ENVIRONMENTAL CHANGE IN DRYLANDS: PAST, PRESENT, FUTURE

EDITED BY: Kathryn Elizabeth Fitzsimmons, Zhuolun Li and Zhiwei Xu
PUBLISHED IN: Frontiers in Earth Science and Frontiers in Environmental Science

frontiers Research Topics

Frontiers eBook Copyright Statement

The copyright in the text of individual articles in this eBook is the property of their respective authors or their respective institutions or funders. The copyright in graphics and images within each article may be subject to copyright of other parties. In both cases this is subject to a license granted to Frontiers.

The compilation of articles constituting this eBook is the property of Frontiers.

Each article within this eBook, and the eBook itself, are published under the most recent version of the Creative Commons CC-BY licence. The version current at the date of publication of this eBook is CC-BY 4.0. If the CC-BY licence is updated, the licence granted by Frontiers is automatically updated to the new version.

When exercising any right under the CC-BY licence, Frontiers must be attributed as the original publisher of the article or eBook, as applicable.

Authors have the responsibility of ensuring that any graphics or other materials which are the property of others may be included in the CC-BY licence, but this should be checked before relying on the CC-BY licence to reproduce those materials. Any copyright notices relating to those materials must be complied with.

Copyright and source acknowledgement notices may not be removed and must be displayed in any copy, derivative work or partial copy which includes the elements in question.

All copyright, and all rights therein, are protected by national and international copyright laws. The above represents a summary only. For further information please read Frontiers' Conditions for Website Use and Copyright Statement, and the applicable CC-BY licence.

ISSN 1664-8714
ISBN 978-2-88976-916-2
DOI 10.3389/978-2-88976-916-2

About Frontiers

Frontiers is more than just an open-access publisher of scholarly articles: it is a pioneering approach to the world of academia, radically improving the way scholarly research is managed. The grand vision of Frontiers is a world where all people have an equal opportunity to seek, share and generate knowledge. Frontiers provides immediate and permanent online open access to all its publications, but this alone is not enough to realize our grand goals.

Frontiers Journal Series

The Frontiers Journal Series is a multi-tier and interdisciplinary set of open-access, online journals, promising a paradigm shift from the current review, selection and dissemination processes in academic publishing. All Frontiers journals are driven by researchers for researchers; therefore, they constitute a service to the scholarly community. At the same time, the Frontiers Journal Series operates on a revolutionary invention, the tiered publishing system, initially addressing specific communities of scholars, and gradually climbing up to broader public understanding, thus serving the interests of the lay society, too.

Dedication to Quality

Each Frontiers article is a landmark of the highest quality, thanks to genuinely collaborative interactions between authors and review editors, who include some of the world's best academicians. Research must be certified by peers before entering a stream of knowledge that may eventually reach the public - and shape society; therefore, Frontiers only applies the most rigorous and unbiased reviews.
Frontiers revolutionizes research publishing by freely delivering the most outstanding research, evaluated with no bias from both the academic and social point of view. By applying the most advanced information technologies, Frontiers is catapulting scholarly publishing into a new generation.

What are Frontiers Research Topics?

Frontiers Research Topics are very popular trademarks of the Frontiers Journals Series: they are collections of at least ten articles, all centered on a particular subject. With their unique mix of varied contributions from Original Research to Review Articles, Frontiers Research Topics unify the most influential researchers, the latest key findings and historical advances in a hot research area! Find out more on how to host your own Frontiers Research Topic or contribute to one as an author by contacting the Frontiers Editorial Office: frontiersin.org/about/contact

ENVIRONMENTAL CHANGE IN DRYLANDS: PAST, PRESENT, FUTURE

Topic Editors:
Kathryn Elizabeth Fitzsimmons, University of Tübingen, Germany
Zhuolun Li, Lanzhou University, China
Zhiwei Xu, Nanjing University, China

Citation: Fitzsimmons, K. E., Li, Z., Xu, Z., eds. (2022). Environmental Change in Drylands: Past, Present, Future. Lausanne: Frontiers Media SA.
doi: 10.3389/978-2-88976-916-2

Table of Contents

05 ***Blowout Morphometrics and Mass Balances***
Thomas R. Baird, Charles S. Bristow, Wanyin Luo, Erji Du, Robert G. Bryant, Thomas M. Mitchell and Pieter Vermeesch

20 ***Provenance of Aeolian Sediments in the Ordos Deserts and Its Implication for Weathering, Sedimentary Processes***
Guoxiang Chen, Zhibao Dong, Chao Li, Weikang Shi, Tianjie Shao, Weige Nan and Junhuai Yang

39 ***Spatial Patterns of Organic and Inorganic Carbon in Lake Qinghai Surficial Sediments and Carbon Burial Estimation***
Xi Chen, Xianqiang Meng, Yinxian Song, Bin Zhang, Zhiwei Wan, Bingqing Zhou and Enlou Zhang

50 ***The Temporal-Spatial Variations and Potential Causes of Dust Events in Xinjiang Basin During 1960–2015***
Lamei Mu, Jing Su, Xinyue Mo, Nan Peng, Ying Xu, Meihua Wang and Jinyan Wang

63 ***A Late Pleistocene Wetland Setting in the Arid Jurf ed Darawish Region in Central Jordan***
Steffen Mischke, Zhongping Lai, Galina Faershtein, Naomi Porat, Matthias Röhl, Paul Braun, Johannes Kalbe and Hanan Ginat

82 ***Moisture Changes in the Northern Xinjiang Basin Over the Past 2400 years as Documented in Pollen Records of Jili Lake***
Yulin Xiao, Lixiong Xiang, Xiaozhong Huang, Keely Mills, Jun Zhang, Xuemei Chen and Yuan Li

94 ***Hydrological Evolution of a Lake Recharged by Groundwater in the Badain Jaran Desert Over the Past 140 years***
Gaolei Jiang, Nai’ang Wang, Xin Mao, Hua Zhao, Linjing Liu, Jianmei Shen, Zhenlong Nie and Zhe Wang

106 ***Rapid Northwestward Extension of the East Asian Summer Monsoon Since the Last Deglaciation: Evidence From the Mollusk Record***
Yajie Dong, Naiqin Wu, Fengjiang Li and Houyuan Lu

117 ***Analysis of Drought and Flood Disasters During 0–1950 AD in the Hexi Corridor, China, Based on Historical Documents***
Xia Tang and Qi Feng

126 ***Holocene Environmental Changes Inferred From an Aeolian-Palaeosol-Lacustrine Profile in the Mu Us Desert, Northern China***
Xiaokang Liu, Ruijie Lu, Zhiyong Ding, Zhiqiang Lyu, Yijing Li and Zhibao Dong

137 ***Establishing a Luminescence-Based Chronostratigraphy for the Last Glacial-Interglacial Cycle of the Loess-Palaeosol Sequence Achajur (Armenia)***
Johanna Lomax, Daniel Wolf, Urs Tilmann Wolpert, Lilit Sahakyan, Hayk Hovakimyan, Dominik Faust and Markus Fuchs

150 ***Late Pleistocene Climate and Dust Source From the Mobarakabad Loess–Paleosol Sequence, Northern Foothills of the Alborz Mountains, Northern Iran***
Amin Ghafarpour, Farhad Khormali, Xianqiang Meng, Hossein Tazikeh and Thomas Stevens

166 ***Advancement of Megadunes and its Implications in the Badain Jaran Sand Sea***
Peng Dong, Aimin Liang and Yali Zhou

174 ***Revisiting Late Pleistocene Loess–Paleosol Sequences in the Azov Sea Region of Russia: Chronostratigraphy and Paleoenvironmental Record***
Jie Chen, Thomas Stevens, Taibao Yang, Mingrui Qiang, Gennady Matishov, Evgeny Konstantinov, Redzhep Kurbanov, Biao Zeng and Peihong Shi

191 ***Holocene Aeolian Activity Recorded by Mountain Paleosols, Gonghe Basin, Northeast Qinghai-Tibet Plateau***
Chunxia Xu, Chongyi E, Yunkun Shi, Jing Zhang, Manping Sun, Zhaokang Zhang and Yongxin Zeng

202 ***Quantitative Reconstruction of Precipitation and Lake Areas During Early to Middle Holocene in Mu Us Desert, North China***
Dawei Li, Yongqiu Wu, Lihua Tan, Yanglei Wen and Tianyang Fu

215 ***The Effects of Wind Regime and Sand Supply on the Coexistence of Barchans and Linear Dunes in China's Qaidam Basin***
Fang Ma, Ping Lü and Min Cao

229 ***Geochemical Composition of Surface Sediments in the Bashang Area, North China and its Environmental Significance***
Linjing Liu, Gaolei Jiang, Xin Mao, Hongmei Zhao, Yongjie Zhao, Yuecong Li, Hua Zhao and Zhiwei Bi

238 ***Variation in Luminescence Characteristics and Paramagnetic Defect Centres in Fine-Grained Quartz From a Loess-Palaeosol Sequence in Tajikistan: Implications for Provenance Studies in Aeolian Environments***
Aditi K. Dave, Alida Timar-Gabor, Giancarlo Scardia, Nosir Safaraliev and Kathryn E. Fitzsimmons

248 ***Dune Field Patterns and Their Control Factors in the Middle Areas of China's Hexi Corridor Desert***
Yan Zhang and Zhengcai Zhang

261 ***Investigating Potential Links Between Fine-Grained Components in Loess and Westerly Airflow: Evidence From East and Central Asia***
Yue Li, Yougui Song, Kathryn E. Fitzsimmons, Aditi K. Dave, Yuming Liu, Xiulan Zong, Huanyu Sun, Huifang Liu and Rustam Orozbaev

frontiers in Earth Science

ORIGINAL RESEARCH
published: 25 May 2021
doi: 10.3389/feart.2021.669440

Blowout Morphometrics and Mass Balances

Thomas R. Baird[1]*, *Charles S. Bristow*[2], *Wanyin Luo*[3], *Erji Du*[3], *Robert G. Bryant*[4], *Thomas M. Mitchell*[1] *and Pieter Vermeesch*[1]

[1]*Department of Earth Sciences, University College, London, United Kingdom,* [2]*Earth and Planetary Sciences, Birkbeck, University of London, London, United Kingdom,* [3]*Northwest Institute of Eco-Environment and Resources, Chinese Academy of Sciences, Lanzhou, China,* [4]*Department of Geography, University of Sheffield, Sheffield, United Kingdom*

OPEN ACCESS

Edited by:
Zhiwei Xu,
Nanjing University, China

Reviewed by:
Zhengyao Liu,
Shaanxi Normal University, China
Yang Bai,
Huizhou University, China
Leví García-Romero,
University of Las Palmas de Gran Canaria, Spain

***Correspondence:**
Thomas R Baird
thomas.baird.16@ucl.ac.uk

Specialty section:
This article was submitted to Environmental Informatics and Remote Sensing,
a section of the journal Frontiers in Earth Science

Received: *18 February 2021*
Accepted: *04 May 2021*
Published: *25 May 2021*

Citation:
Baird TR, Bristow CS, Luo W, Du E, Bryant RG, Mitchell TM and Vermeesch P (2021) Blowout Morphometrics and Mass Balances. Front. Earth Sci. 9:669440. doi: 10.3389/feart.2021.669440

The Gonghe Basin on the Qinghai-Tibet Plateau has a cold, arid climate and has suffered severe land degradation. Climate change as well as anthropogenic activities including overgrazing have resulted in widespread blowout development and the formation of some of Earth's largest blowouts. The blowouts are part of an aeolian dominated landscape that passes from deflation zone to grass covered plain, and then through blowouts of increasing size and complexity to transverse barchanoid dunes that are migrating into the valley of the Yellow River. A combination of structure-from-motion (SfM) optical drone mapping, ground-penetrating radar (GPR) and soil pits are used to investigate blowout scour hollows and depositional lobes. Comparisons of the volumes of sediment removed from the scour hollows with the volumes of sediment deposited within adjacent lobes varies between sites. The lobe volume is invariably less than the volume of the scour hollow. This can, in part, be attributed to aeolian reworking of the lobe, distributing sand further downwind and uplifting of dust. However, much of the difference in volumes between the scour and lobe can be attributed to the measurement technique, particularly where GPR was employed to calculate lobe volumes. The wavelength of the GPR limits its ability to resolve thin layers of sand resulting in an underestimate of the deposited sand at the margins of a lobe where the sand thickness is equal to, or less than, the wavelength of the GPR. For thin sand layers, beneath the resolution of the GPR, soil pits suggest a closer match between the volume of sand eroded from the scour and the volume of the lobe, albeit with large measurement uncertainty. We put forth two hypotheses to explain the spatio-temporal evolution of the blowout dune field. The downwind increase in blowout dune size could either reflect a downwind propagation of aeolian instability; or it could result from an upwind propagation of the instability, which started at the highest points in the landscape and has subsequently migrated in a northwesterly direction, towards lower elevations. Recent optically stimulated luminescence dating appear to support the latter hypothesis.

Keywords: structure from motion, Qinghai-Tibet Plateau, ground-penetrating radar, aeolian geomorphology, geospatial reconstruction, blowouts

1 INTRODUCTION

Blowouts are aeolian features consisting of an erosional depression and an associated downwind depositional lobe or apron. They play a critical role in diagnosing landscape changes, acting as an initial source of sand in reactivating dune fields as well as supplying sediment to downwind features (Barchyn and Hugenholtz, 2013). Blowouts are found in coastal, semi-arid, sandy grassland, and desert landscapes (Hugenholtz and Wolfe, 2006; Hesp and Walker, 2012) and are found across the world, including Europe (van Boxel et al., 1997; Käyhkö, 2007; Gonzlez-Villanueva et al., 2013; Smyth et al., 2013; García-Romero et al., 2019), North America (Fox et al., 2012; Abhar et al., 2015; Garès and Pease, 2015), Africa (Lancaster, 1986), and Asia (Sun et al., 2016; Kang et al., 2017; Luo et al., 2019a). Blowout morphology varies, with scour hollows being classified as saucer, bowl, or trough-shaped and the eroded sediment deposited immediately downwind as either a large lobe or a thinly spread layer of sediment called an apron (Smyth et al., 2020).

Blowouts develop when a stabilised dune's surface is disturbed, exposing the underlying sand to wind erosion. A positive feedback mechanism is then initiated with the reduction in surface roughness facilitating an increase in wind velocity, allowing for further aeolian deflation to occur (Hesp and Walker, 2012). Additional erosion and subsequent destabilisation of the surface, including any anchorage vegetation, then leads to further reductions in surface roughness, and an increasing rate of deflation. Over time, a small area of exposed sand may erode to form a large hollow, supplying sediment to the downwind environment (Luo et al., 2019a). Once initiated, the positive feedback mechanism is self-sustaining and can continue even if conditions are no longer conducive to blowout initialisation (Käyhkö, 2007). Subsequent morphologic development can be restricted by physical characteristics such as the size of the original stabilised dune, a layer of calcrete, or an armoured surface (Hesp, 2002). Seasonal changes, such as the height of the water table, surface moisture levels, or the magnitude and direction of prevailing winds, can also limit blowout development (Hugenholtz and Wolfe, 2006; Davidson-Arnott et al., 2008; Hesp and Walker, 2012). Blowout stabilization requires primary succession of pioneer flora to re-establish vegetation cover, mitigating blowout development by increasing surface roughness and decreasing bed shear stress (Schwarz et al., 2018).

The initial exposure of underlying sediment to wind erosion can occur through natural processes as well as anthropogenic activity. Natural factors which lead to blowout formation include coastal wave erosion, storm events, vegetation cover change, and increased wind speeds (Barchyn and Hugenholtz, 2013; Smyth et al., 2013; Hesp et al., 2016). Biotic factors associated with the grazing pressures from wild fauna, such as rabbits and bison, have also been found to influence blowout formation (van Boxel et al., 1997; Drees and Olff, 2001; Fox et al., 2012). Natural processes may occur seasonally, with reduced efficacy in months with more precipitation or a weaker wind regime (Gonzlez-Villanueva et al., 2013; Abhar et al., 2015). In addition, anthropogenic activities can cause blowout initiation through direct and indirect actions. Off-road vehicle disturbance, pathway trampling, and poor land-use practices can remove anchorage vegetation facilitating blowout genesis (Hesp et al., 2010; Acosta et al., 2013; Houser et al., 2013; Jewell et al., 2014). Pastoral farming poses a dual threat of increased grazing pressures as well as high-intensity trampling involved with moving livestock between paddocks (Blanco et al., 2008; van der Hagen et al., 2020). Indirectly, infrastructure projects and urbanisation may also divert wind patterns, changing the spatiality of sand transport mechanisms and influencing the formation of deflation landforms (García-Romero et al., 2019; Wernette et al., 2020). Abiotic and biotic factors rarely work independently (Corenblit et al., 2015). As such, blowout initiation may be exacerbated by a number of processes at any given study location.

Measuring up to 40 m deep and 1,000 m long (Luo et al., 2019a), the blowouts in Gonghe Basin, Qinghai-Tibet Plateau (QTP) distinguish themselves from previously studied, smaller features in other parts of the world (Hugenholtz and Wolfe, 2006). In comparison to their coastal counterparts, the mega-blowouts of the QTP defy conventional models of blowout development, exceeding a size in which coastal blowouts would tend towards stabilisation (Hugenholtz and Wolfe, 2009). Yet the scarcity of detailed morphological investigations into blowouts on the QTP means that much remains unknown about these mega features. Of particular interest is the difference in volume between the depositional lobes and erosional scour hollows. An inequality in their mass balance would quantify the amount of sediment lost to the surrounding area. This is either as a fine layer extending beyond the depositional lobe or as atmospherically entrained dust.

In this paper we present morphometrics and a mass balance for a range of blowouts on the QTP. An innovative methodology which combines ground-penetrating radar (GPR) surveys, Structure-from-Motion (SfM) modeling from optical drone footage, and geospatial analysis is used to determine a mass balance between the erosional hollow and depositional lobe of three blowouts. A further two compound mega-blowouts are also assessed. Such quantifications are vital to address both the lack of detailed morphometrics for the full range of blowout features and the lack of parametrization in sediment reactivation processes. This research focuses on the Gonghe Basin on the QTP, but the concepts and methodology can be applied elsewhere.

2 STUDY SITE

The Gonghe Basin on the QTP in China is an important region for agriculture, pastoral farming, and power production. The semi-arid steppe is comprised of grassland, farmland, and semi-shifting dunes (Zhang et al., 2003; Yu and Jia, 2014). In recent years, the cold alpine desert region of the Gonghe Basin has experienced severe land degradation from anthropogenic activities and local climatic warming (Wang et al., 2017). Aeolian sand reactivation, predominantly from wind erosion, has substantially eroded cultivated farmlands (Dong et al., 1993; Zhang et al., 2003) and proceeds to threaten downwind infrastructure projects from the risk of sand encroachment. Of

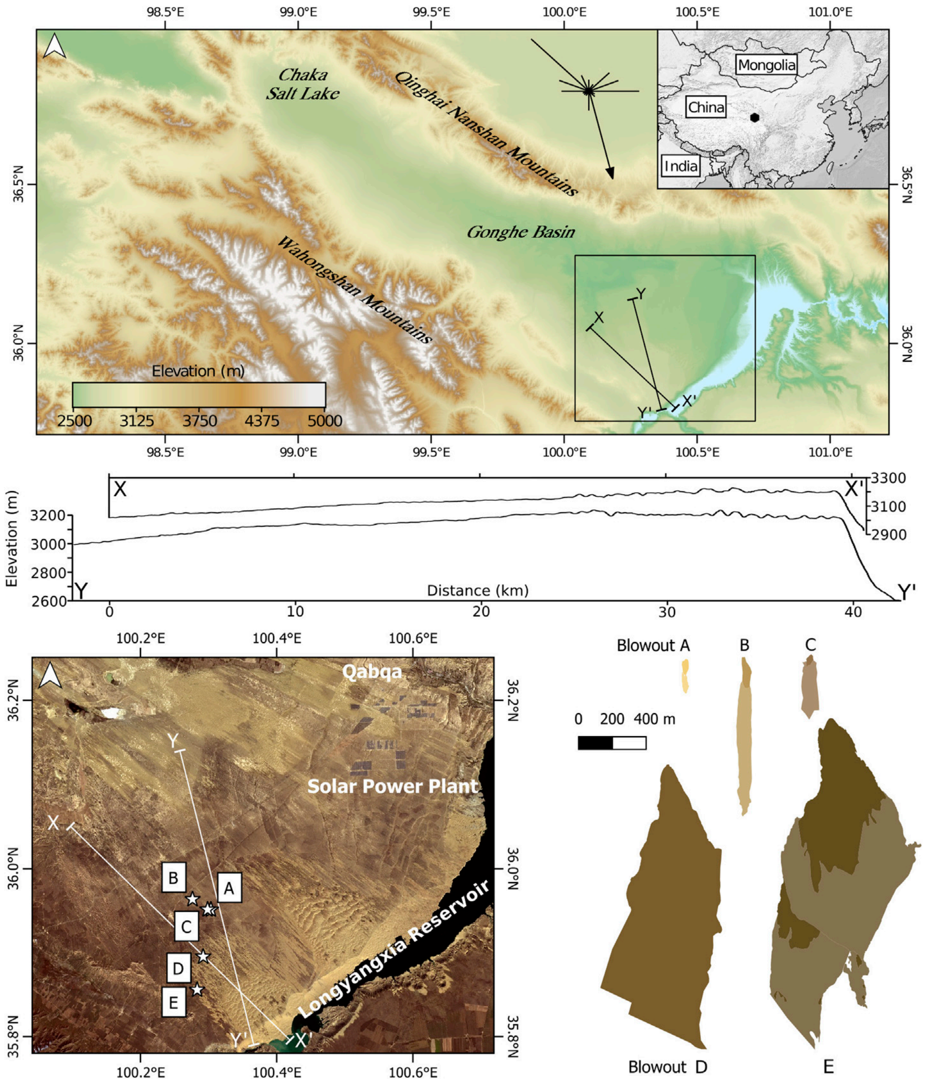

FIGURE 1 | The geographic setting, location, and relative scale of the studied blowout features in Gonghe Basin, Qinghai-Tibet Plateau, China. The presence of upwind blowouts and downwind mobile sand dunes shows clear evidence of dune reactivation. Topographic profile X–X′ is parallel to the direction of net sand transport, which is perpendicular to the orientation of the transverse dune field at the highest point of the plateau. Topographic profile Y–Y′ is parallel to the average wind direction (wind rose from Zhang et al., 2003).

particular note, the Longyangxia Dam and Solar Power Park are located downwind from such eroded farmlands in Gonghe Basin. Attempts have been made to reduce soil degradation by enclosing grasslands with fencing; however, unprotected areas remain overgrazed and the basin continues to be cultivated (Zhang et al., 2003). The threat of further wind erosion is therefore still present. Despite this, the morphology, distributions, and impacts of wind erosion and blowout development in the Gonghe Basin remains a largely understudied phenomena (Luo et al., 2019a).

The mega-blowouts of the QTP are some of the largest on Earth (Luo et al., 2020) and are themselves part of a wider sand flow system from the Gonghe Basin to the Yellow River valley. The Gonghe Basin (**Figure 1**) covers an area of 13,800 km^2 (Liu et al., 2013) and is a northeast to southwest aligned endorheic basin flanked by the Qinghai Nanshan mountains to the north and the Wahongshan Mountains to the south. There is a remarkable coincidence between the orientation of the valley, the mountains on either side, and the winds. Winds blowing along the axis of the basin have caused widespread erosion (Zhang et al., 2003; Luo et al., 2019a). Sand deflated from the valley has accumulated at the downwind end of the valley forming a gently inclined plain that rises around 450 m over 50 km, a gradient of about 1:100, before descending very steeply into the valley of the Yellow River that is around 620 m deep. Across much of the plain the sand-covered slope is vegetated and described as an "alpine meadow" (Yu et al., 2017). The topography includes northeast to southwest elongated ridges of sand that are possibly vegetated linear dunes.

TABLE 1 | Location of the studied blowout features (centroid of the erosional hollow).

Blowout	Latitude (DD)	Longitude (DD)	Hollow depth (m)	Elevation (m)
A	35.9512	100.3034	5.12	3095
B	35.9641	100.2760	8.30	3101
C	35.9514	100.2985	4.81	3096
D	35.8967	100.2897	–	3329
E	35.8600	100.2801	–	3235

The Gonghe Basin experiences average annual temperatures of 2.4—4.1°C and an annual average precipitation of 314.3—414.8 mm (Liu et al., 2013). Approximately 80% of this rainfall occurs between June and September (Yu and Jia, 2014; Yu et al., 2017). Vegetation cover during this wet season increases to a maximum of 20% but remains below 5% during the rest of the year (Wang et al., 2018). The cold alpine desert region in the northeastern QTP is an unusual aeolian environment due to its low temperature and low air pressure (Lu et al., 2005). Sitting at 3750 m above sea level and at the intersection of the westerlies wind belt, Asian, and Indian monsoon, the fragile ecosystem is extremely sensitive to global climate change (Qiang et al., 2016; Luo et al., 2019b). Strong northerly and northwest winds of up to 40 ms^{-1} occur from February to May (Qiang et al., 2013) with average annual speeds ranging from 2.1–2.7 ms^{-1} (Yan and Shi, 2004; Yu and Jia, 2014).

The Longyangxia Power Park is located within the Basin and is comprised of a hydroelectric dam and a solar power farm. It was the largest photovoltaic power station in the world until 2017 (Gautam et al., 2017) and generates an average of 5.94 GW h hydroelectric power and 0.48 GW h photovoltaic power a year (An et al., 2015). Aeolian sediment transport in the basin poses three main threats to the Longyangxia Power Park, including the burial of solar panels, obscuration of solar panels by dust, and the in-filling of the Longyangxia Dam Reservoir.

Five blowouts were surveyed in the Gonghe Basin (**Table 1**), located approximately 50 km south-west of Qabqa, Gonghe County, Qinghai Province (**Figure 1**). Blowouts A, B, and C are located within grazed pastures. Vehicular disturbance and animal activity in the area contribute heavily to blowout initiation. Access to the gated pastures intensifies trampling pressures at egresses and channels vehicles through corridors between paddocks. Additionally, small depressions in the landscape are used by cattle, either for shelter of dust bathing, causing similar fauna pressures on the landscape to those described in Canadian prairies by Fox et al. (2012). Downwind, the size of the blowouts increases until the sand cover increases to form a field of transverse and barchanoid dunes that migrate into the valley of the Yellow River. The larger, more complex blowouts D and E are close to the interface between the blowouts and the active sand dunes and appear to be developed within vegetation-stabilised parabolic dunes. Blowouts B, D, and E were previously studied by Luo et al. (2019a), who looked at their development and growth from 1967 to 2015 with historical satellite imagery, and monitored the expansion of their erosional hollows with annual surveys from 2015 to 2018 as well as drone images (Luo et al., 2020). Here we present updated morphometrics for these blowouts using finer-resolution DEM reconstructions and imaging of the internal structures within depositional lobes. The five blowouts exemplify the range of features found in the Gonghe Basin and are discussed in order of ascending complexity.

3 METHODOLOGY

This study employs an innovative combination of surface and subsurface imaging. SfM optical drone mapping was combined with GPR surveys to provide a high-resolution, non-invasive approach that leaves the fragile landscape undisturbed. We extend the technical work of Luo et al. (2020) to provide geomorphometry and geospatial analysis of the Gonghe Basin using a consistent suit of SfM data. The fieldwork for this study was conducted in July 2018.

Two Phantom four drones were used to survey the full extent of the blowouts. Images were first collected at nadir angles with additional images then captured inside the scour hollows to ensure lateral coverage. A Digital Elevation Model (DEM) and ortho-mosaic were created for each blowout feature using the established SfM approach within Agisoft Photoscan Professional Edition (Scarelli et al., 2016; Lin et al., 2019). Firstly, the optical drone images were aligned and a dense point cloud calculated. Outlying points within the dense clouds were removed manually and a mesh built from the cleaned dataset. This mesh was converted into a DEM and an orthorectified true colour composite texture of the optical drone images was created. Ground control points were recorded using a differential GPS, allowing the SfM data to be precisely georeferenced. Flight details and DEM reconstruction metrics are listed in the Supplementary Material (**Supplementary Table S4**). The three-dimensional models of the study areas were then used to determine the erosional hollow boundary and lobe extent for each blowout feature where it could be discerned. The elevation of the erosional hollow boundary was sampled at 0.2 m intervals and an original surface interpolated using ordinary kriging. This surface was differenced from the DEM to determine the volume of the erosional hollow.

GPR surveys have been successfully conducted to investigate the internal structure of aeolian features (Hugenholtz et al., 2008; Bristow et al., 2010), but relatively few studies have combined the technique with remote sensing to analyse blowout features (Neal and Roberts, 2001; González-Villanueva et al., 2011; Jewell et al., 2017). The low conductivity of sand and large-scale structures contained within aeolian features lend themselves well to GPR surveys (Bristow, 2009) which use the transmission of high-

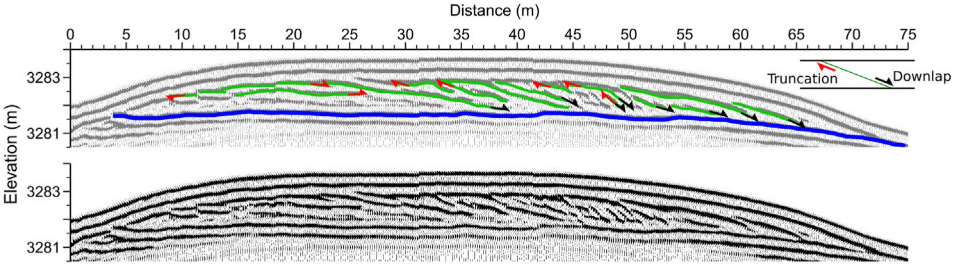

FIGURE 2 | A ground-penetrating radar transect bisecting the depositional lobe of Blowout A from NW to SE. The vertical axis is exaggerated by a factor of 2.5. The extracted base is denoted by the thicker blue line and interpretations of the internal bounding surfaces are shown by thinner green lines. The uninterpreted GPR survey is shown for reference.

frequency electromagnetic fields to image subsurface structures. The GPR profiles within this paper were collected using 200 MHz antennas, a step size of 0.2 m, and an antenna separation of 1 m. CMP surveys indicated a velocity of 0.08 mns^{-1}, that of damp sand. This corresponds well with field observations as short rainfall events occurred frequently throughout the duration of the fieldwork. Similar to the drone mapping, a differential GPS was used to precisely co-locate the GPR survey transects. Topographic corrections were reconstructed from the SfM-determined DEMs. Where a depositional lobe was evident, its depth was traced and extracted at the same resolution as the step size (0.2 m). Ordinary kriging was then used to interpolate a basal surface of the lobe, which was subtracted from the DEM to determine lobe volume.

The uncertainty of the volumetric calculations was determined by the GPR parameters. The signal had a wavelength of 0.4 m, and thus a resolution one quarter that of the wavelength, 0.1 m. The volumetric uncertainty (m^3) was therefore calculated by multiplying the area of the lobe footprint (m^2) by ±0.05 m.

4 GROUND-PENETRATING RADAR IMAGE ANALYSIS

Interpretation of the GPR profiles follows the radar stratigraphy and radar facies methodology (Gawthorpe et al., 1993; Neal and Roberts, 2001; Jol and Bristow, 2003), where reflections on the GPR profile are interpreted as stratigraphic horizons and reflection terminations mark breaks in deposition or truncation due to erosion. The top of the soil horizon at the base of the lobe forms a continuous high-amplitude sub-horizontal reflection at Blowout A (**Figures 2**, **3**).

At Blowout B the basal reflection has a very low-angle dip downwind parallel to the blowout lobe and a relatively steep slope to the west perpendicular to the lobe (**Figures 4**, **5**), because the lobe runs along the flank of a vegetated linear dune. The GPR profile along the axis of the lobe at Blowout A shows inclined reflections that dip in the downwind direction (**Figure 2**). These are interpreted as former positions of the lobe surface and record the extension of the lobe downwind. Changes in the dip of the reflections suggest that the downwind margin of the lobe steepened and then flattened out. The dip of the reflections shows that the downwind margin did not reach the angle of repose. Truncation of the reflections within the lobe indicate periods of erosion, when the lobe was reshaped by changes in the wind. Reflections on the GPR profiles across the lobe are dominated by convex reflections that are interpreted to come from former positions of the lobe surface (**Figure 3**).

The convex morphology mirrors the lobe surface at the time of survey. However, the convex reflections are not symmetrical; some are truncated and others are only preserved on the east side of the lobe. Truncation of the reflections marks erosion, most notably at the upwind end of the lobe where a central scour has eroded into the upwind end of the lobe. Truncation of reflections within the lobe are interpreted as reactivation surfaces where the lobe was reshaped by a change in the wind. The asymmetric development of the lobe with local advance towards the west indicates a change in wind direction.

The presence of downlap and truncation surfaces within the lobes indicates reshaping of the lobe surface due to changes in the wind strength and direction similar to reactivation surfaces identified in sand dunes (Kocurek, 1996) as well as GPR profiles across sand dunes (e.g., Bristow et al., 2005). The abundance of truncation and downlap terminations within the lobe strata indicates extensive reworking of the lobe, with episodes of erosion as well as periods of deposition.

5 MORPHOMETRIC ANALYSIS

5.1 Blowout A

Blowout A (**Figure 6**) exemplifies the standard blowout model with one active erosional hollow and a subsequent clearly defined downwind depositional lobe. The blowout, including the deflation hollow and depositional lobe, measures 170 m in length, 33 m in width, and has a total footprint of 4,015 m^2. The hollow accounts for just under half of the total feature length (79 m). The blowout is oriented to the south-east yet deposited sediment is evident on the south-west edge of the hollow. This is likely caused by a slight deviation from a perfect elongated concave shape, allowing eroded material to be deposited at an angle when exiting the hollow. The maximum width of the hollow is similar to that of the lobe, reaching 33 m and 31 m, respectively.

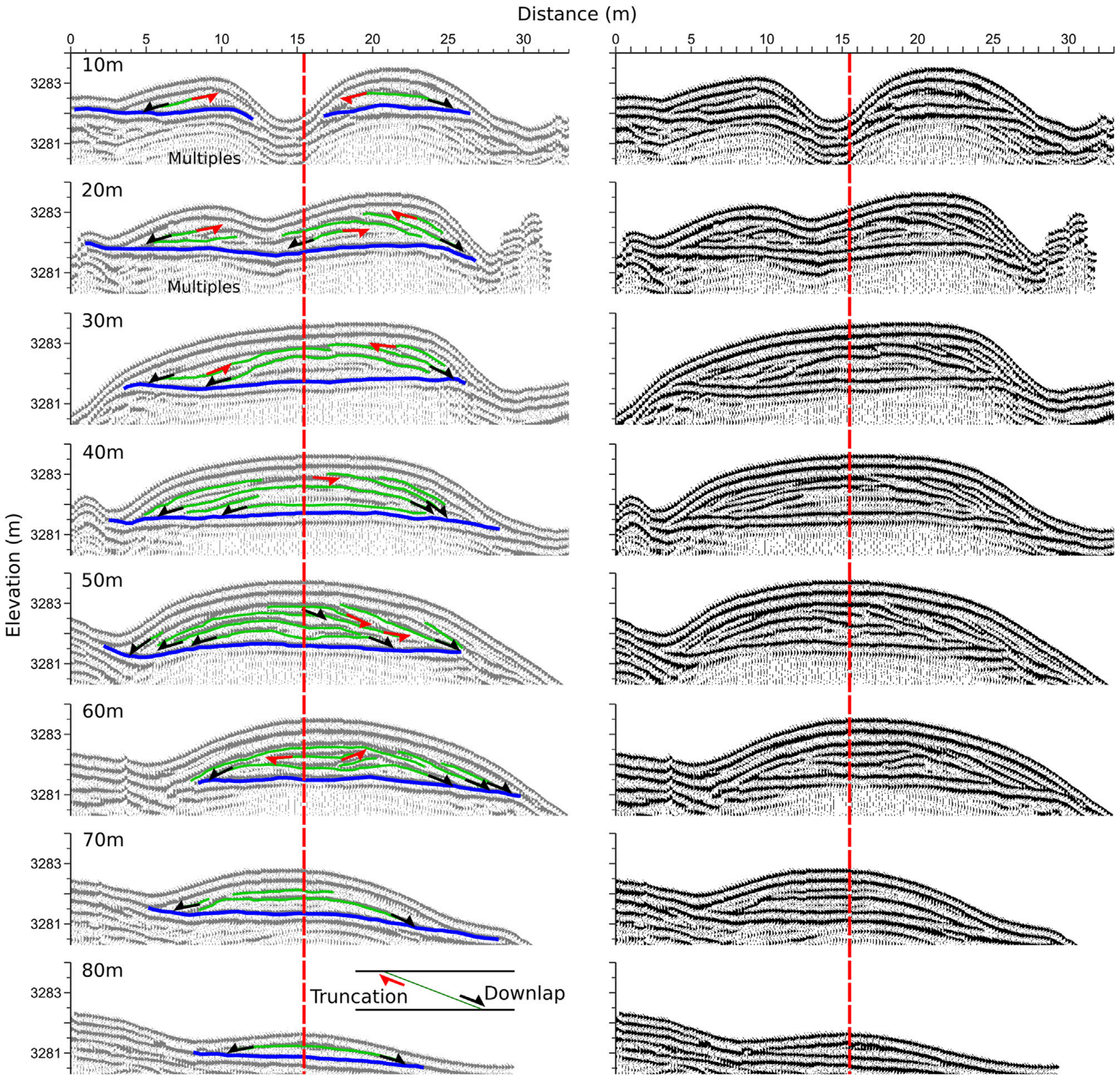

FIGURE 3 | Ground-penetrating radar transect at 10 m intervals perpendicular to the NW-SE bisect. Transects are shown from SE to NW going from left to right. The vertical axis is exaggerated by a factor of 2.5. The extracted base is denoted by the thicker blue line and interpretations of the internal bounding surfaces are shown by thinner green lines. The red dotted line indicates the intersection with the NW to SE bisect (**Figure 3**). The uninterpreted GPR surveys are shown for reference.

A GPR survey was conducted to determine the volume of the depositional lobe. A single longitudinal transect bisected the depositional lobe from NW to SE (**Figure 2**). Eight transects were then made from SW to NE at 10 m intervals perpendicular to the longitudinal transect (**Figure 3**). The continuous lines at the top of the transects in **Figures 2**, **3** denote the direct signals between the transmitter and the receiver. The first signal is the airwave, the fastest direct signal that travels from the transmitter to the receiver directly through the air at the speed of light. The second signal represents the groundwave, a signal that travels directly to the receiver through the near-surface without reflecting off of any soil horizons at a lower velocity. These direct arrivals effectively obscure the top 0.5 m of strata, limiting the use of the GPR to detect the thickness of layers of sand where the thickness is less than 0.5 m. The NW-SE bisect shows inclined reflections dipping in the downwind direction as well as a reflection from the base of the lobe (**Figure 2**). The continuous sub-horizontal reflection at the base of the lobe marks the contact between the lobe and the underlying soil horizon and is coloured blue on **Figure 2**. Inclined reflections within the lobe

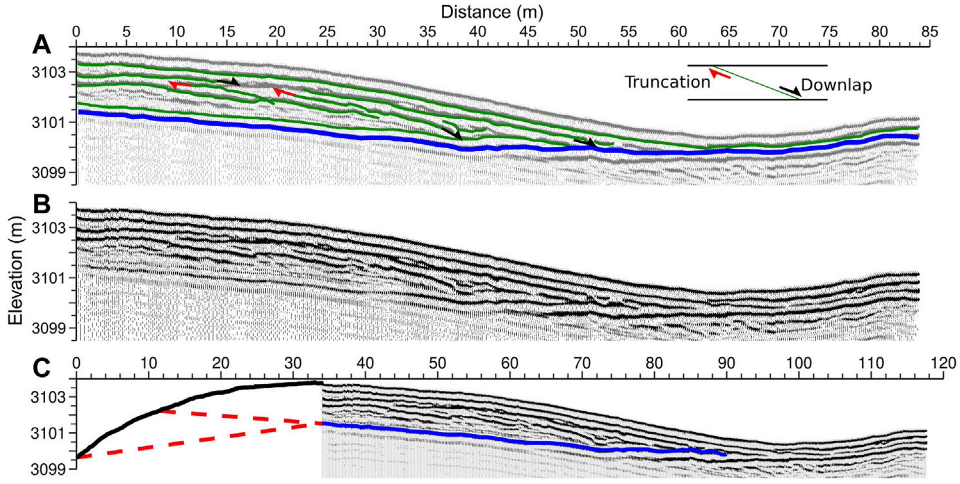

FIGURE 4 | (**A**) Longitudinal GPR transects of the depositional lobe of Blowout B. The vertical axis is exaggerated by a factor of 2.5. The extracted base is denoted by the thicker blue line and interpretations of the internal bounding surfaces are shown by thinner green lines. (**B**) The uninterpreted GPR survey is shown for reference. (**C**) The extrapolations used to calculate volume estimates for the lobe of Blowout B. The interpreted base of the lobe is shown in the solid blue line. The solid black line shows the DEM surface. A linear model extrapolating the first 10 m of the basal surface is shown in the higher red dashed line. The lower red dashed line shows a linear model between the start of the lobe and the identified base.

increase in dip downwind until it reaches an angle of around 30 degrees and then decreases again (**Figure 2**) The downwind dipping reflections are evidence of progradation, with high-angle reflections indicating the angle of repose and development of a slipface on the downwind end of the lobe. Truncation of the inclined reflections at the upwind end of the lobe indicates erosion and is attributed to aeolian reworking of the lobe deposits. Bounding surfaces between sets of inclined reflections are attributed to aeolian reworking of the lobe, possibly during storm events. In conjunction with the sub-horizontal reflections in the perpendicular transects, the lobe shows that tabular cross-strata have formed at the leeward slope. The GPR profiles across the lobe show a central scour at the upwind end that is eroding through the lobe deposits and the underlying soil, truncating the basal blue reflection (**Figure 2**). Reflections within the cross-section profiles show convex-upwards reflections as well as low-angle inclined reflections (**Figure 3**). The convex-upward reflections are attributed to the dome-like morphology of the lobe recording aggradation on the lobe surface. This is most likely wind ripple laminae that are beneath the resolution of the GPR. The low-angle inclined reflections overlay bounding surfaces and are interpreted to indicate changes in the accretion direction of the lobe, with the lobe building out towards the east, most likely a response to changes in wind direction.

The DEM indicates that the scour hollow is 3 m deeper than the lobe is thick. However, the lobe extends over a larger area, 2,133 m^2 compared to 1,882 m^2 of the hollow. The erosional hollow has a volume of 5,806 m^3 and the lobe has a volume of 2,230 ± 110 m^3. The volumes calculated for the depositional lobe appear to account for only 38% of the material eroded from the hollow, suggesting that a significant amount of sediment (3,570 m^3) is lost to the surrounding area, either as a fine layer of sediment or entrained in the atmosphere as dust. It is likely that most of this volume can be attributed to downwind distribution of sand and dispersion into the surrounding grassland in layers that are too thin to be imaged using a 200 MHz GPR system.

5.2 Blowout B

Blowout B (**Figure 7**) differs from Blowout A (**Figure 6**) in that it is eroding into the flank of an elongated ridge, possibly a vegetated linear dune. The blowout lobe is not readily apparent in the DEM or in the orthorectified true colour composite. Instead, an apron of sediment is evident, measuring 633 m in length and 73 m in width at its maximum.

A partially broken barbed wire fence precluded the first 30 m of a bisecting GPR transect from being surveyed. Despite this, a 84 m NW-SE bisect was completed (**Figure 4**). Five SW-NE transects were made perpendicular to the bisect at approximately 20 m intervals (**Figure 5**). In contrast to Blowout A, the transects show a much more complex history. Low-angle reflections and truncated erosion surfaces indicate several periods of reconstruction and erosion. Reworking of the lobe sediment has produced clear scour surfaces and saddle morphology is evident. The increased internal complexity of the lobe could be indicative of maturity, or result from the slope exposing the lobe to a more complex wind regime.

When extracting the basal surface from the GPR transects, the resulting lobe depth is surprisingly symmetrical despite the topographic gradient. Analysis based solely on the DEM without knowledge of the subsurface would therefore overestimated the plume depth. Interpolating the basal surface covered by GPR surveys produces a volume estimate of 6,310 ± 260 m^3. To estimate the total lobe volume, the first 10 m of the baseline was extrapolated to cover the area underneath the barbed wire. This produced an estimated volume of 8,700 m^3. The

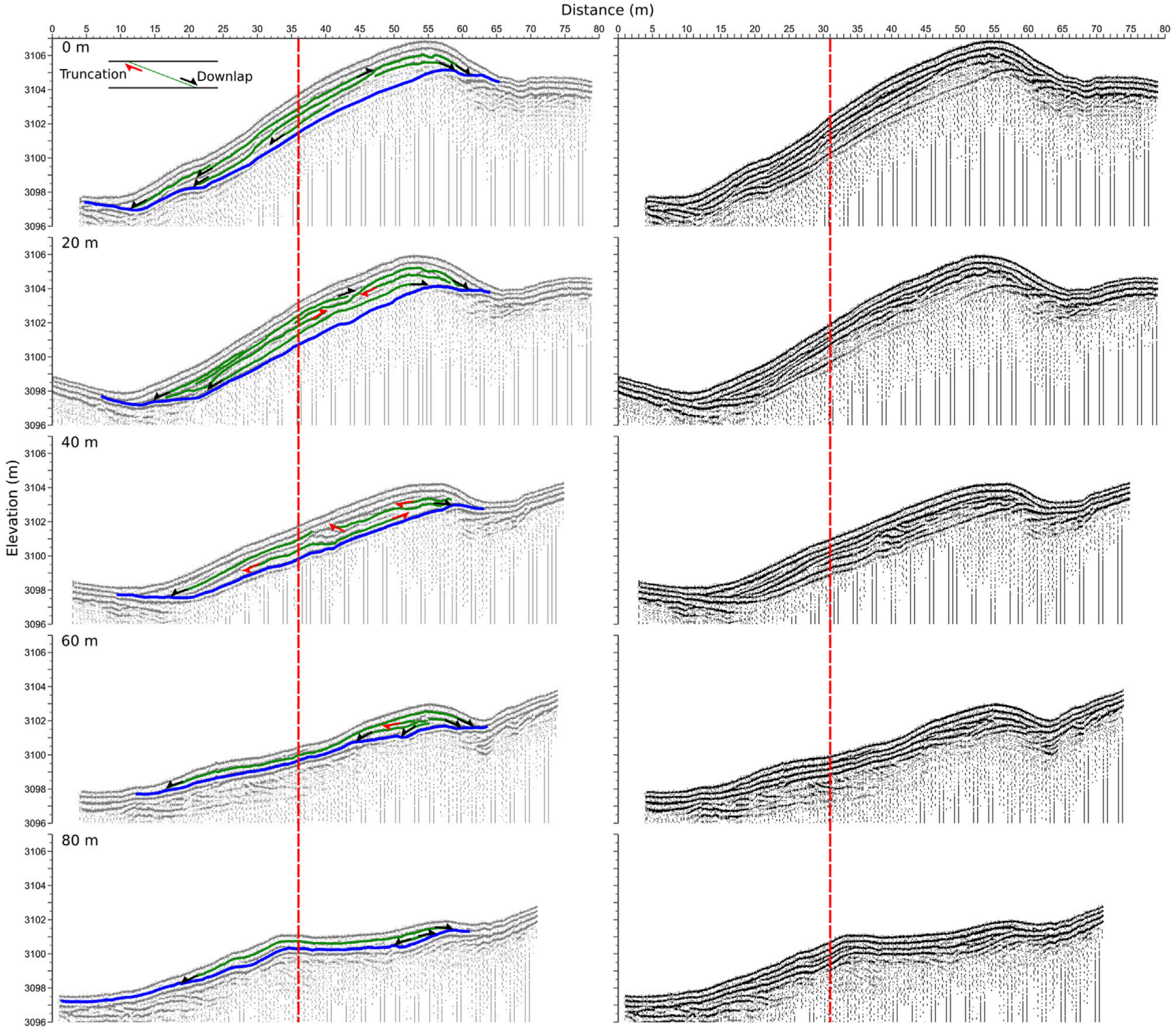

FIGURE 5 | Transverse GPR transects across the lobe of Blowout B at 20 m intervals perpendicular to the NW to SE bisect. The vertical axis is exaggerated by a factor of 2.5. The extracted base is denoted by the thicker blue line and interpretations of the internal bounding surfaces are shown by thinner green lines. The red dotted line indicates the intersection with the NW to SE bisect (**Figure 6**). The uninterpreted GPR surveys are shown for reference.

maximum volume, calculated by extending the base of the lobe to the identified hollow-lobe transition area, is 9,920 m^3. The lobe therefore accounts for roughly half the volume of the hollow (19,900 ± 1,900 m^3). The remaining 50–56% of the eroded material may exist as a thin layer extending downwind which is too thin for the GPR to image. Alternatively, the "missing" sand may have escaped the depositional lobe by saltation towards and into the Longyangxia reservoir, or could have been released into the atmosphere as a fine dust.

5.3 Blowout C

The apron of Blowout C (**Figure 8**) is easy to discern in the orthorectified true colour composite, but is harder to delimit in the DEM due to a topographic incline. The apron is more than twice the maximum width of the hollow (58 m and 28 m, respectively), and three times that of its length (257 m and 87 m, respectively). Additionally, the hollow has a footprint only a tenth that of the apron (1,270 m^2 and 13,000 m^2, respectively). Five GPR surveys were conducted across the depositional plume, comprised of two 150 m longitudinal transects and three 50 m latitudinal transects. However, the apron was too thin to be resolved in the GPR surveys. Instead, 88 small pits were dug into the surface at random locations to measure the soil horizon depth (**Supplementary Table S3**). The depth of sand at each pit was measured in centimetres using an extending steel ruler. Pit locations were recorded using DGPS. These soil horizon depths underwent ordinary kriging to interpolate a basal surface (**Figure 8D**). The maximum depth

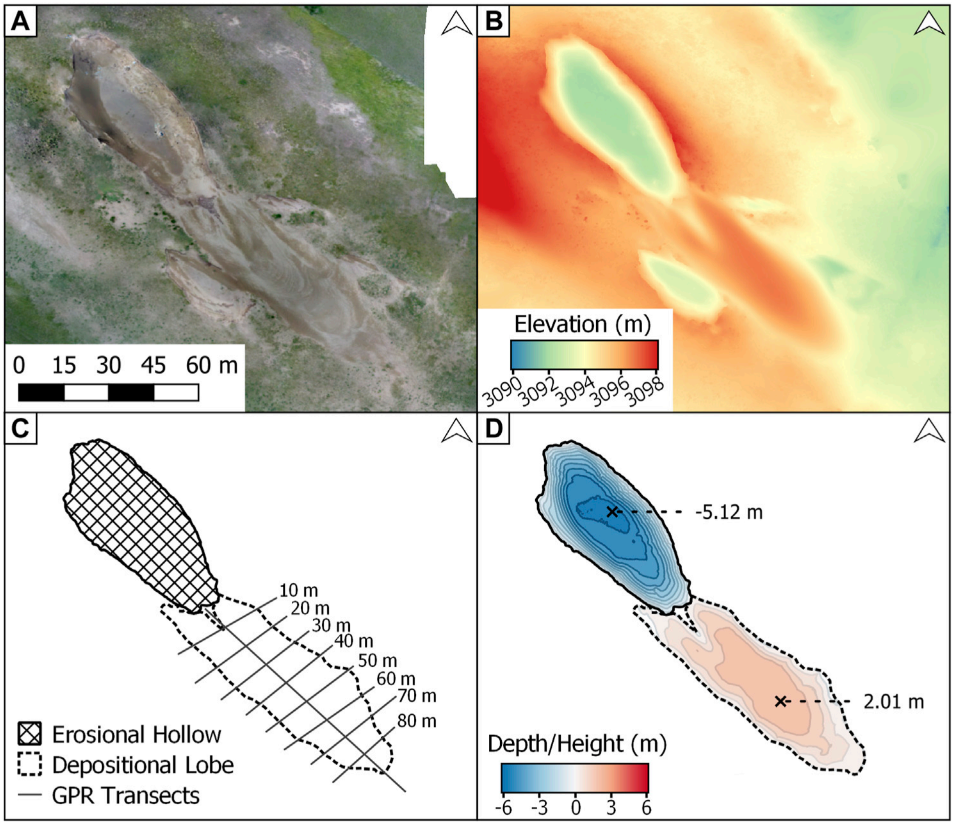

FIGURE 6 | Blowout A viewed as (**A**) a true color composite; (**B**) a digital elevation model; (**C**) a schematic model with ground-penetrating radar transects; and (**D**) interpolated lobe height and hollow depth (contours at 0.5 m spacing). In the true color composite, the light and darker tones on the lobe surface denote moisture content of the sand, showing the former shape and extent of the lobe. Coordinates of the top-left corner of the bounding box: 35.95159N, 100.30301E; bottom-right corner: 35.95015N, 100.30458E.

of the horizon was measured at 0.46 m, and its volume was calculated at 2,290 m^3, albeit with a substantial kriging interpolation uncertainty of 75%. This volume of the depositional lobe is only 980 m^3 less than the erosional hollow's volume (3,270 ± 64 m^3). The relatively small difference between the volume of the topsoil and the hollow may be indicative of lobe deflation with sand distributed into the surrounding grassland and lost as dust. However it would be premature to apply this conclusion to the other blowouts given the large uncertainty for the volume estimate of the soil horizon.

5.4 Blowout D

Blowout D shows a complex mega-blowout feature (**Figure 9**). The boundary between hollow and lobe is hard to discern with a shallow gradient existing throughout its 1,220 m length and 470 m span. The feature covers an area of 446,000 m^2, an order of magnitude larger than Blowouts A–C. With this larger magnitude comes increasing complexity. Multiple secondary hollows are evident on the south-eastern edge of the feature. Some of these hollows are in the process of merging into each other while also simultaneously eroding the side of the primary hollow perpendicular to the direction of the prevailing wind. Juxtaposed to the simplistic model of Blowout A, which has one erosional hollow and one depositional lobe/apron, Blowout D is simultaneously eroding at multiple points along its boundary. Smaller erosional hollows appear on the edge of the larger primary hollow, feeding sediment into the larger system.

The sides of the erosional hollow are oversteepened (**Figure 9E**), with sediment along the scour sides approaching or sitting at the angle of repose. Resistant soils and plant roots flanking the scour sides are maintaining these slopes.

The topography within the hollow also differs from that of Blowouts A–C, with areas of sediment transport evident inside the erosional part of the feature. The mega-blowout appears to facilitate a wind regime that is reworking the sediment below the level of the hollow edge. Further downwind, ripple and proto-dune movement are evident. The hollow-lobe transition is elongated, with a gradual incline over which sand is transported out of the hollow. This complex system is not witnessed in the smaller-scale blowouts, where eroded sediment is immediately transported and deposited at the downwind margin of the hollow.

5.5 Blowout E

Blowout E (**Figure 10**) is another complex mega-blowout. A primary erosional hollow 180,110 m^2 in size has deposited sediment over an

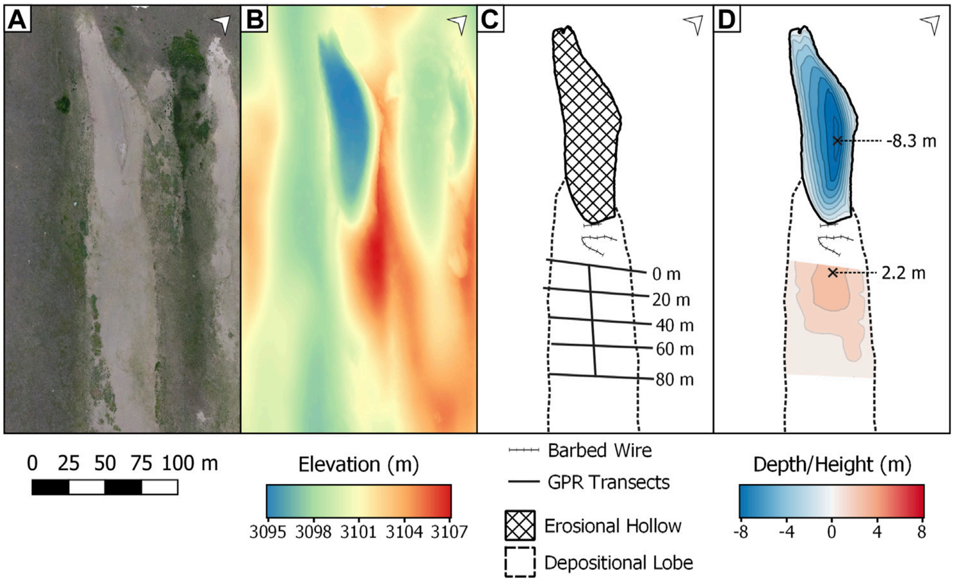

FIGURE 7 | Blowout B viewed as (**A**) a true color composite; (**B**) a digital elevation model; (**C**) a schematic model with ground-penetrating radar transects; and (**D**) interpolated lobe height and hollow depth (contours at 1 m spacing). Note the depositional lobe situated on an incline. Coordinates of the top-left corner of the bounding box: 35.96427N, 100.27499E; bottom-right corner: 35.96310N, 100.27839E.

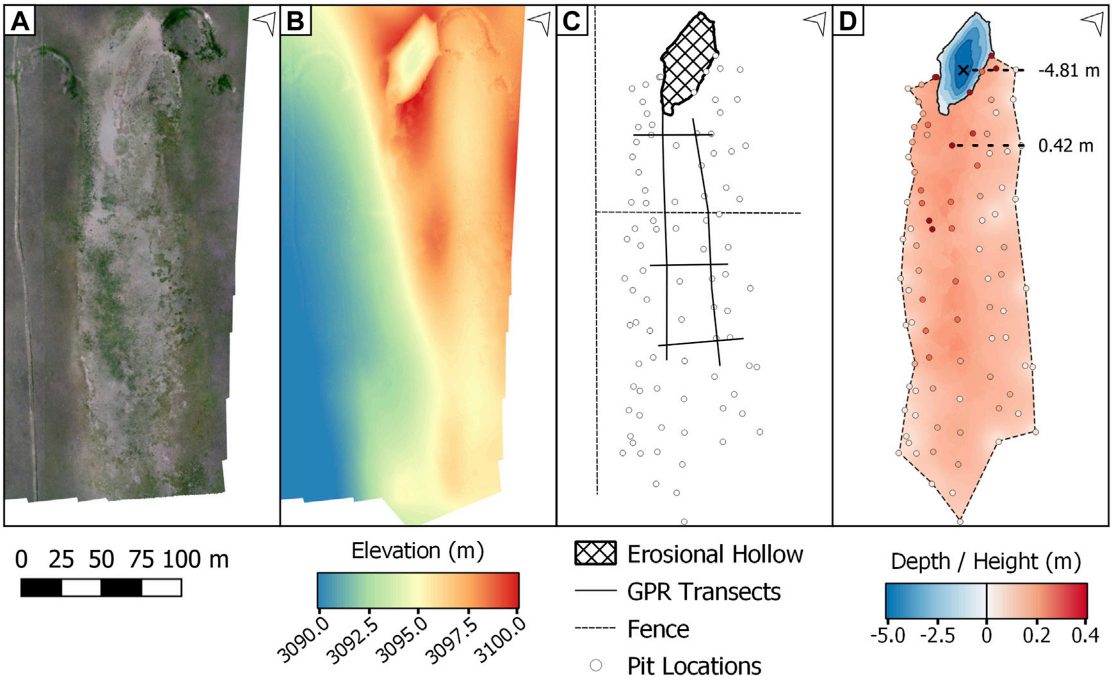

FIGURE 8 | Blowout C viewed as (**A**) a true color composite; (**B**) a digital elevation model; and (**C**) a schematic model with ground-penetrating radar transects; and (**D**) interpolated hollow depth and apron soil thickness with pit sample locations. Coordinates of the top-left corner of the bounding box: 35.95123N, 100.29763E; bottom-right corner: 35.94985N, 100.30134E.

incline to the east while simultaneously infilling historic and vegetated hollows to the south. This primary deposit covers an area of 238,000 m^2. Multiple smaller hollows are evident further south of the primary deposit, and a secondary apron is present. Vegetation is evident both within the second largest hollow and around the edges of the secondary apron.

Two possible interpretations of the mega-blowout's history of sediment reactivation may be drawn from our analysis. Firstly,

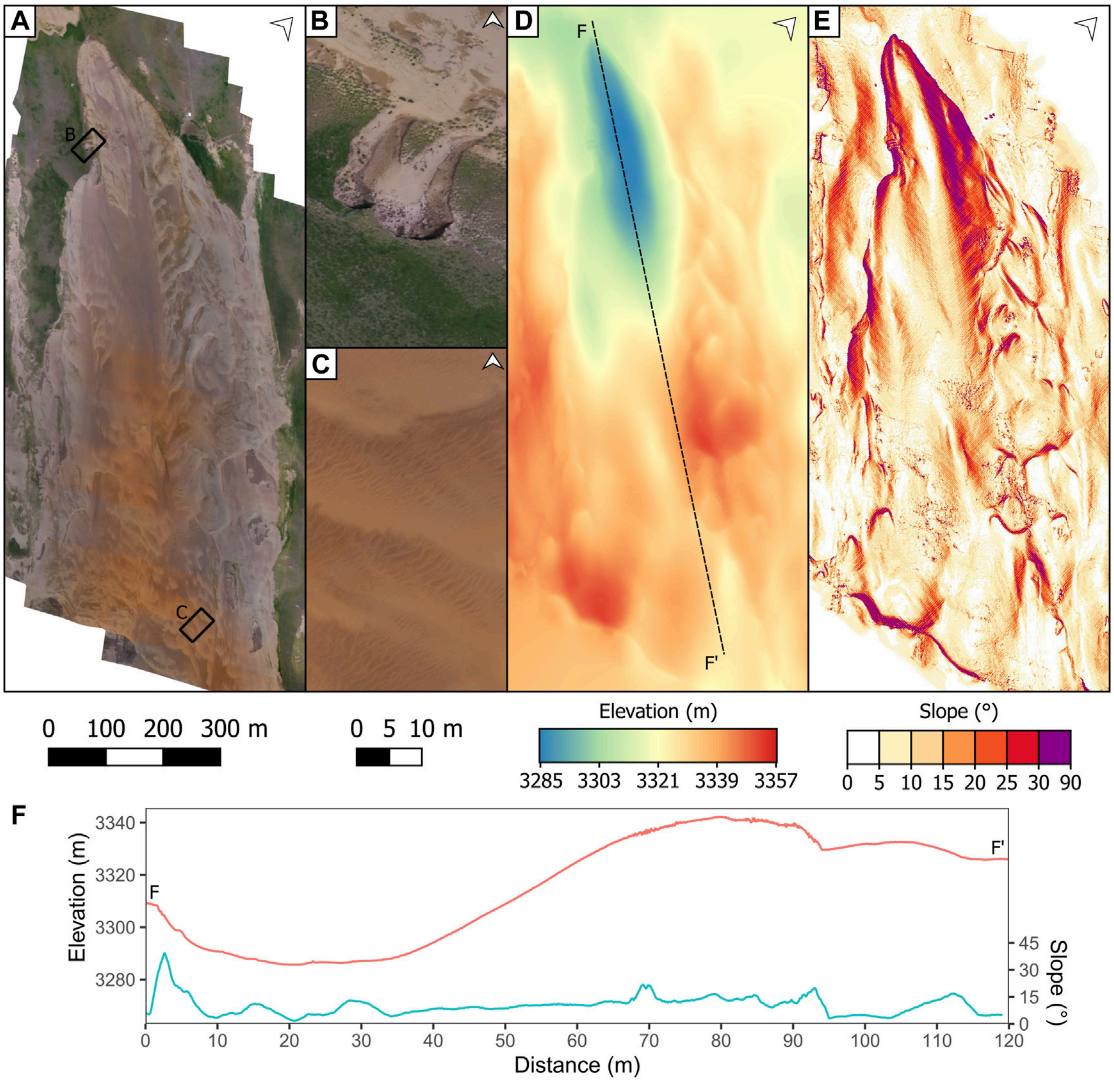

FIGURE 9 | (**A**) A complex mega-blowout with (**B**) multiple merging erosional hollows and (**C**) evidence of active sediment transport. The (**D**) digital elevation model and (**E**) slope map show a (**F**) low gradient incline in the hollow-lobe transition (vertical exaggeration of 2.5). Coordinates of the top-left corner of the bounding box: 35.89694N, 100.28670E; bottom-right corner: 35.89114N, 100.30006E.

the secondary erosional hollow could be mature and inactive, slowly becoming infilled by sediment produced in the active erosional hollow to the north-west. Secondly, the lobe could be in active transport through a larger hollow. The similar depths between the primary and secondary erosional hollows suggest the feature may be a single large hollow. A limit, such as a perched water table, may have been reached with sediment now passing through the feature in a similar way to Blowout D.

6 DISCUSSION

Barchyn and Hugenholtz (2013) suggest that the erosion in a blowout will equal the volume of sediment in the depositional apron due to the conservation of mass. However, we are not aware of any other studies of blowout deflation hollow/depositional lobe volumes with which to compare our results. As a consequence, we can only speculate that the differences observed in this study are not unique but should apply more widely. Barchyn and Hugenholtz (2013) assume that the apron is 100% efficient in trapping wind-blown sand. By analogy with sand dunes it has been shown that dunes with slipfaces are not very efficient sand traps, trapping only a small percentage of the saltation flux, and dunes without slipfaces even less so (Bristow and Lancaster, 2004). The clear implication is that sand derived from deflation hollows can accumulate locally within depositional lobes, but equally it will be distributed more widely downwind. This combination of local sand accumulation and downwind reworking can account for most of the variations in morphology observed in the blowout lobes.

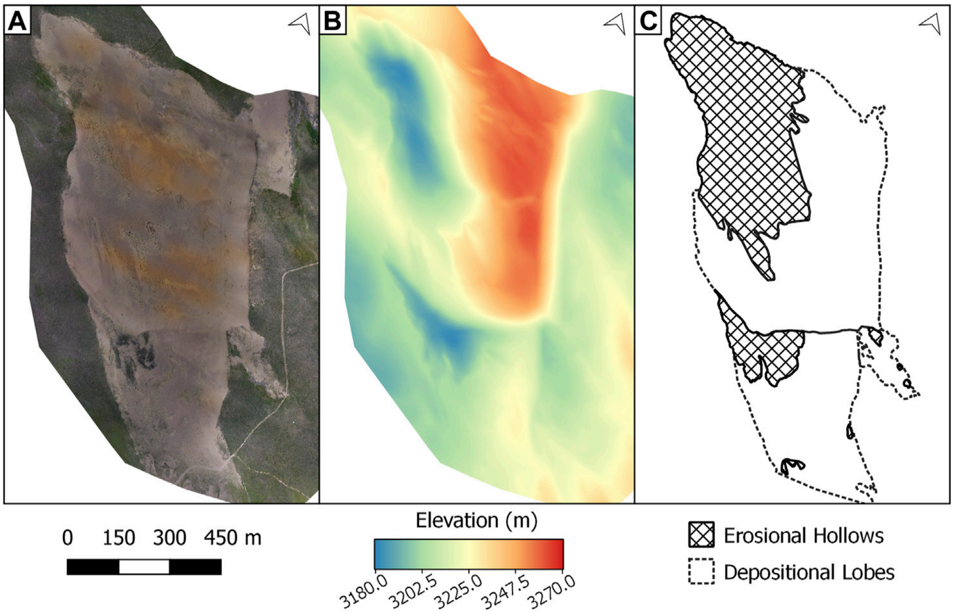

FIGURE 10 | A complex mega-blowout viewed as (**A**) a true color composite; (**B**) a digital elevation model derived from Structure-from-Motion modeling; and (**C**) a schematic model demarcating erosional hollows and depositional lobes. Note infilling of downwind erosional hollows and large slope gradients. Coordinates of the top-left corner of the bounding box: 35.8610N, 100.2761E; bottom-right corner: 35.8516N, 100.2913E.

The other significant influence is the wind direction, which can affect the direction of sediment transport and resulting lobe development.

Truncation of reflections on the GPR profiles provide evidence for erosion and indicates breaks in deposition, as well as reworking of the sand on the surface of the blowout lobe. Changes in the accretion direction of reflections indicates changes in the lobe morphology that is attributed to changes in wind direction. GPR also images the base of the lobes and this has been used to calculate the volume of sediment within two lobes. While the results of the GPR survey in imaging the lobe strata and the base of the lobe are positive, the calculation of lobe volumes using GPR was limited by the inability of the 200 MHz GPR system to image sand layers less than 0.5 m thickness, the section that is covered by arrival of the direct air and ground waves. Higher-frequency GPR systems e.g. 500 MHz antennas with a shorter wavelength would have helped in this respect. The use of soil pits to determine lobe thickness and volume shows a much closer agreement between the volume of the scour hollow and the volume of the depositional lobe at location C. Nonetheless, the kriging interpolation of these point measurements is associated with large statistical uncertainty (**Table 2**).

It would be advantageous for future work to further constrain depositional volumes. There exists, however, two difficulties in this. Firstly, an invasive field campaign risks disturbing the fragile environment and contributing to further land degradation. Secondly, the attribution of widely spread fine material to a particular blowout becomes problematic further downwind. Delimiting the input of upwind features to the amount of sediment in the topsoil surrounding a blowout would require a comprehensive monitoring campaign and/or foreknowledge of sediment emissivity. We have shown that a large amount of material is lost to the surrounding downwind environment, and thus features further downwind are unlikely to be acting in a closed system. The proximity of other blowouts and their level of activity would therefore need to be carefully considered when constraining depositional volumes further. This issue notwithstanding, repeated drone surveys could be conducted to determine lobe accretion and scour deflation through time. While sandy environments pose challenges to photogrammetric methods, studies quantifying sand deposition on beaches using UAV surveys have produced DEMs with centimetre and sub-centimetre vertical accuracies (Jayson-Quashigah et al., 2019; Casella et al., 2020, 2016). Similar applications would be useful to determine volumetric changes through time. However, these studies would be limited to quantifications of topographic changes as sub-surface imaging is still required to identify the lobe base.

TABLE 2 | Volume deficit measurement of the three small blowouts.

Blowout	A	B	C
Volume of hollow (m^3)	5806±100	19900±1900	3270±64
Volume of depositional lobe (m^3)	2230±110	8700–9920	570–(4000)
Volume deficit (%)	62±2	53±6	30 +52/−30

6.1 Elevation and Scour Depth

The scour depth of blowouts in the coastal zone is limited by the presence of the water table and associated capillary zone that restricts sand entrainment, as well as the presence of coarse-grained beach deposits beneath coastal dunes. As a consequence the scour depth in coastal dunes is restricted because wind cannot deflate sand beneath the water table, which is close to mean sea level at the coast, nor can it entrain coarse-grained beach deposits that are commonly raised slightly above the high tide line in a backshore setting. In contrast, the blowouts of the QTP lack a shallow water table and the deflation depth is limited instead by the thickness of aeolian sand and depth to underlying strata. In the Gonghe Basin the sand thickness and blowout dimensions appear to increase in the downwind direction until they join the active sand dunes. We speculate that the increased sand thickness away from the deflation zone in the Gonghe Basin is a legacy of a downwind decrease in transport capacity as wind flow expanded away from the topographic confines of the basin. Drought conditions during the Little Ice Age are believed to have resulted in the reactivation of the blowouts (Luo et al., 2019b).

6.2 Upwind Propagation of Instability and Blowouts

The upwind decrease in blowout dimensions, away from the active dunes, and towards the vegetated plain suggests an upwind propagation of the blowout system, propagating upwind, away from the active dunes. This pattern can be viewed as a systematic downwind propagation of blowout morphology, from small blowouts (localities A, B, and C, this study), to larger mega-blowouts downwind (localities D and E, this study) and sites described by Luo et al. (2019a) Luo et al. (2019b). This pattern suggests a downwind propagation of instability with blowout dimensions increasing downwind. However, an alternative hypothesis is that the sizes of the blowouts relate to their age. In which case the larger blowouts which are downwind started earlier than the smaller blowouts upwind. This explanation suggests the opposite, that the instability started at the downwind end and propagated upwind even though individual blowouts tend to propagate downwind. This hypothesis appears to be supported by OSL ages (Luo et al., 2019a; Luo et al., 2019b). One possible reason for what appears at first to be a counter-intuitive explanation for the blowout pattern is that the downwind areas which are at a higher elevation (**Figure 1**) were closer to the threshold for blowout development and it is only as anthropogenic impacts have increased in the grazed pastures at lower elevations that blowouts have developed upwind, suggesting a bio-geomorphic control on the wider pattern of climatically driven blowout development.

7 CONCLUSION

High resolution topographic surveys of blowouts including erosional hollows and adjacent depositional lobes were collected using SfM optical drone mapping and DGPS to create digital elevation models (DEMs) of the blowouts. In addition, ground-penetrating radar (GPR) profiles were collected along and across the depositional lobes at three of the smaller and less complex blowouts. Volumes of the erosional hollows and their adjacent depositional lobes are calculated from the DEMs, GPR data, and soil pits. The results show that although the areas of the hollows and lobes are similar, the volume of the lobes is much less than the volume of the adjacent hollows with the lobe volume amounting to around 50% of the hollow. Part of the difference in volumes can be attributed to the method used to calculate the lobe volumes. The wavelength of the GPR prevents measurement of sand layers that are thinner than the section covered by the first arrivals of the direct groundwaves and airwaves. Despite this, the results indicate that blowout lobes are not very efficient sand traps, capturing only 50% of the sand eroded from the hollow. The remaining 50% is probably distributed further downwind, as a thin sand layer captured by local vegetation, with an undetermined fraction transported further downwind as saltating sand or a "dust" plume during storm events.

DATA AVAILABILITY STATEMENT

The original contributions presented in the study are included in the article/Supplementary Material, further inquiries can be directed to the corresponding author.

AUTHOR CONTRIBUTIONS

Drone footage collected by RB and TM with support from TB, WL, and PV. GIS field data collection from PV, TB, and WL. GPR surveys conducted by ED and CB, with additional support from TB. GPR interpretations by CB. Models created by TB and RB. Morphometrics and data analysis from TB. Manuscript written by TB, with substantial contributions from CB and edits from PV.

FUNDING

TB is supported by the Natural Environment Research Council (NERC) through Grant No. NE/L002485/1. This reseach was funded by Grant No. 41771015 of the Chinese National Natural Science Foundation, awarded to WL, and a Thesiger Oman fellowship (THES 02/18) of the Royal Geographical Society, awarded to PV.

ACKNOWLEDGMENTS

We would like to thank Mark Bateman, Mei Shao, Songnian Luo, Wanli Luo, and Binhua Xu for field assistance, and the farmers of Gonghe for granting us access to their land. We would also like to thank LG-R and the anonymous reviewers for their critical and constructive comments.

SUPPLEMENTARY MATERIAL

The Supplementary Material for this article can be found online at: https://www.frontiersin.org/articles/10.3389/feart.2021.669440/full#supplementary-material

REFERENCES

Abhar, K. C., Walker, I. J., Hesp, P. A., and Gares, P. A. (2015). Spatial-temporal Evolution of Aeolian Blowout Dunes at Cape Cod. *Geomorphology* 236, 148–162. doi:10.1016/j.geomorph.2015.02.015 Available at: https://linkinghub.elsevier.com/retrieve/pii/S0169555X15000987.

Acosta, A. T. R., Jucker, T., Prisco, I., and Santoro, R. (2013). Passive Recovery of Mediterranean Coastal Dunes Following Limitations to Human Trampling, 187–198. doi:10.1007/978-3-642-33445-0_12 Available at: http://link.springer.com/10.1007/978-3-642-33445-0_12.

An, Y., Fang, W., Ming, B., and Huang, Q. (2015). Theories and Methodology of Complementary Hydro/photovoltaic Operation: Applications to Short-Term Scheduling. *J. Renew. Sustain. Energ.* 7 (6). doi:10.1063/1.4939056

Barchyn, T. E., and Hugenholtz, C. H. (2013). Dune Field Reactivation from Blowouts: Sevier Desert, UT, USA. *Aeolian Res.* 11, 75–84. doi:10.1016/j.aeolia.2013.08.003

Blanco, P. D., Rostagno, C. M., del Valle, H. F., Beeskow, A. M., and Wiegand, T. (2008). Grazing Impacts in Vegetated Dune Fields: Predictions from Spatial Pattern Analysis. *Rangeland Ecol. Manage.* 61 (2), 194–203. doi:10.2111/06-063.1 Available at: https://linkinghub.elsevier.com/retrieve/pii/S1550742408500194.

Bristow, C., Augustinus, P., Wallis, I., Jol, H., and Rhodes, E. (2010). Investigation of the Age and Migration of Reversing Dunes in Antarctica Using GPR and OSL, with Implications for GPR on Mars. *Earth Planet. Sci. Lett.* 289 (1–2), 30–42. doi:10.1016/j.epsl.2009.10.026

Bristow, C. S. (2009). *'Ground Penetrating Radar in Aeolian Dune Sands',* Ground Penetrating Radar: Theory and Applications, 273–297.

Bristow, C. S., Lancaster, N., and Duller, G. A. T. (2005). Combining Ground Penetrating Radar Surveys and Optical Dating to Determine Dune Migration in Namibia. *J. Geol. Soc.* 162 (2), 315–321. doi:10.1144/0016-764903-120

Bristow, C. S., and Lancaster, N. (2004). Movement of a Small Slipfaceless Dome Dune in the Namib Sand Sea, Namibia. *Geomorphology* 59 (1-4), 189–196. doi:10.1016/j.geomorph.2003.09.015

Casella, E., Drechsel, J., Winter, C., Benninghoff, M., and Rovere, A. (2020). Accuracy of Sand Beach Topography Surveying by Drones and Photogrammetry. *Geo-mar Lett.* 40 (2), 255–268. doi:10.1007/s00367-020-00638-8 Available at: http://link.springer.com/10.1007/s00367-020-00638-8.

Casella, E., Rovere, A., Pedroncini, A., Stark, C. P., Casella, M., Ferrari, M., et al. (2016). Drones as Tools for Monitoring Beach Topography Changes in the Ligurian Sea (NW Mediterranean). *Geo-mar Lett.* 36 (2), 151–163. doi:10.1007/s00367-016-0435-9 Available at: http://link.springer.com/10.1007/s00367-016-0435-9.

Corenblit, D., Baas, A., Balke, T., Bouma, T., Fromard, F., Garófano-Gómez, V., et al. (2015). Engineer Pioneer Plants Respond to and Affect Geomorphic Constraints Similarly along Water-Terrestrial Interfaces World-wide. *Glob. Ecol. Biogeogr.* 24 (12), 1363–1376. doi:10.1111/geb.12373 Available at: http://doi.wiley.com/10.1111/geb.12373.

Davidson-Arnott, R. G. D., Yang, Y., Ollerhead, J., Hesp, P. A., and Walker, I. J. (2008). The Effects of Surface Moisture on Aeolian Sediment Transport Threshold and Mass Flux on a Beach. *Earth Surf. Process. Landforms* 33 (1), 55–74. doi:10.1002/esp.1527 Available at: http://doi.wiley.com/10.1002/esp.1527.

Dong, G., Gao, S., and Jin, J. (1993). *The Desertification and its Control in the Gonghe Basin, Qinghai Province.* Beijing, China: Scientific Press.

Drees, M., and Olff, H. (2001). *'Rabbit Grazing and Rabbit Counting',* Coastal Dune Management Shared Experience of European Conservation Practice. Liverpool, United Kingdom: Liverpool University Press, 86–95.

Fox, T. A., Hugenholtz, C. H., Bender, D., and Gates, C. C. (2012). Can bison Play a Role in Conserving Habitat for Endangered Sandhills Species in Canada? *Biodivers Conserv* 21 (6), 1441–1455. doi:10.1007/s10531-012-0255-9 Available at: http://link.springer.com/10.1007/s10531-012-0255-9.

García-Romero, L., Delgado-Fernández, I., Hesp, P. A., Hernández-Calvento, L., Hernández-Cordero, A. I., and Viera-Pérez, M. (2019). Biogeomorphological Processes in an Arid Transgressive Dunefield as Indicators of Human Impact by Urbanization. *Sci. Total Environ.* 650, 73–86. doi:10.1016/j.scitotenv.2018.08.429 Available at: https://linkinghub.elsevier.com/retrieve/pii/S0048969718334041.

Garès, P. A., and Pease, P. (2015). Influence of Topography on Wind Speed over a Coastal Dune and Blowout System at Jockey's Ridge, NC, USA. *Earth Surf. Process. Landforms* 40 (7), 853–863. doi:10.1002/esp.3670 Available at: http://doi.wiley.com/10.1002/esp.3670.

Gautam, B. K., Khan, F. A., and Singh, A. (2017). Performance Analysis of 5 MWP Grid-Connected Solar PV Power Plant Using IEC 61724. *Int. Res. J. Eng. Technology(IRJET)* 4 (7), 2801–2805.

Gawthorpe, R. L., Collier, R. E. L., Alexander, J., Bridge, J. S., and Leeder, M. R. (1993). Ground Penetrating Radar: Application to Sandbody Geometry and Heterogeneity Studies. *Geol. Soc. Lond. Spec. Publications* 73 (1), 421–432. doi:10.1144/gsl.sp.1993.073.01.24

González-Villanueva, R., Costas, S., Duarte, H., Pérez-Arlucea, M., and Alejo, I. (2011). Blowout Evolution in a Coastal Dune: Using GPR, Aerial Imagery and Core Records. *J. Coastal Res.* 64, 278–282. doi:10.1016/j.geomorph.2012.12.019

Gonzlez-Villanueva, R., Costas, S., Prez-Arlucea, M., Jerez, S., and Trigo, R. M. (2013). Impact of Atmospheric Circulation Patterns on Coastal Dune Dynamics, NW Spain. *Geomorphology* 185, 96–109. doi:10.1016/j.geomorph.2012.12.019 Available at: https://linkinghub.elsevier.com/retrieve/pii/S0169555X12005776.

Hesp, P. A., Smyth, T. A. G., Walker, I. J., Gares, P. A., and Wasklewisz, T. (2016). Flow within a Trough Blowout at Cape Cod. *J. Coastal Res.* 75 (sp1), 288–292. doi:10.2112/si75-058.1

Hesp, P. A., and Walker, I. J. (2012). Three-dimensional Æolian Dynamics within a Bowl Blowout during Offshore Winds: Greenwich Dunes, Prince Edward Island, Canada. *Aeolian Res.* 3 (4), 389–399. doi:10.1016/j.aeolia.2011.09.002

Hesp, P. (2002). Foredunes and Blowouts: Initiation, Geomorphology and Dynamics. *Geomorphology* 48 (1-3), 245–268. doi:10.1016/s0169-555x(02)00184-8

Hesp, P., Schmutz, P., Martinez, M. M., Driskell, L., Orgera, R., Renken, K., et al. (2010). The Effect on Coastal Vegetation of Trampling on a Parabolic Dune. *Aeolian Res.* 2 (2-3), 105–111. doi:10.1016/j.aeolia.2010.03.001 Available at: https://linkinghub.elsevier.com/retrieve/pii/S1875963710000042.

Houser, C., Labude, B., Haider, L., and Weymer, B. (2013). Impacts of Driving on the Beach: Case Studies from Assateague Island and Padre Island National Seashores. *Ocean Coastal Manage.* 71, 33–45. doi:10.1016/j.ocecoaman.2012.09.012 Available at: https://linkinghub.elsevier.com/retrieve/pii/S0964569112002670.

Hugenholtz, C. H., and Wolfe, S. A. (2009). Form-flow Interactions of an Aeolian Saucer Blowout. *Earth Surf. Process. Landforms* 34 (November), 919–928. doi:10.1002/esp.1776

Hugenholtz, C. H., Wolfe, S. A., and Moorman, B. J. (2008). Effects of Sand Supply on the Morphodynamics and Stratigraphy of Active Parabolic Dunes, Bigstick Sand Hills, Southwestern SaskatchewanGeological Survey of Canada Contribution 20060654.. *Can. J. Earth Sci.* 45 (3), 321–335. doi:10.1139/e08-001

Hugenholtz, C. H., and Wolfe, S. A. (2006). Morphodynamics and Climate Controls of Two Aeolian Blowouts on the Northern Great Plains, Canada. *Earth Surf. Process. Landforms* 31 (12), 1540–1557. doi:10.1002/esp.1367

Jayson-Quashigah, P.-N., Appeaning Addo, K., Amisigo, B., and Wiafe, G. (2019). Assessment of Short-Term Beach Sediment Change in the Volta Delta Coast in Ghana Using Data from Unmanned Aerial Vehicles (Drone). *Ocean Coastal Manage.* 182, 104952. doi:10.1016/j.ocecoaman.2019.104952 Available at: https://linkinghub.elsevier.com/retrieve/pii/S0964569118309578.

Jewell, M., Houser, C., and Trimble, S. (2014). Initiation and Evolution of Blowouts within Padre Island National Seashore, Texas. *Ocean Coastal Manage.* 95, 156–164. doi:10.1016/j.ocecoaman.2014.04.019

Jewell, M., Houser, C., and Trimble, S. (2017). Phases of Blowout Initiation and Stabilization on Padre Island Revealed through Ground-Penetrating Radar and Remotely Sensed Imagery. *Phys. Geogr.* 38 (6), 556–577. doi:10.1080/02723646.2017.1338042

Jol, H. M., and Bristow, C. S. (2003). GPR in Sediments: Advice on Data Collection, Basic Processing and Interpretation, a Good Practice Guide. *Geol. Soc. Lond. Spec. Publications*, 211, 9–27. doi:10.1144/gsl.sp.2001.211.01.02

Kang, J., Zhao, W., and Zhao, M. (2017). Remediation of Blowouts by Clonal Plants in Maqu Degraded Alpine Grasslands of Northwest China. *J. Plant Res.* 130 (2), 291–299. doi:10.1007/s10265-016-0884-2 Available at: http://link.springer.com/10.1007/s10265-016-0884-2.

Käyhkö, J. (2007). Aeolian Blowout Dynamics in Subarctic Lapland Based on Decadal Levelling Investigations. *Geografiska Annaler: Ser. A, Phys. Geogr.* 89 (1), 65–81. doi:10.1111/j.1468-0459.2007.00308.x

Kocurek, G. (1996). "Deserts Aeolian Systems," in *Sedimentary Environments : Processes, Facies and Stratigraphy*. Editor H. Reading (Oxford: Blackwell Publishing), 125–153.

Lancaster, N. (1986). Dynamics of Deflation Hollows in the Elands Bay Area, Cape Province, South Africa. *CATENA* 13 (1-2), 139–153. doi:10.1016/s0341-8162(86)80009-1 Available at: https://linkinghub.elsevier.com/retrieve/pii/S0341816286800091.

Lin, J., Wang, R., Li, L., and Xiao, Z. (2019). A Workflow of SfM-Based Digital Outcrop Reconstruction Using Agisoft PhotoScan, in '2019 IEEE 4th International Conference on Image, Vision and Computing (ICIVC)'(. IEEE), 711–715.

Liu, B., Jin, H., Sun, L., Sun, Z., Su, Z., and Zhang, C. (2013). Holocene Climatic Change Revealed by Aeolian Deposits from the Gonghe Basin, Northeastern Qinghai-Tibetan Plateau. *Quat. Int.* 296, 231–240. doi:10.1016/j.quaint.2012.05.003

Lu, H., Miao, X., Zhou, Y., Mason, J., Swinehart, J., Zhang, J., et al. (2005). Late Quaternary aeolian activity in the Mu Us and Otindag dune fields (north China) and lagged response to insolation forcing. *Geophys. Res. Letters* 32. doi:10.1029/2005GL024560

Luo, W., Shao, M., Che, X., Hesp, P. A., Bryant, R. G., Yan, C., et al. (2020). Optimization of UAVs-SfM Data Collection in Aeolian Landform Morphodynamics: a Case Study from the Gonghe Basin, China. *Earth Surf. Process. Landforms* 45 (13), 3293–3312. doi:10.1002/esp.4965

Luo, W., Wang, Z., Lu, J., Yang, L., Qian, G., Dong, Z., et al. (2019a). Mega-blowouts in Qinghai-Tibet Plateau: Morphology, Distribution and Initiation. *Earth Surf. Process. Landforms* 44 (2), 449–458. doi:10.1002/esp.4507

Luo, W., Wang, Z., Shao, M., Lu, J., Qian, G., Dong, Z., et al. (2019b). Historical Evolution and Controls on Mega-Blowouts in Northeastern Qinghai-Tibetan Plateau, China. *Geomorphology* 329, 17–31. doi:10.1016/j.geomorph.2018.12.033

Neal, A., and Roberts, C. L. (2001). Internal Structure of a Trough Blowout, Determined from Migrated Ground-Penetrating Radar Profiles. *Sedimentology* 48 (4), 791–810. doi:10.1046/j.1365-3091.2001.00382.x

Qiang, M., Chen, F., Song, L., Liu, X., Li, M., and Wang, Q. (2013). Late Quaternary Aeolian Activity in Gonghe Basin, Northeastern Qinghai-Tibetan Plateau, China. *Quat. Res.* 79 (3), 403–412. doi:10.1016/j.yqres.2013.03.003

Qiang, M., Jin, Y., Liu, X., Song, L., Li, H., Li, F., et al. (2016). Late Pleistocene and Holocene Aeolian Sedimentation in Gonghe Basin, Northeastern Qinghai-Tibetan Plateau: Variability, Processes, and Climatic Implications. *Quat. Sci. Rev.* 132, 57–73. doi:10.1016/j.quascirev.2015.11.010

Scarelli, F. M., Cantelli, L., Barboza, E. G., Rosa, M. L. C. C., and Gabbianelli, G. (2016). Natural and Anthropogenic Coastal System Comparison Using DSM from a Low Cost UAV Survey (Capão Novo, RS/Brazil). *J. Coastal Res.* 75 (sp1), 1232–1236. doi:10.2112/si75-247.1

Schwarz, C., Brinkkemper, J., and Ruessink, G. (2018). Feedbacks between Biotic and Abiotic Processes Governing the Development of Foredune Blowouts: A Review. *Jmse* 7 (1), 2. doi:10.3390/jmse7010002 Available at: http://www.mdpi.com/2077-1312/7/1/2.

Smyth, T. A. G., Jackson, D. W. T., and Cooper, J. A. G. (2013). Three Dimensional Airflow Patterns within a Coastal Trough-Bowl Blowout during Fresh Breeze to Hurricane Force Winds. *Aeolian Res.* 9, 111–123. doi:10.1016/j.aeolia.2013.03.002 Available at: https://linkinghub.elsevier.com/retrieve/pii/S1875963713000232.

Smyth, T., Thorpe, E., and Rooney, P. (2020). Blowout Evolution between 1999 and 2015 in *Ainsdale Sand Dunes National Nature Reserve*. (England: North West Geography), 1 (20).

Sun, Y., Hasi, E., Liu, M., Du, H., Guan, C., and Tao, B. (2016). Airflow and Sediment Movement within an Inland Blowout in Hulun Buir Sandy Grassland, Inner Mongolia, China. *Aeolian Res.* 22, 13–22. doi:10.1016/j.aeolia.2016.05.002 Available at: https://linkinghub.elsevier.com/retrieve/pii/S1875963716300647.

van Boxel, J. H., Jungerius, P. D., Kieffer, N., and Hampele, N. (1997). Ecological Effects of Reactivation of Artificially Stabilized Blowouts in Coastal Dunes. *J. Coast Conserv* 3 (1), 57–62. doi:10.1007/bf02908179 Available at: http://link.springer.com/10.1007/BF02908179.

van der Hagen, H. G. J. M., Assendorp, D., Calame, W., van der Meulen, F., Sýkora, K. V., and Schaminée, J. H. J. (2020). Is Livestock Grazing a Key Factor for Changing Vegetation Patterns in Lime Rich Coastal Dunes in the Netherlands?. *J. Coastal Conservation* 24 (2), 15. doi:10.1007/s11852-020-00733-z Available at: http://link.springer.com/10.1007/s11852-020-00733-z.

Wang, X., Lang, L., Hua, T., Li, H., Zhang, C., and Ma, W. (2018). Effects of Aeolian Processes on Soil Nutrient Loss in the Gonghe Basin, Qinghai-Tibet Plateau: an Experimental Study. *J. Soils Sediments* 18 (1), 229–238. doi:10.1007/s11368-017-1734-0

Wang, Z., Luo, W., Dong, Z., Lu, J., Qian, G., and Xu, G. (2017). Grain Size Characteristics of the Blowout Surface Sediments and its Aerodynamic Significance in the Alpine Meadow Region of the Gonghe Basin. *J. Desert Res.* 37 (1). doi:10.7522/j.issn.1000-694X.2016.00064

Wernette, P., Houser, C., Lehner, J., Evans, A., and Weymer, B. (2020). Investigating the Impact of Hurricane Harvey and Driving on Beach-Dune Morphology. *Geomorphology* 358, 107119. doi:10.1016/j.geomorph.2020.107119

Yan, P., and Shi, P. (2004). Using the 137Cs Technique to Estimate Wind Erosion in Gonghe Basin, QInghai Province, China. *Soil Sci.* 169 (4), 295–305. doi:10.1097/01.ss.0000126843.88716.d3

Yu, C., Zhang, J., Pang, X. P., Wang, Q., Zhou, Y. P., and Guo, Z. G. (2017). Soil Disturbance and Disturbance Intensity: Response of Soil Nutrient Concentrations of Alpine Meadow to Plateau Pika Bioturbation in the Qinghai-Tibetan Plateau, China. *Geoderma* 307 (July), 98–106. doi:10.1016/j.geoderma.2017.07.041

Yu, Y., and Jia, Z. Q. (2014). Changes in Soil Organic Carbon and Nitrogen Capacities of Salix Cheilophila Schneid along a Revegetation Chronosequence in Semi-arid Degraded Sandy Land of the Gonghe Basin, Tibet Plateau. *Solid Earth* 5 (2), 1045–1054. doi:10.5194/se-5-1045-2014

Zhang, C., Gong, J., Zou, X., Dong, G., Li, X., Dong, Z., et al. (2003). Estimates of Soil Movement in a Study Area in Gonghe Basin, North-East of Qinghai-Tibet Plateau. *J. Arid Environments* 53 (3), 285–295. doi:10.1006/jare.2002.1048

Conflict of Interest: The authors declare that the research was conducted in the absence of any commercial or financial relationships that could be construed as a potential conflict of interest.

Copyright © 2021 Baird, Bristow, Luo, Du, Bryant, Mitchell and Vermeesch. This is an open-access article distributed under the terms of the Creative Commons Attribution License (CC BY). The use, distribution or reproduction in other forums is permitted, provided the original author(s) and the copyright owner(s) are credited and that the original publication in this journal is cited, in accordance with accepted academic practice. No use, distribution or reproduction is permitted which does not comply with these terms.

frontiers in Earth Science

ORIGINAL RESEARCH
published: 05 July 2021
doi: 10.3389/feart.2021.711802

Provenance of Aeolian Sediments in the Ordos Deserts and Its Implication for Weathering, Sedimentary Processes

Guoxiang Chen[1], Zhibao Dong[1]*, Chao Li[1], Weikang Shi[1], Tianjie Shao[1], Weige Nan[1] and Junhuai Yang[2]

[1]School of Geography and Tourism, Shaanxi Normal University, Xi'an, China, [2]College of Earth and Environmental Sciences, Lanzhou University, Lanzhou, China

Identifying the provenance of aeolian deposits in semi-arid zones of China is beneficial in understanding Earth's surface processes and helping to alleviate ecological stress. In this paper, we use grain-size, geochemical elements, heavy-minerals, and quartz grain morphology data to investigate the potential source of aeolian sands from the Ordos Deserts (Mu Us Sandy Land and Hobq Desert). Sedimentological, geochemical and geomorphological results indicate that significant provenance differences exist among various parts of the Mu Us Sandy Land, i.e., aeolian sediments from the southwest region are obviously distinct from other areas in the Mu Us Sandy Land but show the same external provenance with the Hobq Desert referring to the sorting, mineralogical maturity, geochemical characteristics, heavy-minerals, and quartz grain morphology. Comparing the samples from the Ordos Deserts with felsic rocks from potential sources *via* a serious of geochemical methods, we conclude that: 1) Aeolian sands from other regions of the Mu Us are a mixture of binary provenance, i.e., one originated from local lacustrine sediments and underlying sandstones, and another from the Alxa Plateau (AP) carried by northwesterly Asian winter monsoon. 2) The fluvial deposits denuded from the Qilian Orogenic Belt in the Northeastern Tibetan Plateau (NTP) and carried by the Yellow River are likely the initial material source for the southwest region of the Mu Us Sandy Land and the Hobq Desert. 3) The Yellow River plays a significant and critical role in sediment transport for sand seas in arid and semi-arid areas of northern China.

Keywords: sediment provenance, grain size, geochemical element, heavy mineral, quartz grain morphology, Ordos Deserts

OPEN ACCESS

Edited by:
Kathryn Elizabeth Fitzsimmons, Max Planck Institute for Chemistry, Germany

Reviewed by:
Benli Liu, Northwest Institute of Eco-Environment and Resources (CAS), China
Xiaodong Miao, Linyi University, China

***Correspondence:**
Zhibao Dong
zbdong@snnu.edu.cn

Specialty section:
This article was submitted to Quaternary Science, Geomorphology and Paleoenvironment, a section of the journal Frontiers in Earth Science

Received: *19 May 2021*
Accepted: *21 June 2021*
Published: *05 July 2021*

Citation:
Chen G, Dong Z, Li C, Shi W, Shao T, Nan W and Yang J (2021) Provenance of Aeolian Sediments in the Ordos Deserts and Its Implication for Weathering, Sedimentary Processes. Front. Earth Sci. 9:711802. doi: 10.3389/feart.2021.711802

INTRODUCTION

Desert sand seas, characterized by various dune types, make up a significant part of the Earth's surface sediment systems (Goudie and Middleton, 2001). Sand seas and dune fields are widely distributed across China, from semi-arid zones with annual precipitation greater than 400 mm in the northeast to hyper-arid zones with annual precipitation less than 50 mm in the northwest (Dong et al., 2013). Previous studies have demonstrated that extensive sand seas in northern and western China are a significant component of the Asian aeolian dust system (Chen and Li, 2011). Dust from these areas has drawn widespread public attention because of its potential influence on the Asian system including radiation balance, hydrological and biogeochemical cycles, as well as air quality (Arimoto, 2001; Goudie, 2009). Also, no matter what state a dune field is in (active or stable), as well as what sort of the dune forms evolve, a better understanding of the sand source is significant in judging the origin and subsequent evolution of a dune field (Dong et al., 2017). Therefore, tracing the provenance of aeolian sediment is fundamental to understanding the formation and evolution of deserts, the interaction between surface processes and climatic changes, the operation of the Earth system (Molnar, 2004). Also, it is beneficial for establishing effective environmental governance policies for such sensitive areas in China (Du et al., 2018). Diverse methods have been adopted to investigate the origin of desert sediments, such as grain size analysis, geochemical tracing, detrital mineralogy, scanning electron microscopy (SEM), satellite imagery, environmental magnetism, detrital zircon, and numerical modeling (Honda et al., 2004; Howari et al., 2007; Pan et al., 2016). For example, the grain-size characteristics of dune sands contain a mass of information about the transport pathways and potential sources of the sediment (Li et al., 2019). Geochemical analysis, especially of trace and rare Earth elements (REE), has great potential in identifying the provenance and transport pathways of sediments since they are less fractionated during weathering, transport, and sedimentation (Dehghani et al., 2018). Examining the provenance of heavy minerals has been used because their composition directly reflects the parent lithologies and primary provenance signals (Garzanti et al., 2008). Furthermore, some peculiar morphologies related to specific sedimentary processes and environments can be discriminated by the analysis of quartz grains using SEM, which provides new insights into the provenance of the sediments (Moral Cardona et al., 2005).

The Ordos Deserts, including the Mu Us Sandy Land and the Hobq Desert, are located in a transitional climatic zone in northern China (**Figure 1**). However, aeolian landforms are differentiated between them, i.e., the Mu Us is characterized by fixed and semi-fixed dunes, whereas active dunes are dominant in the Hobq Desert. In recent years, diverse techniques have been employed to explore the provenance of aeolian sands in the Mu Us, including geochemical indices (Rao et al., 2011b; Rao et al., 2014; Liu and Yang, 2018), zircon U-Pb, heavy mineral analysis, framework petrography (Stevens et al., 2013; Nie et al., 2015; Zhang et al., 2016; Wang et al., 2019; Sun et al., 2020), quartz crystallinity and magnetic susceptibility (Sun et al., 2013; Hällberg et al., 2020). Detailed results from the above provenance analyses have demonstrated that there exist distinct provenance differences between the western and eastern regions of the Mu Us, and diverse opinions about the region's provenance remain. Furthermore, previous studies have either ignored provenance with respect to regional variation or are based on a small number of samples of the Mu Us, which may bias interpretations of the provenance in terms of its regional variation.

Therefore, to better reflect the regional variation in the provenance of these desert sediments, we conducted detailed fieldwork and collected aeolian sand samples from different parts in the Ordos Deserts. Furthermore, we used an integrated approach to identify the provenance of the aeolian sediments in the Ordos Deserts, including grain size, geochemical tracing, mineralogy, and SEM analysis. Based on sedimentological and geomorphological data, this paper aims to present a more complete understanding of the regional variations in the provenance of the sediments that make up the Ordos Deserts and to further ascertain the critical role of the Yellow River in supplying sediments to the sand sea.

FIELD SITE, MATERIAL, AND METHODS

The Study Area

The Ordos Plateau, tectonically situated in the western part of the North China Plate, is enclosed by the Yellow River on its western, northern, and eastern boundaries and is mainly covered by the Ordos Deserts. The Alxa Plateau (AP) and the Chinese Loess Plateau (CLP) are distributed in the upwind and downwind areas of the Ordos Desert, respectively (**Figure 1**). The Alxa Desert is mainly composed of the Badain Jaran Desert (BJD), the Tengger Desert (TD), the Ulan Buh Desert (UBD), and some small deserts in north-central China. The bedrock of the Ordos Plateau are composed of Archaean and Proterozoic metamorphic rocks (Rao et al., 2011b).

Located in the transitional zone between agriculture farming and animal grazing in the Ordos Plateau, the Mu Us Sandy Land (37°27′-39°22′N, 107°20′-111°30′E) is bordered by the Hobq Desert in the north, and the Yellow River in the east and west, and covers an area of $3.2 \times 10^4\,\mathrm{km}^2$ (**Figure 1**). It lies on the margin of the area impacted by the East Asian monsoon, and the mean annual precipitation ranges from 440 mm in the southeast to 250 mm in the northwest, of which 60–80% is concentrated during the period from June to August (Shang et al., 2001). The annual mean temperature is about 6–9°C, and the annual mean evaporation and aridity are 1,800–2,500 mm and 1.0–2.5, respectively (Liu et al., 2015). The ground surface is characterized by semi-fixed, fixed, and mobile dunes, i.e., honeycomb dunes, parabolic dunes, vegetated dunes, crescent dunes, dune networks, etc. The present surface is dominated by substantial aeolian, lacustrine, and fluvial landforms (Wang et al., 2019). Owing to the elevation increasing gradually from the southeast to the northwest, the majority of the rivers flow from the northwest to the southeast. According to the calculation of the resultant drift direction, the wind system that controls aeolian transport in the Mu Us is from the northwest to the southeast (**Figure 2**).

The Hobq Desert, with an area of $1.64 \times 10^4\,\mathrm{km}^2$, is located on the margin of the northern Ordos Plateau. The mean annual precipitation ranges from 360 mm in the southeast to 240 mm in the northwest. Compared to the Mu Us, the majority of dunes in the Hobq Desert are active (Zhu et al., 1980). One prominent characteristic is that ten tributaries of the Yellow River flow through the desert northwards (**Figure 2**).

Material and Methods

The Mu Us Sandy Land was evenly divided into a 10 km × 10 km grid. Sand samples were collected from the dune crest (to a depth

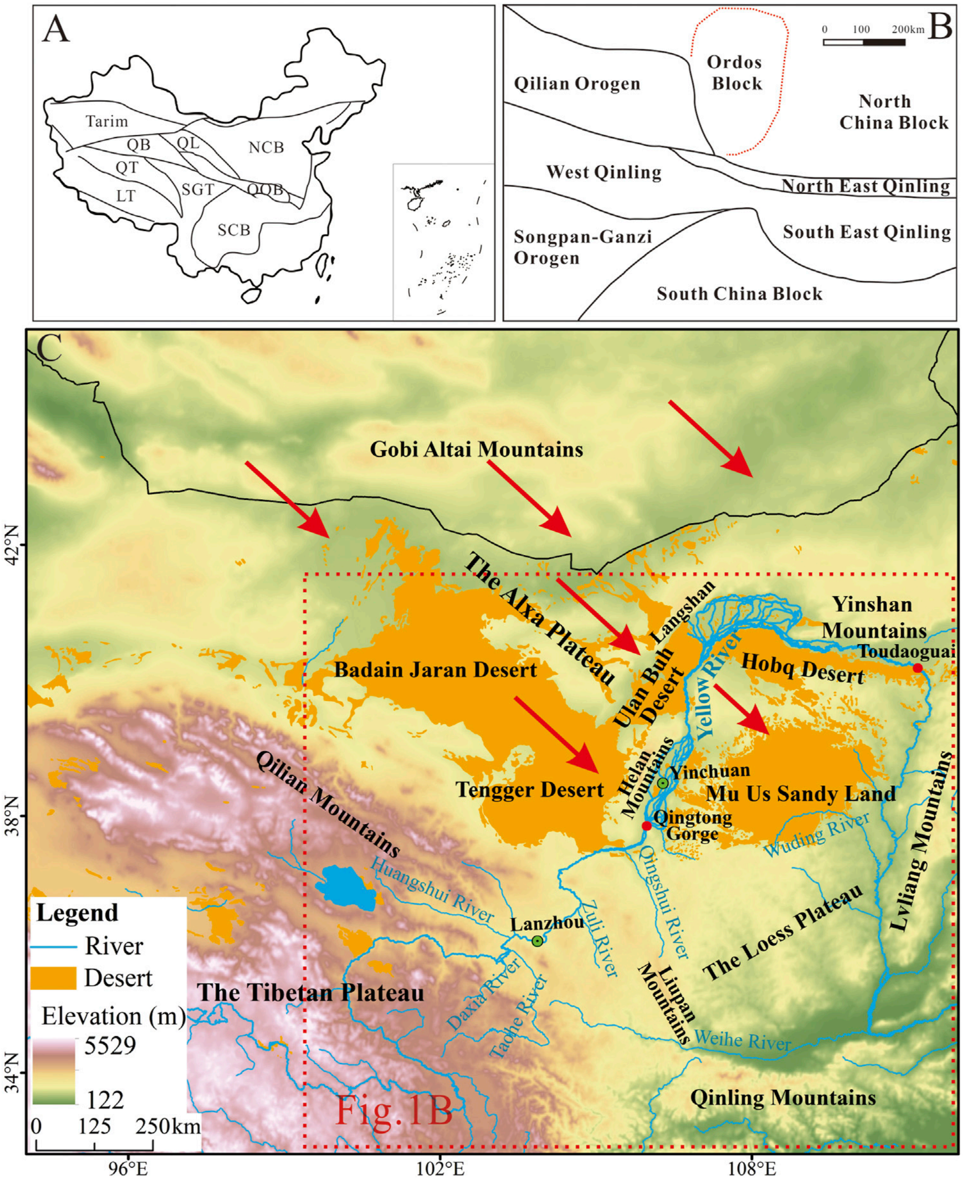

FIGURE 1 | (A) Simplified geological map of China. (NCB: North China Block; SCB: South China Block; SGT: Songpan-Ganzi terrane; QB: Qaidam Basin; QT: Qiangtang terrane; LT: Lhasa terrane; QOB: Qinling Orogenic Belt). **(B)** Simplified regional geological map of study area (modified after Zhu et al., 2011). **(C)** Geographical location of the Ordos Deserts. The red arrows refer to the dominant wind direction.

of 2 cm in a 20 cm × 20 cm area), with a total of 261 surface samples collected from 261 grid cells covering different regions (solid circles with different colors in four different regions, **Figure 2**) of the Mu Us and 7 samples (marked by H1 to 7) were collected from the Hobq Desert (**Figure 2**).

Samples were oven-dried and then analyzed using a Mastersizer 2000 (Malvern Instruments, Malvern, United Kingdom) at the School of Geography and Tourism of Shaanxi Normal University. Gain-size parameters, i.e., mean grain size (*Mz*) and sorting (σ_I) were calculated based on the method of Folk and Ward (1957).

Given that different sediment particles reflect different transport processes and sources, we separated the fine fractions (<125 μm) from the coarse fractions by dry sieving. The concentrations of major and trace elements (except REE) were analyzed using X-ray fluorescence (XRF) spectrometry at the School of Geography and Tourism of Shaanxi Normal University. The procedures for sample preparation are the same as described in Liang et al. (2019). The estimated error for repeat measurements was less than 5%. The chemical weathering intensity evaluation index (CIA) was calculated using the following formula (Nesbitt and Young, 1982):

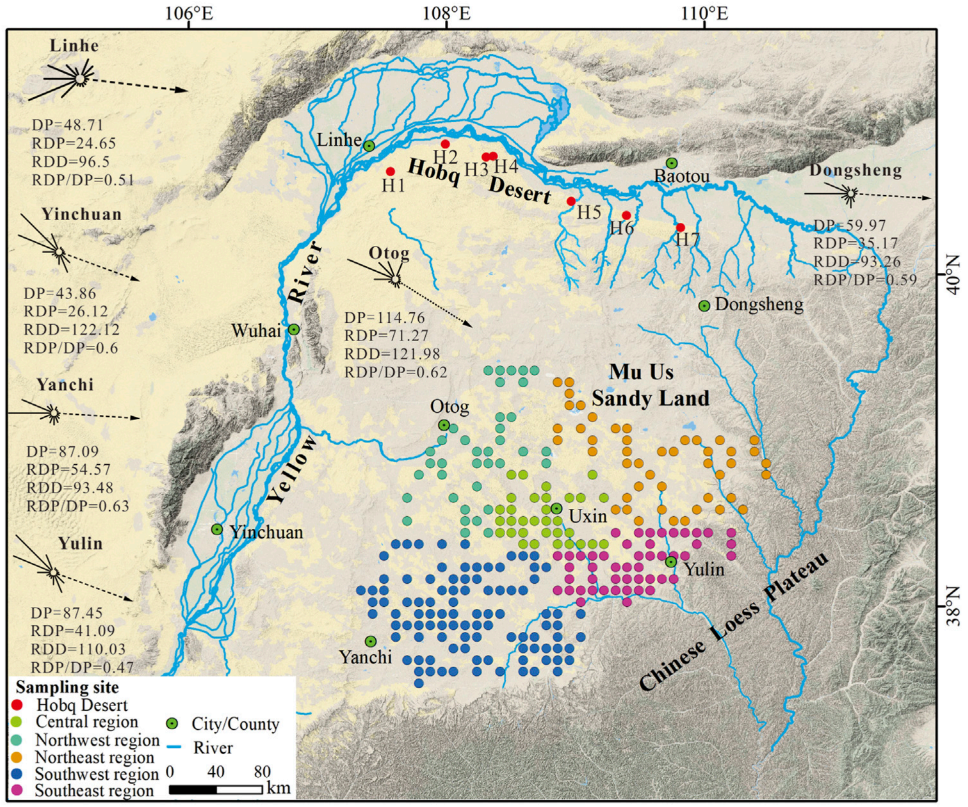

FIGURE 2 | Locations of sand dune samples in the Ordos Deserts. Sand transport roses are calculated based on the descriptions of the wind environment proposed by (Fryberger, 1979) with data from the U.S. National Climate Data Center (NCDC). Abbreviations: DP, drift potential; RDP, resultant drift potential; RDD, resultant drift direction; RDP/DP, directional variability.

$$CIA = \left[Al_2O_3 / (Al_2O_3) + CaO^* + Na_2O + K_2O\right] \times 100 \qquad (1)$$

where the values for each component are given in molecular units. This calculation assumes that CaO* refers to the amount of CaO incorporated only in silicate fraction. Here, the CIA values were calculated assuming $CaO^* = Na_2O$ (in moles), following McLennan (1993). In addition, the plagioclase index of alteration (PIA) was calculated by the following formula (Fedo et al., 1995):

$$PIA = \left[(Al_2O_3 - K_2O) / + (Al_2O_3 + CaO^* + Na_2O - K_2O)\right] \times 100 \qquad (2)$$

The concentrations of REE were determined by inductively coupled plasma-mass spectrometry (ICP-MS) at the Institute of Geochemistry, Chinese Academy of Sciences. The preparation of samples strictly comply with the pretreatment procedures of Yang et al. (2007). Analytical uncertainties (relative standard deviation) were less than ±1% for REE.

Heavy-mineral analyses were performed at the Hebei Central Laboratory of Geology and Mineral Resources. Dried samples were flushed in a washing pan for removing all impurities and then were separated with bromoform (2.89 g/cm^3) from a settling tube via gravity. The types and volume of heavy-minerals were determined by using the "area method" under a binocular microscope and a polarizing microscope (Mange and Maurer, 1992). Given that the experimental conditions and the representativeness of the samples, we selected five representative samples for heavy minerals analysis from each region of the Mu Us.

The analysis of grain-morphology was conducted by using Hitachi Desktop Scanning Electron Microscope TM3000 at the School of Geography and Tourism of Shaanxi Normal University. The preparation of quartz grains strictly complies with the pretreatment procedures of Pan et al. (2016). We selected fifteen to twenty quartz grains from each sample randomly using a binocular microscope and then was sprayed gold film for ensuring electrical conductivity in an ion plating machine before testing. The surface micro-textures from each studied grain were recognized and interpreted according to the concepts of previous studies (Krinsley and Doornkamp, 1973).

RESULTS

Grain-Size Parameters

Figure 3 shows the parameters of the sediments in the Mu Us. Here, the main grain size (*Mz*) for the Mu Us samples averaged 186.86 μm (2.42Φ), which is finer than sediments from the Hobq Desert, which averaged 201.66 μm (2.31Φ). Most regions in the

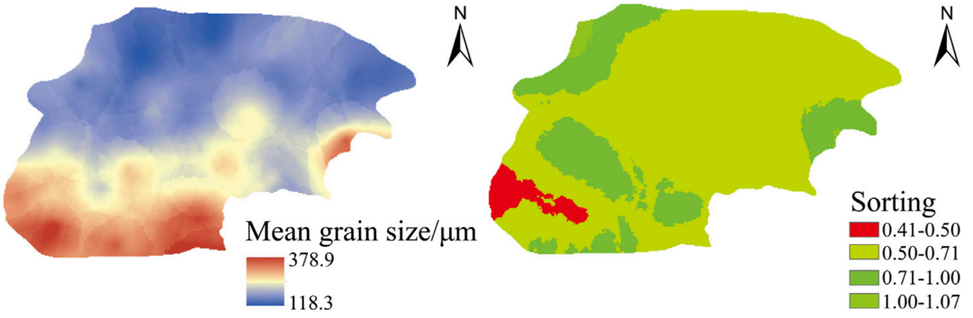

FIGURE 3 | Grain size parameters of sands in the Mu Us Sandy Land.

TABLE 1 | Grain-size parameters of sands in the Hobq Desert.

	H1	H2	H3	H4	H5	H6	H7	H8
Mz	2.29	2.27	2.28	2.13	2.49	2.33	2.38	2.31
σI	0.56	0.50	0.40	0.48	0.51	0.45	0.50	0.49

Mu Us show moderate sorting, whereas the southwest region shows better sorting (**Figure 3**). Similarly, the sorting of the Hobq Desert samples includes two gradations: moderately sorted and better sorted (**Table 1**).

Geochemical Elements

The spatial variation of all major and trace elements in the Mu Us Sandy Land and the Hobq Desert are listed as supplementary materials (**Supplementary Figures S1, S2**, and Appendix A). Key features are described below.

Major Elements

Except for SiO_2, the major elements of the bulk fractions are depleted in the Mu Us and the Hobq Desert, compared to the Upper Continental Crust (UCC) (**Figure 4**). What stands out in **Figure 4** is the markedly higher SiO_2 content, but lower content of Fe_2O_3, MgO, P_2O_5, TiO_2, and MnO of the bulk fractions when compared with the fine fractions of aeolian sands, indicating that the bulk fractions have a higher amount of quartz and feldspar. One prominent characteristic is that Ti in the fine sands is enriched, which means that the Ti-bearing minerals (ilmenite, rutile, and titanite) can be found in the Ordos Deserts. Additionally, aeolian sands collected from the southwest

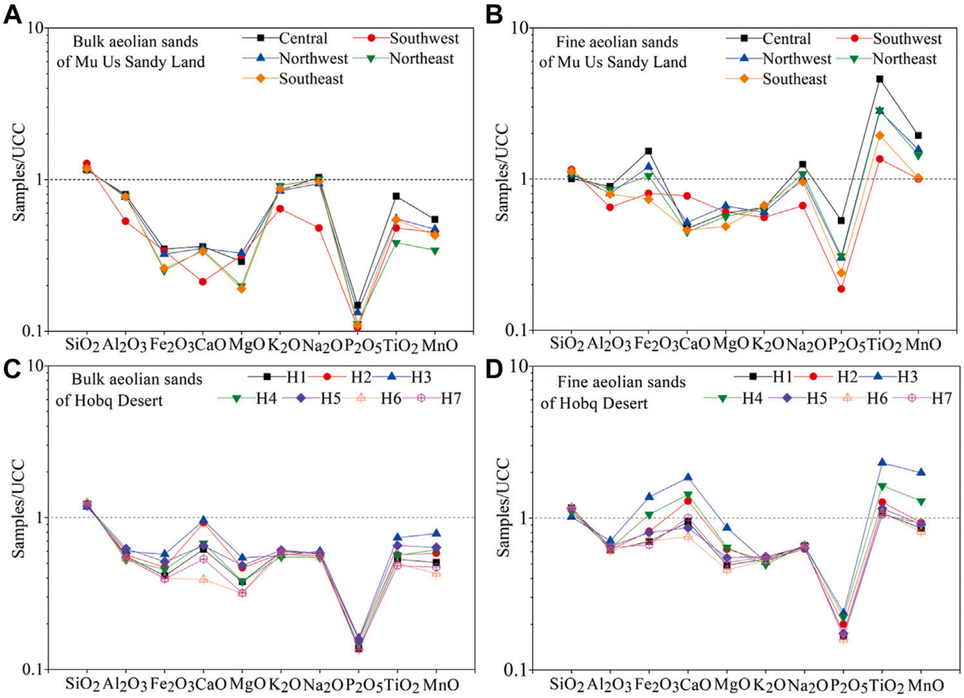

FIGURE 4 | UCC-normalized diagrams of major elements. **(A,B)** are for bulk and fine fraction sands in the Mu Us Sandy Land, respectively. **(C,D)** are for bulk and fine fraction sands in the Hobq Desert, respectively. UCC values from Taylor and McLennan (1985).

region of the Mu Us have higher SiO_2 but lower Al_2O_3, K_2O, Na_2O, and P_2O_5 when compared with other areas (**Figure 4**). According to the UCC-normalized diagram of major elements, both bulk and fine fractions of aeolian sands from the Hobq Desert are relatively uniform, whereas this trend is not found in the Mu Us, as the southwest region differs from other parts of the Mu Us (**Figure 4**).

Trace Elements

UCC-normalized plots of trace elements for various grain size fractions are shown in **Figure 5**. Most trace elements of the bulk fractions experience a varying degree of depletion, except for Co in the Mu Us and Cr in the Hobq Desert. It must be noted, however, that the elements Cr, Zr, and Hf are distinctly enriched in the fine fractions, and the content of most trace elements in the fine fraction sands are higher than in the bulk fractions. Notably, the distribution patterns of fine sands are consistent both in the Mu Us and the Hobq Desert (**Figure 5**).

Rare Earth Elements

The mean total REE contents for bulk aeolian sands of different regions in the Mu Us varies from 61.8 to 96 ppm, and the fine fractions range from 180.4 to 270.5 ppm. The content of bulk fractions and fine fractions in the southwest regions is distinctly lower than that in other parts of the Mu Us. Furthermore, the total REE contents varies from 53.4 to 80.9 ppm for bulk fractions and from 114.2 to 217.3 ppm for fine aeolian sands in the Hobq Desert (Appendix A).

The chondrite-normalized REE distribution patterns of both samples from the Mu Us and the Hobq Desert are characterized by steep light-REE (LREE) and smooth heavy-REE (HREE), which is similar to UCC (**Figure 6**). Compared with bulk aeolian sands, the Eu anomalies show more negative in the fine fractions in both the Mu Us and the Hobq Desert. In addition, Eu anomalies for bulk aeolian sands are not obvious in other areas of the Mu Us except for the southwest (**Figure 6**).

Mineralogy

Figure 7 provides an overview of the composition of heavy minerals, with significant differences in heavy minerals existing across the Mu Us. Amphibole (24.9–38.4%) and garnet (30.8–39.8%) are the dominant heavy minerals in most areas of the Mu Us, except for the southwest. However, samples from the southwest display significantly higher haematite and limonite (average 18.1%), pyroxene (average 6.7%), and epidote (average 2%) contents, and lower garnet content (average 25.3%) (**Figure 7**).

Quartz Grain Morphology

The quartz grain morphologies of the Mu Us include micro-textures produced by mechanical and chemical actions (**Figure 8**). Previous studies of quartz grains from different sedimentary environments concluded that butterfly-shaped pits, pitted surfaces, and crescent-shaped pits are commonly shown in aeolian environments, whereas V-shaped fractures, conchoidal fractures, straight/curved grooves, and parallel striations are characteristics of aqueous environments (Mahaney, 2002; Vos et al., 2014). Quartz grains of all regions in the Mu Us display butterfly-shaped (**Figure 8B**) and crescent-

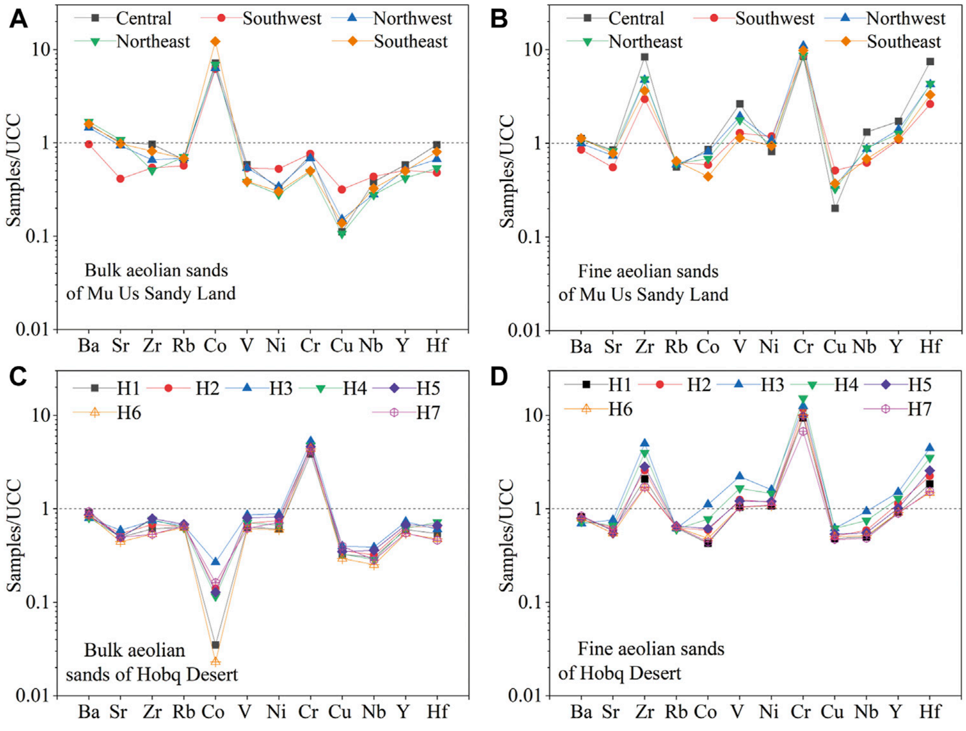

FIGURE 5 | UCC-normalized distribution patterns of trace elements. **(A,B)** are for bulk and fine fraction sands in the Mu Us Sandy Land, respectively. **(C,D)** are for bulk and fine fraction sands in the Hobq Desert, respectively. UCC values from Taylor and McLennan (1985).

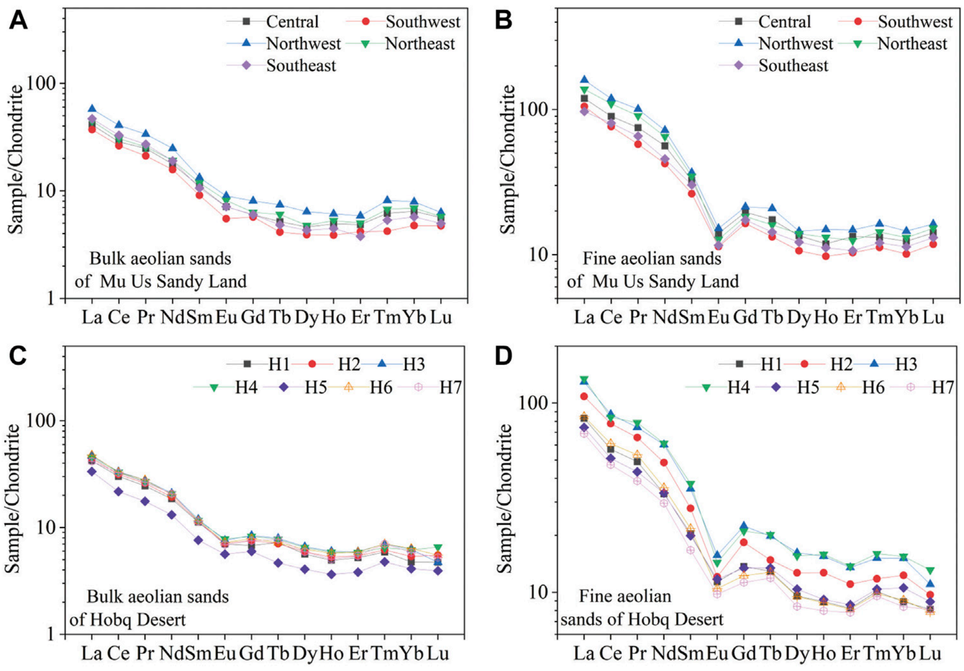

FIGURE 6 | Chondrite-normalized REE patterns for different fractions. **(A,B)** are for bulk and fine fraction sands in the Mu Us Sandy Land, respectively. **(C,D)** are for bulk and fine fraction sands in the Hobq Desert, respectively. UCC values from Taylor and McLennan (1985).

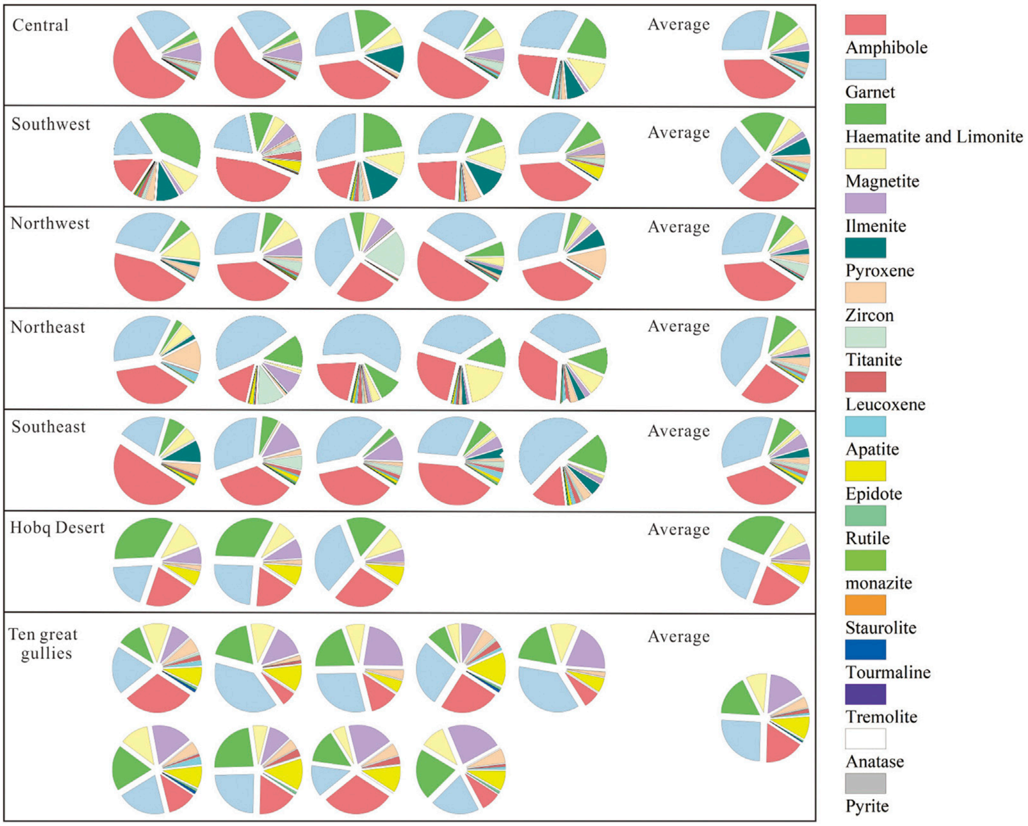

FIGURE 7 | Heavy-mineral assemblages of the samples. The data of Hobq Desert and Ten great gullies from Pan et al. (2016).

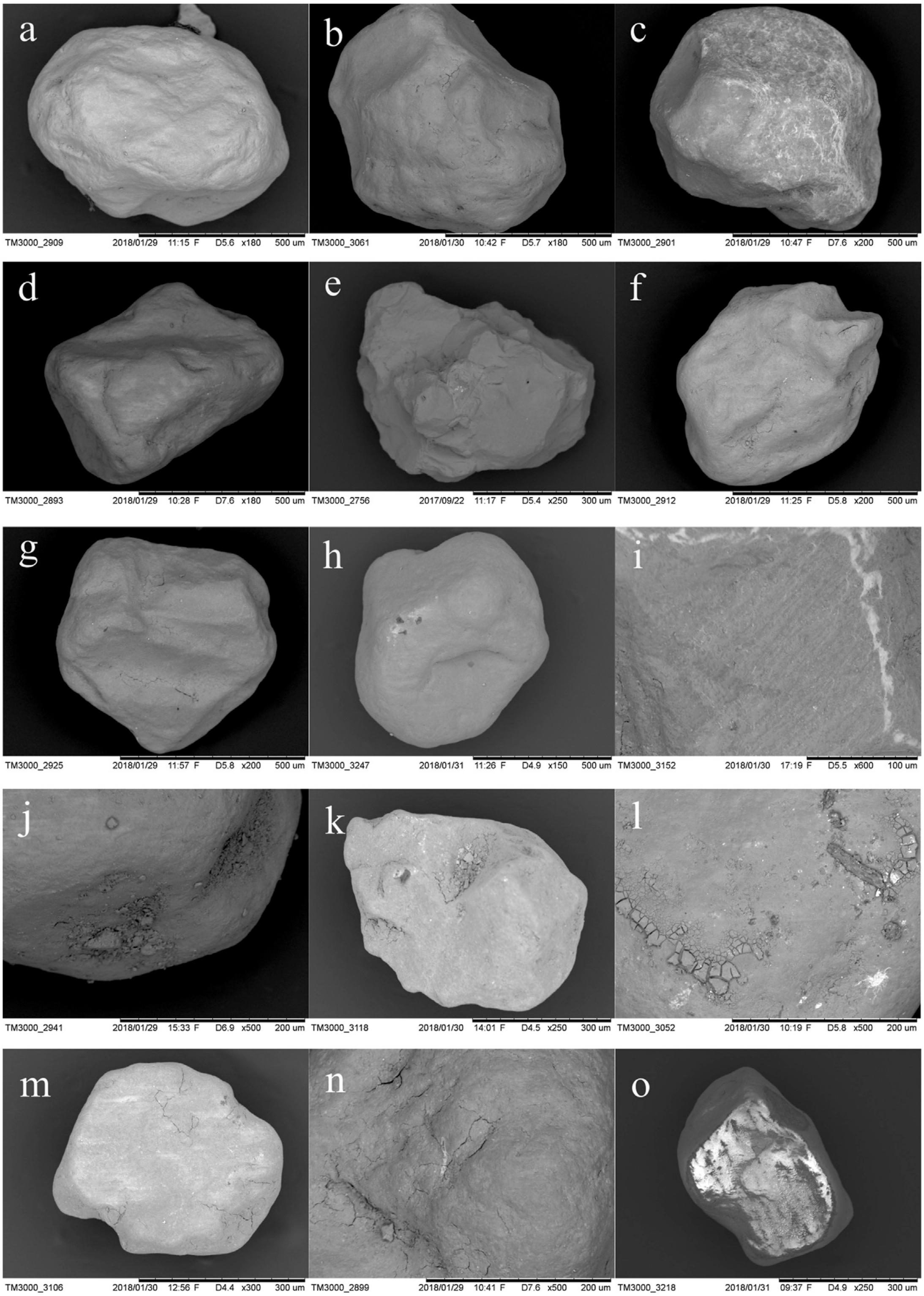

FIGURE 8 | Typical surface microstructures for quartz grains in the Mu Us Sandy Land. **(A)** Rounded grain from the southwest region of the Mu Us Sandy Land. **(B)** rounded grain showing butterfly-shaped pits. **(C)** pitted surface. **(D)** crescent-shaped pits. **(E)** conchoidal fractures produced in the high-energy subaqueous environment. **(F)** large V-shaped fractures with high relief indicates a typical subaqueous environment. **(G)** straight grooves. **(H)** curved grooves; **(I)** parallel striations. **(J)** rounded grains with silica globules. **(K)** sub-angular grains showing silica flowers. **(L)** silica flowers. **(M)** angular grains with solution crevasses. **(N)** solution crevasses founded around silica globule. **(O)** silicon compounds.

shaped pits (**Figure 8D**) typical of aeolian environments, which indicates that the sands had suffered intense aeolian activities. In addition, pitted surfaces are found in some grains (**Figure 8C**). However, some micro-textures such as conchoidal fractures (**Figure 8E**), V-shaped pits (**Figure 8F**), straight/curved grooves (**Figures 8G,H**), and parallel striations (**Figure 8I**) are also found in the quartz grains, and are especially more pronounced in samples from the southwest region, which suggests that those sands may have been subjected originally to an aqueous environment with intense collisions and frictions between grains. Moreover, other structures, such as silica globules on rounded grains (**Figure 8J**), silica flowers (**Figures 8K,L**), solution crevasses (**Figures 8M,N**), and silicon compounds (**Figure 8O**) are common, indicating noticeable chemical processes.

DISCUSSIONS

Provenance Differences Over the Ordos Deserts

Generally, the sands in downwind areas tend to be finer and more well sorted than those in upwind areas, and this trend had been validated in many deserts (Lancaster, 1989, 1995; Zhang et al., 2015; Zhang and Dong, 2015). The mean grain size of dunes in the Mu Us clearly shows a regional variation that tends to be finer from the northwest to the southeast (**Figure 3**), which is consistent with the compound direction of the regional wind system (NW, WNW, **Figure 2**). However, the best-sorted sands occur in the southwest region, which is located in the upwind direction of the prevailing wind in the Mu Us (**Figure 3**). It is evident that this trend is not in accord with the Mu Us, as no systematic trend in the variation of sorting was found with decreasing M_Z, indicating that the spatial variation of sands in the Mu Us cannot be viewed simplistically as a response to the regional wind patterns. Generally, the distribution of grain size over a large sand sea is primarily controlled by wind and the characteristics of the source material (Livingstone et al., 1999). Hence, we conclude that the sediments in the southwest area of the Mu Us may have undergone long-term transportation, thus showing a better sorting than in other areas, or to go a step further, the provenance of sediments in the southwest area of the Mu Us is likely to be different from other regions.

Mineralogical maturity is considered as a compositional state of the clastic sedimentary body wherein quartz is dominant in its resistant minerals, which can be used to ascertain sediment sources (Muhs et al., 2013). Generally, mineralogical maturity can be portrayed by Log (Na_2O/K_2O) vs. Log (SiO_2/Al_2O_3) presented by Pettijohn et al. (1972). As illustrated by **Figure 9**, higher Log (SiO_2/Al_2O_3) values of sands from the southwest region indicate that more quartz and less feldspar existed in this region. Hence, we infer that sands from the southwest region have been subjected to long-distance transport, and their provenance draws the most essential part in terms of their differentiation of mineralogical maturity in the Mu Us. Heavy-mineral assemblages in fluvial deposits are controlled by source-rock lithology, chemical weathering, and the sorting of detrital materials (Garzanti et al., 2007; Garzanti et al., 2013a). However, evidence indicates that sediments in the Mu Us have undergone a low degree of chemical weathering (**Figure 10**). Garzanti et al. (2012) found that although sorting may give rise to the separation of heavy and light minerals during sediment transport, it would not cover up information about the provenance. According to our analysis of the heavy-mineral assemblages, aeolian sediments in the Mu Us can be classified into two groups (**Figure 7**). One group is the southwest region, which is dominated by amphibole, garnet, hematite, and limonite, and some pyroxenes, whereas the other group covers other areas of the Mu Us, which are dominated by amphibole and garnet. Therefore, the distinctive heavy-mineral assemblages between these two groups manifest how the source-rock lithology plays the most critical role in their different provenances. In addition, the roundness of the quartz grain in the southwest region of the upwind direction is significantly higher than that for other areas, also indicating that the deposits from the southwest region may have experienced a longer transport before being deposited (**Supplementary Figure S3**).

Taken together, these results suggest that there is a distinct difference of provenance between the southwest region and other areas in the Mu Us, whereas the southwest region of the Mu Us may have the same sources as the Hobq Desert.

Feasibility of Using Chemical Composition to Determine Provenance

Although the geochemical composition of detrital sediments is widely used for tracing the provenance and composition of sediments, the chemical composition of clastic sediments is the combined result of source-rock composition, the weathering of the source area, sorting, and recycling (Fedo et al., 1995; Perri et al., 2013). As an example, the clastic sediments may not reflect the provenance directly due to the depletion of the mobile elements (like alkali and alkaline Earth metals) and the enrichment of non-mobile elements (such as Al_2O_3, TiO_2, REE) resulting from weathering processes (Nesbitt et al., 1996). It is, hence, necessary to first evaluate whether the effects of these factors have hidden potential provenance signatures before identifying the provenance of the Ordos Deserts as inferred from the geochemical composition.

The chemical index of alteration (CIA), proposed by Nesbitt and Young (1982), is an ideal chemical indicator for estimating the chemical weathering intensity of sediments. Generally, higher weathering intensity tends to result in a larger CIA value of the sediment (Taylor and McLennan, 1985). The range of CIA values for the Mu Us is extremely narrow (45.03–53.89, average 50), indicating that aeolian sands are in the initial stage of weathering and have undergone a low degree of weathering (**Figure 10A**). Also, the Plagioclase Index of Alteration (PIA) is an essential chemical indicator to evaluate the chemical weathering intensity (Fedo et al., 1995). The PIA values of the studied samples are similar to those of the CIA, ranging from 43.2 to 55.87, which also indicates a low degree of chemical weathering (**Figure 10B**). Sediments from the Hobq Desert also show a low degree of chemical weathering (Appendix A). In addition, the diagram of

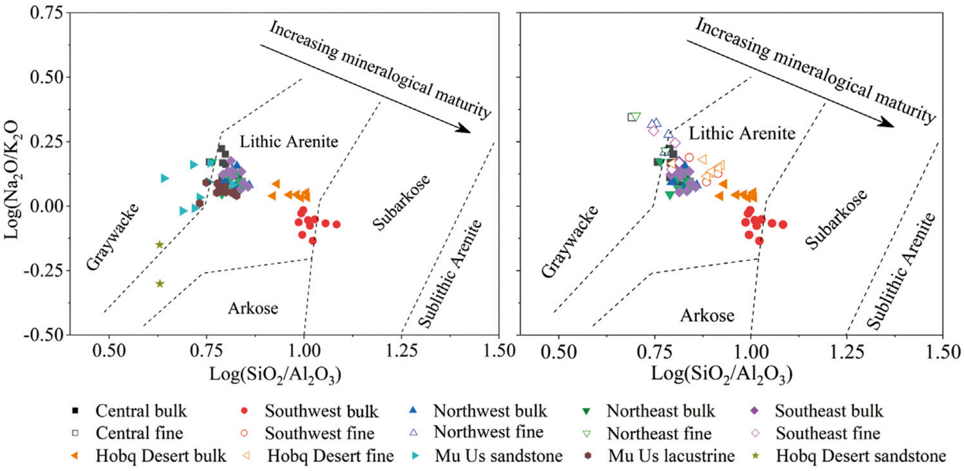

FIGURE 9 | Plots of mineralogical maturity for sediments in the Ordos Deserts. Data of sandstone and lacustrine sediments in Mu Us and the Hobq Desert is from Liu and Yang (2018).

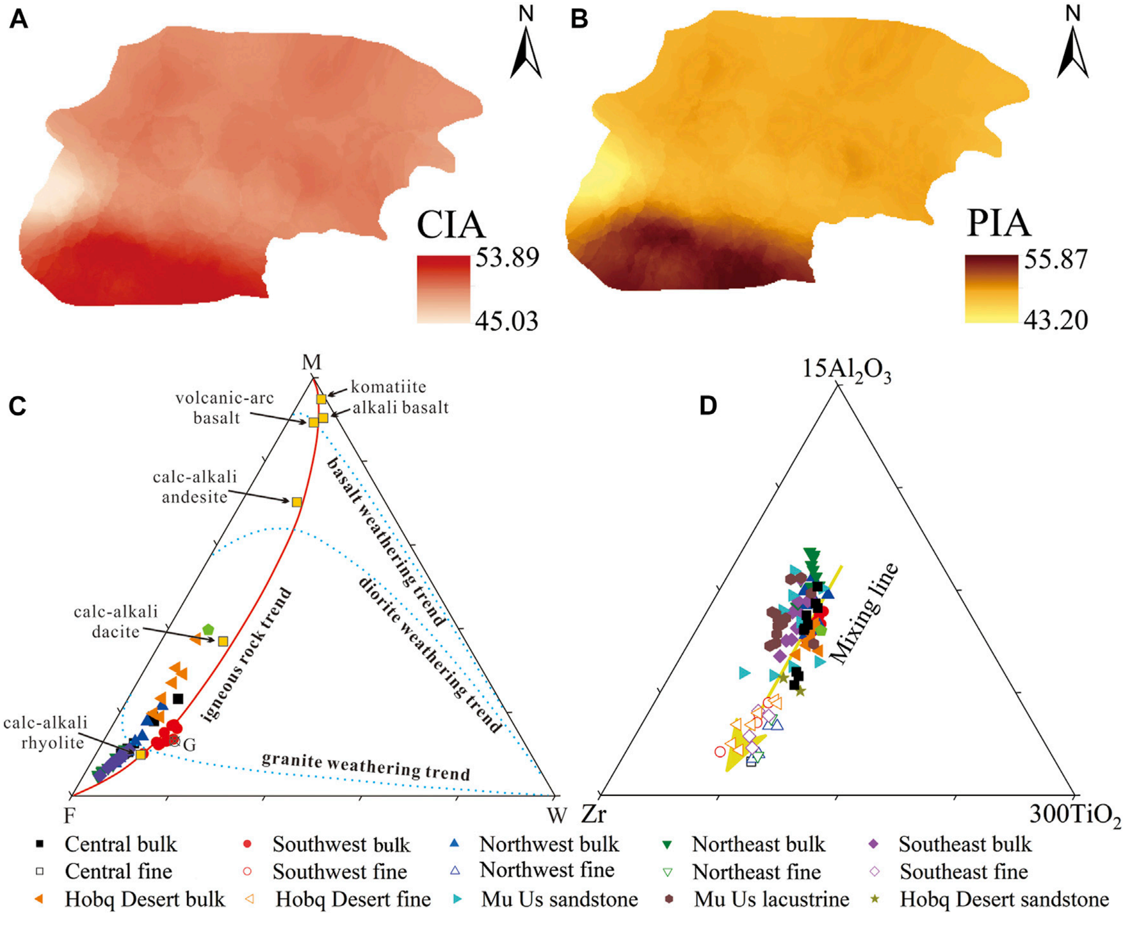

FIGURE 10 | Spatial patterns of CIA **(A)** and PIA **(B)** for sands in the Mu Us Sandy Land. Plots of MFW (Mafic-Felsic-Weathering) characterizing weathering trends **(C)** and Al-Zr-Ti diagram **(D)** for sediments in the Ordos Deserts. M and F denote the mafic and felsic rocks source, respectively, whereas the W used to identify the degree of weathering of these igneous rocks. Data of sandstone and lacustrine sediments in Mu Us and the Hobq Desert is from Liu and Yang (2018).

mafic-felsic-weathering (MFW) can also evaluate the intensity and tendency of weathering (Ohta and Arai, 2007). Compared with the diagram of A-CN-K (where A = Al_2O_3, CN = $CaO^{*}+Na_2O$, K = K_2O), the MFW diagram is more sensitive for characterizing the chemical weathering as a result of it being defined by eight major elements. A linear compositional trend extending from the M apex to the F apex can be defined by igneous rocks ranging from felsic to mafic and ultramafic (Ohta and Arai, 2007). The weathering trend of mafic rocks tends to be closer to the M-W join, which is evidently different from the weathering trend of felsic rocks that is extended from the F apex to the W apex. Samples in the Ordos Deserts near the igneous rock compositional trend (solid red line in **Figure 10C**) and close to the F-W line (dotted blue line in **Figure 10C**), but far away from W apex, indicate a low degree of chemical weathering, as illustrated by the CIA and PIA values. Overall, therefore, the CIA, PIA, and MFW values of the sediments from the Ordos Deserts all indicate a low degree of chemical weathering, with the degree of chemical weathering gradually increasing from north to south in the Mu Us (**Figure 10**).

As a significant sedimentary process, the mechanical sorting of grains occurs in the process of transport and deposition (Perri et al., 2013). As suggested by Garcia et al. (1994), the ternary diagram of Al_2O_3-TiO_2-Zr can highlight the effects of sorting-related fractionations due to Al, Ti and Zr are generally viewed as the least mobile elements in the process of chemical weathering of the major and trace elements, i.e., these elements show little or no change when they are transported from the source areas to the sedimentary areas. Generally, the ratios of TiO_2/Zr or Al_2O_3/Zr of mature sediments show a wide variation, contrary to the immature sediments that exhibit a limited variation. We can see that samples from the Ordos Deserts, especially fine fractions, show a mixing trend toward the Zr apex, indicating that the effect of sedimentary sorting and the increase in zircon results from robust sedimentary recycling (**Figure 10D**).

It is acknowledged that mechanical sorting may cause the separation of coarse and fine particles, and thus have an effect on the chemical composition of clastic sediments in the process of transport and deposition (Perri et al., 2013). However, evidence shows that mechanical sorting in obscuring sediment provenance is inefficient in fluvial and aeolian environments (Garzanti et al., 2012). In addition, chemical weathering tends to break the source rocks down to clays, which usually occurs in the source area (Sawyer, 1986). Hence, we believe that chemical composition can be used for provenance analysis in the Ordos Deserts since it is rarely affected by the above factors.

Types of Main Source Rocks of the Aeolian Sediments in the Ordos Deserts

Previous studies have illustrated that the chemical composition of sedimentary rocks is closely connected to that of their source regions (Fralick and Kronberg, 1997; Kalsbeek and Frei, 2010). Therefore, many discrimination diagrams related to the major and trace elements, and REE have been put forward to allow the discrimination of the provenance of source rocks (Hayashi et al., 1997).

According to the provenance discrimination diagram proposed by Roser and Korsch (1988), the DF1 and DF2 were calculated by the following equations:

$$\begin{aligned}DF1 = {} & 36.6038 \times TiO_2/Al_2O_3 - 12.541 \times Fe_2O_3/Al_2O_3 + 7.329 \\ & \times MgO/Al_2O_3 + 12.031 \\ & \times Na_2O/Al_2O_3 + 35.402 \times K_2O/Al_2O_3 - 6.382\end{aligned} \tag{3}$$

$$\begin{aligned}DF2 = {} & 56.500 \times TiO_2/\mathrm{Al_2O_3} - 10.879 \times Fe_2O_3/\mathrm{Al_2O_3} + 30.875 \\ & \times MgO/\mathrm{Al_2O_3} - 5.404 \\ & \times \mathrm{Na_2O}/\mathrm{Al_2O_3} + 11.112 \times \mathrm{K_2O}/\mathrm{Al_2O_3} - 3.89\end{aligned} \tag{4}$$

we conclude that the majority of aeolian sands from the Ordos Deserts plotted in the field of felsic igneous, indicating that their source rocks are mainly felsic igneous (**Figure 11A**). The elements Ti and Zr show little or no change when they are transported from the source areas to the sedimentary areas for they are generally viewed as the least mobile elements in the process of chemical weathering (Garcia et al., 1994). Therefore, the TiO_2/Zr ratio can reveal useful information on the chemical nature of parent rock. As suggested by Hayashi et al. (1997), different source rock types, i.e., felsic rocks, intermediate rocks and mafic rocks, can be distinguished by the ratio of TiO2/Zr. The TiO2/Zr ratio in felsic rocks is greater than 200, while in intermediate rocks is between 55 and 200. A TiO2/Zr ratio less than 55 is suggestive of felsic source rocks. Ratio of TiO_2/Zr for bulk particle from the Ordos Deserts tends to be less than 55, indicating they may originate from a felsic provenance (**Figure 11B**). With further analysis of the Zr to Hf ratio (**Supplementary Figure S4**), we conclude that all samples from the Ordos Deserts (average 33) are close to the ratio of the UCC (32.8), providing evidence for a crustal origin of the zircons and further demonstrating a granitoid source of the zircons in the Ordos Deserts (Batchelor and Bowden, 1985). Furthermore, the trends of weathering and the composition of the source rocks can also be determined by the triangular diagram of A-CN-K and A-CNK-FM (Nesbitt and Young, 1984) where A = Al_2O_3, CN = $CaO^{*}+Na_2O$, K = K_2O, CNK = $CaO^{*}+Na_2O+K_2O$, and FM = Fe_2O_3 + MgO (all in mol%). All samples from the Ordos Deserts when plotted in the A-CN-K diagram (in molecular proportions) show that the weathering trend shown by our data is obviously parallel to the A-CN join, but does not tend toward the K apex (**Figure 11C**). It can be concluded that the sediments in the Ordos Deserts have not been influenced by potash metasomatism and they are in the early stage of Na and Ca removal. What stands out in **Figure 11C** is that the intersection between the weathering trend line and the feldspar line (Pl-Ks) appears in the field between granite (G) and granodiorite (Gd), indicating the main source rocks of sands in the Ordos Deserts are probably granite and granodiorite (Hu and Yang, 2016). In the ternary diagram of A-CNK-FM, all samples lie between granite (G) and granodiorite (Gd) and cluster near the feldspar-FM joins, which is commonly recognized as an igneous compositional linear trend (**Figure 11D**). Therefore, these samples show a low degree of weathering and an igneous source as illustrated by the ternary diagram of A-CN-K, showing that aeolian sands in the Ordos Deserts tend to have a felsic rocks source.

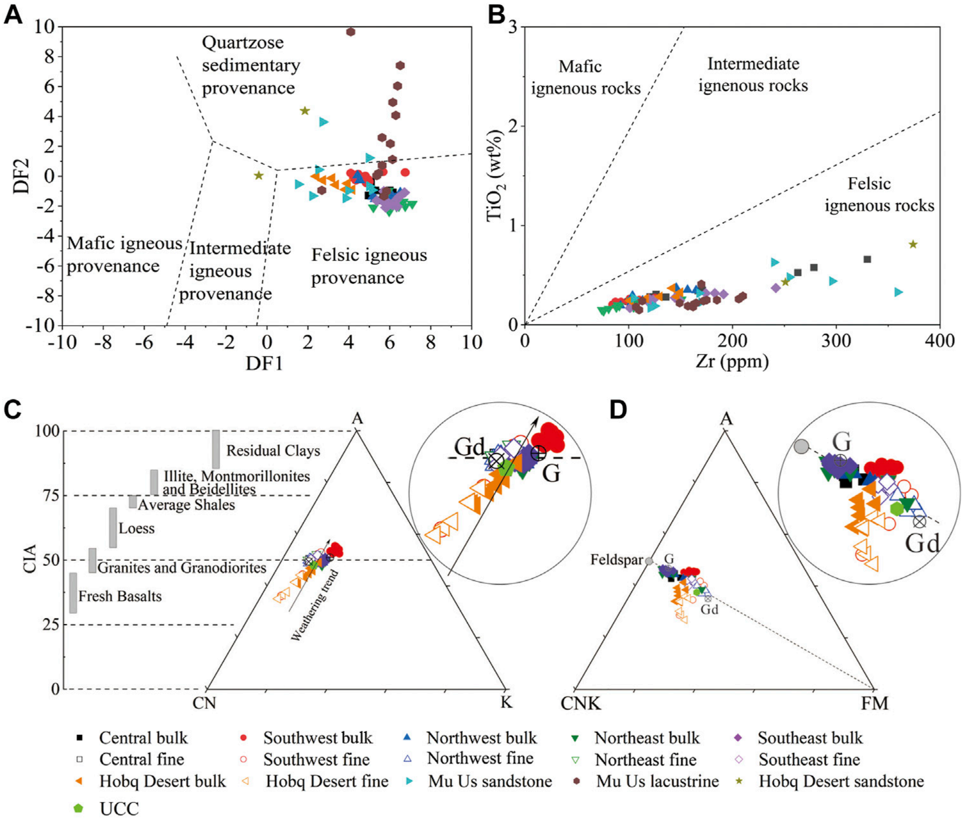

FIGURE 11 | Diagrams characterizing primitive source rock nature for the sediments in the Ordos Deserts. **(A)** DF1 vs. DF2. **(B)** Zr vs. TiO_2 plot. The triangular diagram of A-CN-K **(C)** and A-CNK-FM **(D)** for sediments in the Ordos Deserts. Gd and G represent granitoid and granite, respectively. The CIA values of fresh basalts, granitoid and granite, loess, average shales, illites, montmorillonites, beidellites, and residual clays are from Taylor and McLennan (1985) and Nesbitt and Young (1982). Data of sandstone and lacustrine sediments in Mu Us and the Hobq Desert is from Liu and Yang (2018).

Identification of the Provenance of the Ordos Deserts

The Provenance of Aeolian Sands in the Southwest Region of Mu Us and the Hobq Desert

As we discussed above, a series of geochemical diagrams show that sediments in the Ordos Desert are mainly derived from felsic rocks. Therefore, we can determine the provenance of these sediments by comparing the relevant geochemical parameters between the sediments of the Ordos Desert and its potential source rocks.

Clastic sediments, as the source of Quaternary aeolian depositions, are the result of a combination of multiple processes, such as active tectonics, glacial erosion, fluvial washout, chemical, and mechanical weathering, etc. They are then transported, with the aid of wind or rivers (Harvey, 2012; Lancaster et al., 2015). As clearly shown in **Figure 1**, the east, north, and west of the Ordos Deserts are surrounded by the Yellow River, and to the south, there is the CLP. The Langshan Mountain is an offshoot of the Yinshan Mountain range. Considering that the Helan Mountains and the Langshan Mountain are located in the upwind areas of the Ordos Deserts (**Figure 2**), we concluded that the Helan Mountains, the Langshan Mountain, and the sediments from the surrounding Yellow River might contribute tremendous amounts of material to the Ordos Deserts.

Although the Helan Mountains and the Langshan Mountain are located in the upwind areas of the Mu Us Sandy Land, their detritus could not be the source for the southwest of the Mu Us because significant differences exist in the elemental composition (**Figure 12**). It is clear that the samples from the southwest region of the Mu Us did not concentrate in the field of its potential source area, indicating the Helan Mountains and the Langshan Mountain are not the source areas for the Ordos Deserts. Thus, we conclude that the fluvial sediments from the upper Yellow River may be the potential source of the southwest region of the Mu Us for its unique geographic location (located in the upwind direction of the Ordos Plateau). The evidence presented in **Figure 12** provides support for the above-mentioned hypothesis. The geochemical characteristics of sediments from the upper reach of Yellow River are similar to the samples from the Hobq Desert and the southwest region of the Mu Us, indicating that fluvial deposits from the upper reach of the Yellow River are the primary sources for the Hobq Desert and the southwest region of the Mu Us.

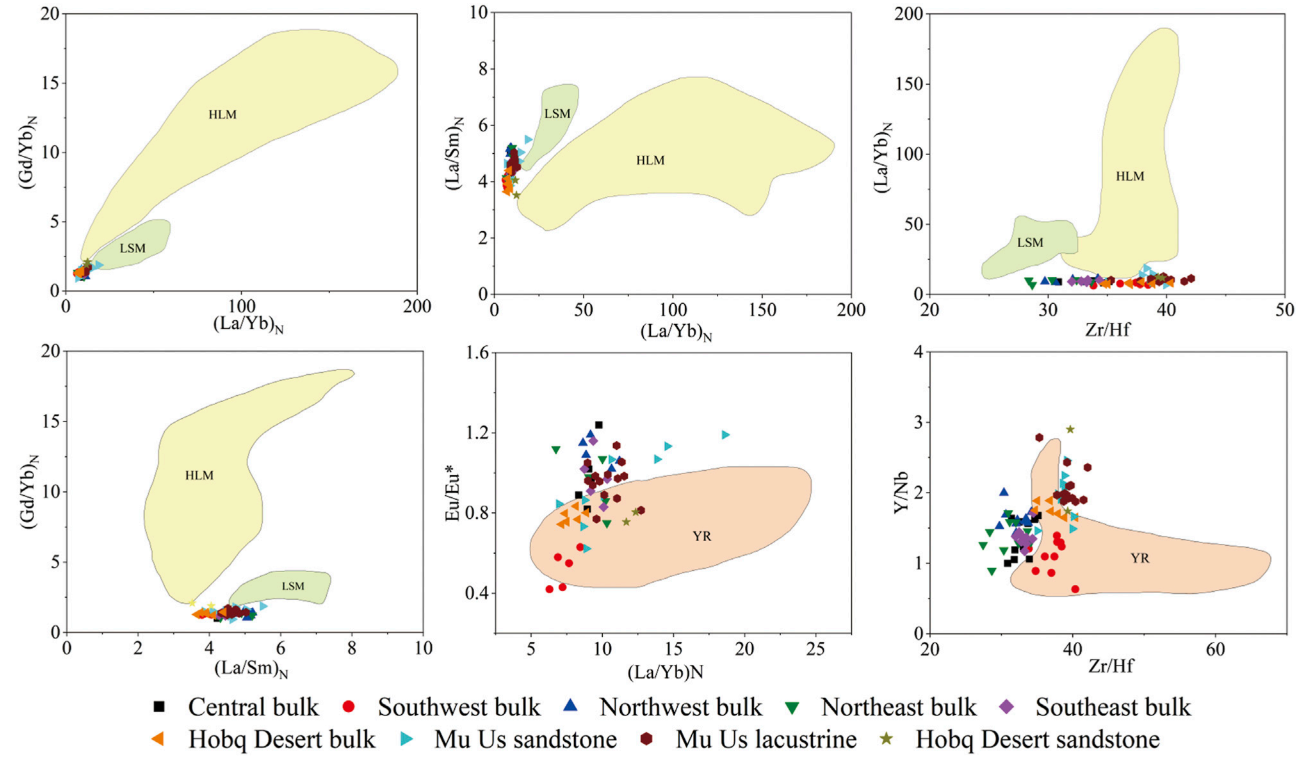

FIGURE 12 | Bivariate diagrams of geochemical elements ratios of samples between the Ordos Deserts and their potential source areas. Data from other potential areas including those from the Helan Mountains (Dan et al., 2014; Li W. et al., 2017), the Langshan Mountain (Wang et al., 2017; Wang et al., 2018), the Yellow River (data from Rao et al., 2011b; Liu et al., 2013; Pang et al., 2018). Data of sandstone and lacustrine sediments in Mu Us and the Hobq Desert is from Liu and Yang (2018). Abbreviations: HLM, the Helan Mountains; LSM, the Langshan Mountain; YR, the Yellow River.

As the second-longest river in China, the Yellow River can be divided into three reaches: the upper, middle, and lower reaches. The upper reach of the Yellow River (from the headwater to Toudaoguai) flows through the Northeastern Tibetan Plateau (NTP), CLP, and the Inner Mongolia Plateau, which is characterized by loose riverbed sediments (**Figure 1**). As the last canyon in the upper reach of the Yellow River, the average gradient of the reach above Qingtong Gorge is 0.001605, and vast valleys and inter-mountainous basins are widely distributed in this area. Therefore, rivers in this section produce tremendous sediments and transport them downstream. In contrast, the downstream of the Qingtong Gorge flows through two plains, i.e., the Yinchuan Plain and the Hetao Plain, characterized by an average gradient of 0.000159 (Wang et al., 2012). Large quantities of deposits from the upper reaches of the Qingtong Gorge and upwind deserts near the Yellow River cause the Ningxia-Inner Mongolian section to appear as a “hanging river”. Studies illustrated that the total accumulated sediments of the Ningxia-Inner Mongolian section were about 20.1×10^8 t during the period 1954–2000, which supplies abundant material for aeolian activities in the surrounding area (Ta et al., 2003). Hence, the detrital deposits brought from the Yellow River and then deposited in the reach of Ningxia-Inner Mongolian are probably the immediate material source of the Hobq Desert and the southwest region of the Mu Us.

According to previous studies, the sediment feeding the Ningxia-Inner Mongolian section originates from three major sources: the UBD, the Hobq Desert, and the tributaries between Lanzhou and Toudaoguai (the Huangshui, Daxia, Tao, Zuli, and Qinshui Rivers). Among these three major sources, the contribution from the tributaries in the upstream basin is the largest (Ta et al., 2003; Ta et al., 2008; Liu, 2015). As discussed earlier, the UBD, which was blocked by the Helan Mountains, could not provide material for the southwest region of the Mu Us, and new evidence of heavy mineral assemblages in the UBD (Zhang et al., 2020) shows differences with what was found in the Mu Us (**Figure 7**). The tributaries between Lanzhou and Toudaoguai belong to the Qilian Orogenic Belt and the western Qinling Orogenic Belt according to the geotectonic units of China (**Figure 1**). Thus, it can be concluded that the detrital deposits from these belts may be source areas for sediments of the reach between Lanzhou and Toudaoguai. However, when geochemical comparisons between the sediments from the Ordos Deserts and the felsic rocks of the potential source areas are conducted, an overlapped field was only found among the Hobq Desert, the southwest region of Mu Us, and the Qilian Orogenic Belt (**Figure 13**). Therefore, we conclud that the original source area is likely to be the Qilian Orogenic Belt.

The heavy mineral assemblages of the Hobq Desert and the southwest region of the Mu Us is consistent with that in the upper reach of the Yellow River (Pan et al., 2016), which further corroborates the previous views that there is a genetic lineage between the sediments transported from the NTP *via* the Yellow River and aeolian sediments in the southwest of the Mu Us (Stevens et al., 2013; Nie et al., 2015). The latest published data of heavy mineral assemblages in the southwest of the Mu Us has revealed that the Yellow River is a potential source for this region, which is exactly matched with the results of this article (Wang et al., 2019). Also, the quartz grains in the upper Yellow River displays typical aqueous characteristics such as V-shaped fractures and conchoidal fractures (Pan et al., 2016). Such characteristics resulting from the action of aqueous processes are also found in the southwest region of the Mu Us (**Supplementary Figure S3**), but the edges of these features tend to be smooth, indicating that the sand has been affected by aeolian activities after being transported to the sedimentary area by fluvial processes (**Figure 8**). Together, these results provide overwhelming evidence to conclude that the detrital sediments brought by the Yellow River from the NTP provide the sediments for the Hobq Desert and the southwest region of the Mu Us.

Our interpretation of the sediment source is also strongly supported by previous studies of detrital zircons from the Ordos Deserts. Stevens et al. (2013) and Nie et al. (2015) suggested that the U-Pb ages of detrital zircons from the NTP closely matched those from the western Mu Us (referred to as the southwest region in this article), indicating that substantial amounts of sediments were eroded from the NTP and, carried by the upper Yellow River, and then stored in the western Mu Us desert.

The Provenance of Aeolian Sands in Other Areas of the Mu Us

In the 1950s, Petrov (1959) suggested that the mineral characteristics of aeolian sands in the Mu Us inherited the nature of bedrock. That is, the potential source of the Mu Us is its underlying sandstone. However, this conclusion was based on samples from areas other than the southwest of the Mu Us. Zhu et al. (1980) and Wang (2013) also confirmed such conclusion through evidence from sedimentology and geomorphology. In recent years, some studies have confirmed multiple sources areas of the Mu Us by using diverse technologies, which are either from local sediments (Stevens et al., 2013; Liu and Yang, 2018; Wang et al., 2019) or from exterior sediments (Nie et al., 2015; Zhang et al., 2016; Hällberg et al., 2020), or both (Rao et al., 2011a; Rao et al., 2011b). The bedrocks of Cretaceous and Jurassic and lacustrine landforms are widely distributed in the central and western parts of the Mu Us (Wen et al., 2018), which may provide substantial detrital sediments for local aeolian activities (Zhu et al., 1980). Overlapped fields are found among the sandstone and lacustrine sediments, and the bulk and fine aeolian sands of other areas in the Mu Us (**Figure 14**), illustrating that the bedrock and lacustrine sediments are important potential sources.

Furthermore, the combined actions of tectonic activities, frost weathering, fluvial comminution, and glacial abrasion have occurred in the Gobi Altay Mts and the AP may provide vast amounts of detrital material for downwind areas, i.e., the CLP (Sun, 2002). The comparisons of elemental ratios of fine sands between the Alxa Deserts and other areas of the Mu Us reveals more or less overlapped fields among them, whereas the fine sands of the Taklimakan Desert show no overlapped fields at all (Figure 14). Although the contribution of the Altay Mountains and the Mongolian Gobi is relatively small, it is one of the significant sources for the BJD (Hu and Yang, 2016). Therefore, we can conclude that the Alxa Deserts may also be a potential source of other areas of the Mu Us, which is supported by previous studies (Zhang et al., 2016; Sun et al., 2018; Hällberg et al., 2020).

The Link Between the Ordos Plateau and Its Surrounding Areas

As the longest and most continuous dust archive known, the CLP is an ideal and critical area for understanding the wind circulation patterns in East Asia. However, substantial issues, especially the source areas and transport pathways, remain controversial. Due to the wide extend of sandy deserts, mountain belts, and playas that lie to the north and northwest of the CLP, these areas are considered as the original dust sources of the CLP (Sun, 2002; Sun et al., 2007; Che and Li, 2013; Bird et al., 2020). Investigations into these areas have used various methods, including zircon U-Pb, isotopes, magnetic susceptibility, major and trace element chemistry, and heavy-mineral assemblage analysis, with each of these techniques providing different interpretations for the dust sources of the CLP. For example, the Ordos Plateau and its upwind areas, including the BJD, the TD, and the UBD, are located in the arid areas in the north of China, and their materials are considered to be the crucial sources of loess on the CLP (Che and Li, 2013; Zhang et al., 2016; Sun et al., 2018). However, some studies have suggested that dust from the northwestern inland basins, such as the Junggar Basin, the Tarim Basin, and the Qaidam Basin, are important dust sources for the CLP (Liu et al., 1994; Pullen et al., 2011). In addition, the north Tibetan Plateau also supplies substantial materials to the CLP through westerly winds, and by the Yellow River as outlined in other studies (Stevens et al., 2013; Nie et al., 2015). Therefore, we can see that the difference and diversity of provenance in the CLP implies a far more complex relationship between the Ordos Plateau and the CLP than previously envisioned.

The Ordos Deserts (the Mu Us Sandy Land and the Hobq Desert) and the Alxa Deserts (the BJD, the TD, and the UBD) are the proximal areas upwind of the CLP (**Figure 1**). The latest geochemical data has demonstrated that Qilian Mountains of the NTP contributes more to the BJD than the AP, but this does not exclude that the AP is not the provenance area of the BJD (Hu and Yang, 2016), since Che and Li (2013) proposed that the zircons in the Alxa arid lands are mixture of those from NTP and Gobi Altay Mountains, and are better matched with zircons from the CLP. In addition, Liu et al. (2017) suggested that Alxa arid lands and the Mu Us desert were the dominant dust sources of the CLP during interglacial and interstadial warm stages, and this has been confirmed by additional studies (Sun et al., 2018; Zhang et al., 2018; Fan et al., 2019; Hällberg et al., 2020). As a consequence, our findings that the AP may be a potential source for the Mu Us is credible. It can therefore be seen from the complexity of the loess provenances that the identification of aeolian sediment provenances

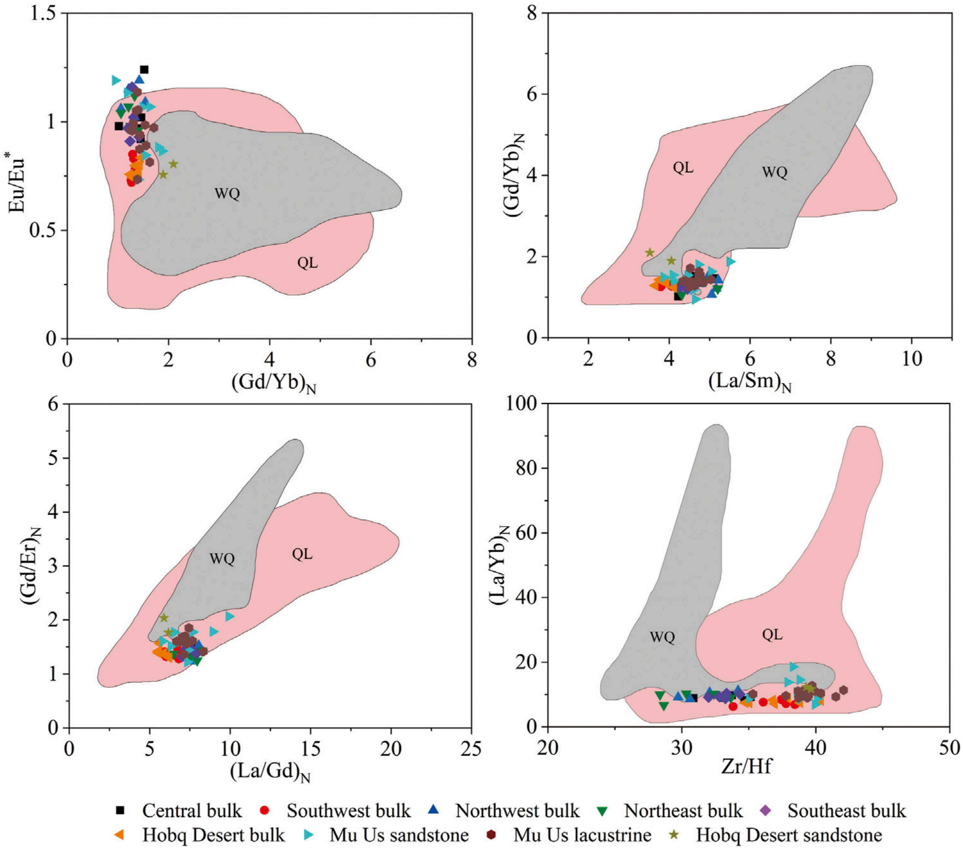

FIGURE 13 | Bivariate diagrams of geochemical elements ratios of samples between the Ordos Deserts and their potential source areas. Data from other potential source areas including those from the Qilian Orogenic Belt (Wu et al., 2010; Tung et al., 2013; Li J. et al., 2017), the western Qinling Orogenic Belt (Zhang et al., 2007; Xin, 2014). Data of sandstone and lacustrine sediments in Mu Us and the Hobq Desert is from Liu and Yang (2018). Abbreviations: QL, the Qilian Orogenic Belt; WQ, the western Qinling Orogenic Belt.

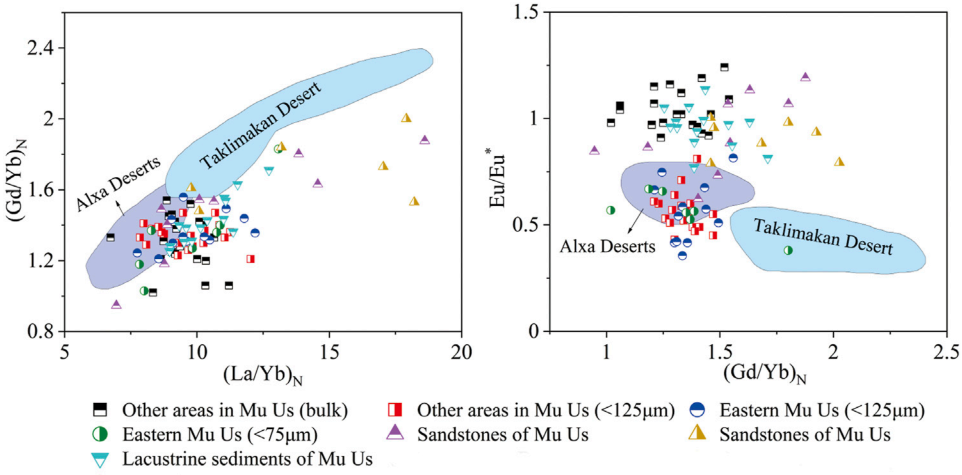

FIGURE 14 | Bivariate diagrams of geochemical elements ratios of samples from other areas of the Mu Us Sandy Land and their potential source areas. Data from other studies include those from the eastern Mu Us, sandstone, and lacustrine sediments of the Mu Us (Rao et al., 2011b; Liu and Yang, 2018), the sands of Taklimakan Desert and Alxa Deserts (Hu and Yang, 2016; Jiang and Yang, 2019).

in arid and semi-arid areas of China needs a variety of comprehensive analytical methods.

Sedimentary Process

Generally, wind is considered as the significant transport agent that contributes to the accumulation of sand in arid areas, whereas fluvial processes often play a substantial role in presorting and concentrating the products of weathering before aeolian transport takes place (Pye and Tsoar, 2009). Go to a step further, sediment transport are usually the combined results of fluvial-aeolian systems in some inland sand seas, such as the Great Sand Dunes of Colorado (Pye and Tsoar, 2009), the Namib Sand Sea (Garzanti et al., 2012), the Wahiba Sand Sea (Garzanti et al., 2013b), the Taklamakan Desert (Jiang and Yang, 2019), the Badain Jaran Desert (Hu and Yang, 2016), the Kumtagh Sand sea (Liang et al., 2020), etc. The weathering products were denudated from the NTP and then undergone long-distance fluvial transport by the Yellow River. These detrital sediments deposited in the southwest region of the Mu Us Sandy Land and then reworked by the aeolian activities, which shows better sorting, higher mineralogical maturity, and typical quartz grains characteristics in aqueous environments (**Figures 3**, **8**, **9**, Figure 8 and Figure 9). In addition, the weathering products from Altay Mountains and the Mongolian Gobi were transported by fluvial processes and reworked by wind and then deposited in other regions of the Mu Us Sandy Land through westerly winds. It is evident that the role of the fluvial system is significant and must be taken seriously for it may exert considerable control on sediment transport in a sand sea.

CONCLUSIONS

We have systematically collected aeolian sediments from Ordos Deserts, to characterize their textural, mineralogical, geochemical, sedimentological signatures and to discriminate their potential sources. The main conclusions are as follows:

1) Provenance differences exist between the southwest region of the Mu Us Sandy Land and other areas. The evidence obtained by other methods also support this conclusion, i.e., the heavy-mineral assemblages and mineralogical maturity, the content of major, trace, and REE elements, the surface micro-textures of quartz grains of southwest region in the Mu Us Sandy Land and the Hobq Desert shows similarity, but their characteristics are obviously different from other regions of the Mu Us.

2) Based on low values of CIA and PIA, as well as MFW diagrams, aeolian sediments from the Ordos Plateau have experienced a low degree of chemical weathering in the source area. The source of aeolian sands in the Ordos Deserts tend to have felsic igneous rocks detected by a series of diagrams, such as DF1 vs. DF2 diagram, Zr vs. TiO_2, as well as A-CN-K and A-CNK-FM diagrams.

3) By comparing to geochemical elements of felsic rocks in potential source areas, it is found that aeolian sands from the Hobq Desert and southwest regions of the Mu Us are mainly originated from fluvial sediments denuded from the NTP and deposited in the section of Ningxia-Inner Mongolian of the Yellow River, whereas aeolian sands from other areas of the Mu Us are a mixture of binary provenance, with one sourced from local lacustrine sediments and underlying sandstones, and another from the AP *via* northwesterly Asian winter monsoon.

4) Fluvial action often plays a significant role in the process of sediment transport and supply for sand seas, and sometimes even plays a decisive role. Therefore, for understanding modern sand seas formation and evolution, we must take the role of fluvial processes seriously.

DATA AVAILABILITY STATEMENT

The original contributions presented in the study are included in the article/**Supplementary Material**, further inquiries can be directed to the corresponding author.

AUTHOR CONTRIBUTIONS

Conceptualization: GC and ZD; Data Curation and Methodology: GC and CL; Analysis and Supervision: WS, TS, WN, and JY.

FUNDING

This study was financially supported by the National Natural Science Foundation of China (41930641) and the Fundamental Research Funds for the Central Universities (2019TS012).

SUPPLEMENTARY MATERIAL

The Supplementary Material for this article can be found online at: https://www.frontiersin.org/articles/10.3389/feart.2021.711802/full#supplementary-material

Supplement Table 1 | Results of major, trace and rare earth elements for different sediments and grain size fractions in the Mu Us Sandy Land and the Hobq Desert.

REFERENCES

Arimoto, R. (2001). Eolian Dust and Climate: Relationships to Sources, Tropospheric Chemistry, Transport and Deposition. *Earth-Science Rev.* 54, 29–42. doi:10.1016/S0012-8252(01)00040-X

Batchelor, R. A., and Bowden, P. (1985). Petrogenetic Interpretation of Granitoid Rock Series Using Multicationic Parameters. *Chem. Geology.* 48, 43–55. doi:10.1016/0009-2541(85)90034-8

Bird, A., Millar, I., Rodenburg, T., Stevens, T., Rittner, M., Vermeesch, P., et al. (2020). A Constant Chinese Loess Plateau Dust Source since the Late Miocene. *Quat. Sci. Rev.* 227, 106042. doi:10.1016/j.quascirev.2019.106042

Che, X., and Li, G. (2013). Binary Sources of Loess on the Chinese Loess Plateau Revealed by U-Pb Ages of Zircon. *Quat. Res.* 80, 545–551. doi:10.1016/j.yqres.2013.05.007

Chen, J., and Li, G. (2011). Geochemical Studies on the Source Region of Asian Dust. *Sci. China Earth Sci.* 54, 1279–1301. doi:10.1007/s11430-011-4269-z

Dan, W., Li, X.-H., Wang, Q., Wang, X.-C., Liu, Y., and Wyman, D. A. (2014). Paleoproterozoic S-type Granites in the Helanshan Complex, Khondalite Belt, North China Craton: Implications for Rapid Sediment Recycling during Slab Break-Off. *Precambrian Res.* 254, 59–72. doi:10.1016/j.precamres.2014.07.024

Dehghani, S., Moore, F., Vasiluk, L., and Hale, B. A. (2018). The Geochemical Fingerprinting of Geogenic Particles in Road Deposited Dust from Tehran metropolis, Iran: Implications for Provenance Tracking. *J. Geochem. Explor.* 190, 411–423. doi:10.1016/j.gexplo.2018.04.011

Dong, Z., Qian, G., Lv, P., and Hu, G. (2013). Investigation of the Sand Sea with the Tallest Dunes on Earth: China's Badain Jaran Sand Sea. *Earth-Science Rev.* 120, 20–39. doi:10.1016/j.earscirev.2013.02.003

Dong, Z., Hu, G., Qian, G., Lu, J., Zhang, Z., Luo, W., et al. (2017). High-Altitude Aeolian Research on the Tibetan Plateau. *Rev. Geophys.* 55, 864–901. doi:10.1002/2017RG000585

Du, S., Wu, Y., and Tan, L. (2018). Geochemical Evidence for the Provenance of Aeolian Deposits in the Qaidam Basin, Tibetan Plateau. *Aeolian Res.* 32, 60–70. doi:10.1016/j.aeolia.2018.01.005

Fan, Y., Li, Z., Wang, F., Ma, J., Mou, X., Li, X., et al. (2019). Provenance Variations of the Tengger Desert since 2.35 Ma and its Linkage with the Northern Tibetan Plateau: Evidence from U-Pb Age Spectra of Detrital Zircons. *Quat. Sci. Rev.* 223, 1–10. doi:10.1016/j.quascirev.2019.105916

Fedo, C., Nesbitt, H. W., and Young, G. (1995). Unraveling the Effects of Potassium Metasomatism in Sedimentary Rocks and Paleosols, with Implications for Paleoweathering Conditions and Provenance. *Geology* 23, 921–924. doi:10.1130/0091-7613(1995)023<0921:UTEOPM>2.3.CO;2

Folk, R. L., and Ward, W. C. (1957). Brazos River Bar [Texas]; a Study in the Significance of Grain Size Parameters. *J. Sediment. Res.* 27, 3–26. doi:10.1306/74D70646-2B21-11D7-8648000102C1865D

Fralick, P. W., and Kronberg, B. I. (1997). Geochemical Discrimination of Clastic Sedimentary Rock Sources. *Sediment. Geology.* 113, 111–124. doi:10.1016/S0037-0738(97)00049-3

Fryberger, S. G. (1979). "Dune Forms and Wind Regime," in *A Study of Global Sand Seas: United States Geological Survey Professional Paper*. Editor E. McKee (Washington: Government Printing Office).

Garcia, D., Fonteilles, M., and Moutte, J. (1994). Sedimentary Fractionations between Al, Ti, and Zr and the Genesis of Strongly Peraluminous Granites. *J. Geology.* 102, 411–422. doi:10.1086/629683

Garzanti, E., Vezzoli, G., Andò, S., Lavé, J., Attal, M., France-Lanord, C., et al. (2007). Quantifying Sand Provenance and Erosion (Marsyandi River, Nepal Himalaya). *Earth Planet. Sci. Lett.* 258, 500–515. doi:10.1016/j.epsl.2007.04.010

Garzanti, E., Andò, S., and Vezzoli, G. (2008). Settling Equivalence of Detrital Minerals and Grain-Size Dependence of Sediment Composition. *Earth Planet. Sci. Lett.* 273, 138–151. doi:10.1016/j.epsl.2008.06.020

Garzanti, E., Andò, S., Vezzoli, G., Lustrino, M., Boni, M., and Vermeesch, P. (2012). Petrology of the Namib Sand Sea: Long-Distance Transport and Compositional Variability in the Wind-Displaced Orange Delta. *Earth-Sci. Rev.* 112, 173–189. doi:10.1016/j.earscirev.2012.02.008

Garzanti, E., Padoan, M., Andò, S., Resentini, A., Vezzoli, G., and Lustrino, M. (2013a). Weathering and Relative Durability of Detrital Minerals in Equatorial Climate: Sand Petrology and Geochemistry in the East African Rift. *J. Geology.* 121, 547–580. doi:10.1086/673259

Garzanti, E., Vermeesch, P., Andò, S., Vezzoli, G., Valagussa, M., Allen, K., et al. (2013b). Provenance and Recycling of Arabian Desert Sand. *Earth-Sci. Rev.* 120, 1–19. doi:10.1016/j.earscirev.2013.01.005

Goudie, A. S., and Middleton, N. J. (2001). Saharan Dust Storms: Nature and Consequences. *Earth-Sci. Rev.* 56, 179–204. doi:10.1016/S0012-8252(01)00067-8

Goudie, A. S. (2009). Dust Storms: Recent Developments. *J. Environ. Manage.* 90, 89–94. doi:10.1016/j.jenvman.2008.07.007

Hällberg, L. P., Stevens, T., Almqvist, B., Snowball, I., Wiers, S., Költringer, C., et al. (2020). Magnetic Susceptibility Parameters as Proxies for Desert Sediment Provenance. *Aeolian Res.* 46, 100615. doi:10.1016/j.aeolia.2020.100615

Harvey, A. (2012). *Introducing Geomorphology: A Guide to Landforms and Processes*. Edinburgh: Dunedin Academic Press.

Hayashi, K.-I., Fujisawa, H., Holland, H. D., and Ohmoto, H. (1997). Geochemistry of ~1.9 Ga Sedimentary Rocks from Northeastern Labrador, Canada1.9 Ga Sedimentary Rocks from Northeastern Labrador, Canada. *Geochim. Cosmochim. Acta* 61, 4115–4137. doi:10.1016/S0016-7037(97)00214-7

Honda, M., Yabuki, S., and Shimizu, H. (2004). Geochemical and Isotopic Studies of Aeolian Sediments in China. *Sedimentology* 51, 211–230. doi:10.1111/j.1365-3091.2004.00618.x

Howari, F. M., Baghdady, A., and Goodell, P. C. (2007). Mineralogical and Gemorphological Characterization of Sand Dunes in the Eastern Part of United Arab Emirates Using Orbital Remote Sensing Integrated with Field Investigations. *Geomorphology* 83, 67–81. doi:10.1016/j.geomorph.2006.06.015

Hu, F., and Yang, X. (2016). Geochemical and Geomorphological Evidence for the Provenance of Aeolian Deposits in the Badain Jaran Desert, Northwestern China. *Quat. Sci. Rev.* 131, 179–192. doi:10.1016/j.quascirev.2015.10.039

Jiang, Q., and Yang, X. (2019). Sedimentological and Geochemical Composition of Aeolian Sediments in the Taklamakan Desert: Implications for Provenance and Sediment Supply Mechanisms. *J. Geophys. Res. Earth Surf.* 124, 1217–1237. doi:10.1029/2018JF004990

Kalsbeek, F., and Frei, R. (2010). Geochemistry of Precambrian Sedimentary Rocks Used to Solve Stratigraphical Problems: An Example from the Neoproterozoic Volta basin, Ghana. *Precambrian Res.* 176, 65–76. doi:10.1016/j.precamres.2009.10.004

Krinsley, D., and Doornkamp, J. (1973). *Atlas of Quartz Sand Surface Textures*. Cambridge: Cambridge University Press.

Lancaster, N., Baker, S., Bacon, S., and McCarley-Holder, G. (2015). Owens Lake Dune fields: Composition, Sources of Sand, and Transport Pathways. *Catena* 134, 41–49. doi:10.1016/j.catena.2015.01.003

Lancaster, N. (1989). Star Dunes. *Prog. Phys. Geogr. Earth Environ.* 13, 67–91. doi:10.1177/030913338901300105

Lancaster, N. (1995). *Geomorphology of Desert Dunes*. New York: Routledge.

Li, J., Zhou, L., Yan, J., Cui, X., and Cai, Y. (2019). Source of Aeolian Dune Sands on the Northern Margin of Qarhan Salt Lake, Qaidam Basin, NW China. *Geol. J.* 55, 3643–3653. doi:10.1002/gj.3624

Li, J., Niu, Y., Chen, S., Sun, W., Zhang, Y., Liu, Y., et al. (2017). Petrogenesis of Granitoids in the Eastern Section of the Central Qilian Block: Evidence from Geochemistry and Zircon U-Pb Geochronology. *Miner Petrol.* 111, 23–41. doi:10.1007/s00710-016-0461-3

Li, W., Yin, C., Long, X., Zhang, J., Xia, X., and Wang, L. (2017). Paleoproterozoic S-type Granites from the Helanshan Complex in Inner Mongolia: Constraints on the Provenance and the Paleoproterozoic Evolution of the Khondalite Belt, North China Craton. *Precambrian Res.* 299, 195–209. doi:10.1016/j.precamres.2017.07.0097

Liang, X., Niu, Q., Qu, J., Liu, B., Liu, B., Zhang, C., et al. (2019). Geochemical Analysis of Yardang Strata in the Dunhuang Yardang National Geopark, Northwest China, and Implications on its Palaeoenvironment, Provenance, and Potential Dynamics. *Aeolian Res.* 40, 91–104. doi:10.1016/j.aeolia.2019.06.003

Liang, A., Dong, Z., Su, Z., Qu, J., Zhang, Z., Qian, G., et al. (2020). Provenance and Transport Process for Interdune Sands in the Kumtagh Sand Sea, Northwest China. *Geomorphology* 367, 107310. doi:10.1016/j.geomorph.2020.107310

Liu, Q., and Yang, X. (2018). Geochemical Composition and Provenance of Aeolian Sands in the Ordos Deserts, Northern China. *Geomorphology* 318, 354–374. doi:10.1016/j.geomorph.2018.06.017

Liu, C.-Q., Masuda, A., Okada, A., Yabuki, S., and Fan, Z.-L. (1994). Isotope Geochemistry of Quaternary Deposits from the Arid Lands in Northern China. *Earth Planet. Sci. Lett.* 127, 25–38. doi:10.1016/0012-821X(94)90195-3

Liu, J., Lai, Z., and Liu, Y. (2013). Study on Speciation and Fractionation of Rare Earth Eleinents in Surface Sediments in Gansu, Ningxia and Inner Mongolia Sections of Yellow River. *Spectroscopy Spectral Analy.* 33, 798–803. doi:10.3964/j.issn.1000-0593(2013)03-0798-06

Liu, B., Jin, H., Sun, L., Sun, Z., and Zhao, S. (2015). Geochemical Evidence for Holocene Millennial-Scale Climatic and Environmental Changes in the South-Eastern Mu Us Desert, Northern China. *Int. J. Earth Sci. (Geol Rundsch)* 104, 1889–1900. doi:10.1007/s00531-015-1161-7

Liu, X.-J., Xiao, G., E, C., Li, X., Lai, Z., Yu, L., et al. (2017). Accumulation and Erosion of Aeolian Sediments in the Northeastern Qinghai-Tibetan Plateau and Implications for Provenance to the Chinese Loess Plateau. *J. Asian Earth Sci.* 135, 166–174. doi:10.1016/j.jseaes.2016.12.034

Liu, C. (2015). *Analysis of Sediment Source of the Inner Mongolia Section of the Yellow River*. Lan Zhou: University of Lanzhou. doi:10.2495/feem140411

Livingstone, I., Bullard, J. E., Wiggs, G. F. S., and Thomas, D. S. T. (1999). Grain-Size Variation on Dunes in the Southwest Kalahari, Southern Africa. *J. Sediment. Res.* 69, 546–552. doi:10.1306/D4268A31-2B26-11D7-8648000102C1865D10.2110/jsr.69.546

Mahaney, W. (2002). *Atlas of Sand Grain Surface Textures and Applications*. New York: Oxford University Press.

Mange, M., and Maurer, H. (1992). *Heavy Minerals in Colour*. London, UK: Chapman & Hall. doi:10.1007/978-94-011-2308-2

McLennan, S. M. (1993). Weathering and Global Denudation. *J. Geology.* 101, 295–303. doi:10.1086/648222

Molnar, P. (2004). Late Cenozoic Increase in Accumulation Rates of Terrestrial Sediment: How Might Climate Change Have Affected Erosion Rates?. *Annu. Rev. Earth Planet. Sci.* 32, 67–89. doi:10.1146/annurev.earth.32.091003.143456

Moral Cardona, J. P., Gutiérrez Mas, J. M., Sánchez Bellón, A., Domínguez-Bella, S., and Martínez López, J. (2005). Surface Textures of Heavy-mineral Grains: a New Contribution to Provenance Studies. *Sediment. Geology.* 174, 223–235. doi:10.1016/j.sedgeo.2004.12.006

Muhs, D. R., Roskin, J., Tsoar, H., Skipp, G., Budahn, J. R., Sneh, A., et al. (2013). Origin of the Sinai-Negev Erg, Egypt and Israel: Mineralogical and Geochemical Evidence for the Importance of the Nile and Sea Level History. *Quat. Sci. Rev.* 69, 28–48. doi:10.1016/j.quascirev.2013.02.022

Nesbitt, H. W., and Young, G. M. (1982). Early Proterozoic Climates and Plate Motions Inferred from Major Element Chemistry of Lutites. *Nature* 299, 715–717. doi:10.1038/299715a0

Nesbitt, H. W., and Young, G. M. (1984). Prediction of Some Weathering Trends of Plutonic and Volcanic Rocks Based on Thermodynamic and Kinetic Considerations. *Geochim. Cosmochim. Acta* 48, 1523–1534. doi:10.1016/0016-7037(84)90408-3

Nesbitt, H. W., Young, G. M., McLennan, S. M., and Keays, R. R. (1996). Effects of Chemical Weathering and Sorting on the Petrogenesis of Siliciclastic Sediments, with Implications for Provenance Studies. *J. Geology.* 104, 525–542. doi:10.1086/629850

Nie, J., Stevens, T., Rittner, M., Stockli, D., Garzanti, E., Limonta, M., et al. (2015). Loess Plateau Storage of Northeastern Tibetan Plateau-Derived Yellow River Sediment. *Nat. Commun.* 6, 8511. doi:10.1038/ncomms951110.1038/ncomms9511

Ohta, T., and Arai, H. (2007). Statistical Empirical index of Chemical Weathering in Igneous Rocks: A New Tool for Evaluating the Degree of Weathering. *Chem. Geology.* 240, 280–297. doi:10.1016/j.chemgeo.2007.02.017

Pan, B., Pang, H., Gao, H., Garzanti, E., Zou, Y., Liu, X., et al. (2016). Heavy-mineral Analysis and Provenance of Yellow River Sediments Around the China Loess Plateau. *J. Asian Earth Sci.* 127, 1–11. doi:10.1016/j.jseaes.2016.06.006

Pang, H., Pan, B., Garzanti, E., Gao, H., Zhao, X., and Chen, D. (2018). Mineralogy and Geochemistry of Modern Yellow River Sediments: Implications for Weathering and Provenance. *Chem. Geology.* 488, 76–86. doi:10.1016/j.chemgeo.2018.04.010

Perri, F., Critelli, S., Martín-Algarra, A., Martín-Martín, M., Perrone, V., Mongelli, G., et al. (2013). Triassic Redbeds in the Malaguide Complex (Betic Cordillera - Spain): Petrography, Geochemistry and Geodynamic Implications. *Earth-Sci. Rev.* 117, 1–28. doi:10.1016/j.earscirev.2012.11.002

Petrov, M. П. (1959). The mineral Element and Origin of Sand in the Ordos, East Alxa and Middle valley of Yellow River. *Acta Geogr. Sinica* 5, 1–20.

Pettijohn, F. J., Potter, P. E., and Siever, R. (1972). *Sand and Sandstone*. Berlin: Springer-Verlag.

Pullen, A., Kapp, P., McCallister, A. T., Chang, H., Gehrels, G. E., Garzione, C. N., et al. (2011). Qaidam Basin and Northern Tibetan Plateau as Dust Sources for the Chinese Loess Plateau and Paleoclimatic Implications. *Geology* 39, 1031–1034. doi:10.1130/G32296.1

Pye, K., and Tsoar, H. (2009). *Aeolian Sand and Sand Dunes*. Berlin: Springer. doi:10.1007/978-3-540-85910-9

Rao, W., Chen, J., Tan, H., Jiang, S., and Su, J. (2011a). Sr-Nd Isotopic and REE Geochemical Constraints on the Provenance of fine-grained Sands in the Ordos Deserts, north-central China. *Geomorphology* 132, 123–138. doi:10.1016/j.geomorph.2011.05.003

Rao, W., Tan, H., Jiang, S., and Chen, J. (2011b). Trace Element and REE Geochemistry of fine- and Coarse-Grained Sands in the Ordos Deserts and Links with Sediments in Surrounding Areas. *Geochemistry* 71, 155–170. doi:10.1016/j.chemer.2011.02.003

Rao, W., Chen, J., Tan, H., Weise, S. M., and Wang, Y. (2014). Nd-Sr Isotopic and REE Geochemical Compositions of Late Quaternary Deposits in the Desert-Loess Transition, north-central China: Implications for Their Provenance and Past Wind Systems. *Quat. Int.* 334-335, 197–212. doi:10.1016/j.quaint.2013.06.009

Roser, B. P., and Korsch, R. J. (1988). Provenance Signatures of sandstone-mudstone Suites Determined Using Discriminant Function Analysis of Major-Element Data. *Chem. Geology.* 67, 119–139. doi:10.1016/0009-2541(88)90010-1

Sawyer, E. W. (1986). The Influence of Source Rock Type, Chemical Weathering and Sorting on the Geochemistry of Clastic Sediments from the Quetico Metasedimentary Belt, Superior Province, Canada. *Chem. Geology.* 55, 77–95. doi:10.1016/0009-2541(86)90129-4

Shang, K., Dong, G., Wang, S., and Yang, D. (2001). Response of Climatic Change in North China Deserted Region to the Warming of the Earth. *J. Desert Res.* 21, 387–392. doi:10.3321/j.issn:1000-694X.2001.04.012

Stevens, T., Carter, A., Watson, T. P., Vermeesch, P., Andò, S., Bird, A. F., et al. (2013). Genetic Linkage between the Yellow River, the Mu Us Desert and the Chinese Loess Plateau. *Quat. Sci. Rev.* 78, 355–368. doi:10.1016/j.quascirev.2012.11.032

Sun, J., Li, S.-H., Muhs, D. R., and Li, B. (2007). Loess Sedimentation in Tibet: Provenance, Processes, and Link with Quaternary Glaciations. *Quat. Sci. Rev.* 26, 2265–2280. doi:10.1016/j.quascirev.2007.05.003

Sun, Y., Chen, H., Tada, R., Weiss, D., Lin, M., Toyoda, S., et al. (2013). ESR Signal Intensity and Crystallinity of Quartz from Gobi and sandy Deserts in East Asia and Implication for Tracing Asian Dust Provenance. *Geochem. Geophys. Geosyst.* 14, 2615–2627. doi:10.1002/ggge.20162

Sun, J., Ding, Z., Xia, X., Sun, M., and Windley, B. F. (2018). Detrital Zircon Evidence for the Ternary Sources of the Chinese Loess Plateau. *J. Asian Earth Sci.* 155, 21–34. doi:10.1016/j.jseaes.2017.10.012

Sun, Y., Yan, Y., Nie, J., Li, G., Shi, Z., Qiang, X., et al. (2020). Source-to-sink Fluctuations of Asian Aeolian Deposits since the Late Oligocene. *Earth-Sci. Rev.* 200, 102963. doi:10.1016/j.earscirev.2019.102963

Sun, J. (2002). Provenance of Loess Material and Formation of Loess Deposits on the Chinese Loess Plateau. *Earth Planet. Sci. Lett.* 203, 845–859. doi:10.1016/S0012-821X(02)00921-4

Ta, W., Yang, G., Qu, J., Wang, T., and Dai, F. (2003). The Effect of the Coarse Aeolian Sand on Siltation of the Inner Mongolian Reach of the Yellow River. *Env Geol.* 43, 493–502. doi:10.1007/s00254-002-0666-0

Ta, W., Xiao, H., and Dong, Z. (2008). Long-term Morphodynamic Changes of a Desert Reach of the Yellow River Following Upstream Large Reservoirs' Operation. *Geomorphology* 97, 249–259. doi:10.1016/j.geomorph.2007.08.008

Taylor, S. R., and McLennan, S. M. (1985). *The Continental Crust: Its Composition and Evolution*. United States: Blackwell Press.

Tung, K.-a., Yang, H.-y., Liu, D.-y., Zhang, J.-x., Yang, H.-j., Shau, Y.-h., et al. (2013). The Neoproterozoic Granitoids from the Qilian Block, NW China: Evidence for a Link between the Qilian and South China Blocks. *Precambrian Res.* 235, 163–189. doi:10.1016/j.precamres.2013.06.016

Vos, K., Vandenberghe, N., and Elsen, J. (2014). Surface Textural Analysis of Quartz Grains by Scanning Electron Microscopy (SEM): From Sample Preparation to Environmental Interpretation. *Earth-Sci. Rev.* 128, 93–104. doi:10.1016/j.earscirev.2013.10.013

Wang, S., Yan, Y., and Li, Y. (2012). Spatial and Temporal Variations of Suspended Sediment Deposition in the Alluvial Reach of the Upper Yellow River from 1952 to 2007. *Catena* 92, 30–37. doi:10.1016/j.catena.2011.11.0110.1016/j.catena.2011.11.012

Wang, W., Teng, X., Liu, F., Teng, F., Guo, S., He, P., et al. (2017). Zircon U-Pb Chronology and Geochemical Characteristics of the Wuheertu Granite Mass in the Langshan, Inner Mongolia. *J. Geomech.* 23, 382–396. doi:10.3969/j.issn.1006-6616.2017.03.006

Wang, W., Teng, X., Liu, Y., Teng, F., Guo, S., He, P., et al. (2018). Geochemical Characteristic, LA-ICP-MS Zircon U-Pb Dating and Hf Isotopic Compositions of the Haorigeshan Monzogranite in the Langshan Region, Inner Mongolia. *Acta Geol. Sinica* 92, 2227–2247. doi:10.3969/j.issn.0001-5717.2018.11.004

Wang, Z., Wu, Y., Tan, L., Fu, T., Wen, Y., and Li, D. (2019). Provenance Studies of Aeolian Sand in Mu Us Desert Based on Heavy-mineral Analysis. *Aeolian Res.* 40, 15–22. doi:10.1016/j.aeolia.2019.05.003

Wang, T. (2013). *Deserts and Aeolian Desertification in China*. Hebei: Science and Technology Press. doi:10.2495/isme132472

Wen, Y., Hao, C., Tan, L., Li, D., Fu, T., Zhang, M., et al. (2018). Compilation of Geomorphic Map of the Mu Us Desert. *J. Desert Res.* 38, 508–515. doi:10.7522/j.issn.1000-694X.2017.00030

Wu, C., Xu, X., Gao, Q., Li, X., Lei, M., Gao, Y., et al. (2010). Early Palaezoic Grranitoid Magmatism and Tetonic Evolution in North Qilian, NW China. *Acta Petrologica Sinica* 26, 1027–1044.

Xin, Y. (2014). *Geochemical Features of Granites and Tectonic Significance in the North of West Qinling Orogenic belt*. Hu Nan: Central South University.

Yang, X., Zhu, B., and White, P. D. (2007). Provenance of Aeolian Sediment in the Taklamakan Desert of Western China, Inferred from REE and Major-Elemental Data. *Quat. Int.* 175, 71–85. doi:10.1016/j.quaint.2007.03.005

Zhang, Z., and Dong, Z. (2015). Grain Size Characteristics in the Hexi Corridor Desert. *Aeolian Res.* 18, 55–67. doi:10.1016/j.aeolia.2015.05.006

Zhang, H., Jin, L., Zhang, L., Nigel, H., Zhou, L., Hu, S., et al. (2007). Geochemical and Pb-Sr-Nd Isotopic Compositions of Granitoids from Western Qinling belt: Constraints on Basement Nature and Tectonic Affinity. *Sci. China Ser. D* 50, 184–196. doi:10.1007/s11430-007-2015-3

Zhang, Z., Dong, Z., and Li, J. (2015). Grain-size Characteristics of Dune Networks in china's Tengger Desert. *Geografiska Annaler: Ser. A, Phys. Geogr.* 97, 681–693. doi:10.1111/geoa.12108

Zhang, H., Lu, H., Xu, X., Liu, X., Yang, T., Stevens, T., et al. (2016). Quantitative Estimation of the Contribution of Dust Sources to Chinese Loess Using Detrital Zircon U-Pb Age Patterns. *J. Geophys. Res. Earth Surf.* 121, 2085–2099. doi:10.1002/2016JF003936

Zhang, W., Zhao, J.-x., Chen, J., Ji, J., and Liu, L. (2018). Binary Sources of Chinese Loess as Revealed by Trace and REE Element Ratios. *J. Asian Earth Sci.* 166, 80–88. doi:10.1016/j.jseaes.2018.07.017

Zhang, C., Li, Z., Chen, Q., Dong, S., Yu, X., and Yu, Q. (2020). Provenance of Eolian Sands in the Ulan Buh Desert, Northwestern China, Revealed by Heavy mineral Assemblages. *Catena* 193, 104624. doi:10.1016/j.catena.2020.104624

Zhu, Z., Wu, Z., Liu, S., and Di, X. (1980). *An Outline of Chinese Deserts*. Beijing: Science Press.

Zhu, L.-m., Zhang, G.-w., Chen, Y.-j., Ding, Z.-j., Guo, B., Wang, F., et al. (2011). Zircon U-Pb Ages and Geochemistry of the Wenquan Mo-Bearing Granitioids in West Qinling, China: Constraints on the Geodynamic Setting for the Newly Discovered Wenquan Mo deposit. *Ore Geology. Rev.* 39, 46–62. doi:10.1016/j.oregeorev.2010.10.001

Conflict of Interest: The authors declare that the research was conducted in the absence of any commercial or financial relationships that could be construed as a potential conflict of interest.

Copyright © 2021 Chen, Dong, Li, Shi, Shao, Nan and Yang. This is an open-access article distributed under the terms of the Creative Commons Attribution License (CC BY). The use, distribution or reproduction in other forums is permitted, provided the original author(s) and the copyright owner(s) are credited and that the original publication in this journal is cited, in accordance with accepted academic practice. No use, distribution or reproduction is permitted which does not comply with these terms.

frontiers in Earth Science

ORIGINAL RESEARCH
published: 22 July 2021
doi: 10.3389/feart.2021.714936

Spatial Patterns of Organic and Inorganic Carbon in Lake Qinghai Surficial Sediments and Carbon Burial Estimation

Xi Chen[1,2], Xianqiang Meng[2]*, Yinxian Song[3]*, Bin Zhang[4], Zhiwei Wan[1], Bingqing Zhou[4] and Enlou Zhang[2]

[1]Key Laboratory of Poyang Lake Wetland and Watershed Research Ministry of Education, School of Geography and Environment, Jiangxi Normal University, Nanchang, China, [2]State Key Laboratory of Lake Science and Environment, Nanjing Institute of Geography and Limnology, Chinese Academy of Sciences, Nanjing, China, [3]Department of Geosciences, Faculty of Land Resource Engineering, Kunming Univerity of Science and Technology, Kunming, China, [4]Geological Exploration Technology Institute of Jiangsu Province, Nanjing, China

OPEN ACCESS

Edited by:
Zhuolun Li,
Lanzhou University, China

Reviewed by:
Yu Li,
Lanzhou University, China
Xingqi Liu,
Capital Normal University, China

***Correspondence:**
Xianqiang Meng
xqmeng@niglas.ac.cn
Yinxian Song
songyinxian@gmail.com

Specialty section:
This article was submitted to Quaternary Science, Geomorphology and Paleoenvironment, a section of the journal Frontiers in Earth Science

Received: 26 May 2021
Accepted: 21 June 2021
Published: 22 July 2021

Citation:
Chen X, Meng X, Song Y, Zhang B, Wan Z, Zhou B and Zhang E (2021) Spatial Patterns of Organic and Inorganic Carbon in Lake Qinghai Surficial Sediments and Carbon Burial Estimation. Front. Earth Sci. 9:714936. doi: 10.3389/feart.2021.714936

Lake carbon burial is of vital significance in global carbon cycle and carbon budget, particularly in the large deepwater lakes. However, carbon burial in large deepwater lakes is hard to estimate due to the difficulty in obtaining high spatial-resolution samples. In this study, we investigated distributions of total organic carbon (TOC) and inorganic carbon (TIC), two main carbon components in lake sediments, based on dozens of surficial sedimentary samples ($n = 26$) covering whole Lake Qinghai, the largest saline lake in China. The results showed that the TOC content, with a range of 1.4–4.8%, was significantly higher in the lake area near the northern lakeshore where human activities are concentrated and lower in the lake areas near the Buha River mouth and the eastern lake area. In contrast, the TIC content, ranging from 1.5 to 3.8%, increased from the northwestern and southeastern lake areas toward the lake center, and mainly depended on hydro-chemical and hydraulic characteristics. The inorganic carbon burial (47.77 ± 19.73 Gg C yr^{-1}) was approximately equal to organic carbon burial (47.50 ± 22.68 Gg C yr^{-1}) and accounted for about 50% of the total carbon burial (95.27 ± 37.74 Gg C yr^{-1}), suggesting that saline lakes constitute a large inorganic carbon pool in addition to an organic carbon pool. Because of saline water body type in arid and semiarid regions and alpine Qinghai–Tibet Plateau, lakes in these regions have huge inorganic carbon burial potential and important contributions to the global carbon budget.

Keywords: Lake Qinghai, organic carbon, inorganic carbon, carbon cycle, carbon burial

INTRODUCTION

Because of the rich organism community and/or lots of carbonate precipitation as well as the ideal burial environment, lake sediments have a great burial capacity of atmospheric carbon (Einsele et al., 2001). Organic carbon (OC) burial was estimated to be 1.25 Mt yr^{-1} in European lakes (Kastowski et al., 2011) and ~12.6 Tg C yr^{-1} in lakes/ponds of the conterminous United States (Clow et al., 2015). It was concluded that organic carbon accumulation in global lakes displayed a rate (42 Tg yr^{-1}) that approached half of that in the ocean (100 Tg yr^{-1}) (Dean and Gorham, 1998). Therefore, lakes play an important role in the carbon cycle and budget and are given considerable official and scientific concerns.

Carbon in lake sediments mainly comprises OC and inorganic carbon (IC). The former stems from terrestrial organism residues derived from watershed and aquatic organism residues derived from lake (Meyers and Ishiwatari, 1993), while the latter consists of lithogenic carbonate inputted by runoff, wind, and endogenic carbonate (including biogenic carbonate) (Anas et al., 2015). Little attention, however, was paid to IC burial in lake sediments. In fact, the inorganic carbon content in sediments of many hydrologically closed temperate lakes was comparable to or even higher than that of organic carbon (Einsele et al., 2001; Gyawali et al., 2019; Chen et al., 2021). Particularly, inorganic carbon could be an essential component in carbon burial in those hydrologically closed lakes.

Previous studies on carbon burial in large lakes mainly focused on several specific sites and lack high-resolution systematic investigation. However, spatial patterns of organic and inorganic carbon in sediments of large deepwater lake and related controlling factors remain complicated and rarely studied on account of the higher cost of high spatial-resolution sampling. Since sedimentary organic and inorganic carbon tend to be susceptible to plenty of drivers, such as carbon sources, climate, sedimentary environments, and human activities (i.e. land use and nutrient supply) (Tenzer et al., 1997; Rumolo et al., 2011; Yu et al., 2015; He et al., 2021), estimation of carbon burial in a large lake based merely on several sites is questionable. High-resolution sampling in a large lake is advantageous to eliminate the inaccuracy of several sites and identify the impacts of human activities and natural conditions on carbon as an implication for environmental restoration and construction surrounding the lake.

Lake Qinghai is located in the northeastern Tibetan Plateau and is the largest saline lake in China. It has been endowed with an enormous scientific and social value for its unique location and high climatic sensitivity (Qin and Huang, 1998; Ji et al., 2005; Henderson et al., 2007; An et al., 2012). Both organic and inorganic carbon contents in sediments were considered to be indicators of environmental and climatic changes, and thus were used for paleoclimatic reconstruction on different timescales (Yu and Kelts, 2002; An et al., 2012; Liu et al., 2014b). In the context of global warming and intensified human activity, as a geographical and paleoclimatic archive at the third pole, the carbon sequestration capacity of Lake Qinghai also needs to be evaluated based on a systematic investigation of the carbon content. For Lake Qinghai, Einsele et al. (2001) and Xu et al. (2013) evaluated carbon burial of its Holocene sediments and modern sediments, respectively. However, the distribution of the sedimentation rate (Xu et al., 2010), eutrophic elements (Chen et al., 2012), and the modern sedimentation process (Shang et al., 2009) in Lake Qinghai surficial sediments showed significant spatial variability. Similarly, to a certain degree, as human-induced changes occur manifestly around and in the lake (Zhang et al., 2013; Luo et al., 2017; Lian et al., 2019), carbon in the sediments of Lake Qinghai could also exhibit spatial heterogeneity due to non-anthropogenic and anthropogenic factors, which is currently unknown.

Here, high-resolution surficial sediments (n = 26) uniformly covering the whole Lake Qinghai were collected. Based on total organic carbon (TOC), total inorganic carbon (TIC), total nitrogen content (TN), organic matter C/N atomic ratio, mineralogical methods, and regional socioeconomic statistics, this study aims to 1) explore the source of OC and IC in Lake Qinghai sediments, 2) investigate the contributions of natural and anthropogenic factors to the spatial variation of TOC and TIC across the lake basin, and 3) further estimate the carbon burial in Lake Qinghai.

MATERIALS AND METHODS

Lake Qinghai (99°36′-100°47′E, 36°32′-37°15′N, ~3,193.8 m a s^{1}.) (**Figure 1**), located in the temperate continental climate and arid/semiarid region in the northeastern Tibetan Plateau, is the largest saline lake in China (lake size: ~4,400 km^2, average water depth: ~21 m, maximum depth of 31.4 m) (Liu et al., 2003; Dong et al., 2018). The mean annual air temperature and precipitation are 1.2 °C and 336.6 mm, respectively (Wang et al., 1998). Strong westerlies and/or northwesterly winds prevail over Lake Qinghai during all seasons, except summer (Dong et al., 2018). The Buha River, Shaliu River, Haergai River, Quanji River, and Heima River are the main tributaries of the lake; of which, the Buha River on the west is the largest with a runoff contribution of ~46.9% (Chang et al., 2017). Catchment zonal soil mainly consists of chestnut soil; the bedrock of the lake's surrounding is dominated by metamorphic rocks and acidic magmatic rocks, and there is limited limestone in the west (Xu et al., 2013). Main vegetation comprises temperate steppe, shrub, alpine grassland, and meadow (Shang et al., 2009).

As an important tourist attraction and one of the national nature reserves, Lake Qinghai is significantly affected by humans with environmental damage or/and ecological construction in recent years. There are four counties in the Lake Qinghai Basin: Tianjun County where the Buha River flows through, Gonghe County in the area south of Lake Qinghai, Gangcha County near to the Shaliu River, and Haiyan County in the area north of the lake where industrial and agricultural activities are concentrated. The Lake Qinghai Basin is an important livestock base, within which there are five large state-owned farms and ranches. Tourism around the lake is under rapid development. Besides, various ecosystem protection and construction projects covering the Lake Qinghai Basin are being implemented, such as degraded grassland management projects, desertification land control projects, and wetland protection projects.

Twenty-six surficial sediment samples (top of 1 cm) covering the whole lake were altogether collected from Lake Qinghai with Kajak gravity corer in September 2017, and 3 surficial soil and 6 fluvial sediment samples from the drainage area were sampled in September 2019 (**Figure 1** and **Table 1**). We measured the volume of each sample before lyophilization and weighed each dry sample after lyophilization for 26 lake sediments.

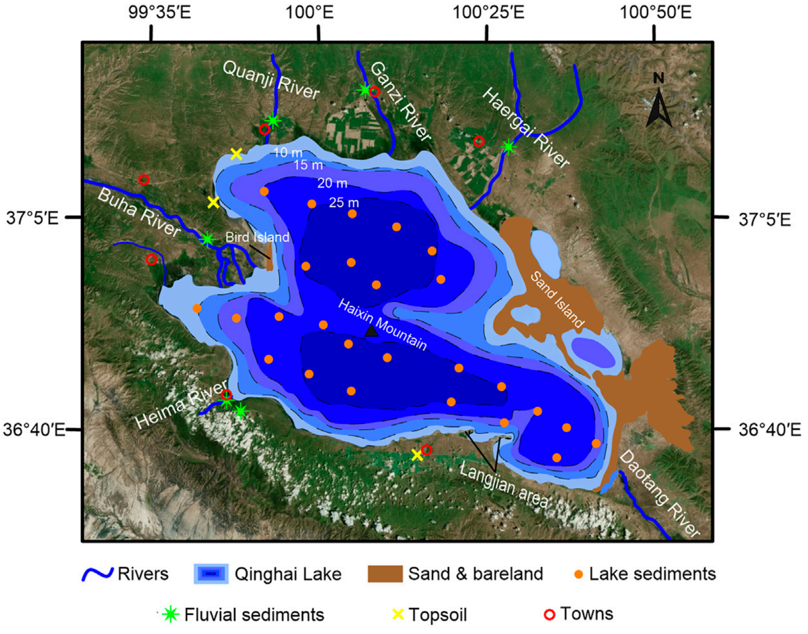

FIGURE 1 | Lake Qinghai Basin and sampling sites.

Total organic carbon, total nitrogen content, total inorganic carbon, and mineral compositions in collected samples were measured. For TOC and TN measurements, 0.5 g of each sample was weighed into a 50 ml centrifuge tube, pretreated with HCl (10%) and heated in a water bath (60°C) for 3 h, rested for 12 h to remove the carbonates, and then rinsed with distilled water repeatedly after 3–4 times centrifugation (5,000 r/min). Finally, samples were freeze-dried and ground, and measured on the EA 3000 elemental analysis instrument at the State Key Laboratory of Lakes and Environment, Nanjing Institute of Geography and Limnology, Chinese Academy of Sciences. Measured TOC was the organic carbon content of the carbonate-free sample. Thus, the TOC content in the bulk sample should be calibrated as $\mathrm{TOC}_{\mathrm{measured}}$ × (1- carbonate content).

For TIC measurement, Fourier transform infrared spectrometry (FTIR) was used to quantify the carbonate content of each sample following the specific steps of Ji et al. (2009) and Meng et al. (2015) because this technique has high precision, small measurement error, simply pretreatment, and high measurement efficiency (Ji et al., 2009). Samples were ground and dried at 70 °C and placed in a sample cup for analyzing in a Thermo Nicolet 6700 FTIR with a diffuse reflectance attachment from wavenumbers 4000–400 cm^{-1} at Nanjing University. The absorption peaks at 2,513–2,522 cm^{-1} representing total carbonate was measured for its reflectance band area (**Figure 2A**). The quantitative equation of the total carbonate content, namely, $y = 0.000181x+0.0237$ (y: total carbonate content, x: band area at 2,513 cm^{-1}; $R^2 = 0.988$, RMSE = 0.0197), was constructed by adding a certain amount of pure carbonate into the carbonate-free matrix that was made by thoroughly removing the carbonate of Lake Qinghai sediments using HCl. The detection limit of carbonate in sediments was 0.1%, and the measuring error of this method was lower than 2% (Meng et al. (2015). Concerning the content of authigenic carbonate relative to the total carbonate content (TCC), we decided to use the calculation results of Xu et al. (2010) that authigenic carbonates accounted for approximately 95% of the total carbonates in Lake Qinghai sediments. Therefore, the TIC content of Lake Qinghai sediments could be estimated with TCC×95% × 12/100. To further determine mineralogical types of carbonates in Lake Qinghai sediments, surrounding soils, and fluvial sediments, the X-ray diffraction analysis (XRD) was also performed on selected representative samples with the Panalytical multifunctional X-ray powder diffractometer at the State Key Laboratory of Lakes and Environment, Nanjing Institute of Geography and Limnology, Chinese Academy of Sciences.

The organic carbon burial rate (OCBR) and the inorganic carbon burial rate (ICBR) were calculated based on TOC, TIC, sedimentation rate (SR), and dry bulk density (DBD), according to Dean and Gorham. (1998):

$$\mathrm{OCBR} = \mathrm{TOC} \times \mathrm{SR} \times \mathrm{DBD}, \tag{1}$$

$$\mathrm{ICBR} = \mathrm{TIC} \times \mathrm{SR} \times \mathrm{DBD}, \tag{2}$$

$$\mathrm{DBD} = M_{\mathrm{d}}/V, \tag{3}$$

where M_{d} = weight of dry sample and V = volume of wet bulk sample (measured before lyophilization). Sedimentation rates of 26 sites were roughly evaluated by Kriging interpolation with the sedimentation rates reported in the study by Xu et al. (2010). As an alpine deepwater lake, previous studies found that Lake Qinghai has stable sedimentary environment in each site, showing a relatively low and stable modern deposition rate in

TABLE 1 | Location, water depth, total organic carbon content (TOC), total nitrogen content (TN), total inorganic carbon content (TIC), and atomic C/N ratio of surficial samples.

Samples	Longitude(E)	Latitude (N)	Water depth (m)	TOC (%)	TN (%)	TIC (%)	C/N
QHH-1[a]	99.880361	37.132358	20.1	3.5	0.42	1.5	9.3
QHH-2[a]	99.993894	37.107975	26.6	4.8	0.70	2.8	7.5
QHH-3[a]	100.096543	37.087114	28	3.4	0.32	3.0	12.55
QHH-4[a]	100.203045	37.063362	27.5	3.5	0.48	3.1	8.5
QHH-5[a]	100.289308	37.01611	26.7	4.6	0.55	3.3	9.8
QHH-6[a]	100.311155	36.960505	26.3	2.1	0.19	3.3	12.42
QHH-8[a]	100.153319	36.949207	27.3	2.6	0.39	3.8	7.9
QHH-9[a]	100.09104	36.992795	28	4.1	0.53	3.0	9.0
QHH-10[a]	99.981435	36.986548	27.4	2.7	0.37	2.9	8.5
QHH-11[a]	99.711628	36.905486	12	1.7	0.21	2.7	9.8
QHH-12[a]	99.809412	36.884322	18.6	1.6	0.20	3.1	9.4
QHH-13[a]	99.913588	36.887739	24.7	2.7	0.48	3.0	6.5
QHH-14[a]	100.021982	36.871759	27.8	3.3	0.50	3.5	7.8
QHH-15[a]	100.083171	36.836496	28	4.3	0.72	3.3	6.9
QHH-16[a]	100.178293	36.808335	27.7	3.3	0.40	3.4	9.4
QHH-17[a]	100.090199	36.742439	26.6	1.4	0.14	3.3	11.76
QHH-18[a]	99.986649	36.776789	25.1	4.7	0.53	3.1	10.4
QHH-19[a]	99.888801	36.803265	21.9	3.5	0.56	2.8	7.2
QHH-20[a]	100.692207	36.640219	24.5	1.9	0.33	2.8	6.8
QHH-21[a]	100.619016	36.670668	26.5	3.1	0.38	3.4	9.6
QHH-22[a]	100.546961	36.703588	25.2	1.9	0.28	3.1	8.1
QHH-23[a]	100.460871	36.75204	27	3.5	0.48	3.2	8.5
QHH-24[a]	100.356369	36.786932	27.5	3.9	0.56	3.1	8.0
QHH-25[a]	100.335989	36.720764	27	4.0	0.55	2.8	8.4
QHH-26[a]	100.468641	36.677763	23.5	1.8	0.22	2.7	9.3
QHH-27[a]	100.595719	36.611497	26	3.3	0.50	2.9	7.6
QHH19-2[b]	100.253677	36.617973	—	—	—	2.7	—
QHH19-6[b]	99.755945	37.109203	—	—	—	1.2	—
QHH19-7[b]	99.810662	37.204389	—	—	—	2.8	—
QHH19-3[c]	99.81916	36.705414	—	—	—	0.63	—
QHH19-4[c]	99.784312	36.722319	—	—	—	0.68	—
QHH19-5[c]	99.736698	37.03716	—	—	—	3.7	—
QHH19-8[c]	99.899197	37.268998	—	—	—	0.84	—
QHH19-9[c]	100.126498	37.329748	—	—	—	0.78	—
QHH19-10[c]	100.477309	37.218026	—	—	—	2.4	—

[a] *Lake sediments.*

[b] *Soils.*

[c] *Fluvial sediments.*

recent decades (Zhang et al., 2009; Fu et al., 2015). Modern SR data of Lake Qinghai reported by Xu et al. (2010) were derived from 11 cores covering the whole Lake Qinghai. Therefore, we believe the SR data of Xu et al. (2010) were relatively reliable.

RESULTS

The distribution of TOC showed great spatial difference in Lake Qinghai surficial sediments ranging from 1.4 to 4.8% (with average of 3.1%, *CV* = 0.32) (**Figure 3A** and **Table 1**). The western and eastern lake areas had a low TOC value (mean value of 2.4%), while a high content (mean value of 3.7%) occurred in the northern and central areas. (**Figure 3A**). Specifically, there were eight prominent low-content sites (i.e., QHH-11 (1.7%) and QHH-12 (1.6%) near the Buha river mouth, QHH-17 (1.4%) in the southern lake area, and QHH-20 (1.9%), QHH-22 (1.9%), and QHH-26 (1.8%) in the eastern lake area) and seven relative higher content sites (i.e., QHH-2 (4.8%), QHH-5 (4.6%), QHH-9 (4.1%), QHH-15 (4.3%), QHH-18 (4.7%), QHH-24 (3.9%), and QHH-25 (4.0%)) (**Table 1**). TN ranged in concentration from 0.14 to 0.72% (**Table 1**). Atomic C/N ratios varied but were all between 6.5 and 12.5 (mean 8.9) (**Table 1**; **Figure 4A**).

The range of TIC content was 1.5–3.8% in Lake Qinghai sediments (3.0% on average, *CV* = 0.14) (**Table 1**). The spatial distribution of TIC content is shown in **Figure 3B**. There was a general increasing trend of TIC content from the northwestern and southeastern lake areas to the central lake area, with the lowest value (1.5%) near the northwestern shore of the lake (QHH-1) and the highest in the central QHH-8 (3.8%) (**Figure 3B** and **Table 1**).

DISCUSSION

Source of Organic and Inorganic Carbon

The carbon source in lake sediments is related to the budget of carbon burial. There was a strong linear relationship between

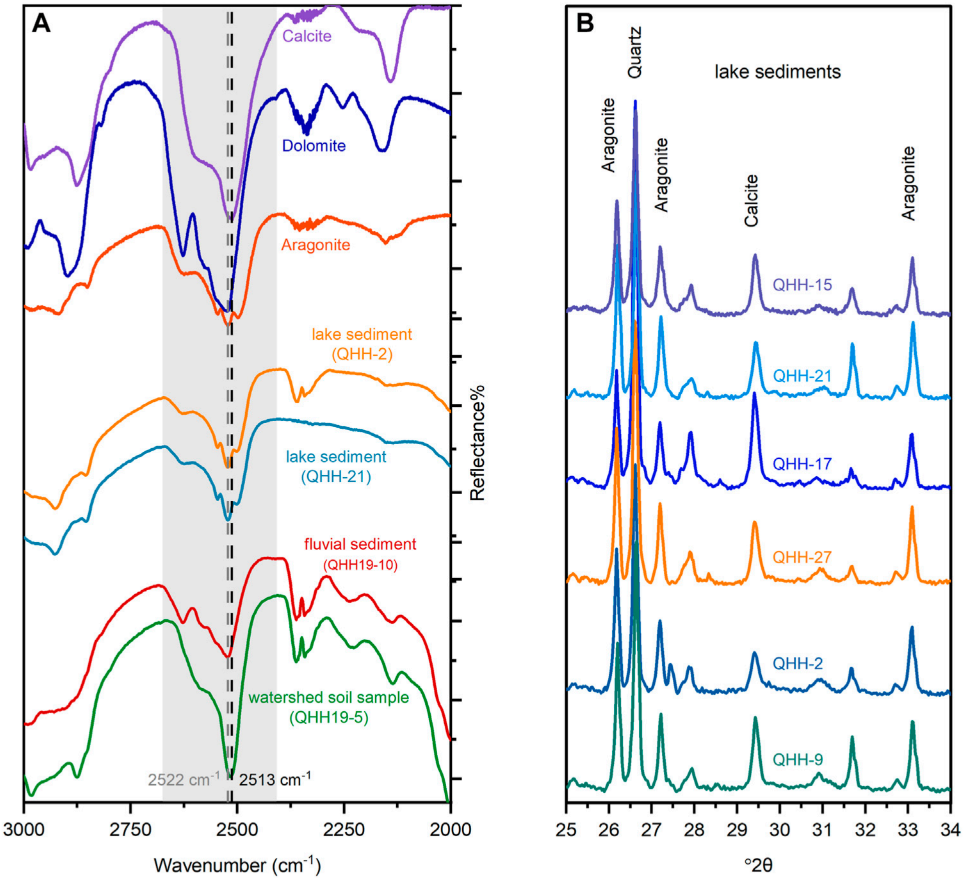

FIGURE 2 | FTIR and XRD analyses on Lake Qinghai sediments and watershed fluvial sediments. **(A)** FTIR spectrum of pure standard calcite, dolomite, aragonite mineral, of samples in the lake sediments (QHH-2 and QHH-21), and of samples in the watershed fluvial sediments (QHH19-10 and QHH19-5). Lake sediments have similar FTIR spectrum features with pure aragonite rather than calcite and dolomite, while watershed samples show a FTIR spectrum feature close to calcite or dolomite rather than aragonite. **(B)** XRD results of lake sediments (QHH-2, QHH-9, QHH-15, QHH-17, QHH-21, and QHH-27) also indicate that aragonite is the main component of carbonate mineral and followed by calcite.

TOC and TN ($R^2 = 0.81$, $p < 0.01$, **Figure 4B**), demonstrating that organic nitrogen was the dominant form of total nitrogen (Schubert and Calvert, 2001; Liu et al., 2010). The organic matter C/N atomic ratio is commonly used to qualitatively distinguish the contribution of terrestrial vegetation and aquatic organisms to organic carbon in lake sediments. Terrestrial vascular plants are poor in nitrogen, so the C/N ratio is high, while aquatic plants are nitrogen rich with a low C/N ratio (Meyers and Lallier-vergés, 1999; Müller and Mathesius, 1999). It was suggested that the C/N ratio of phytoplankton is less than 10 (Hedges and Oades, 1997). C/N ratios greater than 20 were believed to denote terrestrial sources of organic matter, while values in 10–20 were considered to be signals of a mixture of aquatic plants and higher plants (Talbot and Johannessen, 1992; Tyson, 1995; Talbot and Lærdal, 2000). The C/N atomic ratios of Lake Qinghai surficial sediments ranged from 6.5 to 12.5, with values of 22 samples below 10 (**Table1**; **Figure 4A**). Therefore, organic matter in Lake Qinghai sediments may be mainly of endogenous origin. The investigation of organic carbon isotopic compositions of long-chain n-alkanes of modern sediments and aquatic plants also revealed that the organic matter in Lake Qinghai sediments was mainly derived from the endogenous aquatic organisms (Liu et al., 2015). In addition, the preservation of organic carbon in sediments is an important aspect of OC burial. A recent study found that the contribution of TOC degradation to dissolved inorganic carbon was less than 10% in Lake Qinghai (Sun et al., 2019). This may result from the stratification of lake water and the permanently anoxic bottom environment (Sobek et al., 2009). Therefore, TOC in Lake Qinghai was mainly derived from aquatic organisms and well preserved in sediments.

Mineralogical and geochemical methods were used to determine the source and composition of TIC (carbonate) in Lake Qinghai sediments. Among the carbonate mineral types, aragonite is unstable so it hardly exists in ancient bedrock (Kunzler and Goodell, 1970; Martín-García et al., 2019), which is consistent with investigation of modern sediments around the Lake Qinghai Basin (Meng et al., 2019). Thus, aragonite in lake sediments should be autogenetic that precipitated from lake water or/and derived from biogenic origin; this was also supported by

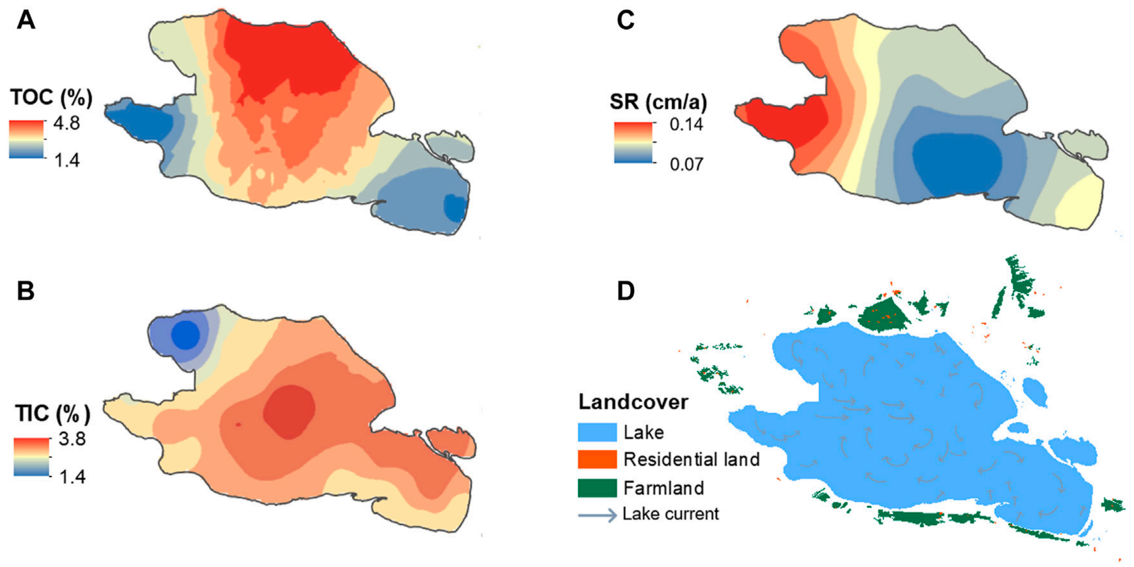

FIGURE 3 | Spatial distribution of **(A)** TOC, **(B)** TIC, **(C)** sediment accumulation rate (Xu et al., 2010), and **(D)** land use around Lake Qinghai in 2000 modified from Liu et al. (2014a) and lake current characteristics modified from Han et al. (2016).

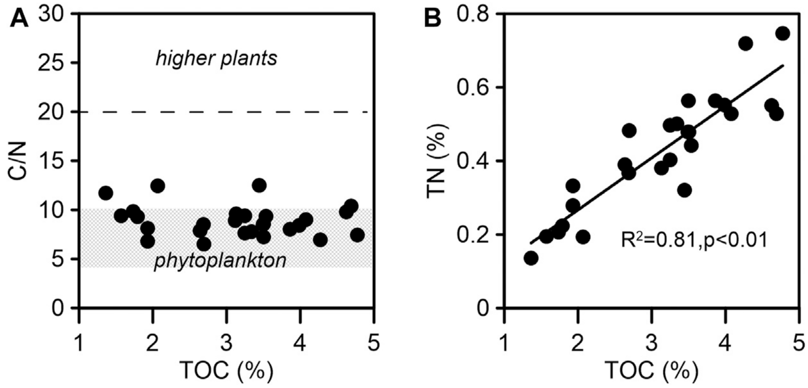

FIGURE 4 | (A) Plot between C/N and TOC. Typical C/N ratio ranges for higher plants and phytoplankton referred to the study by Hedges and Oades. (1997) and Talbot and Lærdal. (2000) were labeled. **(B)** Relationship between total nitrogen (TN) and TOC.

the result that no aragonite was found in the basin soil and fluvial sediments (**Figure 2**). The mineralogical measurement using both FTIR and XRD found that aragonite dominated the carbonate mineral in Lake Qinghai sediments. Within FTIR spectra, the absorption peak shapes of fluvial sediments and topsoil samples are similar to those of pure calcite, and the characteristic peak position is at ca. 2,513 cm^{-1} (**Figure 2A**), whereas the shapes of lacustrine sediments are similar to those of pure aragonite, and the characteristic peak position is at ca. 2,522 cm^{-1} (**Figure 2A**). The XRD results (**Figure 2B**) further supported the judgment that aragonite (d_{104} = 3.39) was the dominant component of carbonate in Lake Qinghai surficial sediments, which was consistent with the results from the study by Yu and Kelts. (2002). In addition, the $\delta^{18}O$ values of carbonate in Lake Qinghai sediments were more positive than those in the surrounding topsoil and were close to equilibrium $\delta^{18}O$ values of lake water (Liu et al., 2018), which also supported the mainly authigenic origin of carbonate in the lake. The evidence demonstrated the rationalization of the assumption selected in this study that authigenic carbonates accounted for approximately 95% of the total carbonates in Lake Qinghai surface sediments based on estimation of Xu et al. (2010).

Spatial Variation of Organic and Inorganic Carbon

TOC and TIC contents in Lake Qinghai had different spatial patterns. TOC content was the highest in the northern lake area and declined outward, with a prominent low value in the shallow part facing the Buha River mouth and the eastern lake area (**Figure 3A**). The spatial variation of TOC was associated with different driving forces. High TOC content in the northern lake area was corresponding to a relatively lower sedimentation rate and intense human activities in the north bank, along which farmland and residential land concentrates (**Figures 3C**,D). The sedimentation rate in the northern lake area was relatively lower despite the three rivers' inflow (**Figure 1**, **Figure 3C**). The limited dilution effect of terrestrial detrital materials was conducive to the accumulation of organic carbon. In addition, anthropogenic nutrient loading by fertilizer use and domestic wastewater increased the trophic level of the northern lake area, generating such high level of TOC concentration in this part.

The low TOC content at the shallow part near the Buha River mouth (water depth: 10–18 m, **Figure 1** and **Table 1**) was the result of the high sedimentation rate and low fine-grain proportion. The high sedimentation rate in the Buha River mouth (**Figure 3C**) reflected a wealth of terrestrial debris input diluting sedimentary organic carbon concentration (Xu et al., 2010). Besides, a good correlation was found between organic matter concentration and the surface area of grains in sediment (Mayer, 1994; Hedges and Keil, 1995) because fine-grained components are effective to organic carbon preservation and are easily resuspended and migrated away from shallow water to the deep water zone (Thompson and Eglinton, 1978; Tenzer et al., 1997). The proportion of coarse particles in the littoral zone and estuary areas is greater than that of coarse particles in the deep lake zone due to continually discharged terrestrial clastic minerals (Håkanson and Jansson, 2002). Therefore, there was quite a low TOC content in the area near the Buha River mouth. For the eastern lake area with a low TOC content, there was a considerable area of sand and bare land in the east bank with no river flowing in (**Figure 1**). Rare human settlements appeared there, resulting in no point source pollution. These possibly resulted jointly in a lower TOC content. In summary, the distributions of TOC in Lake Qinghai were mainly related to sedimentation rates, human activities, and the grain size.

In contrast to TOC, the TIC content displayed a pattern that approximated concentric circles rising from the lakeshore to the center (**Figure 3B**). Supersaturation of carbonate in lake water determined TIC deposition in Lake Qinghai (Liu et al., 2003). However, inflow rivers are unevenly distributed (**Figure 1**). The lake area accepting riverine fresh water may experience salinity reduction and a decrease in carbonate saturation, hence a diminishment of carbonate deposition and TIC content in the sediment. Quite the opposite, in the central part of the lake where there is shortage of freshwater replenishment, evaporation has more intensive influence on the lake water, which may cause relatively more carbonate precipitation (Shen et al., 2001).

On the other hand, the prevailing northwest wind-induced overall eastward and clockwise water currents (**Figure 3D**) (Han et al., 2016). Sediment focusing related to waves and currents may redistribute carbonate minerals to the central and deep basins (Håkanson and Jansson, 2002; Terasmaa and Punning, 2006). This can be reflected by the significantly low TIC content in the upwind northwestern lake area (**Figure 3B**). Therefore, TIC distribution in Lake Qinghai can be mainly attributed to the hydro-chemical characteristics of its lake water and hydraulic conditions controlled by prevailing northwest wind.

Total C Burial Estimation in Lake Qinghai Surficial Sediments

In order to investigate how much carbon was sequestered in Lake Qinghai in recent years, total organic and inorganic carbon burial were estimated by multiplying carbon burial rates with the lake area. Consequently, OCBRs ranged from 4.54 to 30.50 (average value of 10.80) $g\,C\,m^{-2}\,yr^{-1}$, while ICBRs were between 3.32–24.46 (mean value of 10.86) $g\,C\,m^{-2}\,yr^{-1}$. Correspondingly, total OC burial was 47.50 ± 22.68 $Gg\,C\,yr^{-1}$ and IC burial was 47.77 ± 19.73 $Gg\,C\,yr^{-1}$. Thus, total annual carbon burial in Lake Qinghai was concluded to be 95.27 ± 37.74 $Gg\,C\,yr^{-1}$, which is slightly higher than 76 $Gg\,C\,yr^{-1}$ as reported in the study by Xu et al. (2013), which is estimated based on samples mainly derived from central and eastern Lake Qinghai. On the one hand, at least for the last 100–200 years, contemporary lake C burial was likely to be higher than that of the historical value (Dietz et al., 2015; Heathcote et al., 2015; Zhang et al., 2019). On the other hand, the difference in carbon burial estimation for this large lake might be made possible by sampling at different sites. In this study, estimated from OCBRs and ICBRs of each sedimentary sample at 26 sites, total OC and IC burial were vastly different with coefficients of variation of 0.48 and 0.41, respectively. To prevent over/underestimation, it is necessary to consider the spatial heterogeneity while assessing the total C burial of a whole lake based merely on a single sample or sedimentary core, even if sampling in deepwater areas with a stable sedimentary environment of a lake.

The OCBR of Lake Qinghai (14.7 $g\,C\,m^{-2}\,yr^{-1}$) was in line with the global mean value of 10–15 $g\,m^{-2}\,yr^{-1}$ (Tranvik et al., 2009) and close to the average level in the Tibet Plateau Lake Region (14.3 $g\,m^{-2}\,yr^{-1}$) (Zhang et al., 2017), but it was lower than that of other lake regions in China (Zhang et al., 2017). To be specific, for the last 150 years, the mean OCBR of lakes was 25.4 $g\,m^{-2}\,yr^{-1}$ in the Northeast Mountain and Plain Lake Region, 30.6 $g\,m^{-2}\,yr^{-1}$ in the Eastern Plain Lake Region, 30.4 $g\,m^{-2}\,yr^{-1}$ in the Inner Mongolian-Xinjiang Lake Region, and 24.3 $g\,m^{-2}\,yr^{-1}$ in the Yunnan-Guizhou Plateau Lake Region (Zhang et al., 2017). A possible reason of lower OCBRs in Lake Qinghai may be the lower trophic level and primary productivity, owing to a lower temperature and less anthropogenic pollution (Wang et al., 1998; Bi et al., 2018). The oligotrophic Lake Alchichica, Mexico, with similar hypolimnetic anoxia conducive to organic carbon preservation, had OCBRs (14.9 $g\,m^{-2}\,yr^{-1}$) (Alcocer et al., 201 4) comparable to those of Lake Qinghai. Taken equally, lakes of the high northern latitudes had low OCBRs due to frigid climatic patterns and scarce anthropogenic impacts. For example, OCBRs ranged

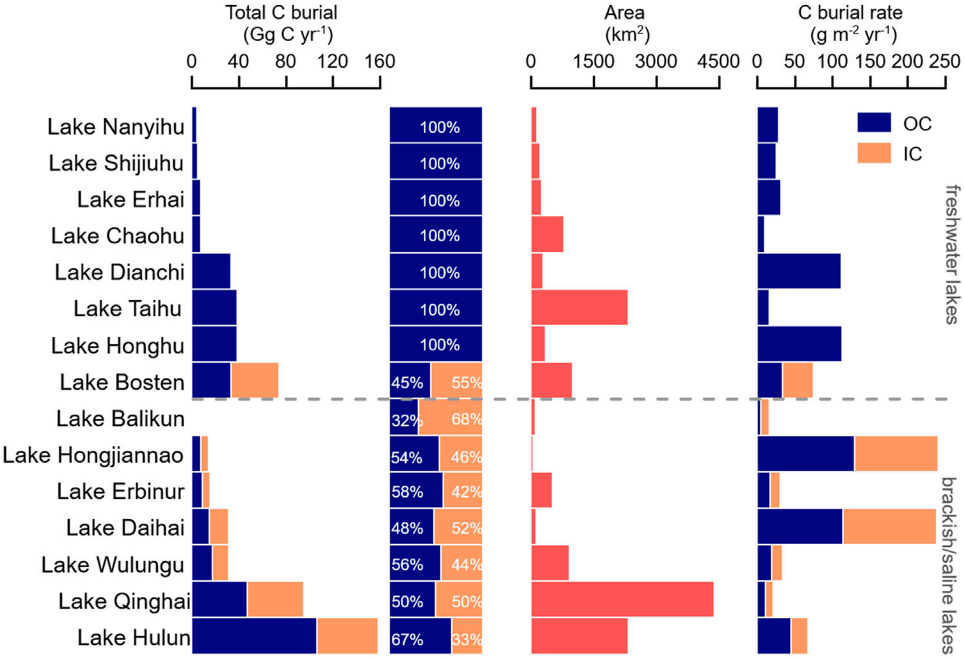

FIGURE 5 | Area, organic, and inorganic carbon burial rate of Lake Qinghai, Lake Balikun, Lake Hongjiannao, Lake Hulun, Lake Erbinur, Lake Daihai, Lake Wulungu, Lake Bosten (Lan et al., 2015), Lake Erhai (Liu et al., 2019), Lake Dianchi (Huang et al., 2018), Lake Shijiuhu, Lake Taihu, Lake Honghu, Lake Nanyihu (Gui et al., 2012), and Lake Chaohu (Dong et al., 2012). Total C burial was calculated by multiplying carbon burial rates with lake area.

1–10 $g\,m^{-2}\,yr^{-1}$ for SW Greenland lakes (Anderson et al., 2019) and from 5.3 to 24.6 $g\,m^{-2}\,yr^{-1}$ for Arctic Sweden (Lundin et al., 2015).

Lake Qinghai had obviously lower OCBRs than many eutrophic lakes, such as Lake Greifen in Switzerland (50–60 $g\,C\,m^{-2}\,yr^{-1}$) (Hollander et al., 1992), Rostherne Mere (96.10 $g\,C\,m^{-2}\,yr^{-1}$), and Tatton Mere (62.51 $g\,C\,m^{-2}\,yr^{-1}$) in the United Kingdom (Scott, 2014). In Minnesota, the United States, OCBRs in ~89% of agriculturally affected lakes were above 50 $g\,C\,m^{-2}\,yr^{-1}$ (Anderson et al., 2013). Notably, the eutrophic Lake Chaohu that has undergone heavy pollution had a lower OCBR of 10.01 $g\,m^{-2}\,yr^{-1}$ than Lake Qinghai (Wu et al., 2016) (**Figure 5**). The exorbitant nutrient levels even led to a decreased carbon sequestration capacity of Lake Chaohu. It was deduced that this owed much to the degradation and decomposition of macrophytes when the lake switched to be cyanobacteria-dominated (Wu et al., 2016).

Large lakes generally have slow C sedimentation rates (Algesten et al., 2004), however, the large Lake Hulun (2,330 km^2) showed a relatively higher OCBR (45.5 $g\,m^{-2}\,yr^{-1}$) (Lan et al., 2015) (**Figure 5**). Lake Hulun has long suffered natural eutrophication resulting from the combined influences of climate warming and drying, water volume reduction, and increased evaporation (Chuai, 2011). In brief, increased primary productivity of a lake, whether it is the consequence of growing temperature or anthropogenic nutrient loading, can thereby promote organic carbon accumulation, resulting in high OCBRs in lake sediments.

Different from open freshwater lakes that mainly deposit organic carbon, inorganic carbon burial contributed approximately 50% to the total carbon burial in Lake Qinghai (**Figure 5**). Because of the supersaturation of carbonate minerals in water bodies, inorganically precipitated carbonate generally exists in brackish and saline lakes (Einsele et al., 2001; Lammers and Depaolo, 2010; Balci et al., 2018). The semi-enclosed status and high salinity condition in Lake Qinghai lead to a mass of carbonate precipitation and sequestration, resulting in a large IC burial proportion. High IC burial proportion was also found in multiple lakes that have similar hydro-chemical characteristics to Qinghai-Tibet alpine and arid/semiarid regions (**Figure 5**). For example, IC burial accounted for 68, 46, 42, 52, 44, and 33% of the total C burial in Lake Balikun, Lake Hongjiannao, Lake Erbinur, Lake Daihai, Lake Wulungu, and Lake Hulun, respectively (Lan et al., 2015) (**Figure 5**). It should be noted that a tiny minority of freshwater lakes also have abundant carbonate minerals. For example, IC burial in freshwater Lake Bosten was even higher than OC burial (Lan et al., 2015), possibly due to the formation of biogenic carbonate or seasonal changes in water chemistry (Kelts and Hsü, 1978; Loeppert and Suarez, 1996). Anyway, saline lakes compose a crucial inorganic carbon pool in addition to an organic carbon pool.

Owing to a large area and high IC burial, total annual C burial of Lake Qinghai surficial sediments (95.27 ± 37.74 $Gg\,C\,yr^{-1}$) was higher than that in many other lakes. Among the 15 lakes shown in **Figure 5**, Lake Qinghai ranked first in the area and second in total annual C burial despite the relatively lower carbon burial rates. Most lakes (10 of 15) with a smaller surface area showed a lower total C burial even with a much higher organic and/or inorganic carbon burial rate (**Figure 5**). Based on a total lake area of 3,185.06 km^2, only 11.5 Gg C yr^{-1} of organic carbon was estimated to be sequestrated annually in sediments of lakes in SW Greenland (Anderson et al., 2019). The organic form of carbon exists in all lakes, but some specific lakes have additional authigenic IC precipitation (Cole et al., 2007), which increases the total carbon burial (**Figure 5**). Therefore, the lake area and water body types are main factors that strongly affect the carbon burial in different lakes, which tallies with the conclusion of Clow et al. (2015).

A large number of lakes (most are closed or semi-closed saltwater type) are spread over the Qinghai–Tibet Plateau, with an area more than 50% of the total area of lakes in China (Wan et al., 2016). Carbon burial in Tibet Plateau lakes is therefore undoubtedly an important component of regional and even global carbon cycle which remain unstudied. More attention and exploration are required for comprehensive understanding of organic and inorganic carbon burial in lake sediments at the Third Pole.

CONCLUSION

Organic carbon of Lake Qinghai was mainly derived from aquatic organisms and well preserved in lake sediments. The TOC content ranged from 1.4 to 4.8% (mean 3.1%) with significant spatial divergence. It was higher in the northern lake area adjacent to the bank with strong human activities and lower in the Buha River mouth and the eastern lake area. The inorganic carbon was dominated by authigenic aragonite with content ranging 1.5–3.8% (mean 3.0%), showing a high value in the lake central area and a significantly low level in the northwestern lake area. This spatial pattern of TIC can be mainly attributed to hydro-chemical characteristics of its lake water and hydraulic conditions controlled by prevailing northwest wind. The OCBR of Lake Qinghai surficial sediments ranged from 4.54 to 30.50 g C m^{-2} yr^{-1}, while ICBRs varied from 3.32 to 24.46 g C m^{-2} yr^{-1}. Correspondingly, total annual organic carbon burial (47.50 ± 22.68 Gg C yr^{-1}) was approximately equal to inorganic carbon burial (47.77 ± 19.73 Gg C yr^{-1}). Both OC burial and IC burial contributed about 50%, suggesting that saline lakes are not only a crucial organic carbon pool but also an important inorganic carbon pool. Lake Qinghai sequestered 95.27 ± 37.74 Gg C yr^{-1}, demonstrating a huge carbon sequestration potential due to its large area. Our study provides scientific and technological support for understanding, under the influence of human activities and hydraulic condition, the spatial variation characteristics of carbon in large and deepwater lakes with conditions analogous with Lake Qinghai. This is also an archive for further research on carbon burial in plateau lakes on different timescales.

DATA AVAILABILITY STATEMENT

The original contributions presented in the study are included in the article/Supplementary Material; further inquiries can be directed to the corresponding authors.

AUTHOR CONTRIBUTIONS

CX performed the test, data processing, analysis and wrote the manuscript. MX conceptualized and designed the research, and reviewed the manuscript. SY reviewed and edited the manuscript. WZ processed the data and plotted. ZB processed the data and plotted. ZB analyzed the data and plotted. ZE funded the research.

FUNDING

This work was supported by the National Science Foundation of China (Nos. 42025707 and 41790423) and the Second Tibetan Plateau Scientific Expedition and Research Program (STEP) (Grant No. 2019QZKK0202) and Jiangxi Normal University's Domestic and Overseas Study Program for Postgraduates.

ACKNOWLEDGMENTS

The data set is provided by National Tibetan Plateau Data Center (http://data.tpdc.ac.cn/). We thank Zhenyu Ni and Rong Chen from the State Key Laboratory of Lake Science and Environment, Nanjing Institute of Geography and Limnology, and Dongliang Ning from the School of Geography Sciences, Nantong University, for field sampling and their constructive suggestions. We also thank Jianru Cheng from the School of Earth Sciences and Engineering, Nanjing University for assistance in carbonate testing.

REFERENCES

Alcocer, J., Ruiz-Fernández, A. C., Escobar, E., Pérez-Bernal, L. H., Oseguera, L. A., and Ardiles-Gloria, V. (2014). Deposition, Burial and Sequestration of Carbon in an Oligotrophic, Tropical lake. *J. Limnol* 73 (2), 223–235. doi:10.4081/jlimnol.2014.783

Algesten, G., Sobek, S., Bergström, A.-K., Ågren, A., Tranvik, L. J., and Jansson, M. (2004). Role of Lakes for Organic Carbon Cycling in the Boreal Zone. *Glob. Change Biol.* 10, 141–147. doi:10.1111/j.1365-2486.2003.00721.x

An, Z., Colman, S. M., Zhou, W., Li, X., Brown, E. T., Jull, A. J. T., et al. (2012). Interplay between the Westerlies and Asian Monsoon Recorded in Lake Qinghai Sediments since 32 Ka. *Sci. Rep.* 2, 619. doi:10.1038/srep00619

Anas, M. U. M., Scott, K. A., and Wissel, B. (2015). Carbon Budgets of Boreal Lakes: State of Knowledge, Challenges, and Implications. *Environ. Rev.* 23 (3), 275–287. doi:10.1139/er-2014-0074

Anderson, N. J., Appleby, P. G., Bindler, R., Renberg, I., Conley, D. J., Fritz, S. C., et al. (2019). Landscape-Scale Variability of Organic Carbon Burial by SW Greenland Lakes. *Ecosystems* 22 (8), 1706–1720. doi:10.1007/s10021-019-00368-8

Anderson, N. J., Dietz, R. D., and Engstrom, D. R. (2013). Land-use Change, Not Climate, Controls Organic Carbon Burial in Lakes. *Proc. R. Soc. B.* 280 (1769), 20131278. doi:10.1098/rspb.2013.1278

Balci, N., Demirel, C., Akcer Ön, S., Gültekin, A. H., and Kurt, M. A. (2018). Evaluating Abiotic and Microbial Factors on Carbonate Precipitation in Lake Acigöl, a Hypersaline lake in Southwestern Turkey. *Quat. Int.* 486, 116–128. doi:10.1016/j.quaint.2017.12.046

Bi, r., Zhang, h., Li, h., Chang, f., Duan, l., He, y., et al. (2018). Characteristics and Changes of Water Quality Parameters of Qinghai Lake in 2015. *J. Water Resour. Res.* 7 (1), 74. doi:10.12677/JWRR.2018.71009

Chang, B., He, K.-N., Li, R.-J., Sheng, Z.-P., and Wang, H. (2017). Linkage of Climatic Factors and Human Activities with Water Level Fluctuations in Qinghai Lake in the Northeastern Tibetan Plateau, China. *Water* 9 (7), 552. doi:10.3390/w9070552

Chen, H., Zhu, L., Wang, J., Ju, J., Ma, Q., and Xu, T. (2021). Paleoclimate Changes over the Past 13,000 Years Recorded by Chibuzhang Co Sediments in the Source Region of the Yangtze River, China. *Palaeogeogr. Palaeoclimatol. Palaeoecol.* 573, 110433. doi:10.1016/j.palaeo.2021.110433

Chen, x., Zhu, y., Fu, x., and Luo, y. (2012). Investigation of Eutrophic Elements Distribution and Their Correlation in Qinhai Lake Surface Sediments. *J. Agro-Environment Sci.* 31 (02), 181–187.

Chuai, X. (2011). *Study on Lake Eutrophication as Well as the Criteria and Control Standard for Phosphorus in China*. Nanjing: Nanjing University.

Clow, D. W., Stackpoole, S. M., Verdin, K. L., Butman, D. E., Zhu, Z., Krabbenhoft, D. P., et al. (2015). Correction to Organic Carbon Burial in Lakes and Reservoirs of the Conterminous United States. *Environ. Sci. Technol.* 49 (24), 14741. doi:10.1021/acs.est.5b00373

Cole, J. J., Prairie, Y. T., Caraco, N. F., McDowell, W. H., Tranvik, L. J., Striegl, R. G., et al. (2007). Plumbing the Global Carbon Cycle: Integrating Inland Waters into the Terrestrial Carbon Budget. *Ecosystems* 10 (1), 172–185. doi:10.1007/s10021-006-9013-8

Dean, W. E., and Gorham, E. (1998). Magnitude and Significance of Carbon Burial in Lakes, Reservoirs, and Peatlands. *Geology* 26 (6), 535. doi:10.1130/0091-7613(1998)026<0535:masocb>2.3.co;2

Dietz, R. D., Engstrom, D. R., and Anderson, N. J. (2015). Patterns and Drivers of Change in Organic Carbon Burial across a Diverse Landscape: Insights from 116 minnesota Lakes. *Glob. Biogeochem. Cycles* 29 (5), 708–727. doi:10.1002/2014gb004952

Dong, H., Song, Y., and Zhang, M. (2018). Hydrological Trend of Qinghai Lake over the Last 60 years: Driven by Climate Variations or Human Activities? *J. Water Clim. Change* 10 (3), 524–534. doi:10.2166/wcc.2018.033

Dong, X., Anderson, N. J., Yang, X., chen, X., and Shen, J. (2012). Carbon Burial by Shallow Lakes on the Yangtze Floodplain and its Relevance to Regional Carbon Sequestration. *Glob. Change Biol.* 18 (7), 2205–2217. doi:10.1111/j.1365-2486.2012.02697.x

Einsele, G., Yan, J., and Hinderer, M. (2001). Atmospheric Carbon Burial in Modern lake Basins and its Significance for the Global Carbon Budget. *Glob. Planet. Change* 30, 167–195. doi:10.1016/S0921-8181(01)00105-9

Fu, g.-y., Sha, z.-j., Zhang, k., Zhao, s., and Guo, l. (2015). Research of Deposition Rate in Northwestern Qinghai Lake Based on the137Cs and 210Pb Dating. *J. Salt Lake Res.* 23 (2), 7–14.

Gui, Z.-f., Xue, B., Yao, S.-c., Wei, W.-j., and Yi, S. (2012). Organic Carbon Burial in lake Sediments in the Middle and Lower Reaches of the Yangtze River Basin, China. *Hydrobiologia* 710 (1), 143–156. doi:10.1007/s10750-012-1365-9

Gyawali, A. R., Wang, J., Ma, Q., Wang, Y., Xu, T., Guo, Y., et al. (2019). Paleo-environmental Change since the Late Glacial Inferred from Lacustrine Sediment in Selin Co, central Tibet. *Palaeogeogr. Palaeoclimatol. Palaeoecol.* 516, 101–112. doi:10.1016/j.palaeo.2018.11.033

Håkanson, L., and Jansson, M. (2002). *Principles of Lake Sedimentology*.

Han, y., Hao, l., Wang, q., Ma, d., and Ji, h. (2016). Prevailing Winds Controlled Hydrodynamic Characteristics of Qinghai Lake. *Yellow River* 38 (3), 51–55. doi:10.3969/j.issn.1000-1379.2016.03.015

He, H., Liu, G., Zou, Y., Li, X., Ji, M., and Li, D. (2021). Coupled Action of Rock Weathering and Aquatic Photosynthesis: Influence of the Biological Carbon Pump Effect on the Sources and Deposition of Organic Matter in Ngoring Lake, Qinghai-Tibet Plateau, China. *Catena* 203, 105370. doi:10.1016/j.catena.2021.105370

Heathcote, A. J., Anderson, N. J., Prairie, Y. T., Engstrom, D. R., and del Giorgio, P. A. (2015). Large Increases in Carbon Burial in Northern Lakes during the Anthropocene. *Nat. Commun.* 6 (1), 10016. doi:10.1038/ncomms10016

Hedges, J. I., and Keil, R. G. (1995). Sedimentary Organic Matter Preservation: an Assessment and Speculative Synthesis. *Mar. Chem.* 49 (2), 81–115. doi:10.1016/0304-4203(95)00008-F

Hedges, J. I., and Oades, J. M. (1997). Comparative Organic Geochemistries of Soils and marine Sediments. *Org. Geochem.* 27 (7), 319–361. doi:10.1016/S0146-6380(97)00056-9

Henderson, A., Holmes, J., and Leng, M. (2007). *Atmospheric Circulation Changes during the Little Ice Age in NW China: A Late Holocene Oxygen Isotope Record from Lake Qinghai, NE Tibetan Plateau*. San Francisco, CA: AGU Fall Meeting Abstracts.

Hollander, D. J., McKenzie, J. A., and Haven, H. L. t. (1992). A 200 Year Sedimentary Record of Progressive Eutrophication in Lake Greifen (Switzerland): Implications for the Origin of Organic-Carbon-Rich Sediments. *Geol* 20, 825–828. doi:10.1130/0091-7613(1992)020<0825:aysrop>2.3.co;2

Huang, C., Zhang, L., Li, Y., Lin, C., Huang, T., Zhang, M., et al. (2018). Carbon and Nitrogen Burial in a Plateau lake during Eutrophication and Phytoplankton Blooms. *Sci. Total Environ.* 616-617, 296–304. doi:10.1016/j.scitotenv.2017.10.320

Ji, J., Ge, Y., Balsam, W., Damuth, J. E., and Chen, J. (2009). Rapid Identification of Dolomite Using a Fourier Transform Infrared Spectrophotometer (FTIR): A Fast Method for Identifying Heinrich Events in IODP Site U1308. *Mar. Geology.* 258 (1), 60–68. doi:10.1016/j.margeo.2008.11.007

Ji, J., Shen, J., Balsam, W., Chen, J., Liu, L., and Liu, X. (2005). Asian Monsoon Oscillations in the Northeastern Qinghai-Tibet Plateau since the Late Glacial as Interpreted from Visible Reflectance of Qinghai Lake Sediments. *Earth Planet. Sci. Lett.* 233, 61–70. doi:10.1016/j.epsl.2005.02.025

Kastowski, M., Hinderer, M., and Vecsei, A. (2011). Long-term Carbon Burial in European Lakes: Analysis and Estimate. *Glob. Biogeochem. Cycles* 25 (3), a–n. doi:10.1029/2010GB003874

Kelts, K., and Hsü, K. J. (1978). "Freshwater Carbonate Sedimentation," in *Lakes: Chemistry, Geology, Physics*. Editor A. Lerman (New York, NY: Springer New York), 295–323. doi:10.1007/978-1-4757-1152-3_9

Kunzler, R. H., and Goodell, H. G. (1970). The Aragonite-Calcite Transformation; a Problem in the Kinetics of a Solid-Solid Reaction. *Am. J. Sci.* 269, 360–391. doi:10.2475/ajs.269.4.360

Lammers, L., and Depaolo, D. (2010). *The Influence of Solution Stoichiometry on Surface-Controlled Ca Isotope Fractionation during Ca Carbonate Precipitation from Mono Lake, California*. San Francisco, CA: AGU Fall Meeting Abstracts.

Lan, J., Xu, H., Liu, B., Sheng, E., Zhao, J., and Yu, K. (2015). A Large Carbon Pool in lake Sediments over the Arid/semiarid Region, NW China. *Chin. J. Geochem.* 34 (3), 289–298. doi:10.1007/s11631-015-0047-5

Lian, X., Qi, y., Wang, h., Zhang, j., and Yang, r. (2019). Spatial Pattern of Ecosystem Services under the Influence of Human Activities in Qinghai Lake Watershed. *J. Glaciology Geocryology* 41 (5), 1254–1263. doi:10.7522/j.issn.1000-0240.2019.0531

Liu, E., Shen, J., Zhang, E., Wu, Y., and Yang, L. (2010). A Geochemical Record of Recent Anthropogenic Nutrient Loading and Enhanced Productivity in Lake Nansihu, China. *J. Paleolimnol* 44 (1), 15–24. doi:10.1007/s10933-009-9382-z

Liu, h., Liu, e., Yu, z., Zhang, e., Lin, q., Wang, r., et al. (2019). Spatio-temporal Patterns of Organic Carbon Burial in the Sediment of Lake Erhai in China during the Past 100 Years. *J. Lake Sci.* 31 (1), 282–292. doi:10.18307/2019.0126

Liu, j., Zhuang, d., Wang, j., Zhou, w., and Wu, s. (2014). *Landuse/Landcover Data of the QinghaiLake River Basin (2000)*. Beijing, China: National Tibetan Plateau Data Center.

Liu, W., Yang, H., Wang, H., An, Z., Wang, Z., and Leng, Q. (2015). Carbon Isotope Composition of Long Chain Leaf Wax N -alkanes in lake Sediments: A Dual Indicator of Paleoenvironment in the Qinghai-Tibet Plateau. *Org. Geochem.* 83-84, 190–201. doi:10.1016/j.orggeochem.2015.03.017

Liu, W., Zhang, P., Zhao, C., Wang, H., An, Z., and Liu, H. (2018). Reevaluation of Carbonate Concentration and Oxygen Isotope Records from Lake Qinghai, the Northeastern Tibetan Plateau. *Quat. Int.* 482, 122–130. doi:10.1016/j.quaint.2018.03.038

Liu, X., Colman, S. M., Brown, E. T., An, Z., Zhou, W., Jull, A. J. T., et al. (2014b). A Climate Threshold at the Eastern Edge of the Tibetan Plateau. *Geophys. Res. Lett.* 41 (15), 5598–5604. doi:10.1002/2014gl060833

Liu, X. Q., Shen, J., Wang, S. M., Zhang, E., and Cai, Y. F. (2003). A 16000-year Paleoclimatic Record Derived from Authigenetic Carbonate of Lacustrine Sediment in Qinghai Lake. *Geol. J. China Universities* 9, 38–46. doi:10.3969/j.issn.1006-7493.2003.01.005

Loeppert, R. H., and Suarez, D. (1996). *Carbonate and gypsum, Methods of Soil Analysis*. United States: Soil Science Society of America and American Society of Agronomy, 437–474.

Lundin, E. J., Klaminder, J., Bastviken, D., Olid, C., Hansson, S. V., and Karlsson, J. (2015). Large Difference in Carbon Emission - Burial Balances between Boreal and Arctic Lakes. *Sci. Rep.* 5, 14248. doi:10.1038/srep14248

Luo, c., Xu, c., Cao, y., and Tong, l. (2017). Monitoring of Water Surface Area in Lake Qinghai from 1974 to 2016. *J. Lake Sci.* 29 (5), 1245–1253. doi:10.18307/2017.0523

Martín-García, R., Alonso-Zarza, A. M., Frisia, S., Rodríguez-Berriguete, Á., Drysdale, R., and Hellstrom, J. (2019). Effect of Aragonite to Calcite Transformation on the Geochemistry and Dating Accuracy of Speleothems. An Example from Castañar Cave, Spain. *Sediment. Geology.* 383, 41–54. doi:10.1016/j.sedgeo.2019.01.014

Mayer, L. M. (1994). Relationships between mineral Surfaces and Organic Carbon Concentrations in Soils and Sediments. *Chem. Geology.* 114 (3), 347–363. doi:10.1016/0009-2541(94)90063-9

Meng, X., Liu, L., Balsam, W., li, S., He, T., Chen, J., et al. (2015). Dolomite Abundance in Chinese Loess Deposits: A New Proxy of Monsoon Precipitation Intensity. *Geophys. Res. Lett.* 42, 10391–10398. doi:10.1002/2015GL066681

Meng, X., Liu, L., Zhao, W., He, T., Chen, J., and Ji, J. (2019). Distant Taklimakan Desert as an Important Source of Aeolian Deposits on the Chinese Loess Plateau as Evidenced by Carbonate Minerals. *Geophys. Res. Lett.* 46 (9), 4854–4862. doi:10.1029/2018GL081551

Meyers, P. A., and Ishiwatari, R. (1993). Lacustrine Organic Geochemistry—An Overview of Indicators of Organic Matter Sources and Diagenesis in lake Sediments. *Org. Geochem.* 20 (7), 867–900. doi:10.1016/0146-6380(93)90100-P

Meyers, P. A., and Lallier-vergés, E. (1999). Lacustrine Sedimentary Organic Matter Records of Late Quaternary Paleoclimates. *J. Paleolimnology* 21 (3), 345–372. doi:10.1023/A:1008073732192

Müller, A., and Mathesius, U. (1999). The Palaeoenvironments of Coastal Lagoons in the Southern Baltic Sea, I. The Application of Sedimentary Corg/N Ratios as Source Indicators of Organic Matter. *Palaeogeogr. Palaeoclimatol. Palaeoecol.* 145 (1), 1–16. doi:10.1016/S0031-0182(98)00094-7

Qin, B., and Huang, Q. (1998). Evaluation of the Climatic Change Impacts on the Inland Lake – A Case Study of Lake Qinghai, China. *Climatic Change* 39 (4), 695–714. doi:10.1023/A:1005319616456

Rumolo, P., Barra, M., Gherardi, S., Marsella, E., and Sprovieri, M. (2011). Stable Isotopes and C/N Ratios in marine Sediments as a Tool for Discriminating Anthropogenic Impact. *J. Environ. Monit.* 13 (12), 3399–3408. doi:10.1039/c1em10568j

Schubert, C. J., and Calvert, S. E. (2001). Nitrogen and Carbon Isotopic Composition of marine and Terrestrial Organic Matter in Arctic Ocean Sediments:. *Deep Sea Res. Oceanographic Res. Pap.* 48 (3), 789–810. doi:10.1016/S0967-0637(00)00069-8

Scott, D. R. (2014). *Carbon Fixation, Flux and Burial Efficiency in Two Contrasting Eutrophic Lakes in the UK (Rostherne Mere & Tatton Mere)*. Loughborough: Loughborough University.

Shang, X., Li, X., An, Z., Ji, M., and Zhang, H. (2009). Modern Pollen Rain in the Lake Qinghai basin, China. *Sci. China Ser. D-earth Sci.* 52 (10), 1510–1519. doi:10.1007/s11430-009-0150-8

Shen, J., Zhang, E., and Xia, W. (2001). Records from lake Sediments of the Qinghai Lake to Minor Climatic and Environmental Changes of the Past about 1000 Years. *Quat. Sci. Rev.* 21 (6), 508–513.

Sobek, S., Durisch-Kaiser, E., Zurbrügg, R., Wongfun, N., Wessels, M., Pasche, N., et al. (2009). Organic Carbon Burial Efficiency in lake Sediments Controlled by Oxygen Exposure Time and Sediment Source. *Limnol. Oceanogr.* 54, 2243–2254. doi:10.4319/lo.2009.54.6.2243

Sun, D., He, Y., Wu, J., Liu, W., and Sun, Y. (2019). Hydrological and Ecological Controls on Autochthonous Carbonate Deposition in Lake Systems: A Case Study from Lake Wuliangsu and the Global Perspective. *Geophys. Res. Lett.* 46 (12), 6583–6593. doi:10.1029/2019gl082224

Talbot, M. R., and Johannessen, T. (1992). A High Resolution Palaeoclimatic Record for the Last 27,500 Years in Tropical West Africa from the Carbon and Nitrogen Isotopic Composition of Lacustrine Organic Matter. *Earth Planet. Sci. Lett.* 110 (1-4), 23–37. doi:10.1016/0012-821X(92)90036-U

Talbot, M. R., and Lærdal, T. (2000). The Late Pleistocene - Holocene Palaeolimnology of Lake Victoria, East Africa, Based upon Elemental and Isotopic Analyses of Sedimentary Organic Matter. *J. Paleolimnology* 23 (2), 141–164. doi:10.1023/A:1008029400463

Tenzer, G., Meyers, P., and Knoop, P. (1997). Sources and Distribution of Organic and Carbonate Carbon in Surface Sediments of Pyramid Lake, Nevada. *J. Sediment. Res.* 67 (5), 884–890. doi:10.1306/D4268667-2B26-11D7-8648000102C1865D

Terasmaa, J., and Punning, J.-M. (2006). Sedimentation Dynamics in a Small Dimictic lake in Northern Estonia. *Proc. Estonian Acad. Sci. Biol. Ecol.* 55, 228–242.

Thompson, S., and Eglinton, G. (1978). The Fractionation of a Recent Sediment for Organic Geochemical Analysis. *Geochimica et Cosmochimica Acta* 42, 199–207. doi:10.1016/0016-7037(78)90132-1

Tranvik, L. J., Downing, J. A., Cotner, J. B., Loiselle, S. A., Striegl, R. G., Ballatore, T. J., et al. (2009). Lakes and Reservoirs as Regulators of Carbon Cycling and Climate. *Limnol. Oceanogr.* 54 (6), 2298–2314. doi:10.4319/lo.2009.54.6_part_2.2298

Tyson, R. V. (1995). *Sedimentary Organic Matter*. Heidelberg: Springer Netherlands. doi:10.1007/978-94-011-0739-6

Wan, W., Long, D., Hong, Y., Ma, Y., Yuan, Y., Xiao, P., et al. (2016). A lake Data Set for the Tibetan Plateau from the 1960s, 2005, and 2014. *Sci. Data* 3 (1), 160039. doi:10.1038/sdata.2016.39

Wang, s., Dou, h., Chen, k., Wang, x., and Jiang, j. (1998). *China Lakes Record*. Beijing: Science Press Ltd.

Wu, P., Gao, C., Chen, F., and Yu, S. (2016). Response of Organic Carbon Burial to Trophic Level Changes in a Shallow Eutrophic lake in SE China. *J. Environ. Sci.* 46, 220–228. doi:10.1016/j.jes.2016.05.003

Xu, H., Lan, J., Liu, B., Sheng, E., and Yeager, K. M. (2013). Modern Carbon Burial in Lake Qinghai, China. *Appl. Geochem.* 39, 150–155. doi:10.1016/j.apgeochem.2013.04.004

Xu, H., Liu, X., An, Z., Hou, Z., Dong, J., and Liu, B. (2010). Spatial Pattern of Modern Sedimentation Rate of Qinghai lake and a Preliminary Estimate of the Sediment Flux. *Chin. Sci. Bull.* 55 (4-5), 621–627. doi:10.1007/s11434-009-0580-x

Yu, J. Q., and Kelts, K. R. (2002). Abrupt Changes in Climatic Conditions across the Late-glacial/Holocene Transition on the N. E. Tibet-Qinghai Plateau: Evidence from Lake Qinghai, China. *J. Paleolimnology* 28 (2), 195–206. doi:10.1023/A:1021635715857

Yu, Z. T., Wang, X. J., Zhang, E. L., Zhao, C. Y., and Liu, X. Q. (2015). Spatial Distribution and Sources of Organic Carbon in the Surface Sediment of Bosten Lake, China. *Biogeosciences* 12 (22), 6605–6615. doi:10.5194/bg-12-6605-2015

Zhang, F., Bin, X. U. E., and Shuchun, Y. A. O. (2019). Spatiotemporal Pattern of Inorganic Carbon Sequestration in Lake Hulun since 1850. *J. Lake Sci.* 31, 1770–1782. doi:10.18307/2019.0617

Zhang, F., Yao, S., Xue, B., Lu, X., and Gui, Z. (2017). Organic Carbon Burial in Chinese Lakes over the Past 150 Years. *Quat. Int.* 438, 94–103. doi:10.1016/j.quaint.2017.03.047

Zhang, j., Chen, y., Ge, j., and Nie, x. (2013). Land Use/cover Change and Land Sources Management in the Area Around the Qinghai Lake of China in 1977-2010. *J. Desert Reaseach* 33 (4), 1256–1266. doi:10.7522/j.issn.1000-694X.2013.00177

Zhang, x., Zeng, y., and Long, y. (2009). An Attempt to Use the ^{137}Cs Mass Balance Model for Assessment of Recent Deposition Rates in Lake Qinghai, China. *J. Lake Sci.* 21 (6), 827–833. doi:10.18307/2009.0612

Conflict of Interest: The authors declare that the research was conducted in the absence of any commercial or financial relationships that could be construed as a potential conflict of interest.

Copyright © 2021 Chen, Meng, Song, Zhang, Wan, Zhou and Zhang. This is an open-access article distributed under the terms of the Creative Commons Attribution License (CC BY). The use, distribution or reproduction in other forums is permitted, provided the original author(s) and the copyright owner(s) are credited and that the original publication in this journal is cited, in accordance with accepted academic practice. No use, distribution or reproduction is permitted which does not comply with these terms.

frontiers
in Environmental Science

ORIGINAL RESEARCH
published: 25 August 2021
doi: 10.3389/fenvs.2021.727844

The Temporal-Spatial Variations and Potential Causes of Dust Events in Xinjiang Basin During 1960–2015

Lamei Mu[1,2†], Jing Su[1*], Xinyue Mo[1*†], Nan Peng[1], Ying Xu[1], Meihua Wang[1] and Jinyan Wang[1]

[1]College of Atmospheric Sciences, Lanzhou University, Lanzhou, China, [2]Longxi Meteorological Bureau of Gansu Province, Longxi, China

Dust events not only cause local ecosystem degradation and desertification, but also have profound impacts on regional and global climate system, as well as air quality and human health. Dust events in Xinjiang Basin, as the important dust source of Eastern Asia, have undergone a significant change under the global warming background and may be in a new active period after 2000, which is worthy of study. This study provides the temporal and spatial variations of dust events in the Xinjiang Basin based on surface meteorological station observation data during 1960–2015. The results show that Southern Xinjiang is the main dust occurrence region where dust events are significantly more than that in the Northern Xinjiang, and each year more than 73% of dust events occurred in spring and summer. The dust index (DI), which is defined to represent the large-scale variation of dust event, shows a significant downward trend during the past 56 years with a linear decreasing rate –8.2 years^{-1} in Southern Xinjiang. The DI is positively correlated to surface wind speed with a mean correlation coefficient of 0.79. The declining trend of surface wind speed could explain dust events variation during 1960–2000. But in the new active period after 2000, the increase of DI is not consistent with the rising wind speed with the correlation coefficient decreasing to 0.34. It is found that, compared with 1960–1999, the average annual precipitation and frequency increased by 17.4 and 13% during 2000–2015, respectively, and the NDVI also increased at the same time, which indicates that the surface condition changes induced by the increase of precipitation might suppress the occurrence of dust. Moreover, the analysis of high-altitude wind field shows that the variation of the East Asian general circulation's intensity, dominating the upper-level wind fields in the Xinjiang basin, will change the surface wind speed and precipitation, and further affect the occurrence of dust events.

Keywords: Xinjiang basin, dust event, dust index, temporal-spatial variation, wind, precipitation, NDVI

OPEN ACCESS

Edited by:
Zhiwei Xu,
Nanjing University, China

Reviewed by:
Baofu Li,
Qufu Normal University, China
Wencai Wang,
Ocean University of China, China

***Correspondence:**
Jing Su
jsu@lzu.edu.cn
Xinyue Mo
moxy16@lzu.edu.cn

†These authors have contributed equally to this work and share first authorship

Specialty section:
This article was submitted to Environmental Informatics and Remote Sensing,
a section of the journal Frontiers in Environmental Science

Received: *19 June 2021*
Accepted: *10 August 2021*
Published: *25 August 2021*

Citation:
Mu L, Su J, Mo X, Peng N, Xu Y, Wang M and Wang J (2021) The Temporal-Spatial Variations and Potential Causes of Dust Events in Xinjiang Basin During 1960–2015. Front. Environ. Sci. 9:727844. doi: 10.3389/fenvs.2021.727844

INTRODUCTION

Dust events, which are classified by visibility as dust storm, blowing dust and floating dust, are common phenomena in the arid and semi-arid regions of central Asia (Indoitu et al., 2012). Dust events not only cause ecosystem degradation and desertification in the local region, but also have profound impacts on the regional and global climate system. Dust aerosol could lead to both cooling by reflecting sunlight back to space and warming by absorbing solar and infrared radiation, which is called the direct radiative effect (Sokolik and Toon, 1999; Wang et al., 2013). They also could increase cloud albedo and suppress precipitation by acting as cloud condensation nuclei and ice nuclei to change the microphysical properties (Wang et al., 2015; Wang et al., 2017), which are defined as the indirect radiative effect (Twomey, 1977; Albrecht, 1989). Dust deposition after long-distance transportation is also one of the sources of marine pollutants and nutrients, influencing marine ecosystems (Cabrerizo et al., 2016; Wang et al., 2019b). And the increased flux of iron, nitrogen and phosphorus to ocean by atmospheric dust can promote the primary production and further the particulate organic carbon export to deep ocean, which is an important way for carbon sequestration of ocean (Struve et al., 2020; Xiu and Chai, 2021). Moreover, large amounts of dust significantly influence air quality and play an essential role in disease transmission (Li et al., 2020; Tian et al., 2020; Wallden et al., 2020; Linares et al., 2021).

Xinjiang is located in Central Asia, one of the important dust source areas, covering 1.66×10^6 km^2 with more than 50% areas are desert and Gobi. The Taklimakan Desert, in the southern part of Xinjiang, is the second-largest desert in the world. Dust particles from the Taklimakan Desert are blown into the free troposphere and even can be lofted vertically up to 10 km due to the unique topography and northeasterly winds associated with certain synoptic conditions (Ge et al., 2014). Then they can be transported horizontally to regions far downwind from the Asian continent to the West Pacific by westerlies (Wang et al., 2010; Hu et al., 2020). The Taklimakan Desert is an important source of dust that affects much of Eastern Asia, and is also considered as the dust sediment source for the North Pacific and even North America (Liu et al., 2019; Yasukawa et al., 2019; Chen et al., 2020; Ma et al., 2020). Therefore, the dust of Xinjiang has drawn much attention from researchers all over the world.

Under the background of global warming, like many other regions worldwide, the area of Xinjiang experienced noteworthy climate change in the past few decades. Along with climate change, some studies have shown that the frequency of dust events also changed significantly. Wang et al. (Wang et al., 2008) used ground observational data collected from Xinjiang meteorological stations from 1961–2000 to show that the monthly and annual mean occurrence days of dust in Xinjiang presented a significant decreasing trend. Ma et al. (Ma et al., 2006) applied ground observational data from 1961–2003 and got similar conclusions with Wang et al., and they also found that there existed oscillation periods of dust events, 10–15 years in Northern Xinjiang and 8–10 years in Southern Xinjiang. Pi et al. (Pi et al., 2017) investigated spatial-temporal characteristics of dust events from 1960 to 2007, which shows a long-term decline and there is heavier dust in Southern Xinjiang than in Northern Xinjiang. And the studies of dust events in Southern Xinjiang exhibit obvious fluctuations and wind speed is the dominant factor (Wang et al., 2019b; Jin et al., 2021).

Although dust events in Xinjiang have been studied by many researchers, these studies primarily focus on the period of 1960–2000. With the decrease of dust events in the late 1990s over the globe, relatively less attention was paid to the changes of dust after 2000. However, (Qian et al., 2004), and (Li and Zhong, 2007) both pointed that dust storms in northern China have increased since 2000 and maybe in a new active period. And this phenomenon is more pronounced in 2021, and many people have noticed the increase of dust events. There have been 21 strong storms in northern China by May, and the frequency, intensity, and influenced coverage are all rare in recent years (CCTV-News, 2021). In terms of the broad impacts of Xinjiang dust aerosol, continuous research on variations of dust events in the whole Xinjiang region is needed, especially in the recent 20 years under the global warming background. Based on above all, it is necessary to analyze the recent changes of dust events in this decade to understand its responses to the undergoing climate change and investigate the possible reasons for it. Due to Xinjiang's unique landform, there are observable spatial differences of climate characteristics between the South and North. This study divides Xinjiang into two parts as Southern and Northern Xinjiang, along the Tianshan Mountains. We provide the temporal and spatial distribution of dust events and analyze the long-term trend as well as abrupt changes of the dust index (DI) in these two parts of Xinjiang from 1960–2015. The potential causes for the variations of dust events are also analyzed.

This paper is organized as follows. *Data and Methods* introduces the dataset used in this study and describes the method to calculate the DI. In *Results and Discussion*, the temporal and spatial distribution of dust events over Xinjiang and the trend of dust events as well as the analysis of the abrupt change are presented, and then the potential causes are discussed. Conclusions are given in *Conclusion*.

DATA AND METHODS

Data

Dust events are studied using the ground-based observation of dust storm, blowing dust and floating dust during 1960–2015 from 50 meteorological stations over Xinjiang (**Figure 1**), provided by the Meteorological Information Center of China Meteorological Administration (CMA). The data of surface wind speed and precipitation from 1960 to 2015 of above stations are also obtained from CMA. NCEP-NCAR reanalysis data (NCEP R1) from 1960 to 2015 are adopted to investigate the atmospheric circulation pattern. NCEP R1 data is one of the most widely used reanalysis data, using a three-dimensional variational (3DVAR) data assimilation scheme with $2.5^\circ \times 2.5^\circ$ horizontal resolution and 28 vertical levels (Kang et al., 2016), which are provided by the National Centers for Environmental Prediction and National Center for Atmospheric research (NCEP/NCAR). Moreover, the Normalized Difference Vegetation Index (NDVI) data from 1982 to 2015 are used in this study. The NDVI data are from the Advanced Very High Resolution Radiometer (AVHRR) carried on the National Oceanic and Atmospheric Administration (NOAA) weather satellite, which provides the longest time NDVI product from 1982.

Methods

Dust events are typically classified into three types: dust storm, blowing dust and flowing dust, according to the visibility (Wang et al., 2005). (Niu et al., 2001) found that the dust concentration of

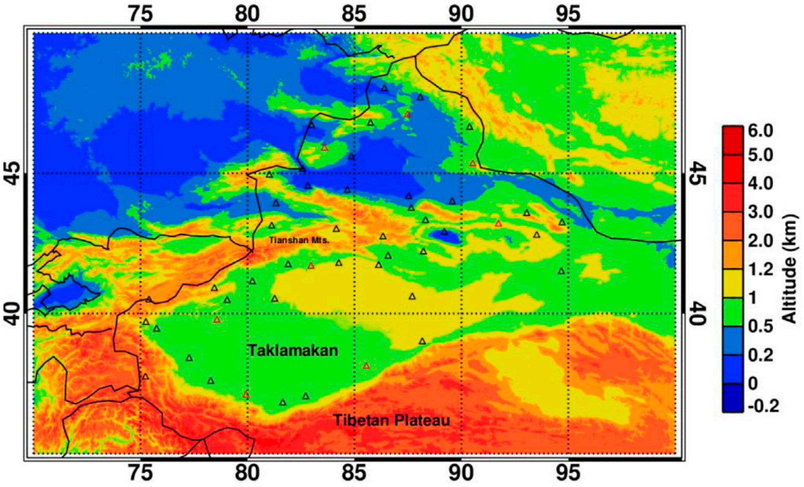

FIGURE 1 | The location of surface observation stations for dust events and the topography of Xinjiang Basin (Triangle: observation station; Red triangle: representative station selected to define DI).

TABLE 1 | Representative stations in Southern and Northern Xinjiang.

Region	Station No.	Station name	Latitude (°N)	Longitude (°E)	Elevation (m)	Correlation coefficient
Southern Xinjiang	51,716	Bachu	39.80	78.57	1,116.5	0.83
	51,644	Kuche	41.72	82.97	1,081.9	0.84
	51,828	Hetian	37.13	79.93	1,375.0	0.80
	51,855	Qiemo	38.15	85.55	1,247.2	0.84
Northern Xinjiang	51,068	Fuhai	47.12	87.48	497.0	0.70
	51,241	Tuoli	45.93	83.60	1,094.2	0.71
	51,288	Beitashan	45.37	90.53	1,653.7	0.67
	51,495	Shisanjianfang	43.22	91.73	721.4	0.72

these three dust events is proportional to each other, and the dust concentration of dust storm is three times higher than that of blowing dust and eight times higher than that of floating dust. Based on this relationship, Wang et al. (Wang et al., 2008) defined the DI for Taklimakan Desert with three dust events data from selected stations. In this study, we use the similar definition to calculate the DI of Xinjiang to describe the statistical characters of the dust events over this region. Firstly, we calculate the correlations of the frequency of monthly dust storm days between each station using the observation data of 50 meteorological stations. Then four stations with the highest correlation coefficients to other stations are selected to calculate the DI, which could present the regional characters of three dust events over the Xinjiang region. The detailed information of representative stations is given in **Table 1**, and the locations are also marked in **Figure 1**. The correlation coefficients of these representative stations are above 0.8 and 0.67 for Southern and Northern Xinjiang, respectively ($p < 0.05$).

Based on the formula proposed by Wang et al. (2008), the equation of DI for Xinjiang is defined as

$$\mathbf{DI} = \mathbf{FD} + 3 \times \mathbf{BD} + 9 \times \mathbf{DS} \tag{1}$$

where FD, BD, and DS are occurrence days of floating dust, blowing dust and dust storm, respectively.

The annual mean occurrence days of three dust events at selected stations are used to calculate the DI.

RESULTS AND DISCUSSION

Temporal and Spatial Distribution of Dust Events

Figure 2 displays the monthly average occurrence days of dust storm, blowing dust and floating dust over Xinjiang region from 1960 to 2015. The frequency of each type of dust event in Southern Xinjiang is significantly greater than that in Northern Xinjiang, according to **Figure 2**. The annual days of dust events in Southern Xinjiang are 12 times more than that in Northern Xinjiang. The most frequent dust event is floating dust in Southern Xinjiang, and its annual occurrence days is larger than 69 days. While, the blowing dust is the most frequent event in Northern Xinjiang, and its annual occurrence days are about 5 days. This tremendous difference is mainly caused by the special terrain. The local dust emission rules Southern Xinjiang due to

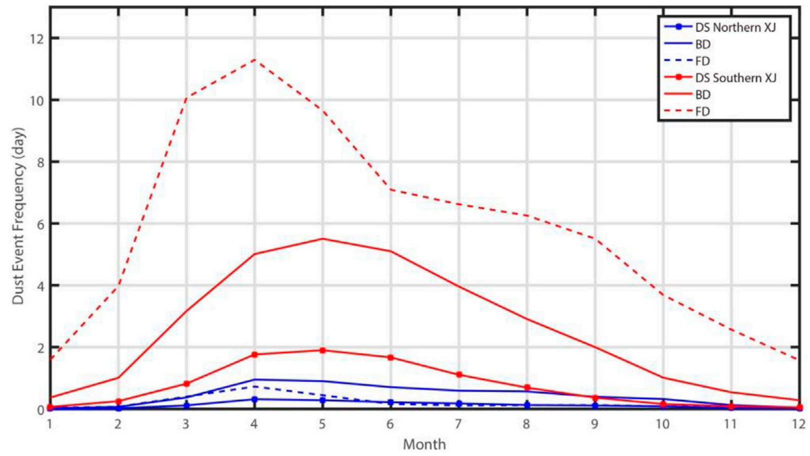

FIGURE 2 | Monthly average occurrence days of dust storm, blowing dust and floating dust during 1960–2015.

TABLE 2 | Seasonal percentage for floating dust, blowing dust and dust storms.

		Spring (%)	Summer (%)	Autumn (%)	Winter (%)
Southern Xinjiang	Dust storm	50.33	38.86	6.86	3.94
	Blowing dust	44.37	38.80	11.50	5.33
	Floating dust	44.43	28.61	16.84	10.12
Northern Xinjiang	Dust storm	47.56	34.88	14.88	2.68
	Blowing dust	43.96	36.84	16.59	2.61
	Floating dust	65.68	16.52	11.76	6.05

the Taklimakan desert, however, only a small amount of dust can be transported to the Northern Xinjiang because of the barrier of Tianshan Mountain. As shown in **Figure 2**, the three types of dust events in both Southern and Northern Xinjiang primarily occur from March to July, which are characterized by a strong unimodal pattern with peaks in April or May. For Southern Xinjiang, the peak of floating dust is in april, while that of dust storm and blowing dust are both in May. The statistical results in **Table 2** show that the total number of dust storm, blowing dust and floating dust in spring and summer accounts for 89.19, 83.17, and 73.04% of these events over the entire year for Southern Xinjiang, respectively, and they are 82.44, 80.80, and 82.20% for Northern Xinjiang, which demonstrates that dust events of Xinjiang mainly occur during Spring and Summer. In spring, the fontal cyclone activity with strong wind is frequent in this region, which induces dust events to happen more often than any other season. In summer, although the wind is not strong as it is in spring due to the rare cold front intrusion, the dust event frequency almost accounts for more than a third of the entire year, only smaller than spring. (Ge et al., 2014) found that although the synoptic situation of spring and summer are quite different, there are also common features for the two seasons: a strong anticyclonic wind anomaly over the Taklimakan at 500 hPa and an enhanced easterly wind over Tarim Basin at 850 hPa, which are all favorable conditions for dust entrainment from the dry desert surface, vertical lofting, and horizontal transportation.

Figure 3 shows the spatial distribution of the annual average occurrence days of floating dust, blowing dust and dust storm over the 56-year in the Xinjiang area. The average occurrence days of three dust events for many Southern Xinjiang stations are more than 130 days, while that in most Northern Xinjiang stations are less than 15 days. As the dominant type of dust event over Xinjiang, the annual mean occurrence days of floating and blowing dust are about 100 days in Southern Xinjiang and less than 10 days in Northern Xinjiang except for stations located along the main dust transport path. This spatial distribution is mainly caused by the special topography. The Taklimakan Desert is located in the Tarim Basin with an average elevation of 1.1 km, where the Pamir Plateau bounds it with an average elevation of 5.5 km to the west and the Kunlun mountain with an average elevation of 5.5 km to the south, as well as the Tianshan mountain with average elevation 4.8 km to the north. The eastern margin of the Taklimakan is the only low-elevation opening for low-level dust to flow out of the desert basin. The dust from Taklimakan Desert rules the local dust emission and induces the flowing dust to dominate the Southern Xinjiang. Lower dust only can be further transported to the northern part by passing through this “gate”. Hence, the blowing dust is the primary dust event in Northern Xinjiang and relatively much less frequent. Combined with the wind rose diagram in **Figure 4**, it is clear that Southern Xinjiang is dominated by easterly winds, which produces great wind shear due to the topographic effect of the

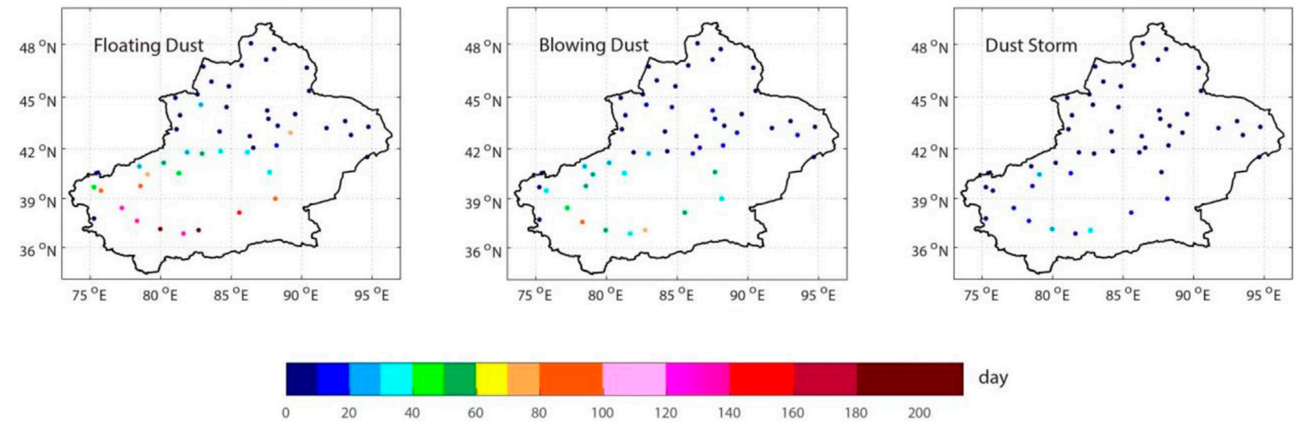

FIGURE 3 | Spatial distribution of floating dust, blowing dust and dust storm in Xinjiang.

Qinghai-Tibet Plateau in the Southern Tarim Basin. The wind shear further facilitates the occurrence of strong dust events, which leads to the primary spatial distribution of dust in Southern Xinjiang along the Taklimakan Desert.

Interannual Variations and Abrupt Changes of Dust Events

The changes of occurrence days of three dust events in Southern and Northern Xinjiang from 1960–2015 are statistically analyzed in **Figure 5**. In general, annual occurrence days of dust events decrease in the Xinjiang region over 56 years. During this period, the number of annual occurrences of dust events increased gradually from 1960 to 1980 with the peak in the late-1970, after that decreased rapidly until the 21st century, and then began to increase after 2005, especially in Southern Xinjiang. This result is consistent with the results presented by Qian et al. (2004). They got the same conclusions of the trend of variations and also pointed that the northern dust has increased since 2000 and a new rising active period will occur.

The DI, describing the large-scale variability of dust events and defined in *Methods*, is a combination of dust storm, blowing dust and floating dust with distinct weight coefficients, which is used to investigate the trend of dust variation over Xinjiang during the past 56 years. **Figure 6** shows the interannual variations of DI and their corresponding sliding *t*-test in Southern and Northern Xinjiang from 1960 to 2015. As shown in **Figure 6A**, the DI in Southern Xinjiang presented a significant downward trend and a linear rate of decrease up to −8.2/year ($p < 0.05$). For Northern Xinjiang, a similar decline trend with a linear rate of −1.37/year since 1985 is shown in **Figure 6B**; however, there is an increase trend during 1960–1984 with the linear rate of 2.52/year. The DI of Northern Xinjiang shows great fluctuation, due to the relatively rare occurrence of dust events in Northern Xinjiang, which is only approximately 10% of that in Southern Xinjiang.

Sliding *t*-test is a widely used statistical method to detect the abrupt change objectively. This method is utilized in this study for DI abrupt change over Southern and Northern Xinjiang, and the results are given in **Figures 6C,D**, respectively. **Figure 6C** illustrates that abrupt changes of DI of Southern Xinjiang occurred in 1975 and 1985, but the sliding *t*-test value decreased significantly after 2005 without passing the 0.05 significance level. The results suggest that although DI has increased since 2005, it does not experience abrupt change. The DI of Northern Xinjiang shows a single peak pattern, with a significant increase before 1984 and a decrease afterward. In combination with the abrupt change detected by the sliding *t*-test in **Figure 6D**, the results show that the years of abrupt change in Northern Xinjiang are generally consistent with that in Southern Xinjiang, which are 1978 and 1986.

Potential Causes for Trends of Dust Events

As an important dust emission region, the declining trend of the dust events in Xinjiang affected the dust activities in the downwind area significantly. Shao et al. (Shao et al., 2013) showed that the global mean dust concentration has decreased by 1.2% yr^{-1} during the latest 20 years, which can be mainly attributed to the decreased frequencies of dust events in these important dust emission regions. To further identify the potential causes of dust event variations over the Xinjiang region, the changes of controlling factors and their correlations with the DI are investigated in this paper.

Surface Wind Speed

It has been recognized that wind is a curial factor in controlling dust events, which plays an essential role not only in the emission but also during the transportation of dust (Kang et al., 2016). **Figure 7** displays variations of annual average surface wind speed in Southern and Northern Xinjiang from 1960 to 2015 based on the data from observation stations. It illuminates that the wind speed in both Southern and Northern Xinjiang shows a consistent decreasing trend over the 56-year study period. The linear rates of decline can be up to −0.014/year and −0.009/year for Southern and Northern Xinjiang, respectively ($p < 0.05$). This downward trend of surface wind

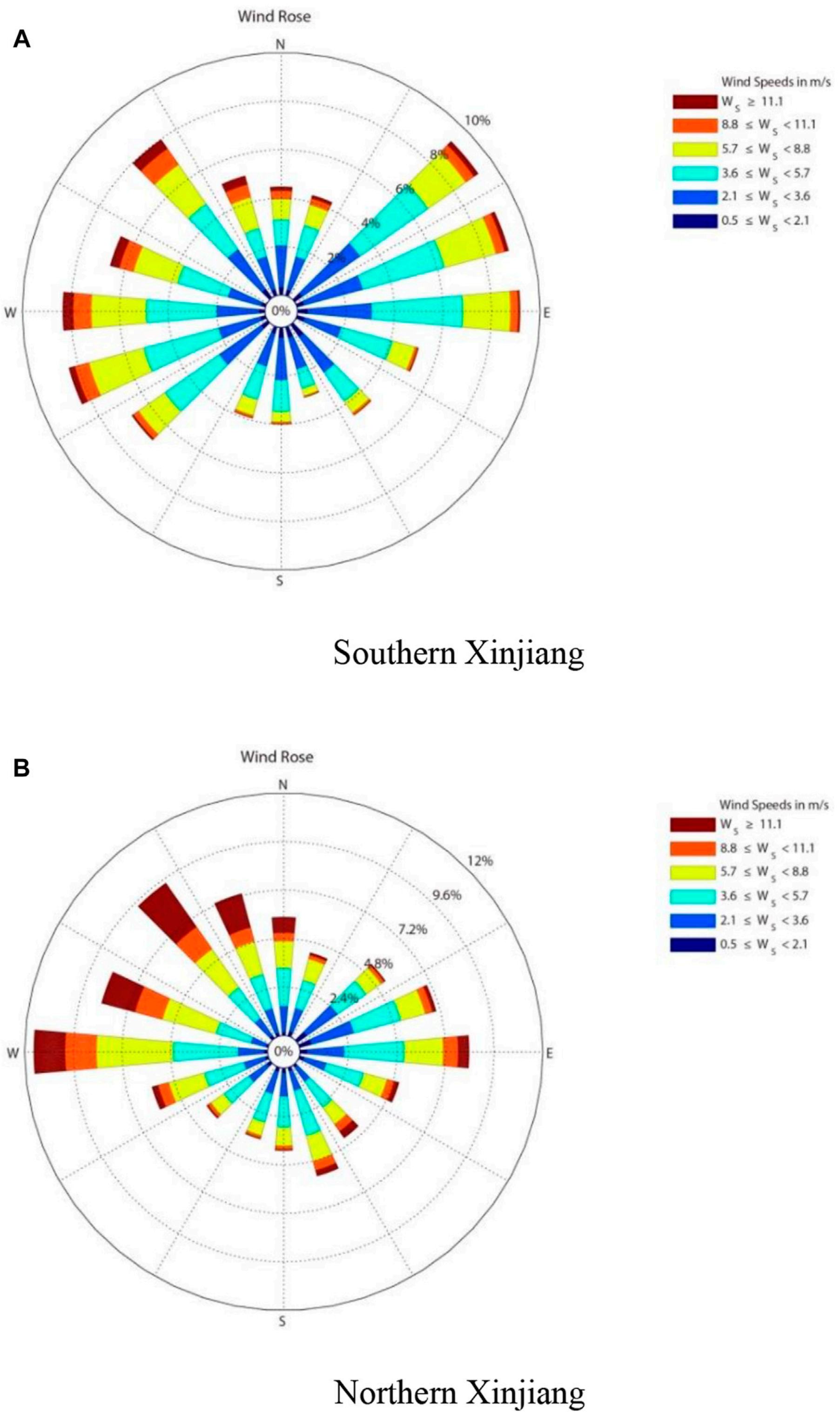

FIGURE 4 | Wind rose diagram: **(A)** Southern Xinjiang. **(B)** Northern Xinjiang.

speed over Xinjiang agrees with the reduction of the global average surface wind speed that has been occurring over land since 1980, which is a phenomenon known as the "global terrestrial stilling" (Zeng et al., 2019). In general, the results of abrupt change of wind are similar to DI; however, there is an evident abrupt change in 2000, which is more significant than

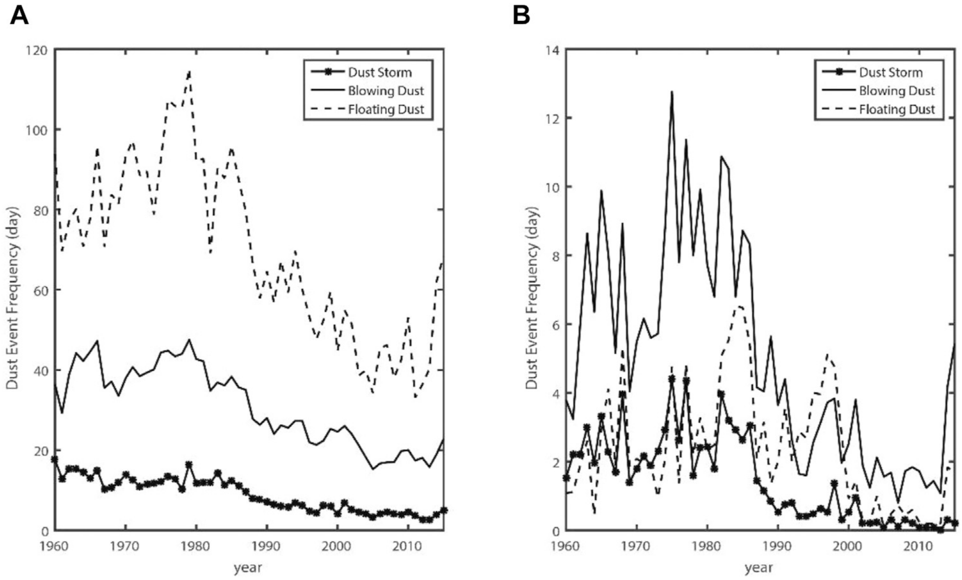

FIGURE 5 | Interannual Variations of dust storm, blowing dust and floating dust in **(A)** Southern Xinjiang and **(B)** Northern Xinjiang.

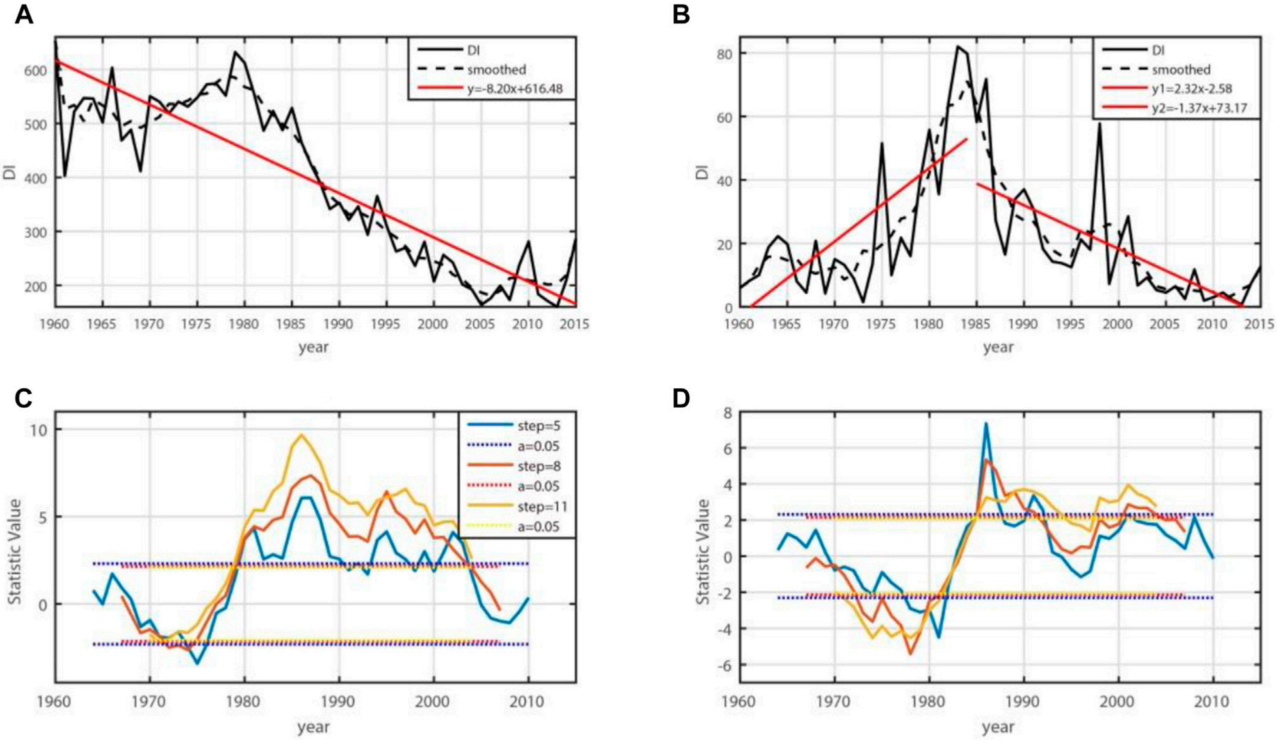

FIGURE 6 | Variations of DI and sliding *t*-test: Southern Xinjiang **(A,C)**, Northern Xinjiang **(B,D)**.

that in the *t*-test of DI (*Interannual Variations and Abrupt Changes of Dust Events*).

The comparison of the trend of DI and average wind speed from 1960 to 2015 in Southern and Northern Xinjiang is shown in **Figure 8**. Since more than 80% of dust events in Xinjiang occurred in spring and summer, DI and wind speed of spring and summer are calculated in **Figure 8**. DI and wind speed are changing synchronously during 1960–2000, which shows a good

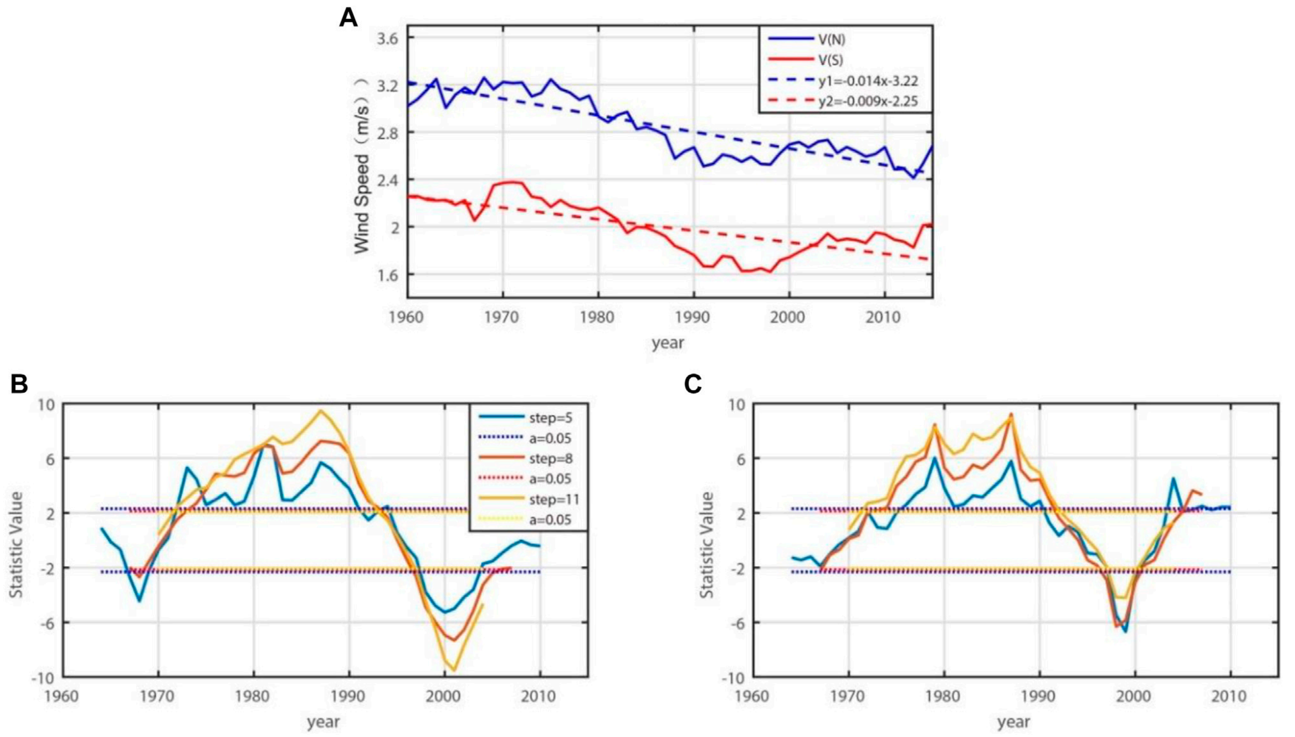

FIGURE 7 | (A) Variations of average wind speed and sliding *t*-test for **(B)** Southern Xinjiang and **(C)** Northern Xinjiang.

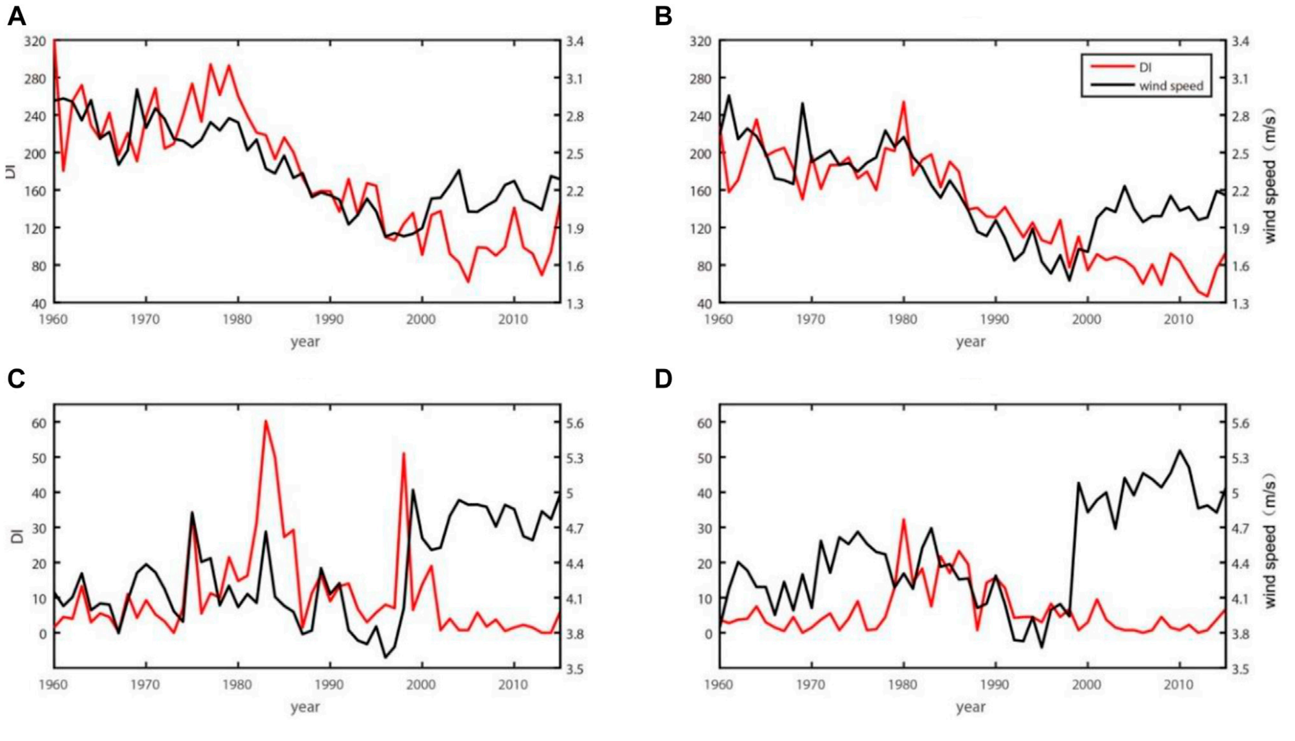

FIGURE 8 | Variations of DI and average surface wind speed: Southern Xinjiang **(A,B)** and Northern Xinjiang **(C,D)** in spring **(A,C)** and summer **(B,D)**.

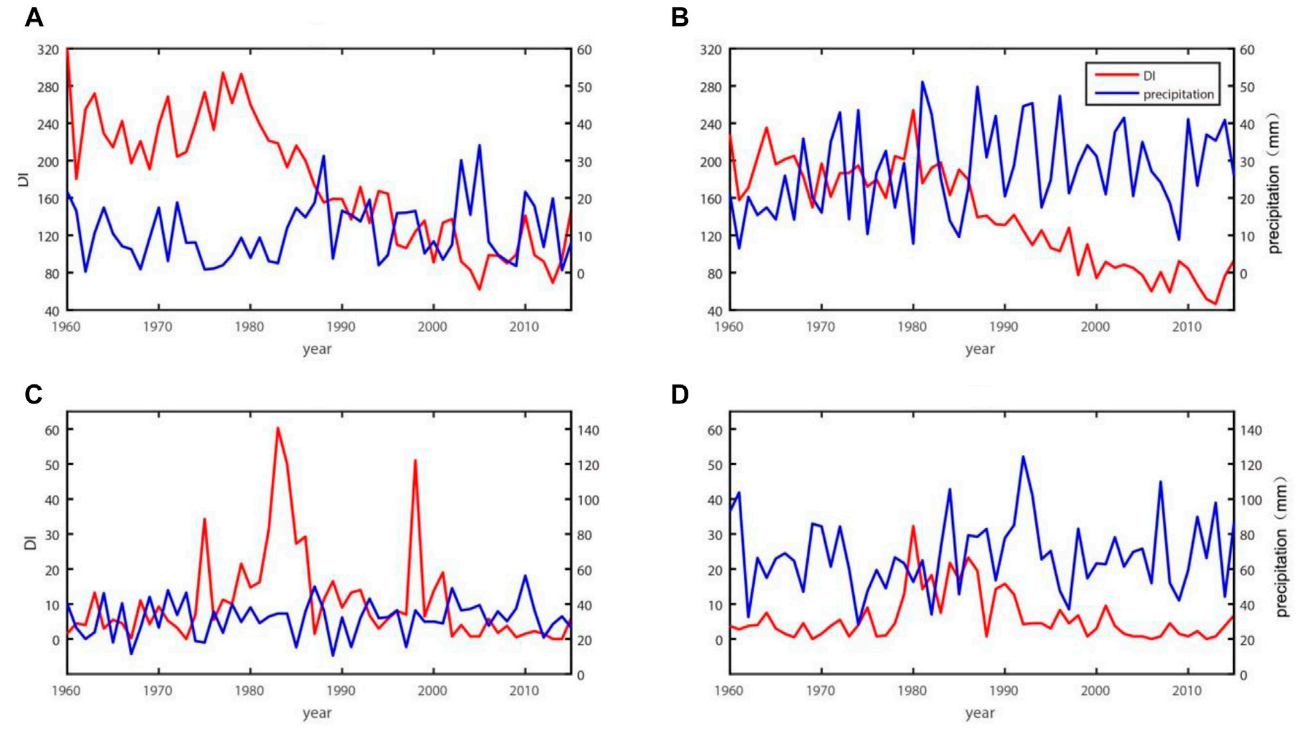

FIGURE 9 | Variations of DI and precipitation of Southern Xinjiang **(A,B)** and Northern Xinjiang **(C,D)** in spring **(A,C)** and summer **(B,D)**.

TABLE 3 | Precipitation and frequency in different periods.

		1960–1999		2000–2015	
		Average spring and summer	Average annual	Average spring and summer	Average annual
Precipitation (mm)	Southern Xinjiang	57.02	72.33	64.79	87.52
	Northern Xinjiang	121.89	176.93	135	202.95
Frequency (day)	Southern Xinjiang	22.33	32.7	23.99	37.03
	Northern Xinjiang	42.62	74.92	41.26	77.01

one to one relationship between variations and peaks of DI and wind speed, especially in Southern Xinjiang. The correlation of DI and wind speed can reach 0.79 over the 56-year ($p < 0.05$), which demonstrates that changes of surface wind speed will significantly and directly affect the dust events of this area. But it is worth pointing that after 2000, the magnitude of wind speed increases considerably greater than that of DI. The correlation coefficient between the DI and wind speed also dramatically dropped to 0.37 during 2000–2015, indicating there must be other factors effectively impacting dust events.

Precipitation and Vegetation

Since the local dust emission is closely associated with surface conditions, the precipitation could indirectly affect dust emission *via* changing surface conditions. Therefore, we further analyze the relationship between DI and precipitation. **Figure 9** illustrates the DI and precipitation in spring and summer during 1960–2015 in Southern and Northern Xinjiang, respectively. It shows a negative relationship between DI and precipitation, especially in summer with more precipitation. Combining with **Table 3** that gives the statistical data on the precipitation and frequency during 1960–1999 and 2000–2015, the average annual precipitation increased from 72.33 to 87.52 mm (17.4%) in Southern Xinjiang, and from 176.93 to 202.95 mm (14.7%) in Northern Xinjiang. Meanwhile, their days of precipitation also increased by 13 and 2.8%, respectively. The synchronous increases in the precipitation and the days of precipitation would suppress the occurrence of dust events. Moreover, the changing of surface vegetation is also studied in this paper. Following the similar analysis of above precipitation studies, the variations of DI and NDVI in spring and summer during 1982–2015 are investigated, which are illustrated in **Figure 10**. The increasing trend of NDVI indicates the improvement of vegetation, especially in summer of Southern Xinjiang. This result is also consistent with other studies

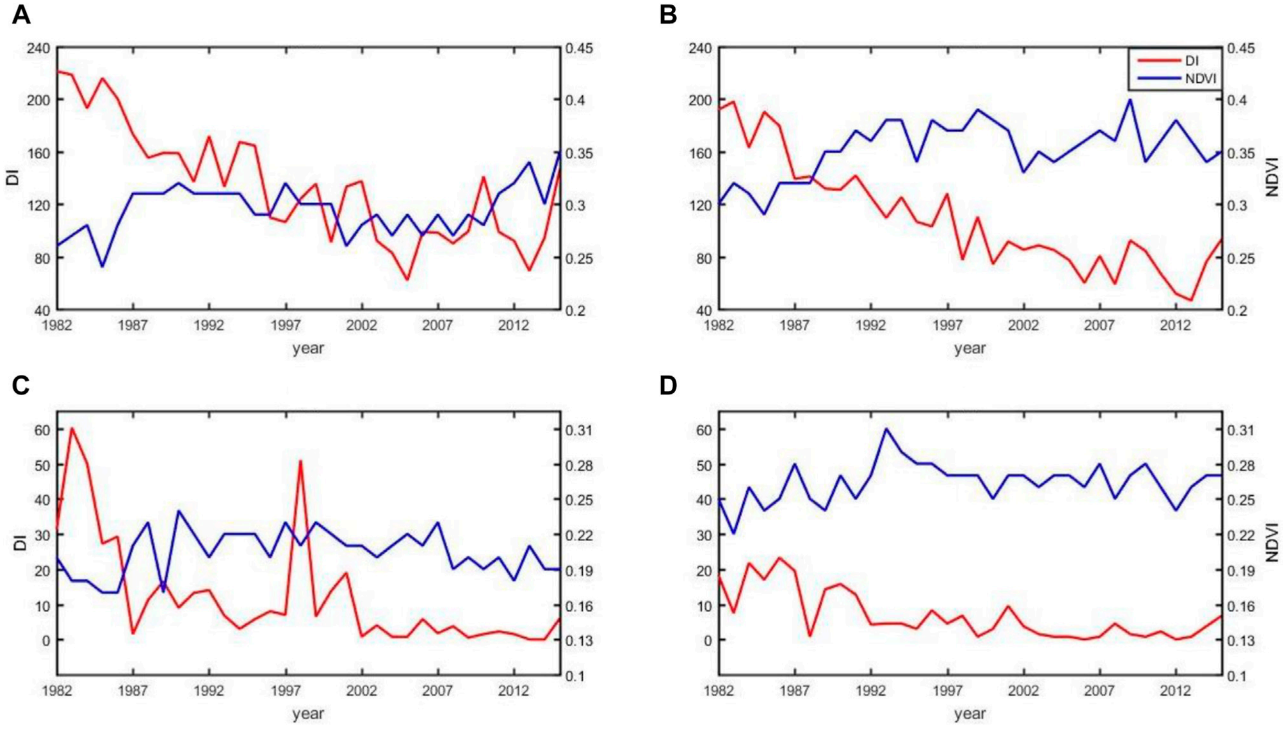

FIGURE 10 | Variations of DI and NDVI of Southern Xinjiang **(A,B)** and Northern Xinjiang **(C,D)** in spring **(A,C)** and summer **(B,D)**.

TABLE 4 | High-frequency and low-frequency dust years.

Classification	Represented year				
rising period (1)	1969	1970	1971	1972	1973
rising period (2)	2004	2009	2010	2014	2015
declining period	1991	1992	1995	1996	1997

which all informed that the vegetation coverage in Xinjiang region had a general increase with fluctuations in recent years (Bao et al., 2017; Yuan et al., 2020; Zhang et al., 2020; Zhou et al., 2021). Therefore this might be another possible reason to explain the change of dust events since 2000. The above analysis suggests that precipitation and vegetation are another factors associated with the variations of dust events in Xinjiang, in view of the change of dust events since 2000.

High-Altitude Wind Field

The westerly circulation of the upper troposphere is an important system for the climate of mid-to-high latitude region. The specific circulation pattern is strongly associated with dust events in northern China (Zhong and Li, 2005; Li and Liu, 2015). To further investigate the atmospheric circulation pattern in the rising and declining periods of dust events, we analyze the changes of high-altitude wind fields by using the NECP data of daily zonal wind speed. As discussed in *Interannual Variations and Abrupt Changes of Dust Events*, the occurrences of dust events increased gradually from 1960 to 1980, peaked in the late-1970, then decreased rapidly until 2000, and started a new active period. Therefore, we chose 1960–1980 and 2000–2015 as the two rising periods and 1981–1999 as the declining period. Meanwhile, the high frequency years and low frequency years are selected during the rising period and declining period respectively as represented years based on the ranking of DI, which are listed in **Table 4**.

Figure 11 shows the difference of zonal wind speed between rising and declining periods for 200 hPa and 500 hPa, respectively. During these two dusts rising periods, both 500 hPa and 200 pha zonal wind speed show the strengthened wind over the entire northern China region. The 500 hPa zonal mean wind speed during the rising period of dust events (1960–1980) over Xinjiang is larger than 1.24 m/s compared to declining period, whereas that is for about 1.10 m/s during 2000–2015, which is weaker than that of 1960–1980. The rising dust events are linked to the intensified westerly jet over Xinjiang.

The cross-section of the mean zonal wind difference of 70°–100°E indicates that the strengthening trends of westerly jet are coherent at all different height levels, shown in **Figure 12**. The difference of the high-altitude wind field between the rising and declining periods of dust events show that the changes of the East Asian atmospheric circulation, which dominates the high-altitude wind fields of the area, would lead to changes in the surface wind and precipitation, thereby changing the frequency of dust events.

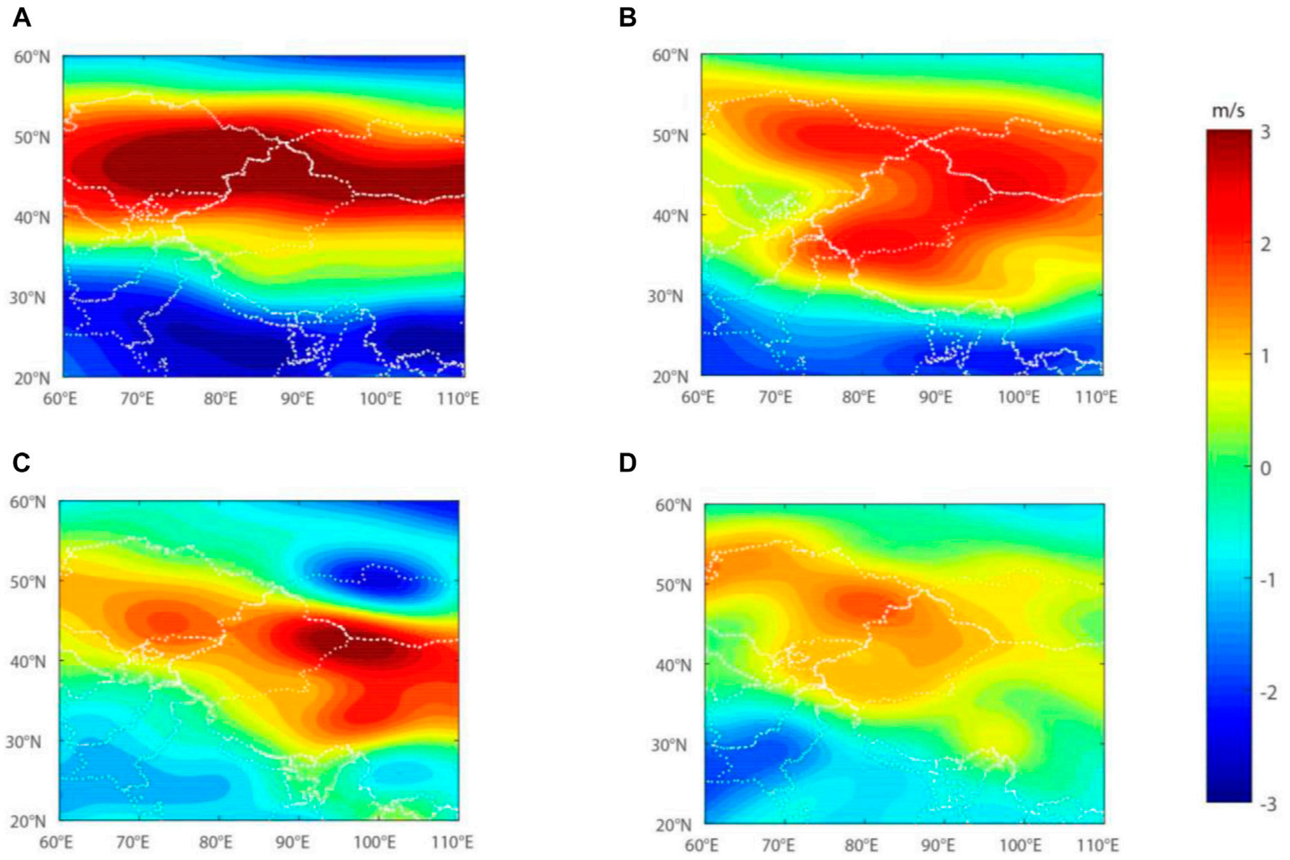

FIGURE 11 | Difference of zonal wind speed between rising period 1960–1980 **(A,C)**, 2000–2015 **(B,D)** and declining period (1981–1999) for 500 hPa **(A,B)** and 200 hPa **(C,D)**.

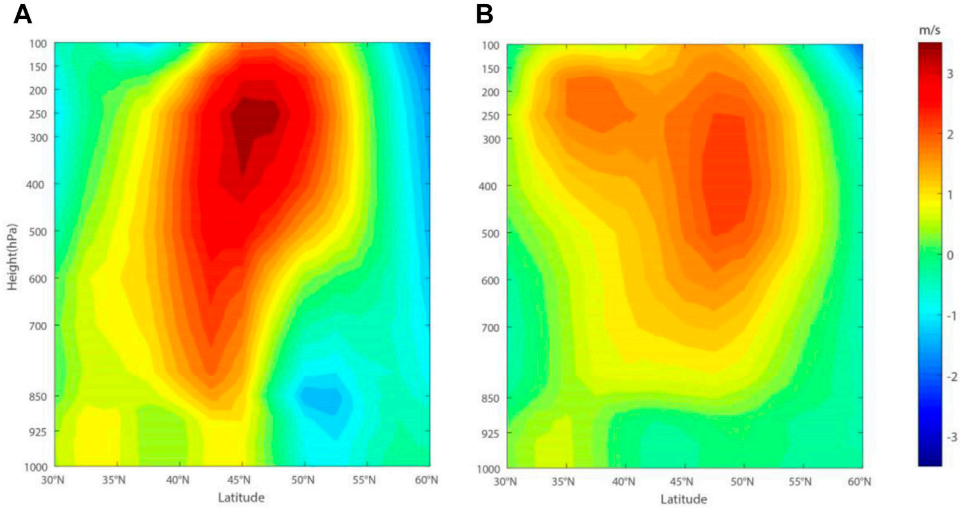

FIGURE 12 | Cross-section of difference of average zonal wind speed (70–100E°) between **(A)** rising period 1960–1979, **(B)** 2000–2015 and declining period (1990–1999).

CONCLUSION

This study investigates the temporal and spatial distribution and the long-term trends of dust events in Xinjiang based on ground-based observation during 1960–2015. The dust events of Xinjiang Basin happen frequently in spring and summer, each year more than 73% of the dust events occurring in these two seasons. The dust events in the Southern Xinjiang are significantly more than that in the northern, and the high incidence area is distributed along the Taklamakan Desert. The DI generally increased during the 1960s–1970s and dramatically decreased in the 1980s–1990s, and then increased in a new active period after 2000. The main factors that influence the variations of dust events are also studied by ground meteorological fields, NECP reanalysis data and NOAA NDVI data. In Southern Xinjiang, there is a significant downward trend of DI in the past 56 years with a linear decreasing rate −8.2years^{-1}. Simultaneously, surface wind speed also indicates a similar decline trend. There is an positive correlation coefficient 0.79 between DI and surface wind, but after 2000 the increase of the DI is not as strong as wind speed rising with the correlation coefficient reducing to 0.34. By analysing the precipitation during different periods, it is found that the average annual total amount and frequency of precipitation increased by 17.4 and 13% in 2000–2015 compared with 1960–1999, respectively, and the NDVI which represents the vegetation condition also shows an increasing trend. That indicates the increase of precipitation and improvement of surface condition will suppress the occurrence of dust events. Furthermore, the high-altitude wind field analysis displays that the variation of the East Asian general circulation's intensity that dominates the upper-level wind fields in the Xinjiang Basin could affect the near-surface wind speed and precipitation, and further the dust activities.

DATA AVAILABILITY STATEMENT

The original contributions presented in the study are included in the article/supplementary material, further inquiries can be directed to the corresponding authors.

AUTHOR CONTRIBUTIONS

All authors listed have made a substantial, direct, and intellectual contribution to the work and approved it for publication.

FUNDING

This research was funded by the National Key Research and Development Program of China (2020YFA0608402) and the National Key Research and Development Program of China (2018YFC1506701).

REFERENCES

Albrecht, B. A. (1989). Aerosols, Cloud Microphysics, and Fractional Cloudiness. *Science* 245 (4923), 1227–1230. doi:10.1126/science.245.4923.1227

Bao, A., Huang, Y., Ma, Y., Guo, H., and Wang, Y. (2017). Assessing the Effect of EWDP on Vegetation Restoration by Remote Sensing in the Lower Reaches of Tarim River. *Ecol. Indicators* 74, 261–275. doi:10.1016/j.ecolind.2016.11.007

Cabrerizo, M. J., Medina-Sánchez, J. M., González-Olalla, J. M., Villar-Argaiz, M., and Carrillo, P. (2016). Saharan Dust Inputs and High UVR Levels Jointly Alter the Metabolic Balance of marine Oligotrophic Ecosystems. *Sci. Rep.* 6 (1), 35892. doi:10.1038/srep35892

CCTV-News (2021). Ministry of Ecology and Environment: There Have Been 21 Dust Weather Events in Northern China This Year. [Online]. Available: http://m.news.cctv.com/2021/05/26/ARTI9tg58ixubbJ2KTKTltBW210526.shtml (Accessed 6 1, 2021).

Chen, S., Tong, B., Dong, C., Wang, F., Chen, B., Cheng, C., et al. (2020). Retrievals of Aerosol Layer Height during Dust Events over the Taklimakan and Gobi Desert. *J. Quantitative Spectrosc. Radiative Transfer* 254, 107198. doi:10.1016/j.jqsrt.2020.107198

Ge, J. M., Huang, J. P., Xu, C. P., Qi, Y. L., and Liu, H. Y. (2014). Characteristics of Taklimakan Dust Emission and Distribution: A Satellite and Reanalysis Field Perspective. *J. Geophys. Res. Atmos.* 119 (20), 11,772–11,783. doi:10.1002/2014JD022280

Hu, Z., Huang, J., Zhao, C., Jin, Q., Ma, Y., and Yang, B. (2020). Modeling Dust Sources, Transport, and Radiative Effects at Different Altitudes over the Tibetan Plateau. *Atmos. Chem. Phys. Discuss.* 20 (3), 1507–1529. doi:10.5194/acp-20-1507-2020

Indoitu, R., Orlovsky, L., and Orlovsky, N. (2012). Dust Storms in Central Asia: Spatial and Temporal Variations. *J. Arid Environments* 85, 62–70. doi:10.1016/j.jaridenv.2012.03.018

Jin, L., He, Q., Li, Z., Deng, M., and Abbas, A. (2021). Interannual and Seasonal Variations of Sand-Dust Events in Tarim Basin, China. *Res. Sq.* doi:10.21203/rs.3.rs-327333/v1

Kang, L., Huang, J., Chen, S., and Wang, X. (2016). Long-term Trends of Dust Events over Tibetan Plateau during 1961-2010. *Atmos. Environ.* 125, 188–198. doi:10.1016/j.atmosenv.2015.10.085

Li, D., and Zhong, H. (2007). The Climatic Formation Cause and the Future Developing Trend of Sand-Dust Storm in China. *China Environ. Sci.* 27 (1), 14–18. doi:10.3321/j.issn:1000-6923.2007.01.005

Li, J., Garshick, E., Al-Hemoud, A., Huang, S., and Koutrakis, P. (2020). Impacts of Meteorology and Vegetation on Surface Dust Concentrations in Middle Eastern Countries. *Sci. Total Environ.* 712, 136597. doi:10.1016/j.scitotenv.2020.136597

Li, X., and Liu, X. (2015). Relation of Spring Dust-Storm Activities in Northern China and Changes of Upper Westerlies. *Plateau Meteorology* 34 (5), 1292–1300. doi:10.7522/j.issn.1000-0534.2014.00067

Linares, C., Culqui, D., Belda, F., López-Bueno, J. A., Luna, Y., Sánchez-Martínez, G., et al. (2021). Impact of Environmental Factors and Sahara Dust Intrusions on Incidence and Severity of COVID-19 Disease in Spain. Effect in the First and Second Pandemic Waves. *Environ. Sci. Pollut. Res.* 16, 1–13. doi:10.1007/s11356-021-14228-3

Liu, L., Guo, J., Gong, H., Li, Z., Chen, W., Wu, R., et al. (2019). Contrasting Influence of Gobi and Taklimakan Deserts on the Dust Aerosols in Western North America. *Geophys. Res. Lett.* 46 (15), 9064–9071. doi:10.1029/2019GL083508

Ma, M., Yang, X., Zhou, C., He, Q., and Mamtimin, A. (2020). Contributions of Dusty Weather and Dust Devil to Dust Emission Amounts at the Northern Margin of the Taklimakan Desert. *Nat. Hazards* 103 (1), 1441–1454. doi:10.1007/s11069-020-04043-3

Ma, Y., Wang, X., Huang, Z., and Chen, C. (2006). Change in Space-Time Distribution of Sand-Dust and Influence of Climatic Factors. *Arid Land Geogr.* 29 (2), 178–185. doi:10.13826/j.cnki.cn65-1103/x.2006.02.003

Niu, S., Sun, J., Chen, Y., and Liu, H. (2001). Observation and Analysis of Mass Concentration of Dust and Sand Aerosol in spring in Helanshan Area. *Plateau Meteorology* 20 (1), 82–87.

Pi, H., Sharratt, B., and Lei, J. (2017). Atmospheric Dust Events in central Asia: Relationship to Wind, Soil Type, and Land Use. *J. Geophys. Res. Atmos.* 122 (12), 6652–6671. doi:10.1002/2016JD026314

Qian, Z. a., Cai, Y., Liu, J. T., Li, D. L., Liu, Z. M., and Song, M. H. (2004). Progress in the Study of Sandstorm in Northern China. *J. Arid Land Resour. Environ.* S1, 1–8. doi:10.3321/j.issn:0001-5733.2006.01.012

Shao, Y., Klose, M., and Wyrwoll, K.-H. (2013). Recent Global Dust Trend and Connections to Climate Forcing. *J. Geophys. Res. Atmos.* 118 (19), 11,107–11,118. doi:10.1002/jgrd.50836

Sokolik, I. N., and Toon, O. B. (1999). Incorporation of Mineralogical Composition into Models of the Radiative Properties of mineral Aerosol from UV to IR Wavelengths. *J. Geophys. Res.* 104, 9423–9444. doi:10.1029/1998JD200048

Struve, T., Pahnke, K., Lamy, F., Wengler, M., Böning, P., and Winckler, G. (2020). A Circumpolar Dust Conveyor in the Glacial Southern Ocean. *Nat. Commun.* 11 (1), 5655. doi:10.1038/s41467-020-18858-y

Tian, Y., Wang, Z., Pan, X., Li, J., Yang, T., Wang, D., et al. (2020). Influence of the Morphological Change in Natural Asian Dust during Transport: A Modeling Study for a Typical Dust Event over Northern China. *Sci. Total Environ.* 739, 139791. doi:10.1016/j.scitotenv.2020.139791

Twomey, S. (1977). The Influence of Pollution on the Shortwave Albedo of Clouds. *J. Atmos. Sci.* 34 (7), 1149–1152. doi:10.1175/1520-0469(1977)034<1149:tiopot>2.0.co;2

Wallden, A., Graff, P., Bryngelsson, I.-L., Fornander, L., Wiebert, P., and Vihlborg, P. (2020). Risks of Developing Ulcerative Colitis and Crohn's Disease in Relation to Silica Dust Exposure in Sweden: a Case-Control Study. *BMJ Open* 10 (2), e034752. doi:10.1136/bmjopen-2019-034752

Wang, S., Wang, J., Zhou, Z., and Shang, K. (2005). Regional Characteristics of Three Kinds of Dust Storm Events in China. *Atmos. Environ.* 39 (3), 509–520. doi:10.1016/j.atmosenv.2004.09.033

Wang, S., Wang, X., Chen, D., Ji, C., Jiang, Y., and Liu, J. (2019a). The Spatial and Temporal Variation Characteristics and Influencing Factors of Dust Weather in the Southern Xinxiang from 1961 to 2017. *J. Arid Land Resour. Environ.* 33 (9), 81–86. doi:10.13448/j.cnki.jalre.2019.269

Wang, W., Huang, J., Minnis, P., Hu, Y., Li, J., Huang, Z., et al. (2010). Dusty Cloud Properties and Radiative Forcing over Dust Source and Downwind Regions Derived from A-Train Data during the Pacific Dust Experiment. *J. Geophys. Res.* 115 (D4), 1–17. doi:10.1029/2010JD014109

Wang, W., Huang, J., Zhou, T., Bi, J., Lin, L., Chen, Y., et al. (2013). Estimation of Radiative Effect of a Heavy Dust Storm over Northwest China Using Fu-Liou Model and Ground Measurements. *J. Quantitative Spectrosc. Radiative Transfer* 122, 114–126. doi:10.1016/j.jqsrt.2012.10.018

Wang, W., Sheng, L., Dong, X., Qu, W., Sun, J., Jin, H., et al. (2017). Dust Aerosol Impact on the Retrieval of Cloud Top Height from Satellite Observations of CALIPSO, CloudSat and MODIS. *J. Quantitative Spectrosc. Radiative Transfer* 188, 132–141. doi:10.1016/j.jqsrt.2016.03.034

Wang, W., Sheng, L., Jin, H., and Han, Y. (2015). Dust Aerosol Effects on Cirrus and Altocumulus Clouds in Northwest China. *J. Meteorol. Res.* 29 (5), 793–805. doi:10.1007/s13351-015-4116-9

Wang, X., Huang, J., Ji, M., and Higuchi, K. (2008). Variability of East Asia Dust Events and Their Long-Term Trend. *Atmos. Environ.* 42 (13), 3156–3165. doi:10.1016/j.atmosenv.2007.07.046

Wang, Y., Zhang, H., Chen, H., and Chai, F. (2019b). The Sources and Transport of Iron in the North Pacific and its Impact on marine Ecosystems. *Atmos. Oceanic Sci. Lett.* 12 (1), 30–34. doi:10.1080/16742834.2019.1545513

Xiu, P., and Chai, F. (2021). Impact of Atmospheric Deposition on Carbon Export to the Deep Ocean in the Subtropical Northwest Pacific. *Geophys. Res. Lett.* 48 (6), e2020GL089640. doi:10.1029/2020GL089640

Yasukawa, K., Ohta, J., Miyazaki, T., Vaglarov, B. S., Chang, Q., Ueki, K., et al. (2019). Statistic and Isotopic Characterization of Deep-Sea Sediments in the Western North Pacific Ocean: Implications for Genesis of the Sediment Extremely Enriched in Rare Earth Elements. *Geochem. Geophys. Geosyst.* 20 (7), 3402–3430. doi:10.1029/2019GC008214

Yuan, J., Bian, Z., Yan, Q., Gu, Z., and Yu, H. (2020). An Approach to the Temporal and Spatial Characteristics of Vegetation in the Growing Season in Western China. *Remote Sensing* 12 (6), 945. doi:10.3390/rs12060945

Zeng, Z., Ziegler, A. D., Searchinger, T., Yang, L., Chen, A., Ju, K., et al. (2019). A Reversal in Global Terrestrial Stilling and its Implications for Wind Energy Production. *Nat. Clim. Chang.* 9 (12), 979–985. doi:10.1038/s41558-019-0622-6

Zhang, H., Xue, L., Wei, G., Dong, Z., and Meng, X. (2020). Assessing Vegetation Dynamics and Landscape Ecological Risk on the Mainstream of Tarim River, China. *Water* 12 (8), 2156. doi:10.3390/w12082156

Zhong, H., and Li, D. (2005). Relationship between Sand-Dust Storm in NorthernChina in April and Westerly Circulation. *Plateau Meteorology* 24 (1), 104–111. doi:10.3321/j.issn:1000-0534.2005.01.016

Zhou, C., Feng, X., Huang, Y., Wang, X., and Zhang, X. (2021). The Indirect Impact of Surface Vegetation Improvement on the Climate Response of Sand-Dust Events in Northern China. *Atmosphere* 12 (3), 339. doi:10.3390/atmos12030339

Conflict of Interest: The authors declare that the research was conducted in the absence of any commercial or financial relationships that could be construed as a potential conflict of interest.

Publisher's Note: All claims expressed in this article are solely those of the authors and do not necessarily represent those of their affiliated organizations, or those of the publisher, the editors and the reviewers. Any product that may be evaluated in this article, or claim that may be made by its manufacturer, is not guaranteed or endorsed by the publisher.

Copyright © 2021 Mu, Su, Mo, Peng, Xu, Wang and Wang. This is an open-access article distributed under the terms of the Creative Commons Attribution License (CC BY). The use, distribution or reproduction in other forums is permitted, provided the original author(s) and the copyright owner(s) are credited and that the original publication in this journal is cited, in accordance with accepted academic practice. No use, distribution or reproduction is permitted which does not comply with these terms.

frontiers
in Earth Science

ORIGINAL RESEARCH
published: 03 September 2021
doi: 10.3389/feart.2021.722435

A Late Pleistocene Wetland Setting in the Arid Jurf ed Darawish Region in Central Jordan

Steffen Mischke[1]*, Zhongping Lai[2], Galina Faershtein[3], Naomi Porat[4], Matthias Röhl[5], Paul Braun[6], Johannes Kalbe[7] and Hanan Ginat[8]

[1]Institute of Earth Sciences, University of Iceland, Reykjavík, Iceland, [2]Institute of Marine Sciences, Shantou University, Shantou, China, [3]Weizmann Institute of Science, Rehovot, Israel, [4]The Geological Survey of Israel, Jerusalem, Israel, [5]Institute of Geological Sciences, Free University of Berlin, Berlin, Germany, [6]Musée National d'Histoire Naturelle, Luxembourg, Luxembourg, [7]Faculty of Agricultural and Environmental Sciences, University of Rostock, Rostock, Germany, [8]Dead Sea and Arava Science Center, Jerusalem, Israel

Current conditions in the southern Levant are hyperarid, and local communities rely on fossil subsurface water resources. The timing of more favourable wetter periods and also their spatial characteristics are not yet well constrained. To improve our understanding of past climate and environmental conditions in the deserts of the southern Levant, sedimentary sections including artefact-bearing beds from Jurf ed Darawish on the Central Jordanian Plateau were investigated using sedimentological and micropalaeontological analyses and OSL dating. Grain-size analysis and structures of the clayey-silty sediments show that they mainly represent reworked loess deposits. The OSL ages suggest that these fine-grained sediments were accumulated during Marine Isotope Stages (MIS) 5-3. Recorded ostracod valves (mostly *Potamocypris*, *Ilyocypris* and *Pseudocandona*), remains of aquatic and terrestrial gastropod shells, and charophyte gyrogonites and stem encrustations indicate that an in-stream wetland existed at the location of Jurf ed Darawish during MIS 5-4 which was replaced by a vegetated alluvial plain in MIS 3. The prevailing aggradational setting was replaced by an erosional setting sometime after 30 ka. Abundant artefacts, distributed over a vertical range of up to 40 cm in a bed covered by a sedimentary sequence of 12-m thickness, provide evidence for the presence of humans in the region during a relatively long period from ca. 85 to 65 ka. The reconstruction of an in-stream wetland at Jurf ed Darawish, and the presence of humans at the site and in other desert regions of the Jordanian Plateau, the Wadi Arava/Araba, and the Negev and the Nefud deserts, show that the regional climate in the late MIS 5 and MIS 4 was significantly wetter than today and provided favourable conditions for humans in the Southern Levant and the northwestern Arabian Peninsula.

Keywords: Southern Levant, OSL dating, granulometry analysis, Ostracoda (Crustacea), human migration

OPEN ACCESS

Edited by:
Zhuolun Li,
Lanzhou University, China

Reviewed by:
Johanna Lomax,
University of Giessen, Germany
Jeff Pigati,
United States Geological Survey (USGS), United States

Correspondence:
Steffen Mischke
smi@hi.is

Specialty section:
This article was submitted to Quaternary Science, Geomorphology and Paleoenvironment, a section of the journal Frontiers in Earth Science

Received: *08 June 2021*
Accepted: *19 August 2021*
Published: *03 September 2021*

Citation:
Mischke S, Lai Z, Faershtein G, Porat N, Röhl M, Braun P, Kalbe J and Ginat H (2021) A Late Pleistocene Wetland Setting in the Arid Jurf ed Darawish Region in Central Jordan. Front. Earth Sci. 9:722435. doi: 10.3389/feart.2021.722435

HIGHLIGHTS

- aggradational setting from >100 to at least 30 ka
- transition from aggradation to incision sometime afterwards
- in-stream wetland during MIS 5 and 4
- vegetated alluvial plain in MIS 3
- presence of humans during ca. 85 to 65 ka

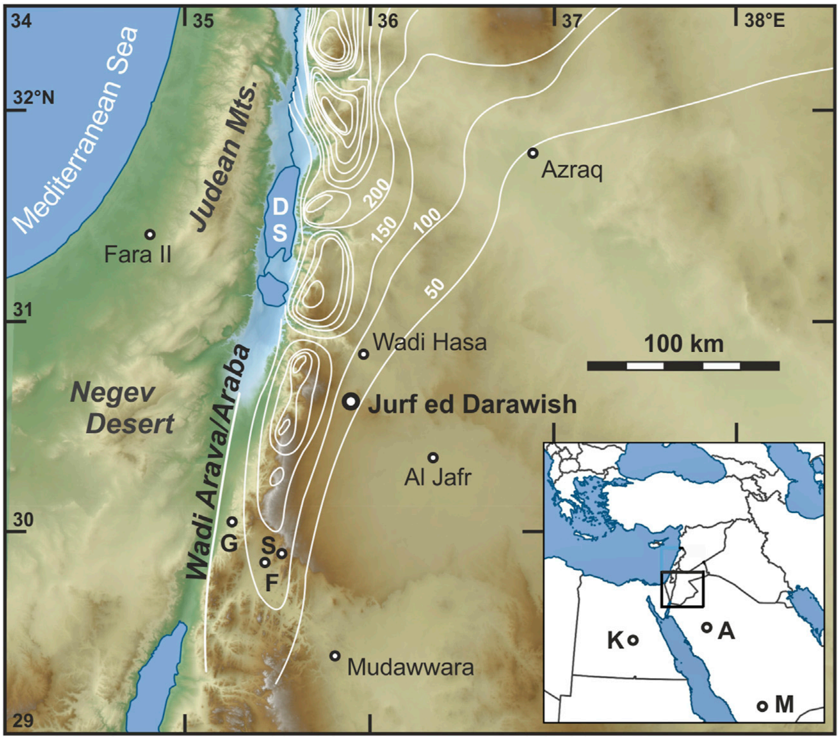

FIGURE 1 | Location of Jurf ed Darawish in the southern Levant and those of other study sites mentioned in the text (DS Dead Sea, A Al Wusta and Alathar, F Tor Faraj, G Gharandal, K Kharga and Kurkur oases, M Mundafan, S Tor Sabiha). Isohyets from Suleiman and Al-Bakri (2011). The colours refer to elevation. Map base prepared by Joe Roe (https://commons.wikimedia.org/wiki/User:Joe_Roe).

INTRODUCTION

The dispersal of anatomically modern humans out of Africa in the Pleistocene was one of the major steps in hominin evolution, but migration timings and the potential role of climate which possibly enabled occupation of previously uninhabited regions, and related landscape changes and available dispersal pathways, are still controversial (Vaks et al., 2007; Garcea, 2012; Groucutt et al., 2018). The region of the southern Levant and the Arabian Peninsula plays a key role in the debate due to its generally arid climate and its crucial geographical position as a barrier or bridge between the wetter regions of northern and eastern Africa on the one side and those of eastern Europe and western Asia on the other (Vaks et al., 2007; Waldmann et al., 2010). Wetter or "pluvial" periods in the southern Levant and the Arabian Peninsula may have provided favourable conditions for human dispersal, and some researchers argue that such conditions typically prevailed during the interglacials when monsoonal circulation was intensified in comparison to the drier glacials (Fleitmann et al., 2003; Groucutt et al., 2018; Stewart et al., 2020a). In contrast, other researchers regard the glacials as the favourable periods when lowered temperature and evaporation possibly caused a higher moisture availability and contraction of desert regions (Vaks et al., 2003; Waldmann et al., 2010).

The increasing number of geological and archaeological studies in northern Africa, the southern Levant and Arabian Peninsula allow the identification of temporal and spatial patterns. Garcea (2012) suggested two distinct periods of human dispersal out-of-Africa, between ca. 130 to 80 and after 50 ka. The time span in between is described as a period of climate deterioration when hyperaridity was established in the Sahara and southern Levant (Shea, 2003; Garcea, 2012). However, this period includes the initiation of the Dead Sea's precursor, Lake Lisan, whose level rose dramatically by 70–80 m, a phase of speleothem growth in the rain-shadow of the Judean Mountains and also of travertine formation in the Western Desert in Egypt (Crombie et al., 1997; Vaks et al., 2003; Waldmann et al., 2007).

In contrast to today's unique characteristic of the Dead Sea as the only major lake of the southern Levant and Arabian Peninsula, additional Quaternary lakes were reconstructed in the region based on analyses of sediments, fossils and shoreline features (Schuldenrein and Clark, 1994; Moumani et al., 2003; Schuldenrein and Clark, 2003; Davies, 2005; Petit-Maire et al., 2010; Rosenberg et al., 2012; Groucutt et al., 2015; Ginat et al., 2018). Inferred surface water bodies must have resulted from significant changes in precipitation or moisture availability (Schuldenrein and Clark, 1994; Davies, 2005; Petit-Maire et al., 2010). Periods of Pleistocene lake formation are disputed for some of these locations (e.g., Mudawwara), whilst some of the earlier inferences of palaeo-lakes were revised as palaeo-wetlands following more recent investigations of previously studied locations (Petit-Maire et al., 2010; Catlett et al., 2013; Winer, 2010; Mischke et al., 2015; **Figure 1**). Most reports of Holocene lakes on the Arabian Peninsula were challenged in a recent reassessment of the available evidence by Enzel et al. (2015).

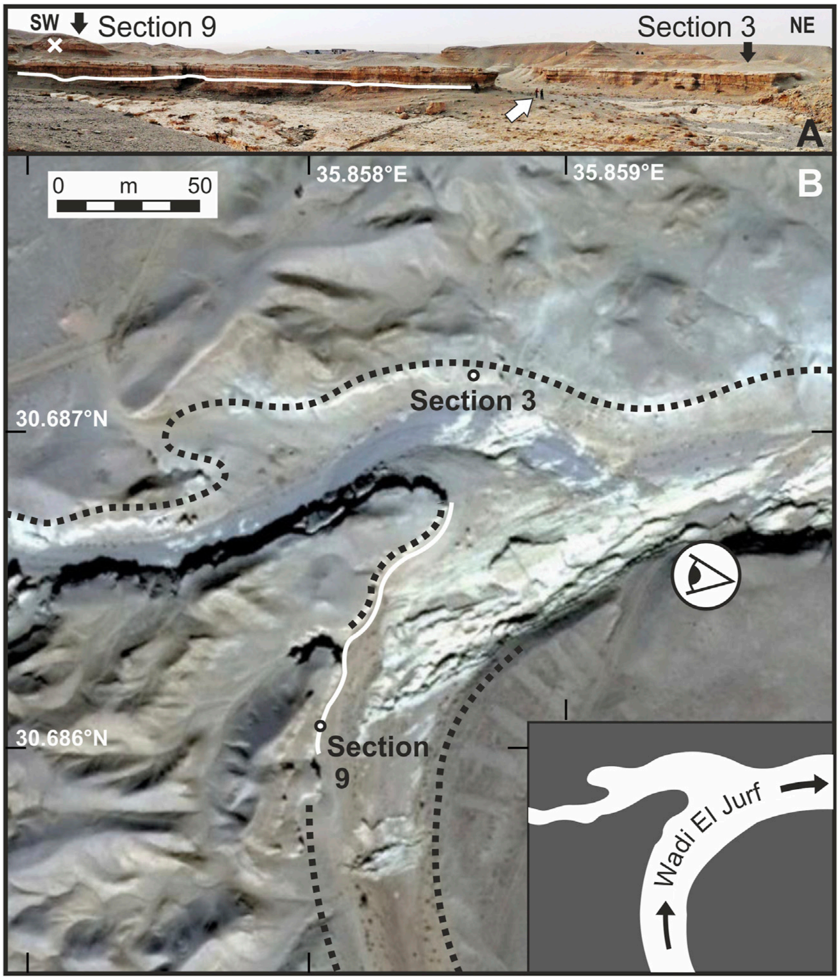

FIGURE 2 | (A) Exposed sediment Section 3 and Section 9. The white line marks the position and lateral distribution of artefacts on the SE-facing slope of the main wadi. The white cross marks the position of one additional artefact in Section 9. South-dipping Maastrichtian limestone beds in foreground. Two persons for scale (white arrow). **(B)** Section 3 and Section 9 at wadi slopes (partly marked by dotted lines). White line shows the position of artefacts as in A. The stylized eye shows the view direction of A, and the inset illustrates the main and tributary wadis.

Thus, thorough multi-proxy studies are required to reconstruct Quaternary landscape change in the region. In addition, robust chronologies are a prerequisite to discuss periods of human presence and potential controls of climate.

We conducted a sedimentological and dating study at Jurf ed Darawish on the Jordanian Plateau where an initial investigation by Moumani et al. (2003) had reported Palaeolithic artefacts embedded in exposed Late Pleistocene lacustrine sediments (**Figure 1**). Our work had the aim to improve knowledge 1) when sediments accumulated at Jurf ed Darawish, 2) when humans were present in the region, and 3) to reassess the inferred depositional setting of a lake proposed by Moumani et al. (2003).

STUDY AREA

The investigated sediment sections are located on the central Jordanian Plateau in the southern vicinity of the village Jurf ed Darawish at ca. 30.687°N and 35.858°E, at an altitude of ca. 940 m above sea level (asl; **Figures 1**, **2**). Unconsolidated Quaternary alluvial sediments are widely distributed in the region, capping the Upper Cretaceous (Maastrichtian) marine limestone bedrock which is exposed on the floors of incised wadis and on hill slopes to the east (Moumani, 1996; **Figure 2**). Eocene limestone is exposed in the southeast of Jurf ed Darawish. In addition, Neogene basalt flows occur within a distance of a few kilometres to the north, west and south (Moumani et al., 2003). There are no natural surface waters near Jurf ed Darawish. However, Wadi El Jurf at the investigated sections is connected to Wadi Juheira, located in the southwest at ca. 1,000 m asl upstream, and to Wadi Al Hasa at ca. 800 m asl in the northeast downstream. Thus, surface runoff following rare rain events in the region is directed to Wadi Al Hasa, and may eventually reach the Dead Sea (**Figure 1**).

Mean January, mean July and mean annual temperatures at Ma'an, 60 km further south, are 7.5, 25.4 and 17.3°C, respectively (www.worldclimate.com). Mean annual precipitation is 41.2 mm with precipitation mostly occurring during the winter season. Potential evaporation exceeds 3,000 mm per year (Suleiman and Al-Bakri, 2011).

Desert vegetation in the region is very sparse and mostly confined to the dry wadi beds. However, steppe vegetation occurs only 30 km to the northwest at the higher altitudes of the eastern Wadi Araba-Dead Sea rift shoulder (Palmer, 2013).

Lower Palaeolithic to Epipalaeolithic artefacts are mostly scattered on the deflated surface in the Jurf ed Darawish region and testify the long history of human presence (Bender, 1968; MacDonald et al., 2000; MacDonald et al., 2001). Current land use is mostly restricted to quarrying of building stones, goat husbandry and small-scale irrigation gardening in the village.

MATERIAL AND METHODS

Logging and Sampling of Sections

Two adjacent sediment sections were investigated and sampled at naturally exposed steep wadi slopes (**Figure 2**). One of the investigated sediment sections represents the "type section of the Burma Member from site 3" which was included in a survey of eight different sediment exposures in the region by Moumani et al. (2003, p. 231). We followed the numbering of Moumani et al. (2003) and called the re-sampled sediment sequence "Section 3" and the newly investigated location "Section 9". The two sediment sections are 130 m apart, and laterally partly traceable sedimentary beds are separated by an incised wadi of ca. 40 m width (**Figure 2**).

The columnar sedimentary Section 3 and Section 9 were logged and sediments from freshly cleaned surfaces sampled for micropalaeontological analysis at 23-cm and 37-cm intervals on average, respectively. Sampling focussed on the non-gravelly sediments at both sections. Sampling density was higher in finer-grained greyish-green sedimentary units presumed to represent the lake sediments described by Moumani (1996), Moumani et al. (2003) and Neeley (2004), in comparison to more brownish sediments possibly representing marsh deposits. However, specific sampling positions also depended on exposure conditions and accessibility. Ca. 250 g of sediment was collected at each sampling location. The position of flaked artefacts, embedded *in situ* in sediments at the Section 9 and partly also distributed in laterally corresponding sediments nearby, was recorded by a handheld GPS device and a Leica DISTO D8 distance-measuring device.

Optically Stimulated Luminescence Dating

Samples for OSL dating were collected from Section 3 and Section 9. Steel tubes were hammered into freshly cleaned and shaded section surfaces. Samples from Section 3 were dated in the Luminescence Dating Laboratory of the China University of Geosciences in Wuhan, and samples from Section 9 in the OSL Dating Laboratory at the Geological Survey of Israel to distribute workload. Comparability of age data was ensured by both lab heads, Zhongping Lai and Naomi Porat, by adapting very similar protocols and using the same water contents for the age calculation of samples from both sections (**Table 1**).

Preparation of OSL samples from Section 3 followed the procedures of Lai and Wintle (2006). Samples were treated with 10% HCl and 30% H_2O_2 to remove carbonates and organics, respectively. After wet sieving, the coarse silt fraction of 38–63 μm was etched by 35% H_2SiF_6 for about ten days to remove feldspars. Infrared (IR; 830 nm) stimulation was used to check for quartz purity, and samples with obvious IR stimulated luminescence signals were treated with H_2SiF_6 again to avoid D_e underestimation (Lai and Brückner, 2008). The purified quartz grains were then mounted on the center (~0.5 cm diameter) of stainless steel discs (1 cm diameter) using silicone oil.

OSL measurements of OSL samples from Section 3 were made using an automated Risø TL/OSL-DA-20 reader equipped with blue diodes ($\lambda = 470 \pm 20$ nm) and infrared laser diodes ($\lambda = 830$ nm). Measurement details are given in **Table 1**.

The concentrations of U, Th and K were measured by neutron activation analysis. For the 38–63 μm grains, the alpha efficiency value was taken as 0.035 ± 0.003 (Lai et al., 2008). The cosmic-ray dose rate was estimated for each sample as a function of depth, altitude and geomagnetic latitude (Prescott and Hutton, 1994). Water content was taken as 25 ± 5%.

For the equivalent dose (D_e) determination in Section 3, the combination of the single aliquot regenerative dose (SAR) protocol (preheat of 10 s at 220°C, a test dose of ~11.5 Gy and a test dose preheat of 10 s at 200°C) and the Standardized Growth Curve (SGC) method was employed (Murray and Wintle, 2000; Roberts and Duller, 2004; Lai, 2006). For each sample, six aliquots were measured using the full SAR protocol to obtain six dose response curves which were then averaged to construct a SGC for this individual sample. Then, more aliquots (from 18 to 22) were measured to obtain the values of test-dose corrected natural signals, and each of the values was interpolated on the SGC to obtain a D_e. The final D_e is the mean of all SAR D_es and SGC D_es (total of 24–28). Further details of the measurement protocol such as preheat conditions are provided in **Table 1**.

Samples for OSL dating from Section 9 were prepared using the routine protocol of Faershtein et al. (2016). Briefly, the very fine sand of 88–125 μm quartz fraction was extracted by sieving, dissolving carbonates with 10% HCl, and removing heavy minerals by magnetic separation. Feldspars were dissolved and quartz grains etched with 42% HF for 40 min, followed by soaking in 16% HCl to dissolve any fluorides which may have precipitated.

Dose recovery tests of OSL samples from Section 9 over a range of preheats showed that a recovery of 100% can be obtained using a preheat of 10 s at 220°C, a test dose of ~9.3 Gy and a test dose preheat of 5 s at 200°C. These measurement conditions were used for all samples.

D_e was measured on 2-mm aliquots with ~200 grains on the disc. Between 13 and 22 aliquots were measured per sample using a modified SAR protocol (**Table 1**; Murray and Wintle, 2000). The average D_e and errors were calculated using the Central Age Model (Galbraith and Roberts, 2012). Single grains (SG) were measured for two samples with a large scatter (JED-2 and JED-4), using green laser stimulation and the same protocol as for the

TABLE 1 | OSL measurement protocols for the two laboratories. The ratios between the signals measured at steps 3 and 6 were used to construct the dose response curve and calculate the D_e. At the GSI at least six dose points were used, including two zero-dose points and one recycling point. All samples showed recycling ratios within 10% of 1.0 for most aliquots and negligible infrared signals. For multi-grain measurements, both labs used blue LEDs for stimulation, and the signal was detected through a 7.5-mm thick U-340 filter (detection window 275–390 nm). For single grain measurements, a green laser was used for stimulation, and detection was as for multi-grains. Irradiations were carried out using calibrated $^{90}Sr/^{90}Y$ beta sources.

	The Geological Survey of Israel, Jerusalem (Section 9)	China University of Geosciences, Wuhan (Section 3)
Grain size	88–125 μm	38–63 μm
Discs/cups	Aluminum discs	Stainless steel discs
Aliquot size	2 mm	5 mm
Signal and background	First 0.2 s and last 5 s	First 0.64 s and last 5 s
Step	—	—
1	β dose (0 for the first run)	β dose
2	Preheat at 220°C for 10 s	Preheat at 220°C for 10 s
3	Blue stimulation at 125°C for 40 s (Lx)	Blue stimulation at 130°C for 40 s (Lx)
4	Test dose (9.3 Gy)	Test dose (11.5 Gy)
5	Preheat at 200°C for 5 s	Preheat at 200°C for 10 s
6	Blue stimulation at 125°C for 40 s (Tx)	Blue stimulation at 130°C for 40 s (Tx)
7	Heat at 280°C for 100 s	—

multi-grain measurements. In total, 500 grains were measured for each sample and selection criteria followed Porat et al. (2006). The finite mixture model was used to isolate the most significantly bleached fraction from the grain population, and the youngest component greater than 15% was selected.

Water contents were estimated at 50% of the saturation-water contents, with associated errors of ±25% of the estimated value. Saturation-water contents, determined using undisturbed sediment samples in the laboratory, represent the water content of the sediments after deposition in the water body and prior to the incision of the modern Wadi El Jurf. Subsequent sediment exposure and the resulting decrease of pore-water contents was accounted for by using 50% of the saturation-water contents as average geological moisture contents.

The alpha, beta and gamma dose rates were calculated from the radioactive elements measured by ICP-MS (U and Th) or ICP-OES (K). Alpha efficiency value was taken as 0.10 ± 0.02 (Aitken, 1985). However, due to HF etching the choice of this value does not affect the ages significantly. Cosmic dose rates were evaluated from the estimated burial depths prior to the down-cutting of the modern channels. For samples JED-12-1 to 4, burial depth was estimated at 11 ± 2 m based on the thickest preserved sedimentary sequence above the sampled sediments (**Figure 2A**); and the calculated cosmic dose rate was 64 ± 13 μGy/a (**Table 2**).

For comparison with ages originally calculated by Moumani et al. (2003) using water contents of ca. 2%, their three ages from Section 3 were recalculated using the data provided in their Table 1 and water contents of 25%, a more realistic value for such fine-grained sediments, that was also used in our age calculations.

Grain-Size Analysis

Subsamples of ca. 50 g from the newly investigated, artefact-rich and thicker sediment Section 9 were used for grain-size analysis with a Coulter LS 200 laser-particle sizer at the Alfred Wegener Institute for Polar and Marine Research in Potsdam, Germany. Subsamples were split in two halves. One group of subsamples was treated with 10% acetic acid to remove carbonate. Carbonate was not removed for the second group of subsamples since we initially assumed that a significant portion of the detrital grains are possibly derived from the local Maastrichtian and Eocene limestone bedrock. Both subsample sets were treated with 35% H_2O_2 to remove organic matter. The dispersant $Na_4P_2O_7$ was added to disaggregate the material before grain-size analysis started. Carbonate-free and carbonate-containing samples did not yield significantly different results, and data reported in the following are based on carbonate-free materials. More detailed information is provided in Röhl (2015).

Analysis of total organic carbon (TOC) and total inorganic carbon (TC) concentrations of eight and 25 samples from Section 3 and Section 9, respectively, were measured on powdered samples with an EuroVector EA3000 elemental analyser (detection limit 0.01%) at the Institute of Geosciences of the University of Potsdam.

Analysis of Organism Remains

Subsamples of ca. 200 g from Section 3 and Section 9 were used for micropalaeontological analysis. Samples were weighed, soaked in a 3% solution of H_2O_2 for two to three days until the reaction was completed, and sieved through 100, 250 and 1000-μm sieves. Fossils were picked under an Olympus SZ-60 microscope and selected fossils were documented with a Zeiss Supra 40 VP scanning electron microscope (SEM) at the Institute of Geological Sciences at Free University of Berlin. Two different ostracod taxa of the genus *Ilyocypris* were identified based on the location and number of marginal ripplets on the inner lamella (Van Harten, 1979; Janz, 1994). These valve features are only visible using a SEM. Thus, valves of *Ilyocypris* identified with a low-power binocular microscope were pooled as *Ilyocypris* spp. Identification of other ostracod valves is based on Meisch (2000) and Fuhrmann (2012).

TABLE 2 | OSL dating results for samples from Section 9 (OD—over-dispersion, the scatter beyond analytical errors. The OD values are low (indicating a homogenous sample) to intermediate (with possible partial bleaching). No. aliquots - the number of aliquots used for the average D_e out of the aliquots measured).

Code JED	Burial depth (m)	Water content (%)	K (%)	U (ppm)	Th (ppm)	Ext. α (µGy/a)	Ext. β (µGy/a)	Ext. γ (µGy/a)	Cosmic (µGy/a)	Dose rate (µGy/a)	No. aliquots	OD (%)	D_e (Gy)	Age (ka)
12–1	11.0	26	1.00	2.4	7.8	9	917	683	64	1,674 ± 54	22/22	33	108 ± 8	64 ± 5
12–2	11.0	24	1.08	2.7	8.2	10	1,017	742	64	1843 ± 63	8/10	47	124 ± 16	67 ± 9
SG	—	—	—	—	—	—	—	—	—	—	126/500	56	122 ± 5	66 ± 3
12–3	11.0	25	1.25	2.4	9.0	10	1,083	781	64	1938 ± 64	20/20	20	148 ± 7	76 ± 5
12–4	11.0	15	0.48	2.7	4.0	9	669	523	64	1,264 ± 39	12/13	46	113 ± 14	89 ± 11
SG	—	—	—	—	—	—	—	—	—	—	152/500	51	106 ± 4	84 ± 4
12–5	1.0	10	0.64	2.6	4.6	10	808	600	185	1,602 ± 49	20/20	14	70 ± 3	44 ± 2

RESULTS

The exposed sediments at the Section 3 and Section 9 are mostly yellowish-brown, homogenous silts. Thick gravel beds occur at the base and thinner gravel layers are exposed within the sections and at their tops (**Figure 3**, **Supplementary Figure S1**). Vertical voids, casts and colourations of a few millimetres to 1-cm diameter are abundant at both sections. The silty sediments partly contain granules and small pebbles which are embedded in the fine-grained matrix. The silty sediments are partly greyish-green in the lower half or middle of both sections; and carbonate-rich units of 1 to 85-cm thickness occur at both sections.

In total, 22 artefacts were recognized in a single sedimentary bed ca. 4.5 m above the base of Section 9 and partly distributed in corresponding sediments over a lateral stretch of 92 m (**Figure 2**). The vertical position of the artefacts within the specific artefact-bearing layer varies by up to 40 cm. One additional artefact was recognized at 11.6 m above the base of Section 9 (**Figures 2**, **3**).

The four OSL ages obtained for the artefact-bearing layer at Section 9 range from 84 ± 4 ka to 64 ± 5 ka (**Table 2**), and are in a stratigraphic order (**Figure 3**). One additional sample from close to the top of the sediment sequence provided an age of 44 ± 2 ka. The nine OSL ages from Section 3 range from 215 ± 34 ka at the base of the section to 30 ± 3 ka near its top (**Table 3**). Two of the samples are not in a stratigraphic order, perhaps due to poor estimation of the dose rates (**Table 2**; **Figure 3**).

Grain-size analysis of the non-gravelly sediments at Section 9 show that silt is the largest grain-size fraction with 42.9% on average (minimum 32.2%, maximum 59.7%), followed by clay (39.3%; minimum 16.3%, maximum 51.8%). Sand constitutes 17.8% on average (minimum 6.3%, maximum 31.9%; **Figure 4**). The main mode of the grain-size frequency curves of most sediment samples is located at ca. 3 µm, and two sub-ordinate modes occur at ca. 50 and 150 µm (**Figure 5**).

TOC concentrations at Section 3 are 0.10% on average (minimum 0.08%, maximum 0.12%) and 0.11% at Section 9 (minimum 0.04%, maximum 0.21%). TIC concentration is 4.60% on average at Section 3 and 4.01% at Section 9 (minima are 2.69 and 1.01%, and maxima are 6.71 and 8.15%, respectively; **Figure 4**).

In total, 11 ostracod taxa, remains of one bivalve, shells of two aquatic and two terrestrial gastropod taxa, gastropod opercula, and charophyte gyrogonites were recorded in sediment samples from Section 9 (**Figure 6**). In addition, Cretaceous ostracod valves and carapaces, foraminifera tests and scaphopod fragments were recorded in the lowermost samples from the section. Valves and carapaces of *Potamocypris fulva* are the most abundant ostracod remains (total number of valves including articulated valves: n_v = 423), followed by unidentified valves of juvenile Candoninae (n_v = 194), remains of *Ilyocypris* spp. (n_v = 91) and those of *Pseudocandona* sp. (n_v = 76). Most abundant gastropod remains are represented by opercula (n = 19). The majority of fossil remains was recorded from the lower half of Section 9 (**Figure 6**).

At Section 3, 11 ostracod taxa, shells of two aquatic and two terrestrial gastropod taxa, and charophyte gyrogonites were recorded (**Figure 7**). A single Cretaceous ostracod valve, foraminifera tests and scaphopod fragments were recorded in addition. Most Quaternary ostracod remains belong to unidentified juvenile valves and carapaces of Candoninae (n_v = 860), to *Ilyocypris* spp. (n_v = 247) and to *Heterocypris salina* (n_v = 50; **Figures 8**, **9**). Ostracod remains were almost exclusively recorded from the lower half of the sediment section (**Figure 7**). Four shells of the terrestrial gastropod family Ferussaciidae were recorded in the upper half of the section, and eight gyrogonites from samples from the lower half. Abundances of all other Quaternary non-ostracod remains at the Section 3 are lower (**Figure 7**).

DISCUSSION

The Age of the Investigated Sediments

A total of 14 samples provide a stratigraphic framework for the two studied sections at Jurf ed Darawish, in addition to the published ages by Moumani et al. (2003) which were recalculated using higher water contents. Three newly determined ages between ca. 100 and more than 200 ka, and the recalculated age of ca. 150 ka of Moumani et al. (2003) near the base of Section 3, represent minimum ages because D_e values higher than

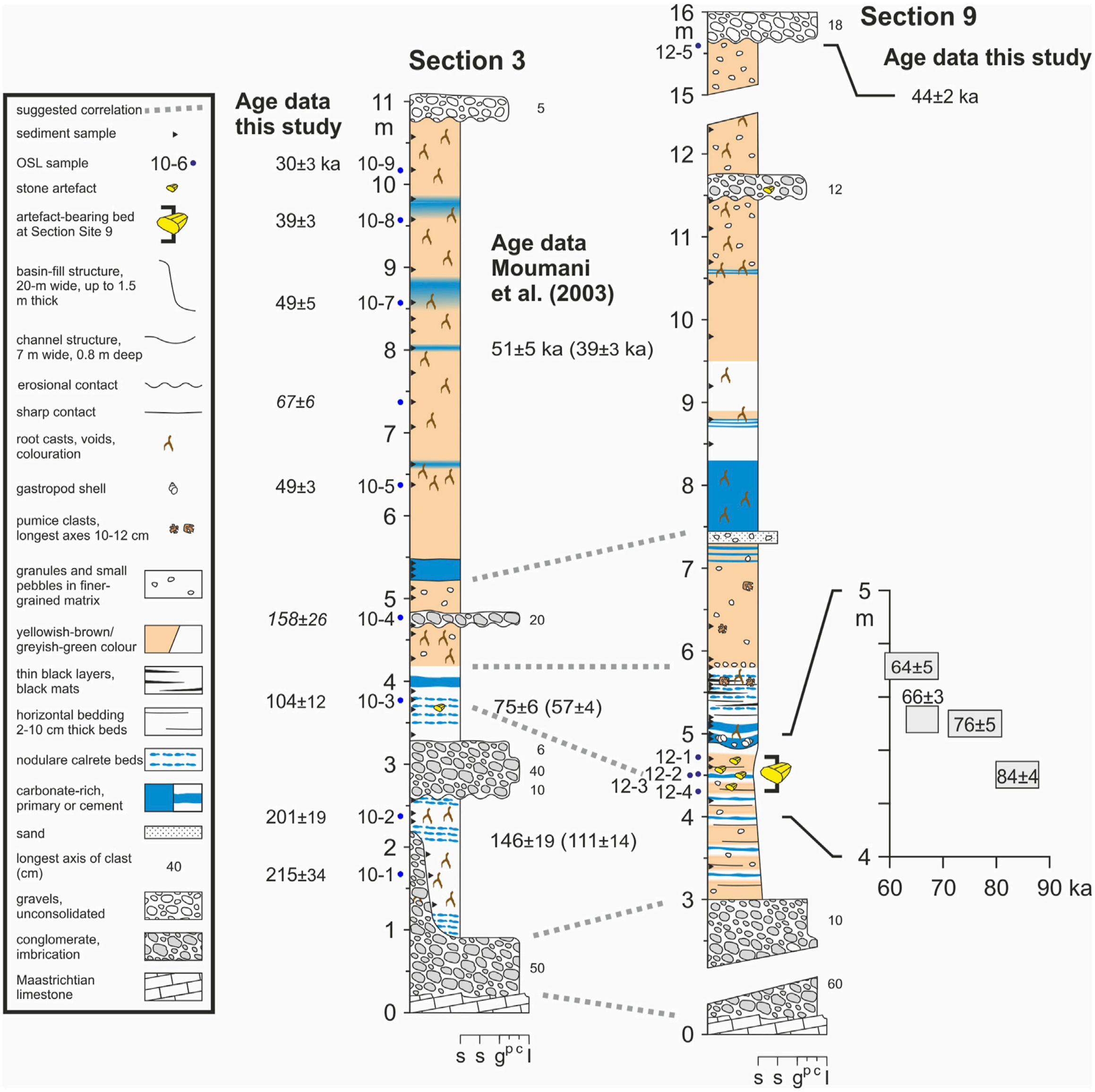

FIGURE 3 | Lithology and OSL age data of Section 3 and Section 9. Positions of three previously dated samples and artefact-bearing layer at Section 3 according to Moumani et al. (2003). *In-situ* artefacts were only recorded at Section 9 in this study. Age data originally reported by Moumani et al. (2003) in brackets, calculated with water contents of ca. 2%, were recalculated using water contents of 25% to enable comparability. The lower three newly obtained age data from Section 3 are minimum ages. Age data of Section 3 in italics are not in stratigraphic order, perhaps due to inaccurate dose rates (**Table 3**). Photos of sections and complete lithological log of Section 9 is available as **Supplementary Figure S1**. (scale of *x*-axis s s g p c l: silt, sand, granules, pebbles, cobbles, limestone, respectively)

~150 Gy are considered as underestimated due to the approach of the dose response curve to saturation (Faershtein et al., 2020; **Table 3**). The minimum ages suggest that the onset of the accumulation of fine-grained sediments pre-dates the Late Pleistocene (**Figure 3**). This onset occurred apparently in the Middle Pleistocene or even earlier.

Sediments near the base of Section 9 provided ages of ca. 85 ka and younger. The age data indicate that the lowermost fine-grained sediments at both sections accumulated during MIS 5 and/or earlier. The stratigraphically mostly consistent ages from the middle and upper part of Section 3 suggest that the accumulation of fine-grained sediments lasted at least until ca. 30 ka, in the later part of MIS 3 (**Figure 3**). The recalculated age of ~50 ka for a sample investigated by Moumani et al. (2003) from a position ca. 2 m below our uppermost OSL sample at Section 3, and the age of 44 ka from Section 9, are all stratigraphically consistent.

Four sediment samples from the artefact-bearing bed at Section 9 yielded stratigraphically consistent ages between ca. 85 to 65 ka, suggesting that humans were present in the region

TABLE 3 | OSL dating results for samples from Section 3 (alpha counting was not used; No. aliquots—the number of aliquots used for the average D_e out of the aliquots measured).

Code JED	Burial depth (m)	Water contents (%)	K (%)	U (ppm)	Th (ppm)	Dose rate (µGy/a)	No. aliquots	D_e (Gy)	Age (ka)
10–1	9.4	25	0.66	3.8	5.6	1,666 ± 119	28	359 ± 50	215 ± 34*
10–2	8.7	25	0.77	1.2	6.0	1,468 ± 105	28	294 ± 19	201 ± 19*
10–3	7.3	25	0.81	2.0	7.1	1,506 ± 106	28	157 ± 14	104 ± 12*
10–4	6.3	25	0.36	1.4	2.9	812 ± 71	26	128 ± 18	158 ± 26
10–5	4.7	25	0.83	2.1	5.3	2,150 ± 117	28	104 ± 4	49 ± 3
10–6	3.7	25	0.99	2.0	5.4	1,584 ± 110	22	106 ± 7	67 ± 6
10–7	2.5	25	0.79	1.8	5.0	1,387 ± 97	24	68 ± 5	49 ± 5
10–8	1.5	25	0.85	2.1	6.1	1,608 ± 109	24	63 ± 3	39 ± 3
10–9	0.9	25	0.92	2.7	6.1	1794 ± 119	24	54 ± 3	30 ± 3

**Minimum age.*

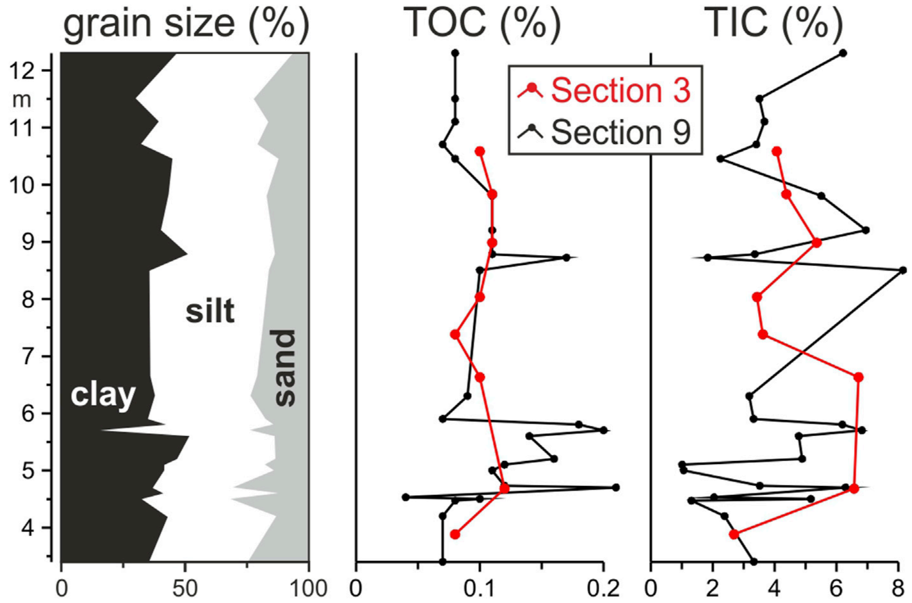

FIGURE 4 | Grain-size fractions at Section 9, and concentrations of total organic (TOC) and inorganic (TIC) carbon. TOC and TIC concentrations at Section 3 shown for comparison in red. Note: TOC and TIC concentrations are shown at height above section base, the data do not necessarily correlate stratigraphically.

during a relatively long period of ca. 20 ka in the later part of MIS 5 and first half of MIS 4. The recalculated age of the sample collected by Moumani et al. (2003) from the artefact-bearing deposits at Section 3, ca. 75 ka, supports the age range for the artefact-bearing sediments at Section 9. In contrast, we determined a significantly older minimum age of ca. 105 ka for the sediments considered to contain artefacts at Section 3. However, this older age potentially results from 1) a stratigraphically lower position of the sampled material in comparison to the sediment with the embedded artefacts dated by Moumani et al. (2003), 2) sampling of a laterally inconsistent sediment layer which pre-dates the accumulation of the artefact-bearing sediment dated by Moumani et al. (2003), or 3) an earlier occupation period than those represented by artefacts in Section 9.

The Depositional Setting at Jurf ed Darawish

The sediments at the two sections represent three main types: 1) gravel deposits, 2) massive yellowish-brown clayey silts with casts, voids or colour traces of roots, and 3) greyish-green clayey silts which are partly carbonate-rich, partly characterized by horizontal bedding and which partly include thin, darker layers (**Figures 3**, **4**). The gravelly deposits were formed either in river channels by fast-flowing water or by overland flow during sporadic flash floods. The thick gravel beds in the lower part of both sections include clasts with up to 60-cm long axes, indicating fast flow. Thinner gravel beds intercalated in the sedimentary sequences and the gravel cover at the top of the sections, which is wide-spread on the surface in the region, probably originate from flash floods.

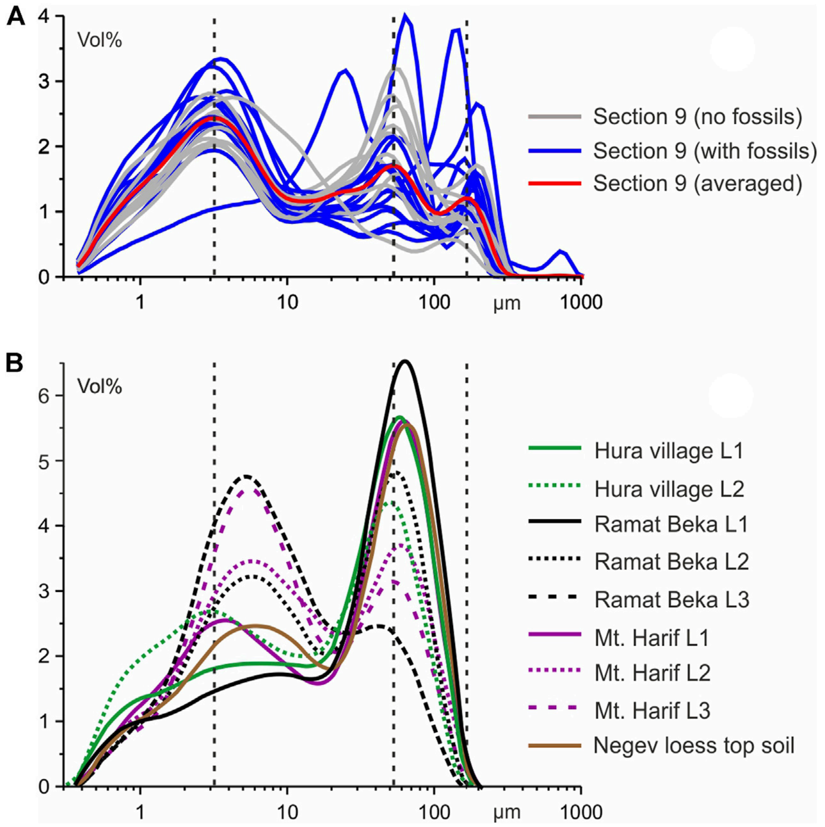

FIGURE 5 | (A) Grain-size-frequency curves for sediment samples from Section 9. Position of three modes at ca. 3, 50 and 150 µm indicated by vertical dotted lines. **(B)** Grain-size frequency curves for loess samples from the Negev Desert redrawn from Amit et al. (2020; Negev loess top soil) and Crouvi et al. (2008; all other) for comparison.

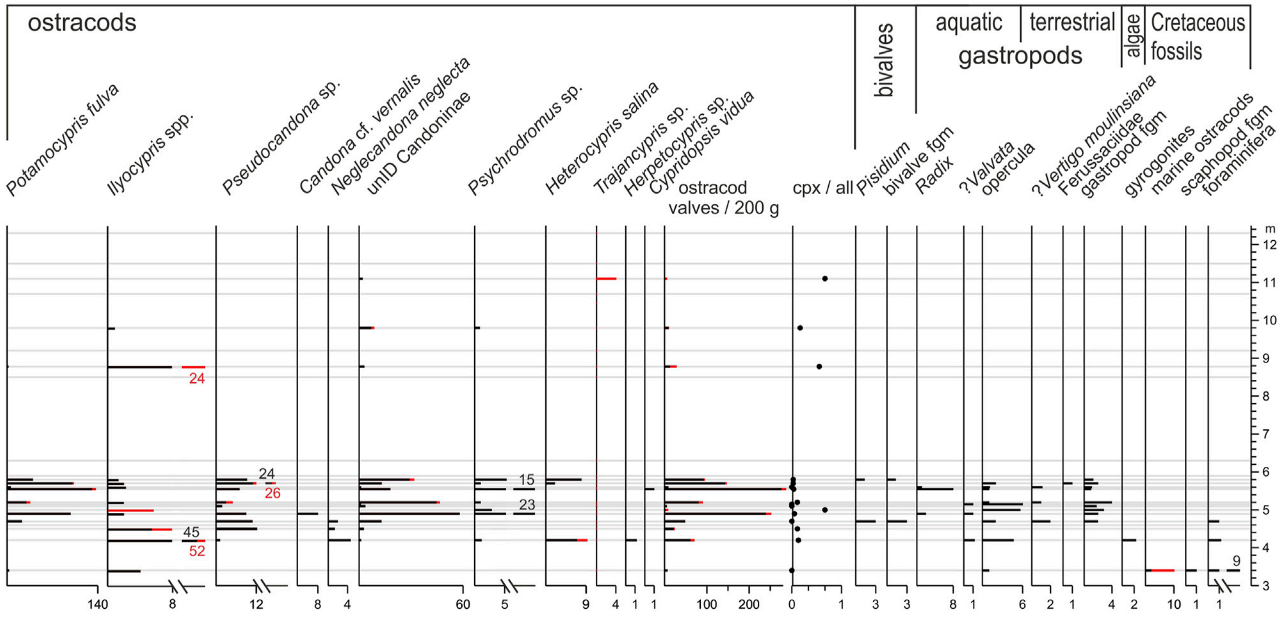

FIGURE 6 | Fossils recorded in sediments of Section 9. Abundances of articulated ostracod valves, i.e., carapaces (cpx), are indicated by red colour. (fgm fragments)

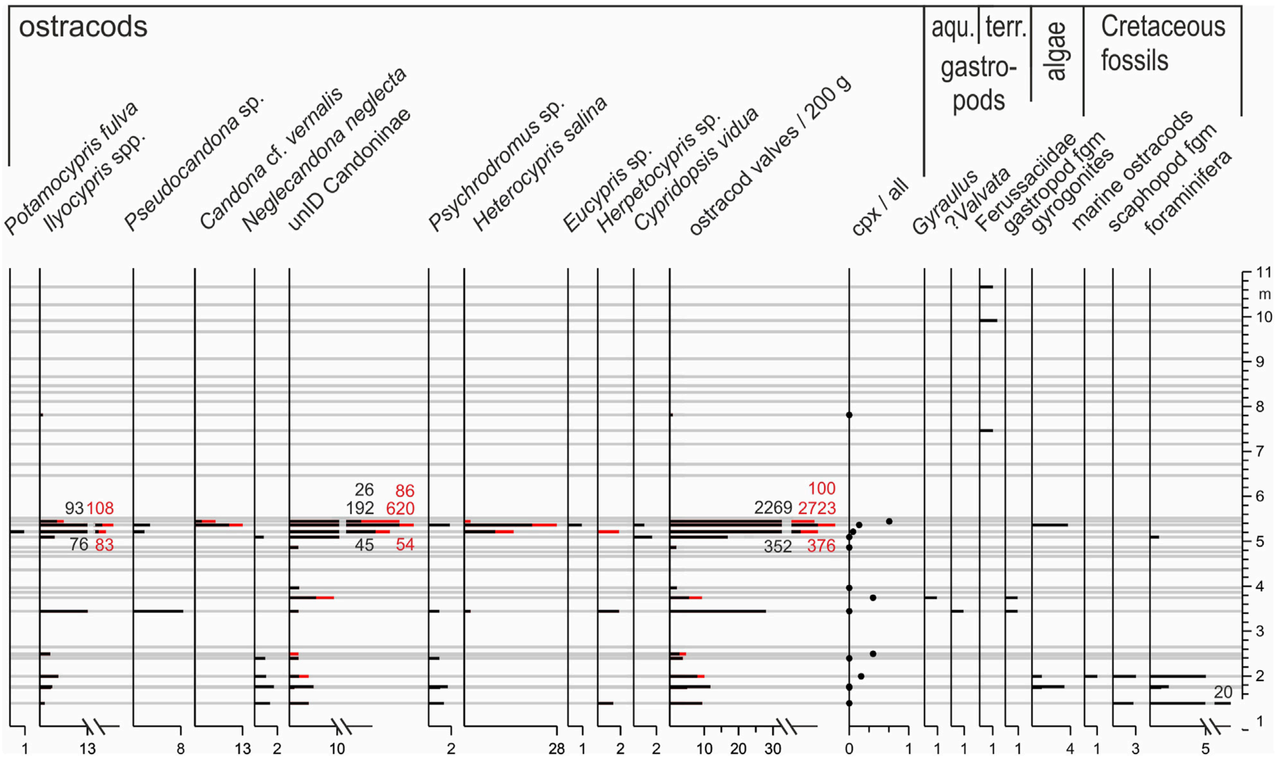

FIGURE 7 | Fossils recorded in sediments of Section 3. Articulated ostracod valves (carapaces, cpx) shown in red as in **Figure 6**. (fgm fragments)

The massive yellowish-brown clayey silts with casts, voids or colour traces of roots dominate at Section 9 and in the middle and upper part of Section 3 (**Figure 3**, **Supplementary Figure S1**). They probably represent reworked alluvial sediments which accumulated in topographically lower locations. The oxidized colour and frequent root traces show that the sediments were mostly exposed and covered by terrestrial plants.

The partly carbonate-rich, partly horizontally bedded greyish-green clayey silts, mostly in the lower halves of both sections, were probably formed in an aquatic to semi-aquatic depositional setting with carbonate precipitation from the open water surface or from groundwater near the surface. Thin sediment layers with darker colour similar to reported "black mats" in other desert environments indicate formation in wetlands (Quade et al., 1998; Pigati et al., 2014).

The fine-grained sediments of Section 9 do not show significant variations of the clay, silt and sand fractions through the stratigraphic sequence (**Figure 4**). Accordingly, grain-size frequency curves of individual samples from the section show three modes at more or less constant grain sizes (**Figure 5**). The two most abundant grain populations characterized by modes at ca. 3 and 50 μm resemble the grain-size patterns of loess samples collected from the Negev Desert (Crouvi et al., 2008; Amit et al., 2020; **Figure 5**). Primary, non-reworked loess in the Negev Desert has a bimodal grain-size frequency distribution with one mode at a fine grain size of 3–8 μm and a second mode at a coarser grain size between 50 and 60 μm (Crouvi et al., 2008, 2009). The finer grain population is regarded as transported mainly from far, distal sources (500–2000 km) such as the Sahara and Arabia, with some contribution from proximal sources (Crouvi et al., 2008; Amit et al., 2020). The coarser grains are described as locally derived dust downwind of active dune fields.

Topsoil sediments of the Judean Mountains in the west and northwest of the Dead Sea were investigated by Amit et al. (2020) who concluded that the clastic particles originated mainly from the Sinai-Negev Erg. The bimodal grain-size frequency distributions of these topsoil samples have one mode centered at ca. 5 μm and a second mode between 42 and 52 μm, comparable to the investigated sediments of the Section 9 which have a similar distance to the Sinai-Negev Erg that could be a potential source area.

In contrast to the loess deposits of the Negev Desert and the topsoil sediments of the Judean Mountains, the sediments of Section 9 have an additional third mode in the fine sand fraction which is comparable to aeolian sand deposits in the Arava/Araba Valley to the west of the central Jordanian Plateau or to dune sands in northeastern Saudi Arabia in its east (Saqqa and Atallah, 2004; Benaafi and Abdullatif, 2015; **Figure 5**). Thus, this coarser grain population probably represents locally derived aeolian sand.

Numerous recorded fossils in the lower part of both sections allow more detailed inferences of the depositional setting. The most abundant fossils, the ostracod assemblages, indicate the existence of a slowly flowing stream and associated wetland

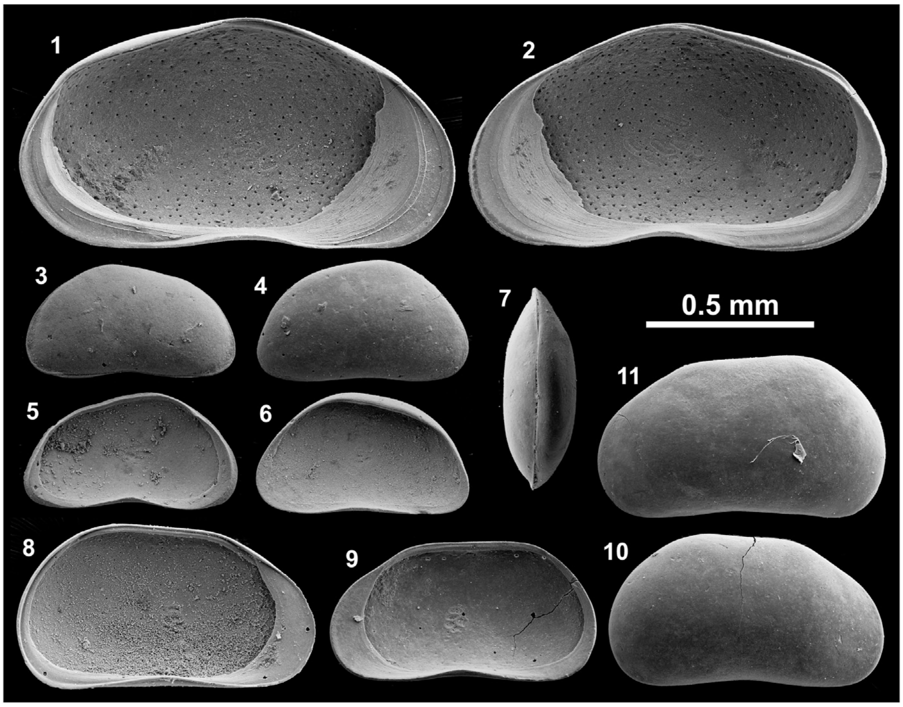

FIGURE 8 | Ostracod valves recorded at Section 9. 1-2 *Psychrodromus* sp., 1 left valve (LV) internal view (iv), 2 right valve (RV) iv; 3-7 *Potamocypris fulva*, 3 LV external view (ev), 4 RV ev, 5 LV iv, 6 RV iv, 7 dorsal view of carapace; 8–11 *Pseudocandona* sp., 8 LV iv, 9 RV iv, 10 RV ev, 11 LV ev. All specimens housed at Institute of Geological Sciences, Free University of Berlin (Germany).

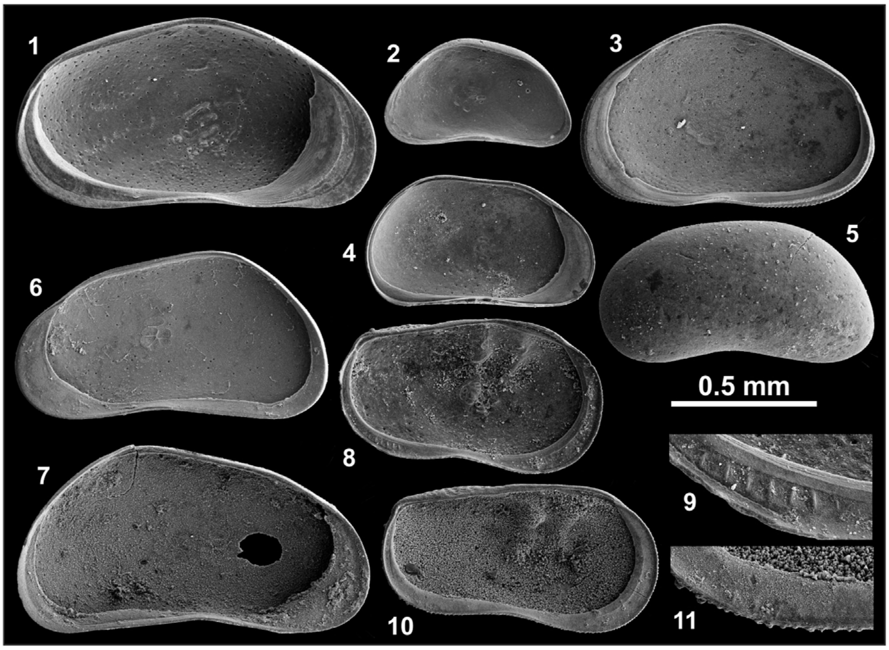

FIGURE 9 | Ostracod valves recorded at Section 3. 1 *Psychrodromus* sp. LV iv; 2 *Potamocypris fulva* RV iv; 3 *Heterocypris salina* RV iv; 4 *Pseudocandona* sp. LV iv; 5 *Neglecandona neglecta* carapace (LV visible); 6-7 *Candona* cf. *vernalis*, 6 RV iv, 7 LV iv; 8-9 *Ilyocypris* cf. *gibba*, 8 LV iv, 9 enlargement of posteroventral part, inner lamella with marginal ripplets; 10–11 *Ilyocypris* cf. *bradyi*, 10 LV iv, 11 enlargement of posteroventral part, partly recrystallized and overgrown inner lamella with poorly preserved marginal ripplets. Scale not valid for 9 and 11. Abbreviations as in Panel 9. All specimens housed at Institute of Geological Sciences, Free University of Berlin (Germany).

FIGURE 10 | In-stream wetland in Wadi Hasa ca. 40 km to the northwest of Jurf ed Darawish. Two cars (black arrows) for scale. Position of stream indicated by white arrows. (Photo by Wolfgang Streicher)

conditions, including springs and temporary ponds at the studied locations. For example, *Potamocypris fulva*, most abundant at Section 9, is typically recorded from very shallow, slowly flowing waters and the interstitial (subterranean) habitat of streams (Meisch, 2000). Similarly, *Ilyocypris gibba* and *I. bradyi* typically occur in small and shallow water bodies such as ponds, springs and streams. Species of *Pseudocandona* are mostly described from permanent and temporary small water bodies such as ponds and springs and the interstitial habitat of streams (Meisch, 2000). Those of *Psychrodromus* are mostly reported from springs, streams flowing from springs, and ponds. *Heterocypris salina* typically inhabits small temporary water bodies. *Cypridopsis vidua* is specifically known from densely vegetated water bodies. *Candona vernalis*, resembling the widely distributed *Neglecandona neglecta*, was only described from modern habitats and Holocene and MIS 9 (Holstein Interglacial ca. 330 ka) deposits in Central Germany so far (Fuhrmann, 2012). The species occurs in temporary small water bodies, often in river plains. The large variations in the number of ostracod valves per sample correspond with typically seen large lateral changes in a stream and wetland setting rather than the minor gradual changes expected in a lake environment. In analogy to modern in-stream wetlands in some segments of Wadi Hasa ca. 40 km northwest of Jurf ed Darawish, an in-stream wetland is inferred from the fossils at Section 3 and Section 9 (**Figure 10**).

The recorded gastropods in sediments of both sections support the inference of a stream and wetland setting due to the occurrence of both aquatic and terrestrial forms. The bivalve genus *Pisidium* was recorded too, whose members occur in a wide range of habitats typically including small and temporary water bodies, springs, streams and lake margins (Welter-Schultes, 2012).

Although only 130 m apart from each other, the distribution of fossils at Section 3 and Section 9 does not support a laterally consistent facies distribution and clear correlation of both sedimentary sequences. For example, valves of *Potamocypris fulva*, abundant at Section 9, were not recorded at Section 3 apart from a single valve (**Figures 6**, **7**). In addition, valves of *Pseudocandona* sp. and *Psychrodromus* sp. are both abundant at Section 9 but rare at Section 3. However, these differences in the assemblage data are supported by the field observation of the lateral coarsening of the artefact-bearing bed at Section 9 towards the north. Lateral litho- and biofacies changes are apparently evident in the Jurf ed Darawish region, and expected in an in-stream wetland setting with slowly flowing waters, stagnant waters, springs and emerged terrestrial habitats occurring close to each other at the same time (Pigati et al., 2014). The inferred lateral facies changes are also evident from the differences of the sedimentary sequences of the Section 3 and Section 9 (**Figure 3**). In addition, they probably explain the seeming discrepancy of the older OSL age determined for the topmost sediments of Section 9 in comparison to the ages of the uppermost sediments at Section 3 in a topographically lower position (**Figure 3**).

In contrast to the sediments in the lower parts of both sections, fossils were only sporadically recorded in the deposits above (**Figures 6**, **7**). However, grain-size frequency curves for these samples are not substantially different from the fossil-bearing samples (**Figure 5**). The middle mode of these samples is more constrained to a grain size of ca. 50 μm, possibly as a result of less significant changes in flow conditions in comparison to the inferred in-stream wetland conditions for sediments below. Clastic material was apparently washed to a topographic low from nearby source areas. The lack of fossils and the oxidized sediment colour suggest that open, stagnant water was not or only rarely present. Abundant traces of plant roots indicate that terrestrial vegetation likely existed most of the time. The in-stream wetland was possibly replaced by a vegetated alluvial plain due to reduced surface runoff which probably resulted from decreased precipitation in the catchment, and/or the increasing down-cutting by flowing waters and possibly lowered groundwater. The timing of the transition from an in-stream wetland setting to a vegetated alluvial plain at Jurf ed Darawish is not well constrained. However, the available age data suggest that this transition occurred sometime between ca. 60 to 50 ka, possibly contemporaneous with the MIS 4/3 transition.

The similarity of the grain-size-frequency curves of samples from Section 9 and those of loess deposits in the Negev Desert suggests that the detrital source material of sediments at Jurf ed Darawish was local loess derived from the catchment of the former wetland. The presence of fossil remains of aquatic organisms, partly recognized horizontal bedding, the dense appearance of the sediments, and the occurrence of granules and small pebbles in the fine-grained matrix, show that the clayey silts represent reworked, secondary fluvial loess rather than primary loess deposits (Cordova et al., 2005). In contrast to the loess deposits of the Negev Desert with a bimodal grain-size frequency distribution, the sediments at Jurf ed Darawish have a significantly higher proportion of the clay and very fine silt fraction in comparison to the coarse silt fraction, consistent with the larger distance to source areas in comparison to the deposits of the Negev Desert (Crouvi et al., 2008; Amit et al., 2020; **Figure 5**).

According to Cordova et al. (2005), primary loess occurs in Jordan in a North-South stretching band which is some tens of kilometres to the east of the highest regions of the Jordanian Plateau and which includes the study area. Red Mediterranean soils are present in the more elevated regions to the west and north of Jurf ed Darawish (Cordova et al., 2005), and Lucke et al. (2013) demonstrated that these soils originated from the long-term accumulation of remote dust (mainly from Egypt and Sudan) rather than the weathering of bedrock.

Periods of dust accumulation are not well constrained in Jordan but studies in the Negev Desert indicate that loess formation occurred as early as the middle Pleistocene ca. 180–130 ka, followed by a major phase of dust deposition and loess formation after 80–75 ka which continued throughout MIS 2 (Ben David, 2003; Enzel et al., 2008; Crouvi et al., 2009). Faershtein et al. (2016) suggested that erosion in the Negev Highlands started after a long period of dust aggradation ca. 24 ka and became predominant at the MIS 2/1 transition. The youngest dated fine-grained deposits near the top of Section 3 with an age of ca. 30 ka and the exposed bedrock in the Wadi El Jurf show that a similar transition from aggradation to incision occurred on the Jordanian Plateau sometime during MIS 2 or 1. According to Neeley (2004), archaeological remains in the Jurf ed Darawish region span the lower Palaeolithic through the Early Epipalaeolithic. Younger than Early Epipalaeolithic (19–16 ka) remains are apparently absent due to diminished resources. Thus, archaeological evidence points to a transition from the former aggradational to the present erosional setting during the last few thousand years before the onset of the Holocene.

Discussion of Previous Inferences From Jurf ed Darawish

The initial investigation of Section 3 and spatial analysis of other nearby sections by Moumani et al. (2003, p. 221) led to the inference of "normal freshwater lacustrine conditions" between >111 and <40 ka at Jurf ed Darawish. Moumani et al. traced sediments similar to those exposed at Section 3 as their newly defined Burma Member of the Wadi Hasa Marl Formation in Wadi El Jurf and upstream in Wadi Burma along an 8-km long southwest-northeast oriented stretch. They argued that a minimum lake depth of 15 m must have existed due to the altitudinal difference of these sediments with an altitude of 940 m asl at Jurf ed Darawish and 955 m asl upstream in Wadi Burma. However, they also stated that the sediment types and recorded fossils rather point to a shallow lake of 10-m depth or less. Shoreline features were not recorded. Additional fine-grained sediments, mapped in Wadi Al Juhiera between 1,008 and 1,014 m asl, ca. 7 km southwest of Jurf ed Darawish, were regarded as deposits of a separate lake basin since a single lake with a required water depth of ca. 70 m was considered as unrealistic for the currently hyperarid region. We argue that 1) the altitudinal distribution of sediments similar to those at Section 3 and Section 9 over a range of ca. 70 m, 2) their spatial documentation along the modern wadis Al Juhiera, Burma and El Jurf, 3) the lack of shoreline deposits, and 4) the sediment types and included fossils recorded at Section 3 and Section 9 are evidence for the former existence of in-stream wetlands and aggradational alluvial plains in the Pleistocene. Similar in-stream wetlands occur in some segments of Wadi Hasa 40 km to the northwest of Jurf ed Darawish today, showing that only slight differences in local climate and groundwater hydrology are required to support a different landscape in an aggradational setting at Jurf ed Darawish (**Figure 10**). In contrast, far-reaching inferences such as those by Findlater (2003, p. 59) who compared the Late Pleistocene landscape at Jurf ed Darawish with a "jungle-like terrain" and nearest modern analogues "in central Africa or South East Asia" are clearly not supported by the accumulated geological evidence.

Comparison With Other Pleistocene Records in the Region

Intensive archaeological surveys and geological studies were conducted in the upper reaches of Wadi Hasa only 20 km to the north of Jurf ed Darawish since the initial surveys by Vita-Finzi (1964) and Clark (1984; **Figure 1**). As a result, Schuldenrein and Clark (1994) and Schuldenrein and Clark (2003) suggested that a relatively large lake existed in the region in the second half of the Late Pleistocene between ca. 70 to 20 ka. However, the detailed sedimentological and dating study of Winer (2010) demonstrated that the sediments in question where formed in an in-stream wetland setting (Rech et al., 2017). Inferred periods of sediment accumulation were before ca. 140, at ca. 120, 98–78, 68–50, 32–24, 16–13 and 10–7 ka (Winer, 2010; **Figure 11**). Remains of gazelle and equids from 'Ain Difla in Wadi Ali, a small tributary of Wadi Hasa, were assigned an age of ca. 100 ka, and suggest that a cool steppe or sub-desert environment existed in the region in the early Late Pleistocene which is more consistent with the inference of in-stream wetlands rather than a long-term presence of a large lake in the Wadi Hasa region (Lindly and Clark, 1987; Shea, 2003).

A lake of ca. 1,000–1,800 km^2 size was also proposed for the Al Jafr Basin ca. 60 km to the southeast of Jurf ed Darawish, based on geomorphological analyses and the examination of surficially exposed sediments by Huckriede and Wiesemann (1968), Bender (1968) and Bandel and Salameh (2013; **Figure 1**). Sediment sections of the uppermost 2 m were subsequently analyzed by Mischke et al. (2015) who concluded that the deposits formed in a wetland including shallow freshwater to slightly oligohaline ponds, streams and swamps. Sediment accumulation occurred during the second half of MIS 3 and was replaced by erosion in MIS 2. However, sediments of pre-MIS 3 age were not included in their study. In contrast, Davies (2005) studied a 31-m long core from the basin which included clay, sandy clays and gravel lenses beneath an 11-m thick aeolian-alluvial sediment cover which was apparently formed in MIS 2. The lower stratigraphic unit was not dated but clays at the base of the core were regarded as formed in a deep lacustrine environment, overlain by multiple sequences of alluvial deposits, possibly formed during individual large flooding events. However, the inference of wetlands in MIS 3 shows that slightly wetter conditions in the Late Pleistocene probably led to a remarkable landscape change at this southeastern, even more arid location in Jordan.

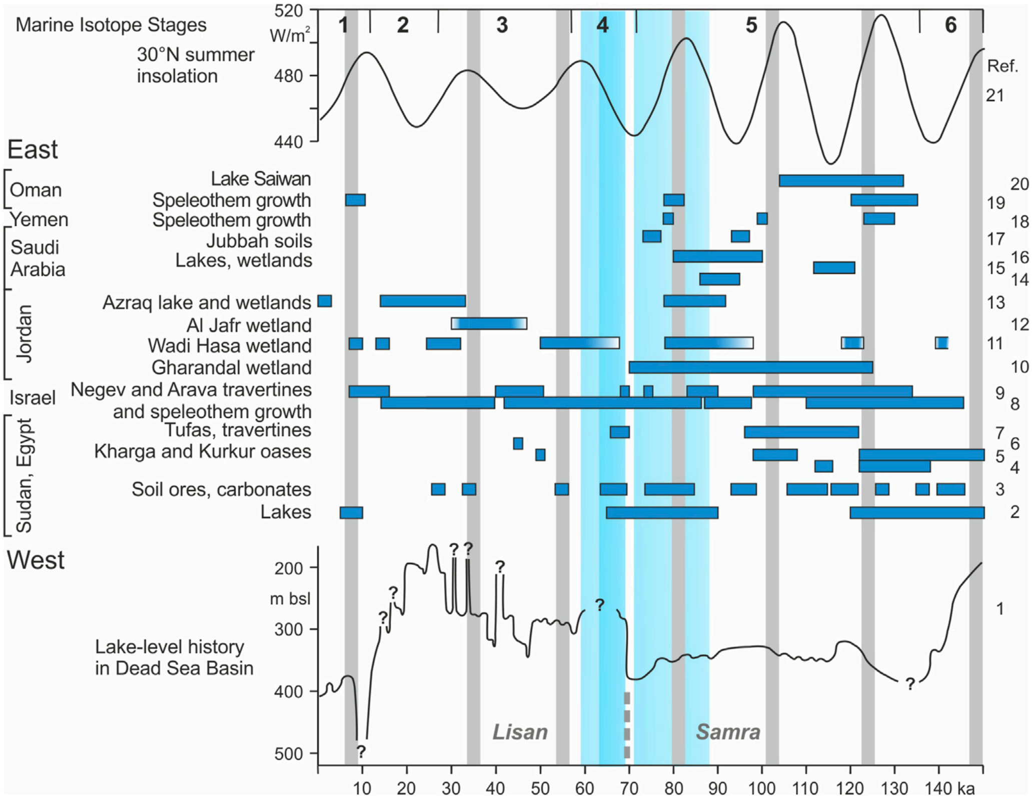

FIGURE 11 | Late Pleistocene and Holocene lake-level history in the Dead Sea Basin, and records of wetter climate conditions (horizontal blue bars) in the region in comparison to the dated artefact-bearing bed at Jurf ed Darawish marked by vertical blue bars. Vertical grey bars indicate sapropels in the eastern Mediterranean Sea north of the Nile delta (Zhao et al., 2011). Broken grey line marks the Samra-Lisan lakes' change. References of other climate records are 1 Bartov et al. (2002), Bartov et al. (2003), Bartov et al. (2007), Waldmann et al. (2007); 2 Szabo et al. (1995); 3 Osmond and Dabous (2004); 4 Smith et al. (2007); 5 Smith et al. (2004); 6 Sultan et al. (1997); 7 Crombie et al. (1997); 8 Vaks et al. (2006), Vaks et al. (2007); 9 Schwarcz et al. (1979), Livnat and Kronfeld (1985), Enmar (1999), Waldmann et al. (2010); 10 Al-Saqarat et al. (2021); 11 Winer (2010); 12 Mischke et al. (2015); 13 Cordova et al. (2013); 14 Groucutt et al. (2018); 15 Stewart et al. (2020b); 16 Groucutt et al. (2015); 17 Petraglia et al. (2011); 18 Fleitmann et al. (2011); 19 Fleitmann et al. (2003); 20 Rosenberg et al. (2012); 21 Berger and Loutre (1991).

Sediments incised by Wadi Gharandal, a tributary of Wadi Araba ca. 90 km southwest of Jurf ed Darawish, were regarded as formed in the Pleistocene Lake Lisan by Bender (1968). The recent reassessment by Al-Saqarat et al. (2021) revealed that the sediments represent a wetland sequence accumulated in the wadi between ca. 125–70 ka. A minimum age of ca. 75 ka was determined for two Levallois flakes which are possibly evidence for the contemporary presence of humans at Jurf ed Darawish and Gharandal. Additional evidence for the presence of springs and densely vegetated areas including reeds, comes from the northern Wadi Arava/Araba ca. 70 km north of Gharandal, where travertines with determined ages of ca. 130, 90 and 70 ka were apparently formed at the same time as the wetlands in Wadi Gharandal and at Jurf ed Darawish (Livnat and Kronfeld, 1985; Waldmann et al., 2010).

Dating of ostrich shells from archaeological excavations of two rock shelters (Tor Sabiha and Tor Faraj; **Figure 1**) ca. 90 km to the south of Jurf ed Darawish yielded ages of ca. 70 ka (Henry and Miller, 1992). Together with 60–50 ka old animal teeth from the excavation of Fara II at the northern margin of the Negev Desert, Henry and Miller (1998, p. 45) already suggested more than two decades ago "an uninterrupted cultural development stretching from ca. 80–45 K bp for the arid zone of the southern Levant" (Schwarcz and Rink, 1998; Goder-Goldberger et al., 2020; **Figure 1**). Our new data from Jurf ed Darawish show that human occupation in the southern Levant was possible not only at few locations characterized by locally specific, very favourable hydrological conditions during the late MIS 5 and in MIS 4. Instead, lowered temperatures and reduced evaporation led to a higher moisture availability and abundant surficially accessible water resources for game and humans.

A wetter climate at ca. 70 ka is also inferred from the coincidence of the reconstructed summer insolation minimum and the dramatic lake-level rise by 70–80 m in the Dead Sea Basin at the Samra-Lisan lakes transition (Berger and Loutre, 1991; Waldmann et al., 2007; **Figure 11**). It is still debated whether precipitation increased mainly in the northernmost catchment of Lake Lisan (i.e., Mount Hermon, the Golan Heights and Upper Galilee) or whether also higher precipitation in its central parts such as the Judean Mountains contributed to the initial rise in lake level and subsequently maintained high level (Waldmann et al., 2007; Enzel et al., 2008). The study at Jurf ed Darawish shows that regions as remote from the seas as precipitation-source areas such as the Jordanian Plateau apparently received higher precipitation than today and likely contributed to high levels of Lake Lisan in MIS 4 and 3.

Further south in the Negev Desert, wetter conditions were inferred from speleothem growth between 84 and 13 ka and from the formation of loess and calcic soils, and thus, the presence of a relatively dense vegetation cover, which started ca. 80–75 ka and mainly prevailed during MIS 4-2 (Vaks et al., 2006; Enzel et al., 2008; Crouvi et al., 2009). Travertines formed in hydrologically favourable conditions of Nahal (i.e., stream) Aqev in the north-central Negev Highlands in the Middle and Late Pleistocene but they are not necessarily evidence of wetter climate conditions since travertine is formed in specific locations in the valley even today. However, Schwarcz et al. (1979) determined ages of 80 and 46 ka for two different artefact-bearing travertine deposits which show that humans inhabited the region at the same time as Jurf ed Darawish.

Wetter conditions in the Late Pleistocene in more distant regions such as the Western Desert in Egypt and Sudan were recorded as a result of studies of lake sediments, travertine and ore deposits, and soil carbonates. For example, Szabo et al. (1995) inferred pluvial conditions and enhanced monsoonal circulation between 90 and 65 ka based on the identification and dating of lake sediments (**Figure 11**). Osmond and Dabous (2004) dated carbonate and oxidized iron deposits, and phosphorite ores as evidence of enhanced groundwater circulation in the Egyptian Sahara. They determined an especially high number of age data between 90 and 70 ka. Dating of travertines in Egypt's Western Desert yielded Middle Pleistocene and younger ages of ca. 150–122, 116–198, 68 and 50 ka (Crombie et al., 1997; Smith et al., 2004, 2007; **Figure 11**).

On the Arabian Peninsula, lakes and wetlands existed between 132 to 104 and 100 to 80 ka (Rosenberg et al., 2012; Groucutt et al., 2015, 2018; Stewart et al., 2020b; **Figure 11**). Soil formation was recorded in Saudi Arabia's hyperarid Nefud Desert ca. 95 and 75 ka (Petraglia et al., 2011). Periods of rapid speleothem growth in the Yemeni Highlands and Oman Mountains as indicators of wetter climate conditions occurred ca. 135–120, 100 and 82–78 ka (Fleitmann et al., 2003, 2011; **Figure 11**). Thus, the presence of humans on the central Jordanian Plateau in the Late Pleistocene falls apparently into a period of generally wetter conditions in the southern Levant, the eastern Sahara and the Arabian Peninsula.

Sediment accumulation at Jurf ed Darawish during most of the late Pleistocene was replaced by an erosional setting sometime after 30 ka (**Figure 3**). As a result, the sequence of the accumulated Pleistocene sediments was removed in the Wadi El Jurf, and the Maastrichtian bedrock became exposed. We assume that similarly dry conditions as occur today with very sparse desert vegetation led to the establishment of the erosional setting. In the Negev Highlands, erosion started after a long period of dust aggradation at ca. 24 ka and incision culminated at the Pleistocene-Holocene transition (Faershtein et al., 2016). In the Al Jafr Basin, wetland deposits were formed in the second half of MIS 3, followed by drier conditions in MIS 2 (Davies 2005; Mischke et al., 2015). The more intensively investigated Lake Lisan experienced a stepwise lake-level decline after the highest level was reached between 27 and 24 ka when the lake was merged with the Sea of Galilee (Hazan et al., 2005; Bartov et al., 2007; Waldmann et al., 2007). However, the most dramatic lake-level fall occurred at ca. 14 ka (Torfstein et al., 2013). Thus, we may speculate that sediment accumulation continued in the Jurf ed Darawish region until ca. 24 ka, followed by erosion which probably became most intensive before and during the Pleistocene-Holocene transition.

CONCLUSION

Evidence from Jurf ed Darawish suggests that an aggradational setting dominated in the present hyperarid region since at least the middle of MIS 5 and during MIS 4 and 3. Dust deposition and loess formation must have resulted from a significantly denser vegetation cover. An in-stream wetland existed at Jurf ed Darawish during MIS 5-4, and was replaced by a vegetated alluvial plain in MIS 3. The accumulation of reworked, secondary fluvial loess continued at Jurf ed Darawish until at least 30 ka before erosion started to prevail sometime afterwards. The new data from Jurf ed Darawish and published information from other locations in the southern Levant show that streams and in-stream and spring-fed wetlands occurred on the Jordanian Plateau, in Wadi Arava/Araba and in the Negev in the Late Pleistocene (Schwarcz et al., 1979; Waldmann et al., 2010; Winer, 2010; Al-Saqarat et al., 2021).

The distribution of artefacts in sediments which accumulated at Jurf ed Darawish between ca. 85 to 65 ka is evidence for a relatively long presence of humans in the region. Artefact-bearing sediments at Gharandal with an age of at least 75 ka, ca. 70-ka old ostrich shells from excavations at Tor Sabiha and Tor Faraj in southwestern Jordan, 80-ka old artefacts in travertine deposits in the Negev Desert, 60–50-ka old animal teeth from the excavation at Fara II at its northern margin, and the 85-ka old human remains from Al Wusta in the Nefud Desert show that humans were present in a wide region of the southern Levant and Arabian Peninsula in the late MIS 5 and during MIS 4 (**Figure 1**). Thus, favourable conditions in the middle of the Late Pleistocene had turned at least significant portions of today's desert barrier of the southern Levant and the Arabian Peninsula into a bridge between climatically more favourable regions in the south and north. The described evidence for the presence of humans in the southern Levant and Arabian Peninsula between ca. 85 to 60 ka fills the gap between two distinct movements identified within the Out-of-Africa 2 model between ca. 130 to 80 and after 50 ka (Garcea, 2012). However, our study leaves open whether the embedded artefacts in the sediments of Jurf ed Darawish represent repeated visits or an uninterrupted presence of humans in the region. Detailed archaeological investigations of the sedimentary sequences of Jurf ed Darawish are required to address this question.

According to the temperature record of the Greenland ice cap, the period between 85 and 60 ka includes an initial long-term cooling and later on one of the coldest periods of the entire Late Pleistocene between 70 and 60 ka which was only interrupted by a single short-term warming at ca. 65 ka (Kindler et al., 2014). This latter period represents the largest increase of global ice sheets in the Late Pleistocene (Batchelor et al., 2019). Thus, lower temperatures, rapid sea-level fall and resulting re-arrangements of the atmospheric circulation were apparently key for the reconstructed landscape change in the southern Levant.

Generally wetter conditions represented by reworked, secondary fluvial loess at Jurf ed Darawish during the Late Pleistocene possibly resulted from 1) the lowered temperatures and reduced evaporation effects which caused an increase in available moisture, and 2) more efficient eastern Mediterranean cyclones which also reached relatively far inland. These eastern Mediterranean cyclones, typically called Cyprus Lows, could have transported more moisture to the southern Levant as a result of a generally more southern location of its pathways and/or a higher frequency of arriving lows (Saaroni et al., 2010). Cyprus Lows reach the eastern Mediterranean coast today mostly in the northern Levant, but the glaciations of Scandinavia and the Alps, and extended snow covers at northern and middle latitudes and related katabatic winds probably forced the westerlies circulation of the Mediterranean to a more southern position in comparison to today. Minor temperature reductions in subtropical regions in the Pleistocene probably resulted in a weaker influence of the descending branch of the Hadley cell, also contributing to a more efficient transport of moist air from the Mediterranean Sea to the southern Levant. Enzel et al. (2008) proposed that eastern Mediterranean lows were funnelled by the ice and snow cover in Europe and Turkey, the lower sea level and the Sahara during the Late Pleistocene over the sea and directed to the east. In addition, climate model simulations predict a poleward shift of North Atlantic storm tracks, decrease of winter rain in the Middle East and weakening of Mediterranean storm tracks in a warmer future (Black et al., 2010). Accordingly, an equatorward shift of North Atlantic storm tracks, increase of winter rain in the Middle East and strengthening of Mediterranean storm tracks are expected for globally cooler conditions.

Further downstream, sediments similar to those at Jurf ed Darawish and previously described as lake sediments were reassessed as in-stream wetland deposits by Winer (2010). Similar sediments exist also 6 km upstream of Jurf ed Darawish in Wadi Juheira, where they were assessed as lake deposits (Neeley, 2004). A sedimentological and palaeontological reassessment could show whether these sediments were formed in a lake or similar to those at Jurf ed Darawish and Wadi Hasa in an in-stream wetland setting.

Wetter climate conditions and presence of humans during the late MIS 5 and during MIS 4 were inferred in a wide region from the Negev Desert in the west to the Nefud Desert in the east. A missing piece in the emerging puzzle of contemporaneously accumulated sediments are potentially the clays and sandy clays under an 11-m thick cover of wetland, alluvial and aeolian deposits in the Al Jafr Basin. Sediments between 31 and 11 m depth were partly regarded as lake deposits by Davies (2005) who conducted loss-on-ignition and element geochemistry analyses. Dating of sediments above provided ages of 24 and 16 ka but the age of the finer-grained sediments below is still not determined. New analyses of sediments from the Al Jafr and other endorheic basins further south and east have the potential to shed more light on the environmental and landscape change in the southern Levant during the Late Pleistocene.

DATA AVAILABILITY STATEMENT

The raw data supporting the conclusion of this article will be made available by the authors, without undue reservation.

AUTHOR CONTRIBUTIONS

SM and HG designed the study; SM, GF, HG, PB, MR, and JK conducted fieldwork; GF, NP, and ZL conducted OSL dating; MR conducted grain-size analysis; JK performed sediment geochemistry analysis; SM and PB conducted microfossil analysis; SM wrote the manuscript draft and all contributed to the revision of the manuscript.

FUNDING

This work was funded by the Deutsche Forschungsgemeinschaft (Grant Mi 730/18-1 to SM).

ACKNOWLEDGMENTS

Logistical support of fieldwork of SM, MR, PB, and JK was kindly provided by Bety S. Al-Saqarat (University of Jordan, Amman) and Linah N. Ababneh (Cornell University, Ithaca). Bernhard Diekmann and Ute Bastian (Alfred Wegener Institute for Polar and Marine Research, Potsdam) provided lab access and supported the grain-size analysis, and Stephan Opitz (University of Cologne) and Karsten Adler (GFZ German Research Centre for Geosciences Potsdam) helped with analyses of grain-size data. We thank Antje Musiol who ran the TOC and TC analyses at the Institute of Geosciences at Potsdam University. The photo of **Figure 10** was kindly contributed by Wolfgang Streicher. Very constructive reviews were provided by JP and JL.

SUPPLEMENTARY MATERIAL

The Supplementary Material for this article can be found online at: https://www.frontiersin.org/articles/10.3389/feart.2021.722435/full#supplementary-material

REFERENCES

Aitken, M. J. (1985). *Thermoluminescence Dating*. London: Academic Press.

Al-Saqarat, B. S., Abbas, M., Lai, Z., Gong, S., Alkuisi, M. M., Abu Hamad, A. M. B., et al. (2021). A Wetland Oasis at Wadi Gharandal Spanning 125-70 Ka on the Human Migration Trail in Southern Jordan. *Quat. Res.* 100, 154–169. doi:10.1017/qua.2020.82

Amit, R., Enzel, Y., and Crouvi, O. (2020). Quaternary Influx of Proximal Coarse-Grained Dust Altered Circum-Mediterranean Soil Productivity and Impacted Early Human Culture. *Geology* 49, 61–65. doi:10.1130/g47708.1

Bandel, K., and Salameh, E. M. (2013). *Geologic Development of Jordan - Evolution of its Rocks and Life*. Deposit No. 690/3/2013 of the. Amman: National Library.

Bartov, Y., Enzel, Y., Porat, N., and Stein, M. (2007). Evolution of the Late Pleistocene Holocene Dead Sea Basin from Sequence Statigraphy of Fan Deltas and Lake-Level Reconstruction. *J. Sediment. Res.* 77, 680–692. doi:10.2110/jsr.2007.070

Bartov, Y., Goldstein, S. L., Stein, M., and Enzel, Y. (2003). Catastrophic Arid Episodes in the Eastern Mediterranean Linked with the North Atlantic Heinrich Events. *Geol* 31, 439–442. doi:10.1130/0091-7613(2003)031<0439:caeite>2.0.co;2

Bartov, Y., Stein, M., Enzel, Y., Agnon, A., and Reches, Z. e. (2002). Lake Levels and Sequence Stratigraphy of Lake Lisan, the Late Pleistocene Precursor of the Dead Sea. *Quat. Res.* 57, 9–21. doi:10.1006/qres.2001.2284

Batchelor, C. L., Margold, M., Krapp, M., Murton, D. K., Dalton, A. S., Gibbard, P. L., et al. (2019). The Configuration of Northern Hemisphere Ice Sheets through the Quaternary. *Nat. Commun.* 10, 3713. doi:10.1038/s41467-019-11601-2

Ben David, R. (2003). *Changes in Desert Margin Environments during the Climate Changes of the Late thesosQuaternary: Interaction between Drainage Systems and the Accumulation of Dust (Loess) and the Invasion of Dunes at the North-West Negev Desert*. Jerusalem: Ph.D. Dissertation at The Hebrew University of Jerusalem, 170. (in Hebrew with Engl. abstr.).

Benaafi, M., and Abdullatif, O. (2015). Sedimentological, Mineralogical, and Geochemical Characterization of Sand Dunes in Saudi Arabia. *Arab J. Geosci.* 8, 11073–11092. doi:10.1007/s12517-015-1970-9

Bender, F. (1968). *Geologie von Jordanien*. Stuttgart: Gebrüder Borntraeger, 230.

Berger, A., and Loutre, M. F. (1991). Insolation Values for the Climate of the Last 10 Million Years. *Quat. Sci. Rev.* 10, 297–317. doi:10.1016/0277-3791(91)90033-q

Black, E., Brayshaw, D. J., and Rambeau, C. M. C. (2010). Past, Present and Future Precipitation in the Middle East: Insights from Models and Observations. *Phil. Trans. R. Soc. A.* 368, 5173–5184. doi:10.1098/rsta.2010.0199

Catlett, G. A., Rech, J. A., Pigati, J. S., and Al Kuisi, M. (2013). Paleoclimatic Implications of Pluvial Deposits in Mudawwara, Jordan. *Geol. Soc. Am. Abstr. Programs* 45, 680.

Clark, G. A. (1984). The Negev Model for Paleoclimatic Change and Human Adaptation in the Levant and its Relevance for the Paleolithic of the Wadi El Hasa (West-Central Jordan). *Annu. Department Antiquities Jordan* 28, 225–248.

Cordova, C. E., Foley, C., Nowell, A., and Bisson, M. (2005). Landforms, Sediments, Soil Development, and Prehistoric Site Settings on the Madaba-Dhiban Plateau, Jordan. *Geoarchaeology* 20, 29–56. doi:10.1002/gea.20036

Cordova, C. E., Nowell, A., Bisson, M., Ames, C. J. H., Pokines, J., Chang, M., et al. (2013). Interglacial and Glacial Desert Refugia and the Middle Paleolithic of the Azraq Oasis, Jordan. *Quat. Int.* 300, 94–110. doi:10.1016/j.quaint.2012.09.019

Crombie, M. K., Arvidson, R. E., Sturchio, N. C., El Alfy, Z., and Zeid, K. A. (1997). Age and Isotopic Constraints on Pleistocene Pluvial Episodes in the Western Desert, Egypt. *Palaeogeogr. Palaeoclimatol. Palaeoecol.* 130, 337–355. doi:10.1016/s0031-0182(96)00134-4

Crouvi, O., Amit, R., Enzel, Y., Porat, N., and Sandler, A. (2008). Sand Dunes as a Major Proximal Dust Source for Late Pleistocene Loess in the Negev Desert, Israel. *Quat. Res.* 70, 275–282. doi:10.1016/j.yqres.2008.04.011

Crouvi, O., Amit, R., Porat, N., Gillespie, A. R., McDonald, E. V., and Enzel, Y. (2009). Significance of Primary Hilltop Loess in Reconstructing Dust Chronology, Accretion Rates, and Sources: An Example from the Negev Desert, Israel. *J. Geophys. Res.* 114, F02017. doi:10.1029/2008jf001083

Davies, C. P. (2005). Quaternary Paleoenvironments and Potential for Human Exploitation of the Jordan Plateau Desert interior. *Geoarchaeology: Int. J.* 20, 381–400. doi:10.1002/gea.20055

Enmar, L. (1999). The Travertines in the Northern and Central Arava: Stratigraphy, Petrology and Geochemistry. *Geol. Surv. Isr. Rep.* 1/99, 111.

Enzel, Y., Amit, R., Dayan, U., Crouvi, O., Kahana, R., Ziv, B., et al. (2008). The Climatic and Physiographic Controls of the Eastern Mediterranean over the Late Pleistocene Climates in the Southern Levant and its Neighboring Deserts. *Glob. Planet. Change* 60, 165–192. doi:10.1016/j.gloplacha.2007.02.003

Enzel, Y., Kushnir, Y., and Quade, J. (2015). The Middle Holocene Climatic Records from Arabia: Reassessing Lacustrine Environments, Shift of ITCZ in Arabian Sea, and Impacts of the Southwest Indian and African Monsoons. *Glob. Planet. Change* 129, 69–91. doi:10.1016/j.gloplacha.2015.03.004

Faershtein, G., Porat, N., Avni, Y., and Matmon, A. (2016). Aggradation-incision Transition in Arid Environments at the End of the Pleistocene: an Example from the Negev Highlands, Southern Israel. *Geomorphology* 253, 289–304. doi:10.1016/j.geomorph.2015.10.017

Faershtein, G., Porat, N., and Matmon, A. (2020). Extended-Range Luminescence Dating of Quartz and Alkali Feldspar from Aeolian Sediments in the Eastern Mediterranean. *Geochronology* 2, 101–118. doi:10.5194/gchron-2-101-2020

Findlater, G. M. (2003). *Imperial Control in Roman and Byzantine Arabia: A Landscape Interpretation of Archaeological Evidence in Southern Jordan*. Edinburgh: Ph.D. Dissertation at The University of Edinburgh, 484.

Fleitmann, D., Burns, S. J., Neff, U., Mangini, A., and Matter, A. (2003). Changing Moisture Sources over the Last 330,000 Years in Northern Oman from Fluid-Inclusion Evidence in Speleothems. *Quat. Res.* 60, 223–232. doi:10.1016/s0033-5894(03)00086-3

Fleitmann, D., Burns, S. J., Pekala, M., Mangini, A., Al-Subbary, A., Al-Aowah, M., et al. (2011). Holocene and Pleistocene Pluvial Periods in Yemen, Southern Arabia. *Quat. Sci. Rev.* 30, 783–787. doi:10.1016/j.quascirev.2011.01.004

Fuhrmann, R. (2012). Atlas quartärer und rezenter Ostrakoden Mitteldeutschlands. *Altenburger Naturwissenschaftliche Forschungen* 15, 1–320.

Galbraith, R. F., and Roberts, R. G. (2012). Statistical Aspects of Equivalent Dose and Error Calculation and Display in OSL Dating: an Overview and Some Recommendations. *Quat. Geochronol.* 11, 1–27. doi:10.1016/j.quageo.2012.04.020

Garcea, E. A. A. (2012). Successes and Failures of Human Dispersals from North Africa. *Quat. Int.* 270, 119–128. doi:10.1016/j.quaint.2011.06.034

Ginat, H., Opitz, S., Ababneh, L., Faershtein, G., Lazar, M., Porat, N., et al. (2018). Pliocene-Pleistocene Waterbodies and Associated Deposits in Southern Israel and Southern Jordan. *J. Arid Environments* 148, 14–33. doi:10.1016/j.jaridenv.2017.09.007

Goder-Goldberger, M., Crouvi, O., Caracuta, V., Kolska Horwitz, L., Neumann, F. H., Porat, N., et al. (2020). The Middle to Upper Paleolithic Transition in the Southern Levant: New Insights from the Late Middle Paleolithic Site of Far'ah II, Israel. *Quat. Sci. Rev.* 237, 106304. doi:10.1016/j.quascirev.2020.106304

Groucutt, H. S., Grün, R., Zalmout, I. A. S., Drake, N. A., Armitage, S. J., Candy, I., et al. (2018). *Homo sapiens* in Arabia by 85,000 Years Ago. *Nat. Ecol. Evol.* 2, 800–809. doi:10.1038/s41559-018-0518-2

Groucutt, H. S., White, T. S., Clark-Balzan, L., Parton, A., Crassard, R., Shipton, C., et al. (2015). Human Occupation of the Arabian Empty Quarter during MIS 5: Evidence from Mundafan Al-Buhayrah, Saudi Arabia. *Quat. Sci. Rev.* 119, 116–135. doi:10.1016/j.quascirev.2015.04.020

Hazan, N., Stein, M., Agnon, A., Marco, S., Nadel, D., Negendank, J. F. W., et al. (2005). The Late Quaternary Limnological History of Lake Kinneret (Sea of Galilee), Israel. *Quat. Res.* 63, 60–77. doi:10.1016/j.yqres.2004.09.004

Henry, D. O., and Miller, G. H. (1992). The Implications of Amino Acid Racemization Dates of Levantine Mousterian Deposits in Southern Jordan. *paleo* 18, 45–52. doi:10.3406/paleo.1992.4572

Huckriede, R., and Wiesemann, G. (1968). Der jungpleistozäne Pluvial-See von El-Jafr und weitere Daten zum Quartär Jordaniens. *Geologica et Paleontologica* 2, 73–95.

Hunt, C. O., Elrishi, H. A., Gilbertson, D. D., Grattan, J., Mclaren, S., Pyatt, F. B., et al. (2004). Early-Holocene Environments in the Wadi Faynan, Jordan. *The Holocene* 14, 921–930. doi:10.1191/0959-683604hl769rp

Janz, H. (1994). Zur Bedeutung des Schalenmerkmals ‚Marginalrippen' der Gattung *Ilyocypris* (Ostracoda, Crustacea). *Stuttgarter Beiträge zur Naturkunde Serie B* 206, 1–19.

Kindler, P., Guillevic, M., Baumgartner, M., Schwander, J., Landais, A., and Leuenberger, M. (2014). Temperature Reconstruction from 10 to 120 Kyr

B2k from the NGRIP Ice Core. *Clim. Past* 10, 887–902. doi:10.5194/cp-10-887-2014

Lai, Z.-P., and Wintle, A. G. (2006). Locating the Boundary between the Pleistocene and the Holocene in Chinese Loess Using Luminescence. *The Holocene* 16, 893–899. doi:10.1191/0959683606hol980rr

Lai, Z., and Brückner, H. (2008). Effects of Feldspar Contamination on Equivalent Dose and the Shape of Growth Curve for OSL of Silt-Sized Quartz Extracted from Chinese Loess. *Geochronometria* 30, 49–53. doi:10.2478/v10003-008-0010-0

Lai, Z. P., Zöller, L., Fuchs, M., and Brückner, H. (2008). Alpha Efficiency Determination for OSL of Quartz Extracted from Chinese Loess. *Radiat. Measurements* 43, 767–770. doi:10.1016/j.radmeas.2008.01.022

Lai, Z. (2006). Testing the Use of an OSL Standardised Growth Curve (SGC) for Determination on Quartz from the Chinese Loess Plateau. *Radiat. Measurements* 41, 9–16. doi:10.1016/j.radmeas.2005.06.031

Lindly, J., and Clark, G. (1987). A Preliminary Lithic Analysis of the Mousterian Site of 'Ain Difla (WHS Site 634) in the Wadi Ali, West-Central Jordan. *Proc. Prehist. Soc.* 53, 279–292. doi:10.1017/s0079497x00006228

Livnat, A., and Kronfeld, J. (1985). Paleoclimatic Implications of U-Series Dates for lake Sediments and Travertines in the Arava Rift Valley, Israel. *Quat. Res.* 24, 164–172. doi:10.1016/0033-5894(85)90003-1

Lucke, B., Kemnitz, H., Bäumler, R., and Schmidt, M. (2013). Red Mediterranean Soils in Jordan: New Insights in Their Origin, Genesis, and Role as Environmental Archives. *Catena* 112, 4–24.

MacDonald, B., Bradshaw, A., Herr, L., Neeley, M., and Quaintance, S. (2000). The Tafila-Busayra Archaeological Survey: Phase 1 (1999). *Annu. Department Antiquities Jordan* 44, 507–522.

MacDonald, B., Herr, L., Neeley, M. P., Quaintance, S., and Bradshaw, A. (2001). The Tafila-Busayra Archaeological Survey: Phase 2 (2000). *Annu. Department Antiquities Jordan* 45, 395–411.

Meisch, C. (2000). *Freshwater Ostracoda of Western and Central Europe*. Heidelberg: Spektrum.

Mischke, S., Opitz, S., Kalbe, J., Ginat, H., and Al-Saqarat, B. (2015). Palaeoenvironmental Inferences from Late Quaternary Sediments of the Al Jafr Basin, Jordan. *Quat. Int.* 382, 154–167. doi:10.1016/j.quaint.2014.12.041

Moumani, K., Alexander, J., and Bateman, M. D. (2003). Sedimentology of the Late Quaternary Wadi Hasa Marl Formation of Central Jordan: a Record of Climate Variability. *Palaeogeogr. Palaeoclimatol. Palaeoecol.* 191, 221–242. doi:10.1016/s0031-0182(02)00715-0

Moumani, K. A. (1996). *The Geology of Jurf Ed Darawish, Map Sheet (3151 II), 1:50 000 National Mapping Project, Natural Resources Authority*. Amman: Geological Directorate, Mapping Division.

Neeley, M. (2004). "Late Epipaleolithic Settlement in the Wadi Juheira, West-central Jordan," in *The Last Hunter-Gatherer Societies in the Near East*. Editor C. Delage (Oxford: John and Erica Hedges), 39–54.

Osmond, J. K., and Dabous, A. A. (2004). Timing and Intensity of Groundwater Movement during Egyptian Sahara Pluvial Periods by U-Series Analysis of Secondary U in Ores and Carbonates. *Quat. Res.* 61, 85–94. doi:10.1016/j.yqres.2003.09.004

Palmer, C. (2013). "Biogeography," in *Atlas of Jordan; History, Territories and Society*. Editor M. Ababsa (Beyrouth: Presses de l'Ifpo), 77–87. doi:10.4000/books.ifpo.4871

Petit-Maire, N., Carbonel, P., Reyss, J. L., Sanlaville, P., Abed, A., Bourrouilh, R., et al. (2010). A Vast Eemian Palaeolake in Southern Jordan (29°N). *Glob. Planet. Change* 72, 368–373. doi:10.1016/j.gloplacha.2010.01.012

Petraglia, M. D., Alsharekh, A. M., Crassard, R., Drake, N. A., Groucutt, H., Parker, A. G., et al. (2011). Middle Paleolithic Occupation on a Marine Isotope Stage 5 Lakeshore in the Nefud Desert, Saudi Arabia. *Quat. Sci. Rev.* 30, 1555–1559. doi:10.1016/j.quascirev.2011.04.006

Pigati, J. S., Rech, J. A., Quade, J., and Bright, J. (2014). Desert Wetlands in the Geologic Record. *Earth-Science Rev.* 132, 67–81. doi:10.1016/j.earscirev.2014.02.001

Porat, N., Rosen, S. A., Boaretto, E., and Avni, Y. (2006). Dating the Ramat Saharonim Late Neolithic Desert Cult Site. *J. Archaeological Sci.* 33, 1341–1355. doi:10.1016/j.jas.2006.01.008

Prescott, J. R., and Hutton, J. T. (1994). Cosmic Ray Contributions to Dose Rates for Luminescence and ESR Dating: Large Depths and Long-Term Time Variations. *Radiat. Measurements* 23, 497–500. doi:10.1016/1350-4487(94)90086-8

Quade, J., Forester, R. M., Pratt, W. L., and Carter, C. (1998). Black Mats, Spring-Fed Streams, and Late-Glacial-Age Recharge in the Southern Great Basin. *Quat. Res.* 49, 129–148. doi:10.1006/qres.1997.1959

Rech, J. A., Ginat, H., Catlett, G. A., Mischke, S., Winer Tully, E., and Pigati, J. S. (2017). "Pliocene-Pleistocene Water Bodies and Associated Deposits in Southern Israel and Southern Jordan," in *Quaternary of the Levant: Environments, Climate Change, and Humans*. Editors Y. Enzel and O. Bar-Yosef (Cambridge University Press), 127–134.

Roberts, H. M., and Duller, G. A. T. (2004). Standardised Growth Curves for Optical Dating of Sediment Using Multiple-Grain Aliquots. *Radiat. Measurements* 38, 241–252. doi:10.1016/j.radmeas.2003.10.001

Röhl, M. (2015). *Rekonstruktion pleistozäner Ablagerungsräume im südlichen Israel und Jordanien anhand von Korngrößendaten*. Berlin: M.Sc. thesis at the Institute of Geological Sciences, Free University Berlin, 74. (in German with English abstract).

Rosenberg, T. M., Preusser, F., Blechschmidt, I., Fleitmann, D., Jagher, R., and Matter, A. (2012). Late Pleistocene Palaeolake in the interior of Oman: a Potential Key Area for the Dispersal of Anatomically Modern Humans Out-Of-Africa? *J. Quat. Sci.* 27, 13–16. doi:10.1002/jqs.1560

Saaroni, H., Halfon, N., Ziv, B., Alpert, P., and Kutiel, H. (2010). Links between the Rainfall Regime in Israel and Location and Intensity of Cyprus Lows. *Int. J. Climatol.* 30, 1014–1025. doi:10.1002/joc.1912

Saqqa, W., and Atallah, M. (2004). Characterization of the Aeolian Terrain Facies in Wadi Araba Desert, Southwestern Jordan. *Geomorphology* 62, 63–87. doi:10.1016/j.geomorph.2004.02.002

Schuldenrein, J., and Clark, G. A. (1994). Landscape and Prehistoric Chronology of West-central Jordan. *Geoarchaeology* 9, 31–55. doi:10.1002/gea.3340090103

Schuldenrein, J., and Clark, G. A. (2003). Prehistoric Landscapes and Settlement Geography along the Wadi Hasa, West-central Jordan. Part II: Towards a Model of Palaeoecological Settlement for the Wadi Hasa. *Environ. Archaeology* 8, 1–16. doi:10.1179/env.2003.8.1.1

Schwarcz, H. P., Blackwell, B., Goldberg, P., and Marks, A. E. (1979). Uranium Series Dating of Travertine from Archaeological Sites, Nahal Zin, Israel. *Nature* 277, 558–560. doi:10.1038/277558a0

Schwarcz, H. P., and Rink, J. W. (1998). "Progress in ESR and U-Series Chronology of the Levantine Paleolithic," in *Neandertals and Modern Humans in Western Asia*. Editors T. Akazawa, K. Aoki, and O. Bar-Yosef (New York: Plenum), 57–68.

Shea, J. J. (2003). The Middle Paleolithic of the East Mediterranean Levant. *J. World Prehistory* 17, 313–394. doi:10.1023/b:jowo.0000020194.01496.fe

Smith, J. R., Giegengack, R., Schwarcz, H. P., McDonald, M. M. A., Kleindienst, M. R., Hawkins, A. L., et al. (2004). A Reconstruction of Quaternary Pluvial Environments and Human Occupations Using Stratigraphy and Geochronology of Fossil-spring Tufas, Kharga Oasis, Egypt. *Geoarchaeology: Int. J.* 19, 1–34. doi:10.1002/gea.20004

Smith, J. R., Hawkins, A. L., Asmerom, Y., Polyak, V., and Giegengack, R. (2007). New Age Constraints on the Middle Stone Age Occupations of Kharga Oasis, Western Desert, Egypt. *J. Hum. Evol.* 52, 690–701. doi:10.1016/j.jhevol.2007.01.004

Stewart, M., Clark-Wilson, R., Breeze, P. S., Janulis, K., Candy, I., Armitage, S. J., et al. (2020b). Human Footprints Provide Snapshot of Last Interglacial Ecology in the Arabian interior. *Sci. Adv.* 6, eaba8940. doi:10.1126/sciadv.aba8940

Stewart, M., Louys, J., Breeze, P. S., Clark-Wilson, R., Drake, N. A., Scerri, E. M. L., et al. (2020a). A Taxonomic and Taphonomic Study of Pleistocene Fossil Deposits from the Western Nefud Desert, Saudi Arabia. *Quat. Res.* 95, 1–22. doi:10.1017/qua.2020.6

Suleiman, A., and Al-Bakri, J. (2011). "Estimating Actual Evapotranspiration Using ALARM and the Dimensionless Temperature," in *Evapotranspiration*. Editor L. Labedzki. doi:10.5772/13918*IntechOpen*

Sultan, M., Sturchio, N., Hassan, F. A., Hamdan, M. A. R., Mahmood, A. M., Alfy, Z. E., et al. (1997). Precipitation Source Inferred from Stable Isotopic Composition of Pleistocene Groundwater and Carbonate Deposits in the Western Desert of Egypt. *Quat. Res.* 48, 29–37. doi:10.1006/qres.1997.1907

Szabo, B. J., Haynes, C. V., and Maxwell, T. A. (1995). Ages of Quaternary Pluvial Episodes Determined by Uranium-Series and Radiocarbon Dating of Lacustrine Deposits of Eastern Sahara. *Palaeogeogr. Palaeoclimatol. Palaeoecol.* 113, 227–242. doi:10.1016/0031-0182(95)00052-n

Torfstein, A., Goldstein, S. L., Stein, M., and Enzel, Y. (2013). Impacts of Abrupt Climate Changes in the Levant from Last Glacial Dead Sea Levels. *Quat. Sci. Rev.* 69, 1–7. doi:10.1016/j.quascirev.2013.02.015

Vaks, A., Bar-Matthews, M., Ayalon, A., Matthews, A., Frumkin, A., Dayan, U., et al. (2006). Paleoclimate and Location of the Border between Mediterranean Climate Region and the Saharo-Arabian Desert as Revealed by Speleothems from the Northern Negev Desert, Israel. *Earth Planet. Sci. Lett.* 249, 384–399. doi:10.1016/j.epsl.2006.07.009

Vaks, A., Bar-Matthews, M., Ayalon, A., Matthews, A., Halicz, L., and Frumkin, A. (2007). Desert Speleothems Reveal Climatic Window for African Exodus of Early Modern Humans. *Geol* 35, 831–834. doi:10.1130/g23794a.1

Vaks, A., Bar-Matthews, M., Ayalon, A., Schilman, B., Gilmour, M., Hawkesworth, C. J., et al. (2003). Paleoclimate Reconstruction Based on the Timing of Speleothem Growth and Oxygen and Carbon Isotope Composition in a Cave Located in the Rain Shadow in Israel. *Quat. Res.* 59, 182–193. doi:10.1016/s0033-5894(03)00013-9

Van Harten, D. (1979). Some New Shell Characters to Diagnose the Species of the *Ilyocypris gibba-biplicata-bradyi* Group and Their Ecological Significance. In 7th International Symposium on Ostracodes. Belgrade: Serbian Geological Society, 71–76.

Vita-Finzi, C. (1964). Observations on the Late Quaternary of Jordan. *Palestine Exploration Q.* 96, 19–33. doi:10.1179/peq.1964.96.1.19

Waldmann, N., Starinsky, A., and Stein, M. (2007). Primary Carbonates and Ca-Chloride Brines as Monitors of a Paleo-Hydrological Regime in the Dead Sea basin. *Quat. Sci. Rev.* 26, 2219–2228. doi:10.1016/j.quascirev.2007.04.019

Waldmann, N., Torfstein, A., and Stein, M. (2010). Northward Intrusions of Low- and Mid-latitude Storms across the Saharo-Arabian belt during Past Interglacials. *Geology* 38, 567–570. doi:10.1130/g30654.1

Welter-Schultes, F. (2012). *European Non-marine Molluscs, a Guide for Species Identification*. Göttingen: Planet Poster Editions.

Winer, E. R. (2010). *Interpretation and Climatic Significance of Late Quaternary valley-fill Deposits in Wadi Hasa, West-central Jordan*. Oxford: M.Sc. thesis at Department of GeologyMiami University, 90.

Zhao, Y., Liu, Z., Colin, C., Paterne, M., Siani, G., Cheng, X., et al. (2011). Variations of the Nile Suspended Discharges during the Last 1.75Myr. *Palaeogeogr. Palaeoclimatol. Palaeoecol.* 311, 230–241. doi:10.1016/j.palaeo.2011.09.001

Conflict of Interest: The authors declare that the research was conducted in the absence of any commercial or financial relationships that could be construed as a potential conflict of interest.

Publisher's Note: All claims expressed in this article are solely those of the authors and do not necessarily represent those of their affiliated organizations, or those of the publisher, the editors and the reviewers. Any product that may be evaluated in this article, or claim that may be made by its manufacturer, is not guaranteed or endorsed by the publisher.

Copyright © 2021 Mischke, Lai, Faershtein, Porat, Röhl, Braun, Kalbe and Ginat. This is an open-access article distributed under the terms of the Creative Commons Attribution License (CC BY). The use, distribution or reproduction in other forums is permitted, provided the original author(s) and the copyright owner(s) are credited and that the original publication in this journal is cited, in accordance with accepted academic practice. No use, distribution or reproduction is permitted which does not comply with these terms.

frontiers in Earth Science

ORIGINAL RESEARCH
published: 30 September 2021
doi: 10.3389/feart.2021.741992

Moisture Changes in the Northern Xinjiang Basin Over the Past 2400 years as Documented in Pollen Records of Jili Lake

Yulin Xiao[1]†, Lixiong Xiang[1]†, Xiaozhong Huang[1]*, Keely Mills[2], Jun Zhang[1], Xuemei Chen[3] and Yuan Li[3]

[1]Key Laboratory of Western China's Environmental System (Ministry of Education), College of Earth and Environmental Sciences, Lanzhou University, Lanzhou, China, [2]British Geological Survey, Nottingham, United Kingdom, [3]Northwest Institute of Eco-Environmental and Resources Research, Chinese Academy of Sciences, Lanzhou, China

Regional humidity is important for terrestrial ecosystem development, while it differs from region to region in inland Asia, knowledge of past moisture changes in the lower basin of northern Xinjiang remains largely unclear. Based on a pollen record from Jili Lake, the *Artemisia*/(Amaranthaceae + *Ephedra*) (Ar/(Am + E)) ratio, as an index of regional humidity, has recorded four relatively dry phases: 1) 400 BCE to 1 CE, 2) the Roman Warm Period (RWP; c. 1–400 CE), 3) the Medieval Warm Period (MWP; c. 850–1200 CE) and 4) the Current Warm Period (CWP; since 1850 CE). In contrast, the Dark Age Cold Period (DACP; c. 400–850 CE) and the Little Ice Age (LIA; c. 1200–1850 CE) were relatively wet. Lower lake levels in a relatively humid climate background indicated by higher aquatic pollen (*Typha* and *Sparganium*) after c. 1700 CE are likely the result of intensified irrigation for agriculture in the catchment as documented in historical records. The pollen Ar/(Am + E) ratio also recorded a millennial-scale wetting trend from 1 CE to 1550 CE which is concomitant with a long-term cooling recorded in the Northern Hemisphere.

Keywords: moisture change, pollen records, the historical period, climate change, arid central asia

OPEN ACCESS

Edited by:
Zhuolun Li,
Lanzhou University, China

Reviewed by:
John Dodson,
Institute of Earth Environment,
Chinese Academy of Sciences, China
Chun Mei Ma,
Nanjing University, China

***Correspondence:**
Xiaozhong Huang
xzhuang@lzu.edu.cn

†These authors have contributed equally to this work

Specialty section:
This article was submitted to Quaternary Science, Geomorphology and Paleoenvironment, a section of the journal Frontiers in Earth Science

Received: *15 July 2021*
Accepted: *16 September 2021*
Published: *30 September 2021*

Citation:
Xiao Y, Xiang L, Huang X, Mills K, Zhang J, Chen X and Li Y (2021) Moisture Changes in the Northern Xinjiang Basin Over the Past 2400 years as Documented in Pollen Records of Jili Lake. Front. Earth Sci. 9:741992. doi: 10.3389/feart.2021.741992

INTRODUCTION

During the Holocene, the "westerlies-dominated climatic regime" (WDCR) is characterized by warm-dry and cold-wet phases in inland Asia on different timescales (Chen et al., 2016; Chen et al., 2019). On millennial timescales, the moisture in the WDCR gradually increased, with the wettest period occurring in the late Holocene, while in arid central Asia (ACA), the wettest phase occurred in the mid-to late Holocene (Chen et al., 2016; Chen et al., 2019). At centennial timescales, the WDCR was generally dry during the Medieval Warm Period (WMP) and relatively wet during the Little Ice Age (LIA), but there were some exceptions in Xinjiang (Chen J. et al., 2015), an important part of the WDCR. It has been suggested that the moisture balance has changed from warm-dry to warm-wet over the last few decades (Shi et al., 2006; Wang et al., 2007). Paleoclimate records from the region that span the late Holocene are mostly located at high altitudes (Huang et al., 2018; Lan et al., 2018; Yang et al., 2019); the lack of paleoclimatic records from low altitude areas, where most people are living, hampers understanding of regional climate change both in the past and into the future.

Recent global warming has resulted in the expansion of drylands around the world, and seriously threatens freshwater resources (Huang et al., 2015; Fan et al., 2020). Many studies suggest a major

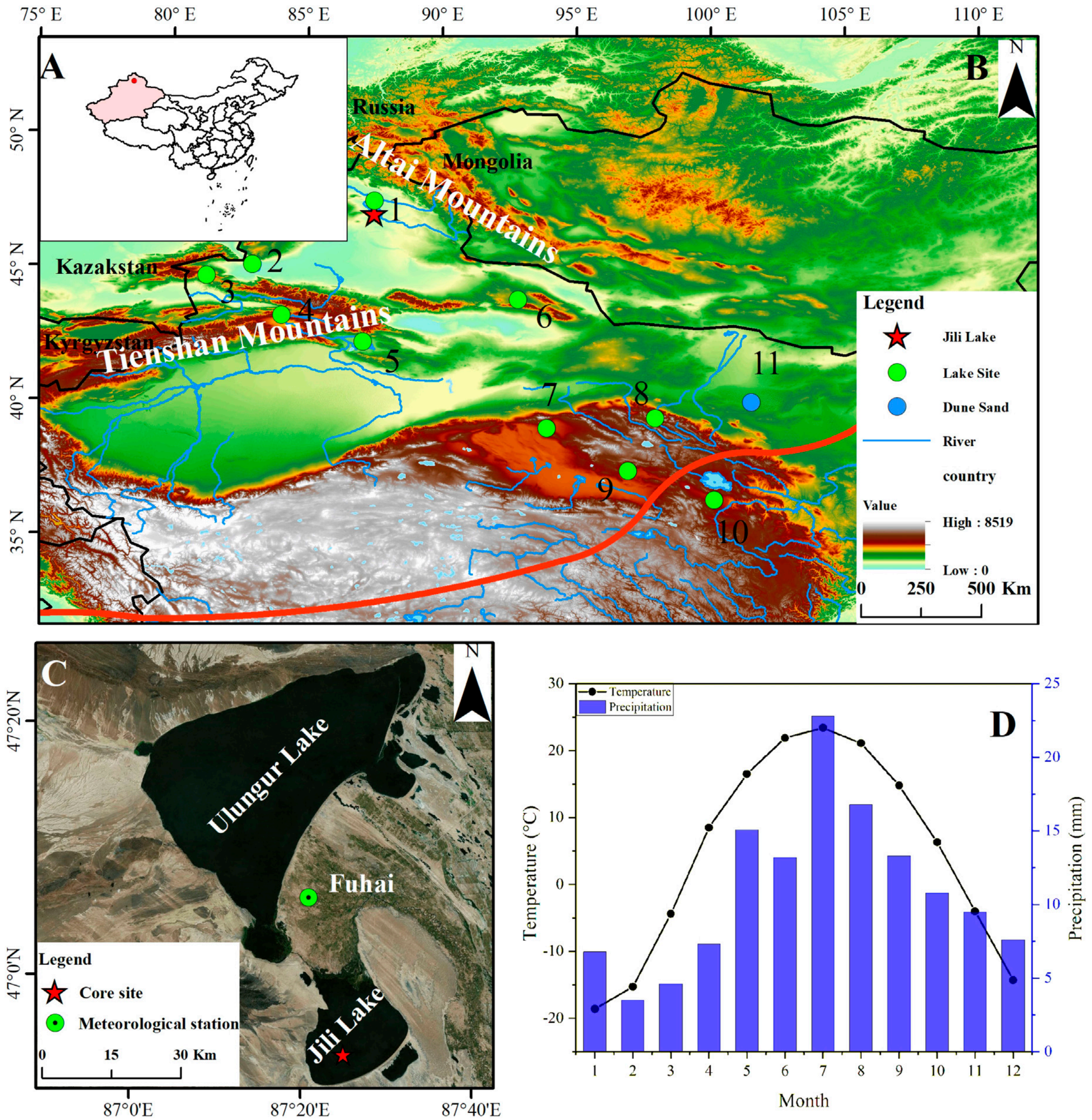

FIGURE 1 | Environmental setting of Jili Lake. **(A)** The study area; **(B)** Location of Jili Lake and other lake sites mentioned in this study: 1 Ulungur Lake; 2 Ebinur Lake; 3 Sayram Lake; 4 Harnur Lake; 5 Bosten Lake; 6 Balikun Lake; 7 Sugan Lake; 8 Tian'E Lake; 9 Hurleg Lake; 10 Genggahai Lake; and 11 BYBS profile. The orange line is the modern limit of the Summer Monsoon (Chen et al., 2008). **(C)** Google Earth image of Jili Lake and Ulungur Lake area, and **(D)** Monthly temperature and precipitation from Fuhai meteorological station (elevation 500 m a.s.l.) for the years 1981–2010 CE.

impact of climate change on regional human activities, with evidence that climate change plays an important role in the abandonment of cities (e.g., Bhattacharya et al., 2015; An et al., 2017; Yao Y.-F. et al., 2020; Jenny et al., 2020). In the Xinjiang area, early cultivation of crops began around 3000 BCE (Li Y., 2020), and an increase in population started at c. 2000 BCE. There is evidence for a widespread prehistoric culture in Xinjiang area, associated with a relatively wetter climate during the late Holocene (An et al., 2019). However, abrupt climate and environment changes might have led to the collapse of some civilizations, such as Xiaohe Culture (Zhang et al., 2017) and Loulan civilization (Fontana et al., 2019; Hao et al., 2019). A diatom record from Bosten Lake indicated that changes in hydro-climate was the main reason for the collapse of the Loulan Kingdom (Fontana et al., 2019). The record of RIK_{37} index from Sayram Lake suggested that humid conditions might have been conducive to the spread of the Mongol Empire across the ACA area during 1206–1260 CE (Yao Y.

et al., 2020). Pollen records from Tian'E Lake in the Qilian Mountains suggested that continuous droughts were an important driving force of the abandonment of several archaeological sites and ancient cities along the Silk Road (Zhang J. et al., 2018). However, there are few humid records from the Northern Xinjiang area that span the last 2,000 years, which can be used to understand the relationship between human activities and climate change.

Lake sediments are an excellent archive of past climate change (Birks et al., 2012), and pollen analysis from lacustrine sediments can help to understand the regional climatic changes through time (Bartlein et al., 1986; Wen et al., 2010). Changes in the relative abundance of fossil pollen preserved in lake sediment archives reflect changes in vegetation in response to various driving force (e.g., precipitation, temperature, human impact), and pollen assemblages from lakes with a larger catchment reflect regional, not just local, changes in climate and vegetation (Sugita, 1994; Nielsen and Sugita, 2005; Xu et al., 2016). Here, we present the results of pollen analysis from Jili Lake (174.0 km^2) located in the northern Xinjiang area to infer the history of climate and vegetation change over the last c. 2400 years. By combining these data with other evidence, for example, charcoal and historical documents (e.g., regional population and cultivation history), we explore the relationship between environment and human activities in this study area.

STUDY AREA

Jili lake (46°51′–47°00′ N, 87°20′–87°32′ E, 483 m a.s.l.) is a large and shallow lake in the inland area of the Eurasian continent, located in the Junggar Basin between the Tianshan Mountains and the Altai Mountains (**Figures 1A**, **B**). The study area sits within a mid-latitude temperate continental climate. As recorded at the nearby Fuhai meteorological station (47°06′ N, 87°21′ E, **Figure 1C**), the mean annual temperature in the region is 4.7°C and the average annual precipitation is 131 mm (**Figure 1D**). Jili Lake receives water mainly from the Ulungur River from the Altai Mountains to the north, and it outflows to Ulungur Lake (**Figures 1B,C**). In 2015, the lake covered a surface area of c. 170 km^2, and had an average depth of c. 10 m (Wang and Dou, 1998; Liu et al., 2018).

In recent decades the surface area of Jili Lake has expanded, and its main water supply comes from the Ulungur river; the water level in Jili Lake has been affected by dam construction and intensified water exploitation (Li et al., 2015; Cheng et al., 2016). Desert vegetation in the vicinity of Jili Lake comprises mostly Amaranthaceae, but the northern part of the catchment mainly has many shrub-coppice covered dunes. The Gobi Desert area lies to the west, and a shrub-coppice dune chain to the south (Lang, 2020). In the Jili Lake area, Amaranthaceae and *Artemisia* accounted for more than 60% of the surface pollen sum, except for *Ephedra*, *Tamarix*, *Jujube*, *Nitraria*, Poaceae and *Allium* (Yan and Xu, 1989). The aquatic plants mainly consist of *Phragmites*, *Myriophyllum spicatum* and *Potamogeton pectinatus*, which are distributed in shallow water areas along the lake shore (Wang et al., 1981; Wang and Dou, 1998).

MATERIALS AND METHODS

Core Sampling and Age-Depth Model

In February 2018 a sediment core, 253 cm in length (JL18-02-A), was collected from the southwestern area of Jili Lake using a Piston corer. The core was frozen and transported to Lanzhou University, sampled at a 1-cm intervals, and freeze-dried. The lithology of the c. 120 cm of the core can be divided into three intervals: 0–6 cm - cyan mud with loose sediments; 6–34 cm - the color of sediments is brown; 34–123 cm - pale silty clay with relatively compact sediments.

We focused on the upper 120 cm of the core because there was a hiatus in the sediment below this depth based on 7 radiocarbon dates (Lang, 2020). For the age-depth model of the upper 120 cm, three bulk organic samples from the core were processed for accelerator mass spectrometry (AMS) radiocarbon dating at the Beta Analytic Radiocarbon Dating Laboratory in Miami, Florida, United States (**Table 1**) (Lang, 2020). The ^{14}C specific activity values of the lake-water DIC sample and the samples from the upper most layers of cores largely approximate to the pMC (percent modern carbon) values of the modern atmosphere (105.4 ± 1.0 pMC in 2007; Fellner and Rechberger, 2009), indicating that the CO_2 exchange between the lake and atmosphere tends to be balanced, reflecting that the "reservoir effect" of the lake water is low. The age-depth model for Jili Lake (**Figure 2**) was calculated using "Clam" version 2.2 (Blaauw, 2010) and the IntCal13 calibration curve (Reimer et al., 2013). The core depth-chronology has a linear relationship and it provides a record of sediment deposition over the last 2400 years.

Pollen and Charcoal Analyses

A total of 96 samples were taken from the core for pollen analysis. Pollen grains were extracted from 1–3 g of dried sample, and preparation used HCl (10%) and HF (40%) to remove carbonates and silicates (Fægri and Iversen, 1989). Samples were sieved through a 10-μm mesh to remove small clay-sized particles, and clean samples were mounted in glycerin on glass slides. Pollen grains and charcoal particles were identified and counted using a Nikon ECLIPSE 80i optical microscope at ×400 magnification. More than 500 pollen grains and 300 charcoal particles were counted for each sample, and charcoal particles were grouped by long axis length: >100, 50–100, and <50 μm. To calculate pollen and charcoal concentration, one *Lycopodium* tablet (27,637 grains) was added to each sample prior to chemical pre-treatment (Maher, 1981). The percentages of pollen were calculated based on the sum of all counted terrestrial pollen grains, and the aquatic pollen percentages were calculated based on the sum of all counted pollen grains. The pollen diagrams were plotted using Tilia software (Grimm, 2011), and the pollen zones were divided by stratigraphically constrained cluster analysis using CONISS (Grimm, 1987).

TABLE 1 | Results of AMC ^{14}C dating of core JL18-02-A.

Samples No.	Beta No.	Depth (cm)	Material	δ^{13}C (‰)	^{14}C age (yr BP)	Calendar age (cal. yr BP, 2σ)
JL18-02A1-001	503015	1.24	BOM	−27.7	101.63 ± 0.38 pMC	-
JL18-02A1-048	503016	59.43	BOM	−24.2	1050 ± 30 BP	1050–924
JL18-02A1-096	515954	118.86	BOM	−25.3	2350 ± 30 BP	2464–2324
JL18-07 (20 cm)	509850	—	DIC	—	93.5 ± 0.30 pMC	-

Note: BOM, Bulk organic matter; DIC, Dissolved inorganic carbon.

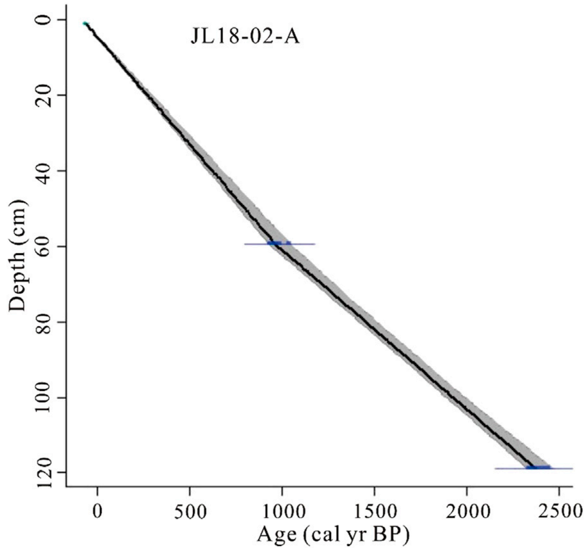

FIGURE 2 | Clam age-depth model for core JL18-02-A from Jili Lake.

Indicators of Climatic Humidity and Human Activities

Based on the investigations of modern surface pollen in northern Xinjiang, it has shown that *Artemisia* and Amaranthaceae (old name is Chenopodiaceae) (APG, 1998), are dominant species in desert-steppe and desert areas (Yu et al., 1998; Luo et al., 2009; Li et al., 2017). A lot of modern pollen investigations have shown that the *Artemisia* and Chenopodiaceae ratio (A/C ratio) is a valid indicator/proxy of humidity in desert and desert-steppe areas (e.g., El-Moslimany, 1990; Sun et al., 1994; Huang et al., 2009; Zhao et al., 2009; Li et al., 2010; Zhao et al., 2012; Zhang D. et al., 2018). As *Ephedra* is also one of the main taxa in desert areas like Amaranthaceae (Huang et al., 2009; Huang et al., 2018), here we use the sum of Amaranthaceae and *Ephedra* (Am + E) to indicate a relatively dry condition, and use the ratio of *Artemisia* (Ar) and (Am + E) as a new indicator of climatic humidity like A/C ratio.

The signal of regional human activity can be indicated by some specific pollen types and charcoal abundance. For example, Poaceae pollen grains among the 35–50 μm size range were considered to be cereal-type Poaceae (mostly might be wheat pollen), which can be used as an indicator of agricultural activity (Li et al., 2008; Li et al., 2012). Charcoal is a particularly useful proxy for recording the disturbance of vegetation by humans, in which macro-charcoal (>100 μm) could indicate changes in local fire occurrence in the past (Whitlock and Larsen, 2001; Li et al., 2008).

RESULTS

A total of 62 pollen taxa and spore types were identified and 53477 pollen grains were counted, with an average of 557 pollen grains per sample. The main herbaceous taxa were *Artemisia*, Amaranthaceae, Poaceae and Asteraceae. Across the three zones as identified by CONISS, the percentages of *Artemisia* and Amaranthaceae exceeded 80% of the terrestrial pollen sum. The arboreal taxa with lower percentages were mainly *Betula* and *Pinus*. The percentage abundance of fern spores was very low, and aquatic pollen types were mainly *Sparganium* and *Typha*. The assemblage characteristics of each pollen zone are briefly described as follows (**Figure 3**).

Zone Ⅰ (119–87 cm, c. 380 BCE-400 CE)

The major pollen types included Asteraceae (0.2–3.6%, mean 2.3%), *Ephedra* (0.6–3.09%, mean 2%), Polygonaceae (0.2–3.6%, mean 2.74%), Rosaceae (1.0–5.8%, mean 2.1%), and *Typha* (1.0–2.8%, mean 1.60%). The sum of tree pollen types is c. 5.1% and including *Pinus*, *Picea*, *Betula* and *Salix*. The abundance of Poaceae (0.3–2.5%, mean 1.4%) and Cyperaceae (0–0.9%, mean 0.3%) was low, and the Ar/(Am + E) ratio (0.2–0.7, mean 0.4) had the lowest value in the whole core sequence. Overall, this zone had the lowest pollen concentration (c. 18873 grains/g). The pollen assemblages in this zone, can be further divided into two sub-zones. Sub-zone Ⅰ-1 (119–106 cm, c. 380–70 BCE) can be readily distinguished from sub-zone Ⅰ-2 (106–87 cm, c. 70 BCE-400 CE) by the decreasing percentage of Poaceae pollen.

Zone Ⅱ (87–40 cm, c. 400–1350 CE)

This zone was typified by an increase in Poaceae (0.5–13.2%, mean 6.5%) and Cyperaceae (0.2–1.5%, mean 0.8%) at the expense of *Artemisia* (mean 34%), Asteraceae (0.5–2.6%, mean 1.4%), and Rosaceae (0–2.4%, mean 0.5%) whose percentages decreased. This zone also sees the first appearance of cereal-type Poaceae (0–0.6%, mean 0.3%).

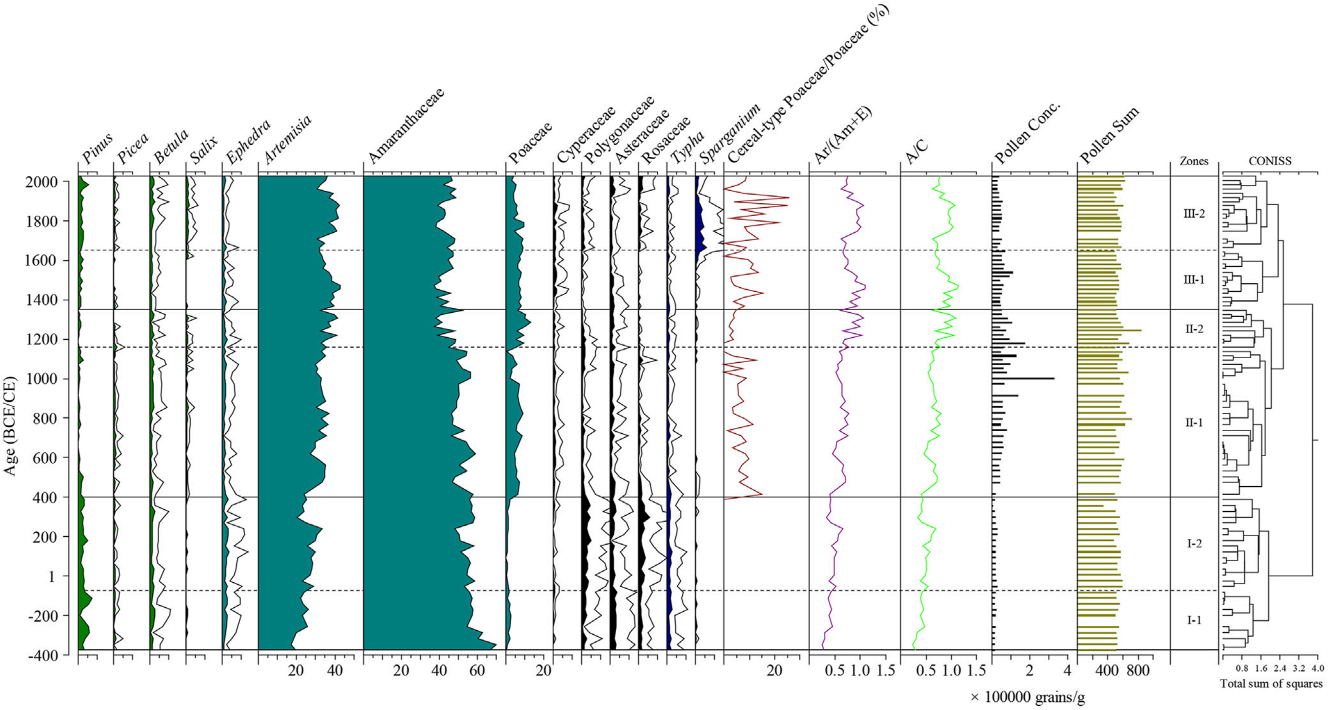

FIGURE 3 | Pollen percentage diagram for core JL18-02-A spanning the last 2400 years.

This zone can be further divided into two sub-zones. Sub-zone II-2 (52–40 cm, c. 1160–1350 CE) can be readily distinguished from Sub-zone II-1 (86–52 cm, c. 400–1160 CE) by the following features: further increases in *Artemisia* (32.6–41.7%, mean 36.8%), Poaceae (5.6–13.2%, mean 9%) percentages and Ar/(Am + E) ratio (0.6–1.1, mean 0.8) and the presence of cereal-type Poaceae/Poaceae, Amaranthaceae (37.3–52.3%, mean 43%), and a decrease in pollen concentration (now with a mean 82166 grains/g).

Zone III (40–0 cm, c. 1350 CE to Present)

There were no obvious changes in the percentage of Poaceae pollen (3.1–9.8%, mean 6.7%) but there was a higher abundance of Cyperaceae pollen (0.4–2.2%, mean 1.1%) compared to the previous zone. In Zone III, there was an obvious increase in aquatic pollen (*Typha* and *Sporangium*) percentages (0.4–6.5%, mean 2.3%), tree pollen percentages (0.8–9.6%, mean 3.9%) and Cereal-type Poaceae/Poaceae (0–33.3%, mean 10.6%). The Ar/(Am + E) ratio was relatively higher (0.6–1.1, mean 0.8), but was interrupted by a brief period (c. 1550–1700 CE) with lower values (0.7–0.8, mean 0.7).

Sub-zone III-2 (23–0 cm, c. 1650 CE to present) is distinguished from sub-zone III-1 (40–23 cm, c. 1350–1650 CE) by an apparent increase in *Artemisia* (30.7–42.3%, mean 32.3%), *Salix* (0.2–2.7%, mean 0.9%), *Sparganium* (1.8–6.5%, mean 2.6%), Rosaceae (0–2.3%, mean 1.0%), and Cereal-type Poaceae/Poaceae (0–33.3%, mean 12.1%) and a slight decrease in Poaceae (3.1–9.8%, mean 6.1%).

DISCUSSION

Pollen Source Area and a Test of Pollen Humidity Indicator of Jili Lake

The size of pollen source area depends on the size of the depositional basin, characteristics of pollen types and spatial distribution of the plant species (Jackson, 1990; Sugita, 1994). Sugita (1994) suggests that pollen assemblages of sedimentary basins with a radius larger than 750 m is mainly influenced by regional pollen rather than local pollen, and hence we considered the pollen assemblages in Jili Lake (~174 km^2) can reflect regional vegetation variations. Because of strong aeolian activity in Northern Xinjiang, we suggested pollen assemblages are a mixed signal to the regional vegetation in the basin. As modern vegetation types show there are less forest around Jili Lake except some specific planted poplar trees to protect farmlands (Xinjiang Comprehensive Investigation Team, Chinese Academy of Sciences, 1978), the tree pollen types in the lake could have been transported by wind and/or river from the southern slopes of the Altai Mountains.

The *Sparganium* is adapted to growing in wet conditions, and the high content of *Sparganium* might indicate a low lake level (Davis, 1999). The aquatic plants in JL18-02-A core from Jili Lake were mainly *Typha* and *Sparganium*, both of which are emergent plants. A previous study showed the higher content of aquatic pollen and lower total pollen concentration may indicate a shallower lake environment (Huang et al., 2010).

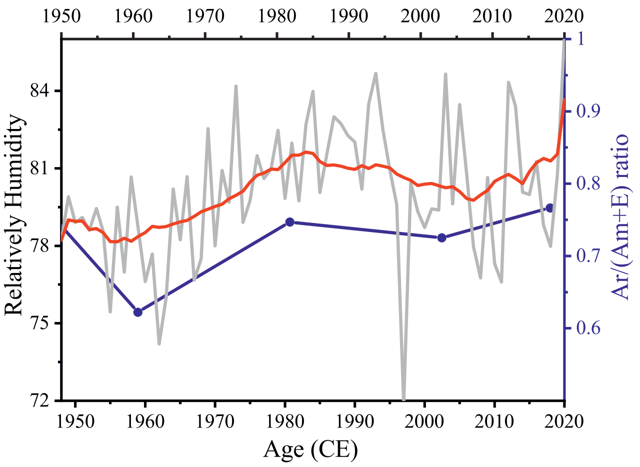

FIGURE 4 | Comparison of Ar/(Am + E) for the core JL18-02-A with various Relative Humidity records from the Fuhai station (data from https://psl.noaa.gov/data/index.html): grey line: relative humidity; red line: relative humidity result of 25-point smoothing; blue dot line: Ar/(Am + E) ratio.

To verify the reliability of Ar/(Am + E) ratio as an indicator of climatic humidity, we compared it to the relative humidity records from meteorological stations (**Figure 4**). It was demonstrated that the Ar/(Am + E) ratio fluctuations of JL18-02-A generally follow the relative humidity records from the Fuhai station, both showing an increasing trend in humidity during the 1950–2018 CE (**Figure 4**).Therefore, the Ar/(Am + E) ratio was a reliable indicator of humidity in this region, which is similar to A/C ratio used by many other previous studies (e.g., Huang et al., 2009; Zhang J. et al., 2018).

Comparison of Regional Moisture Changes in the Late Holocene

The moisture variations inferred from the Ar/(Am + E) ratio from Jili Lake (**Figure 5A**) over the last 2400 years is consistent with other regional records (e.g., Sayram Lake (**Figure 5C**) and Ebinur Lake (**Figure 5D**), and suggested that an increase in regional moisture, which is consistent with an increase in the average moisture index of Xinjiang towards the present (Wang et al., 2013). The nearby Lake Ulungur (**Figure 5B**) also showed an increase in moisture prior to 1450 CE, but then decreased sharply (Liu et al., 2008).

From 400 BCE-400 CE, there is lower water level and lower effective moisture recorded in Jili Lake, which is also seen in other records. For instance, climate conditions were drier at Sayram Lake (**Figure 5C**) and Ebinur Lake (**Figure 5D**) during this period (as interpreted from a low A/C ratio). This period of drying is coincident with strong solar activity (**Figure 5J**), and the known warming associated with the Roman Warm Period (RWP, 0–400 CE) (Biintgen et al., 2011). In low-elevation areas in northern Xinjiang, there are many sites that suggest a dry climate during the RWP (Feng et al., 2017). In the Aral Sea area, there was a period of low lake level from 1 CE to 425 CE (Sorrel et al., 2006), and at Bosten Lake, a period of high salinity and lower lake level occurred from 280 to 480 CE (Fontana et al., 2019; Li et al., 2021). Historical documents show that in the 4th Century, the city of the Loulan Kingdom experienced a severe drought (Li et al., 1991), which might also have been recorded in Jili Lake, as indicated by a lower pollen humidity index (PHI) at 300–400 CE. The results of lithological and grain-size analyses from Jili Lake suggest the lake was shallower before 400 CE, hence the hydrodynamics caused by wave action on the lake was relatively strong (Lang, 2020). We interpret the low pollen concentration as evidence of strong hydrodynamics and/or drier conditions. There are also differences in the records of humidity at different altitudes in the Xinjiang region. From 400 BCE to 400 CE, a decrease in moisture occurred in high altitude areas [e.g., Tielishahan Peat (Zhang et al., 2016) and Narenxia Peat (Zhang D. et al., 2018), Yushenkule Peat (Yang et al., 2019), and Sayram Lake (Lan et al., 2020)], while a slight increase in moisture occurred in low altitude areas [e.g., Jili Lake (**Figure 5A**), Ulungur Lake (**Figure 5B**) and Ebinur Lake (**Figure 5D**)]. In addition, during this period moisture records from Bosten Lake in the southern Tienshan Mountains (**Figure 5H**; Huang et al., 2009) showed a slight decreasing in moisture during this period, which is inconsistent with low latitude lakes in northern Xinjiang.

From 400 CE to 850 CE [Dark Ages Cold Period (DACP)], the PHI indicates an increase in regional moisture, overlain by fluctuations in wet and dry phases at a centennial scale. The water level in Jili Lake began to increase, likely reaching its present-day level after c. 400 CE (Lang, 2020). Similarly, the moisture record from Ebinur Lake (**Figure 5D**) shows an increase in regional moisture, and pollen records from Kanas Lake suggests an increase in effective humidity from 550–1050 CE (Huang et al., 2018).

During the MWP (850–1200 CE), the climate was warm and dry. Although warm climatic conditions prevailed in the Northern Hemisphere (**Figures 5I, J**), the PHI suggests relatively dry conditions in the Jili Lake region. These drier conditions may be related to a period of higher evaporation at Bosten Lake, and also coincided with a glacial retreat event recorded at Karakuli Lake (Liu et al., 2014). During this period, there is a higher content of coarse grain sizes (40–200 μm) from Jili Lake suggests an intensification of storm activity at Jili Lake (Lang, 2020). Likewise, the increased coarse fraction in the record from Harnur Lake (**Figure 5E**) and decreased A/C ratios at Ebinur Lake (**Figure 5D**) corroborate this interpretation.

During the Little Ice Age (LIA: 1200–1850 CE), there was an increase in moisture from 1200 CE (**Figure 5A**), consistent with the A/C ratios of Sayram Lake (**Figure 5C**), Ebinur Lake (**Figure 5D**) and Harnur Lake (**Figure 5E**). Cold climate also recorded in Manas Lake (Song et al., 2015) and Bosten Lake (**Figure 5G**) during this period. This period is not characterized by uniform wet conditions. For example, the period 1560–1700 CE was relatively dry with a lower PHI, though the regional climate was still wetter than the period prior to 1200 CE (**Figure 5A**). At Jili Lake the abundance of aquatic pollen (*Typha* and *Sparganium*) peaked at 1665 CE, with a brief interval of lower water level at 1600–1855 CE. Other regional records also attest to relatively dry conditions during 1560–1700 CE: Sichanghu peatland, Hutubi River Basin, Manas Lake, Kesang Cave and Dalong Pond (Chen F. et al., 2015; Song et al., 2015; Cai et al., 2017; Lan et al., 2019; Ren et al., 2019). At Bosten Lake, the

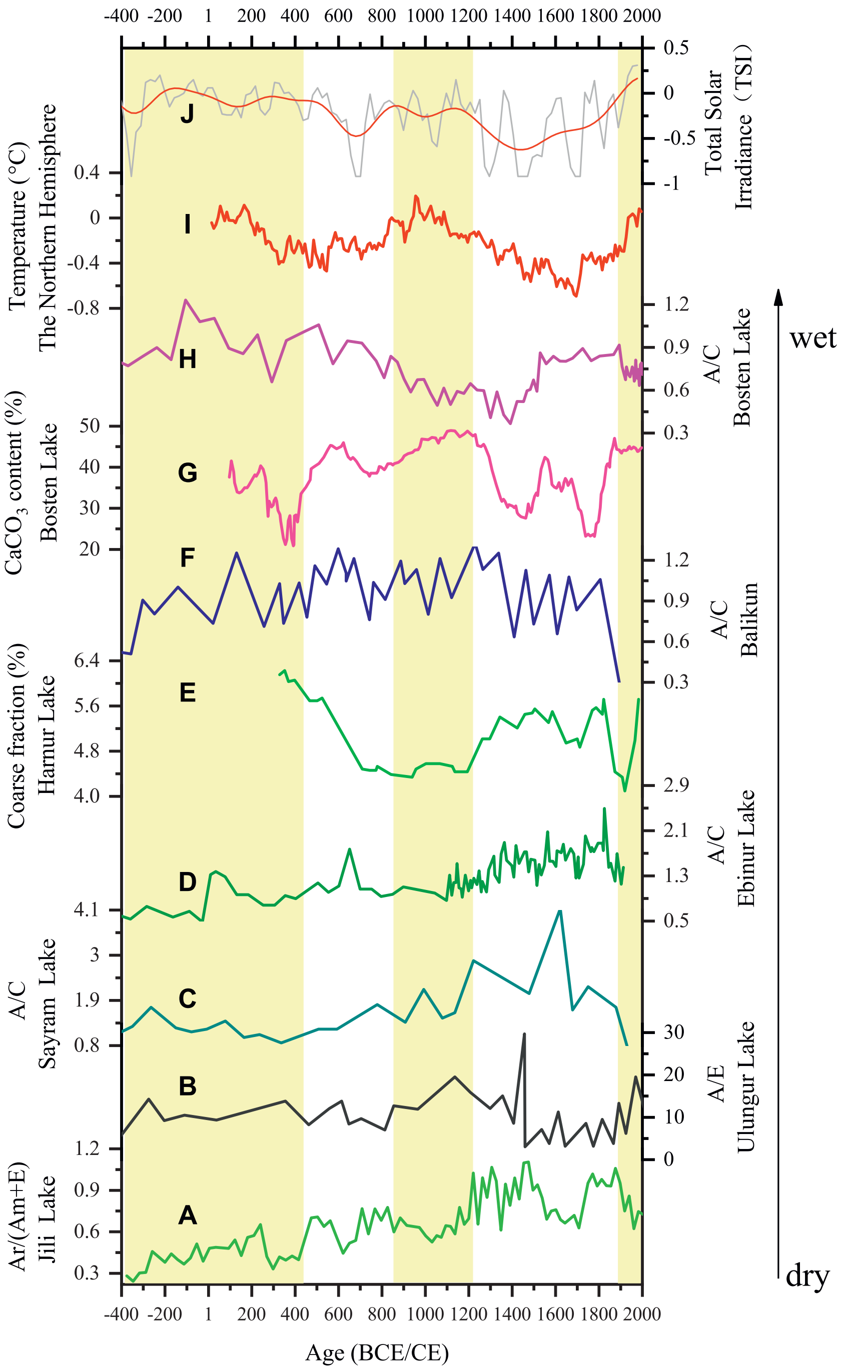

FIGURE 5 | Comparison of Ar/(Am + E) for the core JL18-02-A with various paleoclimatic records: **(A)** Ar/(Am + E) ratio from Jili Lake (this study); **(B)** A/E ratio from Ulungur Lake (Liu et al., 2008); **(C)** A/C ratio from Sayram Lake (Jiang et al., 2013); **(D)** A/C ratio from Ebinur Lake (Wang et al., 2013); **(E)** Coarse fraction from Harnur Lake (Lan et al., 2018); **(F)** A/C ratio from Balikun Lake (Tao et al., 2010); **(G)** $CaCO_3$ content from Bosten Lake (Fontana et al., 2019); **(H)** A/C ratio from Bosten Lake (Huang et al., 2009); **(I)** Temperature in the Northern Hemisphere (Ljungqvist, 2016); **(J)** Reconstructed Total Solar Irradiance (TSI) (Steinhilber et al., 2012).

carbonate content (**Figure 5G**) suggests an interval of high evaporation during 1550–1700 CE; higher temperatures are recorded at the same times [e.g., at Manas Lake (Song et al., 2015) and Belukha glacier (Eichler et al., 2011)], suggesting that temperature was the main driving force of decreased moisture during this period. After 1850 CE, the PHI derived from the Jili Lake record suggests a drier climate, which is consistent with the records of other lakes in northern Xinjiang (Huang et al., 2009; Feng et al., 2016; Li et al., 2017; Yang et al., 2019; Yang et al., 2020).

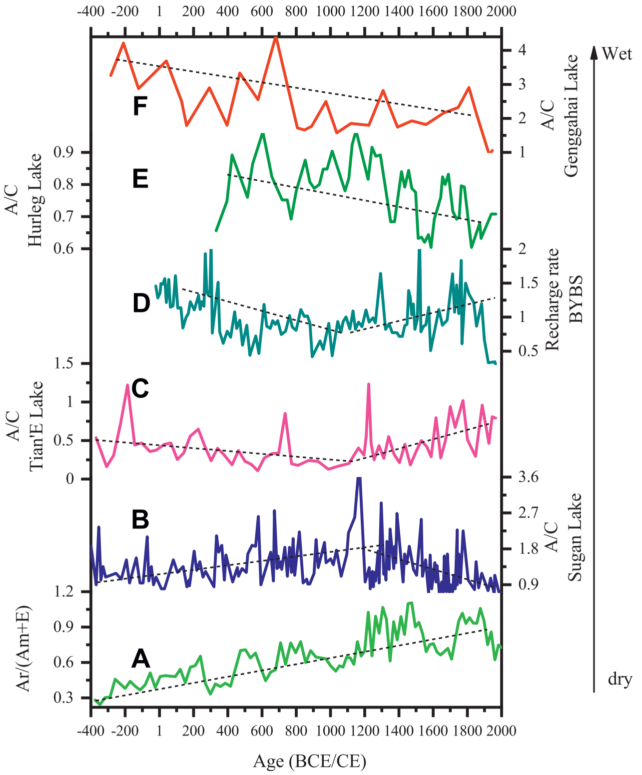

FIGURE 6 | Comparison of Ar/(Am + E) ratio for the core JL18-02-A with various paleoclimatic records in the monsoon marginal region: **(A)** Ar/(Am + E) ratio from Jili Lake (this study); **(B)** A/C ratio from Sugan Lake (Li, 2020); **(C)** A/C ratio from Tian'E Lake (Zhang J. et al, 2018); **(D)** Recharge rate from BYBS profile (Ma et al., 2009); **(E)** A/C ratio from Hurleg Lake (Zhao et al., 2010); **(F)** A/C ratio from Genggahai Lake (Liu et al., 2016).

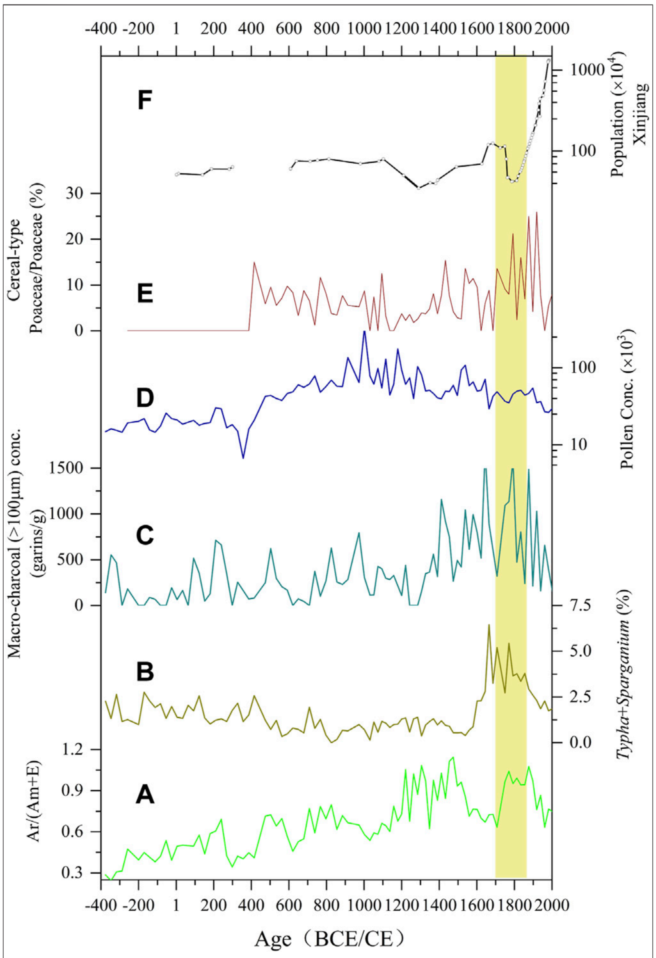

FIGURE 7 | Comparison of Ar/(Am + E) ratio for the core JL18-02-A with population in Xinjiang: **(A)** Ar/(Am + E) ratio from Jili Lake (this study); **(B)** The percentage of *Typha* and *Sparganium* from Jili Lake (this study); **(C)** Macro-charcoal (>100 μm) concentration from Jili Lake (this study); **(D)** Pollen concentration form Jili Lake (this study, Y-axis is a log scale); **(E)** Cereal-type Poaceae/Poaceae (Ce/Po) from Jili Lake (this study); **(F)** Population in Xinjiang, Y-axis is a log scale (Zhao and Xie, 1988). The orange area indicates a population growth period.

Previous studies from northern Xinjiang showed that the region alternated between "cold-wet" and "warm-dry" during the late Holocene (Feng et al., 2006). Combining the Northern Hemisphere temperature (**Figure 5I**) with the PHI derived from the Jili Lake record, there is support for the climate model of "warm-dry" and "cold-wet" (Chen et al., 2019), overlain by a millennial timescale wetting trend from 1 CE to 1550 CE.

By comparison of regional moisture changes with records in monsoon marginal region (**Figure 6**), it was found that there was an increasing trend in moisture at Jili Lake (**Figure 6A**) during 400 BCE-2000 CE, which is in contrast to records from Hurleg Lake (**Figure 6E**) and Genggahai Lake (**Figure 6F**). The reason for these differences may be the climate of Hurleg Lake and Genggahai Lake being mainly driven by the Asia Summer Monsoon (Liu et al., 2016; Zhao et al., 2010). Records from Tian'E Lake (in the Qilian Mountains) and BYBS profile (in the western part of the Badain Jaran Desert) show a decrease in moisture during 400 BCE-1100 CE and an increase in moisture from 1100 BCE to 1800 CE, which was in antiphase to the moisture record at Sugan Lake (**Figures 6B–D**). An increase in moisture during 1100–1800 CE at Tian'E Lake and BYBS profile may be due to the weakening of the Asian Summer Monsoon caused by the reducing solar radiation (Steinhilber et al., 2012; Gao et al., 2020). In general, a wetting record from Jili Lake over 2400 years (**Figure 6A**) is obviously different from that in the monsoon marginal region.

The water vapor in ACA originates from the North Atlantic Ocean, the Mediterranean Sea, Caspian Sea, and regional water recycling within inland Asia, and is transported from west to east by the westerlies (Aizen et al., 2006; Chen et al., 2008). The southward shift of the westerly jet stream facilitates the infiltration of water vapor from the Indian Ocean to ACA and leads to more rainfall over northern Xinjiang (Yang and Zhang., 2008; Zhao et al., 2014). Solar activity plays an important role in atmospheric circulation (Reid, 1991; Steinhilber et al., 2012). Yan et al. (2019) suggesting that changes in solar activity and the intensity and location of the westerly jet stream are the dominant control on hydroclimatic variations in ACA. The stronger westerly and the southern migration of the westerly jet stream, which corresponds to lower total solar irradiance (TSI) and colder conditions, could favor more water vapor transport to ACA, and vice versa (Yan et al., 2019). During 400 BCE-400 CE and the MWP, the Jili Lake region had a warm-dry climate when the solar activity was higher (**Figures 5A, J**). During the LIA, there was a period of higher evaporation (1560–1700 CE) and an associated low moisture index.

Human Activity in the Region and Its Impact on the Lake Level of Jili Lake

Since 1700 CE, there were higher concentrations of macro-charcoal (>100 μm) (**Figure 7C**), accompanied by an increase in the Ce/Po ratio (**Figure 7E**). These indicators suggest that a period of intensified human activity played an important role in influencing the vegetation in the region, and this can be matched with local and state historical documents. The population of Xinjiang gradually increased during 1626–1760 CE (**Figure 7F**). Irrigation for agriculture in northern Xinjiang began in the early Qing Dynasty (from 1716 CE) (Zhao and Xie, 1988) with a rapid phase of development during 1749–1840 CE (Fang, 1989). After 1755 CE, there was an upsurge in urban construction in northern Xinjiang, driven by political, economic and military factors, as well as expended cultivation and trade development (Yang, 2018). Likewise, during the 1600–1850 CE, Jili Lake had a lower lake level as indicated by the higher percentage of aquatic pollen (*Typha* and *Sparganium*) (**Figure 7B**) and the lower pollen concentration (**Figure 7D**). Notably, the PHI derived from the Jili Lake sediments was relatively higher during 1700–1850 CE and indicated relatively wet conditions (**Figure 7A**), which is in contrast to the lower lake level. Therefore, the wetter climate during 1700–1850 can't explain the lower lake level and we infer that the lower water level in Jili Lake during 1600–1850 CE may have been caused by human activities or the more extensive exploitation of water resources. Similarly, the decline of water level in Ulungur Lake was likely caused by the greatly increased regional population and the associated development of oasis irrigation agriculture along the rivers in the lower basin during the Ming and Qing Dynasties (Liu et al., 2008; Tuerhong, 2011; Ni et al., 2021). Consequently, lower lake level may be mainly influenced by stronger irrigation agricultural activities during 1700–1850 CE.

CONCLUSION

The high-resolution pollen record from core JL18-02-A reveals the evolution of vegetation in Jili Lake and its surrounding area over the last 2400 years in response to climate drivers and human impact. The comparison of moisture availability, as inferred by the Ar/(Am + E) ratios to other regional records suggest that the moisture in the northern Xinjiang region study area shows an increase of humidity from 1 CE to 1550 CE, corresponding to a long-term cooling in the Northern Hemisphere. Pollen assemblages indicated that regional vegetation dominated by desert gradually shifted into a desert steppe. The moisture was characterized by the "warm-dry" periods of RWP (c. 1 to c. 400 CE), MWP (c. 850 to c. 1200 CE) and CWP (since 1850 CE), and the "cold-wet" periods of DACP (c. 400 to c. 850 CE) and LIA (c. 1200 to c. 1850 CE). Over the last 2400 years, the monsoon had little influence on moisture changes in the Jili Lake basin. Notably, during 1700–1850 CE, the increase of the percentages in aquatic pollen (*Typha* and *Sparganium*) and cereal-type Poaceae pollen reflecting anthropogonic impacts, and the rise of macro-charcoal and population may result from the intensified irrigation for agriculture in the catchment.

DATA AVAILABILITY STATEMENT

The raw data supporting the conclusions of this article will be made available by the authors, without undue reservation.

AUTHOR CONTRIBUTIONS

XH conceived this study. YX and LX identified the pollen. YX, LX, and XH wrote and revised the manuscript. KM, JZ, YL, and XC discussed the data. KM improved the language.

FUNDING

This study was funded by the National Key Research and Development Program of China (Grant No. 2017YFA0603403), Sub-project "Climatic and environmental evolution in the QTP for the past 40,000 years" (Project No. XDA2009000003) and National Natural Science Foundation of China (award 41991251).

ACKNOWLEDGMENTS

We thank Prof. Mingrui Qiang from South China Normal University for coring the samples. We gratefully acknowledge the editor Prof. Zhuolun Li, and the two reviewers Prof. Chun Mei Ma and Prof. John Dodson for extensive comments and helpful revisions.

REFERENCES

Aizen, V. B., Aizen, E. M., Joswiak, D. R., Fujita, K., Takeuchi, N., and Nikitin, S. A. (2006). Climatic and Atmospheric Circulation Pattern Variability from Ice-Core Isotope/geochemistry Records (Altai, Tien Shan and Tibet). *Ann. Glaciol.* 43, 49–60. doi:10.3189/172756406781812078

An, C., Wang, W., Duan, F., Haung, W., and Chen, F. (2017). Environmental Changes and Cultural Exchange between East and West along the Silk Road in Arid Central Asia (In Chinese). *Acta Geogr. Sin.* 72, 875–891. doi:10.11821/dlxb201705009

An, C., Zhang, M., Wang, W., Liu, Y., Duan, F., and Dong, W. (2019). The Pattern of Xinjiang Physical Geography and its Relationship with the Temporal-Spatial Distribution of Agriculture and Husbandry (in Chinese). *Sci. Sin.-Terrae* 50, 295–304. doi:10.1360/SSTe-2019-0050

APG (1998). An Ordinal Classification for the Families of Flowering Plants. *Ann. Mo. Bot. Gard.* 85, 531–553. doi:10.2307/2844848

Bartlein, P. J., Prentice, I. C., and Webb, T. (1986). Climatic Response Surfaces from Pollen Data for Some Eastern North American Taxa. *J. Biogeogr.* 13, 35–37. doi:10.2307/2844848

Bhattacharya, T., Byrne, R., Böhnel, H., Wogau, K., Kienel, U., Ingram, B. L., et al. (2015). Cultural Implications of Late Holocene Climate Change in the Cuenca Oriental, Mexico. *Proc. Natl. Acad. Sci. USA* 112, 1693–1698. doi:10.1073/pnas.1405653112

Buntgen, U., Tegel, W., Nicolussi, K., Mccormick, M., Frank, D., Trouet, V., et al. (2011). 2500 Years of European Climate Variability and Human Susceptibility. *Science* 331, 578–582. doi:10.1126/science.1197175

Birks, H. J. B., Lotter, A. e. F., and Smol, S. J. J. P. (2012). *Tracking Environmental Change Using Lake Sediments: Data Handling and Numerical Techniques*. Dordrecht: Springer. doi:10.1111/j.1365-2427.2004.01211.x

Blaauw, M. (2010). Methods and Code for 'classical' Age-Modelling of Radiocarbon Sequences. *Quat. Geochronol.* 5 (5), 512–518. doi:10.1016/j.quageo.2010.01.002

Cai, Y., Chiang, J. C. H., Breitenbach, S. F. M., Tan, L., Cheng, H., Edwards, R. L., et al. (2017). Holocene Moisture Changes in Western China, Central Asia, Inferred from Stalagmites. *Quat. Sci. Rev.* 158, 15–28. doi:10.1016/j.quascirev.2016.12.014

Chen, F., Yu, Z., Yang, M., Ito, E., Wang, S., Madsen, D. B., et al. (2008). Holocene Moisture Evolution in Arid central Asia and its Out-of-phase Relationship with Asian Monsoon History. *Quat. Sci. Rev.* 27, 351–364. doi:10.1016/j.quascirev.2007.10.017

Chen, F., Yuan, Y.-j., Wei, W.-s., Yu, S.-l., Zhang, T.-w., Shang, H.-m., et al. (2015a). Tree-ring Recorded Hydroclimatic Change in Tienshan Mountains during the Past 500 Years. *Quat. Int.* 358, 35–41. doi:10.1016/j.quaint.2014.09.057

Chen, J., Chen, F., Feng, S., Huang, W., Liu, J., and Zhou, A. (2015b). Hydroclimatic Changes in China and Surroundings during the Medieval Climate Anomaly and Little Ice Age: Spatial Patterns and Possible Mechanisms. *Quat. Sci. Rev.* 107, 98–111. doi:10.1016/j.quascirev.2014.10.012

Chen, F., Jia, J., Chen, J., Li, G., Zhang, X., Xie, H., et al. (2016). A Persistent Holocene Wetting Trend in Arid central Asia, with Wettest Conditions in the Late Holocene, Revealed by Multi-Proxy Analyses of Loess-Paleosol Sequences in Xinjiang, China. *Quat. Sci. Rev.* 146, 134–146. doi:10.1016/j.quascirev.2016.06.002

Chen, F., Chen, J., Huang, W., Chen, S., Huang, X., Jin, L., et al. (2019). Westerlies Asia and Monsoonal Asia: Spatiotemporal Differences in Climate Change and Possible Mechanisms on Decadal to Sub-orbital Timescales. *Earth-Science Rev.* 192, 337–354. doi:10.1016/j.earscirev.2019.03.005

Cheng, Y., Li, S., and Mengubieke, E. (2016). Changes of Water and Salt Characteristic of Ulungur Lake and the Corresponding Cause Analysis (In Chinese with English Abstract). *Environ. Protect Xinjiang* 38, 1–7. doi:10.3969/j.issn.1008-2301.2016.01.001

Davis, O. K. (1999). Pollen Analysis of Tulare Lake, California: Great Basin-like Vegetation in Central California during the Full-Glacial and Early Holocene. *Rev. Palaeobotany Palynol.* 107, 249–257. doi:10.1016/S0034-6667(99)00020-2

Eichler, A., Tinner, W., Brütsch, S., Olivier, S., Papina, T., and Schwikowski, M. (2011). An Ice-Core Based History of Siberian forest Fires since AD 1250. *Quat. Sci. Rev.* 30, 1027–1034. doi:10.1016/j.quascirev.2011.02.007

El-Moslimany, A. P. (1990). Ecological Significance of Common Nonarboreal Pollen: Examples from Drylands of the Middle East. *Rev. Palaeobotany Palynol.* 64, 343–350. doi:10.1016/0034-6667(90)90150-H

Fægri, K., and Iversen, J. (1989). *Textbook of Pollen Analysis*. 4th Edition. London, England: John Wiley & Sons.

Fan, M., Xu, J., Chen, Y., Li, D., and Tian, S. (2020). How to Sustainably Use Water Resources-A Case Study for Decision Support on the Water Utilization of Xinjiang, China. *Water* 12, 3564. doi:10.3390/w12123564

Fang, Y. (1989). *The History of Xinjiang Culticating*. Xinjiang Uygur Autonomous Region: Xinjiang Juvenile Publishing House. (in Chinese).

Fellner, J., and Rechberger, H. (2009). Abundance of 14C in Biomass Fractions of Wastes and Solid Recovered Fuels. *Waste Manag.* 29 (5), 1495–1503. doi:10.1016/j.wasman.2008.11.023

Feng, X., Ni, J., Yan, S., Kong, Z., and Yang, Z. (2006). Lake fluctuation and environmental change in the late Holocene recorded by plain lakes in northern Xinjiang (in Chinese). *Chin. Sci. Bull.* 51, 49–55.

Feng, Z., Sun, A., Abdusalih, N., Ran, M., Kurban, A., Lan, B., et al. (2016). Vegetation Changes and Associated Climatic Changes in the Southern Altai Mountains within China during the Holocene. *Holocene* 27, 683–693. doi:10.1177/0959683616670469

Feng, Z., Zhang, T., and Ran, M. (2017). *Climatic and Hydrological Changes in Northern Xinjiang and Surrounding Areas in the Past Ten Thousand Years*. Lanzhou: Lanzhou University Press. in Chinese.

Fontana, L., Sun, M., Huang, X., and Xiang, L. (2019). The Impact of Climate Change and Human Activity on the Ecological Status of Bosten Lake, NW China, Revealed by a Diatom Record for the Last 2000 Years. *Holocene* 29, 1871–1884. doi:10.1177/0959683619865586

Gao, Y., Li, Z., Zhu, R., and Wang, N. a. (2020). Quantitative Reconstruction of Holocene Millennial-Scale Precipitation in the Asian Monsoon Margin of Northwest China, Revealed by Phytolith Assemblages from Calcareous Root Tubes in the Tengger Desert. *Clim. Dyn.* 55, 755–770. doi:10.1007/s00382-020-05293-4

Grimm, E. C. (1987). CONISS: A FORTRAN 77 Program for Stratigraphically Constrained Cluster Analysis by the Method of Incremental Sum of Squares. *Comput. Geosci.* 13 (1), 13–35. doi:10.1016/0098-3004(87)90022-7

Grimm, E. C. (2011). *Tilia 1.7.16 Software*. Springfield, IL: Illinois State Museum, Research and Collection Center.

Hao, Z., Zheng, J., Yu, Y., Xiong, D., Liu, Y., and Ge, Q. (2019). Climatic Changes during the Past Two Millennia along the Ancient Silk Road. *Prog. Phys. Geogr. Earth Environ.* 44, 605–623. doi:10.1177/0309133319893919

Huang, X. Z., Chen, F. H., Fan, Y. X., and Yang, M. L. (2009). Dry Late-Glacial and Early Holocene Climate in Arid central Asia Indicated by Lithological and Palynological Evidence from Bosten Lake, China. *Quat. Int.* 194, 19–27. doi:10.1016/j.quaint.2007.10.002

Huang, X., Zhou, G., Ma, Y., Xu, Q., and Chen, F. (2010). Pollen Distribution in Large Freshwater lake of Arid Region: a Case Study on the Surface Sediments from Bosten Lake, Xinjiang, China. *Front. Earth Sci. China* 4, 174–180. doi:10.1007/s11707-009-0060-2

Huang, J., Yu, H., Guan, X., Wang, G., and Guo, R. (2015). Accelerated Dryland Expansion under Climate Change. *Nat. Clim Change* 6, 166–171. doi:10.1038/NCLIMATE2837

Huang, X., Peng, W., Rudaya, N., Grimm, E. C., Chen, X., Cao, X., et al. (2018). Holocene Vegetation and Climate Dynamics in the Altai Mountains and Surrounding Areas. *Geophys. Res. Lett.* 45, 6628–6636. doi:10.1029/2018GL078028

Jackson, S. T. (1990). Pollen Source Area and Representation in Small Lakes of the Northeastern United States. *Rev. Palaeobotany Palynol.* 63, 53–76. doi:10.1016/0034-6667(90)90006-5

Jenny, J.-P., Koirala, S., Gregory-Eaves, I., Francus, P., Ahrens, B., Brovkin, V., et al. (2020). Reply to Li et al.: Human societies began to play a significant role in global sediment transfer 4,000 years ago. *Proc. Natl. Acad. Sci. USA* 117, 5571–5572. doi:10.1073/pnas.1922723117

Jiang, Q., Ji, J., Shen, J., Matsumoto, R., Tong, G., Qian, P., et al. (2013). Holocene Vegetational and Climatic Variation in westerly-dominated Areas of Central Asia Inferred from the Sayram Lake in Northern Xinjiang, China. *Sci. China Earth Sci.* 56, 339–353. doi:10.1007/s11430-012-4550-9

Lan, J., Xu, H., Sheng, E., Yu, K., Wu, H., Zhou, K., et al. (2018). Climate Changes Reconstructed from a Glacial lake in High Central Asia over the Past Two Millennia. *Quat. Int.* 487, 43–53. doi:10.1016/j.quaint.2017.10.035

Lan, B., Zhang, D., Yang, Y., He, L., Zhang, X., and Zhong, R. (2019). Diatom-based Reconstructions of Hydrological Variations and the Underlying Mechanisms during the Past ~520 Years in the central Tianshan Mountains. *J. Hydrol.* 575, 945–954. doi:10.1016/j.jhydrol.2019.06.001

Lan, J., Zhang, J., Cheng, P., Ma, X., Ai, L., Chawchai, S., et al. (2020). Late Holocene Hydroclimatic Variation in central Asia and its Response to Mid-latitude Westerlies and Solar Irradiance. *Quat. Sci. Rev.* 238, 106330. doi:10.1016/j.quascirev.2020.106330

Lang, W. (2020). *The History of Sandstorm Activity Recorded by the Sedimentation of Jili Lake in Northern Xinjiang during the Last 1600 Years the Master's Thesis of*. Lanzhou University. (in Chinese). doi:10.27204/d.cnki.glzhu.2020.000173

Li, J., Sang, X., Ji, Y., and Chen, R. (1991). *The Climate in Xinjiang*. Beijing: Meteorology Press. (in Chinese).

Li, Y., Zhou, L., and Cui, H. (2008). Pollen Indicators of Human Activity. *Sci. Bull.* 53, 1281–1293. doi:10.1007/s11434-008-0181-0

Li, F., Sun, J., Zhao, Y., Guo, X., Zhao, W., and Zhang, K. (2010). Ecological Significance of Common Pollen Ratios: A Review. *Front. Earth Sci. China* 4, 253–258. doi:10.1007/s11707-010-0112-7

Li, M., Li, Y., Xu, Q., Pang, R., Ding, W., Zhang, S., et al. (2012). Surface Pollen Assemblages of Human-Disturbed Vegetation and Their Relationship with Vegetation and Climate in Northeast China. *Chin. Sci. Bull.* 57, 535–547. doi:10.1007/s11434-011-4853-9

Li, Q., Lu, L., Wang, C., Li, Y., Sui, Y., and Guo, H. (2015). MODIS-derived Spatiotemporal Changes of Major Lake Surface Areas in Arid Xinjiang, China, 2000-2014. *Water*. 7, (10). 5731–5751. doi:10.1007/s11430-019-9550-710.3390/w7105731

Li, Y., Qiang, M., Zhang, J., Huang, X., Zhou, A., Chen, J., et al. (2017). Hydroclimatic Changes over the Past 900 Years Documented by the Sediments of Tiewaike Lake, Altai Mountains, Northwestern China. *Quat. Int.* 452, 91–101. doi:10.1016/j.quaint.2016.07.053

Li, Y., Hu, L., Zhao, Y., Wang, H., Huang, X., Chen, G., et al. (2021). Meltwater-Driven Water-Level Fluctuations of Bosten Lake in Arid China over the Past 2,000 Years. *Geophys. Res. Lett.* 48, 2020GL090988. doi:10.1029/2020GL090988

Li, Q. (2020). Solar Forcing of Desert Vegetation and Drought Frequency during the Last 2700 Years in the interior Qaidam Basin, Northeastern Tibetan Plateau. *Sci. China Earth Sci.* 63, 561–574. doi:10.1007/s11430-019-9550-7

Li, Y. (2020). Agriculture and Palaeoeconomy in Prehistoric Xinjiang, China (3000-200 Bc). *Veget Hist. Archaeobot* 30, 287–303. doi:10.1007/s00334-020-00774-2

Liu, X., Herzschuh, U., Shen, J., Jiang, Q., and Xiao, X. (2008). Holocene Environmental and Climatic Changes Inferred from Wulungu Lake in Northern Xinjiang, China. *Quat. Res.* 70, 412–425. doi:10.1016/j.yqres.2008.06.005

Liu, X., Herzschuh, U., Wang, Y., Kuhn, G., and Yu, Z. (2014). Glacier Fluctuations of Muztagh Ata and Temperature Changes during the Late Holocene in Westernmost Tibetan Plateau, Based on Glaciolacustrine Sediment Records. *Geophys. Res. Lett.* 41, 6265–6273. doi:10.1002/2014GL060444

Liu, S., Huang, X., Qiang, M., Lin, X., Bai, Z., and Peng, W. (2016). Vegetation and Climate Change during the Mid-late-holocene Reflected by the Pollen Record from Lake Genggahai, Northeastern Tibetan Plateau. *Quat. Sci.* 36 (2), 247–256. (in Chinese). doi:10.11928/j.issn.1001-7410.2016.02.01

Liu, Y., Yang, J., Chen, Y., Fang, G., and Li, W. (2018). The Temporal and Spatial Variations in Lake Surface Areas in Xinjiang, China. *Water* 10, 431. doi:10.3390/w10040431

Ljungqvist, F. C. (2016). A New Reconstruction of Temperature Variability in the Extra-tropical Northern Hemisphere during the Last Two Millennia. *Geografiska Annaler: Ser. A, Phys. Geogr.* 92, 339–351. doi:10.1111/j.1468-0459.2010.00399.x

Luo, C., Zheng, Z., Tarasov, P., Pan, A., Huang, K., Beaudouin, C., et al. (2009). Characteristics of the Modern Pollen Distribution and Their Relationship to Vegetation in the Xinjiang Region, Northwestern China. *Rev. Palaeobotany Palynol.* 153, 282–295. doi:10.1016/j.revpalbo.2008.08.007

Ma, J., Edmunds, W. M., He, J., and Jia, B. (2009). A 2000 Year Geochemical Record of Palaeoclimate and Hydrology Derived from Dune Sand Moisture. *Palaeogeogr. Palaeoclimatol. Palaeoecol.* 276, 38–46. doi:10.1016/j.palaeo.2009.02.028

Maher, L. J. (1981). Statistics for Microfossil Concentration Measurements Employing Samples Spiked with Marker Grains. *Rev. Palaeobotany Palynol.* 32, 153–191. doi:10.1016/0034-6667(81)90002-6

Ni, Z., Zhang, E., Sun, W., Meng, X., Ning, D., Jiang, Q., et al. (2021). Response of the Chironomid Community to Late Holocene Climate Change and Anthropogenic Impacts at Lake Ulungur, Arid Central Asia. *Quat. Int.* doi:10.1016/j.quaint.2021.08.007

Nielsen, A. B., and Sugita, S. (2005). Estimating Relevant Source Area of Pollen for Small Danish Lakes Around AD 1800. *The Holocene* 15, 1006–1020. doi:10.1191/0959683605hl874ra

Reid, G. C. (1991). Solar Total Irradiance Variations and the Global Sea Surface Temperature Record. *J. Geophys. Res.* 96, 2835. doi:10.1029/90JD02274

Reimer, P. J., Bard, E., Bayliss, A., Beck, J. W., Blackwell, P. G., Ramsey, C. B., et al. (2013). Intcal13 and Marine13 Radiocarbon Age Calibration Curves 0-50,000 Years Cal BP. *Radiocarbon* 55 (4), 1869–1887. doi:10.1017/S0033822200048864 10.2458/azu_js_rc.55.16947

Ren, W., Zhao, Y., Li, Q., and Chen, J. (2019). Changes in vegetation and moisture in the northern Tianshan of China over the past 450 years. *Front. Earth Sci.* 14, 479–491. doi:10.1007/s11707-019-0788-2

Shi, Y., Shen, Y., Kang, E., Li, D., Ding, Y., Zhang, G., et al. (2006). Recent and Future Climate Change in Northwest China. *Clim. Change* 80, 379–393. doi:10.1007/s10584-006-9121-7

Song, M., Zhou, A., Zhang, X., Zhao, C., He, Y., Yang, W., et al. (2015). Solar Imprints on Asian Inland Moisture Fluctuations over the Last Millennium. *Holocene* 25, 1935–1943. doi:10.1177/0959683615596839

Sorrel, P., Popescu, S.-M., Head, M. J., Suc, J. P., Klotz, S., and Oberhänsli, H. (2006). Hydrographic Development of the Aral Sea during the Last 2000 Years Based on a Quantitative Analysis of Dinoflagellate Cysts. *Palaeogeogr. Palaeoclimatol. Palaeoecol.* 234, 304–327. doi:10.1016/j.palaeo.2005.10.012

Steinhilber, F., Abreu, J. A., Beer, J., Brunner, I., Christl, M., Fischer, H., et al. (2012). 9,400 Years of Cosmic Radiation and Solar Activity from Ice Cores and Tree Rings. *Proc. Natl. Acad. Sci.* 109, 5967–5971. doi:10.1073/pnas.1118965109/-/DCSupplemental

Sugita, S. (1994). Pollen Representation of Vegetation in Quaternary Sediments: Theory and Method in Patchy Vegetation. *J. Ecol.* 82, 881–897. doi:10.2307/2261452

Sun, X., Du, N., Weng, C., Lin, R., and Wei, K. (1994). Paleovegetation and paleoenvironment of Manas Lake, Xinjiang, N. W. China during the last 14000 years (in Chinese). *Quat. Sci.* 239–248.

Tao, S., An, C., Chen, F., Tang, L., Wang, Z., Lü, Y., et al. (2010). Pollen-inferred Vegetation and Environmental Changes since 16.7 Ka BP at Balikun Lake, Xinjiang. *Chin. Sci. Bull.* 55, 2449–2457. doi:10.1007/s11434-010-3174-8

Tuerhong, M. (2011). A Brief Account of Chinese Ancient Thought and Literatures about Stationing Troops to Garrison the Frontiers. *J. Libr. Inf. Sci.* 21, 64–66. doi:10.3969/j.issn.1005-6033.2011.12.029 (in Chinese with English abstract).

Wang, S., and Dou, H. (1998). *Chinese Journal of Lakes*. Beijing: Science Publishing House. (in Chinese).

Wang, X., Wang, H., Zhang, K., Lian, G., Zhang, L., Zhou, W., et al. (1981). A Preliminary Study on the Natural Conditions of Wulungu Lake in Xinjiang and its Fishery Biology Basis(in Chinese). *Trans. Oceanol. Limnol.* 4, 19–28. doi:10.13984/j.cnki.cn37-1141.1981.04.004

Wang, J., Li, J., Chen, F., Gou, X., Peng, J., and Liu, P. (2007). Variation of the Dryness in the Recent 200 a Derived from Tree-Rings Width Records in the East Tianshan Mountains. *J. Glaciol. Geocryol.* 29, 209–216. (in Chinese).

Wang, W., Feng, Z., Ran, M., and Zhang, C. (2013). Holocene Climate and Vegetation Changes Inferred from Pollen Records of Lake Aibi, Northern Xinjiang, China: A Potential Contribution to Understanding of Holocene Climate Pattern in East-central Asia. *Quat. Int.* 311, 54–62. doi:10.1016/j.quaint.2013.07.034

Wen, R., Xiao, J., Chang, Z., Zhai, D., Xu, Q., Li, Y., et al. (2010). Holocene Precipitation and Temperature Variations in the East Asian Monsoonal Margin from Pollen Data from Hulun Lake in Northeastern Inner Mongolia, China. *Boreas* 39, 262–272.

Whitlock, C., and Larsen, C. V. (2001). "Charcoal as a Fire Proxy," in *Tracking Environmental Changes Using Lake Sediments,Terrestrial, Algal, and Siliceous Indicators*. Editors J.P. Smol, H.J.B. Birks, and W.M. Last (Dordrecht: Kluwer Academic Publishers), Vol. 3, 75e96.

Xu, Q., Chen, F., Zhang, S., Cao, X., Li, J., Li, Y., et al. (2016). Vegetation Succession and East Asian Summer Monsoon Changes since the Last Deglaciation Inferred from High-Resolution Pollen Record in Gonghai Lake, Shanxi Province, China. *Holocene* 27, 835–846. doi:10.1177/0959683616675941

Yan, S., and Xu, Y. (1989). Spore-pollen Association in Surface-Soil in Altay(in Chinese), Xinjiang. *Arid Zone Res.* 26, 26–33. doi:10.13866/j.azr.1989.01.005

Yan, D., Xu, H., Lan, J., Zhou, K., Ye, Y., Zhang, J., et al. (2019). Solar Activity and the Westerlies Dominate Decadal Hydroclimatic Changes over Arid Central Asia. *Glob. Planet. Change* 173, 53–60. doi:10.1016/j.gloplacha.2018.12.006

Yang, L., and Zhang, Q. (2008). Interannual Variation of Summer Precipitation in Xinjiang and Asian Subtropical Westerly Jet Stream (In Chinese). *J. Appl. Meteorol. Sci.* 19, 171–179. doi:10.3724/SP.J.1011.2008.00323

Yang, Y., Zhang, D., Lan, B., Abdusalih, N., and Feng, Z. (2019). Peat δ13Ccelluose-signified Moisture Variations over the Past ~2200 Years in the Southern Altai Mountains, Northwestern China. *J. Asian Earth Sci.* 174, 59–67. doi:10.1177/0959683619854510.1016/j.jseaes.2018.11.019

Yang, Y., Ran, M., and Sun, A. (2020). Pollen-recorded Bioclimatic Variations of the Last ~2000 Years Retrieved from Bayan Nuur in the Western Mongolian Plateau. *Boreas* 49, 350–362. doi:10.1111/bor.12423

Yang, J. (2018). Study on the Reasons of the Rise of Northern Xinjiang during the Reign of Qianlong(in Chinese). *J. Kashi Univ.* 39, 33–40. doi:10.13933/j.cnki.2096-2134.2018.04.007

Yao, Y., Lan, J., Zhao, J., Vachula, R. S., Xu, H., Cai, Y., et al. (2020a). Abrupt Freshening since the Early Little Ice Age in Lake Sayram of Arid Central Asia Inferred from an Alkenone Isomer Proxy. *Geophys. Res. Lett.* 47. doi:10.1029/2020GL089257

Yao, Y.-F., Wang, X., Guo, W., Jiang, H.-E., Li, M., Ferguson, D. K., et al. (2020b). Archaeobotanical Evidence Reveals the Human-Environment Interactions during the 9th-13th Centuries at Turpan, Xinjiang on the Ancient Silk Road. *Veget Hist. Archaeobot* 29, 539–552. doi:10.1007/s00334-019-00764-z

Yu, G., Prentice, I. C., Harrison, S. P., and Sun, X. (1998). Pollen-based Biome Reconstructions for China at 0 and 6000 Years. *J. Biogeogr.* 25, 1055–1069. doi:10.1046/j.1365-2699.1998.00237.x

Zhang, D., and Feng, Z. (2018a). Holocene Climate Variations in the Altai Mountains and the Surrounding Areas: A Synthesis of Pollen Records. *Earth-Science Rev.* 185, 847–869. doi:10.1016/j.earscirev.2018.08.007

Zhang, Y., Meyers, P. A., Liu, X., Wang, G., Ma, X., Li, X., et al. (2016). Holocene Climate Changes in the central Asia Mountain Region Inferred from a Peat Sequence from the Altai Mountains, Xinjiang, Northwestern China. *Quat. Sci. Rev.* 152, 19–30. doi:10.1016/j.quascirev.2016.09.016

Zhang, Y., Mo, D., Hu, K., Bao, W., Li, W., Abuduresule, I., et al. (2017). Holocene Environmental Changes Around Xiaohe Cemetery and its Effects on Human Occupation, Xinjiang, China. *J. Geogr. Sci.* 27, 752–768. doi:10.1007/s11442-017-1404-6

Zhang, D., Feng, Z., Yang, Y., Lan, B., Ran, M., and Mu, G. (2018b). Peat δ13Ccelluose-recorded Wetting Trend during the Past 8000 Years in the Southern Altai Mountains, Northern Xinjiang, NW China. *J. Asian Earth Sci.* 156, 174–179. doi:10.1016/j.jseaes.2018.01.029

Zhang, J., Huang, X., Wang, Z., Yan, T., and Zhang, E. y. (2018c). A Late-Holocene Pollen Record from the Western Qilian Mountains and its Implications for Climate Change and Human Activity along the Silk Road, Northwestern China. *Holocene* 28, 1141–1150. doi:10.1177/0959683618761548

Zhao, W., and Xie, S. (1988). *Population History of China*. Beijing: People's Publishing House, 1–645. in Chinese.

Zhao, Y., Xu, Q., Huang, X., Guo, X., and Tao, S. (2009). Differences of Modern Pollen Assemblages from lake Sediments and Surface Soils in Arid and Semi-arid China and Their Significance for Pollen-Based Quantitative Climate Reconstruction. *Rev. Palaeobotany Palynol.* 156, 519–524. doi:10.1016/j.revpalbo.2009.05.001

Zhao, Y., Yu, Z., Liu, X., Zhao, C., Chen, F., and Zhang, K. (2010). Late Holocene Vegetation and Climate Oscillations in the Qaidam Basin of the Northeastern Tibetan Plateau. *Quat. Res.* 73, 59–69. doi:10.1016/j.yqres.2008.11.007

Zhao, Y., Li, F., Hou, Y., Sun, J., Zhao, W., Tang, Y., et al. (2012). Surface Pollen and its Relationships with Modern Vegetation and Climate on the Loess Plateau and Surrounding Deserts in China. *Rev. Palaeobotany Palynol.* 181, 47–53. doi:10.1016/j.revpalbo.2012.05.007

Zhao, Y., Wang, M., Huang, A., Li, H., Huo, W., and Yang, Q. (2014). Relationships between the West Asian Subtropical westerly Jet and Summer Precipitation in Northern Xinjiang. *Theor. Appl. Climatol* 116, 403–411. doi:10.1007/s00704-013-0948-3

Conflict of Interest: The authors declare that the research was conducted in the absence of any commercial or financial relationships that could be construed as a potential conflict of interest.

The handling editor declared a shared affiliation with the authors (JZ, YX, LX, and XH) at time of review.

Publisher's Note: All claims expressed in this article are solely those of the authors and do not necessarily represent those of their affiliated organizations, or those of the publisher, the editors and the reviewers. Any product that may be evaluated in this article, or claim that may be made by its manufacturer, is not guaranteed or endorsed by the publisher.

Copyright © 2021 Xiao, Xiang, Huang, Mills, Zhang, Chen and Li. This is an open-access article distributed under the terms of the Creative Commons Attribution License (CC BY). The use, distribution or reproduction in other forums is permitted, provided the original author(s) and the copyright owner(s) are credited and that the original publication in this journal is cited, in accordance with accepted academic practice. No use, distribution or reproduction is permitted which does not comply with these terms.

frontiers in Earth Science

ORIGINAL RESEARCH
published: 01 October 2021
doi: 10.3389/feart.2021.721724

Hydrological Evolution of a Lake Recharged by Groundwater in the Badain Jaran Desert Over the Past 140 years

Gaolei Jiang[1,2,3]*, Nai'ang Wang[1]*, Xin Mao[2,3], Hua Zhao[2,3], Linjing Liu[2,3], Jianmei Shen[2], Zhenlong Nie[2] and Zhe Wang[2]

[1]Centre for Glacier and Desert Research, College of Earth and Environmental Sciences, Lanzhou University, Lanzhou, China, [2]Institute of Hydrogeology and Environmental Geology, Chinese Academy of Geological Sciences, Shijiazhuang, China, [3]Key Laboratory of Quaternary Chronology and Hydro-Environmental Evolution, China Geological Survey, Shijiazhuang, China

OPEN ACCESS

Edited by:
Zhiwei Xu,
Nanjing University, China

Reviewed by:
José Darrozes,
UMR5563 Géosciences
Environnement Toulouse (GET),
France
Li Wu,
Anhui Normal University, China
Steffen Mischke,
University of Iceland, Iceland

***Correspondence:**
Gaolei Jiang
jianggl198899@163.com
Nai'ang Wang
wangna@lzu.edu.cn

Specialty section:
This article was submitted to
Quaternary Science, Geomorphology
and Paleoenvironment,
a section of the journal
Frontiers in Earth Science

Received: 07 June 2021
Accepted: 23 August 2021
Published: 01 October 2021

Citation:
Jiang G, Wang N, Mao X, Zhao H,
Liu L, Shen J, Nie Z and Wang Z (2021)
Hydrological Evolution of a Lake
Recharged by Groundwater in the
Badain Jaran Desert Over the
Past 140 years.
Front. Earth Sci. 9:721724.
doi: 10.3389/feart.2021.721724

Understanding the evolution of lakes in arid areas is very important for water resource management. Previous studies have mainly focused on lakes with runoff recharge, while the evolution of groundwater recharge lakes in hyper-arid areas is still less known. In this study, an 86 cm-long sediment core was extracted from Sayinwusu Lake, one of groundwater-recharge lakes in the southeastern Badain Jaran Desert, Northwest China. ^{210}Pb and ^{137}Cs dating, total organic carbon (TOC) and total nitrogen (TN) contents, and mineral content analysis were used to reconstruct the lake evolution over the past 140 years. The evolution of Sayinwusu Lake since 1880 can be divided into two periods. In the first period from 1880 to 1950, the TOC and TN contents were low, and the minerals consisted of all detrital minerals, which indicate that the lake's primary productivity and salinity were low. During the second period from 1950 to 2018, the contents of TOC, TN, and carbonate minerals increased rapidly at the beginning of the 1950s, indicating that the lake's primary productivity and salinity increased. Comprehensive analysis of regional climate data suggests that the increase in evaporation caused by rising temperature is an important factor affecting lake evolution in the desert. Although precipitation has increased in the arid region of Northwest China in recent decades with increasing temperature, the enhancement of the evaporation effect is much greater. As a record from groundwater recharge lakes in deserts, our study provides new insight into projecting future lake changes in hyper-arid areas.

Keywords: lake evolution, groundwater recharge, global warming, evaporation, arid areas

INTRODUCTION

Lakes are important water resources, especially in hyper-arid areas. Understanding lake evolution patterns can help us predict lake development trends and manage water resources (Panizzo et al., 2013; Creutz et al., 2016; Lopez et al., 2019; Wan et al., 2019; Woolway et al., 2020). Previous studies of lake evolution have mainly focused on the important role of runoff, precipitation, and/or snow melt water in hydrological systems (Zhai et al., 2011; Long et al., 2012; Liu et al., 2013; Li et al., 2016). In hyper-arid areas, including Xinjiang Province and Gansu Province, recharge by groundwater plays a crucial role in the evolution of the main inland basin and is at least equal to, if not greater than, the

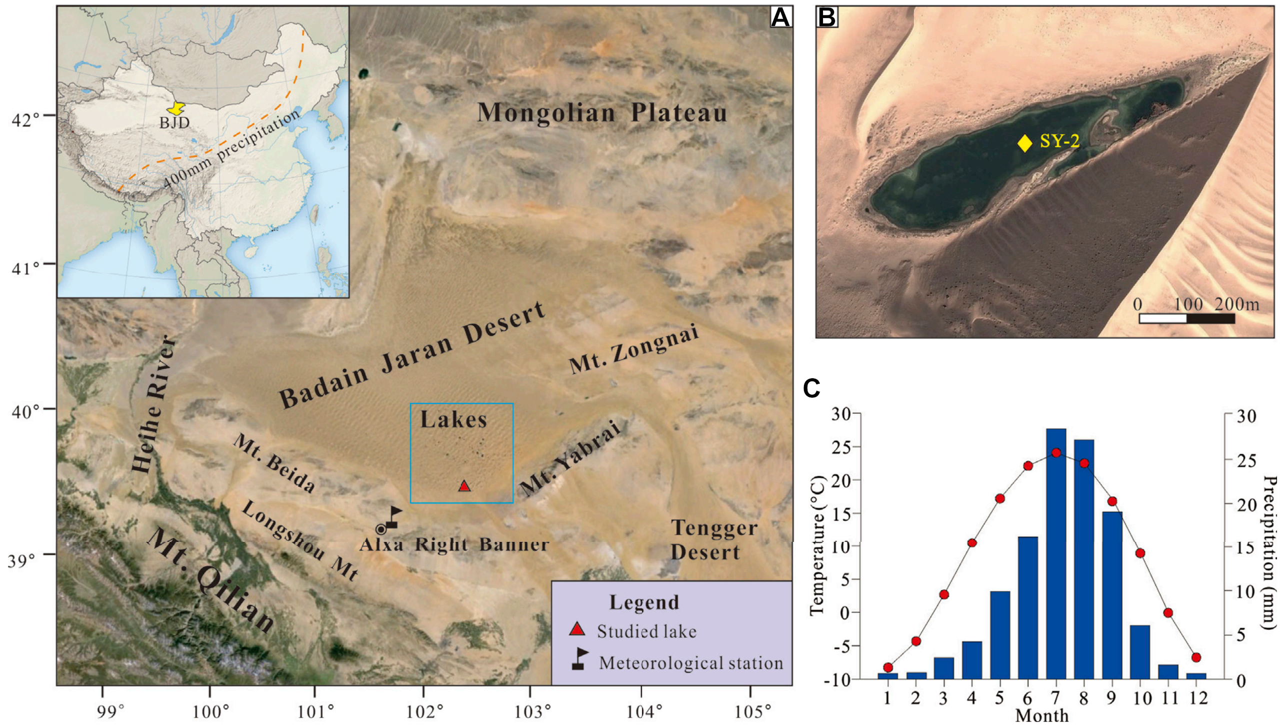

FIGURE 1 | Sketch map showing the geographic setting of the BJD **(A)**, the location of the SY-2 sediment core from Sayinwusu Lake **(B),** and the variation in monthly temperature (red circles) and precipitation (blue pillars) [**(C)**, data are the averages for 1960–2017].

amount of runoff and precipitation (Zhang and Li, 2005a; Zhang and Li, 2005b). The evolution of lakes recharged by groundwater is characterized by intense vertical intersphere water recharge from other areas and no discharge except evaporation; this situation is different from the previous lake evolution model. Many studies have been conducted and have achieved much progress on the evolution pattern, driving factors of lake evolution, and response to climate change for lakes recharged by runoff and/or precipitation (Chen et al., 2009; Long et al., 2012; Liu et al., 2013; Wang et al., 2014; Wu et al., 2020; Fu et al., 2021). However, much less work has been done on the evolution of groundwater recharge lakes.

The Badain Jaran Desert (BJD), located in western Inner Mongolia in a hyper-arid area of China, is sensitive to climate change, with an increase in the temperature of 0.34°C per decade (**Figure 1**; Yang et al., 2011; Ning et al., 2021). The BJD, with an area of 5.2 × 104 km^2, is the second largest desert in China (Zhu et al., 2010). It is characterized by the coexistence of more than 110 perennial lakes and thousands of mega-dunes (Dong et al., 2013). The BJD has the tallest mega-dunes on Earth, with mega-dunes more than 100 m tall covering 68% of the area and concentrated in the southeastern part of the sand sea (Dong et al., 2013). More than 90% of the recharge of lakes between mega-dunes is from groundwater (Dong et al., 2016; Wang et al., 2016). Therefore, the BJD is an ideal region to study the evolution pattern of lakes recharged by groundwater. Previous studies in the BJD were mainly based on the dating of discontinuous lake sediments during the late Quaternary, especially the Holocene at the millennial scale (Yang and Williams, 2003; Yang et al., 2010; Bai et al., 2011; Wang et al., 2016; Chen et al., 2019). This is not sufficient for a detailed understanding of the factors influencing lake evolution during past decades, which is important for predicting the development trend in future decades or centuries.

The global environment has experienced dramatic change, with the highest rate of increase in global temperature over the last century (Woolway et al., 2020). Arid zones are recognized to be more sensitive than other areas to temperature variations associated with global climate change (Huang et al., 2016), and the resulting changes in evaporation are an important factor in lake evolution (Li et al., 2016; Wang et al., 2016). Therefore, the past century is a key period for understanding lake evolution and predicting its trend in the context of global warming (Neukom et al., 2019). Unfortunately, few studies on lake evolution have been conducted during this period in the BJD. In this study, we reconstructed the lake evolution history over the last 140 years based on continuous lake sediments, which may provide new insight into projecting the trend of lake evolution responses to future climate change.

STUDY AREA

The BJD is located on the northwestern Alxa Plateau in Northwest China (**Figure 1A**). It has an elevation of 900–1800 m a.s.l., falling from the southeast to the northwest.

To the south, it is bounded by the Beida Mountains (Mt) and the Heishantou Mt (maximum elevation 1963 m a.s.l.), which separate it from the Gobi of the Hexi Corridor (Dong et al., 2013). To the southeast, it is bounded by the Yabrai Mt (maximum elevation 1957 m a.s.l.), which separate it from the Tengger Desert. To the west and northwest, it stretches down to Ugrian Lake and the Heihe River. To the north, it is bounded by Guaizi Lake, close to the Mongolian Gobi (Dong et al., 2013). Stratigraphic studies of the Badain Jaran Basin demonstrate that Cretaceous strata are widely distributed in the piedmont area of the surrounding mountains and the Badain Jaran Desert. They are several thousand metres thick and mainly consist of red and brick-red sandstone, siltstone with calcareous nodules intercalated with a small amount of conglomerate, and calcareous sandstone (BGMIMAR, 1991). Cenozoic sediments are distributed in the western and southern intermontane areas, which unconformably underlie the upper Quaternary deposits and are less than 200 m thick. The Quaternary aeolian sand has a thickness of 200–400 m and is intercalated with several lacustrine layers (Wang et al., 2015a). Studies have assumed that the sandy materials in the Badain Jaran should have been derived from the weathered extensive lacustrine sediments of dry lake beds in the west and northwest (Yang, 1991; Yan et al., 2001) and the giant alluvial fan of the Heihe River (Mischke, 2005; Hu and Yang, 2016).

The lakes lying among mega-dunes are concentrated within an area of approximately 4,000 km^2 (Dong et al., 2013). Most lakes are less than 0.6 km^2, and the largest is 1.46 km^2. Water depth is generally a few metres up to 10 m, and the deepest lake depth is 15.9 m (Zhang et al., 2013; Wang et al., 2016). The hydrological properties of the lakes vary greatly, with the total dissolved solids (TDS) ranging from less than 1 to 400 g/L (Yang and Williams, 2003; Lu et al., 2010). Most lakes from the southeast edge to the hinterland are of the sulfate–carbonate–chloride type with increasing salinity (Lu et al., 2010). Although the origin of groundwater in the desert remains a hotly debated issue, it is generally agreed that groundwater is the main water source of the lakes and is primarily from the south and southeast areas, such as the Yabrai Mt, and Qilian Mt (Ma and Edmunds, 2006; Gates et al., 2008a; Dong et al., 2013; Wang et al., 2016).

The BJD has an extreme continental desert-type climate (Dong et al., 2004). The mean precipitation ranges from 40 to 90 mm, decreasing from the southeast to the northwest. Most of the precipitation occurs in summer (**Figure 1C**). The evaporation from lake surfaces is 1,450 mm, which is more than 20 times the amount of precipitation (Hu et al., 2015). The mean annual air temperature ranges from 9.5 to 10.3°C, with the lowest monthly mean temperature of 8.3°C in January and the highest of 24.1°C in July (**Figure 1C**). The mean annual wind speed ranges from 2.8 to 4.6 $m\ s^{-1}$, and the wind direction is mainly northwest (Hu and Yang, 2016).

The surface vegetation coverage of the BJD ranges from 5 to 50, with most areas having very low coverage; the vegetation is dominated by xerophytic and ultraxerophytic shrubs and subshrubs, and herbacea is dominated by annual plants. On the sandy hills, the vertical distribution of vegetation is obvious. In the dry lake basin, the *Nitraria tangutorum* community is widely distributed, accompanied by *Zygophyllum xanthoxylum* and *Calligonum mongolicum* (Cui et al., 2014; Wang et al., 2015b). Around the modern lake shore, the vegetation is distributed in a ribbon with a width of a few metres to a dozen metres. Along the lake, there is a marsh-shaped halophytic meadow, mainly composed of *Trigolochin maritimum, Glaux maritima*, and *Aeluro littorlis*. In the periphery, there is a halophytic meadow, mainly composed of *Phragmites communis* and *Achnatherum splendens*. Due to the government's relocation policy and the improvement of living conditions, there are only a few herders living around a few lakes. In 2009, the BJD became a global desert geopark, and thousands of people visited it every year, mainly in October.

The distribution of lakes in the BJD is relatively concentrated in the southeastern region. Lakes with lower salinities are more sensitive to the environmental changes and are easily observed for hydrochemical changes. Sayinwusu Lake, located at the southeastern margin of the BJD, has an area of approximately 0.12 km^2 (**Figure 1B**). The lake is 720 m long and 170 m at the widest point, with the largest water depth of approximately 2 m. The lake water has a pH of 9.5 and salinity of 18.0 g/L with major cations of K^+ (384 mg/L), Na^+ (5,330 mg/L), Ca^{2+} (37 mg/L), and Mg^{2+} (751 mg/L) and major anions of Cl^- (6,440 mg/L), $SO_4{}^{2-}$ (4,166 mg/L), $HCO_3{}^-$ (693 mg/L), and $CO_3{}^{2-}$ (531 mg/L) (team unpublished data). Due to the high salinity, there are no fish in the lake, and no animals, such as camels, drink the lake water. Terrestrial vegetation is distributed in belts around the lake shores, with areal extents of tens of metres. The dominant plant species around the lake are mainly xerophytes, super-arid shrubs, and semi-shrubs, and are mainly composed of *Trigolochin maritimum, Glaux maritima, and Aeluro littorlis* inside and *Phragmites communis* and *Achnatherum splendens* outside.

MATERIALS AND METHODS

Field Sampling

An 86 cm long sediment core (SY-2) was drilled from the centre of Sayinwusu Lake (102°19.82′ E, 39°34.00′ N) in September 2018 A.D. using a gravity corer. The water depth of the sampling point is approximately 1.6 m. The sediment core was sectioned at 1.0 cm intervals (86 samples) and then fully dried in a vacuum-freezing dryer at −25°C for 48–72 h. Before laboratory analysis, these samples were stored in a dry place at room temperature.

^{210}Pb and ^{137}Cs Dating

Twenty-five subsamples were selected at 2-cm intervals for the upper 50 cm part of the sediment core and were ground to fine powder (< 63 μm) in an agate mortar. The activities of ^{137}Cs, ^{210}Pb, and ^{226}Ra in the samples were determined by a low-background well-type germanium detector (EG and GOrtec Gamma Spectrometry) at the State Key Laboratory of Lake Sciences and Environment, CAS. ^{137}Cs was detected at 662 keV, ^{210}Pb was determined via gamma emission at 46.5 keV, ^{226}Ra was measured at 295 keV, and 352 keV g-rays were emitted by its daughter isotope ^{214}Pb. Standard errors (2σ) were calculated from the counting statistics. The excess ^{210}Pb ($^{210}Pbex$) activity was calculated by subtracting the activity of ^{226}Ra

from the total ^{210}Pb activity. ^{210}Pb$_{ex}$ activity is employed to calculate a chronology using the constant rate of supply (CRS) dating model (Appleby and Oldfield, 1978; Appleby, 2001; Swarzenski, 2014). The calculated equation is as follows:

$$A_h = A_0 e^{-\lambda t},$$

where Ah is the cumulative residual unsupported or excess ^{210}Pb activity beneath sediment of depth h, A_0 is the total unsupported ^{210}Pb activity in the sediment column, λ is the ^{210}Pb decay constant, 0.03114 years^{-1}, and t represents time.

TOC and TN Analysis

Eighty-four subsamples at 1 cm intervals were ground to fine powder (< 63 μm) in an agate mortar, treated with 1 N HCl to remove inorganic carbonates, and then rinsed repeatedly with deionized water to remove soluble salts. The residual samples were dried for measurement. The total carbon and total nitrogen contents were determined by an EA 3,000 elemental analyser at the State Key Laboratory of Lake Sciences and Environment, Chinese Academy of Science (CAS). The repetitive errors were less than 3%. The total organic carbon contents were calculated by subtracting the inorganic carbon contents in carbonates from the total carbon contents.

The total organic carbon (TOC)/total nitrogen (TN) ratios of lacustrine sediments are usually used to evaluate the predominance of autochthonous versus allochthonous sources of organic matter (Meyers, 2003). In general, carbon-to-nitrogen (C/N) ratios less than 10 indicate that the organic matter is from protein-rich and cellulose-poor aquatic organisms (Meyers, 2003), the mean C/N value of benthos is approximately 3, and algae and phytoplankton have values of approximately 5–12 and generally less than 10 (Hedges et al., 2002). However, when the organic matter is from protein-poor and cellulose-rich terrestrial plants, the C/N ratio is greater than 20 (Meyers, 2003).

Mineral Analysis

Eighty-six subsamples at 1 cm intervals were ground to fine powder prior to measurement. The mineralogy was measured at the Key Laboratory of Western China's Environmental Systems (Ministry of Education) by a powder X-ray diffractometer (XRD, PANalytical X'Pert Pro MPD). Each sample was spread and leveled onto a 1.5 cm^2 × 1.5 cm^2 concave glass plate for XRD determinations. XRD employs the radiation of a Cu target at 40 kV and 40 mA to generate X-rays that irradiate a sample at a scanning angle of 2ϴ (5–75°) with a 0.01° minimum step size and produce the diffraction peaks of the sample. Other equipment settings are automatic variable divergence detector slits. Corundum (α-Al_2O_3) was selected as the internal standard. The compositions of minerals in samples were determined by comparison of the characteristic diffraction peaks with the standard card spectrum using the software X'Pert HighScore Plus. The detailed calculation method of mineral content can be found in Last (2001).

RESULTS

^{210}Pb and ^{137}Cs

In the studied sediment core, the vertical distributions of the activities of ^{210}Pb and ^{137}Cs are shown in **Table 1** and **Figure 2A**. The first appearance of ^{137}Cs activity occurs at a depth of 36 cm with a corresponding activity of 1.83 Bq/kg. The peak of ^{137}Cs activity is identified at a depth of 30 cm with a corresponding activity of 18.47 Bq/kg. Above 30 cm, the ^{137}Cs activity gradually decreased to approximately about 3 Bq/kg (**Figure 2A**). The excess ^{210}Pb (^{210}Pb$_{ex}$) activity in the core decreases from 253.39 Bq/kg at the core surface to near zero at 50 cm depth (**Figure 2A**).

TOC, TN, and TOC/TN

The TOC and TN contents are very low and constant around 0.1% for TOC and ~0.05% for TN, and no clear peak is observed during this period. The C/N ratio is very noisy during this period except for 1885 A.D., where a very strong peak is observed. The TOC content increases rapidly at 40–41 cm (1948–1950 A.D.) and then maintains a higher content (0.40–1.47%), and **Figure 3** shows four main peaks compared to the geochemical background of approximately 0.5% for TOC and 0.15% for TN. These main peaks correspond to the years 1950–1952 (TOC = 0.85%, TN = 0.10%), 1960 (TOC = 0.8%, TN = 0.12%), 1995 (TOC = 1.47%, TN = 0.24%), ~2004–2007 (TOC = 1.13%, TN = 0.18%), and the highest peak (TOC = 2.01%, TN = 0.35%) observed for 2015–2018. Overall, the TOC/TN ratios are less than 10 with an average value of 6.25. The C/N ratio during 1950–2018 decreased slowly from 8 to 5, and the noise strongly decreased compared to the 1880–1950 period (**Figure 3**).

Mineral Variations

The mineral constituents of core SY-2 at 44–85 cm (1880–1944 A.D.) are detrital minerals, including quartz, feldspars, and mica and a small amount of clay minerals, such as chamosite and clinochlore. The upper part (0–40 cm; 1945–2018 A.D.) is still dominated by detrital minerals but is characterized by various carbonates, including monohydrocalcite, calcite, and dolomite and a small amount of halite. In this part, the average content of carbonates is 9.5%, with two higher phases for 29–36 cm (1955–1968 A.D.) with a value 11% and 0–16 cm (1998–2018 A.D.) with a value 13%. In carbonates, monohydrocalcite is predominant, with a maximum content of 26% (**Figure 4**).

DISCUSSION

Core Chronology

The ^{137}Cs activity versus depth shows no tailing effect, indicating that the vertical migration of ^{137}Cs can be neglected in Sayinwusu Lake (Audry et al., 2004). The first appearance of ^{137}Cs activity at a depth of 36 cm can be dated to the early 1950s (most likely 1952 A.D.) (Jin et al., 2010; Liu et al., 2012). The peak of ^{137}Cs activity at a depth of 30 cm is assigned to the maximum atmospheric global fallout corresponding to 1963 A.D. (Robbins and Edgington, 1975). The CRS dating model suggests an age of 1968 (+11/−16) A.D. at 30 cm and an age of 1955 (+16/−33) A.D. at 36 cm (**Figure 2B**). The ^{137} Cs dating yields ages of 1955 A.D. at 36 cm and 1963 A.D. at 30 cm, which is in general agreement with the ^{210}Pb dates. However, the Chernobyl accident in 1986 A.D. is not identified in the studied core, similar to other lacustrine

TABLE 1 | Measured results and standard errors (2σ) for ^{210}Pb and ^{137}Cs dating.

Sample ID	Depth (cm)	Mass depth (g/cm^2)	^{137}Cs (Bq/kg)	Errors (± 2σ)	^{210}P$_{bex}$ (Bq/kg)	Errors (± 2σ)	^{226}Ra (Bq/kg)	^{210}Pb$_T$ (Bq/kg)
SY-2-2	2	0.43	8.52	2.65	253.39	22.60	42.84	296.23
SY-2-4	4	1.21	3.54	1.85	221.00	20.43	35.51	256.51
SY-2-6	6	2.31	2.40	1.22	159.48	12.85	36.30	195.78
SY-2-8	8	3.61	3.22	1.90	148.99	12.04	30.84	179.83
SY-2-10	10	4.96	3.05	2.45	99.54	10.33	32.96	132.50
SY-2-12	12	6.65	5.01	2.84	106.84	10.24	45.12	151.96
SY-2-14	14	7.99	10.88	3.10	54.84	7.67	44.89	99.73
SY-2-16	16	9.29	7.40	2.40	69.47	8.26	44.03	113.49
SY-2-18	18	10.73	5.08	2.14	107.76	10.22	42.91	150.67
SY-2-20	20	11.95	14.91	3.75	74.20	9.65	58.19	132.40
SY-2-22	22	13.53	4.07	1.66	97.94	10.36	35.01	132.96
SY-2-24	24	14.88	14.81	2.78	67.85	8.49	54.98	122.84
SY-2-26	26	16.33	8.09	2.44	78.36	8.69	59.72	138.09
SY-2-28	28	18.03	10.46	2.80	59.49	8.03	43.05	102.54
SY-2-30	30	19.70	18.47	3.51	62.64	8.80	48.31	110.95
SY-2-32	32	21.23	10.54	3.06	38.47	5.05	32.64	71.11
SY-2-34	34	23.02	4.28	1.73	23.32	4.20	34.76	58.07
SY-2-36	36	24.92	1.83	1.41	34.64	5.11	33.92	68.55
SY-2-38	38	26.95	0.00	—	85.83	10.66	34.89	120.72
SY-2-40	40	29.01	0.00	—	14.32	2.87	34.51	48.83
SY-2-42	42	31.91	0.00	—	7.62	2.49	40.44	48.06
SY-2-44	44	34.99	0.00	—	13.15	3.01	35.24	48.38
SY-2-46	46	38.28	0.00	—	12.18	3.33	32.28	44.47
SY-2-48	48	41.92	0.00	—	5.74	2.12	51.04	56.78
SY-2-50	50	45.36	0.00	—	6.74	2.50	41.85	48.60

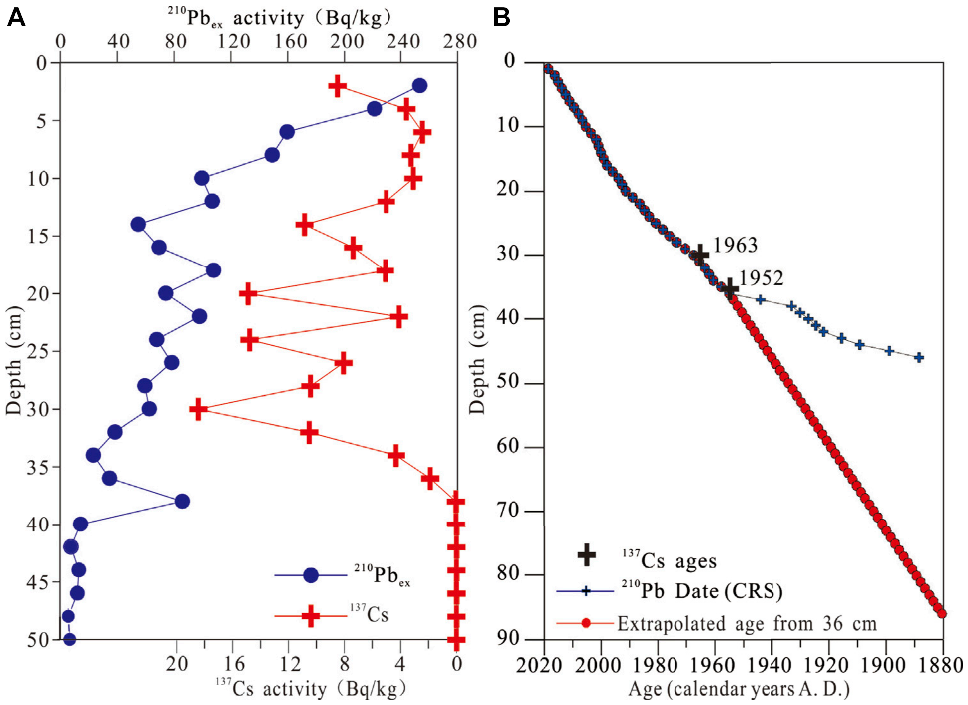

FIGURE 2 | Age model for sediment core SY-2. **(A)** ^{137}Cs and excess ^{210}Pb (^{210}Pb$_{ex}$) activity versus depth. **(B)** Age-depth relation from ^{210}Pb and ^{137}Cs dating.

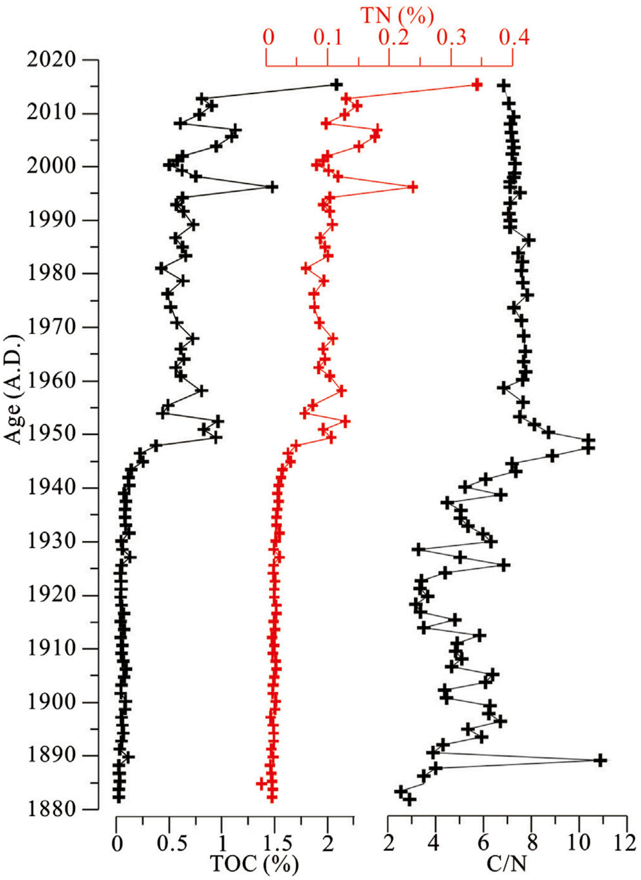

FIGURE 3 | TOC and TN contents and the C/N ratios in sediment core SY-2.

sediment records in China and Japan, because of its small impact on ^{137}Cs activity in these areas (Liu et al., 2012; Zhang et al., 2012).

Based on the CRS dating model, the sedimentation rate decreases below 36 cm (**Figure 2B**). Clearly, this fact does not accord with the lacustrine sedimentary characteristics, which indicates that the chronology of the ^{210}Pb CRS dating model is not reliable in the lower part of the sediment core (> 36 cm, before 1952 A.D.). Considering that: 1) there is no surface runoff recharge to the lakes in the BJD, and more than 90% of the lake recharge depends on groundwater (Dong et al., 2016; Wang et al., 2016); 2) although the lake sediments are from the surrounding aeolian sand, most of the aeolian sand was transported to the lake shore by saltation and creep (Wang et al., 2018), and sand from the shores is eroded by waves and then distributed in the lake (Li et al., 2018); 3) the locations of lakes and mega-dunes are relatively fixed (Yang et al., 2011; Wang et al., 2016); 4) human and animal activities are limited in the desert, so the lake sediment sequence is considered as formed continuously; 5) the ^{210}Pb and ^{137}Cs dating of adjacent lakes indicate that the sediment accumulation rates were relatively stable in the last century (Herzschuh et al., 2006; Liu et al., 2016); and 6) the average content of carbonate is only 9.5% in the upper part of the sediment core SY-2, which has a limited effect on the deposition rate. Therefore, the age of lower sediments (> 36 cm) can be dated by the average mass accumulation rate and that of the upper sediments (< 36 cm) can be determined by the CRS dating model. Finally, the obtained results show that the sediment core covers a period of ~1880–2018 A.D. and that the average sedimentation rate of the upper sediments is 0.57 (+0.19/−0.20) cm/a by CRS age model, which is consistent with those of other lakes in the BJD (Liu et al., 2016).

Proxy Interpretation

TOC, TN, and C/N

The C/N ratios of sediment core SY-2 are less than 10, with an average of 6.25, indicating that the organic matter of these sediments is autochthonous, which is consistent with results from other lakes in the BJD (Dong et al., 2018). The lack of a relationship between TOC and C/N (**Figure 5A**) also suggests that the organic matter of these sediments is autochthonous and reflects primary productivity (Lu and An, 2010). Due to the high salinity, no fish are found in the lake, and no animals, such as camels, drink the lake water. In addition, the administrative region of Alxa Right Banner was established in 1961. Due to government policies and the improvement of living conditions, most herders moved away from the desert in the last 20 or 30 years (based on communications with local herders). Therefore, grazing and local people have little effect on primary productivity. The TOC content reflects primary productivity, which mostly includes endogenous plants in the lake, such as algae and aquatic plants (Kai et al., 2019).

The significant positive relationship between TOC and TN (R^2 = 0.98, $p < 0.001$; **Figure 5B**) observed for SY-2 core sediments suggests that TOC and TN are mainly autochthonous in the lake and that inorganic nitrogen from terrestrial materials is negligible (~0.05%) (e.g., Liu et al., 2009). Changes in TN indicate the nutritional status of the lake, which is strongly subject to changes in water temperature. Water temperature not only affects the change in TN but also directly and significantly affects the growth of plankton in lakes, thus changing the content of endogenous organic carbon (Lu and An, 2010). Therefore, the significant positive relationship between TOC and TN indicates that higher values of TOC and TN represent higher primary productivity and higher temperatures.

Mineralogy

For the lakes in the hinterland of the BJD, the lacustrine sediments were mainly from the aeolian deposits around the lakes (Li et al., 2018). The mineral compositions of surface sediments in lakes show that detrital minerals compose more than 90% and that the saline minerals in lakes are autochthonous (Suhui et al., 2015).

Authigenic carbonate deposition is related to many factors, such as temperature, salinity, and primary productivity within lakes (Kelts and Hsü, 1978; Tucker and Wright, 1990). In this study, the contents of organic matter and carbonate increased almost simultaneously. Due to the increased productivity, more CO_2 (aq) assimilation occurs by thriving algae photosynthesis

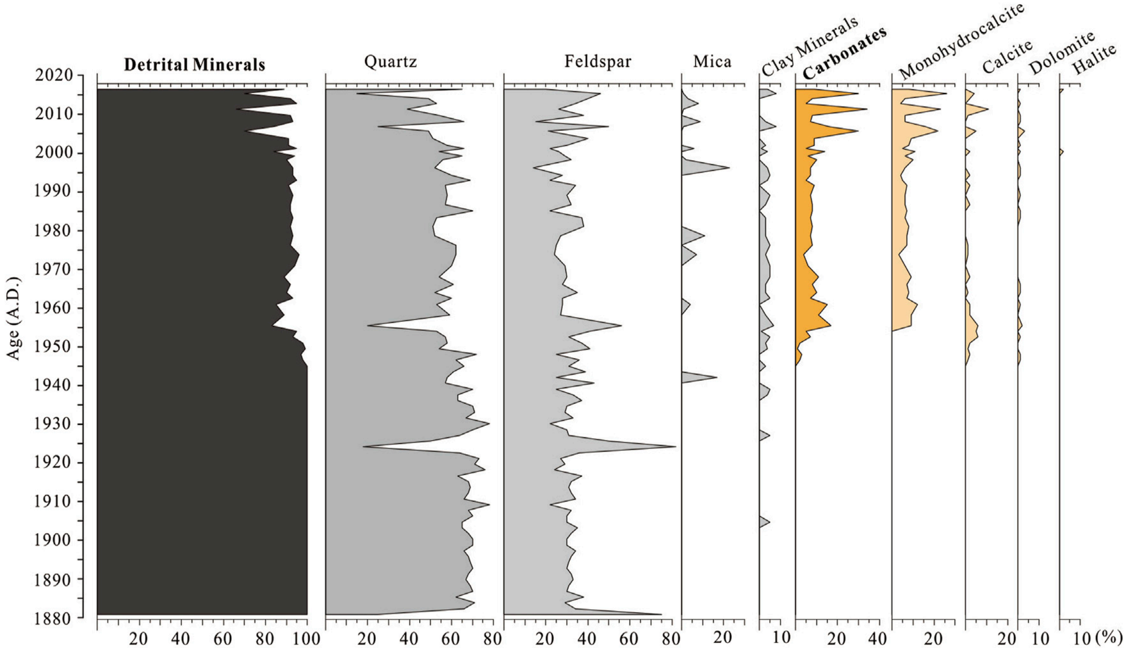

FIGURE 4 | Variations in mineral composition in core SY-2 from the BJD.

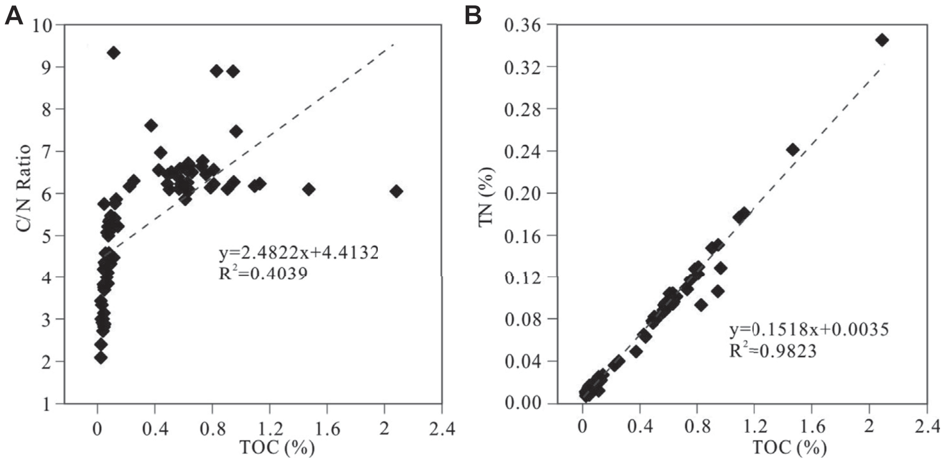

FIGURE 5 | Relationships of TOC content with C/N ratio and TN content in the SY-2 core.

(Opitz et al., 2012), leading to supersaturation of CO_3^{2-}, and promoting the deposition of carbonates via the reaction $2HCO_3^- \rightarrow CO_2\,(aq) + H_2O + CO_3^{2-}$ (Kelts and Hsü, 1978; Zhang et al., 2010). However, in the studied lake, the TOC and TN contents are very low, with average values of 0.77 and 0.13% in the 1950–2018 periods, respectively. This indicated that the primary productivity is very low compared to other lakes, such as Qinghai Lake (Chen et al., 2021) and Bosten Lake (Zhang et al., 2010). Therefore, the primary productivity may be minimal for carbonate precipitation.

Many previous studies suggest that salinity is the most important factor for carbonate precipitation in arid areas (Qiang et al., 2005; Wang et al., 2013; Li et al., 2016). The mineral composition of the surface sediments of the lakes in the BJD also indicated that the saline mineralogical composition and content in lake sediments vary with lake water salinity (Suhui et al., 2015). In core SY-2, the saline minerals are mainly carbonates, including monohydrocalcite, calcite, and dolomite. In the natural environment, monohydrocalcite is predominantly found in water with a high Mg/Ca ratio (high salinity) (Han et al.,

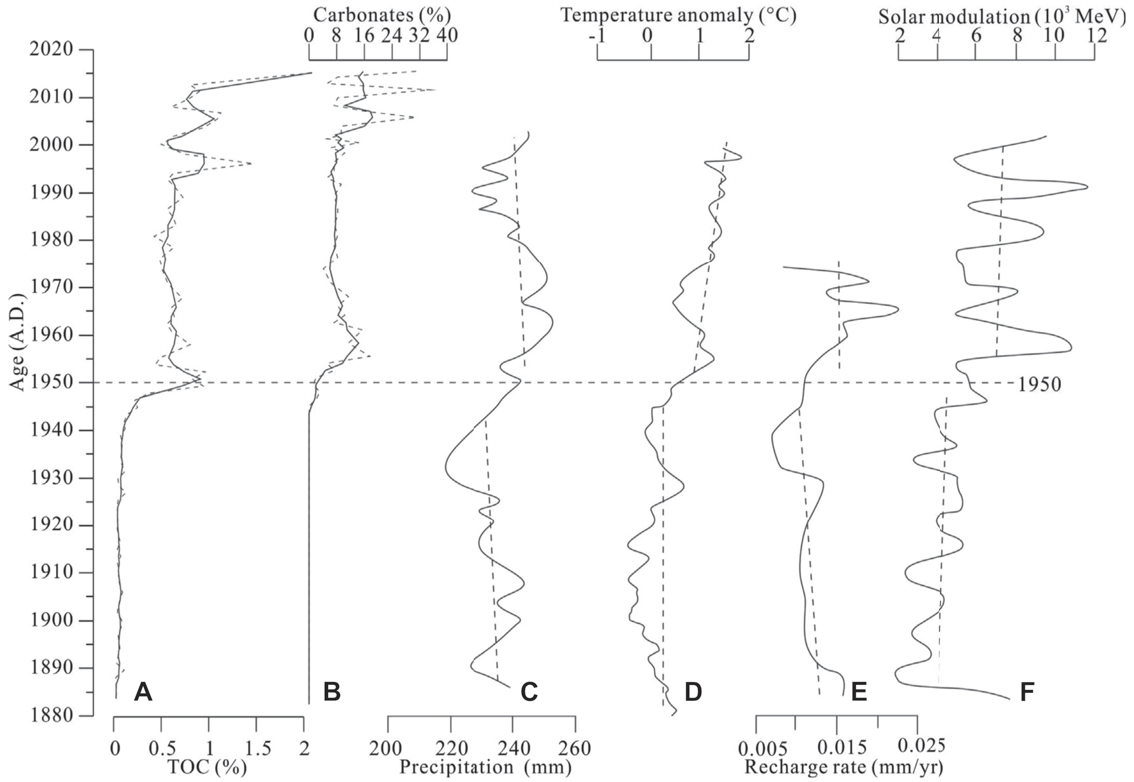

FIGURE 6 | TOC and carbonate contents of the SY-2 sedimentary core and comparisons with other regional climate records. **(A)-(B)** The TOC and carbonate contents of the SY-2 sedimentary core in this study. **(C)** Reconstruction of precipitation at the southern margin of the BJD (Zhang et al., 2015). **(D)** Temperature changes in Northwest China (Ding, 2010). **(E)** Recharge rate of the BJD (Gates et al., 2008b). **(F)** Solar activity (Muscheler et al., 2007).

2020), such as in the limestone of Ikka Fjord, Greenland (Mg/Ca > 5) (Dahl and Buchardt, 2006); Manito Lake sediments, Canada (Mg/Ca > 40) (Last, 2001); and Namco Lake sediments, Tibet (Mg/Ca > 10) (Li et al., 2009). High salinity, high Mg/Ca ratio, and high alkalinity in lake water facilitate the precipitation of dolomite (i.e., environments with high evaporation intensity) (Deckker and Last, 1988), and dolomite has also been considered an evaporative salt mineral in some studies (Qiang et al., 2005). Therefore, the carbonate content is regarded as an indicator of salinity in studies of lake change (Qiang et al., 2005; Wang et al., 2013).

Lake Evolution and Local Climate Records Over the Past 140 Years

Based on the TOC, TN, and carbonate mineral contents, the evolution of Sayinwusu Lake since 1880 can be divided into two periods. The first period dates from 1880 to 1950 (86–43 cm). During this period, the low contents of TOC and TN and predominantly detrital mineral composition indicate that the lake primary productivity and salinity were low (**Figures 6A,B**). The second period represents the time from 1950 to 2018 (above 43 cm). The contents of TOC, TN, and carbonate minerals increased rapidly at the beginning of the 1950s, indicating that the primary productivity and salinity of the lake increased (**Figures 6A,B**). Meanwhile, the simultaneous increases in TOC, TN, and carbonate minerals suggest an increase in regional temperature and evaporation effects. During the second period, the TOC, TN, and carbonate minerals were higher during 1955–1968 and 1998–2018, indicating relatively high temperatures and evaporation effects.

Due to the special geographical conditions, there have been a few studies on the reconstruction of regional climate and environment during the last several 100 years. A palynological study of Baoritaolegai Lake sediments in the southeastern BJD over the last 160 years identified three dry periods: the mid 1870s to the beginning of the 1900s, the beginning of the 1920s to the late 1930s, and the beginning of the 1960s to the present (Herzschuh et al., 2006). The tree rings of the shrub (*Zygophyllum xanthoxylum Maxim*) were affected by precipitation during the last 160 years, and three dry phases were identified: 1840s to early 1850s, early 1890s–1900s, and late 1970s to mid 1980s (Xiao et al., 2012). However, the salinity changes from the lake sediment archives in this study do not agree well with the climatic records of tree rings and palynology in the desert hinterland. There are two possible reasons for the differences. One explanation is that the local precipitation in the desert could not sustain the lakes (Ma et al., 2014). The lakes in the desert area are mainly recharged by groundwater, and the recharge source is from adjacent areas and/or other areas (e.g., Chen et al., 2004; Ma and Edmunds, 2006; Gates et al., 2008a; Shao et al., 2012; Dong et al., 2016; Wang et al., 2016). Similar to the groundwater recharge lakes in the Sahara Desert, lake evolution has little relevance in terms of the local climate but much pertinence regarding changes in groundwater recharge (Creutz et al., 2016). The other explanation is that the climate records of vegetation in the hinterland of the desert reflect precipitation before and during the vegetation growing season, especially the summer (Xiao et al., 2012). The hydrogen and oxygen isotopes of modern precipitation show that the precipitation in the desert is mainly from westerly moisture and that part of the summer is affected by the East Asian summer monsoon (Cao et al., 2020). Therefore, the climate reconstructed by vegetation records in desert areas is a mixed signal of westerly moisture and East Asian summer monsoon precipitation. Consequently, it is reasonable that there is no significant relationship between lake evolution and local precipitation in the BJD.

The Factors Influencing Lake Evolution

In this study, the simultaneous increases in TOC and TN contents indicate that the regional temperature rose at the beginning of the 1950s. Research integrating ice cores, stalagmites, and lake records reveals that the temperature of Northwest China warmed rapidly at the beginning of the 1950s (**Figure 6D**; Ding, 2010), which is consistent with the rapid warming trend in China (Ge et al., 2015). With rising temperatures, precipitation in the arid region of Northwest China has increased in recent decades (Chen et al., 2020; Liu et al., 2021). The reconstructed precipitation from tree rings shows that the annual precipitation began to increase at the beginning of the 1950s on the southern margin of the desert and the northeastern Tibetan Plateau (**Figure 6C**; Yang et al., 2010; Yang et al., 2014; Zhang et al., 2015; Liu et al., 2021). Although the recharge source of groundwater in the BJD is still controversial, previous studies have suggested that it is mainly the mountain areas in the southern BJD and/or the northern Tibetan Plateau (Chen et al., 2004; Ma and Edmunds, 2006; Gates et al., 2008a; Gates et al., 2008b; Dong et al., 2016). Therefore, the precipitation in recharge source areas has increased in recent decades. The recharge rate of groundwater in the southeastern BJD shows a high value after 1950 A.D. (Gates et al., 2008b), which indicates that the groundwater recharge amount of the lakes in the BJD increased (**Figure 6E**).

Although precipitation is important for lake evolution, evaporation is also an important control on the water balance, especially in arid and semiarid regions (Wu et al., 2020). Modern observations suggest that the evaporation of lakes is closely correlated with air temperature and water temperature in the BJD (Han et al., 2018). Due to the warm island effect of lakes in the BJD, the annual temperature in the lake group region is approximately 1.6°C higher than those in other regions (Liang et al., 2020), which may cause a more intense evaporation effect. When the enhancement of the evaporation effect caused by the temperature rise is much greater than the increased precipitation, the effective moisture decreases (Li et al., 2016; Wu et al., 2020). The salinization of lakes in the BJD at the beginning of the 1950s and the increased temperature simultaneously suggest that the increase in evaporation induced by the temperature rise was greater than that in groundwater recharge (Li et al., 2016; Wu et al., 2020). Wind speed is another important factor for evaporation. Due to the high sand mountains, the wind speed is low in the hinterland of the BJD (Ma and Wang, 2016). The carbonate content has no obvious relationship with the wind speed in the last 60 years but has good consistency with the temperature changes (**Figure 7**). This phenomenon is consistent with modern instrumental observations (Han et al., 2018).

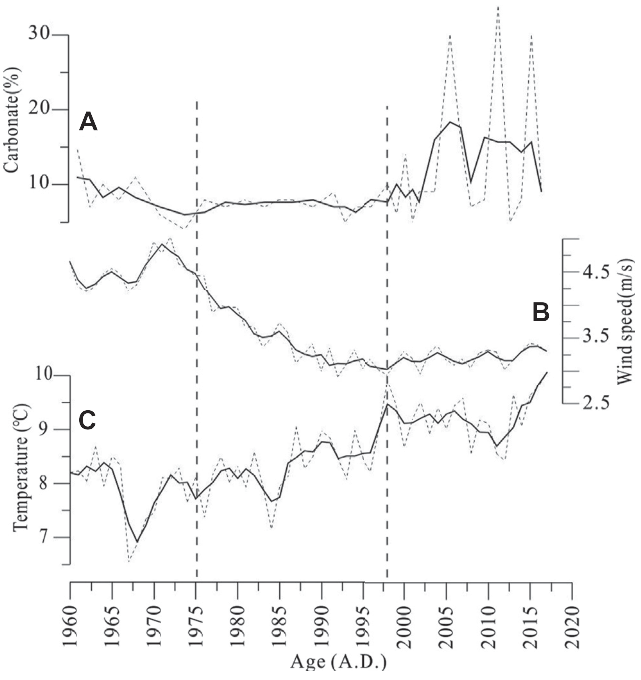

FIGURE 7 | Relationships between the carbonate contents of the SY-2 core **(A)** and the annual average temperature **(B)** and wind speed **(C)** during 1960–2017.

Regionally, tree-ring records suggest that the last dry period was from the beginning of the 1950s to the present in the Hexi Corridor (Deng et al., 2017). In the long term, the drought periods in the Hexi Corridor tend to coincide with solar activity, which may be a possible external driving factor (**Figure 6F**; Muscheler et al., 2007; Deng et al., 2017). Several lakes in the northeastern Tibetan Plateau have also shown salinization resulting from high temperatures in recent decades, such as Hala Lake (Cao et al., 2007), Sugan Lake (Chen et al., 2009), and Qinghai Lake (Zhang et al., 2004). Furthermore, dry basins or shrinking lakes in the geological period also occurred under the high temperature and precipitation climate in the northeastern Tibetan Plateau and Hexi Corridor (Liu et al., 2013; Wang et al., 2014; Wu et al., 2020). Therefore, for other areas of the world, although there are differences in the timing of temperature increases, they all lead to droughts and extreme events (Hegerl et al., 2018; Neukom et al., 2019; Woolway et al., 2020; Che et al., 2021).

In the context of global warming (Neukom et al., 2019), lake surface water temperatures have increased worldwide at a global average rate of 0.34°C decade^{-1}, and global annual mean lake evaporation rates are forecast to increase 16% by 2,100 relative to 2006–2015 (Woolway et al., 2020). Arid zones are more sensitive than other areas to temperature changes during global climate change, especially desert areas (Chen et al., 2015; Huang et al., 2016; Liang et al., 2020). Remote sensing data show that the lake areas in the BJD and central Asia have decreased in recent decades (Zhang et al., 2013; Che et al., 2021). With ongoing global warming, our results suggest that lakes in arid areas, especially in desert areas, will become increasingly salty, and this issue should have been addressed earlier.

CONCLUSION

^{210}Pb and ^{137}Cs dating, TOC, TN, and mineral content analysis were used to reconstruct the lake hydrological changes during the past 140 years. From 1880 to 1950, the primary productivity and salinity of Sayinwusu Lake were low. From 1950 to 2018, the TOC, TN, and carbonate minerals increased rapidly at the beginning of the 1950s, indicating that the primary productivity and salinity of the lake increased.

At the beginning of the 1950s, the TOC and TN contents increased synchronously, indicating increases in primary productivity and temperature. Regional climate reconstruction data also suggest that precipitation and temperature have increased in recent decades. However, the enhancement of the evaporation effect caused by the temperature rise is much greater than the increased precipitation in arid areas, especially in desert areas.

DATA AVAILABILITY STATEMENT

The original contributions presented in the study are included in the article/Supplementary Material; further inquiries can be directed to the corresponding authors.

AUTHOR CONTRIBUTIONS

All authors listed have made substantial, direct, and intellectual contributions to the work and approved it for publication.

FUNDING

This research was financially supported by the National Natural Science Foundation of China (41807420 and 41871021), the National Key R and D Programme of China (No. 2019YFC0409201), the project of the China Geological Survey (121201106000150093) and the Basic Research Programme of Institute of Hydrogeology and Environmental Geology, Chinese Academy of Geological Sciences (CAGS) (SK202007).

ACKNOWLEDGMENTS

We are grateful to Li Zhuolun at Lanzhou University and Le Cao, Pucheng Zhu, Jinsong Yang, Dejun Wan, Kai Ning, Min Liu, and other colleagues at the Institute of Hydrogeology and Environmental Geology, CAGS, who have contributed to our field work and data analysis.

REFERENCES

Appleby, P. G. (2001). "Chronostratigraphic Techniques in Recent Sediments," in *Tracking Environmental Change Using Lake Sediments: Basin Analysis, Coring, and Chronological Techniques*. Editors W.M. Last and J.P. Smol (Dordrecht, Netherlands: Springer Netherlands), 171–203.

Appleby, P. G., and Oldfield, F. (1978). The Calculation of Lead-210 Dates Assuming a Constant Rate of Supply of Unsupported 210Pb to the Sediment. *Catena.* 5, 1–8. doi:10.1016/s0341-8162(78)80002-2

Audry, S., Schäfer, J., Blanc, G., and Jouanneau, J.-M. (2004). Fifty-Year Sedimentary Record of Heavy Metal Pollution (Cd, Zn, Cu, Pb) in the Lot River Reservoirs (France). *Environ. Pollut.* 132, 413–426. doi:10.1016/j.envpol.2004.05.025

Bai, Y., Wang, N. A., He, R. X., Li, J. M., and Lai, Z. P. (2011). Ground Penetrating Radar Images and Optically Stimulated Luminescence Dating for Lacustrine Deposition of the Badain Jaran Desert. *J. Desert Res.* 31, 842–847.

BGMIMAR (Bureau of Geology Mineral Resources of Inner Mongolia Autonomous Region) (1991). *Regional Geology of Inner Mongolia Autonomous Region*. Beijing, China: Geological Publishing House.

Cao, J., Zhang, J. W., Zhang, C. J., and Chen, F. H. (2007). Environmental Changes During the Past 800 Years Recorded in Lake Sediments From Hala Lake on the Northern Tibetan Plateau. *Quat. Sci.* 27, 100–107.

Cao, L., Shen, J. M., Nie, Z. L., Meng, L. Q., Liu, M., and Wang, Z. (2020). Stable Isotopic Characteristics of Precipitation and Moisture Recycling in the Badain Jaran Desert. *Earth Sci.* doi:10.3799/dqkx.2020.273

Che, X., Feng, M., Sun, Q., Sexton, J. O., Channan, S., and Liu, J. (2021). The Decrease in Lake Numbers and Areas in Central Asia Investigated Using a Landsat-Derived Water Dataset. *Remote Sensing.* 13, 1032. doi:10.3390/rs13051032

Chen, C., Zhang, X., Lu, H., Jin, L., Du, Y., and Chen, F. (2020). Increasing Summer Precipitation in Arid Central Asia Linked to the Weakening of the East Asian Summer Monsoon in the Recent Decades. *Int. J. Climatol.* 41, 1024–1038. doi:10.1002/joc.6727

Chen, J., Chen, F., Zhang, E., Brooks, S. J., Zhou, A., and Zhang, J. (2009). A 1000-Year Chironomid-Based Salinity Reconstruction From Varved Sediments of Sugan Lake, Qaidam Basin, Arid Northwest China, and its Palaeoclimatic Significance. *Chin. Sci. Bull.* 54, 3749–3759. doi:10.1007/s11434-009-0201-8

Chen, J. S., Li, L., Wang, J. Y., Barry, D. A., Sheng, X. F., Gu, W. Z., et al. (2004). Groundwater Maintains Dune Landscape. *Nature.* 432, 459–460. doi:10.1038/432459a

Chen, T., Lai, Z., Liu, S., Wang, Y., Wang, Z.-t., Miao, X., et al. (2019). Luminescence Chronology and Palaeoenvironmental Significance of Limnic Relics From the Badain Jaran Desert, Northern China. *J. Asian Earth Sci.* 177, 240–249. doi:10.1016/j.jseaes.2019.03.024

Chen, X., Meng, X., Song, Y., Zhang, B., Wan, Z., Zhou, B., et al. (2021). Spatial Patterns of Organic and Inorganic Carbon in Lake Qinghai Surficial Sediments and Carbon Burial Estimation. *Front. Earth Sci.* 9. doi:10.3389/feart.2021.714936

Chen, Y., Li, Z., Fan, Y., Wang, H., and Deng, H. (2015). Progress and Prospects of Climate Change Impacts on Hydrology in the Arid Region of Northwest China. *Environ. Res.* 139, 11–19. doi:10.1016/j.envres.2014.12.029

Creutz, M., Van Bocxlaer, B., Abderamane, M., and Verschuren, D. (2016). Recent Environmental History of the Desert Oasis Lakes at Ounianga Serir, Chad. *J. Paleolimnol.* 55, 167–183. doi:10.1007/s10933-015-9874-y

Cui, X. J., Dong, Z. B., Lu, J. F., Wang, M., Li, J. Y., and Luo, W. Y. (2014). Relationship Between Vegetation Feature and Physiognomy Morphology of Mega-Dunes in Badain Jaran Desert. *Bull. Soil Water Conserv.* 34, 278–283.

Dahl, K., and Buchardt, B. (2006). Monohydrocalcite in the Arctic Ikka Fjord, SW Greenland: First Reported Marine Occurrence. *J. Sediment. Res.* 76, 460–471. doi:10.2110/jsr.2006.035

Deckker, P. D., and Last, W. M. (1988). Modern Dolomite Deposition in Continental, Saline Lakes, Western Victoria, Australia. *Geology.* 16, 29. doi:10.1130/0091-7613(1988)016<0029:mddics>2.3.co;2

Deng, Y., Gou, X., Gao, L., Yang, M., and Zhang, F. (2017). Tree-Ring Recorded Moisture Variations Over the Past Millennium in the Hexi Corridor, Northwest China. *Environ. Earth Sci.* 76, 272. doi:10.1007/s12665-017-6581-1

Ding, Z. L. (2010). *Integrated Study on Environmental Evolution in Western China*. Meteorological Press.

Dong, C., Wang, N. a., Chen, J., Li, Z., Chen, H., Chen, L., et al. (2016). New Observational and Experimental Evidence for the Recharge Mechanism of the Lake Group in the Alxa Desert, north-central China. *J. Arid Environments.* 124, 48–61. doi:10.1016/j.jaridenv.2015.07.008

Dong, S., Li, Z., Chen, Q., and Wei, Z. (2018). Total Organic Carbon and its Environmental Significance for the Surface Sediments in Groundwater Recharged Lakes From the Badain Jaran Desert, Northwest China. *J. Limnol.* 77, 121–129. doi:10.4081/jlimnol.2017.1667

Dong, Z., Qian, G., Lv, P., and Hu, G. (2013). Investigation of the Sand Sea With the Tallest Dunes on Earth: China's Badain Jaran Sand Sea. *Earth-Science Rev.* 120, 20–39. doi:10.1016/j.earscirev.2013.02.003

Dong, Z., Wang, T., and Wang, X. (2004). Geomorphology of the Megadunes in the Badain Jaran Desert. *Geomorphology.* 60, 191–203. doi:10.1016/j.geomorph.2003.07.023

Fu, C., Wu, H., Zhu, Z., Song, C., Xue, B., Wu, H., et al. (2021). Exploring the Potential Factors on the Striking Water Level Variation of the Two Largest Semi-Arid-Region Lakes in Northeastern Asia. *Catena.* 198, 105037. doi:10.1016/j.catena.2020.105037

Gates, J. B., Edmunds, W. M., Darling, W. G., Ma, J., Pang, Z., and Young, A. A. (2008a). Conceptual Model of Recharge to Southeastern Badain Jaran Desert Groundwater and Lakes From Environmental Tracers. *Appl. Geochem.* 23, 3519–3534. doi:10.1016/j.apgeochem.2008.07.019

Gates, J. B., Edmunds, W. M., Jinzhu Ma, M., and Sheppard, P. R. (2008b). A 700-Year History of Groundwater Recharge in the Drylands of NW China. *The Holocene.* 18, 1045–1054. doi:10.1177/0959683608095575

Ge, Q. S., Zheng, J. Y., and Hao, Z. X. (2015). PAGES Synthesis Study on Climate Changes in Asia over the Last 2000 years: Progresses and Perspectives. *Acta Geogr. Sin.* 70, 355–363.

Han, L., Li, Y., Liu, X., and Yang, H. (2020). Paleoclimatic Reconstruction and the Response of Carbonate Minerals During the Past 8000 Years Over the Northeast Tibetan Plateau. *Quat. Int.* 553, 94–103. doi:10.1016/j.quaint.2020.06.009

Han, P. F., Wang, X. S., Hu, X. N., Jiang, X. W., and Zhou, Y. Y. (2018). Dynamic Relationship Between Lake Surface Evaporation and Meterorological Factors in the Badian Jaran Desert. *Arid Zone Res.* 35, 1013–1020.

Hedges, J. I., Baldock, J. A., Gélinas, Y., Lee, C., Peterson, M. L., and Wakeham, S. G. (2002). The Biochemical and Elemental Compositions of Marine Plankton: a NMR Perspective. *Mar. Chem.* 78, 47–63. doi:10.1016/s0304-4203(02)00009-9

Hegerl, G. C., Brönnimann, S., Schurer, A., and Cowan, T. (2018). The Early 20th Century Warming: Anomalies, Causes, and Consequences. *Wires Clim. Change.* 9, e522. doi:10.1002/wcc.522

Herzschuh, U., Kürschner, H., Battarbee, R., and Holmes, J. (2006). Desert Plant Pollen Production and a 160-Year Record of Vegetation and Climate Change on the Alashan Plateau, NW China. *Veget Hist. Archaeobot.* 15, 181–190. doi:10.1007/s00334-005-0031-9

Hu, F., and Yang, X. (2016). Geochemical and Geomorphological Evidence for the Provenance of Aeolian Deposits in the Badain Jaran Desert, Northwestern China. *Quat. Sci. Rev.* 131, 179–192. doi:10.1016/j.quascirev.2015.10.039

Hu, W. F., Wang, N. A., Zhao, L. Q., Ning, K., Zhang, H. X., and Sun, J. (2015). Water-Heat Exchange Over a Typical Lake in Badain Jaran Desert, China. *Prog. Geogr.* 34, 1061–1071.

Huang, J., Yu, H., Guan, X., Wang, G., and Guo, R. (2016). Accelerated Dryland Expansion Under Climate Change. *Nat. Clim Change.* 6, 166–171. doi:10.1038/nclimate2837

Jin, Z., Han, Y., and Chen, L. (2010). Past Atmospheric Pb Deposition in Lake Qinghai, Northeastern Tibetan Plateau. *J. Paleolimnol.* 43, 551–563. doi:10.1007/s10933-009-9351-6

Kai, N., Naiang, W., Xiaonan, L., Zhuolun, L., Jiaqi1, S., Ran, A., et al. (2019). A Grain Size and N-Alkanes Record of Holocene Environmental Evolution From a Groundwater Recharge Lake in Badain Jaran Desert, Northwestern China. *The Holocene.* 29, 1045–1058. doi:10.1177/0959683619831430

Kelts, K., and Hsü, K. J. (1978). "Freshwater Carbonate Sedimentation," in *Lakes: Chemistry, Geology, Physics*. Editor A. Lerman (New York: Springer-Verlag), 295–323. doi:10.1007/978-1-4757-1152-3_9

Last, W. M. (2001). "Tracking Environmental Change Using lake Sediments: Physical and Geochemical Methods," in *Mineralogical Analysis of Lake Sediments*. Editor W.M. Last (Last (Netherlands: Springer), 143–187.

Li, M., Kang, S., Zhu, L., Wang, F., Wang, J., Yi, C., et al. (2009). On the Unusual Holocene Carbonate Sediment in Lake Nam Co, Central Tibet. *J. Mt. Sci.* 6, 346–353. doi:10.1007/s11629-009-1020-8

Li, Z., Wang, N. a., Cheng, H., and Li, Y. (2016). Early-Middle Holocene Hydroclimate Changes in the Asian Monsoon Margin of Northwest China Inferred From Huahai Terminal lake Records. *J. Paleolimnol.* 55, 289–302. doi:10.1007/s10933-016-9880-8

Li, Z., Wei, Z., Dong, S., and Chen, Q. (2018). The Paleoenvironmental Significance of Spatial Distributions of Grain Size in Groundwater-Recharged Lakes: A Case Study in the Hinterland of the Badain Jaran Desert, Northwest China. *Earth Surf. Process. Landforms.* 43, 363–372. doi:10.1002/esp.4248

Liang, X., Zhao, L., Xu, X., Niu, Z., Zhang, W., and Wang, N. a. (2020). Plant Phenological Responses to the Warm Island Effect in the Lake Group Region of the Badain Jaran Desert, Northwestern China. *Ecol. Inform.* 57, 101066. doi:10.1016/j.ecoinf.2020.101066

Liu, S., NarentuyaXia, B., Xia, G., and Tian, M. (2012). Using 210Pbuns and 137Cs to Date Recent Sediment Cores From the Badain Jaran Desert, Inner Mongolia, China. *Quat. Geochronol.* 12, 30–39. doi:10.1016/j.quageo.2012.06.001

Liu, S. W., Chu, G. Q., and Lai, Z. P. (2016). Determination of Age and Sedimentation Rates Using Radionuclide (210Pbuns and 137Cs) Dating in Inter-Dune Lakes of the Badain Jaran Desert, China. *Acta Geol. Sin.* 90, 2013–2022.

Liu, W., Gou, X., Li, J., Huo, Y., Yang, M., Zhang, J., et al. (2021). Temperature Signals Complicate Tree-Ring Precipitation Reconstructions on the Northeastern Tibetan Plateau. *Glob. Planet. Change.* 200, 103460. doi:10.1016/j.gloplacha.2021.103460

Liu, W., Li, X., An, Z., Xu, L., and Zhang, Q. (2013). Total Organic Carbon Isotopes: a Novel Proxy of Lake Level From Lake Qinghai in the Qinghai-Tibet Plateau, China. *Chem. Geology.* 347, 153–160. doi:10.1016/j.chemgeo.2013.04.009

Liu, X., Dong, H., Yang, X., Herzschuh, U., Zhang, E., Stuut, J.-B. W., et al. (2009). Late Holocene Forcing of the Asian Winter and Summer Monsoon as Evidenced by Proxy Records From the Northern Qinghai-Tibetan Plateau. *Earth Planet. Sci. Lett.* 280, 276–284. doi:10.1016/j.epsl.2009.01.041

Long, H., Lai, Z., Fuchs, M., Zhang, J., and Li, Y. (2012). Timing of Late Quaternary Palaeolake Evolution in Tengger Desert of Northern China and its Possible Forcing Mechanisms. *Glob. Planet. Change.* 92-93, 119–129. doi:10.1016/j.gloplacha.2012.05.014

Lopez, L. S., Hewitt, B. A., and Sharma, S. (2019). Reaching a Breaking point: How Is Climate Change Influencing the Timing of Ice Breakup in Lakes Across the Northern Hemisphere? *Limnol. Oceanogr.* 64, 2621–2631. doi:10.1002/lno.11239

Lu, F. Y., and An, Z. S. (2010). Pretreatment Methods for Analyzing the Total Organic Carbon and Nitrogen Contents of Heqing Core Sediments and Their Environmental Significances. *J. Geomech.* 46, 393–401.

Lu, Y., Wang, N. A., Li, G. P., Li, Z. L., Dong, C. Y., and Lu, J. W. (2010). Spatial Distribution of Lakes Hydro-Chemical Types in Badain Jaran Desert. *J. Lake Sci.* 22, 774–782.

Ma, J., and Edmunds, W. M. (2006). Groundwater and Lake Evolution in the Badain Jaran Desert Ecosystem, Inner Mongolia. *Hydrogeol. J.* 14, 1231–1243. doi:10.1007/s10040-006-0045-0

Ma, N., and Wang, N. A. (2016). On the Simulation of Evaporation From Lake Surface in the Hinterland of the Badain Jaran Desert. *Arid Zone Res.* 33, 1141–1149.

Ma, N., Wang, N., Zhao, L., Zhang, Z., Dong, C., and Shen, S. (2014). Observation of Mega-Dune Evaporation after Various Rain Events in the Hinterland of Badain Jaran Desert, China. *Chin. Sci. Bull.* 59, 162–170. doi:10.1007/s11434-013-0050-3

Meyers, P. A. (2003). Applications of Organic Geochemistry to Paleolimnological Reconstructions: a Summary of Examples From the Laurentian Great Lakes. *Org. Geochem.* 34, 261–289. doi:10.1016/s0146-6380(02)00168-7

Mischke, S. (2005). New Evidence for Origin of Badain Jaran Desert of Inner Mongoliafrom Granulometry and Thermoluminescence Dating. *J. Palaeogeogr.* 7, 79–97.

Muscheler, R., Joos, F., Beer, J., Müller, S. A., Vonmoos, M., and Snowball, I. (2007). Solar Activity During the Last 1000yr Inferred From Radionuclide Records. *Quat. Sci. Rev.* 26, 82–97. doi:10.1016/j.quascirev.2006.07.012

Neukom, R., Steiger, N., Gómez-Navarro, J. J., Wang, J., and Werner, J. P. (2019). No Evidence for Globally Coherent Warm and Cold Periods Over the

Preindustrial Common Era. *Nature.* 571, 550–554. doi:10.1038/s41586-019-1401-2

Ning, W. X., Liu, X. Y., and Wang, Z. T. (2021). Temperature and Precipitation Characteristics and Spatial Stratified Heterogeneity in Badain Jaran Desert. *J. Univ. Chin. Acad. Sci.* 38, 103–113.

Opitz, S., Wünnemann, B., Aichner, B., Dietze, E., Hartmann, K., Herzschuh, U., et al. (2012). Late Glacial and Holocene Development of Lake Donggi Cona, North-Eastern Tibetan Plateau, Inferred From Sedimentological Analysis. *Palaeogeogr. Palaeoclimatol. Palaeoecol.* 337-338, 159–176. doi:10.1016/j.palaeo.2012.04.013

Panizzo, V. N., Mackay, A. W., Rose, N. L., Rioual, P., and Leng, M. J. (2013). Recent Palaeolimnological Change Recorded in Lake Xiaolongwan, Northeast China: Climatic versus Anthropogenic Forcing. *Quat. Int.* 290-291, 322–334. doi:10.1016/j.quaint.2012.07.033

Qiang, M., Chen, F., Zhang, J., Gao, S., and Zhou, A. (2005). Climatic Changes Documented by Stable Isotopes of Sedimentary Carbonate in Lake Sugan, Northeastern Tibetan Plateau of China, since 2 kaBP. *Chin. Sci Bull.* 50, 1930–1939. doi:10.1360/04wd0285

Robbins, J. A., and Edgington, D. N. (1975). Determination of Recent Sedimentation Rates in Lake Michigan Using Pb-210 and Cs-137. *Geochimica et Cosmochimica Acta.* 39, 285–304. doi:10.1016/0016-7037(75)90198-2

Shao, T., Zhao, J., Zhou, Q., Dong, Z., and Ma, Y. (2012). Recharge Sources and Chemical Composition Types of Groundwater and Lake in the Badain Jaran Desert, Northwestern China. *J. Geogr. Sci.* 22, 479–496. doi:10.1007/s11442-012-0941-2

Suhui, M., Li, Z. L., Zhuolun, L., Naiang, W., Kai, N., and Meng, L. (2015). Mineralogical Assemblages in Surface Sediments and its Formation Mechanism in the Groundwater Recharged Lakes: a Case Study of Lakes in the Badain Jaran Desert. *J. Lake Sci.* 27, 727–734. doi:10.18307/2015.0422

Swarzenski, P. W. (2014). "210Pb Dating," in *Encyclopedia of Scientific Dating Methods*. Editors W. J. Rink and J. Thompson (Dordrecht, Netherlands: Springer Netherlands), 1–11. doi:10.1007/978-94-007-6326-5_236-1

Tucker, M. E., and Wright, V. P. (1990). "Carbonate Mineralogy and Chemistry," in *Carbonate Sedimentology*. Editors M. E. Tucker and V. P. Wright (Oxford, UK: Blackwell Science), 284–313.

Wan, D., Mao, X., Jin, Z., Song, L., Yang, J., and Yang, H. (2019). Sedimentary Biogeochemical Record in Lake Gonghai: Implications for Recent Lake Changes in Relatively Remote Areas of China. *Sci. Total Environ.* 649, 929–937. doi:10.1016/j.scitotenv.2018.08.331

Wang, F., Li, Z., Wang, X., Li, B., and Chen, F. (2018). Variation and Interplay of the Siberian High and Westerlies in Central-East Asia During the Past 1200kyr. *Aeolian Res.* 33, 62–81. doi:10.1016/j.aeolia.2018.05.003

Wang, F., Sun, D., Chen, F., Bloemendal, J., Guo, F., Li, Z., et al. (2015a). Formation and Evolution of the Badain Jaran Desert, North China, as Revealed by a Drill Core from the Desert centre and by Geological Survey. *Palaeogeogr. Palaeoclimatol. Palaeoecol.* 426, 139–158. doi:10.1016/j.palaeo.2015.03.011

Wang, M., Dong, Z., Luo, W., Lu, J., Li, J., Cui, X., et al. (2015b). Species Diversity of Vegetation and its Relationship With Soil Characteristics in the Southern Marginal Zone of the Badain Jaran Desert. *Acta Bot. Boreal. – Occident. Sin.* 35, 379–388.

Wang, H., Dong, H., Zhang, C. L., Jiang, H., Zhao, M., Liu, Z., et al. (2014). Water Depth Affecting Thaumarchaeol Production in Lake Qinghai, Northeastern Qinghai-Tibetan Plateau: Implications for Paleo Lake Levels and Paleoclimate. *Chem. Geology.* 368, 76–84. doi:10.1016/j.chemgeo.2014.01.009

Wang, N. a., Li, Z., Li, Y., and Cheng, H. (2013). Millennial-Scale Environmental Changes in the Asian Monsoon Margin During the Holocene, Implicated by the Lake Evolution of Huahai Lake in the Hexi Corridor of Northwest China. *Quat. Int.* 313-314, 100–109. doi:10.1016/j.quaint.2013.08.039

Wang, N., Ning, K., Li, Z., Wang, Y., Jia, P., and Ma, L. (2016). Holocene High Lake-Levels and Pan-Lake Period on Badain Jaran Desert. *Sci. China Earth Sci.* 59, 1633–1641. doi:10.1007/s11430-016-5307-7

Woolway, R. I., Kraemer, B. M., Lenters, J. D., Merchant, C. J., O'Reilly, C. M., and Sharma, S. (2020). Global Lake Responses to Climate Change. *Nat. Rev. Earth Environ.* 1, 388–403. doi:10.1038/s43017-020-0067-5

Wu, D., Zhou, A., Zhang, J., Chen, J., Li, G., Wang, Q., et al. (2020). Temperature-Induced Dry Climate in Basins in the Northeastern Tibetan Plateau During the Early to Middle Holocene. *Quat. Sci. Rev.* 237, 106311. doi:10.1016/j.quascirev.2020.106311

Xiao, S. C., Xiao, H. L., Dong, Z. B., and Peng, X. M. (2012). Dry/wet Variation Recorded by Shrub Tree-Rings in the Central Badain Jaran Desert of Northwestern China. *J. Arid Environments.* 87, 85–94. doi:10.1016/j.jaridenv.2012.06.013

Yan, M., Wang, G., Li, B., and Dong, G. (2001). Formation and Growth of High Mega-Dunes in Badain Jaran Desert. *Acta Geogr. Sin.* 56, 83–91.

Yang, B., Qin, C., Wang, J., He, M., Melvin, T. M., Osborn, T. J., et al. (2014). A 3,500-Year Tree-Ring Record of Annual Precipitation on the Northeastern Tibetan Plateau. *Proc. Natl. Acad. Sci.* 111, 2903–2908. doi:10.1073/pnas.1319238111

Yang, X. (1991). Geomorphologische Untersuchungen in Trockenräumen NW-Chinas Unter Besonderer Berücksichtigung von Badanjilin und Takelamagan. *Gött. Geogr. Abh.* 96, 1–124.

Yang, X., Ma, N., Dong, J., Zhu, B., Xu, B., Ma, Z., et al. (2010). Recharge to the Inter-Dune Lakes and Holocene Climatic Changes in the Badain Jaran Desert, Western China. *Quat. Res.* 73, 10–19. doi:10.1016/j.yqres.2009.10.009

Yang, X., Scuderi, L., Paillou, P., Liu, Z., Li, H., and Ren, X. (2011). Quaternary Environmental Changes in the Drylands of China - A Critical Review. *Quat. Sci. Rev.* 30, 3219–3233. doi:10.1016/j.quascirev.2011.08.009

Yang, X., and Williams, M. A. J. (2003). The Ion Chemistry of Lakes and Late Holocene Desiccation in the Badain Jaran Desert, Inner Mongolia, China. *Catena.* 51, 45–60. doi:10.1016/S0341-8162(02)00088-7

Zhai, D., Xiao, J., Zhou, L., Wen, R., Chang, Z., Wang, X., et al. (2011). Holocene East Asian Monsoon Variation Inferred From Species Assemblage and Shell Chemistry of the Ostracodes from Hulun Lake, Inner Mongolia. *Quat. Res.* 75, 512–522. doi:10.1016/j.yqres.2011.02.008

Zhang Chengjun, C., Feng Zhaodong, Z., Yang Qili, Q., Gou Xiaohui, X., and Sun Feifei, F. (2010). Holocene Environmental Variations Recorded by Organic-Related and Carbonate-Related Proxies of the Lacustrine Sediments from Bosten Lake, Northwestern China. *The Holocene.* 20, 363–373. doi:10.1177/0959683609353428

Zhang, E., Shen, J., Wang, S., Yin, Y., Zhu, Y., and Xia, W. (2004). Quantitative Reconstruction of the Paleosalinity at Qinghai Lake in the Past 900 Years. *Chin.Sci.Bull.* 49, 730–734. doi:10.1007/BF03184273

Zhang, X. B., Long, Y., Wen, A. B., and He, X. B. (2012). Discussion on Applying 137Cs and 210Pbex for Lake Sediment Dating in China. *Quat. Sci.* 32, 430–440.

Zhang, Y. X., Yu, L., and Yin, H. (2015). Annual Precipitation Reconstruction Over Last 191 Years at the South Edge of Badain Jaran Desert Based on Tree Ring Width Data. *Desert Oasis Meteorol.* 9, 12–16.

Zhang, Z. G., and Li, L. R. (2005a). *Groundwater Resource of China (Gansu Vol).* Peking, China: Sino Maps Press.

Zhang, Z. G., and Li, L. R. (2005b). *Groundwater Resource of China (Xinjiang Vol).* Peking, China: Sino Maps Press.

Zhenyu, Z., Wang, N. A., Nai'ang, W., Yue, W., Shiping, S., Xunhe, Z., et al. (2013). Remote Sensing on Spatial Changes of Lake Area in Badain Jaran Desert Hinterland during 1973 2010. *J. Lake Sci.* 25, 514–520. doi:10.18307/2013.0408

Zhu, J., Wang, N. A., Chen, H. B., Dong, C., and Zhang, H. A. (2010). Study on the Boundary and the Area of Badain Jaran Desert Based on Remote Sensing Imagery. *Prog. Geogr.* 29, 1087–1094.

Conflict of Interest: The authors declare that the research was conducted in the absence of any commercial or financial relationships that could be construed as a potential conflict of interest.

Publisher's Note: All claims expressed in this article are solely those of the authors and do not necessarily represent those of their affiliated organizations, or those of the publisher, the editors and the reviewers. Any product that may be evaluated in this article, or claim that may be made by its manufacturer, is not guaranteed or endorsed by the publisher.

Copyright © 2021 Jiang, Wang, Mao, Zhao, Liu, Shen, Nie and Wang. This is an open-access article distributed under the terms of the Creative Commons Attribution License (CC BY). The use, distribution or reproduction in other forums is permitted, provided the original author(s) and the copyright owner(s) are credited and that the original publication in this journal is cited, in accordance with accepted academic practice. No use, distribution or reproduction is permitted which does not comply with these terms.

frontiers in Earth Science

ORIGINAL RESEARCH
published: 01 November 2021
doi: 10.3389/feart.2021.788738

Rapid Northwestward Extension of the East Asian Summer Monsoon Since the Last Deglaciation: Evidence From the Mollusk Record

Yajie Dong[1]*, *Naiqin Wu*[1]*, *Fengjiang Li*[1,2,3] *and Houyuan Lu*[1,4]

[1]Key Laboratory of Cenozoic Geology and Environment, Institute of Geology and Geophysics, Chinese Academy of Sciences, Beijing, China, [2]Innovation Academy for Earth Science, Chinese Academy of Sciences, Beijing, China, [3]Center for Excellence in Life and Paleoenvironment, Chinese Academy of Sciences, Beijing, China, [4]College of Earth and Planetary Sciences, University of Chinese Academy of Sciences, Beijing, China

The magnitude and rate of the expansion of the East Asian summer monsoon (EASM) rain belt under future climatic warming are unclear. Appropriate ecological proxy data may provide an improved understanding of the spatial extension of the EASM during past warming intervals. We reconstructed the spatiotemporal pattern of the extension of the EASM since the Last Glacial Maximum (LGM), using six well-dated mollusk fossil sequences from Chinese loess sections located on the modern northern edge of the EASM. The abundance of typical dominant mollusk species indicative of EASM intensity shows a delayed response, from ~17 ka in the southeastern sections to ~9 ka in the northwestern sections, during the last deglacial warming. Isoline plots based on a mollusk data synthesis show that the mollusk EASM indicators have a northeast–southwest zonal distribution for both the present-day, the cold LGM, and the warm mid-Holocene, which is consistent with the spatial pattern of modern precipitation. The resulting estimated expansion rate of EASM intensity accelerated during ~12–9 ka (~50 km/ka), which corresponds to the early Holocene interval of rapid climatic warming, a northwestward shift of ~150 km compared to today. This implies that the northern fringe of the EASM in northern China will become wetter in the coming century, under moderate warming scenarios.

Keywords: last deglaciation, land snails, monsoon margin, climatic warming, loess plateau

OPEN ACCESS

Edited by:
Zhuolun Li,
Lanzhou University, China

Reviewed by:
Pál Sümegi,
University of Szeged, Hungary
Daniel Enrique Ibarra,
Brown University, United States

Correspondence:
Yajie Dong
dongyajie@mail.iggcas.ac.cn
Naiqin Wu
nqwu@mail.iggcas.ac.cn

Specialty section:
This article was submitted to Quaternary Science, Geomorphology and Paleoenvironment, a section of the journal Frontiers in Earth Science

Received: *03 October 2021*
Accepted: *19 October 2021*
Published: *01 November 2021*

Citation:
Dong Y, Wu N, Li F and Lu H (2021) Rapid Northwestward Extension of the East Asian Summer Monsoon Since the Last Deglaciation: Evidence From the Mollusk Record. Front. Earth Sci. 9:788738. doi: 10.3389/feart.2021.788738

INTRODUCTION

The East Asian summer monsoon (EASM) serves as an interhemispheric heat transfer mechanism and is the main mechanism of moisture transport to East Asia (Webster et al., 1998; Ding, 2004). In recent decades, the summer monsoon rain belt has retreated southward, increasing the incidence of droughts in northern China and flooding in southern China (Wang, 2001; Chase et al., 2003; Ding et al., 2008). Several researchers have linked these monsoon migrations to recent global warming (Li et al., 2010), and argue that as the world warms, dry regions will become drier and wet regions will become wetter (Held and Soden, 2006). However, this scenario, which is based on limited decadal-scale observational data, has made it difficult to establish a long-term linkage between monsoon rainfall and climatic warming and has been challenged by paleo-records of the monsoon (Yang and Ding, 2008; Yang et al., 2015; Huang et al., 2019; Cheng et al., 2020).

Current paleoclimate records reflecting the variability of EASM rainfall intensity come mainly from oxygen isotopic records from cave deposits (Wang Y. J. et al., 2001; Cheng et al., 2006; Cheng et al., 2009), and physical and geochemical proxies (e.g., magnetic susceptibility, $\delta^{13}C$ of organic matter) from loess deposits and lake sediments (Lu et al., 2007; Peterse et al., 2011; Lu et al., 2013; Chen et al., 2015; Goldsmith et al., 2017; Wen et al., 2017). These studies addressing the response of the EASM to past warming focus on two main aspects: 1) Reconstructing the history of EASM rainfall intensity and exploring its relationship with the external drivers of climate forcing. Based on well-documented speleothems oxygen isotopic records, the debate over whether the EASM reached its maximum intensity in the early Holocene (Wang Y. J. et al., 2001; Cheng et al., 2006; Cheng et al., 2009) or the mid-Holocene (Lu et al., 2013; Chen et al., 2015) still challenges our understanding of the response of EASM intensity to summer insolation and the associated temperature fluctuations. 2) Spatial characterization of the magnitude of shifts in the EASM rain belt during past warming intervals, especially on the sensitive northern fringe, which is of particular eco-environmental concern. Recent paleorecords based on the spatial distribution of C_4 plant biomass and loess grain size suggest that the EASM moved northwestward by ~300 km from the cold Last Glacial Maximum (LGM) to the warm mid-Holocene (~6 ka) (Yang and Ding, 2008; Yang et al., 2015). This northward shift in the EASM rainfall belt would have increased the precipitation in the semi-arid region of northern China, which is supported by PlioMIP climate simulations (Huang et al., 2019; Cheng et al., 2020).

Although these paleo-records and climate simulations indicate the same trend of northwestward migration of the northern extent of the EASM, the spatial estimates show only two time-slice scenarios (a warm mid-Holocene and a cold LGM). However, the rate and spatial extent of the movement of the EASM rain belt since the last deglaciation, and their relationship with warming rates, remain unclear. Since the validity of Chinese cave isotope-based reconstructions of EASM precipitation intensity has been questioned (Tan, 2009; Maher and Thompson, 2012; Liu et al., 2015), and other geological evidence is mainly from a few records from single sites, the extent to which the spatial migration of the EASM rain belt fluctuated under past climatic warming requires further investigation. Absent from the debate are multi-site records of ecological indicators sensitive to summer monsoon precipitation amount.

Terrestrial mollusks are one of the most diverse and abundant invertebrates inhabiting various environments of the East Asian monsoon regions (Nekola, 2003; Dong et al., 2019). They are abundantly preserved as fossils, for example in loess sediments (Rousseau and Wu, 1997; Wu et al., 2002; Sümegi et al., 2015; Horsák et al., 2018; Richter et al., 2019). Previous studies have shown that mollusks are sensitive to the advance and retreat of the East Asian monsoon, and several mollusks have been identified as indicator species of the EASM, such as *Punctum orphana* and *Macrochlamys angigyra* (Rousseau and Wu, 1997; Wu et al., 2002). These characteristics make mollusks a unique model taxon for exploring spatiotemporal changes in the EASM and their linkage with climatic warming.

Here we present the first modern distribution of terrestrial mollusks in northern China, together with six high-resolution mollusk fossil sequences spanning the interval from 25 ka (in the LGM) to the Holocene, along environmental gradients in the Chinese Loess Plateau (CLP), located in the northwestern part of the EASM region (**Figure 1**). The peripheral location of these loess sections with respect to the monsoon region provides an excellent opportunity to examine the magnitude of the spatial expansion of the EASM in response to climate change. The temperature of the Holocene climatic optimum (~8–4 ka) was ~2°C higher than today in the Northern Hemisphere (Wang S. et al., 2001; Shakun et al., 2012), which is equivalent to predicted warming. Our aims were to estimate the shift of the monsoon rain belt associated with past global warming and to predict future hydroclimatic trends in the region.

MATERIALS AND METHODS

Study Area and Sites

The six studied loess-palaeosol sections are Linxia (35°38′N, 103°09′E, H = 2,179 m), Huanxian (36°32′N, 107°20′E, H = 1,232 m), Shuozhou (39°23′N, 112°09′E, H = 1,579 m), Jingchuan (35°15′N, 107°43′E, H = 1,244 m), Jixian (36°06′N, 110°38′E, H = 995 m), and Yaoxian (34°53′N, 108°58′E, H = 673 m). They are located along a northwest–southeast transect across the CLP (**Figure 1A**). The northernmost sites (Linxia, Huanxian) are currently located near the northwestern limit of the EASM domain. The modern mean annual temperature (MAT) of these sites increases from ~6 to ~13°C, and the mean annual precipitation (MAP) from ~300 to ~650 mm, from northwest to southeast (**Figure 1A**). Daily backward moisture trajectories of rainfall events in the central CLP show that the moisture transported by the EASM accounts for ~85% of the annual rainfall (**Figure 1B**). About 70% of the precipitation falls in the summer and autumn seasons when the EASM circulation transports tropical and subtropical moisture inland (Qian, 1991).

Modern mollusk species distributions are from Li et al. (2016), Dong et al. (2019), Dong et al. (2020a). The dataset comprises 356 samples collected from surface soils across an ~800 km climatic gradient across northern China. This extensive dataset of modern mollusk samples covering all fossil sites ensures a comprehensive survey of species distributions.

Loess Sequences and Chronology

The six profiles are geographically located in “Yuan” areas (flat-topped loess highlands, covered with thick loess deposits), one of the major topographic units in the CLP (Liu, 1985). Sampling was undertaken on 1) the upper part of loess unit L1 (L1-1) which was deposited since marine isotope stage 2 (MIS2); and 2) the lower part of the Holocene paleosol

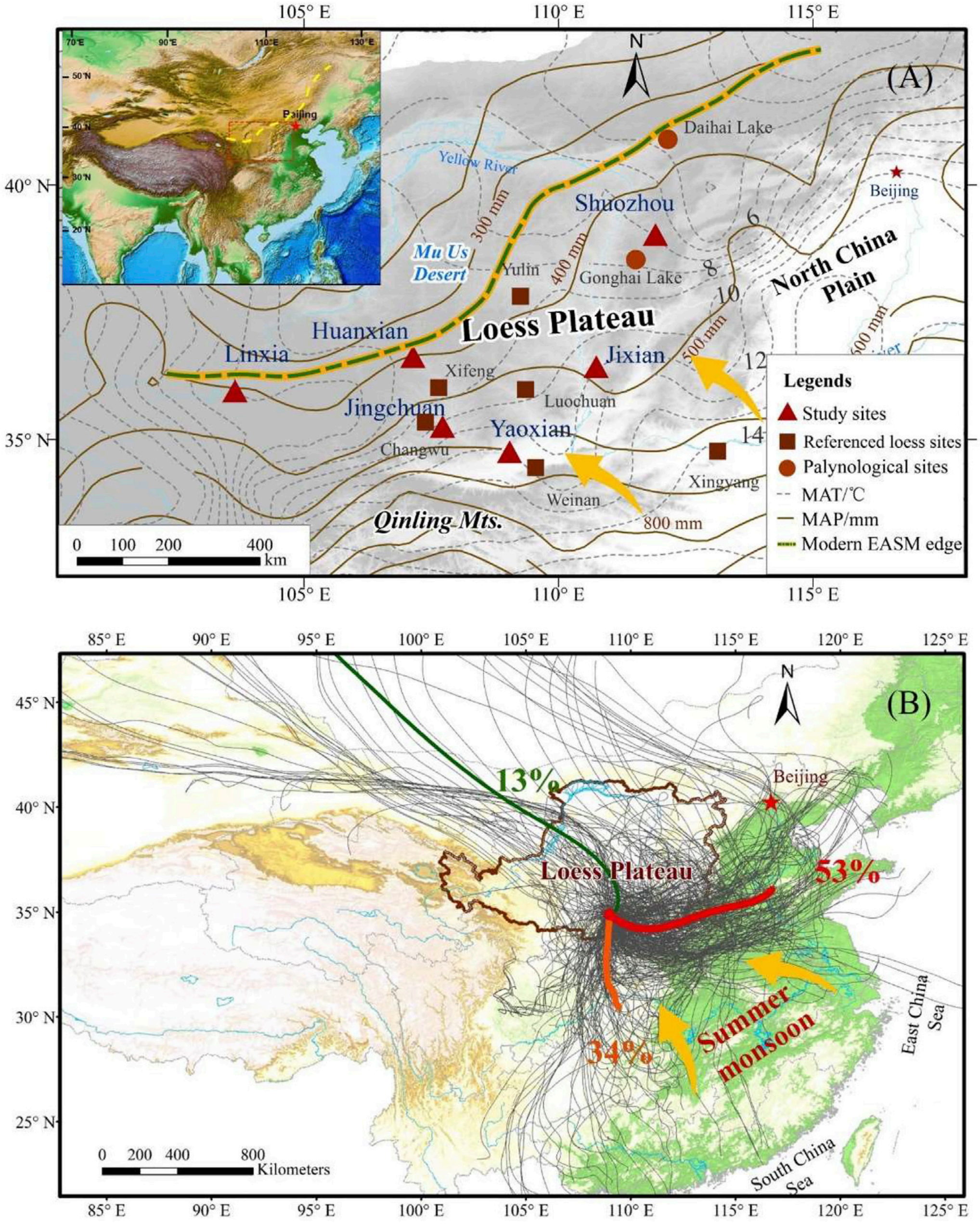

FIGURE 1 | Locations of the studied sections (solid red triangles) along climatic gradients from the northwest to southeast across the Chinese Loess Plateau **(A)**. The inset map shows the location of the study area and the modern northern edge of the EASM region. The arrows indicate the direction of the summer monsoonal winds. Brown squares and red circles denote locations of the loess sites and palynological sites referenced in the text. The isohyets (in mm; gray lines) and isotherms (in °C; brown dashed lines) are 50-years averages (Lin et al., 2002). **(B)** Ensembles of backward air-parcel trajectories (Draxler and Hess, 1997) of the source moisture for the Yaoxian loess site. Grey lines indicate daily backward (144 h) moisture trajectories of rainfall events (>0 mm/day) from January 2005 to December 2011, at the height of 1,000 m above ground level. Three primary moisture transport paths to the Yaoxian loess site were generated using cluster analysis of moisture trajectories. The green paths denote the Westerlies; the green paths denote the eastern branch of the East Asian summer monsoon; the red path denotes southern branches of the East Asian summer monsoon. The data for backward trajectories analysis were downloaded from (ftp://arlftp.arlhq.noaa.gov/pub/archives/reanalysis/).

unit (S0) (**Supplementary Figure S1**). The chronology of the six loess-paleosol sequences is based on high-resolution optically stimulated luminescence (OSL) dating for the Linxia, Huanxian, Jingchuan and Yaoxian sections (Lai and Wintle, 2006; Dong et al., 2015), and on the ^{14}C ages of mollusk shells from the Jixian (Dong et al., 2021a) and Shuozhou sections (**Supplementary Figure S2**). The age-depth models were constructed by polynomial fits through a number of successive absolute dates. The age-depth models for the loess sequence show that most of the loess profiles

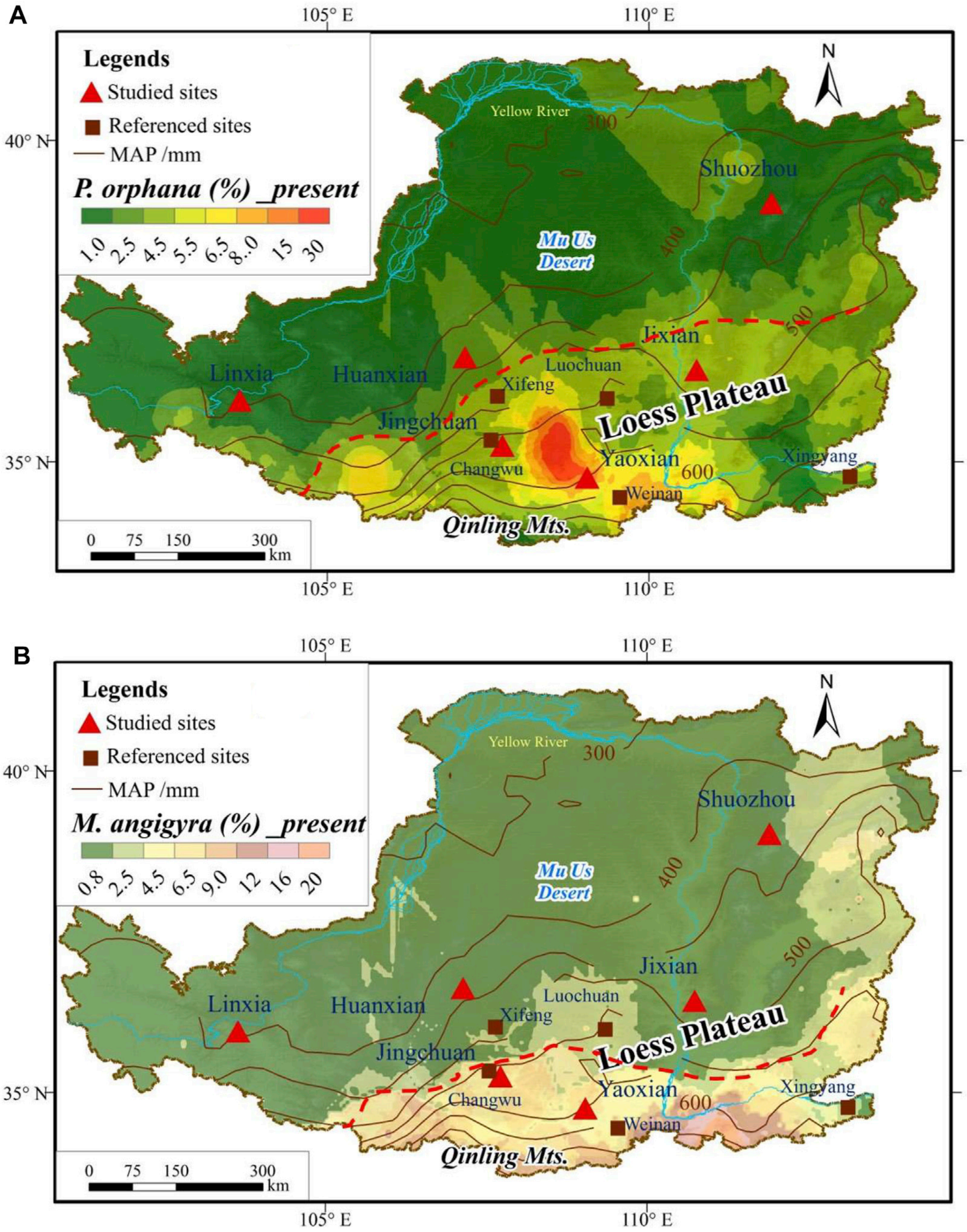

FIGURE 2 | Maps of the abundance of *P. orphana* **(A)** and *M. angigyra* **(B)** based on modern surveys (Li et al., 2016; Dong et al., 2019, 2020a), together with modern mean annual precipitation over the past 50 years. Red dotted lines show the reference values of the 4.5%, 2.5% isolines of *P. orphana* and *M. angigyra*, respectively.

span the past 25 ka, including the Last Glacial Maximum (LGM), the Last deglacial, and the Holocene (**Supplementary Figure S2**).

Mollusk Samples

A total of 522 mollusk samples were taken from the L1 and S0 strata in six loess sections spanning the last 22 ka. A sampling of each loess section was conducted at the equal intervals which equates to an average temporal resolution of ~200–600 years for each sample (**Supplementary Figure S1**). The mollusk data for the Yaoxian, Jingchuan, Linxia and Jixian loess profiles are from Dong et al. (2020a, 2020b, 2021b). Each sample comprised ~15 kg of soil material, and all samples were washed and sieved in the field using a 0.5-mm mesh sieve to remove fine soil. The mollusk shells were then picked and identified under a binocular microscope; the identification procedures followed Yen (1939) and Chen and Gao (1987). All mollusk taxa in the deposits were identified and the abundance of summer monsoon indicator species was determined at each site.

Spatial Analysis

Compared with the long geological period, the morphological and ecological characteristics of terrestrial mollusks, from the study area in northern China, have not changed since the LGM (Li et al., 2006), indicating that the range of potential evolutive variations remains very tight and negligible. This allows therefore to apply the present ecological requirements of the studied mollusk species to the Late glacial and Holocene malacofauna to assess the spatial dynamics of their distribution.

Interpolation analysis was used to produce a map of the spatial abundance of typical mollusk species for the whole study area. There are many spatial interpolation methods, such as Inverse Distance Weighted interpolation, Kriging interpolation algorithm and Natural Neighbor interpolation method (Sibson, 1981; Isaaks and Srivastava, 1989), used to predict the distribution of variables in different disciplines. Among them, Kriging interpolation, a geostatistical method, has been widely used to predict many environmental and ecological variables, such as annual rainfall and species richness, as long as the data are spatially dependent (Isaaks and Srivastava, 1989; Webster and Oliver, 2001). The Kriging interpolation involves a process of semi-variogram to model the spatial autocorrelation of the data to assign weights, which can result in better interpolations under an appropriate sampling design. In this study, this method was used for spatial analysis of the distribution of the mollusk species.

RESULTS

Mollusk Taxa Indicative of EASM Intensity

P. orphana and *M. angigyra* were two of the most abundant thermo-humidiphilous taxa, both in the modern mollusk samples and in the loess-paleosol sequences. Modern surveys based on the 356 surface mollusk samples (Li et al., 2016; Dong et al., 2019, 2020a) show that *P. orphana* has a mean abundance of ~5.3% in the CLP, with a maximum of ~46% (**Figure 2A**). The *P. orphana* isolines using the Kriging interpolation show a northeast–southwest trend (**Figure 2A**), which is consistent with the modern climatic pattern: i.e., a northeast–southwest trend (**Figure 1**). Its modern distribution is mainly in the southeastern CLP where the MAP ranges from ~450 to 860 mm, an area presently dominated by the summer monsoon.

M. angigyra, another typical thermo-humidiphilous species, requires a higher temperature and wetter conditions than *P. orphana* (Chen and Gao, 1987). Although its distribution is more southerly than that of *P. orphana*, they both show a similar spatial abundance pattern. From northwest to southeast, the abundance of *M. angigyra* increases substantially, reaching ~85%, and with an average of ~4.9% (**Figure 2B**). The abundance of these two mollusk species increases linearly with the increase in MAP in the CLP. Their spatial distribution shows that their abundance is sensitive to the hydrothermal regime in northern China and thus they reflect fluctuations in EASM intensity. Their occurrence on the northern fringe of EASM is regarded as a proxy of EASM strength and an indicator of the northward migration of the warm and wet summer monsoon into the Loess Plateau (Wu et al., 1996, 1999, 2002; Rousseau and Wu, 1997).

Spatial Patterns of Mollusk Abundance Since the LGM

Considering the sensitivity of the two mollusk species to the summer monsoon, and the fact that they are the dominant thermo-humidiphilous species in the entire mollusk assemblage, we now examine their spatiotemporal distribution since the LGM. The abundances of the two mollusk species show a striking and regular pattern of variability within the six loess sequences. In the southern region of the CLP (Yaoxian), *P. orphana* is abundant throughout the time series (**Figure 3A**). Large fluctuations in abundance occurred during 25–9 ka, but the species generally maintained a high level of abundance, with the average number of individuals remaining at ~30/15 kg (**Figure 3A**). The number of individuals of *P. orphana* was significantly reduced in the eastern and central CLP (Jixian, Jingchuan), and was almost absent before and during the LGM. The species began to be continuously distributed at ~20 ka at the Jixian site, and reached its maximum abundance during the early to middle Holocene. In the northern part of the CLP, the continuous presence of *P. orphana* in the Huanxian and Shuozhou sections was delayed by ~16 ka and 12.5 ka, respectively. In the far northwest Linxia section, the numbers of this species were even lower, and it did not appear until ~9 ka, although it increased substantially during the mid-Holocene (**Figure 3A**). At most of the sites *P. orphana* reached its maximum abundance between ~8 ka and ~4 ka, although there was a slight variability between the sites. Continuously declining abundances occurred during ~4–3 ka. In general, the sites in the northern CLP had a substantially lower abundance of *P. orphana* compared to the southern and eastern sites. During the last deglacial warming, the continuous occurrence of *P. orphana* was gradually delayed from southeast to northwest across the CLP.

The spatial abundance of *M. angigyra* is similar to that of *P. orphana*. Sites from the southern to the eastern CLP (Yaoxian, Jixian) contained more *M. angigyra* than most of the northern sites (Jingchuan, Huanxian, Shuozhou and Linxia) (**Figure 3B**). All of the sites had a low abundance of *M. angigyra* during the cold LGM. Between ~17 and 15 ka, there was a rapidly increasing abundance at sites in the eastern and southern CLP (Jixian, Yaoxian). Different from *P. orphana*, the northern boundary of the distribution of *M. angigyra* is much more southerly, being

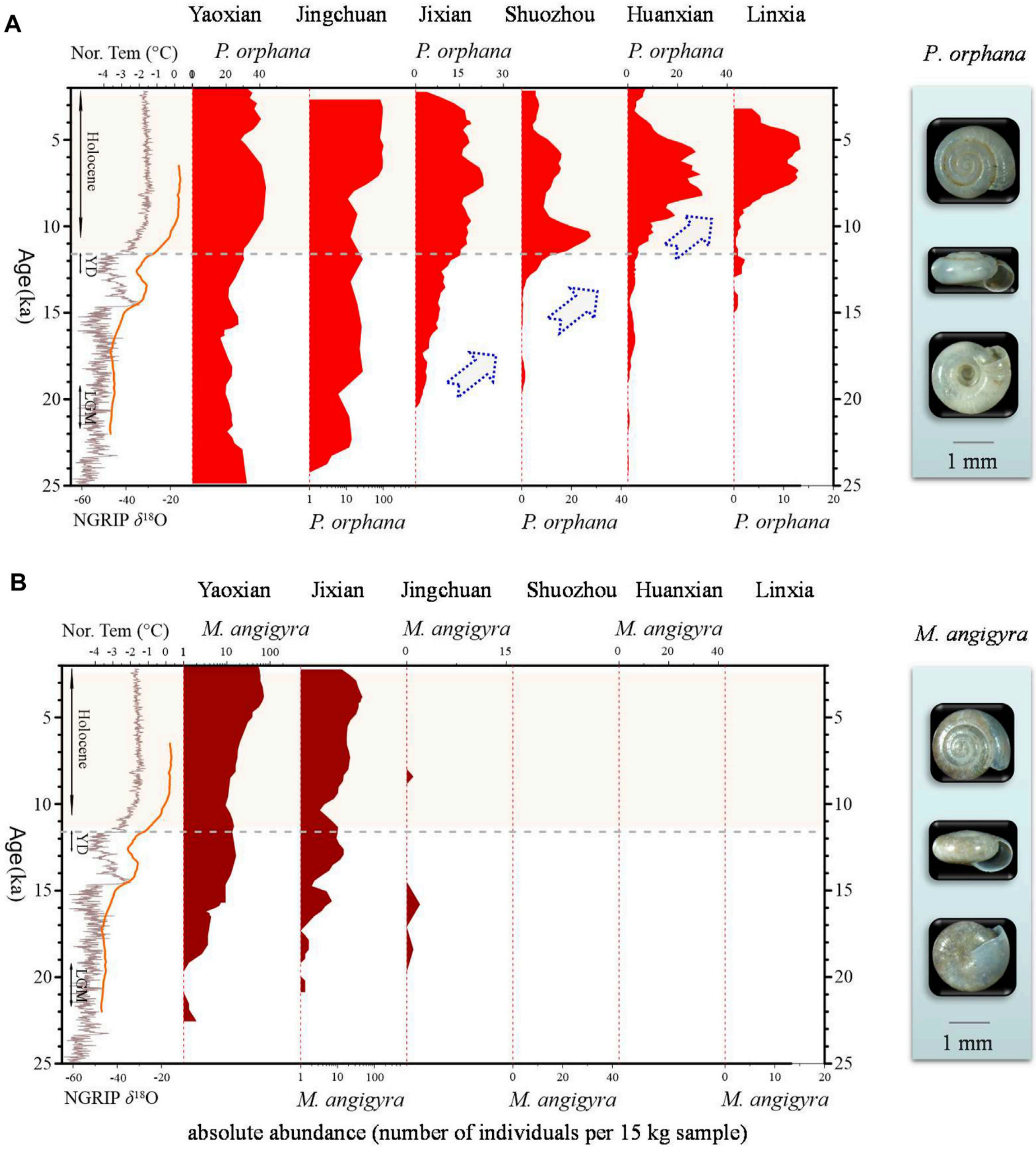

FIGURE 3 | Abundance of *P. orphana* **(A)** and *M. angigyra* **(B)** in the six loess sections from southeast to northwest across the Chinese Loess Plateau, and correlation with the Greenland NGRIP ice-core δ^{18}O record (Huber et al., 2006) and Northern Hemisphere average temperature (Nor. Tem) (°C) (Shakun et al., 2012). The Holocene, Younger Dryas (YD) and LGM intervals are indicated. The shaded zones indicate the Holocene soil layer.

rare or nearly absent from the central and northern areas, such as Jingchuan, Huanxian, Shuozhou and Linxia, during the entire Holocene.

Migration of the EASM Rain Belt From the LGM to the Middle Holocene

In order to characterize the spatial variation of the abundance of typical summer monsoon-sensitive mollusk species and to evaluate the extent of the summer monsoon, we plotted contour maps of their abundance based on a synthesis of the data from the present study and published fossil mollusk records (Wu et al., 1996, 1999, 2000, 2001, 2002, 2007; Rousseau and Wu, 1997; Rousseau et al., 2000, 2009). The isolines of the abundance of the two indicator mollusks all show a northeast–southwest zonal distribution during both the cold LGM, the warm Holocene, and at the present day (**Figure 4**). This pattern is consistent with the northeast–southwest trend of modern annual

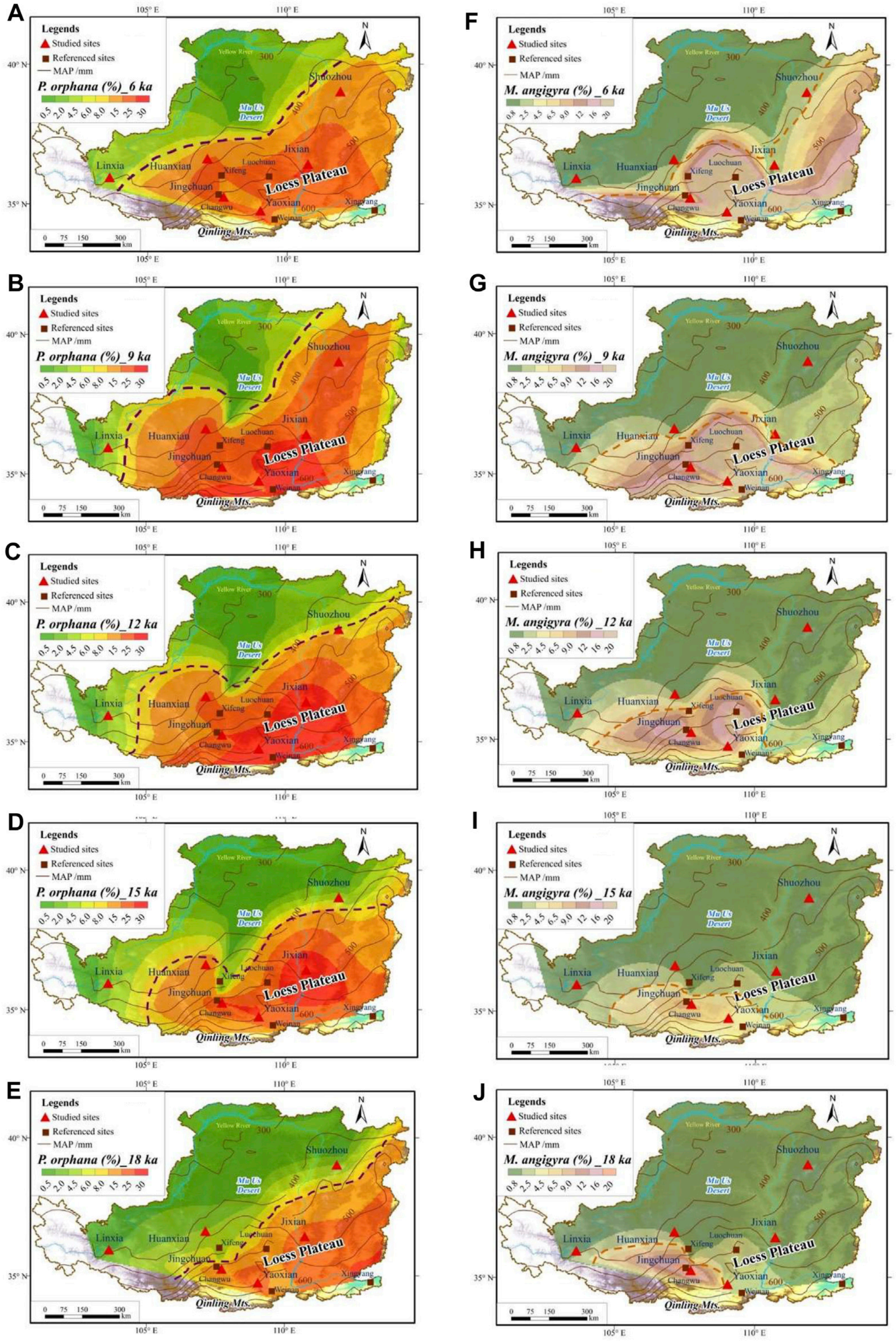

FIGURE 4 | Contour maps of the abundance of *P. orphana* and *M. angigyra* for the time slices of ~6 ka **(A, F)**, ~ 9 ka **(B, G)**, ~12 ka **(C, H)**, ~15 ka **(D, I)**, and ~18 ka **(E, J)** since the last deglaciation. The modern mean annual precipitation distribution over the past 50 years is also shown. Red dotted lines show the reference values of the 4.5 and 2.5% isolines of *P. orphana* and *M. angigyra*, respectively.

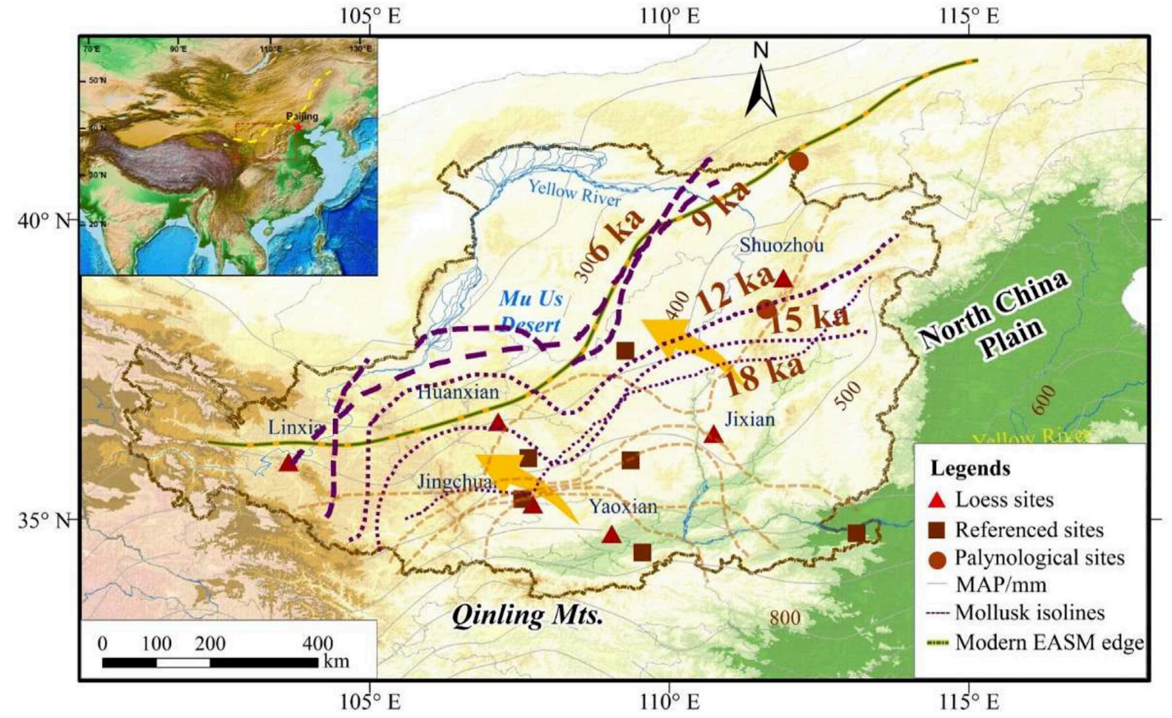

FIGURE 5 | Migration of the East Asian summer monsoon rain belt since the last deglaciation (~18 ka, ~15 ka, ~12 ka, ~9 ka, and ~6 ka) reconstructed using the abundance isolines for *P. orphana* (purple dotted line) and *M. angigyra* (orange dotted line).

isohyets. Therefore, changes in the zonal distribution of indicator mollusk abundance in the CLP can serve as a useful analog for shifts in the EASM rain belt. Since the 4.5% isoline of *P. orphana* abundance is close to the current northern limit of the EASM, we can use it as a reference value to estimate the spatial migration of the EASM margin since the LGM. Correspondingly, there is an estimated 350-km migration distance between the LGM and the mid-Holocene, and a minimum 150-km northwestward migration of the monsoon rain belt during the warm Holocene, compared with the present day (**Figure 4**). Similarly, using an *M. angigyra* abundance of 2.5% as a reference, we estimate a northwesterly monsoon rain belt advance of ~300 km for the warm Holocene compared with the cold LGM, and a ~100-km northwestward migration compared with the present day (**Figure 5**). We estimate that the distributions of mollusk species shifted to the northwestern sites at average rates of ~30 km/ka during ~15–12 ka (from the onset of the deglacial warming) and ~50 km/ka during ~12–9 ka (roughly corresponding to the early Holocene).

DISCUSSION

Precipitation and related humidity conditions are important first-order factors affecting mollusk communities at large regional scale, especially on the northern margin of the EASM in northern China (Chen and Gao, 1987; Wu et al., 2018; Dong et al., 2019). Previous studies have shown that the two mollusk species are highly sensitive to monsoonal precipitation, which is supported by our surveys of modern mollusk abundance, and their abundance in Chinese loess deposits has been widely used to reconstruct changes in EASM intensity during the Quaternary (Wu et al., 2002; Wu et al., 2018). Our records show that the abundance of these mollusks increased substantially with climatic warming during the last deglaciation, reaching a maximum during ~8–4 ka. The maximum timing of EASM intensity indicated by the mollusk records during the mid-Holocene is consistent with that documented by climatically-sensitive records of magnetic susceptibility, organic matter content and carbon isotopes from Chinese loess deposits (Lu et al., 2013). It is also supported by pollen-based precipitation reconstructions from lake deposits in northern China (Chen et al., 2015; Zhou et al., 2016; Wen et al., 2017; Cheng et al., 2020), indicating that the maximum summer monsoon precipitation on the northern EASM margin occurred in the mid-Holocene, rather than during the early Holocene, as inferred from speleothem oxygen isotope records.

The northern margin of the EASM rain belt, as inferred from the two mollusk indicator species, shifted from northwest to southeast, consistent with records of loess grain-size and C_4 plant biomass records (Yang and Ding, 2008; Yang et al., 2015). Previous studies have presented only two time slices and did not demonstrate a statistical linkage between spatial shifts of the rain belt and climatic warming. We found that observed spatial shifts were significantly greater during intervals of high-amplitude warming. Specifically, a pronounced extension of the EASM rain belt occurred at ~16 ka, corresponding to the beginning of the last deglaciation. The estimated maximum advance rate reached ~50 km/ka during ~12–9 ka, corresponding to the interval of rapid warming from the last deglaciation to the Holocene. These results indicate that the rate and extent of EASM rainfall expansion were strongly related to the concurrent level of warming since the last deglaciation.

It is noteworthy that the ecological requirements of the two EASM indicator mollusk species are not the same. The distribution of the maximum abundance and extension of the two species differ slightly due mainly to the different optimum ranges of hydrothermal conditions. *M. angigyra* requires warmer and wetter conditions for its survival and growth and tends to be located in the south with higher precipitation. As shown in our fossil record, their fossils are only distributed at a few sites in the southeastern Loess Plateau, such as at Weinan during the cold LGM (Wu et al., 2002). The most obvious expansion (characterized by continuous occurrence and 3–5% abundance isolines) of *M. angigyra* has been from the southern CLP to the central CLP since deglaciation, while *P. orphana* can extend northwestward from the central CLP to the northwest. Thus, the extension rate and amplitude of the EASM rain belt indicative of their reference abundance value may deviate slightly, but the path and direction of their expansion still coincide with the modern precipitation pattern. Both two mollusks indicate a roughly 300-km northwestward migration of the monsoon rain belt for the warm Holocene compared with the cold LGM. Although our reconstruction would be improved by a higher temporal resolution, better chronological accuracy, and more fossil sites, our data provide the best estimates of extension rates and is an improvement over previous study.

Our estimated migration distance is similar to that of the desert margin from the LGM to the mid-Holocene inferred from loess grain-size records (Yang and Ding, 2008). This estimate is also consistent with the 300-km northwestward migration of the monsoon rain belt inferred from the spatial distribution of C_4 plant biomass in the CLP (Yang et al., 2015). Although the migration distance estimated by different proxies may vary due to proxy sensitivity and the accuracy of the chronology, the same northwestward trend provides firm evidence of the extension of the EASM rain belt based on both ecological and geochemical proxies.

Our data, together with previous geological records, confirm that increased global temperatures strengthened the EASM and resulted in at least 150 km concomitant northward advance of the monsoon rain belt during the mid-Holocene compared to today. This long-term linkage between climatic warming and monsoon rainfall extent is supported by recent climate models, namely the coincidence of the increased land-ocean thermal contrast with the Asian monsoon domain, which was forced mainly by Earth orbital parameters and atmospheric CO_2 content, since the last deglaciation (Cheng et al., 2020). This evidence supports the scenario proposed by Broecker and Putnam (2013) that the Northern Hemisphere warms more rapidly than the Southern Hemisphere oceans. This leads to an increase in the interhemispheric temperature contrast which induces a northward shift of the thermal equator (ITCZ), ultimately leading to increased precipitation on the northern margin of monsoonal Asia. These scenarios occurred during earlier warm periods, such as the mid-Pliocene (Huang et al., 2019). As a result, northern China may become wetter over the next century as global warming continues. We, therefore, suggest that the drying trend in northern China, which has already lasted for several decades, will eventually reverse with ongoing global warming.

CONCLUSION

Based on 356 surface-soil mollusk assemblages we demonstrate that two dominant mollusk species, *Punctum orphana* and *Macrochlamys angigyra*, can be used as an indicator of the movement of the EASM rain belt. Based on this, we present changes in the abundance of the two species from six loess sections across the Chinese Loess Plateau, and examine spatiotemporal changes in the EASM rain belt during the interval from the cold LGM to the warm Holocene. The spatial distribution of the abundances of the two mollusk species shows a northeast-southwest zonal distribution for both the present-day, the cold LGM, and the warm mid-Holocene, which is consistent with the northeast-southwest trend of modern precipitation. Therefore, the northeast-southwest zonal distribution pattern of mollusk abundance in the CLP is a robust analog for the EASM rain belt. The occurrence of the two EASM indicator species shows a lag from the relatively warm, wet southeast to the relatively cold, dry northwest since the LGM, with their abundance reaching a maximum during the mid-Holocene. Using the 3–5% mollusk abundance isolines as a reference, we estimate that the EASM rain belt during the warm Holocene penetrated 150-km further northwestward compared to today. Our results provide long-term biological evidence suggesting that the northern monsoonal marginal region in China may become wetter as the climate warms, and thus that the observed drought trend of recent decades may be reversed with ongoing global warming.

DATA AVAILABILITY STATEMENT

The original contributions presented in the study are included in the article/**Supplementary Material**, further inquiries can be directed to the corresponding authors.

AUTHOR CONTRIBUTIONS

YD conceived the study, undertook the field work, collected the mollusk data, identified and counted the mollusk species, performed statistical analyses, and wrote the text. NW conceived the study, undertook the field work, collected the mollusk data, and wrote the text; FL undertook the field work, collected the mollusk data, and wrote the text. HL conceived the study, undertook the field work, collected the mollusk data, and wrote the text. All authors commented on the interpretation of the results and gave final approval for publication.

FUNDING

This work was supported by the "Strategic Priority Research Program" of the Chinese Academy of Sciences (XDB26000000) and the National Natural Science Foundation of China (41888101, 42172210, 41830322, and 41430103).

ACKNOWLEDGMENTS

We thank Drs Linpei Huang, Bin Wu, Daojing Wang, and Wenwen Wen for their assistance with the fieldwork.

SUPPLEMENTARY MATERIAL

The Supplementary Material for this article can be found online at: https://www.frontiersin.org/articles/10.3389/feart.2021.788738/full#supplementary-material

REFERENCES

Broecker, W. S., and Putnam, A. E. (2013). Hydrologic Impacts of Past Shifts of Earth's thermal Equator Offer Insight into Those to Be Produced by Fossil Fuel CO_2. *Proc. Natl. Acad. Sci.* 110, 16710–16715. doi:10.1073/pnas.1301855110

Chase, T. N., Knaff, J. A., Pielke, R. A., and Kalnay, E. (2003). Changes in Global Monsoon Circulations since 1950. *Nat. Hazards* 29, 229–254. doi:10.1023/A:1023638030885

Chen, D. N., and Gao, J. X. (1987). *Economic Fauna Sinica of China, Terrestrial Mollusca*. Beijing: Science Press.

Chen, F., Xu, Q., Chen, J., Birks, H. J. B., Liu, J., Zhang, S., et al. (2015). East Asian Summer Monsoon Precipitation Variability since the Last Deglaciation. *Sci. Rep.* 5, 11186. doi:10.1038/srep11186

Cheng, H., Edwards, R. L., Broecker, W. S., Denton, G. H., Kong, X., Wang, Y., et al. (2009). Ice Age Terminations. *Science* 326, 248–252. doi:10.1126/science.1177840

Cheng, H., Edwards, R. L., Wang, Y., Kong, X., Ming, Y., Kelly, M. J., et al. (2006). A Penultimate Glacial Monsoon Record from Hulu Cave and Two-phase Glacial Terminations. *Geology* 34, 217–220. doi:10.1130/G22289.1

Cheng, J., Ma, Y., Wu, H., Long, H., and Liu, Z. (2020). Migration of Afro-Asian Monsoon Fringe since Last Glacial Maximum. *Front. Earth Sci.* 8, 322. doi:10.3389/feart.2020.00322

Cheng, Y., Liu, H., Dong, Z., Duan, K., Wang, H., and Han, Y. (2020). East Asian Summer Monsoon and Topography Co-determine the Holocene Migration of forest-steppe Ecotone in Northern china. *Glob. Planet. Change* 187, 103135. doi:10.1016/j.gloplacha.2020.103135

Ding, Y. (2004). "Seasonal March of the East-Asian Summer Monsoon," in *East Asian Monsoon*. Editor C. P. Chang (Singapore: World Scientific Publishing Co. Pte. Ltd), 3–53. doi:10.1142/9789812701411_0001

Ding, Y., Wang, Z., and Sun, Y. (2008). Inter-decadal Variation of the Summer Precipitation in East China and its Association with Decreasing Asian Summer monsoon.Part I: Observed Evidences. *Int. J. Climatol.* 28, 1139–1161. doi:10.1002/joc.1615

Dong, Y., Wu, N., Jiang, W., Li, F., and Lu, H. (2020b). Cascading Response of flora and Terrestrial Mollusks to Last Deglacial Warming. *Glob. Ecol. Conserv.* 24, e01360. doi:10.1016/j.gecco.2020.e01360

Dong, Y., Wu, N., Li, F., Chen, X., Zhang, D., Zhang, Y., et al. (2019). Influence of Monsoonal Water-Energy Dynamics on Terrestrial Mollusk Species-Diversity Gradients in Northern China. *Sci. Total Environ.* 676, 206–214. doi:10.1016/j.scitotenv.2019.04.292

Dong, Y., Wu, N., Li, F., Huang, L., Lu, H., and Stenseth, N. C. (2021b). Paleorecords Reveal the Increased Temporal Instability of Species Diversity under Biodiversity Loss. *Quat. Sci. Rev.* 269, 107147. doi:10.1016/j.quascirev.2021.107147

Dong, Y., Wu, N., Li, F., Huang, L., and Wen, W. (2015). Time-transgressive Nature of the Magnetic Susceptibility Record across the Chinese Loess Plateau at the Pleistocene/Holocene Transition. *PLoS One* 10, e0133541. doi:10.1371/journal.pone.0133541

Dong, Y., Wu, N., Li, F., and Lu, H. (2021a). Coupled Morphologic and Demographic Responses of *Opeas Striatissimum* (Gastropoda: Subulinidae) to Latest Pleistocene to Early Holocene Climate Fluctuations. *Palaeogeogr. Palaeoclimatol. Palaeoecol.* 562, 110101. doi:10.1016/j.palaeo.2020.110101

Dong, Y., Wu, N., Li, F., Zhang, D., Zhang, Y., Huang, L., et al. (2020a). Anthropogenic Modification of Soil Communities in Northern China for at Least Two Millennia: Evidence from a Quantitative Mollusk Approach. *Quat. Sci. Rev.* 248, 106579. doi:10.1016/j.quascirev.2020.106579

Draxler, R. R., and Hess, G. D. (1997). "Description of the HYSPLIT_4 Modeling System," in *NOAA Tech. Memo. ERL ARL-224* (Silver Spring: Air Resources Laboratory), 24. Available at: https://www.researchgate.net/publication/255682850_Description_of_the_HYSPLIT_4_modelling_system.

Goldsmith, Y., Broecker, W. S., Xu, H., Polissar, P. J., deMenocal, P. B., Porat, N., et al. (2017). Northward Extent of East Asian Monsoon Covaries with Intensity on Orbital and Millennial Timescales. *Proc. Natl. Acad. Sci. USA* 114, 1817–1821. doi:10.1073/pnas.1616708114

Held, I. M., and Soden, B. J. (2006). Robust Responses of the Hydrological Cycle to Global Warming. *J. Clim.* 19, 5686–5699. doi:10.1175/JCLI3990.1

Horsák, M., Juřičková, L., Horsáková, V., Pokorná, A., Pokorný, P., Šizling, A. L., et al. (2018). Forest Snail Diversity and its Environmental Predictors along a Sharp Climatic Gradient in Southern Siberia. *Acta Oecol.* 88, 1–8. doi:10.1016/j.actao.2018.02.009

Huang, X., Jiang, D., Dong, X., Yang, S., Su, B., Li, X., et al. (2019). Northwestward Migration of the Northern Edge of the East Asian Summer Monsoon during the Mid-pliocene Warm Period: Simulations and Reconstructions. *J. Geophys. Res. Atmos.* 124, 1392–1404. doi:10.1029/2018JD028995

Huber, C., Leuenberger, M., Spahni, R., Flückiger, J., Schwander, J., Stocker, T. F., et al. (2006). Isotope Calibrated Greenland Temperature Record over Marine Isotope Stage 3 and its Relation to CH4. *Earth Planet. Sci. Lett.* 243, 504–519. doi:10.1016/j.epsl.2006.01.002

Isaaks, E. H., and Srivastava, R. M. (1989). *An Introduction to Applied Geostatistics*. New York: Oxford University Press.

Lai, Z.-P., and Wintle, A. G. (2006). Locating the Boundary between the Pleistocene and the Holocene in Chinese Loess Using Luminescence. *The Holocene* 16, 893–899. doi:10.1191/0959683606hol980rr

Li, F. J., Wu, N. Q., Dong, Y. J., Lu, H. Y., Chen, X. Y., Zhang, D., et al. (2016). Quantitative Distribution and Calculation of Ecological Amplitude of Land Snail Metodontia in the Chinese Loess Plateau and Adjacent Regions. *Quat. Sci.* 36, 564–574. (In Chinese with English abstract). doi:10.11928/j.issn.1001-7410.2016.03.06

Li, F., Wu, N., and Rousseau, D.-D. (2006). Preliminary Study of Mollusk Fossils in the Qinan Miocene Loess-Soil Sequence in Western Chinese Loess Plateau. *Sci. China Ser. D* 49, 724–730. doi:10.1007/s11430-006-0724-7

Li, J., Wu, Z., Jiang, Z., and He, J. (2010). Can Global Warming Strengthen the East Asian Summer Monsoon? *J. Clim.* 23, 6696–6705. doi:10.1175/2010JCLI3434.1

Lin, Z. H., Mo, X. G., Li, H. X., and Li, H. B. (2002). Comparison of Three Spatial Interpolation Methods for Climate Variables in China. *Acta Geograph. Sin.* 57, 47–56. doi:10.11821/xb200201006

Liu, J., Chen, J., Zhang, X., Li, Y., Rao, Z., and Chen, F. (2015). Holocene East Asian Summer Monsoon Records in Northern China and Their Inconsistency with Chinese Stalagmite $\delta^{18}O$ Records. *Earth-Science Rev.* 148, 194–208. doi:10.1016/j.earscirev.2015.06.004

Liu, T. S. (1985). *Loess and the Environment*. Haidian: China Ocean Press.

Lu, H., Wu, N., Liu, K., Jiang, H., and Liu, T. (2007). Phytoliths as Quantitative Indicators for the Reconstruction of Past Environmental Conditions in China II: Palaeoenvironmental Reconstruction in the Loess Plateau. *Quat. Sci. Rev.* 26, 759–772. doi:10.1016/j.quascirev.2006.10.006

Lu, H., Yi, S., Liu, Z., Mason, J. A., Jiang, D., Cheng, J., et al. (2013). Variation of East Asian Monsoon Precipitation during the Past 21 k.Y. And Potential CO_2 Forcing. *Geology* 41, 1023–1026. doi:10.1130/G34488.1

Maher, B. A., and Thompson, R. (2012). Oxygen Isotopes from Chinese Caves: Records Not of Monsoon Rainfall but of Circulation Regime. *J. Quat. Sci.* 27, 615–624. doi:10.1002/jqs.2553

Nekola, J. C. (2003). Large-scale Terrestrial Gastropod Community Composition Patterns in the Great Lakes Region of North America. *Divers. Distrib.* 9, 55–71. doi:10.1046/j.1472-4642.2003.00165.x

Peterse, F., Prins, M. A., Beets, C. J., Troelstra, S. R., Zheng, H., Gu, Z., et al. (2011). Decoupled Warming and Monsoon Precipitation in East Asia over the Last Deglaciation. *Earth Planet. Sci. Lett.* 301 (1–2), 256–264. doi:10.1016/j.epsl.2010.11.010

Qian, L. Q. (1991). *Climate of the Loess Plateau*. Beijing: China Meteorological Press.

Richter, C., Roettig, C.-B., Wolf, D., Groh, K., Kolb, T., and Faust, D. (2019). Changes in Pleistocene Gastropod Faunas on Fuerteventura (Canary Islands) and Implications on Shifting Palaeoenvironmental Conditions. *Quat. Sci. Rev.* 209, 63–81. doi:10.1016/j.quascirev.2019.02.005

Rousseau, D.-D., and Wu, N. (1997). A New Molluscan Record of the Monsoon Variability over the Past 130 000 Yr in the Luochuan Loess Sequence, China. *Geology* 25, 275–278. doi:10.1130/0091-613(1997)025<0275:ANMROT>2.3

Rousseau, D.-D., Wu, N., Pei, Y., and Li, F. (2009). Three Exceptionally strong East-Asian Summer Monsoon Events during Glacial Times in the Past 470 Kyr. *Clim. Past* 5, 157–169. doi:10.5194/cpd-4-1289-200810.5194/cp-5-157-2009

Rousseau, D.-D., Wu, N. Q., and Guo, Z. T. (2000). The Terrestrial Mollusks as New Indices of the Asian Paleomonsoons in the Chinese Loess Plateau. *Glob. Planet. Change* 26, 199–206. doi:10.1016/S0921-8181(00)00086-2

Shakun, J. D., Clark, P. U., He, F., Marcott, S. A., Mix, A. C., Liu, Z., et al. (2012). Global Warming Preceded by Increasing Carbon Dioxide Concentrations during the Last Deglaciation. *Nature* 484, 49–54. doi:10.1038/nature10915

Sibson, R. (1981). "A Brief Description of Natural Neighbor Interpolation," in *Interpolation Multivariate Data* (New York: John Wiley & Sons), 21–36.

Sümegi, P., Náfrádi, K., Molnár, D., and Sávai, S. (2015). Results of Paleoecological Studies in the Loess Region of Szeged-Öthalom (SE Hungary). *Quat. Int.* 372, 66–78. doi:10.1016/j.quaint.2014.09.003

Tan, M. (2009). Circulation Effect: Climatic Significance of the Short-Term Variability of the Oxygen Isotopes in Stalagmites from Monsoonal China: Dialogue between Paleoclimate Records and Modern Climate Research. *Quatern. Sci.* 29, 851–862. (In English abstract). doi:10.3969/j.issn.1001-7410.2009.05.01

Wang, H. (2001). The Weakening of the Asian Monsoon Circulation after the End of 1970's. *Adv. Atmos. Sci.* 18, 376–386. doi:10.1007/BF02919316

Wang, S., Gong, D., and Zhu, J. (2001a). Twentieth-century Climatic Warming in China in the Context of the Holocene. *The Holocene* 11, 313–321. doi:10.1191/095968301673172698

Wang, Y. J., Cheng, H., Edwards, R. L., An, Z. S., Wu, J. Y., Shen, C.-C., et al. (2001b). A High-Resolution Absolute-Dated Late Pleistocene Monsoon Record from Hulu Cave, China. *Science* 294, 2345–2348. doi:10.1126/science.1064618

Webster, P. J., Magaña, V. O., Palmer, T. N., Shukla, J., Tomas, R. A., Yanai, M., et al. (1998). Monsoons: Processes, Predictability, and the Prospects for Prediction. *J. Geophys. Res.* 103, 14451–14510. doi:10.1029/97JC02719

Webster, R., and Oliver, M. A. (2001). *Geostatistics for Environmental Science*. Toronto: John Wiley & Sons.

Wen, R., Xiao, J., Fan, J., Zhang, S., and Yamagata, H. (2017). Pollen Evidence for a Mid-Holocene East Asian Summer Monsoon Maximum in Northern China. *Quat. Sci. Rev.* 176, 29–35. doi:10.1016/j.quascirev.2017.10.008

Wu, N., Chen, X., Rousseau, D., Li, F., Pei, Y., and Wu, B. (2007). Climatic Conditions Recorded by Terrestrial Mollusc Assemblages in the Chinese Loess Plateau during marine Oxygen Isotope Stages 12-10. *Quat. Sci. Rev.* 26, 1884–1896. doi:10.1016/j.quascirev.2007.04.006

Wu, N., Li, F., and Rousseau, D.-D. (2018). Terrestrial Mollusk Records from Chinese Loess Sequences and Changes in the East Asian Monsoonal Environment. *J. Asian Earth Sci.* 155, 35–48. doi:10.1016/j.jseaes.2017.11.003

Wu, N., Liu, T., Liu, X., and Gu, Z. (2002). Mollusk Record of Millennial Climate Variability in the Loess Plateau during the Last Glacial Maximum. *Boreas* 31, 20–27. doi:10.1111/j.1502-3885.2002.tb01052.x

Wu, N. Q., Rousseau, D. D., and Liu, T. S. (1996). Land Mollusk Records from the Luochuan Loess Sequence and Their Paleoenvironmental Significance. *Sci. China, Ser. D Earth Sci.* 39, 494–502.

Wu, N., Rousseau, D. D., and Liu, D. (1999). Climatic Instability Recorded by the Mollusk Assemblages from the Late Glacial Loess Deposits in China. *Chin.Sci.Bull.* 44, 1238–1242. doi:10.1007/bf02885974

Wu, N., Rousseau, D. D., Liu, T., Lu, H., Zhaoyan, G., Guo, Z., et al. (2001). Orbital Forcing of Terrestrial Mollusks and Climatic Changes from the Loess Plateau of China during the Past 350 Ka. *J. Geophys. Res.* 106, 20045–20054. doi:10.1029/2001JD900224

Wu, N., Rousseau, D. D., and Liu, X. (2000). Response of Mollusk Assemblages from the Luochuan Loess Section to Orbital Forcing since the Last 250 Ka. *Chin.Sci.Bull.* 45, 1617–1622. doi:10.1007/bf02886225

Yang, S., and Ding, Z. (2008). Advance-retreat History of the East-Asian Summer Monsoon Rainfall belt over Northern China during the Last Two Glacial-Interglacial Cycles. *Earth Planet. Sci. Lett.* 274, 499–510. doi:10.1016/j.epsl.2008.08.001

Yang, S., Ding, Z., Li, Y., Wang, X., Jiang, W., and Huang, X. (2015). Warming-induced Northwestward Migration of the East Asian Monsoon Rain belt from the Last Glacial Maximum to the Mid-holocene. *Proc. Natl. Acad. Sci. U.S.A.* 112, 13178–13183. doi:10.1073/pnas.1504688112

Yen, T. C. (1939). Die Chinesischen land-und Süsswasser Gastropoden des natur-museums senckenberg. *Abhandlumgen der Senckenbergischen Naturforschenden Gesellschaft* 444, 1–235.

Zhou, X., Sun, L., Zhan, T., Huang, W., Zhou, X., Hao, Q., et al. (2016). Time-transgressive Onset of the Holocene Optimum in the East Asian Monsoon Region. *Earth Planet. Sci. Lett.* 456, 39–46. doi:10.1016/j.epsl.2016.09.052

Conflict of Interest: The authors declare that the research was conducted in the absence of any commercial or financial relationships that could be construed as a potential conflict of interest.

Publisher's Note: All claims expressed in this article are solely those of the authors and do not necessarily represent those of their affiliated organizations, or those of the publisher, the editors and the reviewers. Any product that may be evaluated in this article, or claim that may be made by its manufacturer, is not guaranteed or endorsed by the publisher.

Copyright © 2021 Dong, Wu, Li and Lu. This is an open-access article distributed under the terms of the Creative Commons Attribution License (CC BY). The use, distribution or reproduction in other forums is permitted, provided the original author(s) and the copyright owner(s) are credited and that the original publication in this journal is cited, in accordance with accepted academic practice. No use, distribution or reproduction is permitted which does not comply with these terms.

frontiers
in Environmental Science

ORIGINAL RESEARCH
published: 23 November 2021
doi: 10.3389/fenvs.2021.781179

Analysis of Drought and Flood Disasters During 0–1950 AD in the Hexi Corridor, China, Based on Historical Documents

Xia Tang[1,2]* *and Qi Feng*[1,2]

[1]*Key Laboratory of Ecohydrology of Inland River Basin, Chinese Academy of Science, Lanzhou, China,* [2]*Northwest Institute of Eco-Environment and Resources, Chinese Academy of Sciences, Lanzhou, China*

It is important to analyze the characteristics of drought and flood change in an arid area over a long timescale for the evolution of the environment. Historical documents were used to reconstruct a drought and flood grade series for the Hexi Corridor from 0 to 1950 AD. The moving average and wavelet transform processing methods were used to determine the temporal evolution characteristics of droughts and floods, as well as the corresponding relationships with climate change and human activities in the Hexi Corridor after 1000 AD. The results showed the occurrence of eight drought phases (370–410 AD, 790–870 AD, 1050–1150 AD, 1260–1340 AD, 1430–1570 AD, 1710–1770 AD, 1800–1890 AD, and 1910–1950 AD), five flood phases (320–360 AD, 1670–710 AD, 1730–1790 AD, 1810–1860 AD, and 1880–1950 AD), and 3 oscillation periods of drought and flood events. Climate change may have been the main factor inducing droughts and floods before 1580 AD, whereas human activities may have increased the frequency of droughts and floods after the 16th century. Therefore, quantifying the impacts of natural factors and human activities on droughts and floods can provide important theoretical guidance for the prevention and reduction of future disasters.

Keywords: hexi corridor, drought and flood grade, historical period, reconstruction, climate chang

OPEN ACCESS

Edited by:
Zhuolun Li,
Lanzhou University, China

Reviewed by:
Guodong Li,
Henan University, China
Yamin Wang,
Changsha Normal University, China

Correspondence:
Xia Tang
tangxia@llas.ac.cn

Specialty section:
This article was submitted to Interdisciplinary Climate Studies, a section of the journal Frontiers in Environmental Science

Received: *22 September 2021*
Accepted: *02 November 2021*
Published: *23 November 2021*

Citation:
Tang X and Feng Q (2021) Analysis of Drought and Flood Disasters During 0–1950 AD in the Hexi Corridor, China, Based on Historical Documents. Front. Environ. Sci. 9:781179. doi: 10.3389/fenvs.2021.781179

INTRODUCTION

Coping with droughts, floods, and extreme hydrological events has been a focus of social concern since the beginning of human civilization. Long-term imbalances between water supply and demand lead to droughts and floods (Kundzewicz and Kaczmarek, 2000) that reflect an extremal process in the natural evolution of the climate (Xing et al., 2013). Extremely high temperatures and heavy rainfall events on the global scale may become frequent at the end of the 21st century, and the overall economic losses caused by extreme climate events could gradually increase (Field et al., 2012). Consequently, the probability and intensity of storms, floods, and drought events will inevitably increase in different regions. The following goal was set in the 2030 Agenda for Sustainable Development adopted by the United Nations in 2015 to reduce disaster risks: “By 2030, significantly reduce the number of deaths and the number of people affected and substantially decrease the direct economic losses relative to the global gross domestic product caused by disasters, including water-related disasters.” (Lv et al., 2015).

Study of the occurrence pattern of extreme climate disaster events on the background of global warming, it is necessary to examine climate events over the long-term climate evolution and analyze

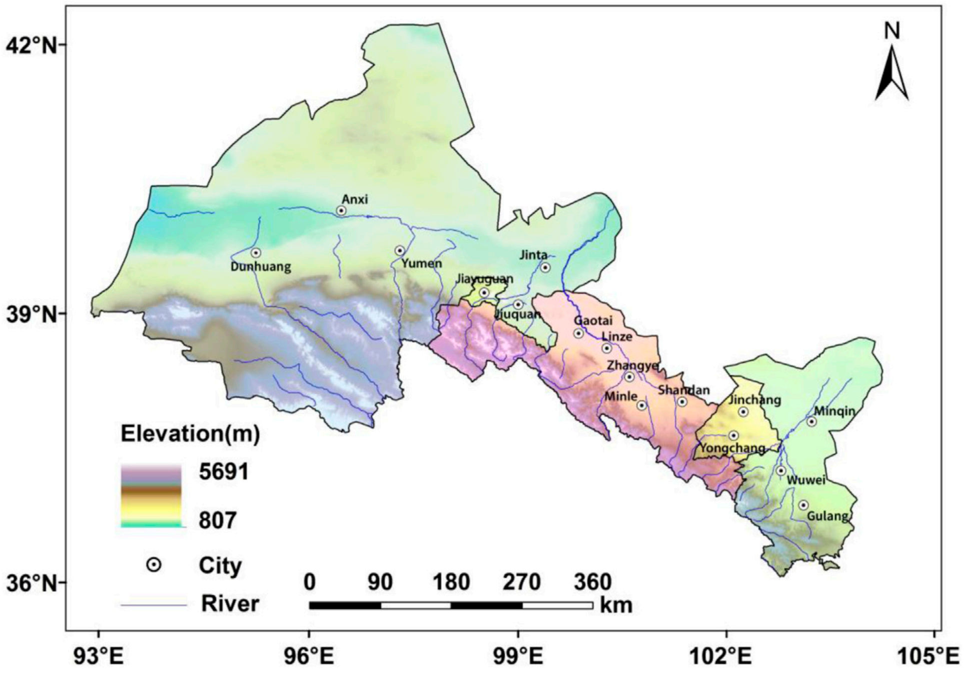

FIGURE 1 | The location of the Hexi Corridor.

the inherent regularity of them. Historical documents have been one of the most important climate records due to their time accuracy, high spatial resolution, and rich information content (Pfister and Wanner, 2002). The Hexi Corridor is located in an inland arid and semiarid climate transition zone in northwestern China with a dry climate and high rainfall variability. Variations in precipitation significantly affect local agricultural production and other aspects of life in the Hexi region and have been the main factor controlling the occurrence of droughts and floods. However, due to the regional differences in the distribution of Chinese historical documents, the previous related studies the climate changes rarely involved the Hexi Corridor of Northwest China. For example, Feng. (1982) compiled climate data from historical documents in the Qilian Mountains and the surrounding areas. Dong et al. (2012) used historical documents to analyze variations in the occurrence of droughts and floods during the Little Ice Age in the Hexi Corridor. Existing studies have mainly been conducted on the Ming and Qing Dynasty periods, for which historical data is relatively abundant. For instance, the consequences of vegetation destruction in the Hexi Corridor have been recorded in historical documents from the Qing Dynasty: 1) The quantity of snow in the Hexi Corridor decreased, the water levels of rivers and streams were low, and the rivers ran dry from time to time. 2) The water level in the rivers was insufficient for irrigation, resulting in drought. 3) The air was dry, and rainfall decreased. (Pan, 2009). However, few studies have been performed on variations in the occurrence of droughts and floods in the Hexi Corridor over the past 2000 years.

A study of the occurrence pattern of extreme climate disaster events against the background of global warming requires an analysis of climate events over a long time scale to discover inherent regularity. Historical documents are one of the most important types of climate records available because of temporal accuracy, a high spatial resolution, and rich informational content (Qian and Zhu, 2002; Ji et al., 2015). Therefore, a variety of historical documents was used to reconstruct a drought and flood series for the Hexi Corridor from 0 to 1950 AD in this study. The wavelet transform was used to analyze the cycle of droughts and floods. The reconstructed drought and flood series was used to discuss the relationship between disasters, human activities and climate change. The results fill in gaps in the understanding of drought and flood characteristics in the Hexi Corridor during 0–1950 AD and lay a foundation for future prevention and mitigation of disasters.

METHODOLOGY

Study Area

The Hexi Corridor is located in western Gansu Province (36°46′-42°49′ N, 96°44′-104°14′ E), with Wushaoling to the east, the intersection of Gansu and Xinjiang to the west, the Qilian Mountains to the south, and the Inner Mongolia Autonomous Region to the north (**Figure 1**). The corridor spans up to 1,100 km from east to west over an area of approximately 276,000 km^2. Since the four counties of Hexi were established in the Western Han Dynasty (121 BC-111 BC), the Hexi Corridor has been formally included in the political system of the Central Plains Dynasties. The Hexi Corridor was a significant route of China's "Silk Road Economic Belt" between Asia and Europe and an important base for China's grain commodity and metallurgy.

The Hexi Chorography records show that oasis cultivation, ditch construction, dam construction, and water diversion for irrigation began in the Hexi Corridor over 2000 years ago (Tang and Feng, 2015). The development of large-scale water conservation and excessive logging of surface vegetation accelerated soil salinization and desertification, leading to frequent flood and drought disasters (Xiao and Xiao, 2008; Tang et al., 2014; Sendai, 2015). The Hexi Corridor has a continental monsoon climate characterized by strong winds, dry soil, and frequent droughts in midsummer. Improper farmland water conservation disrupted the ecological balance and affected the temporal and spatial patterns of extreme hydrological processes in inland rivers (Xing et al., 2013).

Four counties, namely, Wuwei, Jiuquan, Zhangye, and Dunhuang, were established in the Hexi Corridor during the Western Han Dynasty. The names of the administrative districts and counties in the Hexi Corridor were subsequently changed occasionally during the Southern and Northern Dynasty and the Sui, Tang, Song, Yuan, Ming, and Qing Dynasties. However, under the current administrative division scheme, the study area mainly corresponds to the historical Hexi Corridor, including the Jiuquan area (the cities of Jiuquan, Yumen, and Dunhuang and Jinta, Guazhou, Subei, and Aksai Counties); the Zhangye area (the cities of Zhangye and Linze, Gaotai, Shandan, Minle, and Sunan Counties); the Wuwei area (the city of Wuwei and Minqin, Gulang, and Tianzhu Counties); and the two prefecture-level cities of Jinchang (Yongchang County, Jinchuan District) and Jiayuguan.

Historical Document Processing

In ancient times, Chinese governmental agencies generally instituted a special department to compile chorography into an official publication. These typical records are useful for investigating climate change, including natural disasters events and related information (Qian and Zhu, 2002). Data sources of this study are based on "The Chorography of Hexi" (Zhangye Prefectural Committee, 1958) and "Encyclopaedia of China's Meteorological Disasters; Gansu Volume" (Wen and Dong, 2005). Moreover, we further analyzed and verified these collected data with references, including "the History of Disaster and Famine in Northwest China (780 BC-1949 AD) (Yuan, 1994), "the China Meteorological Disaster Encyclopedia: Gansu Fascicule (718 BC-2000 AD)" (Dong et al., 2005), "A Compendium of Chinese Meteorological Records of the Last 3,000 Years" (Zhang, 2000) and "The Atlas of Drought and Flood Distribution over Northwest China in the Past 500 Years" (Bai et al., 2010). These historical records are descriptions of the drought and flood events; thus, they are usually incompleteness and non-continuous. To build a longer record, we synthesized all data sources and then determined a method of replacing missing data. First, we assumed that any year without a flood and drought record was a normal year if the length of missing record was less than 3 years (Chinese Academy of Meteorological Sciences, China Meteorological Administration, 1981). Second, we used the same-year records from other counties that adjoin the Hexi Corridor to identify the missing records.

We selected 0–1950 AD as our study period, spanning approximately 2,000 years. A total of 365 events related to droughts and floods were found. Verbal descriptions of droughts and floods were recorded in the documents, such as "a drought occurred in Ganzhouwei in the summer of the fourth year of the Jingtai Period in the Ming Dynasty (1453 AD)" and "during the first year of the Taiding Period in the Yuan Dynasty (1324 AD), the Heishui River flooded in June, and the rains damaged crops in Ganzhou in September" (Dong et al., 2005). Therefore, this written information was quantitatively analyzed to reconstruct a series of drought and flood grades.

Quantification of Drought and Flood Grades

The descriptive sentences of droughts and floods recorded in historical documents were comprehensively analyzed. The intensity of a disaster was evaluated based on two aspects, socioeconomics and natural phenomena. The grade classification method of historical droughts and floods of the China Meteorological Administration (Bai et al., 2010) was used to standardize the drought and flood grades obtained from the literature. The records were classified into five grades depending on the severity of the disaster (**Table 1**): grade 1 denotes flooding, grade 2 denotes partial waterlogging, grade 3 denotes no drought or flood, grade 4 denotes a partial drought, and grade 5 denotes a drought.

Wavelet Analysis

Morlet first proposed the use of wavelet analysis with a time-frequency multiresolution function for signal processing and analysis in the early 1980s. This method consists of denoising, reconstructing, and extracting signals, such as sound, image, and earthquake signals, to determine the time or frequency domain over which vibration periods of different signals appear. Wavelet analysis is now widely used to study periodic variations in climate and hydrological series (Yuan, et al., 2014; Sang et al., 2013; Ye et al., 2014). Wavelet analysis can clearly reveal local variation characteristics implicit in time series, fully reflect the variations in a system on different timescales, and improve the analysis of the temporal evolution of a series (Abramovich et al., 2000). MATLAB (R2011a) was used in this study to perform a wavelet analysis on the series of drought and flood levels in the Hexi Corridor from 0 to 1950 to determine alternating drought and flood patterns.

RESULTS

Reconstruction of the Drought and Flood Grade Series

The aforementioned documents and disaster quantification criterion were used to statistically analyze the series for Hexi drought and flood grades from 0 to 1950 AD. A total of 365 droughts or floods of different grades occurred in the Hexi Corridor during this period. Among the 256 droughts, 173 were grade 4, and 83 were grade 5 (**Figure 2**). Droughts occurred once every seven to 8 years on average. This frequency is slightly higher than that mentioned in the farmer's almanac: "A major drought occurs every 10 years". There were 109 floods of different grades, of which 84 were grade 2 and 25 were grade

TABLE 1 | Quantification standard for drought and flood grades [1.5].

Grade	Quantification criterion	Natural conditions	Socioeconomic aspects
1 (Flood)	Long-lasting and intense precipitation: large-scale severe flooding	Long-lasting heavy rain in the spring and summer; heavy rain and river flooding in the summer; floods, storms, and heavy rain; continuous rain lasting from days to months; upper and lower reaches of river flooded; rain-damaged crops	People ate each other; the government provided relief to starving people; countless people and animals drowned; severe flooding; most people were homeless
2 (Partial waterlogging)	Moderate flood in a single season or month: regional flooding	Flooding in april; regional floods; heavy/torrential rain; regional flash floods; sudden mountain torrents resulting in farmland destruction; long-lasting heavy rain in autumn resulting in crop damage	Flooding; famine; many people fled their homes; people who had starved to death were seen everywhere; rice prices were extremely high
3 (Normal)	No droughts or floods	Bumper harvest, rich harvest, a year of plenty	—
4 (Partial drought)	Moderate drought in a single season or month: regional drought	Drought in the spring; drought in the autumn; drought and locust infestation; summer rice yield considerably lower than usual; little rain for late crops; drought and plague; drought and famine; drought in the counties of the Hexi Corridor in the summer and autumn	Drought; land tax collection was halted; famine; many people fled their homes; people who had starved to death could be seen everywhere; rice prices were extremely high
5 (Drought)	Drought lasting for months to seasons: large-scale severe drought	Dry rivers and pools; severe drought in the summer and autumn; no rain from spring to autumn; drought lasting years, with many people fleeing their homes; drought from the spring to the autumn, winter drought	People who had starved to death could be seen everywhere; people ate people; no harvest, famine; the government provided relief to starving people and reduced land taxes

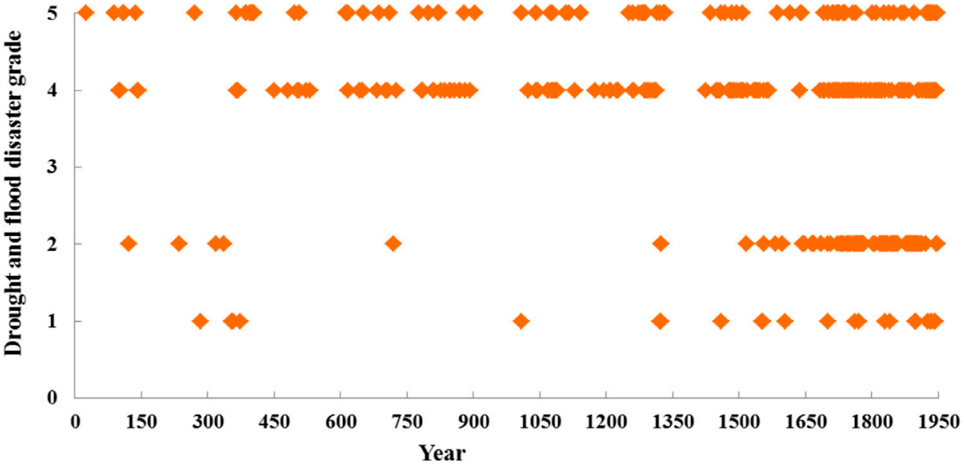

FIGURE 2 | Grades of droughts and floods in the Hexi Corridor from 0 to 1950 AD.

1. Floods occurred once every 17–18 years on average. The number of droughts and floods increased significantly starting in 300 AD. Fluctuations in the occurrence of floods manifested as an increase-decrease-increase pattern. More detailed and accurate records may have been kept in more recent periods. In general, the number of droughts increased continuously, and droughts occurred more frequently than floods in the Hexi Corridor. This result was linked to the location and geographic environment of the area.

Characteristic Changes of Droughts and Floods

A 10-years moving average was calculated from the reconstructed series to determine long-term variations in droughts and floods. A peak value analysis showed that droughts occurred frequently in the Hexi Corridor during eight phases, namely, 370–410, 790–870, 1050–1150, 1260–1340, 1430–1570, 1710–1770, 1800–1890, and 1910–1950. In particular, droughts lasted longer after 1880, with a clear increase in the overall drought duration over time (**Figure 3A**). Floods occurred frequently during five phases, namely, 320–360, 1670–1710, 1730–1790, 1810–1860, and 1880–1950. The highest flood frequency among these five phases occurred during the Guangxu period in the Qing Dynasty (**Figure 3B**). Large fluctuations in the trend line reflected a clear historical increase in the numbers of drought and flood disasters.

We compared the frequencies of droughts and floods over 10-year periods to analyze the characteristics in the Hexi Corridor. The two types of disasters were basically the same in terms of the

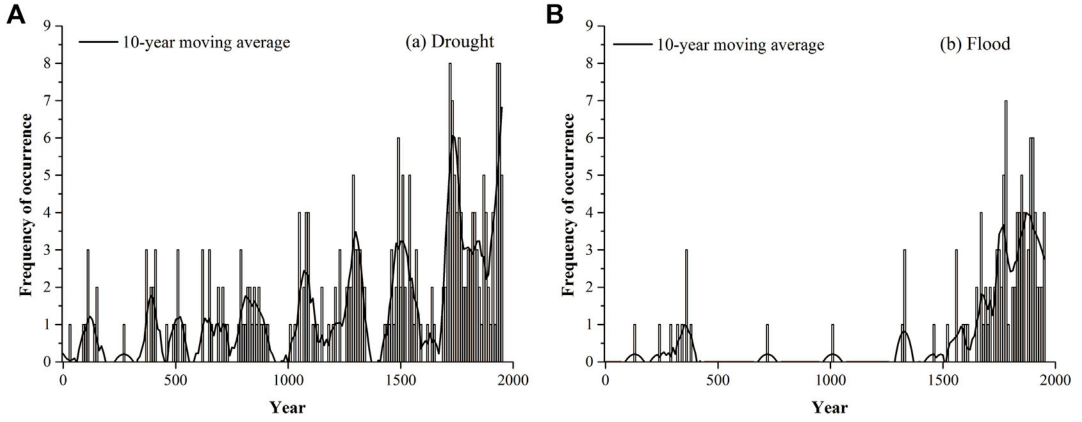

FIGURE 3 | Frequencies of droughts and floods in the Hexi Corridor from 0 to 1950 AD.

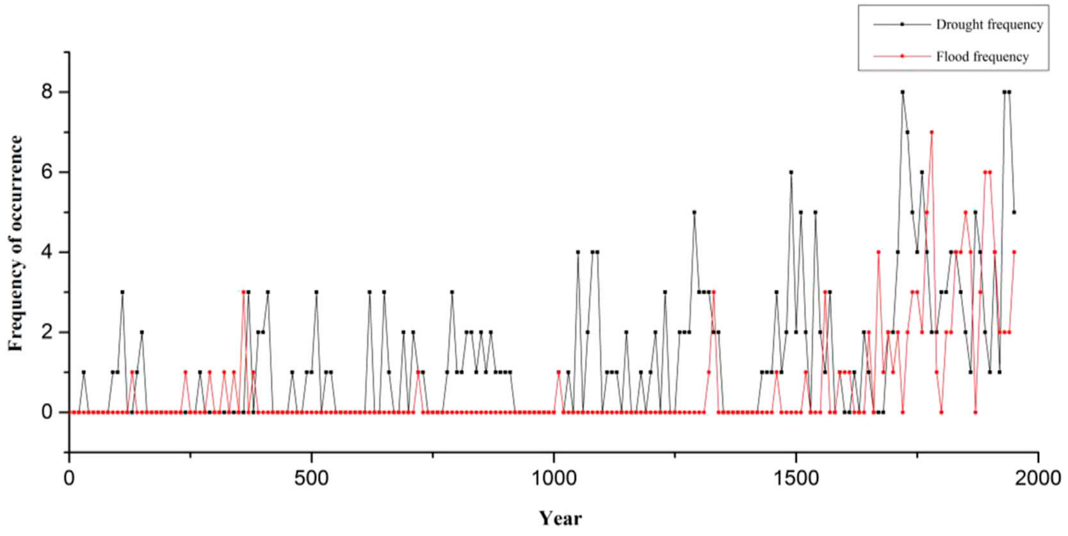

FIGURE 4 | Comparison of drought and flood frequency in the Hexi Corridor from 0 to 1950 AD.

phases of high occurrence and the general trend. The frequencies of droughts and floods have gradually increased over the last 400 years (**Figure 4**). The results showed that during 1600–1950 AD, drought and flood events occurred 194 times in the Hexi Corridor, and the average frequency was 2.78 years. These events occurred more frequently in the middle and late stages of the study period, and the frequency showed an upward trend. The occurrence of droughts and floods in the Hexi Corridor alternated to some extent, with frequent correspondence in intensity between nearby floods and droughts in the time series. Major droughts were generally followed by major floods. For instance, major droughts lasting for years were followed by major floods at approximately 1720–1780 AD, 1830–1860 AD, and 1900–1940 AD. Considering the full time series showed that droughts occurred more frequently and with higher intensity than floods in the Hexi Corridor.

Periodic Characteristics of Droughts and Floods

Droughts and floods occurred during different phases with a well-defined periodicity. The Morlet wavelet was used to analyze the historical data of droughts and floods during the 1950-years study

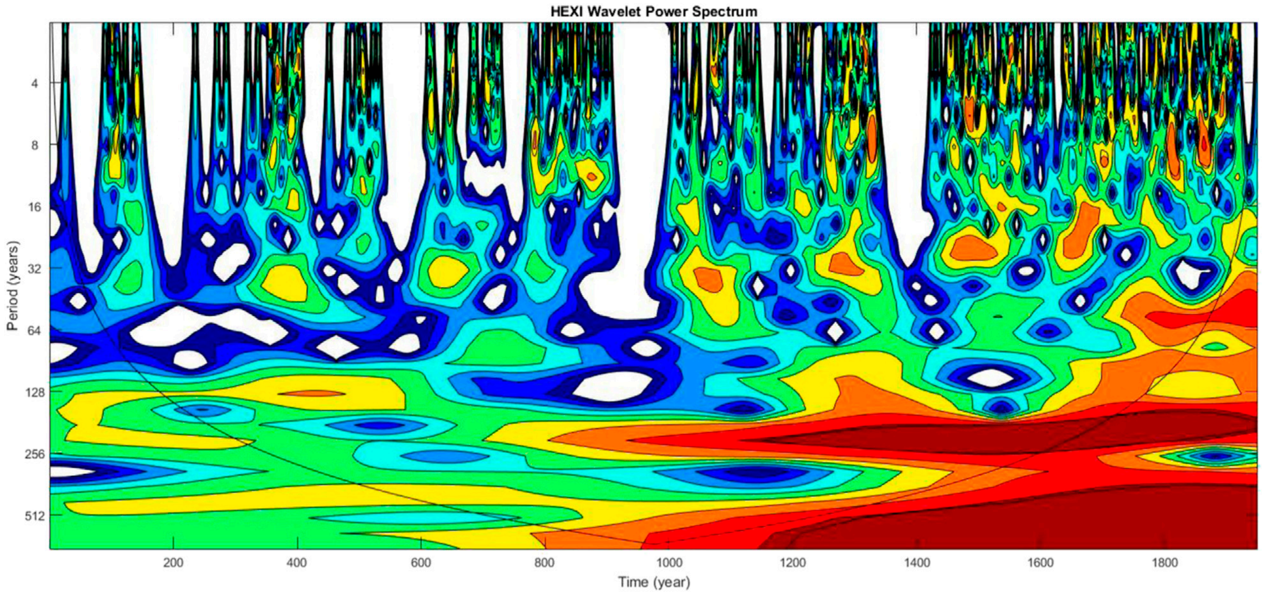

FIGURE 5 | Wavelet analysis of droughts and floods in the Hexi Corridor from 0 to 1950 AD.

period. A wavelet variance analysis (**Figure 5**) showed that there were 3 oscillation periods at approximately 33–34 a, 71–77 a, and 165–220 a, and the oscillation period around 165–185 a was most intense. Our findings match with the research of Li and Zhao. (2008), which demonstrated that there was a period around 168 a for the drought and flood disasters in northwestern China.

Relationship Between the Occurrence of Droughts and Floods and Climate Change

An analysis of the reconstructed drought and flood data shows scarce historical records for the Hexi Corridor in northwestern of China before 1000 AD (the Northern Song Dynasty), such that detailed disaster records were not available. The data from 1000 to 1950 were subsequently used to determine the drought and flood influence factors. Liu et al. (2004) used tree-ring data from the central part of the northern slope of the Qilian Mountains to reconstruct the temperature changes in the Qilian region over a millennial scale. The cold and warm periods in the Qilian juniper tree-ring records match well with the Dunde ice core records and the winter half-year temperature records in eastern China (Thompson et al., 1995; Yao et al., 1996). The results of Liu et al. (2004) were used to classify the cold and warm changes from 1000 to 1950 into eight phases, and the frequencies of droughts and floods were calculated for each phase. The drought frequency was clearly higher during the cold phases than during the warm phases for phases 1 to 6, whereas the reverse occurred during phases 7 and 8. There flood frequency was clearly higher during the warm periods than during the cold periods for phases 5 to 8. However, floods only occurred during the cold phases for phases 1 to 4 (**Table 2**).

Climate change may have been the main influence factor for the occurrence of droughts and floods before 1580. Note that droughts were more frequent during cold periods than during warm periods, and the flood frequency fluctuated but increased over time. Human activities have caused global climatic deterioration since 1581, coupling with frequent extreme drought and flood events (**Table 3**). Human activities have significantly changed the spatial pattern of water resources and surface vegetation coverage, which has conspicuously affected the local climate (Zhang et al., 1997). Consequently, droughts and floods have been affected by climate change and indirectly by human activities. Further study is required to determine whether the frequent droughts and floods in the Hexi Corridor resulted from intensified human activities or natural environmental evolution.

Relationship Between the Occurrence of Droughts and Floods and Land Area Change

The frequencies of droughts and floods per 50 years increased from approximately 2.3 during the Han Dynasty to approximately 43.2 during the Republic of China era over the study period (**Table 3**). The occurrence of droughts and floods increased continuously throughout the study period. Cheng. (2007) reconstructed the desertified land areas of the Hexi Corridor during the last 2000 years, corresponding to three large-scale desertification processes. The desertified land area during the Northern and Southern Dynasties (420–589 AD), the final Tang and Five Dynasties (836–960), and the Ming and Qing Dynasties (1368–1911 AD) was 1070, 1765, and 6,884 km^2, respectively. The changes in the desertified land areas were basically consistent with the occurrences of disasters. The large-scale construction of water conservancy projects and reclamation of oases, have resulted in frequent

TABLE 2 | Droughts and floods disasters during cold and warm phases from 1000 to 1950.

Phase	Year (AD)	Temperature (°C) (Liu et al., 2004)	Period length (years)	Proportion of drought frequency (%)	Proportion of flood frequency (%)	Cold and warm periods (Liu et al., 2004)
1	1000–1050	1.79	50	15.0	2.0	Cold
2	1051–1150	1.92	100	12.0	0.0	Warm
3	1151–1350	1.81	200	15.5	3.0	Cold
4	1351–1440	2.21	90	2.2	0.0	Warm
5	1441–1510	1.8	70	28.6	1.4	Cold
6	1511–1580	1.98	70	17.1	5.7	Warm
7	1581–1890	1.72	310	26.8	21.9	Cold
8	1891–1950	2.06	59	45.8	33.9	warm

TABLE 3 | Frequencies of disasters and changes in desertified land area during historical periods.

Historical periods	Year (AD)	Flood frequency	Drought frequency	Total number of disasters	Frequency (per 50 years)	Desertified land area (km^2)	Population (10^4 Person)
Han Dynasty	0–220[a]	2	8	10	2.3	—	28.02
Wei-Jin Era	220–581	8	19	27	3.8	1070	19.88
Sui-Tang Dynasty	581–907	1	33	34	5.2	1765	27.55
Song-Yuan Dynasty (Western Xia)	960–1368	5	52	57	7.0	—	10.5
Ming-Qing Dynasty	1368–1911	83	122	205	18.9	6,884	30.6
The Republic of China	1912–1950	10	22	32	43.2	—	96.5

[a] *Note: data for the Eastern and Western Han Dynasties were only available from 0 to 220 AD, because of limited historical records.*

and alternating droughts and floods. In particular, great importance was attached to the development and management of Hexi Corridor during the Ming and Qing Dynasties (**Table 3**), such that various measures to restore agricultural production were adopted, and inland immigrants were encouraged to expand oasis cultivation (Tang et al., 2018). For example, the population in the Hexi area reached 2.945 million during the Jiaqing period of the Qing Dynasty (1796–1820 AD) (Cheng, 2009). Although the cultivated land area in the Hexi Corridor reached 341,100 hm^2 at this time, the water conservation system was not complete, and the frequencies of droughts and floods reached 18.9 per 50 years. Thus, disasters occurred in approximately 37.8% of the years comprising the Qing Dynasty. Historical records from the 40th year of the Qianlong Period of the Qing Dynasty (1775) state "there were droughts, hails, and starving people in 31 sub prefectures, departments, and counties, including Gulang, Fuyi, Zhangye, Dongle, Suzhou, Shandan, Gaotai, and Anxi" and that in Linze County, "because the five canals have been dry for the last several years, people have struggled to survive" (Pan 2009).

DISCUSSION

Population growth, the development of water and soil resources, cultivated oasis expansion, indiscriminate reclamation, and deforestation resulted in considerable destruction of forest vegetation in the Hexi Corridor. The ecological environment gradually deteriorated, the lands became infertile, and extreme flood and drought events occurred frequently (Li, 2003; Pan 2009; Yu et al., 2011). Compared with the droughts and floods in the historical period, the more recent disasters striking the Hexi Corridor have been more varied, such as climatic droughts, hydrological droughts, ecological droughts, and artificial droughts in recent years. Modern meteorological records show that droughts and floods occurred frequently in the Hexi Corridor in 1956–1995, especially in the middle and lower reaches of the Heihe River (Ren et al., 2010). From 1951 to 2001, there was a considerable proportion of years with consecutive droughts in Zhangye city in the middle reaches of the Heihe River (Yin and Zhang, 2004). The drought proportion was as high as 78.8% (Chu, 2014). On the background of global warming, the area of irrigated farmland in the Hexi Corridor has increased sharply (Wang and Zhang, 2007), and the amount of agricultural water consumption has gradually increased. These resulted in an average of 60.3 days/year from 1957 to 2000 that the Heihe River dried up (Liu et al., 2008). Intense human activities have greatly changed the natural circulation of water resources in the area, resulting in soil erosion, enhanced desertification, sharp declines in forest and grassland areas, and deterioration of the ecological environment. The frequent occurrence of droughts and floods is further affected by humans. Therefore, the intensity and frequency of human activities should be weakened.

The effect of human activities on droughts and floods, in addition to that of natural evolution, makes the periodicity of droughts and floods more complex. The increasing frequency and intensity of extreme hydrological events has made "two droughts in 3 years" an inescapable reality in the Hexi Corridor (Ke and Lv, 2005). It is necessary to quantify the impacts of natural factors and human activities on the occurrence of droughts and floods in this typical inland arid region the future. Special attention should be paid to the hydrological cycle of the Heihe River, Shiyang River, and Shule River in the Hexi Corridor. (For example, March to May is the peak of spring irrigation in the middle reaches of the rivers. This time coincides with the dry season of the rivers, and the downstream riverbeds dry up. July to September is the high-water season of summer. The peak annual runoff is formed in September.) Attention should also be paid to the potential impact of factors such as river channel relocation, land-use changes, and runoff changes at outlets of rivers on extreme hydrological events.

CONCLUSION

Historical documents were used to reconstruct a series for the occurrence of droughts and floods in the Hexi Corridor from 0 to 1950 AD. Wavelet analysis was used to determine the disaster cycle of the series. Considering the changes in the climate (after 1000 AD) and desertified land area in the region showed that flood and drought disasters were affected by climate change and human activities in the Hexi Corridor. Nevertheless, it is difficult to discriminate between the influence of natural fluctuations and human interventions.

1) Drought was the main influence factor for disasters over time. Droughts occurred more frequently and intensively than floods. Droughts occurred very frequently during eight phases, on average once every seven to 8 years. The drought frequency clearly increased over time. Floods occurred very frequently certain phases, once every 17–18 years on average.
2) Droughts and floods occurred over three distinct periodic lengths, namely, 33–34 a, 71–77 a, and 165–220 a. Comparison with other study that there was a period around 168a for the drought and flood disasters in northwestern China.
3) Climate changes appear to have been the main factor affecting droughts and floods before 1580 AD. However, alternation between droughts and floods became more significant after the 16th century because human activities intensified the frequency of disasters. A preliminary analysis shows that changes in the desertified land area were basically consistent with the occurrence of disasters, indicating that overcultivation of oases, indiscriminate reclamation, and deforestation increased the frequency of droughts and floods. Further studies are required to determine whether this phenomenon was caused by human activities or natural environmental evolution.

DATA AVAILABILITY STATEMENT

The raw data supporting the conclusions of this article will be made available by the authors, without undue reservation.

AUTHOR CONTRIBUTIONS

XT: conceptualization, methodology, and writing draft. QF: supervision and reviewing.

FUNDING

This study was funded by the National Natural Science Foundation of China (Grant Nos. 41801079) and the Natural Science Foundation of Gansu Province, China (Grant Nos. 18JR3RA385). The authors would like to thank the editors and reviewers for detailed and constructive comments that significantly improved the manuscript.

REFERENCES

Abramovich, F., Bailey, T. C., and Sapatinas, T. (2000). Wavelet Analysis and its Statistical Applications. *J. R. Statist Soc. D* 49 (1), 1–29. doi:10.1111/1467-9884.00216

Bai, H. Z., Dong, A. X., and Zheng, G. F. (2010). *The Atlas of Drought and Flood Distribution over Northwest China in Past 500 years: 1470-2000*. Beijing: China Meteorological Press.

Central Meteorological Administration (1981). *Yearly Charts of Dryness-Wetness in China for the Last 500 Years Period*. Beijing: Cartographic Publishing House.

Cheng, G. D. (2009). *Integrated Management of the Water-Ecology-Economy System in the Heihe River Basin*. Beijing: Science Press, 581.

Cheng, H. Y. (2007). *Study on Desertification in Hexi Corridor in Historical Period.* Lanzhou: Lanzhou University.

Chinese Academy of Meteorological Sciences, China Meteorological Administration (1981). *Yearly Charts of Dryness/Wetness in China for the Last 500-Year Period*. Beijing, China: SinoMaps Press.

Chu, C. (2014). Analysis on Change Regulation of Meteorological Disasters in Zhangye City during 1980 to 2010. *Mod. Agric. Sci. Tech.* (3), 258–259.

Dong, A. X., Wang, P. X., and Lin, B. (2005). *China Meteorological Disaster Ency-Clopedia: Gansu Fascicule*. Beijing: China Meteorological Press, 16–220.

Dong, W. M., An, C. B., Zhao, Y. T., and Li, H. (2012). Variation of D/F Records in Historical Documents of Hexi Region during LIA and its Mechanism. *Arid Land Geogr.* 35 (6), 946–951.

Feng, S. W. (1982). The Organization of Historical Climate Data about Qilian Mountain and Surrounding Areas. *Hist. Geogr. Northwest China* 1, 1–19.

Field, C., Barros, V., Stocker, T., Qin, D., Dokken, D., Ebi, K., et al. (2012). *Managing the Risks of Extreme Events and Disasters to advance Climate Change adaptationSpecial Report of the Intergovernmental Panel on Climate Change Working Group.*

Ji, Y., Zhou, G., Wang, S., and Wang, L. (2015). Increase in Flood and Drought Disasters during 1500-2000 in Southwest China. *Nat. Hazards* 77 (3), 1853–1861. doi:10.1007/s11069-015-1679-9

Ke, Y., and Lv, X. Y. (2005). *Focus on Heihe.* Beijing: China Water & Power Press, 72.

Kundzewicz, Z. W., and Kaczmarek, Z. (2000). Coping with Hydrological Extremes. *Water Int.* 25 (1), 66–75. doi:10.1080/02508060008686798

Li, B. C. (2003). *Northwest Development and Sustainable Development Series Book: Researches on the Desertification in the Hexi Corridor during Historical Period.* Beijing: Science Press.

Li, Y. F., and Zhao, J. B. (2008). The Research on the Flooding Disaster in Guanzhong in Recent 200 Years. *Journalof Arid Land Resour. Environ.* 22 (4), 96–99.

Liu, W., Wang, T., and Zheng, H. (2008). Driving Forces of Different Type of Land Desertification in Hiehe River Basin. *J. Desert Res.* 28 (4), 634–641.

Liu, X. H., Qin, D. H., and Shao, X. M. (2004). Temperature Variations Recorded in Tree-Rings of Middle Qilian Mountains during the Last Millennium. *Sci. China (Series D)* 34 (1), 89–95.

Lv, Z. X., Wei, Y. P., and Xiao, H. L. (2015). Evolution of the Human–Water Relationships in Heihe River basin in the Past 2000 Years. *Hydrol. Earth Syst. Sci. Discuss.* 12 (1), 1059–1091.

Pan, C. H. (2009). The Water Conservancy Construction and the Changing of Ecological Environment of the Hexi Corridor in the Qing Dynasty. *Agric. Hist. China* (4), 123–130.

Pfister, C., and Wanner, H. (2002). Documentary Evidence. *PAGES news* 10 (3), 2. doi:10.22498/pages.10.3.2

Qian, W., and Zhu, Y. (2002). Little Ice Age Climate Near Beijing, China, Inferred from Historical and Stalagmite Records. *Quat. Res.* 57, 109–119. doi:10.1006/qres.2001.2283

Ren, C. X., Lu, Y. Q., and Yang, D. Y. (2010). Drought and Flood Disasters and Rebuilding of Precipitation Sequence in Heihe River Basin in the Past 2000 Years. *J. Arid Land Resour. Environ.* 24 (6), 91–95.

Sang, Y. F., Wang, Z. G., and Liu, C. M. (2013). Applications of Wavelet Analysis to Hydrology: Status and Prospects. *Prog. Geogr.* 9 (9), 1413–1422.

Tang, X., and Feng, Q. (2015). An Analysis on Historical Process and Driving Mechanism of Land Use Change in Heihe River Basin. *Res. Soil Water Conservation* 22 (03), 336–340.

Tang, X., Zhang, Z. Q., Wei, Y. P., Xiong, Y. L., and Wang, Q. H. (2014). Quantitative Evaluation of Water Resources Pressure in Heihe River Basin. *Bull. Soil Water Conservation* 6, 219–224.

Tang, X., Zhao, Y., Zhang, Z., Feng, Q., and Wei, Y. (2018). Cultivated Oasis Evolution in the Heihe River basin over the Past 2,000 Years. *Land Degrad. Dev.* 29, 2254–2263. doi:10.1002/ldr.2991

Thompson, L. G., Mosley-Thompson, E., Davis, M. E., Lin, P. N., Dai, J., Bolzan, J. F., et al. (1995). A 1000 Year Climate Ice-Core Record from the Guliya Ice Cap, China: its Relationship to Global Climate Variability. *A. Glaciology.* 21, 175–181. doi:10.1017/s0260305500015780

Sendai: UN Conference Adopts New, People-Centred Disaster Risk Reduction Strategy. (2015) Available at: http://www.un.org/apps/news/story.asp?NewsID=50361&Kw1=Disaster&Kw2=&Kw3=#.VjrEMYWAKrM.

Wang, H. Q., and Zhang, B. (2007). Driving Force of Drought and the Trend Predication in Heihe River Basin. *J. Arid Land Resour. Environ.* 21 (9), 68–72.

Wen, K. G., and Dong, A. X. (2005). *Encyclopaedia of China's Meteorological Disasters: Gansu Volume*. Beijing: China Meteorological Press.

Xiao, S. C., and Xiao, H. L. (2008). Water Balance Assessment and the Lower Reachespwater Regime Processes in Heihe River Basin in the Last 2000 Years. *J. Glaciology Geocryology* 30 (5), 733–739.

Xing, Z. Q., Yan, D. H., Lu, F., and Ma, H. J. (2013). Advances in the Study of Anthropogenic Effects on the Drought and Flood Events. *J. Nat. Resour.* 28 (6), 1070–1082.

Yao, T. D., Qin, D. H., and Tian, L. D. (1996). Variations in Temperature and Precipitation in the Past 2000 a on the Xizang (Tibet) Plateau-Guliya Ice Core Record. *Sci. China* 26 (4), 348–353.

Ye, B. S., Zhao, C. Y., and Jiang, F. Q. (2014). Characteristics of the Flood and Drought Disasters in the Tarim River basin in Recent 300 Years. *J. Glaciology Geocryology* 36 (1), 173–182.

Yin, X. L., and Zhang, D. Y. (2004). The Drought Characteristics Analysis in Zhangye City in 2001 and Some Defending Countermeasures. *Arid Meteorology* 22 (3), 38–43.

Yu, K. K., Zhao, J. B., and Luo, D. C. (2011). Preliminary Study on Drought Disasters and Drought Events in the Hexi Corridor in the Ming and. *Qing Dynasties* 28 (2), 288–293.

Yuan, L. (1994). *History of Disaster and Famine in Northwest China*. Lanzhou: Gansu People's Publishing House.

Yuan, Z., Yan, D. H., Yang, Z. Y., Yin, J., and Yuan, Y. (2014). Research on Temporal and Spatial Change of 400 Mm and 800 Mm Rainfall Contours of China in 1961-2000. *Adv. Water Sci.* 25 (4), 494–502.

Zhang, D. E. (2000). *A Compendium of Chinese Meteorological Records of the Last 3000 Years*. Nanjing: Jiangsu Education Press.

Zhang, P. Y., Ge, Q. S., and Zhang, S. H. (1997). The Modes and Abrupt Changes of Climate in China during Recent 2000 Years. *Quat. Res.* 1, 12–20.

Zhangye Prefectural Committee (1958). *The Chorography of Hexi*. Gansu: Zhengye Press.

Zhou, Z. H., and Ma, J. (2018). Spatial-temporal Evolution Mechanism of Historical Towns in Hexi Corridor: Taking Cultural Relics protection Units as an Example. *Huazhong Architecture* 8, 12–19.

Conflict of Interest: The authors declare that the research was conducted in the absence of any commercial or financial relationships that could be construed as a potential conflict of interest.

Publisher's Note: All claims expressed in this article are solely those of the authors and do not necessarily represent those of their affiliated organizations, or those of the publisher, the editors and the reviewers. Any product that may be evaluated in this article, or claim that may be made by its manufacturer, is not guaranteed or endorsed by the publisher.

Copyright © 2021 Tang and Feng. This is an open-access article distributed under the terms of the Creative Commons Attribution License (CC BY). The use, distribution or reproduction in other forums is permitted, provided the original author(s) and the copyright owner(s) are credited and that the original publication in this journal is cited, in accordance with accepted academic practice. No use, distribution or reproduction is permitted which does not comply with these terms.

frontiers
in Earth Science

ORIGINAL RESEARCH
published: 03 December 2021
doi: 10.3389/feart.2021.799935

Holocene Environmental Changes Inferred From an Aeolian-Palaeosol-Lacustrine Profile in the Mu Us Desert, Northern China

Xiaokang Liu[1,2], Ruijie Lu[2]*, Zhiyong Ding[3], Zhiqiang Lyu[4], Yijing Li[1] and Zhibao Dong[1,5]

[1]School of Geography and Tourism, Shaanxi Normal University, Xi'an, China, [2]Engineering Center of Desertification and Blown-Sand Control of Ministry of Education, Faculty of Geographical Science, Beijing Normal University, Beijing, China, [3]State Key Laboratory of Geohazard Prevention and Geoenvironment Protection, Chengdu University of Technology, Chengdu, China, [4]Georges Lemaître Centre for Earth and Climate Research, Earth and Life Institute, Université Catholique de Louvain, Ottignies-Louvain-la-Neuve, Belgium, [5]Planetary Aeolian Research Institute, Shaanxi Normal University, Xi'an, China

An excavated profile of aeolian-palaeosol-lacustrine sediments (the Wapianliang profile), located at the southeastern part of the Mu Us Desert, Northern China, was studied to reconstruct regional Holocene environmental changes. A chronology was established based on three AMS ^{14}C and two OSL dates, and variations in the lithology and grain size, magnetic susceptibility, soil micromorphology, and chemical elements were used to explore the regional depositional environments during the Holocene. The results showed that since around 14 ka BP, this region had experienced seven alternations of wetting and drying. A shallow lake, which was identified by celadon lacustrine sediments with sporadic freshwater gastropod fossils, occurred in this area from around 13.0 ka BP to 9.9 ka BP. There existed two obvious intervals of soil formation, inferred from the environmental proxies of the palaeosol/sandy palaeosol layers, with relatively fine average grain-size, high magnetic susceptibility value, remarkable pedogenesis features, and strong chemical weathering, in particular, a well-developed palaeosol layer dating from the middle Holocene (8.6 ka BP to 4.2 ka BP). A weakly-developed palaeosol layer (from around 1.2 ka BP) at the upper part of the profile is possibly an indication of the Medieval Warm Period. This implies a forest steppe environment at both of these sedimentary stages. After 0.9 ka BP, a desert environment returned, analogous to before around 13.0 ± 1.4 ka BP, between 9.9 ± 1.1 ka BP to 8.6 ka BP, and between 4.2 ka BP to 1.6 ka BP, indicating the aggravation of aeolian activity and the expansion of mobile sand dunes. The variations in sedimentary environments were mainly triggered by changes in the East Asian Summer Monsoon (EASM).

Keywords: Mu Us Desert, environmental changes, Holocene, sedimentary condition, East Asian summer monsoon

OPEN ACCESS

Edited by:
Zhuolun Li,
Lanzhou University, China

Reviewed by:
Peixian Shu,
Chinese Academy of Sciences, China
Zhengcai Zhang,
Chinese Academy of Sciences, China

****Correspondence:***
Ruijie Lu
ruijielu@bnu.edu.cn

Specialty section:
This article was submitted to Quaternary Science, Geomorphology and Paleoenvironment, a section of the journal Frontiers in Earth Science

Received: *22 October 2021*
Accepted: *10 November 2021*
Published: *03 December 2021*

Citation:
Liu X, Lu R, Ding Z, Lyu Z, Li Y and Dong Z (2021) Holocene Environmental Changes Inferred From an Aeolian-Palaeosol-Lacustrine Profile in the Mu Us Desert, Northern China. Front. Earth Sci. 9:799935. doi: 10.3389/feart.2021.799935

INTRODUCTION

The Holocene (from around 11.7 ka BP to the present) may appear as a blink of an eye considering the long history of the Earth, yet it is vitally important to understanding current and recent environmental conditions (Qin, 2011). As an interglacial period, the climate patterns during the Holocene are relatively warm-moist, particularly the ubiquitous and long-term Holocene Megathermal period

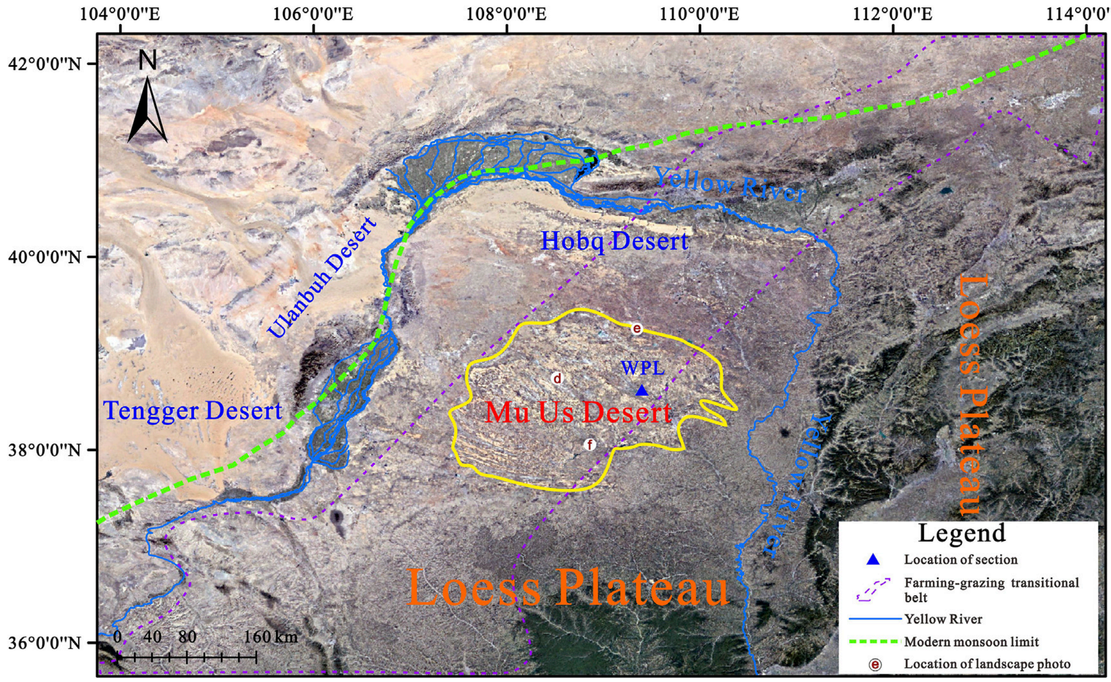

FIGURE 1 | The geographical location of the Mu Us Desert, China. The locations of landscape photo d, e, and f correspond to the picture of **Figures 4D–F**, respectively.

(8.5 ka BP to 3.0 ka BP) (Shi et al., 1994). Previous studies have revealed that this was a prosperous period, with high lake levels (Liu et al., 2018a; Chen et al., 2021), massive glacial thaw (Nesje and Kvamme, 1991; Nesje, 1992), well-developed palaeosol (Lu et al., 2005; Yue et al., 2021), and extensive prehistoric human activities (Nicoll, 2004; Liu et al., 2021). In particular, in ecologically fragile monsoon marginal and agricultural and pastoral interlaced zones, numerous sedimentary profiles or cores have recorded multiple sedimentary facies variations (Zhang et al., 2011; Chen et al., 2015; Shanahan et al., 2015; Liu et al., 2018b; Li et al., 2021). The frequent variations in lacustrine and aeolian activities recorded in individual profiles indicate the quick response and feedback of the regional climatic and environmental changes (Li et al., 2012; Liu et al., 2018a).

The Mu Us Desert in Northern China is located in a desert-loess transitional zone, on the northern margin of the East Asian Summer Monsoon (EASM), within a farming-grazing transitional belt (**Figure 1**). The area is highly sensitive to environmental variation driven by climate change and/or human impacts and is therefore suitable for studying palaeoclimatic and palaeoenvironmental history (Zhou et al., 2002; Ding et al., 2005). Since the 1920s, efforts to understand Holocene palaeoclimate in the Mu Us Desert have found that under the background of climatic variation during the Holocene, aeolian and fluvio-lacustrine deposits coexisted, and the differences that arose concerned the proportion of these different lithologies over time (Liu et al., 2018a), which has been confirmed by various geological records (Ding et al., 2021; Shu et al., 2021). Based on the chronology, lithology, and environmental indices, during the Holocene Climate Optimum period, one or two (perhaps even four) layers of palaeosol and sandy palaeosol were widely developed, corresponding to that the sand dunes were mostly fixed (Gao et al., 2001; Xu Z. et al., 2015; Jia et al., 2015; Zhao S. et al., 2016).

In general, owing to the limits in the distribution area and ideal exposed profiles, together with the frequent meandering Salawusu palaeo-river (a major river in the southern area of Mu Us Desert) (Zhao H. et al., 2016), to date, little attention has been paid to the reconstruction of these sedimentary conditions, especially since an individual profile has identified the presence of multiple sedimentary facies (Zhao H. et al, 2016; Liu et al., 2018b; Jia et al., 2018). Based on extensive field campaigns, a proper section, Wapianliang (WPL), has been found, with aeolian sand, palaeosol, and lacustrine sediments. Therefore, in this paper, we selected the WPL section and used grain size, magnetic susceptibility, soil micromorphology, chemical elements, and lithology analyses to explore the variations in regional depositional environments during the Holocene in the southeastern marginal areas of the Mu Us Desert. Our main objective is to further understand the changes in the regional sedimentary environment during the Holocene.

MATERIAL AND METHODS

Regional Setting

The Mu Us Desert, with a total area of about 39,000 km^2, is located along the margin of a region influenced by the EASM (**Figure 1**),

TABLE 1 | Lithological description of the WPL section.

Unit number	Depth(cm)	Lithology description	Munsell color
A	620–572	Loose medium aeolian sand. Not bottomed	Pale yellow-brown (10YR6/4)
B	572–512	Relatively tight medium and fine lacustrine sand, with sporadic freshwater gastropod fossils	Light gray (2.5Y7/1)
C	512–372	Loose coarse and medium aeolian sand	Light brown (10YR7/3)
D	372–210	Relatively tight medium and fine sandy palaeosol, with sporadic pseudomyceliums. 230–210 and 372–340 cm are the transitional layers	Dark gray-brown (10YR4/2)
E	210–110	Relatively loose fine aeolian sand	Light brown (10YR6/3)
F	110–86	Relatively loose medium weakly developed sandy palaeosol, with one pottery shard	Light brown (10YR6/3)
G	86–0	Loose medium aeolian sand	Pale yellow-brown (10YR6/4)

which dominates the regional climate. The mean annual rainfall is between 250 and 440 mm and the mean annual temperature is between 6.0 and 8.5°C. Warm and humid air brought by the EASM delivers more than 60–70% of the annual precipitation, which falls mainly between June and August (Liu et al., 2018a). The modern vegetation consists mostly of *Artemisia ordosica* Krasch., *Tamarix chinensis* Lour., and *Hippophae rhamnoides* Linn. Regional landscape types are varied, including stabilized, semistabilized, and active sand dunes, grassland, and interlinked sequences of lakes and marshes (Department of Geography of Peking University et al., 1983; Zhou et al., 1996).

Sampling and Laboratory Measurements

An excavation has exposed a stratum in the southeastern margin of the Mu Us Desert, namely section WPL (N38°34′58″, E109°21′39″, altitude 1226 m), which was chosen for study. The WPL section is an aeolian sand-palaeosol-lacustrine sediments sedimentary sequence about 6.20 m thick. The detailed lithological description is presented in **Table 1**.

Three Accelerator Mass Spectrometry (AMS) ^{14}C dates of the organic sediments were obtained from the WPL section. The analyses were made at the Beta Analytic Radiocarbon Dating Laboratory, and details of the pretreatment procedure are given at http://www.radiocarbon.com/pretreatment-carbon-dating.htm#Washes. The AMS ^{14}C dates were converted to calendar ages using the program Calib 7.02 based on the INTCAL 13 calibration (Reimer et al., 2013). In addition, for the lacustrine layer, we collected two samples for Optical Stimulated Luminescence (OSL) dating. The material from the middle part of the sample tube, which had not been exposed to light, were used for equivalent dose (De) measurements. Pure quartz grains 90–125 μm size were extracted using the procedure employed by the OSL Laboratory of the Qinghai Institute of Salt Lakes, Chinese Academy of Sciences. De measurements were conducted using a Risø DA-20 TL/OSL reader equipped with blue diodes (k = 470 ± 20 nm) and a 90Sr/90Y radioactive beta source. The luminescence was detected using a U-340 filter. The material that was possibly exposed to light at each end of the tube was used to measure the concentrations of Uranium (U), Thorium (Th), and Potassium (K) by neutron-activation-analysis (NAA). The water content was measured by weighing the samples before and after drying. Details of the pretreatment procedure of OSL dating samples are presented in Lai and Brückner (2008). Finally, we obtained the boundary ages of the aeolian sand, sandy palaeosol, and the lacustrine deposit units using linear interpolation.

216 samples were collected from the WPL section at 2 or 4 cm intervals for laboratory measurements. The grain size measurements were made using a Mastersizer 2000 with a measurement range of 0.02–2000 μm at the State Key Laboratory of Earth Surface Processes and Resource Ecology, Beijing Normal University (*see* Lu et al. (2015) for a description of the pretreatment procedure). Measurements of magnetic susceptibility were made using a Bartington Instruments MS2 meter and MS2B sensor at the same laboratory, and after air-drying, the samples were disaggregated and packed into 8 cm^3 plastic boxes. The thin sections of the soil sample from 260 cm depth were produced by the Cambrian Geological Technology Limited Company, Langfang City, Hebei Province, and the identification of the soil micromorphology was conducted using a Leica Microscope. The elemental content analyses of samples were made with an Axios wavelength-dispersive X-ray fluorescence spectrometer using a superlong, sharp-pointed ceramic X-ray light tube with a power of 4 kW and a pipe flow of 160 mA at the Key Laboratory of the Desert and Desertification, Northwest Institute of Eco-Environment and Resources, Chinese Academy of Sciences, Lanzhou, China. The pretreatment procedure is presented in Ding et al. (2019).

The Ti/Sr ratio was used to reflect the amount of precipitation indirectly, particularly in the aeolian deposits. Generally, Ti is a stable element, whereas Sr is more active, therefore, the variation in the Ti/Sr ratio depends on the eluviation of Sr (Chen et al., 1999; Liu et al., 2013). The Ratio of Elements (Re) is the ratio of $(K_2O+Na_2O+CaO+MgO)/(Fe_2O_3+MnO_2)$ as proposed by Liu et al. (2002). In Northern China, K, Na, Ca, and Mg are usually concentrated when the climate is dry, while sediments are rich in Fe and Mn when the climate is wet (Guan, 1992).

RESULTS AND DISCUSSION

Patterns of Variation During the Holocene

Chronology

The sandy palaeosol layers contained organic material, which meets the requirements necessary for AMS ^{14}C measurements.

TABLE 2 | ^{14}C dates for the WPL profile.

Sample No	Laboratory No	Depth (cm)	$^{13}C/^{12}C$ ratio	Radiocarbon age (yr BP)	Calendar age (2σ,cal yr BP)
WPL-14C-00	Beta-436306	96–98	−19.9‰	1250 ± 30	1177 ± 96
WPL-14C-02	Beta-436307	230–232	−20.7‰	4210 ± 30	4738.5 ± 110.5
WPL-14C-06	Beta-436308	330–332	−21.6‰	6560 ± 30	7489.5 ± 64.5

TABLE 3 | OSL dates for the WPL profile.

Sample No	Laboratory No	Depth (cm)	U (ppm)	Th (ppm)	K (%)	Moisture (%)	Environmental dose rate (Gy/Ka)	De (Gy)	OSL age (ka)
ISL-LUM2017-93	WPL-OSL-14	490	1.15 ± 0.06	2.44 ± 0.10	2.41 ± 0.07	0	2.79 ± 0.21	27.6 ± 2.1	9.9 ± 1.1
ISL-LUM2017-98	WPL-OSL-17	600	0.68 ± 0.04	2.95 ± 0.11	2.43 ± 0.07	0.01	2.72 ± 0.21	35.4 ± 2.7	13.0 ± 1.4

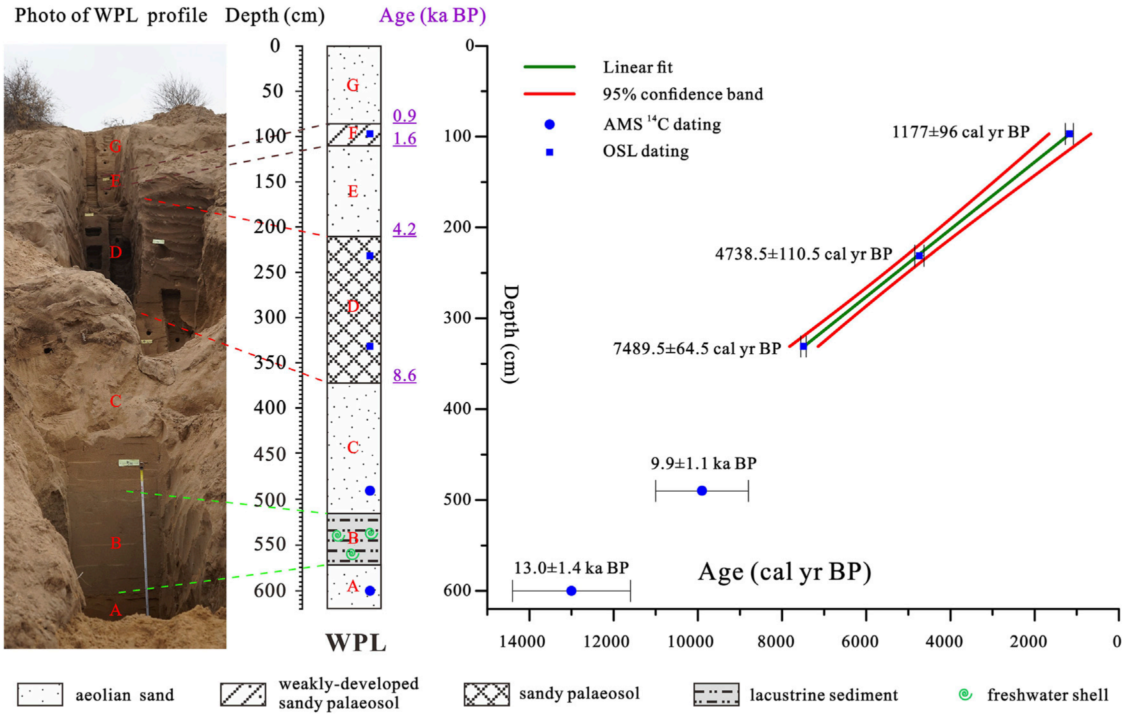

FIGURE 2 | The age-depth model for the WPL profile, based on AMS ^{14}C and OSL ages. 2σ calibrated age or error ranges were shown for each age and the red lines are the 95% confidence interval.

Three samples for dating were chosen and the results for the WPL profile were listed in **Table 2**. All of these dates were obtained from bulk organic matter. For the lower part of the section, to obtain the age of the lacustrine sediment layer, two samples were collected using 4 cm-diameter lucifuge steel tubes for the OSL dating, with the results listed in **Table 3**. Generally, all five ages were in good chronological order. We established a final age model using piecewise linear fitting (**Figure 2**) and the age of the boundary sample was determined by linear interpolation and extrapolation. Because of lack of precise dating data directly derived from the lacustrine layer (Stage B), here we selected the OSL ages from upper and lower aeolian sands to control and

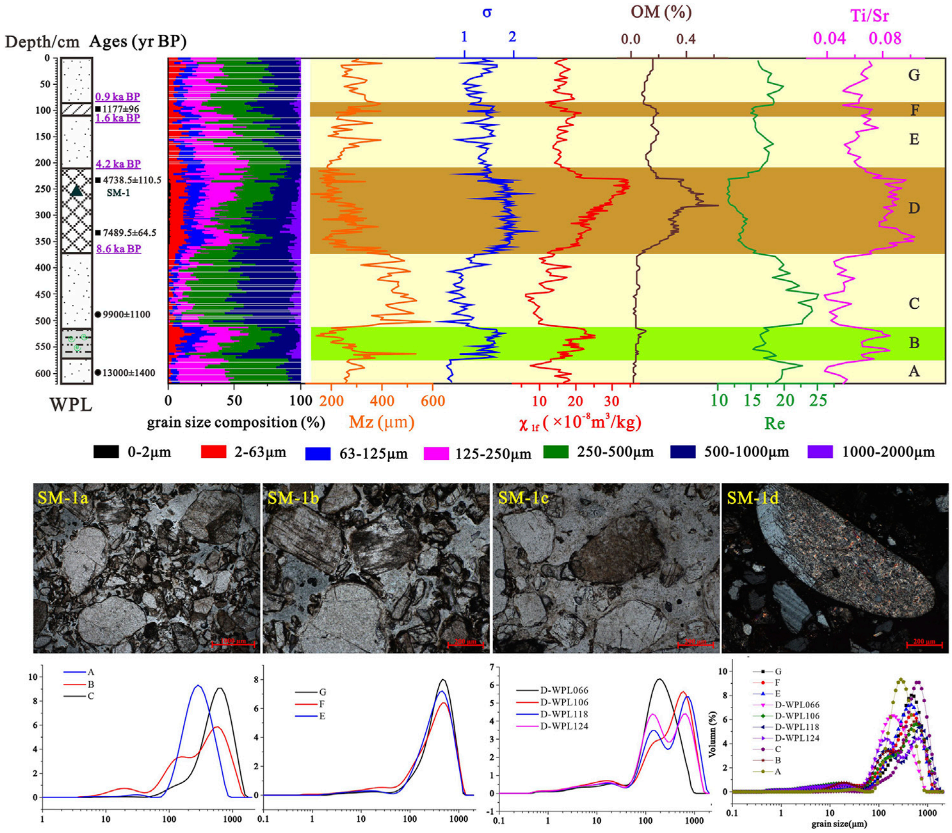

FIGURE 3 | Upper panels: the environmental proxies' variation over the WPL profile. The legend of the profile is same as **Figure 2**. Middle panels: the characteristics of the soil micromorphology of sample SM-1. SM-1a, SM-1b, SM-1c were identified under plane-polarized light and SM-1d was identified under cross-polarized light. The scales are 200 μm. Lower panels: representative grain size frequency distribution curves for the WPL section.

represent the possible development period of the lacustrine sediments Stage B to a certain degree.

Palaeoclimatic Record of the WPL Profile

To summarize the main phases of the site's sedimentary evolution, the record was divided into seven stages, labeled A to G from bottom to top (**Figure 3**).

Stage A. We interpreted the pale yellow-brown aeolian sand layer A to represent the sand of the late glacial period (before 13.0 ± 1.4 ka BP), as indicated by it having the highest medium sand content (47%), the lowest clay and silt contents (0 and 2%), and the best sorting (0.63ϕ, the minimum of all the identified stages). The curve of the grain size frequency distribution for this stage showed a near symmetrical single peak. Meanwhile, the low-frequency magnetic susceptibility (χl_f) and the organic matter content (OM) showed low values (**Figure 3**). Under a same provenance circumstance, the value of χ_{lf} is predominantly affected by climate, particularly precipitation, as characterized by the different degrees of pedogenesis (Tite and Linington, 1975; An et al., 1991; Verosub et al., 1993). The lower values of χ_{lf} and OM mean there was little precipitation, sparse vegetation, and weak pedogenesis.

Considering the geochemical element indices, the value of Ti/Sr was low and Re was high, representing an arid environment with low precipitation. All the selected environmental proxies indicate an aeolian sand-dominated environment, with an arid climate, poor precipitation, and rare vegetation during the late glacial period (before 13.0 ± 1.4 ka BP) in our study area.

Stage B. Between around 13.0 ± 1.4 ka BP and 9.9 ± 1.1 ka BP, the former aeolian sand was succeeded by light gray lacustrine sand, with sporadic freshwater gastropod fossils, which reflects a shallow lake environment. In detail, the grain size parameters exhibit a higher content of silt and very fine sand (13.84%, highest of the whole profile) and worse sorting. The grain size frequency distribution curve for this stage shows three peaks, indicating a mixture of multiple types of interactions between water and wind. For the other indices, the higher χ_{lf} and less obvious crest value of OM indicate the enhancement of the input magnetic materials during this time. In addition, the lower value of Re and higher value of Ti/Sr indicate a relatively humid environment with more precipitation (**Figure 3**). As a whole, we speculate that during this interval, the regional environment existed within a vivifying situation, with lake-dominated conditions and a relatively humid climate, abundant precipitation, and surrounded by lush vegetation at the beginning of the Holocene.

Stage C. For the interval from around 9.9 ± 1.1 ka BP to 8.6 ka BP, the lithology is seen to be typical aeolian sand, characterized by the highest mean grain size (Mz) with medium sand, coarse sand, and very coarse sand, and better sorting. The grain size frequency distribution curve showed a single peak, similar to Stage A. In addition, the low χ_{lf} value and the near-zero content of OM all indicate an extremely weak degree of pedogenesis and a sparsely vegetated environment. The higher value of Re and lower value of Ti/Sr indicate that during this period, there existed a relatively arid climate, with less precipitation (**Figure 3**).

Stage D. This stage represents the period from between 8.6 ka BP and 4.2 ka BP. The lithology is dark gray-brown sandy palaeosol, with sporadic pseudomyceliums. The Mz of this stage was 243.88 μm, the minimum of all the sedimentary layers, with the highest content of clay (the only one, over 1%) and silt, and the worst sorting. The frequency distribution curve for grain size showed a double peak or three-peak patterns (**Figure 3**, low part, D-WPL066, D-WPL106, D-WPL118, D-WPL124), pointing to the diversity of sources, such as the various processes of pedogenesis. Considering soil micromorphology, sample SM-1 displayed a relatively coarse sand structure, which contained quartz, feldspar, mica, and other lithic minerals, with the total content of silt and clay minerals being less than 10%. In detail, the soil particles were loosely arranged, with few clay minerals. The main quartz was single-crystal quartz (41%), with the development of the secondary enlargement, and the distribution of clay line. Its surface was clean and displayed no cleavage. The feldspar was comprised of alkali feldspar and plagioclase (45%) and developed alteration of micacization and kaolinization. As a whole, all of these characteristics imply a relatively weak degree of pedogenesis during Stage D. Given the expression of the soil character, we called this stage sandy palaeosol. In addition, it shows the highest value of χ_{lf} and OM content, indicating the existence of pedogenesis and a flourishing vegetated environment. Together with the results of the element geochemical index, which saw the lowest value of Re and highest value of Ti/Sr, during this period there existed widely developed palaeosol, with a relatively humid climate, more precipitation, and flourishing vegetation (**Figure 3**). Thereinto, at a depth of between 230 and 210 cm, the transitional layer exhibited obvious transitional characteristics, from the stage D to stage E (**Figure 3**).

Stage E. For the interval from 4.2 ka BP to 1.6 ka BP (Late Holocene), the lithology is light brown aeolian sand. The grain composition mainly consists of medium, fine, and coarse sand (approximatively 80%). The sorting for Stage E is better than for Stage D and the grain size frequency curve mainly showed a typical single-peak pattern, similar to stages A and C. In addition, the lower values of χ_{lf} and OM content indicate a weak degree of pedogenesis and less vegetation. The value of Re sightly increased, together with a lower value of Ti/Sr. These results indicate that during this Late Holocene period, the regional climate was relatively arid, with less precipitation, and less vegetation coverage (**Figure 3**).

Stage F. At this stage (from around 1.6 ka BP to 0.9 ka BP, or around 1.2 ka BP), we obtained an AMS ^{14}C dating age (1177 ± 96 yr cal BP) using organic material. In the weakly developed sandy palaeosol layer, the clay content was relatively high, second to the Stage D sandy palaeosol layer. The grain size frequency distribution curve mainly showed a double peak pattern, and the curve was relatively smooth, implying the weak effect of pedogenesis. The higher values of χ_{lf} and OM content all confirmed the development of soil and the existence of more vegetation. For the geochemistry of elements, the valley value of Ti/Sr and the crest value of Re indicate a relatively humid climate, with more precipitation (**Figure 3**). We, therefore, speculate that Stage F was a period of weakly developed palaeosol.

Stage G. For the top layer, we interpreted the pale yellow-brown aeolian sand to represent the sand of recent millennial deposits (around 0.9 ka BP to the present). Its grain composition was composed of medium, coarse, and fine sand (over 80%), and the frequency distribution curve of the grain size showed a single peak pattern. The lower value of χ_{lf} and OM content, together with the geochemistry results (lower Ti/Sr value and higher value of Re) (**Figure 3**) indicated that after 0.9 ka BP, there existed a relatively arid climate with less precipitation.

Based on these proxies', since the late glacial period, the WPL section with aeolian sand, palaeosol, and lacustrine sediments has documented at least seven stratigraphic cycles, varying between desert and non-desert periods. Generally, for the four desert periods, Stages A, C, E, and G, their mean grain sizes were coarser, sorting was better, the frequency curves had mainly single-peaked forms, and the values of χ_{lf} and OM content were lower, with the combination of elements showing obvious arid climate patterns. Conversely, over the three non-desert periods, which include the lacustrine deposits and sandy palaeosol or weakly developed sandy palaeosol, Stages B, D, and F, their mean grain sizes were finer, sorting was worse, the frequency curves showed double-peaked or multimodal patterns, and the values of χ_{lf} and OM content were higher. Furthermore, the combination of elements showed obvious humid climate patterns.

Development of Regional Sedimentary Conditions Inferred From the WPL Profile and Its Climatic Control

At each stage, the sedimentation reflects the different regional environments, hence, the study of sedimentary facies provides perspective on what the environment could have been at that time. In order to better understand the geomorphic processes and variations in the sedimentary conditions, we considered the possible forcing mechanisms.

Based on the results of **section 3.1.2**, we speculated upon the possible regional sedimentary conditions for each stage. As seen from **Figure 4A**, we considered Stages A, C, E, and G, that is, from before 13.0 ± 1.4 ka BP, from between 9.9 ± 1.1 ka BP to 8.6 ka BP, from 4.2 ka BP to 1.6 ka BP, and from 0.9 ka BP to the present, respectively, to indicate cold and dry desert environments, characterized by strong aeolian activity with coarser grain sizes, better sorting, lower OM content, lower χ_{lf}, and Ti/Sr values, and higher Re values (*see* image **Figure 4D**, which was taken at the hinterland of the modern Mu Us Desert). The emergence or disappearance of aeolian sand was strongly affected by the intensity of the EASM, whether during the Last Glaciation period or the Late Holocene (**Figures 5A–F**). This should be detailly introduced and discussed later.

For Stage B, from around 13.0 ± 1.4 ka BP to 9.9 ± 1.1 ka BP as shown in **Figure 4B**, we speculated that it was a shallow lake environment, which is attributed to a relatively warm and moist

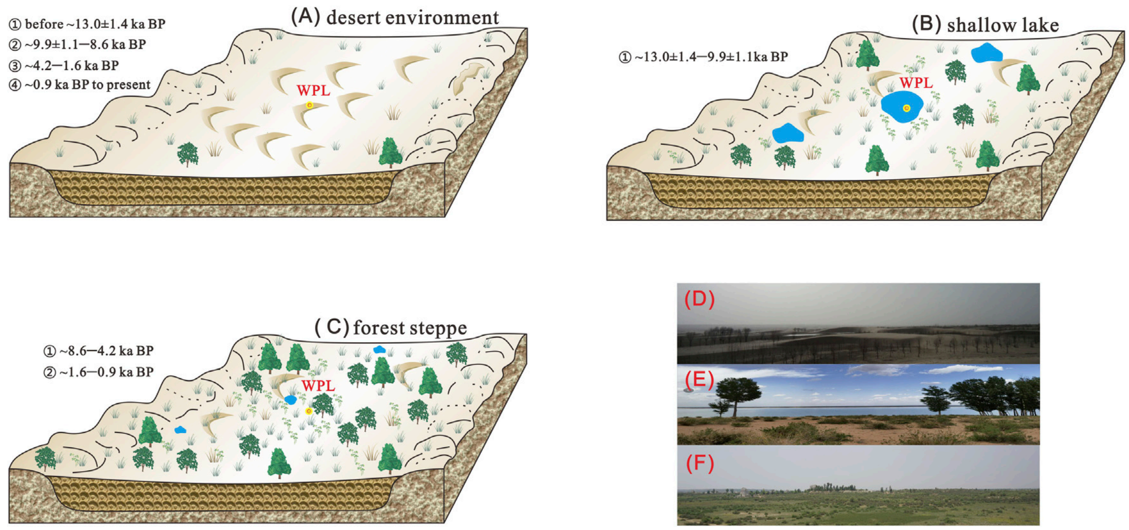

FIGURE 4 | The sketch map of regional sedimentary conditions. **(A)** Desert environment dominated by active dunes. **(B)** Shallow lake environment. **(C)** Forest steppe environment with luxuriant vegetation. Thereinto, the differences between the periods 8.6 ka BP to 4.2 ka BP and from 1.6 ka BP to 0.9 ka BP were influenced by the amount of vegetation in the vicinity; **(D)** landscape photo of a desert environment, which was taken at the hinderland of the modern Mu Us Desert; **(E)** landscape photo of a shallow lake, which was taken at Manai Lake in the modern Mu Us Desert; **(F)** landscape photo of a forest steppe environment, which was taken at Tongwan City in the southern margin of the modern Mu Us Desert.

climate during the Last Deglaciation and early Holocene (Zhou et al., 2002), similar to the landscape shown in **Figure 4E**, showing the area at Manai Lake in the modern Mu Us Desert. As seen from **Figure 5H**, since 15 ka BP, orbital variations have driven changes in summer insolation, which led to thermal contrasts between land and sea (An et al., 2000). The enhanced intensity of monsoons could bring more precipitation (**Figures 5A,C,E,F**), consistent with the lower Re values (**Figure 5B**). On the other hand, it is acknowledged that the lakes or marshes that formed during the Last Deglaciation and early Holocene were related to strong aeolian activity, mainly the formation of blowouts. With regards to blowouts and their relationship to the foundation of lakes, Shen et al. (2005) believed Hongjiannao Lake in the eastern margin of the Mu Us Desert was the result of a wind-erosion lake. Because of the uncertainties in the dating, we can only speculate that within the period between around 13.0 ± 1.4 ka BP to around 9.9 ± 1.1 ka BP, there existed an obvious lake environment stage, as evident by sporadic gastropod fossils. In addition, the rise in temperature (**Figure 5D**) produced meltwater from the permafrost (Xu H. et al., 2015), providing another possible source of lake water. A similar view was expressed by Liu et al. (2018a) and this profile provides new evidence for this idea. In fact, examples of emerging lakes and marshes since 15 ka BP to the early Holocene are very common in our studied area, such as Midiwan (Zhou et al., 2002), Tanyaogou (Jia et al., 2018), and Dishaogouwan Left (Liu et al., 2018b).

Considering Stages D and F, from 8.6 ka BP to 4.2 ka BP and from 1.6 ka BP to 0.9 ka BP, respectively, based on the results of the analysis of the environmental proxies and soil micromorphology, we speculate that these stages indicate a forest steppe environment (**Figure 4C**), with the lithology of sandy palaeosol or weakly developed sandy palaeosol. Therefore, we chose the dense herbal and woody plants symbols in **Figure 4**. The timing of Stages D and F correspond to the Holocene Megathermal and Medieval Warm Period (MWP, 600–1280 AD), with an obvious decrease in the degree of drought (**Figure 4B**). Particularly for Stage D, the soil characteristics are obvious, meaning the fixation of sand dunes, the existence of the process of pedogenesis, and the flourishing of vegetation (Shi et al., 1994; Mason et al., 2009; Xu Z. et al., 2015; Jia et al., 2015). Meanwhile, the suitability of climate is also reflected in these stages having the most precipitation (**Figure 5A**) and higher temperatures (**Figure 5D**) during the middle Holocene. The landscape during this period was close to that shown in **Figure 4F**, which was taken at Tongwan City in the southern margin of the modern Mu Us Desert. We propose that an increased intensity in the EASM was the main reason for the presence of the Holocene Optimum and MWP. The WPL section is mainly located within the positive landform area, therefore, the period of development of the soil corresponds to the lacustrine and sandy peat-dominated period based on the synthesis of variations in hydrological conditions inferred from peat-containing profiles (**Figure 5G**). Therefore, the optimum timing of the climate was mostly similar, i.e., 8.5 to 3.0 ka BP and 8.6 to 4.2 ka BP, respectively. Furthermore, for the return of sandy palaeosol during Stage F, the short-lived enhancement of the summer monsoon might be responsible, with the redness of Qinghai Lake also capturing this returned process (**Figure 5C**).

On the whole, these variations in the sedimentary conditions mentioned above are the products of climatic and environmental changes, which were mainly triggered by the EASM (**Figure 5**). As a result, the alternations between wetting and drying were

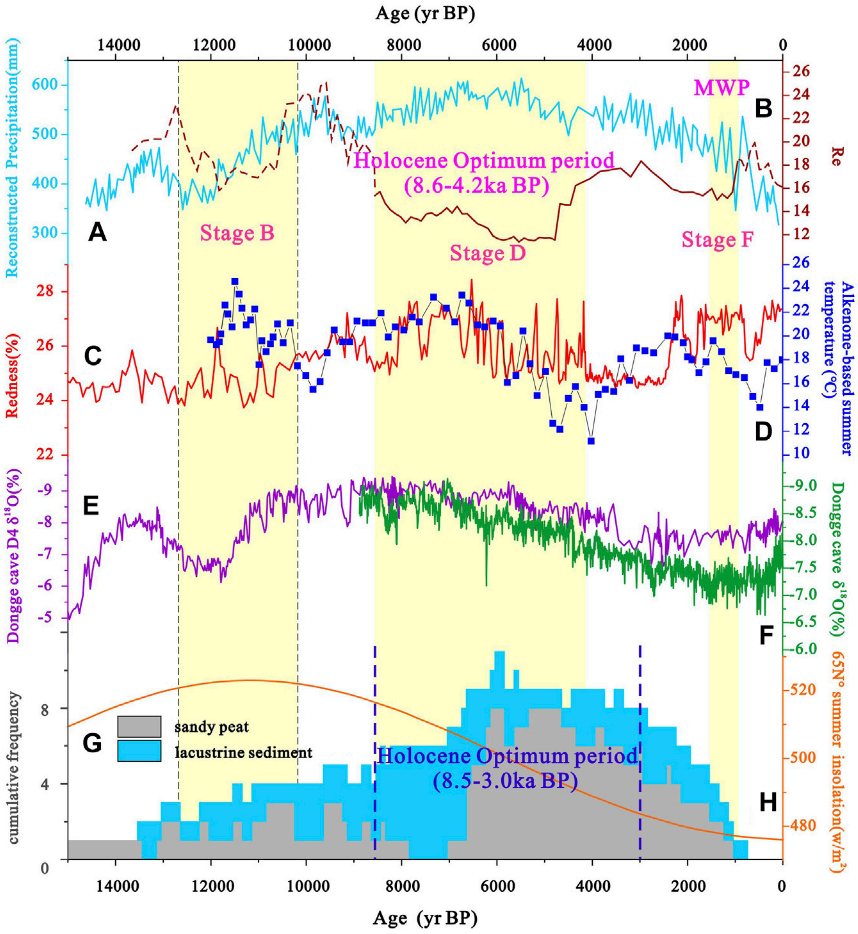

FIGURE 5 | Variations in the Ratio of Elements (Re) representing the degree of drought since the Last Deglaciation period and selected environmental proxies. **(A)** Annual precipitation records from Gonghai Lake, northern China (Chen et al., 2015). **(B)** Re from this paper. **(C)** Redness curve of Qinghai Lake which reflects precipitation (Ji et al., 2005). **(D)** Alkenone-based summer temperature record from Lake Qinghai (Hou et al., 2016). **(E)** Dongge cave stalagmite D4 oxygen isotope record (Dykoski et al., 2005). **(F)** Dongge cave stalagmite oxygen isotope record (Wang et al., 2005). **(G)** Synthesis of variations in hydrological conditions inferred from peat-containing profiles (Liu et al., 2018a). **(H)** Northern Hemisphere summer insolation at 30°N (Berger and Loutre, 1991).

embodied in the identifiable transitions within different landscapes (**Figure 4**).

Regional Comparisons and Environmental Significances

The WPL profile recorded signals of varying temporal scales, from centennial to millennial, characterized by the transition of sedimentary facies and conditions. As mentioned above, in the Mu Us Desert, as a process of the first paludification, peatland development was typically initiated in topographic depressions and in lakeshore and river valley environments (Liu et al., 2018a), as noted in the early-Holocene wetness records widely seen in valleys (Shu et al., 2021). Our studied section belonged to a topographically depressed area, which saw blowout-based shallow lakes forming during Stage B. As the main body of sediments, the Holocene aeolian deposits in our profile were very thick (over 5 m) and lasted for a relatively long time (over 10 ka). The prolonged and prosperous Holocene Optimum, which was characterized by the widely distributed palaeosol and sandy palaeosol stratigraphies, is widely recognized over the Northern China dune fields. In addition to Mu Us Desert region, more sedimentary sequences in the Hulunbuir Sandy Land, the Horqin sandy land, and the Otindag Sandy Land were constantly established (**Figure 6**). Generally, as seen from **Figure 6B**, the light yellow shaded area indicates the age of the middle Holocene palaeosol of the WPL profile and in this regard, it shows that the climate of the middle Holocene in these sandy areas was similarly humid and moist. In particular, between 7.5 and 3.5 ka BP, all the sandy lands in the eastern portion of the desert belt (sand seas and sandy lands) in northern China were stabilized and the intensity of aeolian activity was significantly weakened (Yang et al., 2019). However, previous studies have also demonstrated that the chronological framework about the Holocene palaeosols displayed obvious spatial heterogeneities (Gao et al., 1993; Yang et al., 2019). The differences over time and space could be strongly affected by the East Asian monsoon (Jiang and Liu, 2007). Furthermore, with respect to the reason for these inconsistencies, the instability,

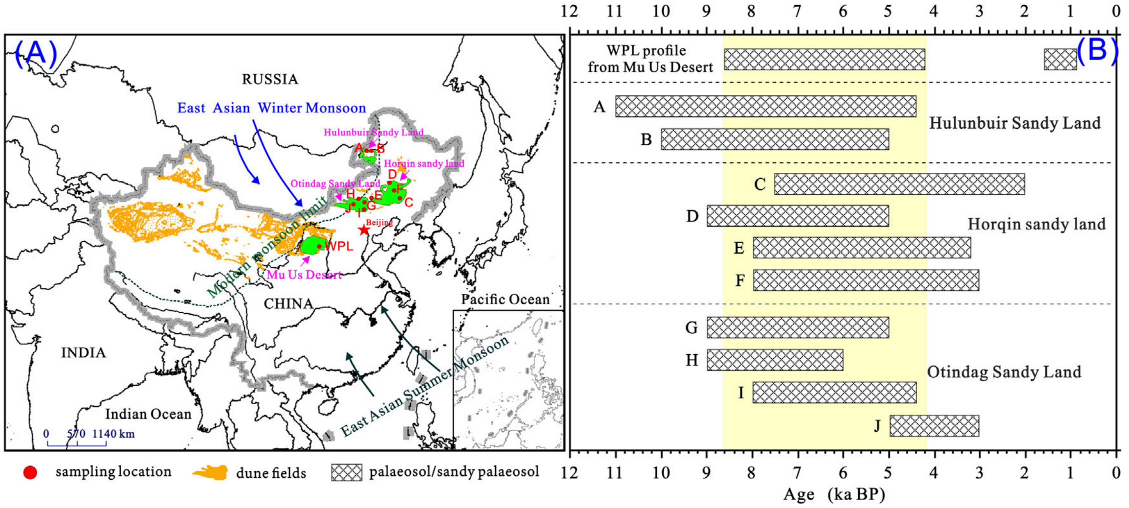

FIGURE 6 | Regional comparisons. **(A)** The location map of our research area, the Mu Us Desert, and a sketch map of the locations of studied points in other sandy lands in Northern China, which were shown in **Figure 6B**. **(B)** The ages of the development of palaeosol/sandy palaeosol in the monsoonal area in Northern China. In detail, A - Li and Sun (2006); B - Yang and Ding (2013); C - Zhao et al. (2007); D - Guo et al. (2017); E - Mu et al. (2016); F - Yang et al. (2012); G - Zhou et al. (2013); H - Jin et al. (2004); I - Gong et al. (2013); J - Yang et al. (2008).

and multiperiod aeolian activities could also impact this region (Jia et al., 2015).

More in-depth palaeoenvironmental studies are required for a full understanding of the relationships between aeolian activity and climate change in northern China (Yang et al., 2019). Profiles such as Wapianliang with aeolian-palaeosol-lacustrine sediments could provide us with more useful information about the varied sedimentary conditions, including the geomorphological processes under Holocene climatic patterns. Furthermore, the study of the transportation and replenishment of materials from centennial to millennial scales may be a way forward in enhancing our understanding of these processes.

CONCLUSION

We have presented a new aeolian-palaeosol-lacustrine profile, Wapianliang, from the Mu Us Desert and have used the results to reconstruct Holocene environmental changes, particularly the sedimentary conditions. The results indicate that since 14 ka BP, this region had experienced seven alternating periods of wetter and dryer climate. Correspondingly, the sedimentary conditions changed from a shallow lake (around 13.0 to 9.9 ka BP), forest steppe environment (around 8.6 ka BP to 4.2 ka BP, and around 1.2 ka BP), and desert environments (the remaining periods). In addition, the variations in depositional environments were mainly triggered by the East Asian monsoon. This section, therefore, provides useful information for enhancing our understanding of the paleoenvironmental evolution of the Mu Us Desert.

DATA AVAILABILITY STATEMENT

The original contributions presented in the study are included in the article/Supplementary Material, further inquiries can be directed to the corresponding author/s.

AUTHOR CONTRIBUTIONS

XL and RL contributed to conception, design of the study and writing of draft of the manuscript. ZDi and ZL conducted investigation and methodology. YL performed the statistical analysis. ZDo provided the funding and resources. All authors contributed to manuscript revision, read, and approved the submitted version.

FUNDING

This study was supported by the National Natural Science Foundation of China (No. 41901094, 41930641, 41330748) and Fundamental Research Funds for the Central Universities (GK202103148).

ACKNOWLEDGMENTS

We thank the editor and anonymous reviewers who have significantly improved this paper. We thank Du Jing for assistance in both field and laboratory, and MJEditor (www.mjeditor.com) for English improvement.

REFERENCES

An, Z., Kukla, G. J., Porter, S. C., and Xiao, J. (1991). Magnetic Susceptibility Evidence of Monsoon Variation on the Loess Plateau of Central China During the Last 130,000 Years. *Quat. Res.* 36 (1), 29–36. doi:10.1016/0033-5894(91)90015-W

An, Z., Porter, S. C., Kutzbach, J. E., Wu, X. H., Wang, S. M., Liu, X. D., et al. (2000). Asynchronous Holocene Optimum of the East Asian Monsoon. *Quat. Sci. Rev.* 19 (8), 743–762. doi:10.1016/S0277-3791(99)00031-1

Berger, A., and Loutre, M. F. (1991). Insolation Values for the Climate of the Last 10 Million Years. *Quat. Sci. Rev.* 10 (4), 297–317. doi:10.1016/0277-3791(91)90033-Q

Chen, C., Tao, S., Zhao, W., Jin, M., Wang, Z., Li, H., et al. (2021). Holocene Lake Level, Vegetation, and Climate at the East Asian Summer Monsoon Margin: A Record from the Lake Wulanhushao Basin, Southern Inner Mongolia. *Palaeogeogr. Palaeoclimatol. Palaeoecol.* 561, 110051. doi:10.1016/j.palaeo.2020.110051

Chen, F., Xu, Q., Chen, J., Birks, H. J. B., Liu, J., Zhang, S., et al. (2015). East Asian Summer Monsoon Precipitation Variability Since the Last Deglaciation. *Sci. Rep.* 5, 1–11. doi:10.1038/srep11186

Chen, J., An, Z., Wang, Y., Ji, J., Chen, Y., and Lu, H. (1999). Distribution of Rb and Sr in the Luochuan Loess- Paleosol Sequence of China During the Last 800 Ka. *Sci. China Ser. D-earth Sci.* 42 (3), 225–232. doi:10.1007/BF02878959

Department of Geography of Peking University (1983). “Commission for Integrated Survey of Natural Resources of Chinese Academy of Sciences,” in *Natural Conditions and its Improvement and Utilization in the Mu Us Sandland* (Beijing: Lanzhou Institute of Desert Research of Chinese Academy of Sciences).

Ding, Z. L., Derbyshire, E., Yang, S. L., Sun, J. M., and Liu, T. S. (2005). Stepwise Expansion of Desert Environment Across Northern China in the Past 3.5 Ma and Implications for Monsoon Evolution. *Earth Planet. Sci. Lett.* 237 (1-2), 45–55. doi:10.1016/j.epsl.2005.06.036

Ding, Z., Lu, R., Lyu, Z., and Liu, X. (2019). Geochemical Characteristics of Holocene Aeolian Deposits East of Qinghai Lake, China, and Their Paleoclimatic Implications. *Sci. Total Environ.* 692, 917–929. doi:10.1016/j.scitotenv.2020.136716

Ding, Z., Lu, R., Wang, L., Yu, L., Liu, X., Liu, Y., et al. (2021). Early-Mid Holocene Climatic Changes Inferred from Colors of Eolian Deposits in the Mu Us Desert. *Geoderma* 401, 115172. doi:10.1016/j.geoderma.2021.115172

Dykoski, C., Edwards, R., Cheng, H., Yuan, D., Cai, Y., Zhang, M., et al. (2005). A High-Resolution, Absolute-Dated Holocene and Deglacial Asian Monsoon Record from Dongge Cave, China. *Earth Planet. Sci. Lett.* 233 (1-2), 71–86. doi:10.1016/j.epsl.2005.01.036

Gao, S. Y., Chen, W. N., Jin, H. L., Dong, G. R., Li, B. S., Yang, G. S., et al. (1993). A Preliminary Study on Desert Evolution in the Northwestern Fringe of Monsoon Area, China. *Sci. China, Ser. B* 23 (2), 202–208. doi:10.3321/j.issn:1006-9240.1993.02.005

Gao, S. Y., Wang, G. Y., Ha, S., and Su, Z. Z. (2001). A Case Study on Desert Evolution in the Northwestern Fringe of Monsoon Area, China Since the Last Glacial Epoch. *Quat. Sci.* 21 (1), 66–71. doi:10.3321/j.issn:1001-7410.2001.01.008

Gong, Z., Li, S.-H., Sun, J., and Xue, L. (2013). Environmental Changes in Hunshandake (Otindag) Sandy Land Revealed by Optical Dating and Multi-Proxy Study of Dune Sands. *J. Asian Earth Sci.* 76, 30–36. doi:10.1016/j.jseaes.2013.07.035

Guan, Y. Z. (1992). The Element, Clay Mineral and Depositional Environment in Horqin Sand Land. *J. Desert Res.* 12 (1), 12–18.

Guo, L., Xiong, S., Yang, P., Ye, W., Jin, G., Wu, W., et al. (2018). Holocene Environmental Changes in the Horqin Desert Revealed by OSL Dating and δ 13 C Analyses of Paleosols. *Quat. Int.* 469 (A), 11–19. doi:10.1016/j.quaint.2017.06.048

Hou, J., Huang, Y., Zhao, J., Liu, Z., Colman, S., and An, Z. (2016). Large Holocene Summer Temperature Oscillations and Impact on the Peopling of the Northeastern Tibetan Plateau. *Geophys. Res. Lett.* 43 (3), 1323–1330. doi:10.1002/2015GL067317

Ji, J., Shen, J., Balsam, W., Chen, J., Liu, L., and Liu, X. (2005). Asian Monsoon Oscillations in the Northeastern Qinghai-Tibet Plateau Since the Late Glacial as Interpreted from Visible Reflectance of Qinghai Lake Sediments. *Earth Planet. Sci. Lett.* 233 (1-2), 61–70. doi:10.1016/j.epsl.2005.02.025

Jia, F., Lu, R., Gao, S., Li, J., and Liu, X. (2015). Holocene Aeolian Activities in the Southeastern Mu Us Desert, China. *Aeolian Res.* 19 (B), 267–274. doi:10.1016/j.aeolia.2015.01.002

Jia, F., Lu, R., Liu, X., Zhao, C., Lv, Z., and Gao, S. (2018). Palaeoenvironmental Implications of a Holocene Sequence of Lacustrine-Peat Sediments from the Desert-Loess Transitional Zone in Northern China. *J. Asian Earth Sci.* 156, 167–173. doi:10.1016/j.jseaes.2018.01.030

Jiang, W. Y., and Liu, T. S. (2007). Timing and Spatial Distribution of Mid-holocene Drying Over Northern China: Response to a Southeastward Retreat of the East Asian Monsoon. *J. Geophys. Res.* 112, D241111–D241118. doi:10.1029/2007JD009050

Jin, H. L., Su, Z. Z., Sun, L. Y., Sun, Z., Zhang, H., and Jin, L. Y. (2004). The Holocene Climate Change in the Hunshandake Sandy Land. *Chin. Sci. Bull.* 49 (15), 1532–1536. doi:10.3321/j.issn:0023-074X.2004.15.01210.1007/bf03184307

Lai, Z., and Brückner, H. (2008). Effects of Feldspar Contamination on Equivalent Dose and the Shape of Growth Curve for OSL of Slt-sized Quartz Extracted from Chinese Loess. *Geochronometria* 30, 49–53. doi:10.2478/v10003-008-0010-0

Li, S.-H., Sun, J., and Li, B. (2012). Holocene Environmental Changes in Central Inner Mongolia Revealed by Luminescence Dating of Sediments from the Sala Us River valley. *The Holocene* 22 (4), 397–404. doi:10.1177/0959683611425543

Li, S.-H., and Sun, J. (2006). Optical Dating of Holocene Dune Sands from the Hulun Buir Desert, Northeastern China. *The Holocene* 16 (3), 457–462. doi:10.1191/0959683606hl942rr

Li, Y., Qiang, M., Huang, X., Zhao, Y., Leppänen, J. J., Weckström, J., et al. (2021). Lateglacial and Holocene Climate Change in the NE Tibetan Plateau: Reconciling Divergent Proxies of Asian Summer Monsoon Variability. *Catena* 199, 1050891–1050897. doi:10.1016/j.catena.2020.105089

Liu, B., Jin, H. L., and Sun, Z. (2013). Desert Evolution and Climate Change in the Horqin Sandy Land in Middle and Late Holocene. *J. Desert Res.* 33 (1), 77–86. doi:10.7522/j.issn.1000-694X.2013.00011

Liu, H., Xu, L., and Cui, H. (2002). Holocene History of Desertification Along the Woodland-steppe Border in Northern China. *Quat. Res.* 57 (2), 259–270. doi:10.1006/qres.2001.2310

Liu, X., Lu, R., Du, J., Lyu, Z., Wang, L., Gao, S., et al. (2018a). Evolution of Peatlands in the Mu Us Desert, Northern China, Since the Last Deglaciation. *J. Geophys. Res. Earth Surf.* 123, 252–261. doi:10.1002/2017JF004413

Liu, X., Lu, R., Jia, F., Chen, L., Li, T., Ma, Y., et al. (2018b). Holocene Water-Level Changes Inferred from a Section of Fluvio-Lacustrine Sediments in the Southeastern Mu Us Desert, China. *Quat. Int.* 469 (B), 58–67. doi:10.1016/j.quaint.2016.12.032

Liu, X., Lu, R., Jia, F., Li, X., Li, X., Li, M., et al. (2021). The Strategy and Environmental Significance of Neolithic Subsistence in the Mu Us Desert, China. *Quat. Int.* 574, 68–77. doi:10.1016/j.quaint.2020.12.006

Lu, H., Miao, X., Zhou, Y., Mason, J., Swinehart, J., Zhang, J., et al. (2005). Late Quaternary Aeolian Activity in the Mu Us and Otindag Dune Fields (north China) and Lagged Response to Insolation Forcing. *Geophys. Res. Lett.* 32 (21), 365–370. doi:10.1029/2005GL024560

Lu, R., Jia, F., Gao, S., Shang, Y., Li, J., and Zhao, C. (2015). Holocene Aeolian Activity and Climatic Change in Qinghai Lake Basin, Northeastern Qinghai-Tibetan Plateau. *Palaeogeogr. Palaeoclimatol. Palaeoecol.* 430, 1–10. doi:10.1016/j.palaeo.2015.03.044

Mason, J. A., Lu, H., Zhou, Y., Miao, X., Swinehart, J. B., Liu, Z., et al. (2009). Dune Mobility and Aridity at the Desert Margin of Northern China at a Time of Peak Monsoon Strength. *Geology* 37 (10), 947–950. doi:10.1130/G30240A.1

Mu, Y., Qin, X., Zhang, L., and Xu, B. (2016). Holocene Climate Change Evidence from High-Resolution Loess/paleosol Records and the Linkage to Fire-Climate Change-Human Activities in the Horqin Dunefield in Northern China. *J. Asian Earth Sci.* 121, 1–8. doi:10.1016/j.jseaes.2016.01.017

Nesje, A., and Kvamme, M. (1991). Holocene Glacier and Climate Variations in Western Norway: Evidence for Early Holocene Glacier Demise and Multiple Neoglacial Events. *Geol* 19 (6), 6102–6612. doi:10.1130/0091-7613(1991)0192.3.CO10.1130/0091-7613(1991)019<0610:hgacvi>2.3.co;2

Nesje, A. (1992). Younger Dryas and Holocene Glacier Fluctuations and Equilibrium-Line Altitude Variations in the Jostedalsbre Region, Western Norway. *Clim. Dyn.* 6 (3), 221–227. doi:10.1007/BF00193534

Nicoll, K. (2004). Recent Environmental Change and Prehistoric Human Activity in Egypt and Northern Sudan. *Quat. Sci. Rev.* 23 (5-6), 561–580. doi:10.1016/j.quascirev.2003.10.004

Qin, D. H. (2011). *Preface to the Holocene Climate Change*. Beijing: China Meteorological Press.

Reimer, P. J., Bard, E., Bayliss, A., Beck, J. W., Blackwell, P. G., Ramsey, C. B., et al. (2013). IntCal13 and Marine13 Radiocarbon Age Calibration Curves 0-50,000 Years Cal BP. *Radiocarbon* 55 (4), 1869–1887. doi:10.2458/azu_js_rc.55.16947

Shanahan, T. M., Mckay, N. P., Hughen, K. A., Overpeck, J. T., Otto-Bliesner, B., Heil, C. W., et al. (2015). The Time-Transgressive Termination of the African Humid Period. *Nat. Geosci* 8 (2), 140–144. doi:10.1038/ngeo2329

Shen, J., Wang, Y., Yang, X., Zhang, E., Yang, B., and Ji, J. (2005). Paleosandstorm Characteristics and Lake Evolution History Deduced from Investigation on Lacustrine Sediments-The Case of Hongjiannao Lake, Shaanxi Province. *Chin.Sci.Bull.* 50, 2355–2361. doi:10.1007/BF03183747

Shi, Y. F., Kong, Z. C., Wang, S. M., Tang, L. Y., Wang, F. B., Yao, T. D., et al. (1994). The Climatic Fluctuation and Important Event of Holocene Megathermal in China. *Sci. China B Chem. Life Sci. Earth Sci.* 37 (3), 353–365. doi:10.1360/yb1994-37-3-353

Shu, P., Wang, H., Zhou, W., Ao, H., Niu, D., Wen, X., et al. (2021). Seasonal Rainfall Patterns in Stable Carbon Isotopes in the Mu Us Desert, Northern China During the Early and Middle Holocene. *Clim. Dyn.* 56, 799–812. doi:10.1007/s00382-020-05504-y

Tite, M. S., and Linington, R. E. (1975). Effect of Climate on the Magnetic Susceptibility of Soils. *Nature* 256 (5518), 565–566. doi:10.1038/256565a0

Verosub, K. L., FineSinger, P. M. J., Singer, M. J., and TenPas, J. (1993). Pedogenesis and Paleoclimate: Interpretation of the Magnetic Susceptibility Record of Chinese Loess-Paleosol Sequences. *Geol* 21 (11), 10112–11014. doi:10.1130/0091-7613(1993)021<1011:PAPIOT>2.3.CO10.1130/0091-7613(1993)021<1011:papiot>2.3.co;2

Wang, Y., Cheng, H., Edwards, R. L., He, Y., Kong, X., An, Z., et al. (2005). The Holocene Asian Monsoon: Links to Solar Changes and North Atlantic Climate. *Science* 308 (5723), 854–857. doi:10.1126/science.1106296

Weijian, Z., Donahue, D. J., Porter, S. C., Jull, T. A., Xiaoqiang, L., Stuiver, M., et al. (1996). Variability of Monsoon Climate in East Asia at the End of the Last Glaciation. *Quat. Res.* 46 (3), 219–229. doi:10.1006/qres.1996.0062

Xu, H., Yeager, K. M., Lan, J., Liu, B., Sheng, E., and Zhou, X. (2015a). Abrupt Holocene Indian Summer Monsoon Failures: A Primary Response to Solar Activity? *The Holocene* 25 (4), 677–685. doi:10.1177/0959683614566252

Xu, Z., Lu, H., Yi, S., Vandenberghe, J., Mason, J. A., Zhou, Y., et al. (2015b). Climate-driven Changes to Dune Activity During the Last Glacial Maximum and Deglaciation in the Mu Us Dune Field, North-central China. *Earth Planet. Sci. Lett.* 427, 149–159. doi:10.1016/j.epsl.2015.07.002

Yang, L.-R., and Ding, Z.-L. (2013). Expansion and Contraction of Hulun Buir Dunefield in North-eastern China in the Last Late Glacial and Holocene as Revealed by OSL Dating. *Environ. Earth Sciearth Sci.* 68 (5), 1305–1312. doi:10.1007/s12665-012-1828-3

Yang, L., Wang, T., Zhou, J., Lai, Z., and Long, H. (2012). OSL Chronology and Possible Forcing Mechanisms of Dune Evolution in the Horqin Dunefield in Northern China Since the Last Glacial Maximum. *Quat. Res.* 78 (2), 185–196. doi:10.1016/j.yqres.2012.05.002

Yang, X., Liang, P., Zhang, D., Li, H., Rioual, P., Wang, X., et al. (2019). Holocene Aeolian Stratigraphic Sequences in the Eastern Portion of the Desert belt (Sand Seas and sandy Lands) in Northern China and Their Palaeoenvironmental Implications. *Sci. China Earth Sci.* 62 (8), 1302–1315. doi:10.1007/s11430-018-9304-y

Yang, X., Zhu, B., Wang, X., Li, C., Zhou, Z., Chen, J., et al. (2008). Late Quaternary Environmental Changes and Organic Carbon Density in the Hunshandake Sandy Land, Eastern Inner Mongolia, China. *Glob. Planet. Change* 61 (1-2), 70–78. doi:10.1016/j.gloplacha.2007.08.007

Yue, D.-P., Zhao, J.-B., Ma, Y.-D., Cao, J.-J., Li, Y.-H., Ma, A.-H., et al. (2021). Mid-Holocene Soil Water and Vegetation in the Xi'an Area of the Southern Chinese Loess Plateau. *Geoderma* 383, 1148021–1148029. doi:10.1016/j.geoderma.2020.114802

Zhang, J., Jia, Y., Lai, Z., Long, H., and Yang, L. (2011). Holocene Evolution of Huangqihai Lake in Semi-arid Northern China Based on Sedimentology and Luminescence Dating. *The Holocene* 21 (8), 1261–1268. doi:10.1177/0959683611405232

Zhao, H., Sheng, Y., Li, B., and Fan, Y. (2016a). Holocene Environment Changes Around the Sara Us River, Northern China, Revealed by Optical Dating of Lacustrine-Aeolian Sediments. *J. Asian Earth Sci.* 120, 184–191. doi:10.1016/j.jseaes.2016.02.002

Zhao, H., Lu, Y., and Yin, J. (2007). Optical Dating of Holocene Sand Dune Activities in the Horqin Sand-fields in Inner Mongolia, China, Using the SAR Protocol. *Quat. Geochronol.* 2 (1-4), 29–33. doi:10.1016/j.quageo.2006.03.008

Zhao, S., Xia, D., Jin, H., Jia, J., Li, G., Gao, F., et al. (2016b). Long-term Weakening of the East Asian Summer and Winter Monsoons During the Mid- to Late Holocene Recorded by Aeolian Deposits at the Eastern Edge of the Mu Us Desert. *Palaeogeogr. Palaeoclimatol. Palaeoecol.* 457, 258–268. doi:10.1016/j.palaeo.2016.06.011

Zhou, W. J., Dodson, J., Head, M. J., Li, B. S., Hou, Y. J., Lu, X. F., et al. (2002). Environmental Variability within the Chinese Desert-Loess Transition Zone Over the Last 20000 Years. *The Holocene* 12 (1), 107–112. doi:10.1191/0959683602hl525rr

Zhou, Y. L., Lu, H. Y., Zhang, X. Y., and Yi, S. W. (2013). Changes of the Border of Hunshandake (Otindag) Sand Field (Northern China) During the Last Glacial Maximum and Holocene. *Quat. Sci.* 33 (2), 228–242. doi:10.3969/j.issn.1001-7410.2013.02.04

Conflict of Interest: The authors declare that the research was conducted in the absence of any commercial or financial relationships that could be construed as a potential conflict of interest.

Publisher's Note: All claims expressed in this article are solely those of the authors and do not necessarily represent those of their affiliated organizations, or those of the publisher, the editors and the reviewers. Any product that may be evaluated in this article, or claim that may be made by its manufacturer, is not guaranteed or endorsed by the publisher.

Copyright © 2021 Liu, Lu, Ding, Lyu, Li and Dong. This is an open-access article distributed under the terms of the Creative Commons Attribution License (CC BY). The use, distribution or reproduction in other forums is permitted, provided the original author(s) and the copyright owner(s) are credited and that the original publication in this journal is cited, in accordance with accepted academic practice. No use, distribution or reproduction is permitted which does not comply with these terms.

frontiers
in Earth Science

ORIGINAL RESEARCH
published: 07 December 2021
doi: 10.3389/feart.2021.755084

Establishing a Luminescence-Based Chronostratigraphy for the Last Glacial-Interglacial Cycle of the Loess-Palaeosol Sequence Achajur (Armenia)

Johanna Lomax[1]*, Daniel Wolf[2], Urs Tilmann Wolpert[1], Lilit Sahakyan[3], Hayk Hovakimyan[3], Dominik Faust[2] and Markus Fuchs[1]

[1]Department of Geography, Justus Liebig University Giessen, Giessen, Germany, [2]Institute of Geography, TU Dresden, Dresden, Germany, [3]Institute of Geological Sciences, National Academy of Science of Armenia, Yerevan, Armenia

OPEN ACCESS

Edited by:
Zhiwei Xu,
Nanjing University, China

Reviewed by:
Shuangwen Yi,
Nanjing University, China
Xiaodong Miao,
Linyi University, China
Aditi Dave,
Max Planck Institute for Chemistry, Germany

****Correspondence:***
Johanna Lomax
johanna.lomax@geogr.uni-giessen.de

Specialty section:
This article was submitted to Quaternary Science, Geomorphology and Paleoenvironment, a section of the journal Frontiers in Earth Science

Received: *07 August 2021*
Accepted: *08 November 2021*
Published: *07 December 2021*

Citation:
Lomax J, Wolf D, Wolpert UT, Sahakyan L, Hovakimyan H, Faust D and Fuchs M (2021) Establishing a Luminescence-Based Chronostratigraphy for the Last Glacial-Interglacial Cycle of the Loess-Palaeosol Sequence Achajur (Armenia). Front. Earth Sci. 9:755084. doi: 10.3389/feart.2021.755084

The loess-palaeosol section Achajur is part of the Sevkar loess area in north-eastern Armenia and comprises three prominent pedocomplexes with intercalated loess units, probably spanning at least three glacial-interglacial cycles. With its central position between the Black Sea and the Caspian Sea, the Sevkar loess area serves as important bridge between loess sections in southeastern Europe and Central Asia. Establishing a numerical chronology of the Achajur loess section enables correlation with other loess-palaeosol sections and a palaeoenvironmental reconstruction of the region. In this paper, we focus on the chronology of the last glacial-interglacial cycle using luminescence dating on fine grain (4–11 µm) material. We compare two post-IR-IRSL protocols on polymineral fine grain using different stimulation temperatures, in order to evaluate the influence of fading and potential unbleachable residuals on our samples. For a backup of the younger ages (<50 ka), we also applied a single aliquot protocol on the quartz fine grain fraction. The results indicate that the upper loess unit was deposited during MIS3 and 4, while MIS2 ages are not present. The underlying pedocomplex and loess unit fall into MIS5 and MIS6, respectively. This confirms that the loess was deposited during dry phases and pedocomplexes formed during wetter phases, as is also shown by comparison with other palaeoenvironmental proxies from the area.

Keywords: loess, post-IR-IRSL, quartz, fine grain dating, Armenia, luminescence dating, palaeoenvironment, tephra

INTRODUCTION

Loess-palaeosol sequences (LPS) play an important role in reconstructing Quaternary climates and environments. They provide information on past climate conditions by comparison with Marine Isotope Stages (MIS) and pollen records (e.g. Antoine et al., 2019; Rousseau et al., 2020; Wolf et al., 2021) or by analyses of mollusc assemblages (e.g. Moine et al., 2005; Richter et al., 2020), on loess source areas (Ujvari et al., 2012; Ujvari et al., 2014), on past vegetation cover (e.g. Hatté et al., 1998, Hatté et al., 2013; Trigui et al., 2019) and former soil formation conditions (e.g. Buggle et al., 2011).

For such environmental reconstructions, precise chronologies are essential. Loess as windblown sediment is considered as ideal material for optically stimulated luminescence (OSL) dating (e.g.

Fuchs et al., 2013; Lomax et al., 2019). However, quartz luminescence ages are often underestimated in high dose ranges, explained by an aberrant behaviour of the laboratory generated dose response curve, which restricts quartz OSL dating to around 50–65 ka in loess when using fine to medium sized grains (Chapot et al., 2012; Timar-Gabor and Wintle, 2013; Avram et al., 2020). Upper age limits in feldspars are much higher (e.g. Avram et al., 2020), but anomalous fading may lead to an unwanted loss of the infrared stimulated luminescence (IRSL) signal (Spooner, 1994) and thus to underestimated IRSL ages. In the recent decade however, feldspar luminescence protocols have been developed which decrease or even overcome the problem of fading in feldspar dating. These protocols use a first lower temperature IRSL which empties luminescence traps prone to fading, followed by a second or consecutive IRSL steps at elevated temperatures, which sample the luminescence of more stable traps (Thomsen et al., 2008; Buylaert et al., 2009; Li and Li, 2011, 2012; Thiel et al., 2011; Zhang and Li, 2020). This measurement procedure is usually termed post-IR-IRSL (pIRIR) dating. Because there seems to be a negative relation between first and second stimulation temperature and fading, and a positive relation between first and second stimulation temperature and residual signals (e.g. Kars et al., 2014), a careful consideration of these two problems needs to be carried out. Younger samples, which usually show smaller fading rates, but in which residuals can contribute largely to the palaeodose, are often measured using lower first and second stimulation temperatures (e.g. Reimann and Tsukamoto, 2012), whereas for older samples, the opposite is the case (Zhang and Li, 2020). For these reasons, there is so far no general protocol for feldspar samples, and therefore, a wide range of protocols and approaches exist and their application is dependent on the individual local geoconditions.

LPS in north-eastern Armenia provide excellent conditions for reconstructing palaeoenvironmental conditions. They contain multiple sequences of loess and pedocomplexes indicating that they represent several glacial-interglacial cycles. Furthermore, several tephra layers within the loess sections provide the possibility of reconstructing past volcanic eruptions and for using these tephra layers as chronological marker horizons. Studies on the chronology of north-eastern Armenian loess sections are rare so far. Wolf et al. (2016) present five pIRIR ages and two OSL ages of the loess section Sevkar, which is located close to the section Achajur studied in this paper. Together with studies of Trigui et al. (2019) and Richter et al. (2020) it is shown that during glacials, dry conditions promoted shrub-steppe and loess accumulation in the area, whereas interglacials were accompanied by forest- and high-grass-steppe and landscape stability with soil formation. The aim of this paper is to refine the chronology of LPS in the Sevkar loess area for the last glacial-interglacial cycle, to enable a correlation between the loess sections Sevkar and Achajur, and to test the reliability of the obtained luminescence ages. Therefore, three different protocols were applied on different mineral fractions, dating a total of 13 samples. The quartz fine grain fraction was measured using a *1*) SAR protocol (Murray and Wintle, 2000; 2003) in order to provide reliable ages for the younger part of the loess section. Furthermore, two different pIRIR protocols, namely a *2*) pIRIR-225 protocol (Buylaert et al., 2009) and a *3*) pIRIR-290 protocol (Thiel et al., 2011; Li and Li, 2012), were applied to the polymineral fine grain fraction. The aim of this approach is to test which protocol yields the most reliable ages, especially for the older part (>50 ka) of the section, in order to apply this protocol to further sections from the Sevkar loess area. For evaluating the reliability of these polymineral feldspar ages, a comparison with the quartz ages from the younger part of the section, stratigraphic information and comparison with regional palaeoclimatic records is used as age control.

STUDY AREA AND SITE DESCRIPTION

The Achajur loess section within the Sevkar loess area is located approximately 75 km north of Lake Sevan in north-eastern Armenia (Tavush region) (**Figure 1**). The section is part of a larger area of loess deposits stretching along the north-eastern foothills of the Southern Caucasus, which forms a NW-SE stretching boundary to the Kura depression. Some of the loess deposits of the Sevkar area form dune-like ridges and show a strong inclination of loess units and soil horizons (Wolf et al., 2016). Furthermore, most of the loess sections contain prominent tephra layers, derived from volcanoes in Armenia, Georgia and Turkey (Neill et al., 2013; Sherriff et al., 2019). The nearby Aghstev River drains the Southern Caucasus and joins the Kura River in Azerbaijan, which in turn drains into the Caspian Sea.

At present, annual precipitation in the study area ranges between 450 and 550 mm with a maximum in May and a minimum in winter. The mean annual temperature averages ca. 11°C (Wolf et al., 2016). The most common type of vegetation of the adjacent Kura Basin is steppe vegetation in lower areas, associated with patches of oak forests on the slopes of the Southern Caucasus.

The section Achajur is located at 41°0′17″N, 45°9′22″E and 891 m a.s.l. The composite profile is derived from compiling four sub-sections and reaches a total thickness of 24 m. It comprises three palaeosol complexes (P-3, P-2, P-1) and the Holocene soil (P-0), intercalated by the loess units L-3, L-2 and L-1 (**Figure 2**). This indicates that the section most probably reaches down to at least the third last glacial.

A short stratigraphic description deals with the section (**Figure 2**) from the bottom to the top: Above a blackish horizon that marks the upper part of pedocomplex P-3, sub-sequence 3 represents a succession of loess deposits (L-3), ending with the formation of pedocomplex P-2. Loess unit L-3 comprises another weakly developed brownish soil (L-3/S1). The lower part of pedocomplex P-2 (P-2/S2) exhibits a greyish-brown soil with large (~10 cm) calcium-carbonate enrichments. Above at least two layers of relocated material, which are characterised by small rounded clay-pebbles (<6 mm), the upper part of pedocomplex P-2 (P-2/S1) reveals another strong dark-brown to reddish-brown soil containing big calcium-carbonate enrichments and concretions. Sub-sequence 3 ends with a greyish colluvial layer. Sub-sequence 2 is characterised by the deposition of thick layers of loess material (L-2) bearing features of strong relocation such as rock fragments or isolated clay-pebbles. Based on field observations, no prominent interstadial palaeosols seem to be

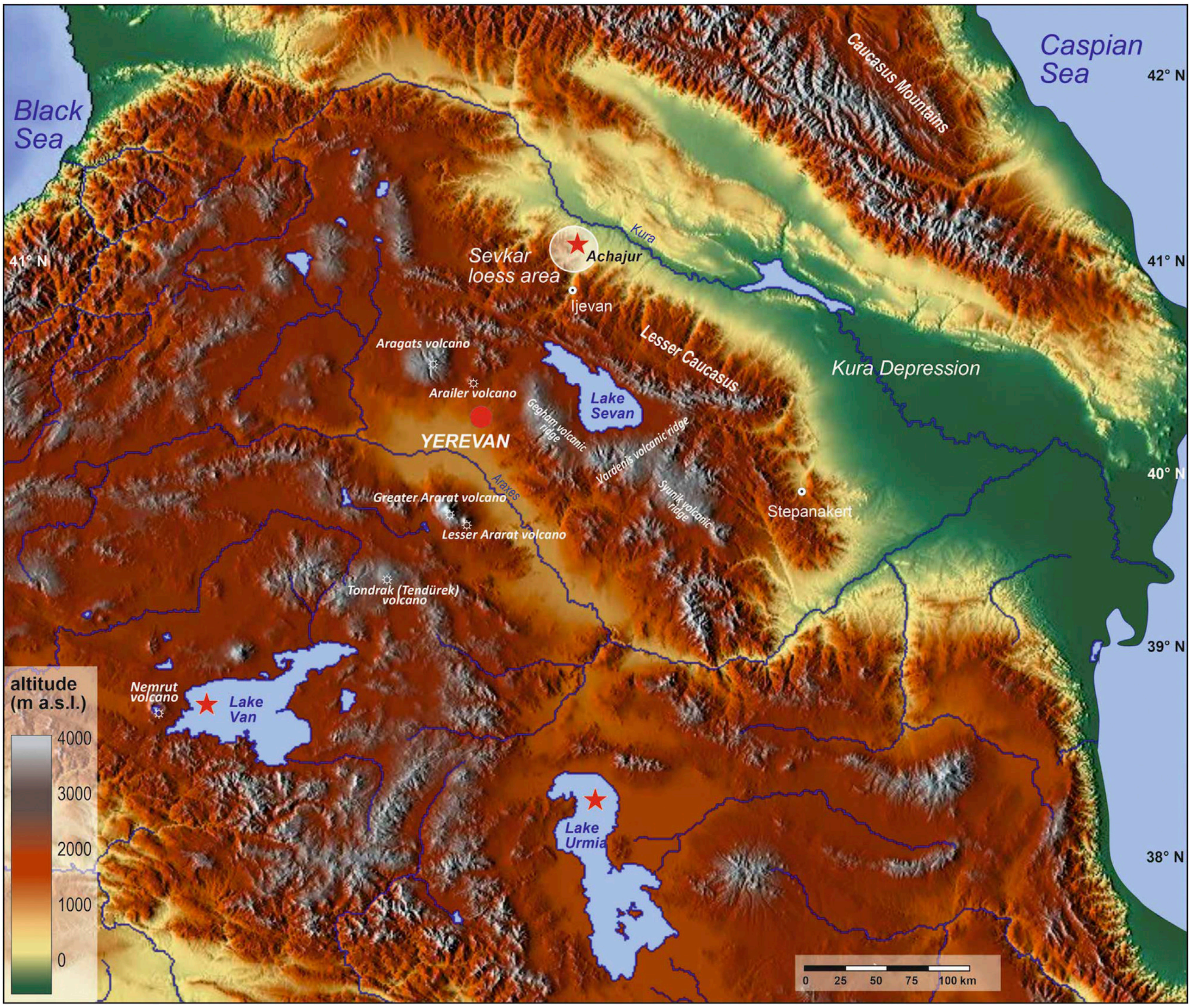

FIGURE 1 | Study area showing the location of the Achajur section and sites of important palynological studies discussed for palaeoclimatic interpretation. (Map modified from maps-for-free.com).

present in this unit. A pale bluish tephra layer interrupts unit L-2, while a couple of relocated greyish tephra-bearing layers are admixed above. Weakly weathered palaeosols were found below the bluish tephra (L-2/S2) as well as in the upper part (L-2/S1). Sub-sequence 2 ends with pedocomplex P-1 that shows a succession of three well-developed palaeosols. While the lowermost palaeosol (P-1/S3) is characterized by a ~60 cm thick strongly weathered brown horizon with large calcium-carbonate enrichments, the overlying palaeosols (P-1/S1 and P-1/S2) reveal a blackish color and crumbly structure and can be classified as chernozems. The uppermost sub-sequence 1 is characterised by a succession of loess deposits (L-1) with interposed pale greyish-brown palaeosols (L-1/S1-S4). At the top of the section, a reddish-brown soil (P-0/S2) with small calcium-carbonate concretions is present and is covered by a sequence of colluvial deposits.

For a further characterisation of the loess section, field magnetic susceptibility (MS) measurements were carried out using a portable Bartington MS2F probe (580 Hz), taking measurements at an interval of 5 cm. Often, MS values represent the degree of soil formation, with high MS values in palaeosols due to the formation of iron oxides during soil formation, and low values in pure loess (Evans and Heller, 1994). In the Sevkar loess area however, high values of magnetic minerals within the loess units, probably related to tephric material, hamper a clear distinction between loess layers and soil horizons (Wolf et al., 2016). Due to this, the loess layers can yield higher MS values than some of the palaeosols.

Eight samples for luminescence dating (Gi538-545) were taken in the L-1 loess layer, and three samples in palaeosols (Gi546 and Gi548) and intercalated loess layers (Gi547) of the pedocomplex P-1. Further two samples (Gi549 and Gi550) are derived from the younger part of

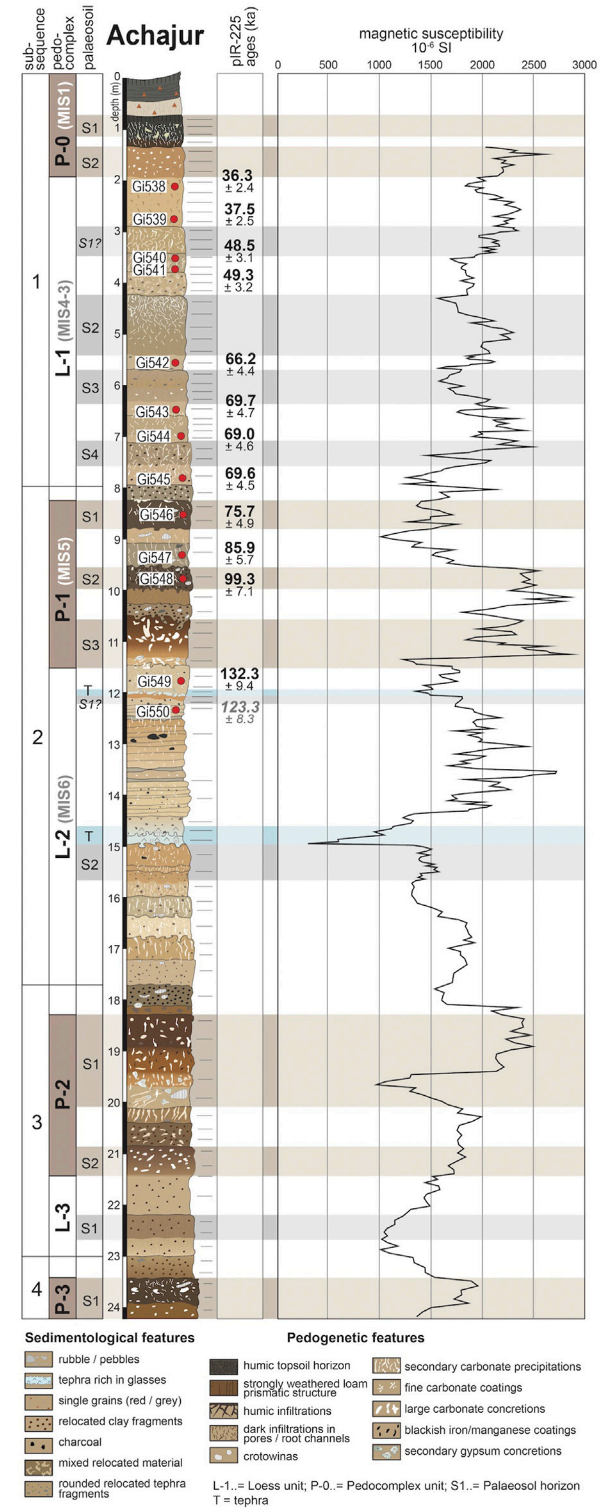

FIGURE 2 | Loess section Achajur with pIRIR-225 ages. The age of Gi550 is set in italics, because it likely underestimates the true depositional age. Magnetic susceptibility (χ) measurements were carried out with a portable Bartington susceptibility meter at an interval of 5 cm.

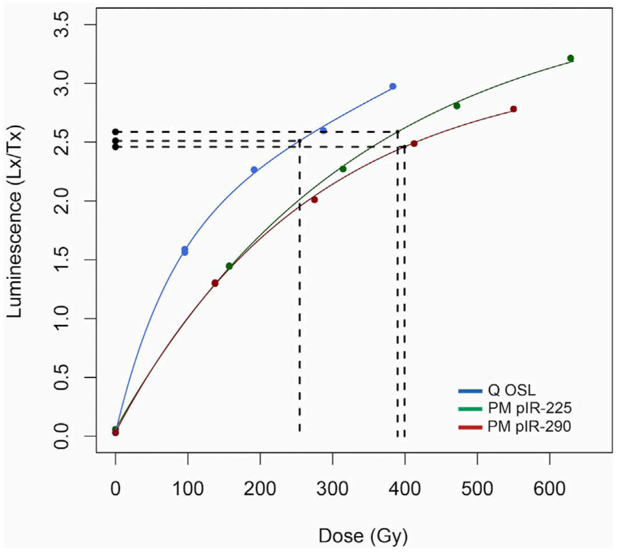

FIGURE 3 | Typical growth curves of one aliquot each of sample Gi549, showing Lx/Tx values, Ln/Tn values and the respective palaeodoses for the quartz fine grain fraction, and the polymineral fine grain fraction measured with an pIRIR-225 and an pIRIR-290 protocol.

the L-2 loess, above the bluish tephra layer at 15 m. At Achajur, it was not possible to take samples below the tephra, since these layers were heavily disturbed by erosional processes, and therefore, a stratigraphical assignment was not possible.

LUMINESCENCE METHODS

Sample Preparation and Instrumental Details

The fine grain fraction (4–11 μm) was separated by settling using Stokes' law. To receive the quartz rich fraction, the polymineral samples were subjected to HCl (10%) and H_2O_2 (10%), and subsequently etched in 34% pre-treated H_2SiF_6 for several days (Fuchs et al., 2005). Removal of the feldspar fraction was tested through IR stimulation in the luminescence reader. 1 mg of material were pipetted onto stainless steel cups, preparing ca. 25 cups per sample.

Luminescence measurements were performed on a Lexsyg Smart luminescence reader using green LEDs for stimulation (525 ± 25 nm, power density 65 mW/cm^2). Signals were detected with a Hamamatsu H7360 photomultiplier after passing a filter combination of a Semrock HC377/50 and a Schott BG3. This combination restricts the detected wavelength to ca. 350–400 nm, encompassing the peak OSL emission of quartz (Huntley et al., 1991; Lomax et al., 2015).

The polymineral fine grain fraction was extracted following the same laboratory procedure as for extracting the quartz fine grain fraction, without the etching step at the end. As for quartz, 1 mg of material was pipetted onto stainless steel cups. Signals

TABLE 1 | Details of the pIRIR-225 and pIRIR-290 protocols used for dating the Achajur polymineral fine grain samples.

	pIRIR-225		pIRIR-290	
1	Irradiation with regeneration dose		Irradiation with regeneration dose	
2	Preheat at 250°C for 60 s		Preheat at 320°C for 60 s	
3	IRSL at 50°C for 300 s		IRSL at 130°C for 600 s	
4	IRSL at 225°C for 300 s	Lx	IRSL at 290°C for 600 s	Lx
5	Irradiation with test dose		Irradiation with test dose	
6	Preheat at 250°C for 60 s		Preheat at 320°C for 60 s	
7	IRSL at 50°C for 300 s		IRSL at 130°C for 600 s	
8	IRSL at 225°C for 300 s	Tx	IRSL at 290°C for 600 s	Tx
9	Return to step 1 with further regeneration doses		IRSL at 325°C for 200 s	
10			Return to step 1 with further regeneration doses	

were stimulated in a Lexsyg Smart luminescence reader using IR LEDs (830 ± 3 nm, 300 or 250 mW/cm^2) and signal detection through an interference filter (AHF Brightline HC414/46 + Schott BG39) centred at 410 nm. All samples were analysed using the R luminescence package (Kreutzer et al., 2012b).

Quartz Fine Grain Measurements

For D_e determination, a single aliquot regenerative (SAR) protocol after Murray and Wintle (2000, 2003) was applied. Preheat and cutheat temperatures in the standard measurements were set to 240–220°C, following preheat and preheat-dose recovery tests (**Supplementary Figure S1**).

OSL signals were measured for 50 s at 125°C and the initial and background integrals were set to 0–0.5 s and 40–50 s. Rejection criteria were set to 10% for each the recycling ratio, the IR depletion ratio (Duller, 2003), the test dose error and the total palaeodose error, and to 5% for the recuperation ratio. An exponential plus linear fit was used for generating a growth curve. Typical OSL and TL signals for sample Gi538 are shown in **Supplementary Figure S2**. A typical growth curve for the fine grain quartz fraction is provided in **Figure 3**.

Per sample, 15 aliquots were measured and at least 14 aliquots passed the rejection criteria. As expected for fine grains, where OSL signals and corresponding doses are averaged over thousands of grains, overdispersion values were low, averaging 2.8%, with a maximum overdispersion of 5.8%. The arithmetic mean was used for final D_e calculation.

Polymineral Fine Grain Measurements

D_e Determination

A pIRIR-225 following Buylaert et al. (2009) and a pIRIR-290 protocol following Thiel et al. (2011) and Li and Li (2012) were applied for dating the polymineral fine grain fraction. **Table 1** gives details for the individual settings of the two protocols. In comparison to the original protocols of Thiel et al. (2011) and Li and Li (2012), the stimulation time in our study was increased to 600 s for the pIRIR-290 protocol, in order to fully deplete the IRSL signals. The first IRSL stimulation temperature was set to 130°C, hence to a larger temperature than the commonly used 50°C stimulation temperature (e.g. Thiel et al., 2011). An even higher first stimulation temperature of 200°C is recommended by Li and Li (2012) in order to reduce fading especially for older samples >400 Gy. We tested first stimulation temperatures of 50, 90, 130, 170 and 210°C for sample Gi544. For the two highest first stimulation temperatures of 170 amd 210°C, the post-IR signal became too weak to clearly distinguish it from the background level (**Supplementary Figure S3**). Apart from this observation, the pIRIR-290 palaeodose agrees within errors for first stimulation temperatures of 50, 90, 130 and 170°C for sample Gi544 (**Supplementary Figure S4**). We therefore decided for 130°C as first stimulation temperature, in order to account for possibly higher fading rates in the older samples, but still yielding a detectable post-IR signal with a low measurement error.

Signals for both protocols were integrated over the first 5 s of the signal, subtracted by a background derived from the last 50 or 100 s for the pIRIR-225 and pIRIR-290 protocol, respectively. Typical growth curves for the pIRIR-225 and pIRIR-290 signal are shown in **Figure 3**. For standard measurements, 10 aliquots for each sample were measured for the pIRIR-225 protocol and five to nine aliquots for the pIRIR-290 protocol. Rejection thresholds were set to 10% each for the recycling ratio, 5% for the recuperation ratio and 15% for the test dose error and the total palaeodose error. Average overdispersion values of 1.8% for the pIRIR-225 and 2.5% for the pIRIR-290 protocol were noticed. For both protocols, the arithmetic mean was applied for final D_e estimation.

TABLE 2 | Residual signals measured for the pIRIR-225 and pIRIR-290 protocol.

Sample	Bleaching type	Bleaching time	Protocol	Residual (Gy)
Gi541	Natural sun light	7 days	pIRIR-225	5.5 ± 0.3
Gi545	Natural sun light	7 days	pIRIR-225	8.5 ± 0.4
Gi549	Natural sun light	7 days	pIRIR-225	42.4 ± 1.7
Gi550	Natural sun light	7 days	pIRIR-225	9.7 ± 0.2
Gi540	Solar simulator	24 h	pIRIR-290	19.1 ± 2.0
Gi543	Solar simulator	24 h	pIRIR-290	17.8 ± 0.2
Gi538	Natural sun light	2 days	pIRIR-290	18.8 ± 1.5
Gi545	Natural sun light	2 days	pIRIR-290	21.3 ± 0.1

Test Measurements

Residual Measurements

Residuals were determined either after bleaching in natural sunlight (2 or 7 days) or after bleaching for 24 h in the solar simulator of the Lexsyg reader, using the sunlight spectrum (Frouin et al., 2015). Respective residuals along with bleaching type and duration are given in **Table 2**, consisting of arithmetic mean values of two to three aliquots per measurement. Assuming that the residual of Gi549 is an outlier, the pIRIR-225 protocol

TABLE 3 | Results of dose recovery tests using a pIRIR-225 and a pIRIR-290 protocol.

Sample	Bleaching	Protocol	Given dose (Gy)	Ratio (recovered/given dose)	Ratio with residual subtraction
Gi541	7d natural	pIRIR-225	210	1.02 ± 0.01	0.99 ± 0.01
Gi545	7d natural	pIRIR-225	262	1.03 ± 0.01	0.98 ± 0.01
Gi549	7d natural	pIRIR-225	524	1.12 ± 0.03	1.04 ± 0.03
Gi550	7d natural	pIRIR-225	524	1.03 ± 0.01	1.01 ± 0.01
Gi538	2d natural	pIRIR-290	275	1.20 ± 0.03	1.13 ± 0.03
Gi540	24h Solar sim	pIRIR-290	188	1.16 ± 0.04	1.06 ± 0.04
Gi541	24h Solar sim	pIRIR-290	275	1.33 ± 0.06	1.27 ± 0.06
Gi538	2d natural	pIRIR-290	271	1.20 ± 0.03	1.13 ± 0.03
Gi545	2d natural	pIRIR-290	215	1.11 ± 0.01	1.01 ± 0.01

produces lower residuals as the pIRIR-290 protocol. Translating these residuals into ages by dividing them by a typical dose rate for our samples of 3.3 Gy/ka, the pIRIR-225 protocol yields residuals of around 2–3 ka, whereas the pIRIR-290 protocol yields a residual of around 6 ka. For final age calculation, residuals for the pIRIR-225 protocol are neglected, whereas for ages based on the pIRIR-290 protocol, a residual of 18.3 Gy is subtracted from each D_e value, representing the arithmetic mean of the two lowest residuals.

Dose Recovery Measurements

Dose recovery tests were carried out after either 2 or 7 days of exposure to natural daylight or after 24 h bleaching in the solar simulator (Frouin et al., 2015). Subsequently, different known doses were administered in the Lexsyg reader and recovered with either the pIRIR-225 or the pIRIR-290 protocol. At least three aliquots were measured for each test and the dose recovery ratios provided in **Table 3** are based on the arithmetic mean of the three D_e values. Ratios are given with and without residual subtraction.

For the pIRIR-225 protocol, dose recovery ratios range between 1.02 ± 0.01 and 1.12 ± 0.03, when no residual subtraction is applied and between 0.98 ± 0.01 and 1.04 ± 0.03, when residual subtraction is applied. Dismissing sample Gi549, which showed an outlier in the recovered dose as well as in the residual dose, the protocol yields acceptable dose recovery ratios without residual subtraction. Therefore, D_e values and ages based on the pIRIR-225 protocol are calculated without residual subtraction in the final results.

The pIRIR-290 protocol yielded one unsatisfactory result in the dose recovery test, with a ratio of 1.33 before and 1.27 after residual subtraction. The reason for the overestimation of the given dose is possibly related to a too low test dose, which in this test was set to 23% of the given dose. In a further dose recovery test, the test dose size was increased to 33% of the given dose, yielding more satisfactory ratios of 1.16 ± 0.04 and 1.06 ± 0.04 (Gi540) and 1.20 ± 0.03 and 1.13 ± 0.03 (Gi538) before and after residual dose subtraction. Dose recovery ratios in dependence of the test dose size were already reported by e.g. Yi et al. (2016). They noticed an overestimation of the given dose in dose recovery tests, when the test dose was below 15% of the total (natural plus given) dose in a pIRIR-290 protocol with a first stimulation temperature of 50°C. It is followed that for the standard measurements, a test dose of 30% of the palaeodose is more appropriate for the samples in this study. Furthermore, the pIRIR-290 seems to perform better with a residual subtraction, therefore, D_e values and ages produced with this protocol are reported after a residual subtraction.

TABLE 4 | g-values measured for the pIRIR-225 protocol, following the procedure of Auclair et al. (2003).

Sample	Given dose (Gy)	Protocol	Mean g-value (%/decade)
Gi541	26	pIRIR-225	0.48 ± 0.30
Gi550	26	pIRIR-225	0.05 ± 0.57
Gi541	158	pIRIR-225	0.94 ± 0.15
Gi545	224	pIRIR-225	1.31 ± 0.10
Gi547	264	pIRIR-225	1.48 ± 0.08
Gi541	330	pIRIR-225	1.30 ± 0.10
Gi550	330	pIRIR-225	1.44 ± 0.20
Gi550	528	pIRIR-225	1.80 ± 0.15

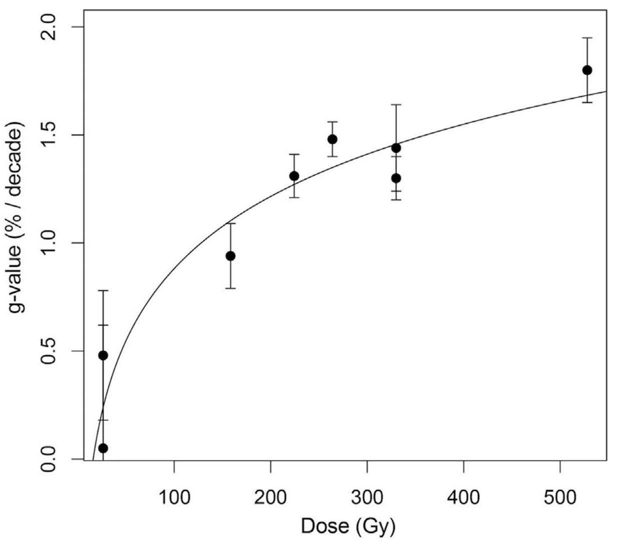

FIGURE 4 | Measured fading rates versus given dose in the fading test, and the potential logarithmic relation between the data.

Fading Measurements

Fading rates for the pIRIR-225 protocol were determined by subjecting the samples to different storage times up to

TABLE 5 | Radionuclide concentrations and resulting dose rates based on Durcan et al. (2015) for the quartz and polymineral fine grain fraction.

Sample	Depth (m)	U (ppm)	Th (ppm)	K (%)	Dose rate PM (Gy/ka)	Dose rate Q (Gy/ka)
Gi538	2.1	1.84 ± 0.28	6.35 ± 0.93	1.57 ± 0.08	3.00 ± 0.18	2.65 ± 0.16
Gi539	2.7	2.08 ± 0.24	6.14 ± 0.80	1.70 ± 0.09	3.18 ± 0.19	2.80 ± 0.17
Gi540	3.5	2.35 ± 0.23	5.14 ± 0.74	1.70 ± 0.09	3.15 ± 0.18	2.78 ± 0.17
Gi541	3.7	2.64 ± 0.23	4.96 ± 0.74	1.75 ± 0.09	3.29 ± 0.19	2.89 ± 0.17
Gi542	5.5	2.30 ± 0.25	6.22 ± 0.81	1.64 ± 0.08	3.17 ± 0.19	2.77 ± 0.17
Gi543	6.4	2.44 ± 0.19	4.17 ± 0.61	1.63 ± 0.08	2.97 ± 0.18	2.62 ± 0.16
Gi544	7.0	2.53 ± 0.20	4.77 ± 0.65	1.56 ± 0.08	3.00 ± 0.18	2.62 ± 0.16
Gi545	7.8	2.38 ± 0.23	6.73 ± 0.76	1.75 ± 0.09	3.32 ± 0.19	2.91 ± 0.17
Gi546	8.5	2.69 ± 0.21	4.96 ± 0.67	1.89 ± 0.09	3.37 ± 0.20	2.97 ± 0.18
Gi547	9.4	2.40 ± 0.21	5.37 ± 0.69	1.63 ± 0.08	3.06 ± 0.18	2.68 ± 0.16
Gi548	9.7	1.93 ± 0.23	7.03 ± 0.77	1.79 ± 0.09	3.20 ± 0.19	2.82 ± 0.17
Gi549	11.7	2.55 ± 0.20	4.88 ± 0.66	1.46 ± 0.07	2.90 ± 0.17	2.51 ± 0.16
Gi550	12.3	2.73 ± 0.24	7.11 ± 0.80	1.60 ± 0.08	3.33 ± 0.20	2.87 ± 0.17

approximately 2 days after irradiation and preheat, following Auclair et al. (2003). From these storage times, a g-value was calculated (Huntley and Lamothe, 2001). **Table 4** provides g-values for the pIRIR-225 protocol in relation to different irradiation times.

As visualised also in **Figure 4**, g-values are higher when the given dose is higher, and possibly the data set can be fitted by a logarithmic function. A similar relationship was recognised by Li and Li (2008), both in modelled and experimental datasets. It is thus likely that the older samples with higher palaeodoses have undergone higher rates of fading. In many studies, fading rates of below ca. 1.5% are treated as laboratory artefacts and are not used for a fading correction (e.g. Thiel et al., 2011; Buylaert et al., 2012). In our dataset, only one sample yields a g-value above 1.5%, which is sample Gi550 with a g-value of 1.8%. So far it is unclear, to which extent this value is a combination of a potential laboratory artefact and a true fading rate. At the current stage of research, we will thus not correct the pIRIR-225 ages for fading, and will treat sample Gi550 as minimum age. In a successive study on further sections from the same area, the need for a fading correction of the older samples may become clearer, because in these sections, a known age tephra is encompassed by luminescence samples. For the pIRIR-290 protocol, no fading tests were carried out, based on the assumption that the signal of the pIRIR-290 protocol does not fade (Thiel et al., 2011; Buylaert et al., 2012). The latter ages are thus used for an internal check on the degree of fading of the pIRIR-225 ages.

Dose Rate Estimation

The dose rate for OSL age calculation was determined by thick source α-counting (U and Th) and ICP-OES (K) at the University of Bayreuth. Cosmic-ray dose rates were calculated according to Prescott and Hutton (1994). An a-value of 0.035 ± 0.02 was applied for the quartz fine grain fraction (Mauz et al., 2006) and of 0.086 ± 0.004 (Rees-Jones, 1995) for the polymineral fraction. For the latter, an internal K-content of 12.5 ± 0.5% (Huntley and Baril, 1997) was also included in dose rate calculation. The water content of the samples was estimated to 15.0 ± 7.5%. Calculation of the total dose rate was carried out using the program DRAC (Durcan et al., 2015).

RESULTS

Table 5 summarises radionuclide concentrations and resulting dose rates for the quartz and the polymineral fine grain fraction. **Table 6** and **Figure 5** show all luminescence ages, obtained from quartz and from uncorrected polymineral fine grain D_e values. It is observed that between 35 and 55 ka, ages of the three protocols and mineral fractions agree very well. Assuming that the quartz ages are reliable in this age range, this argues for negligible fading of the polymineral fine grain ages for samples <55 ka, and for the correctness of the residual subtraction procedure of the polymineral fraction. The quartz ages are younger than the polymineral ages from ca. 60 ka onward, but agree within errors for samples up to ca. 85 ka. Sample Gi549 below the P-1 pedocomplex shows a discrepancy between the quartz and the polymineral fine grain fraction, most likely caused by an underestimation of the quartz fine grain fraction. Underestimation of the quartz fine grain fraction from ca. 60 ka onward have been shown for loess samples from Eastern Europe (e.g. Timar-Gabor et al., 2011, 2015a; Kreutzer et al., 2012a; Constantin et al., 2015). The reason for the underestimation is not yet totally understood, but is probably linked to differences in natural and laboratory generated growth curves (Chapot et al., 2012; Timar-Gabor and Wintle, 2013; Timar-Gabor et al., 2015b; Avram et al., 2020). All polymineral ages, measured with the pIRIR-225 and pIRIR-290 protocol agree within errors, and the mean ratio (pIRIR-290/pIRIR-225) between the two datasets is 1.03. This suggests that there is no significant difference in fading between the two protocols for our samples.

Results of the field magnetic susceptibility measurements are not standardized to mass or volume. However, a comparison with results from other loess areas measured with the same device shows that maximum MS values of the Achajur section are at least 10 times the maximum values in eastern German loess sections (e.g. Meszner et al., 2011) or 100 times the maximum values of loess sections in central Spain (Wolf et al., 2018). Most probably, this is due to a strong admixture of magnetic minerals derived from volcanic clastics such as tephra material or weathered volcanic bedrock.

TABLE 6 | Luminescence ages for the quartz (Q-FG) and polymineral fine (PM-FG) grain fraction.

Sample	Unit	Accepted *n* (Q)	D_e Q-FG (Gy)	Age Q-FG (ka)	Accepted *n* (pIRIR-225)	D_e PM-FG, pIRIR-225 (Gy)	Age PM-FG, pIRIR-225 (ka)	Accepted *n* (pIRIR-290)	D_e PM FG, pIRIR-290 (Gy)	Age PM-FG, pIRIR-290 (ka)
Gi538	L-1	15	97.9 ± 3.0	37.0 ± 2.6	10	109.0 ± 3.3	36.3 ± 2.4	5	105.5 ± 5.2	35.1 ± 2.7
Gi539	L-1				10	119.1 ± 3.6	37.5 ± 2.5			
Gi540	L-1	15	132.7 ± 4.3	47.8 ± 3.3	10	152.8 ± 4.7	48.5 ± 3.1			
Gi541	L-1	15	142.8 ± 4.4	49.4 ± 3.3	10	162.3 ± 4.9	49.3 ± 3.2	8	163.2 ± 7.6	49.7 ± 3.7
Gi542	L-1				10	209.6 ± 6.3	66.2 ± 4.4			
Gi543	L-1	14	173.3 ± 6.0	66.2 ± 4.6	10	206.9 ± 6.3	69.7 ± 4.7	9	228.1 ± 11.4	76.7 ± 5.9
Gi544	L-1	15	172.3 ± 5.5	65.7 ± 4.5	10	207.1 ± 6.3	69.0 ± 4.6			
Gi545	L-1	15	191.8 ± 5.9	66.0 ± 4.5	10	231.2 ± 7.0	69.6 ± 4.5	9	239.5 ± 11.3	72.1 ± 5.4
Gi546	P-1				10	254.9 ± 7.7	75.7 ± 4.9			
Gi547	P-1	15	218.9 ± 6.8	81.8 ± 5.6	10	262.8 ± 7.9	85.9 ± 5.7	8	291.3 ± 13.7	95.2 ± 7.2
Gi548	P-1				10	318.1 ± 12.7	99.3 ± 7.1			
Gi549	L-2	14	260.4 ± 8.6	103.6 ± 7.3	10	383.2 ± 14.5	132.3 ± 9.4	7	396.1 ± 24.9	136.8 ± 11.9
Gi550	L-2				10	410.6 ± 12.7	123.3 ± 8.3	8	391.2 ± 20.7	117.5 ± 9.4

Ages derived from both protocols are not corrected for fading, and ages of the pIRIR-290 protocol include a residual subtraction of 18.3 Gy. All D_e values are based on the arithmetic mean.

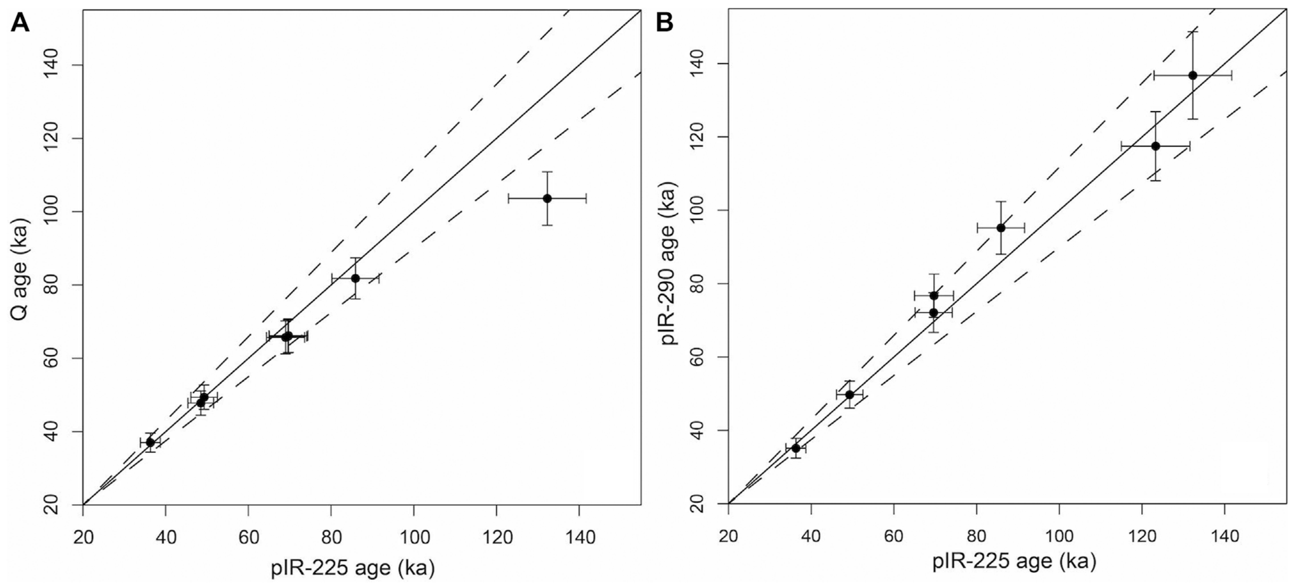

FIGURE 5 | Comparison of luminescence ages, comparing **(A)** quartz fine grain ages with pIRIR-225 polymineral fine grain ages, and **(B)** pIRIR-225 and pIRIR-290 polymineral fine grain ages. The dotted lines indicate 10% deviations from the 1:1 line.

The sequence of the L-2 loess gives a good impression about how the incorporation of volcanic material affects the magnetic susceptibility. Lowest values of ~300×10^{-6} SI-units are linked to the bluish tephra (~15 m), possibly indicating rhyolitic volcanism. Three meters above this tephra numerous thinner and darker tephra layers as well as volcanic rock fragments originating from neighbouring slopes are present. Magnetic susceptibility shows background values in the pure loess of about 1700×10^{-6} SI-units, while in loess with volcanic contaminations, values rise to ca. 2700×10^{-6} SI-units. This clearly illustrates the importance of the respective proportion of volcanic clasts within loess deposits for MS results. Furthermore, it shows that a simple scheme of low MS in loess and pedogenic enrichment of MS in palaeosols is not applicable to the Achajur section.

DISCUSSION

Considering the polymineral fine grain ages as reliable, the LPS Achajur shows a chronology in line with the expected stratigraphy, with the prominent pedocomplex P-1 falling into MIS5, and the overlying loess unit L-1 falling into MIS4 and 3. The MIS2 does not seem to be present at Achajur. The loess unit below the P-1 pedocomplex should probably fall into MIS6, according to stratigraphic expectations, which ends at around

130 ka (Lisiecki and Raymo, 2005). Likewise, at Lake Van in eastern Anatolia, full interglacial conditions assigned to MIS5 are established at ca. 129 ka, following an initial warming phase from ca. 131 ka onwards (Pickarski et al., 2015). The ages of sample Gi550, i.e. 117 ± 9 (pIRIR-290) and 123 ± 8 (pIRIR-225) underestimate this stratigraphic expectation, and they are also slightly younger than the overlying sample Gi549, which in turn agrees with the stratigraphic expectation. Possibly, the age discrepancy can partially be explained by an inaccurate estimation of the dose rate, since both samples and both protocols show agreeing palaeodoses. O'Gorman et al. (2021) for example showed that tephras can have very low internal potassium contents in IR-sensitive grains, e.g. due to a dominance of sanidine which is typical in rhyolitic rocks. The internal K-content of 12.5 ± 0.5% (Huntley and Baril, 1997) used for all our samples may thus be an overestimate in those samples with a large tephric contribution. Nonetheless, the effect on the pIRIR age would be small. For example, a theoretical internal K-content of 5% would only increase the age of sample Gi550 by 0.5%.

A further explanation could be a stronger rate of signal loss due to fading for sample Gi550 due to a thin (relocated?) tephra layer between sample Gi549 and Gi550. Since volcanic feldspar is known to fade to a higher degree than non-volcanic feldspar (Wintle, 1973), this tephra could indeed be responsible for a higher fading rate in sample Gi550. For the pIRIR-225 protocol, the sample showed a measured g-value of 1.8%, higher than for other samples for which g-values were measured. At this stage of research, we can only speculate on the underestimation of sample Gi550 and will thus treat the ages of this sample as most likely underestimated in the following.

With the resulting luminescence ages, the Achajur section provides a similar chronostratigraphy as the nearby LPS Sevkar, published by Wolf et al. (2016). They also present a "too young" age of 110 ± 17 ka for the loess unit below the P-1, and MIS4 to MIS3 ages for the loess unit above the P-1 palaeosol complex. Again, at this stage of research, we consider the age below the P-1 at the Sevkar section as true age underestimate. A similar chronostratigraphy is also recognised in LPS from northern Iran, with high loess deposition rates during MIS4, a three-fold palaeosol assigned to MIS5 and further loess deposition during MIS6 (Lauer et al., 2017; Kehl et al., 2021). In the latter two studies, a non-fading corrected pIRIR-290 protocol (Toshan loess section, Lauer et al., 2017) and a fading-corrrected pIRIR-225 protocol (Neka-Abelou, Kehl et al., 2021) were applied to polymineral fine grain samples. Similar to our results at Achajur, some age uncertainties, i.e. a potential age underestimation at Toshan and potential age overestimation at Neka-Abelou are noted for the MIS5 and MIS6 deposits. This demonstrates that–despite the huge advances made since the development of pIRIR protocols–dating of loess samples >100 ka still remains challenging. In contrast to the LPS at Achajur, the Iranian loess section Toshan also comprises units of significant loess deposition younger than 35 ka (MIS3-MIS2) (Lauer et al., 2017). At Neka Abelou however, the MIS2 is also not fully represented, with a youngest age of 28 ± 2 ka relatively near to the surface (Kehl et al., 2021).

In the following, the chronostratigraphy is compared with the well dated palynological records of Lake Van in Turkey (Litt et al., 2014; Stockhecke et al., 2014) and Lake Urmia in Iran (Djamali et al., 2008). Further comparisons are made with the studies of Richter et al. (2020) and Trigui et al. (2019), who reconstructed palaeoenvironments directly in the Sevkar loess area by gastropod analyses and leaf wax n-alkane analyses, respectively.

MIS6 – L-2 Loess Unit

The L-2 loess unit is presented by samples Gi550 and Gi549, which we expect to represent MIS6 with a slight underestimation. The prominent tephra at 15 m, located ca. 2.5 m below sample Gi550 cannot be bracketed with luminescence ages in this study, because the underlying loess unit was not sampled. However, the age of sample Gi549 provides a minimum age of around 132 ± 9 ka (pIRIR-225) and 137 ± 12 ka (pIRIR-290) for the tephra. A further, thin tephra is located between samples Gi550 and Gi549 at ca. 12 m. Interestingly, the tephra at 15 m is associated with a potential underlying incipient soil unit. The thinner tephra between samples Gi549 and Gi550 also shows a reddish layer below, which may also indicate weak pedogenesis. Possibly, the high vulnerability of volcanic glasses to weathering processes is connected to soil formation processes below the tephra layers (Kirkman and McHardy, 1980). However, relatively low values of magnetic susceptibility (**Figure 2**) do not indicate strong pedogenesis within the respective layers. Thus we are not able to undoubtedly clarify the development of the reddish units below the tephra layers.

A potential derivation of the tephra at 15 m is Nemrut volcano, which is situated ca 350 km to the southwest. Nemrut volcano shows an increase in volcanic activity from 200 ka onward (Sumita and Schmincke, 2013), and Lake Van shows several tephra layers in the MIS6 layers (Stockhecke et al., 2014). Lake Van also provides the possibility for correlation with a nearby palaeoclimatic record derived from the pollen assemblage archived in the lake sediments. In the vicinity of the lake, vegetation is characterised by dwarf-shrub steppe and desert steppe, with very little arboreal pollen during MIS6, indicating dry and cold conditions (Litt et al., 2014). A similar assemblage of Artemisa steppe and grasses is found at Lake Urmia in NE-Iran (Djamali et al., 2008). Richter et al. (2020) deduced a species-poor shrub steppe from gastropod assemblages found in other loess sections from the Sevkar area during MIS6. They also found indications that the limiting factor for tree growth during glacials in north-eastern Armenia is related to dry conditions rather than low temperatures. Similar conclusions were drawn by Trigui et al. (2019) from leaf wax n-alkanes in the Sevkar area.

MIS5 – P-1 Pedocomplex

Three samples were dated within the P-1 palaeosol complex, which are Gi548, Gi547 and Gi546. Field observations show a three-fold character of this unit, with three palaeosol horizons intercalated by two thin loess layers or relocated loessic material, respectively. The magnetic susceptibility record shows a significant increase in MS values for the lower two palaeosols of the P-1 complex. The uppermost palaeosol (P-1/S1) however is not as pronounced, and only shows a little increase in the magnetic susceptibilty in relation to the over- and underlying loess. Hence, especially the field observations seem to follow the three-fold character of MIS5 with its interglacial period 5e, its two interstadial periods 5c and 5a, and the two stadial periods 5d and 5b in between (e.g. Martinson et al., 1987; Lisiecki and Raymo, 2005). The relatively large errors of the pIRIR-ages and the partially diverging ages between the pIRIR-290 and the pIRIR-225 protocols make it difficult to assign the sediments in the P-1 pedocomplex to substages of MIS5. Furthermore, it needs to be considered that luminescence methods do not necessarily date soil formation but the loess deposition prior to pedogenesis, although a rejuvenation of the OSL age may occur in phases of strong bioturbation (e.g. Reimann et al., 2017). Sample Gi548 with an age of 99 ± 7 ka (pIRIR-225) was taken in unit P-1-S2, hence in the older of the two chernozem-like horizons, and is centred at MIS5c (Martinson et al., 1987). The overlying intercalated loess layer with sample Gi547 has a pIRIR-225 age of 86 ± 6 ka and a pIRIR-290 age of 95 ± 7 ka. These two ages cover MIS stages 5a to 5c, with a weighted mean of the two ages of ca. 91 ka centred at MIS5b. Sample Gi546 is located in the younger chernozem-like horizon of unit P-1/S1. With an age of 76 ± 5 ka, deposition of this unit falls into MIS5a/MIS4, hence the soil formation probably postdates MIS5a. With these luminescence ages, it seems plausible that the main pedogenesis developed in the pedocomplex P-1 took place during warmer substages of MIS5e and 5c. However, for the uppermost soil, an assignment to an interstadial of MIS5 is difficult.

Lake Van records a high percentage of arboreal pollen for MIS5e, dominated by Quercus and Pinus nigra. As pine is not present in today's vegetation, Litt et al. (2014) deduced a higher degree of seasonality during MIS5e as compared to today, with colder winters and warmer summers than today. MIS5d is recognised as tree-less stadial and MIS5c again shows a prominent peak of arboreal pollen, although with a lower percentage of Quercus than MIS5e. MIS5b is again associated with colder and/or dryer conditions due to a decline of arboreal pollen (Litt et al., 2014). MIS5a is subdued at Lake Van, which, according to Litt et al. (2014), could possibly be the result of high tephra input, concealing the pollen assemblage in this part of the record. However, Lake Urmia also shows a subdued MIS5a, with only slightly higher arboreal pollen than during the following MIS4 (Djamali et al., 2008), arguing for near-glacial conditions during the late part of MIS5 in the region. For two nearby LPS in the Sevkar area, high-grass steppe and forest-steppe conditions during formation of the P-1 pedocomplex are reconstructed from gastropod and n-alkane analyses (Trigui et al., 2019; Richter et al., 2020).

MIS4/3 – L-1 Loess Unit

With the exception of the pIRIR-290 age of sample Gi543, the samples Gi542-Gi545 yield ages between 66 ± 4 and 72 ± 5 ka, arguing for high rates of loess deposition during MIS4, indicating dry environmental conditions. A similar finding was reported by Malinsky-Buller et al. (2020) who assigned the onset of aeolian sediment deposition in the Hrazdan Valley in central Armenia to the transition from MIS5 to MIS4. Pronounced environmental dryness during MIS4 is likewise supported by the pollen records of Lake Van and Lake Urmia, which are dominated by steppe and desert steppe vegetation (Djamali et al., 2008; Litt et al., 2014), and by the gastropod fauna and n-alkanes at LPS in the Sevkar area (Trigui et al., 2019; Richter et al., 2020).

Further loess deposition is noted at around 49 ± 3 ka (Gi540 and Gi541) and at around 37 ± 3 ka (Gi538 and Gi539). Between these loess layers, the Achajur section incorporates weekly developed palaeosols. Based on the luminescence ages, the most prominent of these palaeosols (L-1/S2) falls into a period between 66 ± 4 and 49 ± 3 ka and can possibly be related to the pronounced Greenland interstadial 14 from 55 to 51.5 ka (Rasmussen et al., 2014). At the site Kalavan 2, 50 km south of the Sevkar loess area, a juxtaposition of surface erosion and pedogenesis was interpreted as evidence for strong seasonality changes in line with a sequence of stadials and interstadials at the end of MIS4 and the beginning of MIS3 (Malinsky-Buller et al., 2021). Intermediate climate conditions during this stage of MIS3 are recognised at Lake Van with a minor increase in Quercus pollen between 50 and 60 ka. Relatively wet conditions–especially with enhanced winter rainfall–are also recorded at the Karaca Cave in NW-Turkey (Rowe et al., 2012), whereas Lake Urmia does not show an increase in arboreal pollen during this time. The maximum of the last glacial, MIS2, does not seem to be present at the Achajur site.

CONCLUSION

In conclusion, the LPS Achajur is generally in line with the expected global stratigraphy and with nearby pollen records of Lake Van and Lake Urmia. It indicates dry glacials promoting loess deposition and wetter interglacials and interstadials with soil formation. The LGM is not represented in the section, either due to prior deposition and later erosion or due to a lack of loess formation. With exception of the lowermost sample, which is located near an overlying tephra, polymineral fine grain samples measured with a pIRIR-225 and pIRIR-290 protocol do not seem to require a fading correction. Quartz ages older than 60 ka appear slightly underestimated, especially for the MIS6 loess layer. Future research will concentrate on the relation between soil and tephra layers and an explanation for the lacking LGM loess layers.

DATA AVAILABILITY STATEMENT

The raw data supporting the conclusions of this article will be made available by the authors, without undue reservation.

AUTHOR CONTRIBUTIONS

JL carried out part of the luminescence dating, wrote the paper and prepared some of the figures. DW carried out field work, prepared some of the figures and is responsible for the stratigraphic description of the loess section, UTW carried out part of the luminescence dating and contributed in field work, LS is the project leader in the Armenian research team, HH carried out field work, and DF and MF are the project leaders of the TU Dresden and the JLU Giessen research teams.

FUNDING

This work was funded by the German Research Foundation (DFG, FU 417/26-1 and FA 239/21-1).

ACKNOWLEDGMENTS

We thank Manfred Fischer (University of Bayreuth) for carrying out the determination of radionuclide concentrations, and Lisett Diehl for help with the figures. We also thank SY, XM and AD for their very constructive and helpful reviews.

SUPPLEMENTARY MATERIAL

The Supplementary Material for this article can be found online at: https://www.frontiersin.org/articles/10.3389/feart.2021.755084/full#supplementary-material

REFERENCES

Antoine, P., Lagroix, F., Jordanova, D., Jordanova, N., Lomax, J., Fuchs, M., et al. (2019). A Remarkable Late Saalian (MIS 6) Loess (Dust) Accumulation in the Lower Danube at Harletz (Bulgaria). *Quat. Sci. Rev.* 207, 80–100. doi:10.1016/j.quascirev.2019.01.005

Auclair, M., Lamothe, M., and Huot, S. (2003). Measurement of Anomalous Fading for Feldspar IRSL Using SAR. *Radiat. Measurements* 37, 487–492. doi:10.1016/s1350-4487(03)00018-0

Avram, A., Constantin, D., Veres, D., Kelemen, S., Obreht, I., Hambach, U., et al. (2020). Testing Polymineral post- IR IRSL and Quartz SAR - OSL Protocols on Middle to Late Pleistocene Loess at Batajnica, Serbia. *Boreas* 49, 615–633. doi:10.1111/bor.12442

Buggle, B., Glaser, B., Hambach, U., Gerasimenko, N., and Marković, S. (2011). An Evaluation of Geochemical Weathering Indices in Loess-Paleosol Studies. *Quat. Int.* 240, 12–21. doi:10.1016/j.quaint.2010.07.019

Buylaert, J.-P., Jain, M., Murray, A. S., Thomsen, K. J., Thiel, C., and Sohbati, R. (2012). A Robust Feldspar Luminescence Dating Method for Middle and Late Pleistocene Sediments. *Boreas* 41, 435–451. doi:10.1111/j.1502-3885.2012.00248.x

Buylaert, J. P., Murray, A. S., Thomsen, K. J., and Jain, M. (2009). Testing the Potential of an Elevated Temperature IRSL Signal from K-Feldspar. *Radiat. Measurements* 44, 560–565. doi:10.1016/j.radmeas.2009.02.007

Chapot, M. S., Roberts, H. M., Duller, G. A. T., and Lai, Z. P. (2012). A Comparison of Natural- and Laboratory-Generated Dose Response Curves for Quartz Optically Stimulated Luminescence Signals from Chinese Loess. *Radiat. Measurements* 47, 1045–1052. doi:10.1016/j.radmeas.2012.09.001

Constantin, D., Cameniţă, A., Panaiotu, C., Necula, C., Codrea, V., and Timar-Gabor, A. (2015). Fine and Coarse-Quartz SAR-OSL Dating of Last Glacial Loess in Southern Romania. *Quat. Int.* 357, 33–43. doi:10.1016/j.quaint.2014.07.052

Djamali, M., de Beaulieu, J.-L., Shah-hosseini, M., Andrieu-Ponel, V., Ponel, P., Amini, A., et al. (2008). A Late Pleistocene Long Pollen Record from Lake Urmia, NW Iran. *Quat. Res.* 69, 413–420. doi:10.1016/j.yqres.2008.03.004

Duller, G. A. T. (2003). Distinguishing Quartz and Feldspar in Single Grain Luminescence Measurements. *Radiat. Measurements* 37, 161–165. doi:10.1016/s1350-4487(02)00170-1

Durcan, J. A., King, G. E., and Duller, G. A. T. (2015). DRAC: Dose Rate and Age Calculator for Trapped Charge Dating. *Quat. Geochronol.* 28, 54–61. doi:10.1016/j.quageo.2015.03.012

Evans, M. E., and Heller, F. (1994). Magnetic Enhancement and Palaeoclimate: Study of a Loess/palaeosol Couplet Across the Loess Plateau of China. *Geophys. J. Int.* 117, 257–264. doi:10.1111/j.1365-246x.1994.tb03316.x

Frouin, M., Huot, S., Mercier, N., Lahaye, C., and Lamothe, M. (2015). The Issue of Laboratory Bleaching in the Infrared-Radiofluorescence Dating Method. *Radiat. Measurements* 81, 212–217. doi:10.1016/j.radmeas.2014.12.012

Fuchs, M., Kreutzer, S., Rousseau, D.-D., Antoine, P., Hatté, C., Lagroix, F., et al. (2013). The Loess Sequence of Dolní Věstonice, Czech Republic: A New OSL-Based Chronology of the Last Climatic Cycle. *Boreas* 42, 664–677. doi:10.1111/j.1502-3885.2012.00299.x

Fuchs, M., Straub, J., and Zöller, L. (2005). Residual Luminescence Signal of Recent River Flood Sediments: A Comparison Between Quartz and Feldspar of fine- and Coarse-Grain Sediments. *Ancient TL* 2, 25–30.

Hatté, C., Fontugne, M., Rousseau, D.-D., Antoine, P., Zöller, L., Laborde, N. T., et al. (1998). δ13C Variations of Loess Organic Matter as a Record of the Vegetation Response to Climatic Changes During the Weichselian. *Geol* 26, 583–586. doi:10.1130/0091-7613(1998)026<0583:cvolom>2.3.co;2

Hatté, C., Gauthier, C., Rousseau, D.-D., Antoine, P., Fuchs, M., Lagroix, F., et al. (2013). Excursions to C4 Vegetation Recorded in the Upper Pleistocene Loess of Surduk (Northern Serbia): An Organic Isotope Geochemistry Study. *Clim. Past* 9, 1001–1014. doi:10.5194/cp-9-1001-2013

Huntley, D., and Baril, M. (1997). The K Content of the K-Feldspars Being Measured in Optical Dating or in Thermoluminescence Dating. *Ancient TL* 15, 11–13.

Huntley, D. J., Godfrey-Smith, D. I., and Haskell, E. H. (1991). Light-induced Emission Spectra from Some Quartz and Feldspars. *Int. J. Radiat. Appl. Instrumentation. D. Nucl. Tracks Radiat. Measurements* 18, 127–131. doi:10.1016/1359-0189(91)90104-p

Huntley, D. J., and Lamothe, M. (2001). Ubiquity of Anomalous Fading in K-Feldspars and the Measurement and Correction for it in Optical Dating. *Can. J. Earth Sci.* 38, 1093–1106. doi:10.1139/e01-013

Kars, R. H., Reimann, T., Ankjaergaard, C., and Wallinga, J. (2014). Bleaching of the post-IR IRSL Signal: New Insights for Feldspar Luminescence Dating. *Boreas* 43, 780–791. doi:10.1111/bor.12082

Kehl, M., Vlaminck, S., Köhler, T., Laag, C., Rolf, C., Tsukamoto, S., et al. (2021). Pleistocene Dynamics of Dust Accumulation and Soil Formation in the Southern Caspian Lowlands - New Insights from the Loess-Paleosol Sequence at Neka-Abelou, Northern Iran. *Quat. Sci. Rev.* 253, 106774. doi:10.1016/j.quascirev.2020.106774

Kirkman, J. H., and McHardy, W. J. (1980). A Comparative Study of the Morphology, Chemical Composition and Weathering of Rhyolitic and Andesitic Glass. *Clay miner.* 15, 165–173. doi:10.1180/claymin.1980.015.2.07

Kreutzer, S., Fuchs, M., Meszner, S., and Faust, D. (2012a). OSL Chronostratigraphy of a Loess-Palaeosol Sequence in Saxony/Germany Using Quartz of Different Grain Sizes. *Quat. Geochronol.* 10, 102–109. doi:10.1016/j.quageo.2012.01.004

Kreutzer, S., Schmidt, C., Fuchs, M., Dietze, M., and Fischer, M. (2012b). Introducing an R Package for Luminescence Dating Analysis. *Ancient TL* 30, 1–8.

Lauer, T., Frechen, M., Vlaminck, S., Kehl, M., Lehndorff, E., Shahriari, A., et al. (2017). Luminescence-chronology of the Loess Palaeosol Sequence Toshan, Northern Iran - A Highly Resolved Climate Archive for the Last Glacial-Interglacial Cycle. *Quat. Int.* 429, 3–12. doi:10.1016/j.quaint.2015.03.045

Li, B., and Li, S.-H. (2012). A Reply to the Comments by Thomsen et al. on "Luminescence Dating of K-feldspar from Sediments: A Protocol Without Anomalous Fading Correction". *Quat. Geochronol.* 8, 49–51. doi:10.1016/j.quageo.2011.10.001

Li, B., and Li, S.-H. (2008). Investigations of the Dose-dependent Anomalous Fading Rate of Feldspar from Sediments. *J. Phys. D: Appl. Phys.* 41, 225502. doi:10.1088/0022-3727/41/22/225502

Li, B., and Li, S.-H. (2011). Luminescence Dating of K-Feldspar from Sediments: A Protocol Without Anomalous Fading Correction. *Quat. Geochronol.* 6, 468–479. doi:10.1016/j.quageo.2011.05.001

Lisiecki, L., and Raymo, M. (2005). A Pliocene-Pleistocene Stack of 57 Globally Distributed Benthic δ18O Records. *Paleocean* 20, 1–17. doi:10.1029/2004pa001071

Litt, T., Pickarski, N., Heumann, G., Stockhecke, M., and Tzedakis, P. C. (2014). A 600,000 Year Long Continental Pollen Record from Lake Van, Eastern Anatolia (Turkey). *Quat. Sci. Rev.* 104, 30–41. doi:10.1016/j.quascirev.2014.03.017

Lomax, J., Fuchs, M., Antoine, P., Rousseau, D.-D., Lagroix, F., Hatté, C., et al. (2019). A Luminescence-Based Chronology for the Harletz Loess Sequence, Bulgaria. *Boreas* 48, 179–194. doi:10.1111/bor.12348

Lomax, J., Mittelstrass, D., Kreutzer, S., and Fuchs, M. (2015). OSL, TL and IRSL Emission Spectra of Sedimentary Quartz and Feldspar Samples. *Radiat. Measurements* 81, 251–256. doi:10.1016/j.radmeas.2015.02.018

Malinsky-Buller, A., Glauberman, P., Ollivier, V., Lauer, T., Timms, R., Frahm, E., et al. (2021). Short-term Occupations at High Elevation During the Middle Paleolithic at Kalavan 2 (Republic of Armenia). *PLOS ONE* 16, e0245700. doi:10.1371/journal.pone.0245700

Malinsky-Buller, A., Glauberman, P., Wilkinson, K., Li, B., Frahm, E., Gasparyan, B., et al. (2020). Evidence for Middle Palaeolithic Occupation and Landscape Change in Central Armenia at the Open-Air Site of Alapars-1. *Quat. Res.* 99, 223–247. doi:10.1017/qua.2020.61

Martinson, D. G., Pisias, N. G., Hays, J. D., Imbrie, J., Moore, T. C., and Shackleton, N. J. (1987). Age Dating and the Orbital Theory of the Ice Ages: Development of a High-Resolution 0 to 300,000-year Chronostratigraphy. *Quat. Res.* 27, 1–29. doi:10.1016/0033-5894(87)90046-9

Mauz, B., Packman, S., and Lang, A. (2006). The Alpha Effectiveness in Silt-sized Quartz: New Data Obtained by Single and Multiple Aliquot Protocols. *Ancient TL* 24, 47–52.

Meszner, S., Fuchs, M., and Faust, D. (2011). Loess-Palaeosol-Sequences from the Loess Area of Saxony (Germany). *E&g Quat. Sci. J.* 60, 47–65. doi:10.3285/eg.60.1.03

Moine, O., Rousseau, D.-D., and Antoine, P. (2005). Terrestrial Molluscan Records of Weichselian Lower to Middle Pleniglacial Climatic Changes from the Nussloch Loess Series (Rhine Valley, Germany): The Impact of Local Factors. *Boreas* 34, 363–380. doi:10.1080/03009480510013060

Murray, A. S., and Wintle, A. G. (2000). Luminescence Dating of Quartz Using an Improved Single-Aliquot Regenerative-Dose Protocol. *Radiat. Measurements* 32, 57–73. doi:10.1016/s1350-4487(99)00253-x

Murray, A. S., and Wintle, A. G. (2003). The Single Aliquot Regenerative Dose Protocol: Potential for Improvements in Reliability. *Radiat. Measurements* 37, 377–381. doi:10.1016/s1350-4487(03)00053-2

Neill, I., Meliksetian, K., Allen, M. B., Navarsardyan, G., and Karapetyan, S. (2013). Pliocene-Quaternary Volcanic Rocks of NW Armenia: Magmatism and Lithospheric Dynamics Within an Active Orogenic Plateau. *Lithos* 180-181, 200–215. doi:10.1016/j.lithos.2013.05.005

O'Gorman, K., Tanner, D., Sontag-González, M., Li, B., Brink, F., Jones, B. G., et al. (2021). Composite Grains from Volcanic Terranes: Internal Dose Rates of Supposed 'potassium-Rich' Feldspar Grains Used for Optical Dating at Liang Bua, Indonesia. *Quat. Geochronol.* 64, 101182. doi:10.1016/j.quageo.2021.101182

Pickarski, N., Kwiecien, O., Djamali, M., and Litt, T. (2015). Vegetation and Environmental Changes During the Last Interglacial in Eastern Anatolia (Turkey): A New High-Resolution Pollen Record from Lake Van. *Palaeogeogr. Palaeoclimatol. Palaeoecol.* 435, 145–158. doi:10.1016/j.palaeo.2015.06.015

Prescott, J. R., and Hutton, J. T. (1994). Cosmic Ray Contributions to Dose Rates for Luminescence and ESR Dating: Large Depths and Long-Term Time Variations. *Radiat. Measurements* 23, 497–500. doi:10.1016/1350-4487(94)90086-8

Rasmussen, S. O., Bigler, M., Blockley, S. P., Blunier, T., Buchardt, S. L., Clausen, H. B., et al. (2014). A Stratigraphic Framework for Abrupt Climatic Changes During the Last Glacial Period Based on Three Synchronized Greenland Ice-Core Records: Refining and Extending the INTIMATE Event Stratigraphy. *Quat. Sci. Rev.* 106, 14–28. doi:10.1016/j.quascirev.2014.09.007

Rees-Jones, J. (1995). Optical Dating of Young Sediments Using Finegrain Quartz. *Ancient TL* 13, 9–14.

Reimann, T., Román-Sánchez, A., Vanwalleghem, T., and Wallinga, J. (2017). Getting a Grip on Soil Reworking - Single-Grain Feldspar Luminescence as a Novel Tool to Quantify Soil Reworking Rates. *Quat. Geochronol.* 42, 1–14. doi:10.1016/j.quageo.2017.07.002

Reimann, T., and Tsukamoto, S. (2012). Dating the Recent Past. *Quat. Geochronol.* 10, 180–187. doi:10.1016/j.quageo.2012.04.011

Richter, C., Wolf, D., Walther, F., Meng, S., Sahakyan, L., Hovakimyan, H., et al. (2020). New Insights into Southern Caucasian Glacial-Interglacial Climate Conditions Inferred from Quaternary Gastropod Fauna. *J. Quat. Sci.* 35, 634–649. doi:10.1002/jqs.3204

Rousseau, D.-D., Antoine, P., Boers, N., Lagroix, F., Ghil, M., Lomax, J., et al. (2020). Dansgaard-Oeschger-like Events of the Penultimate Climate Cycle: The Loess point of View. *Clim. Past* 16, 713–727. doi:10.5194/cp-16-713-2020

Rowe, P. J., Mason, J. E., Andrews, J. E., Marca, A. D., Thomas, L., van Calsteren, P., et al. (2012). Speleothem Isotopic Evidence of Winter Rainfall Variability in Northeast Turkey Between 77 and 6 Ka. *Quat. Sci. Rev.* 45, 60–72. doi:10.1016/j.quascirev.2012.04.013

Sherriff, J. E., Wilkinson, K. N., Adler, D. S., Arakelyan, D., Beverly, E. J., Blockley, S. P. E., et al. (2019). Pleistocene Volcanism and the Geomorphological Record of the Hrazdan Valley, Central Armenia: Linking Landscape Dynamics and the Palaeolithic Record. *Quat. Sci. Rev.* 226, 105994. doi:10.1016/j.quascirev.2019.105994

Spooner, N. A. (1994). The Anomalous Fading of Infrared-Stimulated Luminescence from Feldspars. *Radiat. Measurements* 23, 625–632. doi:10.1016/1350-4487(94)90111-2

Stockhecke, M., Sturm, M., Brunner, I., Schmincke, H. U., Sumita, M., Kipfer, R., et al. (2014). Sedimentary Evolution and Environmental History of L Ake V an (T Urkey) over the Past 600 000 Years. *Sedimentology* 61, 1830–1861. doi:10.1111/sed.12118

Sumita, M., and Schmincke, H.-U. (2013). Impact of Volcanism on the Evolution of Lake Van II: Temporal Evolution of Explosive Volcanism of Nemrut Volcano (Eastern Anatolia) During the Past Ca. 0.4Ma. *J. Volcanology Geothermal Res.* 253, 15–34. doi:10.1016/j.jvolgeores.2012.12.009

Thiel, C., Buylaert, J.-P., Murray, A., Terhorst, B., Hofer, I., Tsukamoto, S., et al. (2011). Luminescence Dating of the Stratzing Loess Profile (Austria) - Testing the Potential of an Elevated Temperature post-IR IRSL Protocol. *Quat. Int.* 234, 23–31. doi:10.1016/j.quaint.2010.05.018

Thomsen, K. J., Murray, A. S., Jain, M., and Bøtter-Jensen, L. (2008). Laboratory Fading Rates of Various Luminescence Signals from Feldspar-Rich Sediment Extracts. *Radiat. Measurements* 43, 1474–1486. doi:10.1016/j.radmeas.2008.06.002

Timar-Gabor, A., Constantin, D., Buylaert, J. P., Jain, M., Murray, A. S., and Wintle, A. G. (2015b). Fundamental Investigations of Natural and Laboratory Generated SAR Dose Response Curves for Quartz OSL in the High Dose Range. *Radiat. Measurements* 81, 150–156. doi:10.1016/j.radmeas.2015.01.013

Timar-Gabor, A., Constantin, D., Marković, S. B., and Jain, M. (2015a). Extending the Area of Investigation of Fine Versus Coarse Quartz Optical Ages from the Lower Danube to the Carpathian Basin. *Quat. Int.* 388, 168–176. doi:10.1016/j.quaint.2014.09.065

Timar-Gabor, A., Vandenberghe, D. A. G., Vasiliniuc, S., Panaoitu, C. E., Panaiotu, C. G., Dimofte, D., et al. (2011). Optical Dating of Romanian Loess: A Comparison Between Silt-sized and Sand-Sized Quartz. *Quat. Int.* 240, 62–70. doi:10.1016/j.quaint.2010.10.007

Timar-Gabor, A., and Wintle, A. G. (2013). On Natural and Laboratory Generated Dose Response Curves for Quartz of Different Grain Sizes from Romanian Loess. *Quat. Geochronol.* 18, 34–40. doi:10.1016/j.quageo.2013.08.001

Trigui, Y., Wolf, D., Sahakyan, L., Hovakimyan, H., Sahakyan, K., Zech, R., et al. (2019). First Calibration and Application of Leaf Wax N-Alkane Biomarkers in Loess-Paleosol Sequences and Modern Plants and Soils in Armenia. *Geosciences* 9 (6), 263. doi:10.3390/geosciences9060263

Újvári, G., Varga, A., Ramos, F. C., Kovács, J., Németh, T., and Stevens, T. (2012). Evaluating the Use of Clay Mineralogy, Sr-Nd Isotopes and Zircon U-Pb Ages in Tracking Dust Provenance: An Example from Loess of the Carpathian Basin. *Chem. Geology.* 304-305, 83–96. doi:10.1016/j.chemgeo.2012.02.007

Újvári, G., Varga, A., Raucsik, B., and Kovács, J. (2014). The Paks Loess-Paleosol Sequence: A Record of Chemical Weathering and Provenance for the Last 800ka in the Mid-carpathian Basin. *Quat. Int.* 319, 22–37. doi:10.1016/j.quaint.2012.04.004

Wintle, A. G. (1973). Anomalous Fading of Thermo-Luminescence in Mineral Samples. *Nature* 245, 143–144. doi:10.1038/245143a0

Wolf, D., Baumgart, P., Meszner, S., Fülling, A., Haubold, F., Sahakyan, L., et al. (2016). Loess in Armenia - Stratigraphic Findings and Palaeoenvironmental Indications. *Proc. Geologists' Assoc.* 127, 29–39. doi:10.1016/j.pgeola.2016.02.002

Wolf, D., Kolb, T., Alcaraz-Castaño, M., Heinrich, S., Baumgart, P., Calvo, R., et al. (2018). Climate Deteriorations and Neanderthal Demise in Interior Iberia. *Sci. Rep.* 8, 7048. doi:10.1038/s41598-018-25343-6

Wolf, D., Kolb, T., Ryborz, K., Heinrich, S., Schäfer, I., Calvo, R., et al. (2021). Evidence for Strong Relations Between the Upper Tagus Loess Formation (Central Iberia) and the Marine Atmosphere off the Iberian Margin During the Last Glacial Period. *Quat. Res.* 101, 84–113. doi:10.1017/qua.2020.119

Yi, S., Buylaert, J.-P., Murray, A. S., Lu, H., Thiel, C., and Zeng, L. (2016). A Detailed Post-IR IRSL Dating Study of the Niuyangzigou Loess Site in Northeastern China. *Boreas* 45, 644–657. doi:10.1111/bor.12185

Zhang, J., and Li, S.-H. (2020). Review of the Post-IR IRSL Dating Protocols of K-Feldspar. *MPs* 3, 7. doi:10.3390/mps3010007

Conflict of Interest: The authors declare that the research was conducted in the absence of any commercial or financial relationships that could be construed as a potential conflict of interest.

Publisher's Note: All claims expressed in this article are solely those of the authors and do not necessarily represent those of their affiliated organizations, or those of the publisher, the editors and the reviewers. Any product that may be evaluated in this article, or claim that may be made by its manufacturer, is not guaranteed or endorsed by the publisher.

Copyright © 2021 Lomax, Wolf, Wolpert, Sahakyan, Hovakimyan, Faust and Fuchs. This is an open-access article distributed under the terms of the Creative Commons Attribution License (CC BY). The use, distribution or reproduction in other forums is permitted, provided the original author(s) and the copyright owner(s) are credited and that the original publication in this journal is cited, in accordance with accepted academic practice. No use, distribution or reproduction is permitted which does not comply with these terms.

frontiers in Earth Science

ORIGINAL RESEARCH
published: 17 December 2021
doi: 10.3389/feart.2021.795826

Late Pleistocene Climate and Dust Source From the Mobarakabad Loess–Paleosol Sequence, Northern Foothills of the Alborz Mountains, Northern Iran

Amin Ghafarpour[1], Farhad Khormali[1]*, Xianqiang Meng[2], Hossein Tazikeh[1] and Thomas Stevens[3]*

[1]Department of Soil Sciences, Loess Research Center, Gorgan University of Agricultural Sciences and Natural Resources, Gorgan, Iran, [2]State Key Laboratory of Lake Science and Environment, Nanjing Institute of Geography and Limnology, Chinese Academy of Sciences, Nanjing, China, [3]Department of Earth Sciences, Uppsala University, Uppsala, Sweden

OPEN ACCESS

Edited by:
Kathryn Elizabeth Fitzsimmons,
University of Tübingen, Germany

Reviewed by:
Charlotte Prud'Homme,
University of Lausanne, Switzerland
György Varga,
Hungarian Academy of Sciences (MTA), Hungary

***Correspondence:**
Amin Ghafarpour
aghafarpour@yahoo.com
Farhad Khormali
fkhormali@gau.ac.ir

Specialty section:
This article was submitted to Quaternary Science, Geomorphology and Paleoenvironment, a section of the journal Frontiers in Earth Science

Received: *15 October 2021*
Accepted: *30 November 2021*
Published: *17 December 2021*

Citation:
Ghafarpour A, Khormali F, Meng X, Tazikeh H and Stevens T (2021) Late Pleistocene Climate and Dust Source From the Mobarakabad Loess–Paleosol Sequence, Northern Foothills of the Alborz Mountains, Northern Iran. Front. Earth Sci. 9:795826. doi: 10.3389/feart.2021.795826

Paleoclimatic investigation of loess-paleosol sequences from northern Iran is important for understanding past changes in a region highly sensitive to shifts in precipitation, and along potential routes of past human migration. Here, we present carbon and oxygen isotopic compositions of bulk carbonate ($\delta^{13}C_{bc}$ and $\delta^{18}O_{bc}$, respectively) coupled with particle size distributions of samples from the Mobarakabad section, northern Iran, to study past wind dynamics and hydroclimate. We also present new initial clay-sized Hf-Nd isotope results from key horizons in order to assess general dust sources. Variations of $\delta^{13}C_{bc}$ and $\delta^{18}O_{bc}$ values of modern soils compared to paleosols allow reconstruction of late Pleistocene–Holocene climate change in the area. Our results show severe drought during a major eolian deposition phase (EDP) after 34 ka. The thickness and PSD of the C horizon of unit 5 suggest significant shifts in loess sources and depositional environments during this EDP after 34 ka. Indeed, based on our new clay-sized Hf-Nd data, we hypothesize that the loess unit 5 might originate from the young crustal source of the Alborz and Kopet Dagh mountains. In general, the PSD of C horizons in the section is bimodal in the silt fraction and the very small, very fine clay fraction, with a mode at c. 1 μm in the modern soil and paleosols possibly produced by weathering and pedogenic processes. There also appears to be a good correlation between $\delta^{13}C_{bc}$ and $\delta^{18}O_{bc}$ values, differentiating phases of loess accumulation and paleosol formation and hence providing quantitative data for reconstructing paleoclimatic conditions in the study area.

Keywords: dust, paleosol, particle size distribution, bulk carbonate isotopes, provenance, northern Iranian loess

INTRODUCTION

Loess sediment in the mid-latitude of Eurasia provides an excellent sedimentary archive for understanding past climate and environmental changes in the continental interior (e.g., Rousseau et al., 2017, 2020; Fenn et al., 2020; Fitzsimmons et al., 2020; Költringer et al., 2020; Song et al., 2021). In northern Iran, loess deposits are found in the so-called Northern Iranian Loess Plateau (NILP) and along the northern foothills of the Alborz Mountain range (NFAM). These deposits represent outstanding archives of past climate in a region highly sensitive to changes in hydroclimate and potentially important in past human migrations (Shoaee et al., 2021) but otherwise poorly represented by past climate records. The loess units in the area are separated by paleosols showing various development degrees, providing valuable sedimentary archives of loess accumulation, soil, and paleosol formation within the loess units (Kehl et al., 2005; Frechen et al., 2009; Kehl, 2010; Khormali and Kehl, 2011; Ghafarpour et al., 2016, 2021; Vlaminck et al., 2016, 2018; Lauer et al., 2017a; Lauer et al., 2017b; Shahriari et al., 2017; Pourmasoumi et al., 2019; Sharifigarmdareh et al., 2020; Kehl et al., 2021). These previous studies of loess–paleosol sequences in northern Iran mainly focused on dating of the deposits, particle size distributions, and paleosol formation in response to paleoprecipitation and paleopedogenic process, with little emphasis on phases of eolian deposition, meaning that additional detailed analyses of the loess units in particular are essential. In addition, there is still considerable uncertainty about the potential source(s) area of the northern Iranian loess, due to the lack of previous provenance analyses.

The particle size distribution (PSD) has proved an appropriate property of loess and eolian sediments for understanding loess sedimentary environment, eolian dynamics, and pedogenesis reconstruction (e.g., Nilson and Lehmkuhl, 2001; Vandenberghe et al., 2006; Jacobs and Mason, 2007; Prins et al., 2009; Stevens and Lu, 2009; Tripaldi et al., 2010; Vriend et al., 2011; Markovic et al., 2013; Vandenberghe, 2013; Sweeney and Mason, 2013; Schaetzl et al., 2014; Forman et al., 2014; Ujvari et al., 2016; Zeeden et al., 2016; Vandenberghe, et al., 2018; Stevens et al., 2020; Wacha et al., 2021). Most loess is dominated by medium silt-sized grains, but a proportion of fine silt and clay particles in fine-grained eolian landforms, and loess is also likely to be transported as silt- or sand-sized aggregates (Pye, 1995; Mason et al., 2003; Qiang et al., 2010; Mason et al., 2011a). The PSD of loess is the result of a combined local/regional signal of atmospheric properties (wind strength and its variations, vertical mixing) and environmental settings such as topography (Vandenberghe et al., 1997; Mason et al., 1999; Rousseau et al., 2002; Nottebaum et al., 2014), vegetation cover (Stevens et al., 2011), source distance (Ding et al., 2005; Yang and Ding, 2008), and regional aridity and/or a change in sediment availability (Forman et al., 2008; Muhs et al., 2013). Bulk loess grain size proxies such as U-ratio and "grain size indexes" (GSIs) have been commonly employed as a measure of wind strength, with application to loess depositional history in Europe, Asia, and North America (e.g., Vandenberghe et al., 1985; Vandenberghe et al., 1997; Rousseau et al., 2007; Machalett et al., 2008; Muhs et al., 2008; Antoine et al., 2009). The U-ratio represents the proportion of medium and coarse-grained silt (44–16 μm) vs. fine-sized silt (5.5–16 μm) (Vandenberghe et al., 1985), and GSI is the ratio of 20- to 50-μm/<20-μm fractions (Rousseau et al., 2002); both indices are designed to assess changes in the silt fraction and exclude larger sand particles, or in the case of the U-ratio, pedogenic clays. Kehl et al. (2005) and Kehl (2010) showed an increase in PSD from west to east and from south to north in northern Iran, coinciding with pronounced east–west and north–south gradients of modern climate from arid to subhumid.

Soil carbonate isotope studies of modern soils and paleosols have typically focused on samples collected from temperate or warm environments (e.g., Quade et al., 2007; Hough et al., 2014; Diaz et al., 2016; Gallagher and Sheldon, 2016; Ringham et al., 2016; Bayat et al., 2017; Dietrich et al., 2017). The carbon and oxygen isotope composition of pedogenic carbonate ($\delta^{13}C_{pc}$ and $\delta^{18}O_{pc}$) and land snail shell carbonate within successions of rapidly buried Quaternary soils exhibit stratigraphic trends that are interpreted to record a history of significant climate variation and provide an additional technique for investigating Quaternary climate and ecologic changes (McDonald and McFadden, 1994; Monger et al., 1998; Lechler et al., 2018; Huth et al., 2019; Újvári et al., 2019, 2021; Zamanian et al., 2021). Recent studies suggest a strong summer seasonal bias in some (Breecker et al., 2009; Passey et al., 2010; Quade et al., 2013; Huth et al., 2019) but not all pedogenic carbonates (Peters et al., 2013). The $\delta^{13}C$ values of soil carbonates are controlled by the $\delta^{13}C$ of soil CO_2, which is mainly determined by the abundance of C_3 and C_4 plants in the local ecosystem (Amundson et al., 1988; Cerling and Quade, 1993; Breecker et al., 2009). The $\delta^{13}C$ values of soil carbonates can also be affected by soil-respired CO_2 concentrations, pCO_2, and the carbon isotope value of atmospheric CO_2 (Fischer-Femal and Bowen, 2021). In addition, water availability and pCO_2 can also significantly affect the discrimination against ^{13}C during photosynthesis, which then changes the carbon isotope value of respired CO_2 (Diefendorf et al., 2010; Kohn, 2010; Schubert and Jahren, 2012; Fischer-Femal and Bowen, 2021). Soil carbonate $\delta^{18}O$ values are controlled by the oxygen isotope composition of soil water ($\delta^{18}O_{sw}$) and the temperature of mineral precipitation (Cerling and Quade, 1993; Quade et al., 2007). The $\delta^{18}O_{sw}$ values predominantly track isotope values of rainfall (Tan et al., 2017; Kelson et al., 2020), even though they can also be affected by evaporation in the near surface (e.g., Breecker et al., 2009; Huth et al., 2019). Soil carbonate $\delta^{18}O$ is thought to decrease with lower temperatures and higher elevation (Dworkin et al., 2005; Quade et al., 2011). Some authors suggested that $\delta^{13}C_{bc}$ in loess represents a mixed signal derived from both detrital carbonate and authigenic pedogenic carbonate (Ning et al., 2007; Liu et al., 2011; Koeniger et al., 2014), and the effects of multiple formation times on bulk soil carbonate isotope composition should also be considered (Burgener et al., 2016). Also, Zamanian et al. (2021) studied isotopic signatures of different types of carbonates in the Nussloch paleosol-loess sequence in Germany, and they excluded the stable isotope composition of bulk carbonate for reconstructing the local paleoenvironment because the bulk carbonates in the section were detrital materials from the diagenetic conditions of carbonates in the deflation area.

$\delta^{13}C_{bc}$ values have been shown to be an indicator of paleovegetation density in response to the intensity of the Asian summer monsoon in arid parts of the Chinese loess plateau (Rao et al., 2006). In addition, some investigations on modern ecosystems have identified that the increase in mean annual precipitation (MAP), to which soil humidity is directly related, influences vegetation density and together, and these factors cause a depletion in $\delta^{13}C_{bc}$ and $\delta^{13}C_{pc}$ values in the

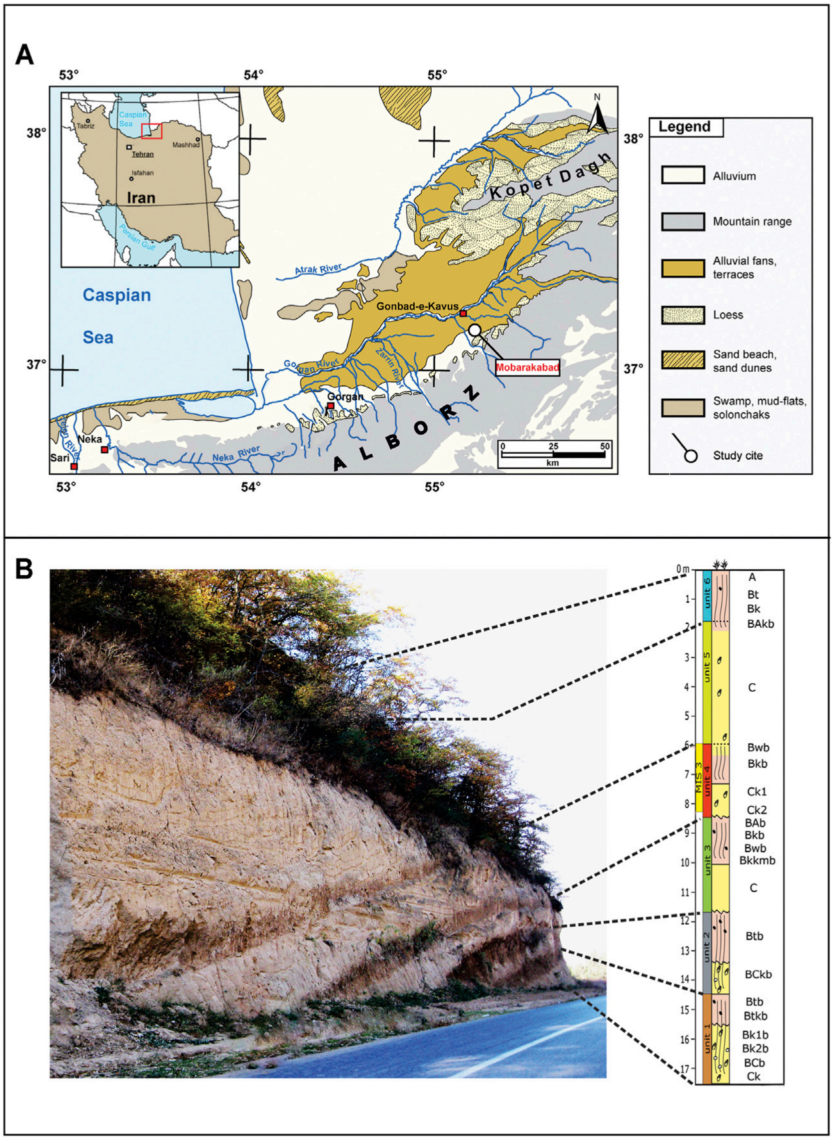

FIGURE 1 | (A) Map of north Iran showing the locations of the study site and the occurrence of loess deposits supplemented by other geomorphological features in the region (after Kehl et al., 2021). **(B)** Photo overview and stratigraphic section of Mobarakabad, showing bedding characteristics, buried soils (paleosols) with recognized horizons (**Figure 3** for legend). The total thickness of the section is about 17 m, and it contains six loess units separated by paleosols. Section location: Mobarakabad (37° 09′ 32″ N, 55° 18′ 14″ E).

northwestern Chinese loess plateau (CLP). Chinese loess $\delta^{13}C_{bc}$ variation therefore likely reflects the regional precipitation change and therefore can be regarded as a sensitive proxy for the summer monsoon intensity (Liu et al., 2011; Sun et al., 2015). Recently, Khormali et al. (2020) investigated δ^{13} C_{bc} and δ^{18} O_{bc} as well as $\delta^{13}C_{pc}$ and $\delta^{18}O_{pc}$ and organic carbon from modern soils and paleosols in northern Iran along a west to east and south to north precipitation gradient. They concluded that $\delta^{13}C_{bc}$ and $\delta^{18}O_{bc}$ values showed a significant relationship with MAP, over the range from 200 to approximately 750 mm/yr, and also suggested a summer bias in carbonate nodule formation in the area. This development opens up an excellent opportunity to reconstruct hydroclimate in northern Iran and yield new insights into climate variability and forcing in the region.

While past climate records based on isotopic and particle size parameters are still much needed to refine the picture of Quaternary climate change from loess in northern Iran, the provenance of loess in this area has not been studied previously. The clay-sized Hf-Nd isotopic composition of dust has been successfully used as a tool for aerosol/dust source discrimination (Pettke et al., 2002; Aciego et al., 2009; Lupker et al., 2010; Pourmand et al., 2014; Ujvari et al., 2015; Zhao et al., 2014, 2015), based on the fact that radiogenic isotopes of these elements differ in source rocks of different ages and weathering histories. Compared with the detailed provenance studies of

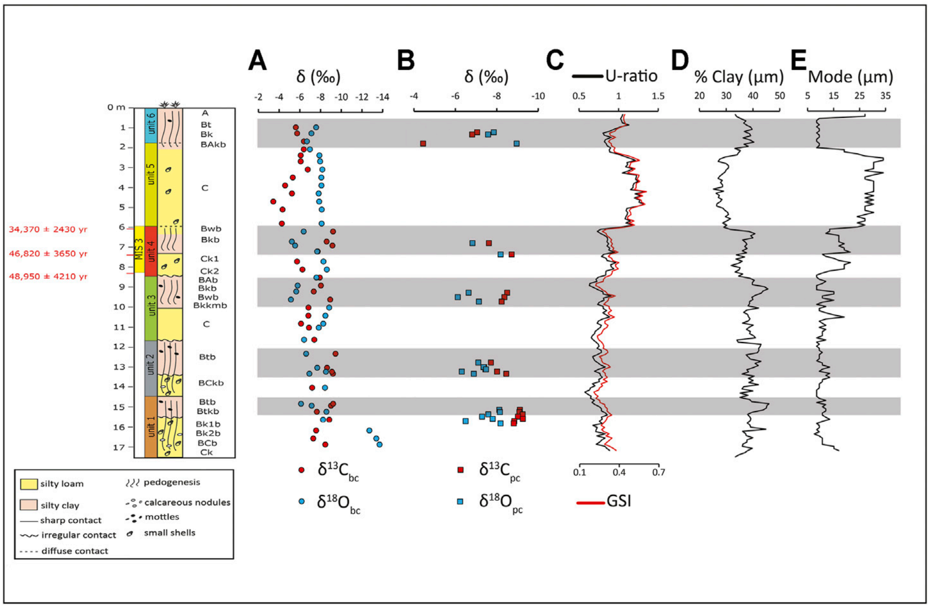

FIGURE 2 | Stratigraphic column for Mobarakabad along with trends of **(A)** $\delta^{13}C_{bc}$ and $\delta^{18}O_{bc}$, **(B)** $\delta^{13}C_{pc}$ and $\delta^{18}O_{pc}$ (Khormali et al., 2020), **(C)** U-ratio and GSI, **(D)** clay (<5.5 µm), **(E)** mode. Note in the stratigraphic column, the capital letters A, B, and C represent the master horizons of loess units (Soil Survey Staff, 2014). Lowercase letters are used as suffixes to designate specific subordinate distinctions within master horizons. The suffix symbol meanings are as follows: b: buried genetic horizon; k: accumulation of secondary carbonates; kk: engulfment of the horizon by secondary carbonates; m: pedogenic cementation; t: accumulation of silicate clay; and w: development of color or structure (Soil Survey Staff, 2014).

aerosol/dust in Greenland (Lupker et al., 2010), Mongolian Plateau (Zhao et al., 2015), CLP (e.g., Zhao et al., 2014), Carpathian Basin (Újvári et al., 2012), and North Africa (e.g., Zhao et al., 2018), the provenance of northern Iranian loess has not been investigated so far and lacks analyses of multiple clay-sized Hf-Nd isotopic compositions. Dust provenance to loess deposits is especially important to constrain in order to understand past sediment routing processes, dust transport, and a possible link to climate change.

This study presents $\delta^{13}C_{bc}$, $\delta^{18}O_{bc}$, and PSD of the late Pleistocene loess–paleosol sequences at Mobarakabad in northern Iran (**Figure 1A**), in order to reconstruct late Pleistocene hydroclimate and eolian processes in the region. Also, we report the first clay-sized Hf-Nd isotopic composition for northern Iranian loess, focusing on the three upper loess units at the section, which accumulated since middle MIS 3. Our aims were to 1) assess the feasibility of using $\delta^{13}C_{bc}$ and $\delta^{18}O_{bc}$ to reconstruct paleoenvironment at the study section, 2) demonstrate how the PSD of the loess–paleosol sequence reflects paleoclimate changes, and 3) make a first general preliminary assessment of potential source(s) of loess on the northern foothills of the Alborz Mountain range since late MIS 3.

GEOGRAPHIC SETTING

The study area is characterized by seasonal rainfall variation, with high precipitation amounts from October to March, dropping sharply in summer when the air temperature reaches its peak in July–August. The section at Mobarakabad is located on the NFAM and lies 310 m above sea level, with forest vegetation cover. The modern climate at Mobarakabad is characterized by ~680 mm MAP and with a mean annual air temperature (MAAT) of 16.5°C. The 17-m-thick section at Mobarakabad contains six loess units separated by paleosols (**Figure 1B**). The uppermost unit (unit 6) is the modern soil that formed under forest vegetation and is classified as a Calcic Argixeroll in the U.S. Department of Agriculture (USDA) soil taxonomic system (Soil Survey Staff, 2014). Unit 5 is ~4 m thick and primarily reflects eolian deposition and contains some shells of mollusks. Unit 4 lies below this, 6–8 m below the surface. The upper 1 m of unit 4 is a pedogenically altered, light brown soil with secondary calcium carbonate (Bwb and Bkb horizons). Furthermore, small shells of mollusks are detected in the Ck1 and Ck2 horizons of this unit (**Figure 2**). The underlying unit 3 exhibits BAb, Bkb, Bwb, Bkkmb, and C horizons and contains Fe mottles, and at the top of the unit, a 5- to 7-cm weak, buried organic-rich horizon is present (**Figure 2**). The uppermost 1.5 m of unit 2 is a well-developed paleosol (Btb) that shows clear signs of secondary accumulation of clay containing and Fe mottles based on visual observation in the field. The BCkb horizons of unit 2 reflect eolian depositional phases composed of detrital carbonate with small shells of mollusks (**Figure 2**). The lowermost unit (unit 1) lies at a depth of ~14.5 below the surface and is mostly pedogenically altered, hosting well-developed Btb and Btkb horizons. The lower 2.5 m of unit 1 contains Bk1b, Bk2b, BCb, and Ck horizons, containing pedogenic carbonate with small shells of mollusks (**Figure 2**).

METHODS

Sampling

A total of 164 samples were taken in 10-cm intervals for particle size measurements down section, while 40 samples were taken from the modern soil, C horizons, and paleosols for carbon and oxygen isotope analyses of bulk carbonates. In addition, four samples from the Bt and Bk horizons of the modern soil (unit 6), C horizon of unit 5, and Bk horizon of unit 4 were selected for clay-sized Hf-Nd isotopic measurements.

Particle Size Measurements

All samples were treated using 0.1 N HCl and 10% H_2O_2 before instrument measurement to remove carbonate and organic matter, respectively. After adding deionized water, sample suspension was left for 48 h prior to pipetting, to remove acidic ions. After that, the samples were dispersed with 10 ml of 30% $(NaPO_3)_6$ and placed in an ultrasonic vibrator for 10 min prior to particle size measurements. Each sample was measured three times repeatedly in a Mastersizer 2000 Laser Particle Analyzer at the Ministry of Education Key Laboratory of Surficial Geochemistry, Nanjing University. A constant of 1.33 was used for the refractive index of dispersant water, while a 1.52 refractive index was used for the solid phases (Özer et al., 2010), and an absorption index of 0.1 was applied. The default ideal range of obscuration on the Mastersizer 2000 (10–20%) is adopted as a working obscuration target for our standard operating procedure. As an assessment of measurement uncertainties, it must be noted that the applied optical parameter settings in laser diffraction may have considerable effects on the grain size results, in particular for the clay fractions (Varga et al., 2019a). At the same time, the clay size content of sediments is typically underestimated by the laser diffraction method in comparison with other methods such as pipette analyses (Beuselinck et al., 1998; Mason et al., 2003; Polakowski et al., 2014). Konert and Vandenberghe (1997) suggested the clay-silt break be set at 8 μm for comparison with traditional, that is, pipette particle size analysis. Our data have suggested better correlations between laser diffractometry and the pipette method (Ghafarpour et al., 2016) when the clay-silt break is set at 5.5 μm. Therefore, we used a 5.5-μm clay-silt break in this study. (For further discussion on the principles and application of laser diffractometry for particle size characterization, see, e.g., Mason et al. (2011b), Miller and Schaetzl (2012), and Varga et al. (2019b).)

$\delta^{13}C_{bc}$ and $\delta^{18}O_{bc}$

The samples were ground to <75 um; ~200 mg of powdered sample was reacted directly with 100% phosphoric acid for 20 min at 70°C to produce carbon dioxide. Carbon dioxide was gathered and analyzed with MAT-253 at the Nanjing Institute of Geology and Palaeontology, Chinese Academy of Sciences. Carbon and oxygen isotope compositions were measured and normalized against international standards (NBS-19). Isotope values are given in per mil (‰) as δ values:

$$\delta\,(‰) = \left[\left(R_{\mathrm{Sample}}/R_{\mathrm{Standard}}\right) - 1\right] \times 1000,$$

where R is the ratio of the heavier to the lighter isotopes of carbon and oxygen ($^{13}C/^{12}C$, $^{18}O/^{16}O$). All δ values are expressed against V-PDB (Vienna Peedee Belemnite). The standard deviation is less than 0.08 and 0.03‰ for $\delta^{18}O$ and $\delta^{13}C$, respectively.

Hf-Nd Isotope Measurements of Units 4-6

Hf and Nd isotopic analyses followed the procedures described by Zhao et al. (2014). To isolate the clay-sized silicate mineral fraction for Hf analysis, organic matter and carbonate were removed. Organic matter was removed with excess hydrogen peroxide (30%) overnight and then a decarbonation step was carried out using excess 1 M acetic acid for 10 h in order to eliminate the influence of secondary carbonate on Hf isotopic composition. The samples were subsequently rinsed at least three times with MilliQ water to completely remove major ions and soluble salts. Different fractions were extracted by sieving the ultrasonically dispersed samples in mesh with MilliQ water, and the 2-μm particles were separated based on Stokes' law and then were recovered by centrifuging. The samples were subsequently rinsed at least three times with MilliQ water to completely remove major ions and soluble salts. The Hf-Nd isotopic ratios of the extracted clay-sized fractions were measured with a Thermo Fisher Scientific Neptune MC-ICP-MS at the State Key Laboratory for Mineral Deposits Research, Nanjing University. These samples were prepared as follows: first, sample digestion; 100 mg of the dry silicate residue was totally dissolved with $HF–HClO_4$ mixture in steel jacketed autoclaves at 180 ~200°C for 72 h, while 100 mg of clay-sized fractions were digested with a mixture of $HF–HClO_4$ 110~140°C for 72 h. The second step is purification for Hf and Nd with ion chromatography. The Hf analysis used a modified method of Yang et al. (2010), which includes dissolving the samples in an HF–HClO4 mixture and separation by chromatographic extraction using a cation exchange resin, Bio-Rad 50WX8 resin + Eichrom® Ln-Spec resin. Hafnium was separated from the matrix by ion-exchange procedures using Eichrom® Ln-Spec resin. The details of the analytical procedure for the Hf isotopic measurement are published elsewhere (Yang et al., 2010). Nd was then separated and purified by ion-exchange procedures (Pu et al., 2005). All chemical digestion and purification were carried out in a Class 100 ultraclean laboratory. $^{179}Hf/^{177}Hf$ was normalized to 0.7325, and $^{143}Nd/^{144}Nd$ was normalized to 0.7219. The analytical blank was <60 pg for Nd and <60 pg for Hf. Reproducibility and accuracy of the Hf and Nd isotopic analyses were periodically checked by running the standards, Nd (JNDi-1) and Hf (MC-475) every two sample runs. The mean standard $^{143}Nd/^{144}Nd$ value was 0.511840 ± 8 (2σ external standard deviation, $n = 6$), and the mean standard $^{176}Hf/^{177}Hf$ value was 0.282160 ± 8 (2σ external standard deviation, $n = 15$). The observed natural variability in Hf and Nd isotopic composition is small and usually expressed in εHf and εNd notations, which are deviations from the Chondritic Uniform Reservoir (CHUR, $^{176}Hf/^{177}Hf = 0.282785$ and $^{143}Nd/^{144}Nd = 0.512630$) and calculated using the equations of Bouvier et al. (2008) as follows:

$$\varepsilon\mathrm{Hf} = 10^4 \times \left[{}^{176}\mathrm{Hf}/{}^{177}\mathrm{Hf}_{\mathrm{sample}} - {}^{176}\mathrm{Hf}/{}^{177}\mathrm{Hf}_{\mathrm{CHUR}}\right]/{}^{176}\mathrm{Hf}/{}^{177}\mathrm{Hf}_{\mathrm{CHUR}},$$

$$\varepsilon\mathrm{Nd} = 10^4 \times \left[{}^{143}\mathrm{Nd}/{}^{144}\mathrm{Nd}_{\mathrm{sample}} - {}^{143}\mathrm{Nd}/{}^{144}\mathrm{Nd}_{\mathrm{CHUR}}\right]/{}^{143}\mathrm{Nd}/{}^{144}\mathrm{Nd}_{\mathrm{CHUR}}.$$

RESULTS AND DISCUSSION

$\delta^{13}C_{bc}$ and $\delta^{18}O_{bc}$ Results

Carbonate $\delta^{18}O$ and $\delta^{13}C$ records and particle size parameters of the Mobarakabad section are shown in **Figures 2A–E**. The samples show $\delta^{13}C_{bc}$ ranging from −9.4 to −3.4‰ (mean value = −7.1‰) and $\delta^{18}O_{bc}$ ranging from −13.7 to −5.1‰, with a mean value of −7.8‰. Comparison of organic and carbonate $\delta^{13}C$ values of samples reveals that both pedogenic and bulk carbonates are enriched 14.5–16.5‰ with respect to associated organic matter, suggesting that organic matter and carbonate are cogenetic (Cerling et al., 1989). In units 1–5, $\delta^{13}C_{bc}$ values decrease with increasing pedogenesis and vegetation cover from loessic C horizons to the paleosols (**Figure 2A**). Additionally, the vegetation in the paleosols of the section is dominated by C_3 plants, with a mean $\delta^{13}C$ value of soil organic matter (−23.6‰) (Khormali et al., 2020). Thus, $\delta^{13}C_{bc}$ values of paleosols are very sensitive to changes in the precipitation-controlled vegetation density and can serve as a reliable proxy of paleoprecipitation. During paleosol formation (interglacials and/or interstadials) in units 1–5, enhanced precipitation can result in increased soil moisture and biomass, strong soil respiration, and high pCO_2, leading to the depleted carbonate $\delta^{13}C$ values in the paleosols (Cerling et al., 1989; Quade et al., 1989; Liu et al., 2011).

The Bkb and BCb horizons of unit 1 produced an average $\delta^{18}O_{bc}$ value of ~ −13.3‰ and an average $\delta^{13}C_{bc}$ value of ~ −8.3‰. In contrast, the average $\delta^{13}C_{bc}$ and $\delta^{18}O_{bc}$ values of upper Btb and Btkb horizons in unit 1 are ~ −9 and ~−7.7‰, respectively. Additionally, the average $\delta^{13}C_{pc}$ and $\delta^{18}O_{pc}$ values in the Btb and Btkb horizon of unit 1 are ~ −8.8 and ~−7.8‰, respectively (**Figure 2B**). Therefore, lower $\delta^{18}O_{bc}$ values of Bkb and BCb horizons relative to $\delta^{18}O_{bc}$ and $\delta^{18}O_{pc}$ values of upper Btb and Btkb horizons in unit 1 suggest that the Bkb and BCb horizons record colder periods of carbonate formation than the Btb and Btkb horizons. Also, a (~5.5‰) increase in the $\delta^{18}O_{pc}$ values of the Btb and Btkb horizons compared to the Bkb and BCb horizons in unit 1 reflects significant evaporative ^{18}O enrichment at shallow soil depths. This observation is in line with other studies suggesting that evaporation affects oxygen isotope values at shallow soil depths (e.g., Quade et al., 1989; Breecker et al., 2009; Stevenson et al., 2010). Thus, we infer that pedogenic carbonates in unit 1 could initially form at the time of the deepest wetting front penetration into the soil during the summer season when soil moisture levels are low (Quade et al., 1989; Stevenson et al., 2010). Furthermore, it is the maximum wetting front that fixes the $\delta^{18}O$ values of the soil carbonates, and therefore, no marked difference between $\delta^{18}O_{pc}$ values compared to $\delta^{18}O_{bc}$ is seen in the paleosol of unit 1.

The $\delta^{18}O_{bc}$ values of the C horizons of units 2–4 are about −7 to −8‰, and the $\delta^{18}O_{bc}$ values of paleosols of units 2–4 range from ~−5.1 to ~ −8.3‰, suggesting a positive shift of ~2–3‰ in $\delta^{18}O_{bc}$ values of these paleosols compared to underlying C horizons (**Figure 2A**). The mean $\delta^{18}O_{bc}$ values of paleosols of units 2–4 (−7.2‰) are similar to mean $\delta^{18}O_{pc}$ values (−7.4‰) of these paleosols, showing no shift in the seasonality throughout the time of accumulation of carbonate nodules in the paleosols of units 2–4. This may suggest that carbonates in the paleosols of units 2–4 formed over the same time periods during the summer seasons when soil temperature and soil water evaporation are high, and so the major driving variables behind the $\delta^{18}O_{bc}$ values might be the temperature of carbonate formation.

The average of $\delta^{13}C_{bc}$ (~−5.3‰) with the maximum values of −3.4‰ of the C horizon of unit 5 is higher than that of the other loessic C horizons. The inferred timing of eolian phases of unit 5 is after 34 ka (Ghafarpour et al., 2017), and the average pH value of the C horizon of this unit is about 7.8 with relatively high carbonate contents (~20%) (Ghafarpour et al., 2016). When vegetation cover is low, due to aridity, the soil zone CO_2 becomes mixed with atmospheric CO_2, which has a more positive value. Furthermore, high rates of soil moisture evaporation result in the degassing of CO_2, preferentially of the lighter $^{12}CO_2$, therefore also resulting in higher δ^{13} C values in the soil carbonates (Dever et al., 1987; Candy et al., 2012; Gallant et al., 2014). Therefore, high $\delta^{13}C_{bc}$ with a pH of 7.8 in the C horizon of unit 5 probably reflects a period of increasing loess accumulation accompanied by an arid environment.

The $\delta^{18}O$ value of rainfall ($\delta^{18}O_{mw}$) can be used to predict $\delta^{18}O_{sw}$ values and determine how they interact on an ecosystem scale (Quade et al., 1989; Stevenson et al., 2010; Hough et al., 2014). In the modern soil, the calculated $\delta^{18}O_{sw}$ from which the soil carbonate formed was −8.3 to −7.1‰ (Kim and O'Neil, 1997), consistent with the local rainfall $\delta^{18}O_{mw}$ value (−8.2‰). This suggests that the Bk horizon of modern soils at ~ 130 cm depth did not undergo significant dewatering by evaporation prior to pedogenic carbonate formation, and thus, the $^{18}O_{pc}$ values (−8.1‰) of Bk horizons have not been influenced by the evaporation of soil water. In the modern soil, $\delta^{13}C_{bc}$ and $\delta^{13}C_{pc}$ are higher than $\delta^{18}O_{bc}$ and $\delta^{18}O_{pc}$ values, respectively. This trend in modern soil differs significantly from that shown in paleosols in which $\delta^{13}C_{bc}$ and $\delta^{13}C_{pc}$ values are lower than $\delta^{18}O_{bc}$ and $\delta^{18}O_{pc}$ values, respectively (**Figure 2A**). The observed shift in average $\delta^{13}C_{pc}$ values from paleosols (−8.5‰) to modern soil (−6.1‰) suggests that the paleosols $\delta^{13}C_{pc}$ values were ~2.5‰ lower than those of the modern soil. Additionally, the $\delta^{13}C_{pc}$ values of the modern soil of Mobarakabad are similar to the average $\delta^{13}C_{pc}$ values of loessic modern soils (−6.2‰) in the NFAM with forest cover, reported in Khormali et al. (2020). Furthermore, the mean $\delta^{13}C$ values of soil organic matter (−23.6‰) of the paleosols in Mobarakabad (Khormali et al., 2020) are within the same range as the $\delta^{13}C$ values of modern soil organic matter, indicating a C_3-dominated environment for both paleosols and the modern soil of Mobarakabad. Therefore, we

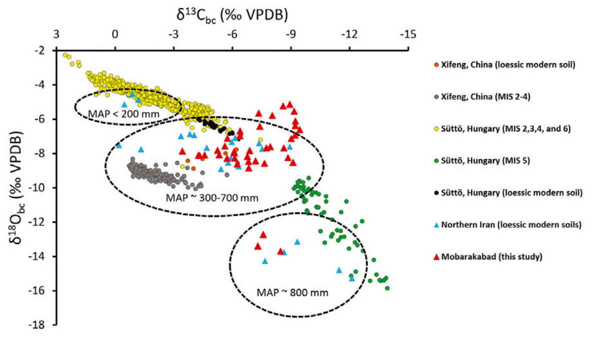

FIGURE 3 | Comparison of $\delta^{13}C_{bc}$ and $\delta^{18}O_{bc}$ values of loess–paleosol samples of Mobarakabad (this study) with $\delta^{13}C_{bc}$ and $\delta^{18}O_{bc}$ of loessic modern soils in northern Iran (Khormali et al., 2020) and loess–paleosol sequences at Xifeng in China (Luo et al., 2020) and at Sütto in Hungary (Koeniger et al., 2014). Note that dashed ovals show mean annual precipitation of the loessic modern soil sections in northern Iran, which correspond to ranges of isotope data from the same sections Khormali et al. (2020).

inferred a ~2.5‰ increase in $\delta^{13}C_{pc}$ values of the modern soil of Mobarakabad and loessic modern soils in northern Iran (Khormali et al., 2020), as compared to paleosols of Mobarakabad section, might result from a drier climate in Holocene, as compared to the paleosol formation periods in late Pleistocene in the NFAM. In contrast, the similarity in average $\delta^{18}O_{pc}$ values of both the modern soil and paleosols in Mobarakabad (−7.3‰) with the average $\delta^{18}O_{pc}$ values of loessic modern soils in the NFAM (−7.4‰) may reflect no shift in the source of late Pleistocene-to-Holocene regional precipitation in the NFAM.

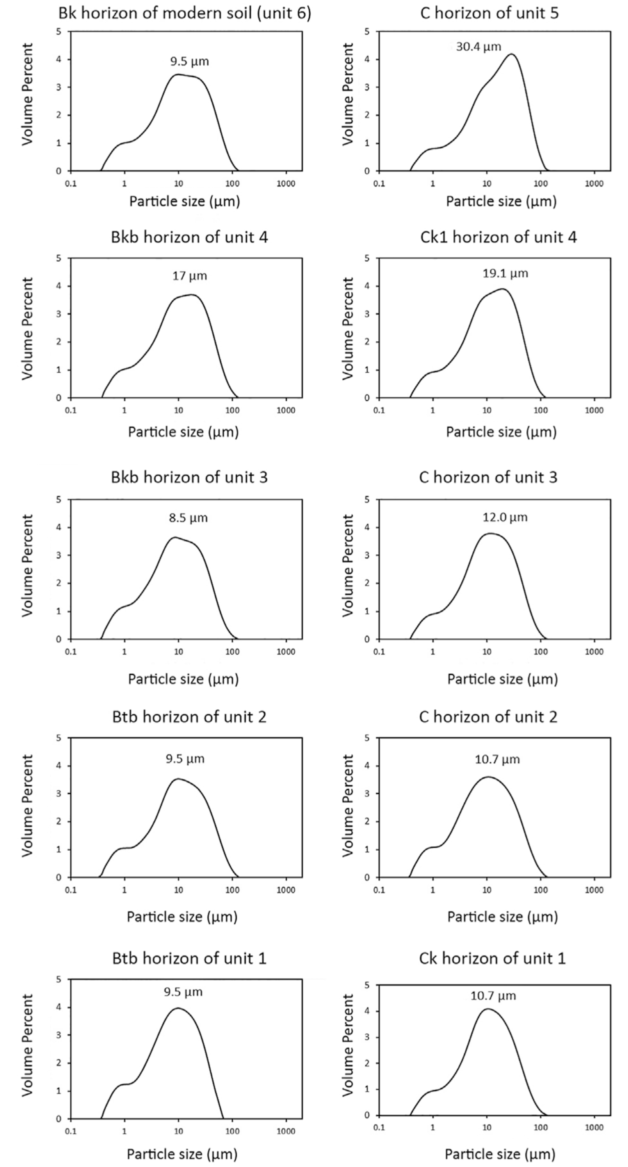

FIGURE 4 | PSD curves with the modal sizes of modern soil, C (k) horizons, and paleosols (Bkb and Btb horizons) at the study section.

A comparison $\delta^{18}O_{bc}$ and $\delta^{13}C_{bc}$ values of Mobarakabad samples with those of loessic modern soils in northern Iran (Khormali et al., 2020), and the loess–paleosol sequences at Xifeng in China (Luo et al., 2020) and at Sütto in Hungary (Koeniger et al., 2014) are shown in **Figure 3**. This illustrates that the $\delta^{18}O_{bc}$ and $\delta^{13}C_{bc}$ values of most Mobarakabad samples match with $\delta^{18}O_{bc}$ and $\delta^{13}C_{bc}$ values of those loessic modern soils in northern Iran (MAP ~300–700 mm), Xifeng in China (MAP = 480 mm), and Sütto in Hungary, each receiving ~600–650 mm of annual precipitation. Interestingly and in contrast, the $\delta^{18}O_{bc}$ values of Bkb and BCb of unit 1 at Mobarakabad are in the range of loessic modern soil isotope values in northern Iran, where MAP is ~800 mm and MIS 5e loess in Hungary (**Figure 3**). In addition, by comparing loess units at Mobarakabad, including the OSL ages of unit 4, with stratigraphy and previously published luminescence ages from other sections at NFAM, this unit 1 at Mobarakabad correlates well with MIS 5e (*Particle Size Parameters of Loess Units*). Corroborating this assignment, based on magnetic depletion in the paleosol of unit 1 at Mobarakabad, Ghafarpour et al. (2021) concluded that the paleosol formation was accompanied by high (winter) rainfall in which dissolution of pedogenic maghemite–magnetite occurred. As such, one way of explaining these observations is high rainfall in winters, probably in MIS 5e, followed by dry and hot summers in which evaporative soil water loss predominates with little meteoric recharge, resulting in enriched $\delta^{18}O_{bc}$ and $\delta^{18}O_{pc}$ values of the upper horizons (Btb and Btkb) compared to those of Bkb and BCb horizons in unit 1 (**Figure 2A**).

Our dataset suggests that the $\delta^{13}C_{bc}$ and $\delta^{18}O_{bc}$ values of the loess–paleosol sequences at Mobarakabad are well correlated with changing phases of increased eolian sedimentation and periods of pedogenesis recorded in the loessic C horizons and paleosols, respectively, and most likely reflect the regional precipitation change. We find that both $\delta^{13}C_{bc}$ and $\delta^{18}O_{bc}$ values decrease with increasing rainfall, pedogenesis, soil humidity, and C_3 biomass, from the loessic C horizons to paleosols. However, it is also essential to take into account that any change in the source of loessic detrital materials in the modern soil reflects the conditions

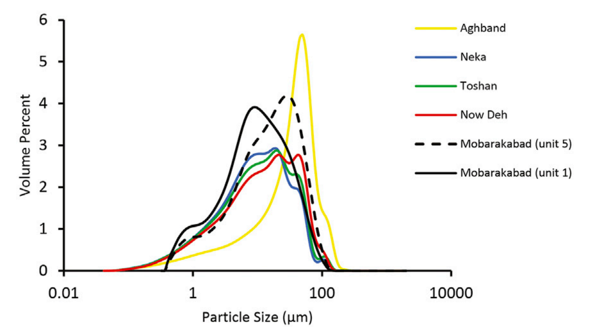

FIGURE 5 | PSD curves of C horizons of unit 1 (black line) and unit 5 (dashed line) at Mobarakabad in comparison with least weathered loess at Toshan (green line) (Vlaminck et al., 2016), Now Deh (red line), and Neka-Abelou (blue line) sections (Kehl et al., 2021) on the NFAM. The yellow line represents PSD of a loess sample from Aghband in the NILP (Lauer et al., 2017a) (see text for discussion).

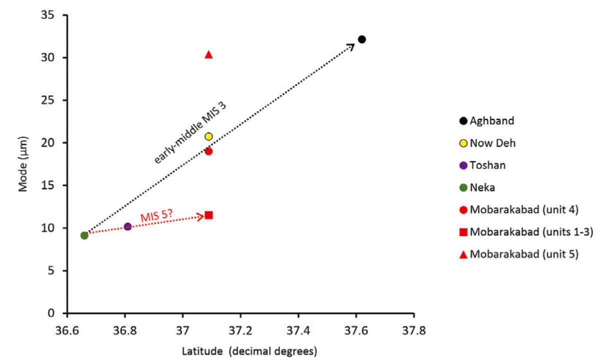

FIGURE 6 | Relationship between the mode size of loessic C horizons and the latitude of Mobarakabad as well as the mode grain size of loess–paleosol sequences located along the NFAM (Vlaminck et al., 2016; Kehl et al., 2021), supplemented by data from the Aghband section (Lauer et al., 2017a) in the NILP. Note that with increasing latitude, the mode size of loess from early to middle MIS 3 increases (r^2 = 0.98), but it appears that there is a weaker trend in the mode size of loess samples in the sections at the NFAM within MIS 5 (see text). There is a noticeable anomaly in the C horizon of unit 5 (red triangle) at Mobarakabad that is accumulated after 34 ka (see text for discussion).

of $\delta^{13}C_{bc}$ and $\delta^{18}O_{bc}$ values in the deflation area, rather than local environmental conditions.

Particle Size Parameters of Loess Units

All the sample particle size distributions from the C horizons of the section are bimodal in the silt fraction. One mode lies at ca. 19 μm, but all the distribution curves show a broad top which consists of two modes, with the second one somewhat coarser at ca. 35 μm. The latter mode dominates only in the C horizons of unit 5. The C and Ck horizons of units 1–3 show a fine modal particle size of 10.7–12 μm, and the Ck1 and Ck2 horizons of unit 4 show a bimodal distribution with a modal particle size of 19.1 μm (**Figure 4**). These fine-grained loess types approximately correspond to the "subgroup 1. c.," with the modal diameter ranging from 4 to 22 μm classified by Vandenberghe (2013). This subgroup is interpreted to be transported and deposited as background dust transported in high-suspension clouds over long distances continuously over time and incorporated in the high-level westerlies (Pye, 1995; Sun et al., 2002; Vandenberghe et al., 2018). Under such a scenario, it is therefore possible that the C horizon samples include loess transported over long distances (c. 10.7–12 μm mode) and loess transported over a short distance (c. 35 μm mode) by lower level suspension. Furthermore, the very small fraction of fine clays with mode at c. 1 μm in the loessic C horizons suggests an origin from high-level background dust mixed with a small amount of clay which might originate from sources that consist of very fine particles such as a very fine-grained alluvium. However, we cannot exclude the possibility that the fine-grain clay-sized particles are also partly a product of weathering or transported as aggregates in lower-level suspension clouds over shorter distances of 10–100 s of km, as discussed previously.

The C horizon of unit 5 is characterized by the lowest clay content (26%) and highest U-ratios (1.3) as well as GSI (0.6), with a mode size around 34 μm, representing the coarsest segment of the section (**Figures 2C–E, 4**). This is exceptionally coarse for the profile and dominates the changes in grain size parameters with depth at the site; the implications will be discussed later. In units 1–3, the modal values of loessic C horizons (10.7–12 μm), U-ratio (~0.8), and GSI (~0.3) are lower than those of unit 5. Also, the average clay content of the loessic C horizons of units 1–3 (38%) is higher than of loessic C horizon of unit 5 (26%). These trends may suggest that the dynamics of the silt population is also reflected in the clay-sized fraction. Therefore, we interpret the increase in clay content of the loessic C horizons of units 1–3 as resulting from source(s) with very fine-grained alluvium and/or were probably carried in high suspension clouds at least hundreds of kilometers (*Comparison With Other Northern Iranian and Global Loess Records*), rather than being produced by weathering or pedogenic process. This may suggest that the % of clay is at least partly influenced by eolian processes, rather than reworking, as in theory, the U-ratio at least ought to reflect changes in the eolian dynamics independent of postdepositional pedogenesis (Vandenberghe et al., 1985). As such, we generally interpret the changes in grain size parameters in the loessic C horizons of the Mobarakabad section as showing more intensive eolian dynamics during phases of loess deposition as than periods of pedogenesis and soil formation, especially higher wind speeds and/or relatively greater coarse sediment availability during loess forming periods. The impact of possible source changes is discussed in *Comparison With Other Northern Iranian and Global Loess Records*.

In marked contrast, the developed Bk(b)-, Bt(b)-, and Btk(b) horizons of the modern soil and paleosols exhibit clay (<5.5 μm) proportions between 38.5 and 45.5% (**Figure 2D**). These buried horizons in modern soil and paleosols have clearly been affected by pedogenic processes, and their high clay content (with an increase in pedogenic smectite content) is the result of weathering and clay illuviation (Ghafarpour et al., 2016). Therefore, we argue that in the modern soil and paleosols, the dominant mode at c. 8.5–9.5 μm, with a secondary one in very fine clay fraction (c.

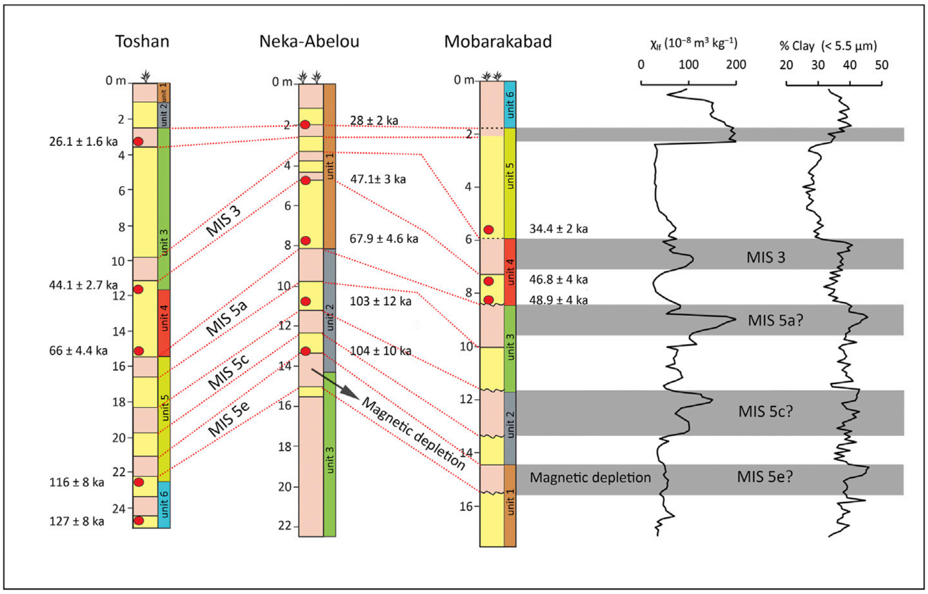

FIGURE 7 | Correlation among loess (in yellow) and paleosols (in pink) of the loess–paleosol sequences located in NFAM based on patterns of magnetic susceptibility (Ghafarpour et al., 2016), clay variations (this study), and OSL ages (Ghafarpour et al., 2017) at Mobarakabad and associated luminescence ages (red circles) of Toshan and Neka-Abelou sections (see Vlaminck et al., 2016; Kehl et al., 2021).

1 μm), was almost certainly produced by pedogenic processes and clay illuviation (Mason et al., 2003; Stevens et al., 2011) but potentially mixed up with clay (illite and kaolinite) derived from background dust input.

Comparison With Other Northern Iranian and Global Loess Records

One possible way to identify local effects on PSD is to compare the spatial patterns of loess thickness and PSD over a depositional area (e.g., Muhs et al., 1999, 2008; Mason, 2001; Mason et al., 2003) as the trends may provide insights into sediment transport pathways or distance from the source, availability of sediment, and sedimentation rate. Furthermore, these comparisons allow wider patterns to be identified that are independent of local topographic or proximal source influences. Previous studies in northern Iran defined the median particle size as 9.12–11 μm for least weathered loess at Neka-Abelou and Toshan sections (**Figure 5**) on the NFAM (Vlaminck et al., 2016; Kehl, et al., 2021). In particular, the modes of the C horizons of units 1–3 (10.7–12 μm) at Mobarakabad are comparable with the modal values of the loess (~11 μm) in unit 5 at Toshan (**Figure 6**) and also with the mode size of loess in unit 3 (~10.5 μm) at Neka-Abelou (**Figure 6**), both forming during MIS 5 (Lauer et al., 2017b; Kehl et al., 2021) (**Figure 7**). This consistency implies similar source and dust transport dynamics for these loess sediments. By comparing the OSL ages (unit 4), magnetic susceptibility, and clay variations of loess units at Mobarakabad with the previously published results from luminescence dating of Neka-Abelou and Toshan sections, we suggest that the units 1–3 at Mobarakabad correlate well with MIS 5 (**Figure 7**), supporting the assignment based on the isotopic analyses above. Therefore, we postulate that the similarity between modal peaks of MIS 5 loess at Mobarakabad, Neka-Abelou, and Toshan sections suggests that the loess was probably carried some hundreds of kilometers over a wider area from its source(s) and that the source material consisted of very fine particles (such as a very fine-grained alluvium). To a great extent, therefore, the fine MIS 5 loess at Mobarakabad and other sites on the NFAM would be consistent with transport in high suspension clouds throughout the year over (relatively) large distances, at least under the model of Vandenberghe (2013). We do however agree that luminescence ages from units 1–3 at Mobarakabad are needed to support these interpretations.

By contrast, the strong correlation between average mode size of early-middle MIS 3 loess at Mobarakabad (unit 4), Toshan, Now Deh, and Neka-Abelou with the geographical latitude of the sections (**Figure 6**) in northern Iran is in agreement with the findings of Kehl et al. (2021), who suggested dust transport by north to northeasterly winds supplying coarse-grained dust to the NILP and finer facies along the NFAM. Currently, north to northeasterly winds are most frequent during late autumn and winter as the influence of the Siberian high-pressure cell intensifies (Kehl et al., 2021). Hence, similar wind dynamics during early-middle MIS 3, almost certainly, would have been responsible for the entrainment of coarse silt from the north and the transport of this coarse sediment to NFAM. However, the influence of source distance or local source activation complicates this possibility.

In contrast to the relatively fine-grained loess at Mobarakabad, the average median particle size of the Aghband loess in NLIP is around 33–38 μm (**Figure 5**), as reported in the study of Lauer et al. (2017a). Kehl (2010) indicated the fining trend of loess from north to south and east to west across northern Iran. Also, the U-ratios of Aghband show values of 2.5–7 (Lauer et al., 2017a) and are indicative of significantly coarser silt dominance than shown in the C horizons of Mobarakabad, with a maximum of 1.3 at Mobarakabad. This difference may again partly reflect the influence of nearby source areas of especially coarse silt and also hint at the transport of dust from the north to northeast.

However, one factor must be considered when interpreting the particle size distributions of fine-grained loess such as at Mobarakabad. Similar particle size distributions to those of the loess–paleosol sequences from Mobarakabad can be seen in Miocene–Pliocene Chinese Red Clay and the parna/loessic clay of Australia (Dare-Edwards, 1984; Xu et al., 2015). In the case of Australian parna, clay size particles are likely transported as aggregates by low-level winds and not via high-altitude suspension clouds (Dare-Edwards, 1984). In China, the Red Clay sequences of the Chinese Loess Plateau have an uncertain or mixed source, but patterns in grain size variability over the depositional area suggest low-level atmospheric transport (Xu et al., 2014). As such, it is hard to use the particle size distribution of these deposits to infer transport mode, and this may also be the case in the NFAM; sediment size and availability in proximal source regions may be a more significant factor on overall distributions.

An Abrupt Shift in Dust Source and Drought Event in Unit 5

As discussed in *Particle Size Parameters of Loess Units*, the C horizon of unit 5 with a modal particle size of 30.4 μm is much coarser than the other C horizons of the section (**Figures 4**, **5**). The inferred eolian phase timing for the C horizon of unit 5 is after 34 ka, and the thickness almost reaches 6 m. The unusual thickness, U-ratio, and GSI values that characterize this unit suggest that the loess was deposited at high accumulation rates in relatively dry and windy conditions, or during a phase with a high availability of relatively coarse sediment in source regions. From this, we infer that the primary loess source for this unit was likely nearby and/or that winds were stronger in this region with more sediment availability during the time of eolian transport than during the deposition time of the C horizon of unit 4 (between 48.9 and 46.8 ka). As discussed in *Comparison With Other Northern Iranian and Global Loess Records*, the U-ratio and GSI values of the C horizon of unit 4 (**Figure 2C**) during middle MIS 3 suggest that loess accumulation at the time of unit 4 formation was mainly controlled by northerly transport winds, probably under Siberian high-pressure cell influence. In contrast, the significant increase in GSI and U-ratio of unit 5 (**Figure 2C**) which accumulated after 34 ka suggests spatiotemporal changes in sedimentary environment related to the local source or transport conditions. Indeed, the PSD of the C horizon of unit 5 at Mobarakabad is significantly coarser than all other units at the section. We therefore suggest that it may reflect the temporary activation of a local source of loess from alluvial plains of Gorgan, Atrek, and other rivers (**Figure 1A**), which originate from the nearby mountains (*Hf-Nd isotopic compositions in units 4–6*). Similar temporary close by source activation has also been seen in some Chinese loess sections and is also reflected in a dramatic increase in loess grain size (Stevens et al., 2013).

We therefore postulate that this EDP in the C horizon of unit 5 indicates an apparent shift to a likely local source and stronger wind dynamics (high GSI and U-ratio (**Figure 2C**)), almost certainly a result of spring–summer winds which dominate for a longer period in the year and eolian deposition keeping ahead of pedogenesis. Also, the EDP in the C horizon of unit 5 is generally associated with a severe drought as evidenced by high $\delta^{13}C_{bc}$ values (**Figure 2A**). This finding is in accordance with a possible drought phase that likely extended to Central Asia, as evidenced by thick loess deposits in Tajikistan and Kazakhstan allocated to MIS 4–2 (last Pleniglacial) (Mestdagh et al., 1999; Dodonov et al., 2006; Machalett et al., 2008; Fitzsimmons et al., 2018).

Hf-Nd Isotopic Compositions in Units 4–6

The $^{176}Hf/^{177}Hf$ and $^{143}Nd/^{144}Nd$ ratios (plotted as εNd (0) and εHf (0)) of clay-sized fractions from the samples are shown in **Figure 8** and **Table 1**. Clay-sized fractions from Bt and Bk horizons of the modern soil (unit 6) have εNd values of −7.18 and −7.37, respectively. The εHf value of the Bt horizon of the modern soil is −0.52, and the Bk horizon of the modern soil has an εHf value of 0.03. The C horizons of unit 5 have the most radiogenic εNd values (−6.73) of samples, and the εHf value of this horizon is −0.42. The least radiogenic εNd and εHf values (−8.06 and −0.64, respectively) are obtained from the paleosol (Bkb horizon) of unit 4. The Hf-Nd isotope data of samples (**Figure 8A**) plot well above the terrestrial array (Vervoort et al., 2011) and clay-sized array (Zhao et al., 2014), which are also above typical published zircon free arrays. Zircons are enriched in Hf and have a low εHf value compared to the average continental crust (Bayon et al., 2009). Zircons in loess will be very fine, but probably, much of the zircon is not <2 μm; the fraction we have analyzed. Also, the wind will tend to sort grains by density, so that relatively more zircon is left behind and hence depleted in the bulk samples of loess to begin with.

The samples at Mobarakabad comprise of much more radiogenic εNd (0) and εHf(0) than last glacial loess and modern and last glacial dust samples of N. America, W. Africa, Greenland, and Europe but are fairly close to some N African and some CLP samples, albeit more radiogenic (references shown in **Figure 8B**). Furthermore, the Hf-Nd isotopic values of the Asian dust end-members are −10.8 < εNd < −9 and 2.5 < εHf <. −4 (Patchett et al., 1984), and similar ranges were reported for Hf-Nd isotope data from the Taklimakan, Badain Jaran, and adjacent Tengger deserts (Zhao et al., 2014). Also, Chauvel et al. (2014) reported −10 < εNd < −9 for Chashmanigar loess deposits in Tajikistan. In addition, while the εNd of Chinese, Tajik, and Central European loess sediments scatters closely around the average Nd isotopic signature of the upper continental crust [εNd (0): 10.3] (Chauvel et al., 2014;

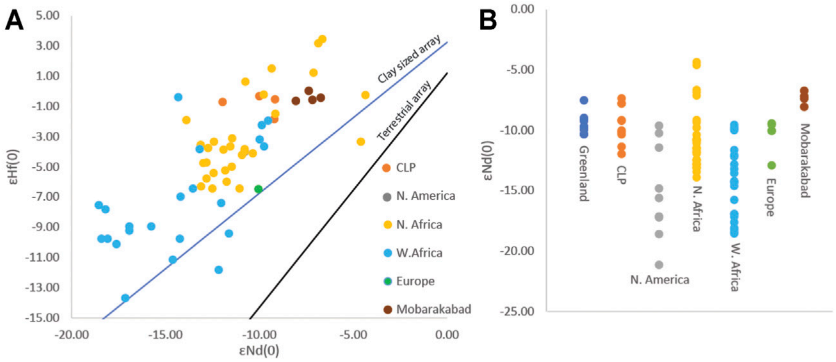

FIGURE 8 | (A) Plot of clay-sized εHf(0) vs. εNd(0) from this study (Mobarakabad) plus a range of published modern and last glacial loess and dust data from the CLP, N. America, N. Africa, W. Africa, and Europe relative to the Terrestrial array (Vervoort et al., 2011) and clay-sized array (Zhao et al., 2014). **(B)** Plot of εNd(0) by area representing more radiogenic Nd in Mobarakabad than loess and dust in Europe, W. Africa, N. America, and last glacial maximum dust in Greenland, but close to some N. African and some CLP samples. Source data are from Biscaye et al. (1997) and Svensson et al. (2000) for Greenland; Biscaye et al. (1997), Feng et al. (2009), Újvári et al. (2015), and Zhao et al. (2015) for Asia; Biscaye et al. (1997) and Újvári et al. (2015) for North America; Zhao et al. (2018) and Skonieczny et al. (2013) for North and West Africa; and Újvári et al. (2015) and Biscaye et al. (1997) for Europe.

TABLE 1 | Hf and Nd isotopic compositions of samples from Mobarakabad.

Horizon/unit	^{143}Nd/^{144}Nd	2δ	εNd	2δ	^{176}Hf/^{177}Hf	2δ	εHf	2δ
Bt horizon of modern soil (unit 6)	0.512262	4	−7.18	0.078029	0.282769	4	−0.56	0.14145
Bk horizon of modern soil (unit 6)	0.512252	16	−7.37	0.312116	0.282786	4	0.03	0.14145
C horizon of unit 5	0.512285	19	−6.73	0.370638	0.282773	5	−0.42	0.176813
Bk horizon (paleosol) of unit 4	0.512217	12	−8.06	0.234087	0.282767	4	−0.64	0.14145

[1] *Errors on ^{176}Hf/^{177}Hf and ^{143}Nd/^{144}Nd represent within-run uncertainty calculated as 2σ ×10^{-6}, expressed as variation in the 6th decimal place.*

[2] *εHf and εNd values are calculated using the chondritic values of ^{176}Hf/^{177}Hf = 0.282785 and ^{143}Nd/^{144}Nd = 0.512630 (Bouvier et al., 2008). Measured values for BCR-2, from Weis et al. (2006, 2007), are 0.512634 ± 0.000012 for ^{143}Nd/^{144}Nd and 0.282857 ± 0.000004 for ^{176}Hf/^{177}Hf.*

Ujvari et al., 2018), reflecting various mixed, homogenized crustal sources, the more radiogenic εNd values of unit 4–6 at Mobarakabad range from −8.06 to −6.73 (**Figure 8B**). Hence, we propose that the more radiogenic εNd of loessic C horizon of unit 5 at Mobarakabad reflects sourcing from the relatively young crust, and the effects of incorporation of radiogenic Hf into clays released during silicate weathering. This implies that the EDP after 34 ka (unit 5) at Mobarakabad is likely sourced from a young, actively weathering crustal source, rather than from (Central) Asian dust. Hence, we presume non-glacial erosion of the tectonically close by active mountains (Alborz and Kopet Dagh) produced fine silt-sized sediment in the area which was then carried into dry basins by fluvial transport of seasonal rivers, where it is deflated as dust to form loess.

SUMMARY AND CONCLUSIONS

Our results yield new insights on the provenance and paleoclimatic implications for loess deposits in northern Iran. The most important result from particle size trends and isotopic signatures of bulk carbonates at the Mobarakabad is that the eolian deposition phase after 34 ka reflects rapid loess accumulation during severe drought associated with windy conditions and potentially activation of close by sediment sources. The different trends of $\delta^{13}C_{bc}$ and $\delta^{18}O_{bc}$ in the modern soil in comparison to paleosols suggest that the regional climate of the northern foothills of the Alborz Mountain range during the Holocene is drier than that of the late Pleistocene. In unit 1, a ~5.5‰ increase in the $\delta^{18}O_{bc}$ and $\delta^{18}O_{pc}$ values of the Btb and Btkb horizons compared to the lower Bkb and BCb horizons may reflect high rainfall (most probably during MIS 5e) in the winters, followed by dry and hot summers in which evaporative soil water loss predominates with little meteoric recharge. This would result in enriched $\delta^{18}O$ values of carbonate in the upper horizons (Btb and Btkb) of unit 1. The compiled dataset from northern Iranian loess plateau, Chinese loess plateau, and loess–paleosol sequences in Hungary suggests that $\delta^{13}C_{bc}$ and $\delta^{18}O_{bc}$ variation in loessic modern soils and paleosols most likely reflects regional precipitation change and can provide valuable, quantitative paleoenvironmental information. Particle size distributions data suggest that the depositional patterns of loess at Mobarakabad are comparable to those of loess at other sites in the northern foothills of the Alborz Mountain range. Finally, based on Hf and Nd isotopic data, we hypothesize that loess unit 5, accumulated after 34 ka at Mobarakabad, might originate from the actively eroding crustal sources of relatively young mountain (Alborz and Kopet Dagh) belts around the loess area.

DATA AVAILABILITY STATEMENT

The raw data supporting the conclusion of this article will be made available by the authors, without undue reservation.

AUTHOR CONTRIBUTIONS

AG, HT, and FK (supervisor) initialized the project and collected samples for the analysis. XM carried out the isotope measurements. TS mentored AG in clay-sized Nd-Hf isotopes and particle size interpretations and had significant contributions to the editing and revision of this work. AG wrote the manuscript, and all coauthors contributed to the article and approved the submitted version.

ACKNOWLEDGMENTS

This study is part of the Ph.D. thesis done at Gorgan University of Agricultural Sciences and Natural Resources, Iran. Wancang Zhao is thanked for providing clay-sized Hf-Nd isotopes and Bradley A. Miller for his help in determining the particle size distributions. We also gratefully thank Jef Vandenberghe and Joseph A. Mason for their highly constructive feedback that enhanced the presentation and clarity of this article.

REFERENCES

Aciego, S. M., Bourdon, B., Lupker, M., and Rickli, J. (2009). A New Procedure for Separating and Measuring Radiogenic Isotopes (U, Th, Pa, Ra, Sr, Nd, Hf) in Ice Cores. *Chem. Geology.* 266 (3–4), 194–204. doi:10.1016/j.chemgeo.2009.06.003

Amundson, R. G., Chadwick, O. A., Sowers, J. M., and Doner, H. E. (1988). Relationship between Climate and Vegetation and the Stable Carbon Isotope Chemistry of Soils in the Eastern Mojave Desert, Nevada. *Quat. Res.* 29, 245–254. doi:10.1016/0033-5894(88)90033-6

Antoine, P., Rousseau, D.-D., Moine, O., Kunesch, S., Hatté, C., Lang, A., et al. (2009). Rapid and Cyclic Aeolian Deposition during the Last Glacial in European Loess: a High-Resolution Record from Nussloch, Germany. *Quat. Sci. Rev.* 28, 2955–2973. doi:10.1016/j.quascirev.2009.08.001

Bayat, O., Karimi, A., and Khademi, H. (2017). Stable Isotope Geochemistry of Pedogenic Carbonates in Loess-Derived Soils of Northeastern Iran: Paleoenvironmental Implications and Correlation across Eurasia. *Quat. Int.* 429, 52–61. doi:10.1016/j.quaint.2016.01.040

Bayon, G., Burton, K. W., Soulet, G., Vigier, N., Dennielou, B., Etoubleau, J., et al. (2009). Hf and Nd Isotopes in marine Sediments: Constraints on Global Silicate Weathering. *Earth Planet. Sci. Lett.* 277, 318–326. doi:10.1016/j.epsl.2008.10.028

Beuselinck, L., Govers, G., Poesen, J., Degraer, G., and Froyen, L. (1998). Grain-size Analysis by Laser Diffractometry: Comparison with the Sieve-Pipette Method. *Catena* 32, 193–208. doi:10.1016/S0341-8162(98)00051-4

Biscaye, P. E., Grousset, F. E., Revel, M., Van der Gaast, S., Zielinski, G. A., Vaars, A., et al. (1997). Asian Provenance of Glacial Dust (Stage 2) in the Greenland Ice Sheet Project 2 Ice Core, Summit, Greenland. *J. Geophys. Res.* 102 (C12), 26765–26781. doi:10.1029/97jc01249

Bouvier, A., Vervoort, J. D., and Patchett, P. J. (2008). The Lu-Hf and Sm-Nd Isotopic Composition of CHUR: Constraints from Unequilibrated Chondrites and Implications for the Bulk Composition of Terrestrial Planets. *Earth Planet. Sci. Lett.* 273, 48–57. doi:10.1016/j.epsl.2008.06.010

Breecker, D. O., Sharp, Z. D., and McFadden, L. D. (2009). Seasonal Bias in the Formation and Stable Isotopic Composition of Pedogenic Carbonate in Modern Soils from central New Mexico, USA. *Geol. Soc. America Bull.* 121, 630–640. doi:10.1130/B26413.1

Burgener, L., Huntington, K. W., Hoke, G. D., Schauer, A., Ringham, M. C., Latorre, C., et al. (2016). Variations in Soil Carbonate Formation and Seasonal Bias over >4 Km of Relief in the Western Andes (30°S) Revealed by Clumped Isotope Thermometry. *Earth Planet. Sci. Lett.* 441, 188–199. doi:10.1016/j.epsl.2016.02.033

Candy, I., Adamson, K., Gallant, C. E., Whitfield, E., and Pope, R. (2012). Oxygen and Carbon Isotopic Composition of Quaternary Meteoric Carbonates from Western and Southern Europe: Their Role in Palaoenvironmental Reconstruction. *Palaeogeogr. Palaeoclimatol. Palaeoecol.* 326-328, 1–11. doi:10.1016/j.palaeo.2011.12.017

Cerling, T. E., and Quade, J. (1993). Stable Carbon and Oxygen Isotopes in Soil Carbonates. *Geophys. Monogr.* 78, 217–231. doi:10.1029/GM078p0217

Cerling, T. E., Quade, J., Wang, Y., and Bowman, J. R. (1989). Carbon Isotopes in Soils and Palaeosols as Ecology and Palaeoecology Indicators. *Nature* 341 (6238), 138–139. doi:10.1038/341138a0

Chauvel, C., Garçon, M., Bureau, S., Besnault, A., Jahn, B.-M., and Ding, Z. (2014). Constraints from Loess on the Hf-Nd Isotopic Composition of the Upper continental Crust. *Earth Planet. Sci. Lett.* 388, 48–58. doi:10.1016/j.epsl.2013.11.045

Dare-Edwards, A. J. (1984). Aeolian Clay Deposits of South-Eastern Australia: Parna or Loessic Clay? *Trans. Inst. Br. Geogr.* 9, 337–344. doi:10.2307/622237

Dever, L., Fontes, J. C., and Riché, G. (1987). Isotopic Approach to Calcite Dissolution and Precipitation in Soils under Semi-arid Conditions. *Chem. Geology. Isotope Geosci. section* 66, 307–314. doi:10.1016/0168-9622(87)90050-9

Diaz, N., King, G. E., Valla, P. G., Herman, F., and Verrecchia, E. P. (2016). Pedogenic Carbonate Nodules as Soil Time Archives: Challenges and Investigations Related to OSL Dating. *Quat. Geochronol.* 36, 120–133. doi:10.1016/j.quageo.2016.08.008

Diefendorf, A. F., Mueller, K. E., Wing, S. L., Koch, P. L., and Freeman, K. H. (2010). Global Patterns in Leaf 13C Discrimination and Implications for Studies of Past and Future Climate. *Proc. Natl. Acad. Sci.* 107 (13), 5738–5743. doi:10.1073/pnas.0910513107

Dietrich, F., Diaz, N., Deschamps, P., Ngounou Ngatcha, B., Sebag, D., and Verrecchia, E. P. (2017). Origin of Calcium in Pedogenic Carbonate Nodules from Silicate Watersheds in the Far North Region of Cameroon: Respective Contribution of *In Situ* Weathering Source and Dust Input. *Chem. Geology.* 460, 54–69. doi:10.1016/j.chemgeo.2017.04.015

Ding, Z. L., Derbyshire, E., Yang, S. L., Sun, J. M., and Liu, T. S. (2005). Stepwise Expansion of Desert Environment across Northern China in the Past 3.5 Ma and Implications for Monsoon Evolution. *Earth Planet. Sci. Lett.* 237, 45–55. doi:10.1016/j.epsl.2005.06.036

Dodonov, A. E., Sadchikova, T. A., Sedov, S. N., Simakova, A. N., and Zhou, L. P. (2006). Multidisciplinary Approach for Paleoenvironmental Reconstruction in Loess-Paleosol Studies of the Darai Kalon Section, Southern Tajikistan. *Quat. Int.* 152-153, 48–58. doi:10.1016/j.quaint.2005.12.001

Dworkin, S. I., Nordt, L., and Atchley, S. (2005). Determining Terrestrial Paleotemperatures Using the Oxygen Isotopic Composition of Pedogenic Carbonate. *Earth Planet. Sci. Lett.* 237 (1-2), 56–68. doi:10.1016/j.epsl.2005.06.054

Feng, J.-L., Zhu, L.-P., Zhen, X.-L., and Hu, Z.-G. (2009). Grain Size Effect on Sr and Nd Isotopic Compositions in Eolian Dust: Implications for Tracing Dust Provenance and Nd Model Age. *Geochem. J.* 43, 123–131. doi:10.2343/geochemj.1.0007

Fenn, K., Durcan, J. A., Thomas, D. S. G., and Banak, A. (2020). A 180 Ka Record of Environmental Change at Erdut (Croatia): a New Chronology for the Loess-Palaeosol Sequence and its Implications for Environmental Interpretation. *J. Quat. Sci* 35 (4), 582–593. doi:10.1002/jqs.3201

Fischer-Femal, B. J., and Bowen, G. J. (2021). Coupled Carbon and Oxygen Isotope Model for Pedogenic Carbonates. *Geochimica et Cosmochimica Acta* 294, 126–144. doi:10.1016/j.gca.2020.10.022

Fitzsimmons, K. E., Nowatzki, M., Dave, A. K., and Harder, H. (2020). Intersections between Wind Regimes, Topography and Sediment Supply:

Perspectives from Aeolian Landforms in Central Asia. *Palaeogeogr. Palaeoclimatol. Palaeoecol.* 540, 109531. doi:10.1016/j.palaeo.2019.109531

Fitzsimmons, K. E., Sprafke, T., Zielhofer, C., Günter, C., Deom, J.-M., Sala, R., et al. (2018). Loess Accumulation in the Tian Shan piedmont: Implications for Palaeoenvironmental Change in Arid Central Asia. *Quat. Int.* 469, 30–43. doi:10.1016/j.quaint.2016.07.041

Forman, S. L., Marín, L., Gomez, J., and Pierson, J. (2008). Late Quaternary Eolian Sand Depositional Record for Southwestern Kansas: Landscape Sensitivity to Droughts. *Palaeogeogr. Palaeoclimatol. Palaeoecol.* 265 (1-2), 107–120. doi:10.1016/j.palaeo.2008.04.028

Forman, S. L., Wright, D. K., and Bloszies, C. (2014). Variations in Water Level for Lake Turkana in the Past 8500 Years Near Mt. Porr, Kenya and the Transition from the African Humid Period to Holocene Aridity. *Quat. Sci. Rev.* 97, 84–101. doi:10.1016/j.quascirev.2014.05.005

Frechen, M., Kehl, M., Rolf, C., Sarvati, R., and Skowronek, A. (2009). Loess Chronology of the Caspian lowland in Northern Iran. *Quat. Int.* 198, 220–233. doi:10.1016/j.quaint.2008.12.012

Gallagher, T. M., and Sheldon, N. D. (2016). Combining Soil Water Balance and Clumped Isotopes to Understand the Nature and Timing of Pedogenic Carbonate Formation. *Chem. Geology.* 435, 79–91. doi:10.1016/j.chemgeo.2016.04.023

Gallant, C. E., Candy, I., van den Bogaard, P., Silva, B. N., and Turner, E. (2014). Stable Isotopic Evidence for Middle Pleistocene Environmental Change from a Loess-Paleosol Sequence: Kärlich, Germany. *Boreas* 43 (4), 818–833. doi:10.1111/bor.12065

Ghafarpour, A., Khormali, F., Balsam, W., Forman, S. L., Cheng, L., and Song, Y. (2021). The Formation of Iron Oxides and Magnetic Enhancement Mechanisms in Northern Iranian Loess-Paleosol Sequences: Evidence from Diffuse Reflectance Spectrophotometry and Temperature Dependence of Magnetic Susceptibility. *Quat. Int.* 589, 68–82. doi:10.1016/j.quaint.2021.02.019

Ghafarpour, A., Khormali, F., Balsam, W., Karimi, A., and Ayoubi, S. (2016). Climatic Interpretation of Loess-Paleosol Sequences at Mobarakabad and Aghband, Northern Iran. *Quat. Res.* 86, 95–109. doi:10.1017/s0033589400039740

Ghafarpour, A., Khormali, F., and Forman, S. L. (2017). "The OSL Chronology of the Loess- Paleosol Sequence Mobarakabad, Northern Iran," in LoessFest2017, Gorgan, Iran, 08-12 October, 68–69.

Hough, B. G., Fan, M., and Passey, B. H. (2014). Calibration of the Clumped Isotope Geothermometer in Soil Carbonate in Wyoming and Nebraska, USA: Implications for Paleoelevation and Paleoclimate Reconstruction. *Earth Planet. Sci. Lett.* 391, 110–120. doi:10.1016/j.epsl.2014.01.008

Huth, T. E., Cerling, T. E., Marchetti, D. W., Bowling, D. R., Ellwein, A. L., and Passey, B. H. (2019). Seasonal Bias in Soil Carbonate Formation and its Implications for Interpreting High-Resolution Paleoarchives: Evidence from Southern Utah. *J. Geophys. Res. Biogeosci.* 124 (3), 616–632. doi:10.1029/2018jg004496

Jacobs, P. M., and Mason, J. A. (2007). Late Quaternary Climate Change, Loess Sedimentation, and Soil Profile Development in the central Great Plains: a Pedosedimentary Model. *Geol. Soc. America Bull.* 119, 462–475. doi:10.1130/b25868.1

Kehl, M. (2010). *Quaternary Loesses, Loess-like Sediments, Soils and Climate Change in Iran*. Stuttgart, Germany: Gebrüder Borntraeger Verlagsbuchhandlung.

Kehl, M., Sarvati, R., Ahmadi, H., Frechen, M., and Skowronek, A. (2005). Loess Paleosoil-Sequences along a Climatic Gradient in Northern Iran. *E&g Quat. Sci. J.* 55, 149–173. doi:10.3285/eg.55.1.08

Kehl, M., Vlaminck, S., Köhler, T., Laag, C., Rolf, C., Tsukamoto, S., et al. (2021). Pleistocene Dynamics of Dust Accumulation and Soil Formation in the Southern Caspian Lowlands - New Insights from the Loess-Paleosol Sequence at Neka-Abelou, Northern Iran. *Quat. Sci. Rev.* 253, 106774. doi:10.1016/j.quascirev.2020.106774

Kelson, J. R., Huntington, K. W., Breecker, D. O., Burgener, L. K., Gallagher, T. M., Hoke, G. D., et al. (2020). A Proxy for All Seasons? A Synthesis of Clumped Isotope Data from Holocene Soil Carbonates. *Quat. Sci. Rev.* 234, 106259. doi:10.1016/j.quascirev.2020.106259

Khormali, F., and Kehl, M. (2011). Micromorphology and Development of Loess-Derived Surface and Buried Soils along a Precipitation Gradient in Northern Iran. *Quat. Int.* 234, 109–123. doi:10.1016/j.quaint.2010.10.022

Khormali, F., Shahriari, A., Ghafarpour, A., Kehl, M., Lehndorff, E., and Frechen, M. (2020). Pedogenic Carbonates Archive Modern and Past Precipitation Change - A Transect Study from Soils and Loess-Paleosol Sequences from Northern Iran. *Quat. Int.* 552, 79–90. doi:10.1016/j.quaint.2019.12.011

Kim, S.-T., and O'Neil, J. R. (1997). Equilibrium and Nonequilibrium Oxygen Isotope Effects in Synthetic Carbonates. *Geochimica et Cosmochimica Acta* 61 (16), 3461–3475. doi:10.1016/s0016-7037(97)00169-5

Koeniger, P., Barta, G., Thiel, C., Bajnóczi, B., Novothny, Á., Horváth, E., et al. (2014). Stable Isotope Composition of Bulk and Secondary Carbonates from the Quaternary Loess-Paleosol Sequence in Süttő, Hungary. *Quat. Int.* 319, 38–49. doi:10.1016/j.quaint.2012.06.038

Kohn, M. J. (2010). Carbon Isotope Compositions of Terrestrial C3 Plants as Indicators of (Paleo)ecology and (Paleo)climate. *Proc. Natl. Acad. Sci.* 107 (46), 19691–19695. doi:10.1073/pnas.1004933107

Költringer, C., Stevens, T., Bradák, B., Almqvist, B., Kurbanov, R., Snowball, I., et al. (2020). Enviromagnetic Study of Late Quaternary Environmental Evolution in Lower Volga Loess Sequences, Russia. *Quat. Res.* 103, 1–25. doi:10.1017/qua.2020.73

Konert, M., and Vandenberghe, J. (1977). Comparison of Laser Grain Size Analysis With Pipette and Sieve Analysis: A Solution for the Underestimation of the Clay Fraction. *Sedimentology* 44, 523–535. doi:10.1046/j.1365-3091.1997.d01-38.x

Lauer, T., Frechen, M., Vlaminck, S., Kehl, M., Lehndorff, E., Shahriari, A., et al. (2017b). Luminescence-chronology of the Loess Palaeosol Sequence Toshan, Northern Iran - A Highly Resolved Climate Archive for the Last Glacial-Interglacial Cycle. *Quat. Int.* 429, 3–12. doi:10.1016/j.quaint.2015.03.045

Lauer, T., Vlaminck, S., Frechen, M., Rolf, C., Kehl, M., Sharifi, J., et al. (2017a). The Agh Band Loess-Palaeosol Sequence - A Terrestrial Archive for Climatic Shifts during the Last and Penultimate Glacial-Interglacial Cycles in a Semiarid Region in Northern Iran. *Quat. Int.* 429, 13–30. doi:10.1016/j.quaint.2016.01.062

Lechler, A. R., Huntington, K. W., Breecker, D. O., Sweeney, M. R., and Schauer, A. J. (2018). Loess-paleosol Carbonate Clumped Isotope Record of Late Pleistocene-Holocene Climate Change in the Palouse Region, Washington State, USA. *Quat. Res.* 90 (2), 331–347. doi:10.1017/qua.2018.47

Liu, W., Yang, H., Sun, Y., and Wang, X. (2011). δ^{13}C Values of Loess Total Carbonate: a Sensitive Proxy for Asian Summer Monsoon in Arid Northwestern Margin of the Chinese Loess Plateau. *Chem. Geol.* 284 (3–4), 317–322. doi:10.1016/j.chemgeo.2011.03.011

Luo, X., Wang, H., An, Z., Zhang, Z., and Liu, W. (2020). Carbon and Oxygen Isotopes of Calcified Root Cells, Carbonate Nodules and Total Inorganic Carbon in the Chinese Loess-Paleosol Sequence: The Application of Paleoenvironmental Studies. *J. Asian Earth Sci.* 201, 104515. doi:10.1016/j.jseaes.2020.104515

Lupker, M., Aciego, S. M., Bourdon, B., Schwander, J., and Stocker, T. F. (2010). Isotopic Tracing (Sr, Nd, U and Hf) of continental and marine Aerosols in an 18th century Section of the Dye-3 Ice Core (Greenland). *Earth Planet. Sci. Lett.* 295, 277–286. doi:10.1016/j.epsl.2010.04.010

Machalett, B., Oches, E. A., Frechen, M., Zöller, L., Hambach, U., Mavlyanova, N. G., et al. (2008). Aeolian dust dynamics in Central Asia during the Pleistocene e driven by the long-termmigration, seasonality and permanency of the Asiatic polar front. *Geochem. Geophys. Geosyst.* 8, Q08Q09. doi:10.1029/2007GC001938

Marković, S. B., Hambach, U., Stevens, T., Jovanović, M., O'Hara-Dhand, K., Basarin, B., et al. (2013). Loess in the Vojvodina Region (Northern Serbia): an Essential Link between European and Asian Pleistocene Environments. *Neth. J. Geosciences* 91 (1-2), 173–188.

Mason, J. A., Greene, R. S. B., and Joeckel, R. M. (2011b). Laser Diffraction Analysis of the Disintegration of Aeolian Sedimentary Aggregates in Water. *Catena* 87, 107–118. doi:10.1016/j.catena.2011.05.015

Mason, J. A., Jacobs, P. M., Hanson, P. R., Miao, X., and Goble, R. J. (2003). Sources and Paleoclimatic Significance of Holocene Bignell Loess, Central Great Plains, USA. *Quat. Res.* 60 (3), 330–339. doi:10.1016/j.yqres.2003.07.005

Mason, J. A., Nater, E. A., Zanner, C. W., and Bell, J. C. (1999). A New Model of Topographic Effects on the Distribution of Loess. *Geomorphology* 28, 223–236. doi:10.1016/s0169-555x(98)00112-3

Mason, J. A., Swinehart, J. B., Hanson, P. R., Loope, D. B., Goble, R. J., Miao, X., et al. (2011). Late Pleistocene Dune Activity in the central Great Plains, USA. *Quat. Sci. Rev.* 30, 3858–3870. doi:10.1016/j.quascirev.2011.10.005

Mason, J. A. (2001). Transport Direction of Peoria Loess in Nebraska and Implications for Loess Sources on the central Great Plains. *Quat. Res.* 56, 79–86. doi:10.1006/qres.2001.2250

McDonald, E. V., and McFadden, L. D. (1994). "Quaternary Stratigraphy of the Providence Mountains piedmont and Preliminary Age Estimates and Regional Stratigraphic Correlations of Quaternary Deposits in the Eastern Mojave Desert, California," in *Geological Investigations of an Active Margin. Geol. Soc. Am. Cordilleran Sect. Fieldtrip Guideb*. Editors S. F. McGill and T. M. Ross, 205–210.

Mestdagh, H., Haesaerts, P., Dodonov, A., and Hus, J. (1999). Pedosedimentary and Climatic Reconstruction of the Last Interglacial and Early Glacial Loess-Paleosol Sequence in South Tadzhikistan. *Catena* 35, 197–218. doi:10.1016/s0341-8162(98)00100-3

Miller, B. A., and Schaetzl, R. J. (2012). Precision of Soil Particle Size Analysis Using Laser Diffractometry. *Soil Sci. Soc. Am. J.* 76, 1719–1727. doi:10.2136/sssaj2011.0303

Monger, H. C., Cole, D. R., Gish, J. W., and Giordano, T. H. (1998). Stable Carbon and Oxygen Isotopes in Quaternary Soil Carbonates as Indicators of Ecogeomorphic Changes in the Northern Chihuahuan Desert, USA. *Geoderma* 82, 137–172. doi:10.1016/s0016-7061(97)00100-6

Muhs, D. R., Aleinikoff, J. N., Stafford, T. W., Jr., Kihl, R., Been, J., Mahan, S. A., et al. (1999). Late Quaternary Loess in Northeastern Colorado: Part I-Age and Paleoclimatic Significance. *Geol. Soc. Am. Bull.* 111, 1861–1875. doi:10.1130/0016-7606(1999)111<1861:lqlinc>2.3.co;2

Muhs, D. R., Bettis, E. A., Aleinikoff, J. N., McGeehin, J. P., Beann, J., Skipp, G., et al. (2008). Origin and Paleoclimatic Significance of Late Quaternary Loess in Nebraska: Evidence from Stratigraphy, Chronology, Sedimentology, and Geochemistry. *Geol. Soc. America Bull.* 120, 1378–1407. doi:10.1130/b26221.1

Muhs, D. R., Shroder, J., and Lancaster, N. (2013). "11.9 Loess and its Geomorphic, Stratigraphic, and Paleoclimatic Significance in the Quaternary," in *Treatise on Geomorphology. Aeolian Geomorphology*. Editors D. J. Sherman and A. C. W. Baas (San Diego, CA: Academic Press), Vol. 11, 149–183. doi:10.1016/b978-0-12-374739-6.00302-x

Nilson, E., and Lehmkuhl, F. (2001). Interpreting Temporal Patterns in the Late Quaternary Dust Flux from Asia to the North Pacific. *Quat. Int.* 76-77 (77), 67–76. doi:10.1016/s1040-6182(00)00090-2

Ning, Y. F., Liu, W. G., and An, Z. S. (2007). Variation of Soil delta C-13 Values in Xifeng Loess- Paleosol Sequence and its Paleoenvironmental Implication. *Chin. Sci. Bull.* 51, 1350–1354.

Nottebaum, V., Lehmkuhl, F., Stauch, G., Hartmann, K., Wünnemann, B., Schimpf, S., et al. (2014). Regional Grain Size Variations in Aeolian Sediments along the Transition between Tibetan highlands and north-western Chinese Deserts - the Influence of Geomorphological Settings on Aeolian Transport Pathways. *Earth Surf. Process. Landforms* 39, 1960–1978. doi:10.1002/esp.3590

Ozer, M., Orhan, M., and Isik, N. S. (2010). Effect of Particle Optical Properties on Size Distribution of Soils Obtained by Laser Diffraction. *Environ. Eng. Geosci.* 16, 163–173. doi:10.2113/gseegeosci.16.2.163

Passey, B. H., Levin, N. E., Cerling, T. E., Brown, F. H., and Eiler, J. M. (2010). High-temperature Environments of Human Evolution in East Africa Based on Bond Ordering in Paleosol Carbonates. *Proc. Natl. Acad. Sci.* 107, 11245–11249. doi:10.1073/pnas.1001824107

Patchett, P. J., White, W. M., Feldmann, H., Kielinczuk, S., and Hofmann, A. W. (1984). Hafnium/rare Earth Element Fractionation in the Sedimentary System and Crustal Recycling into the Earth's Mantle. *Earth Planet. Sci. Lett.* 69, 365–378. doi:10.1016/0012-821x(84)90195-x

Peters, N. A., Huntington, K. W., and Hoke, G. D. (2013). Hot or Not? Impact of Seasonally Variable Soil Carbonate Formation on Paleotemperature and O-Isotope Records from Clumped Isotope Thermometry. *Earth Planet. Sci. Lett.* 361, 208–218. doi:10.1016/j.epsl.2012.10.024

Pettke, T., Lee, D.-C., Halliday, A. N., and Rea, D. K. (2002). Radiogenic Hf Isotopic Compositions of continental Eolian Dust from Asia, its Variability and its Implications for Seawater Hf. *Earth Planet. Sci. Lett.* 202, 453–464. doi:10.1016/s0012-821x(02)00778-1

Polakowski, C., Sochan, A., Bieganowski, A., Ryzak, M., Földényi, R., and Tóth, J. (2014). Influence of the Sand Particle Shape on Particle Size Distribution Measured by Laser Diffraction Method. *Int. Agrophysics* 28, 195–200. doi:10.2478/intag-2014-0008

Pourmand, A., Prospero, J. M., and Sharifi, A. (2014). Geochemical Fingerprinting of Trans-Atlantic African Dust Based on Radiogenic Sr-Nd-Hf Isotopes and Rare Earth Element Anomalies. *Geology* 42, 675–678. doi:10.1130/g35624.1

Pourmasoumi, M., Khormali, F., Ayoubi, S., Kehl, M., and Kiani, F. (2019). Development and Magnetic Properties of Loess-Derived forest Soils along a Precipitation Gradient in Northern Iran. *J. Mt. Sci.* 16, 1848–1868. doi:10.1007/s11629-018-5288-4

Prins, M. A., Zheng, H., Beets, K., Troelstra, S., Bacon, P., Kamerling, I., et al. (2009). Dust Supply from River Floodplains: the Case of the Lower Huang He (Yellow River) Recorded in a Loess-Palaeosol Sequence from the Mangshan Plateau. *J. Quat. Sci.* 24, 75–84. doi:10.1002/jqs.1167

Pu, W., Gao, J., Zhao, K., Ling, H., and Jiang, S. (2005). Separation Method of Rb–Sr, Sm–Nd Using DCTA and HIBA. *J. Nanjing Univ. Natural Sci.* 4, 016.

Pye, K. (1995). The Nature, Origin and Accumulation of Loess. *Quat. Sci. Rev.* 14, 653–667. doi:10.1016/0277-3791(95)00047-x

Qiang, M., Lang, L., and Wang, Z. (2010). Do fine-grained Components of Loess Indicate Westerlies: Insights from Observations of Dust Storm Deposits at Lenghu (Qaidam Basin, China). *J. Arid Environments* 74, 1232–1239. doi:10.1016/j.jaridenv.2010.06.002

Quade, J., Breecker, D. O., Daeron, M., and Eiler, J. (2011). The Paleoaltimetry of Tibet: An Isotopic Perspective. *Am. J. Sci.* 311, 77–115. doi:10.2475/02.2011.01

Quade, J., Cerling, T. E., and Bowman, J. R. (1989). Systematic Variations in the Carbon and Oxygen Isotopic Composition of Pedogenic Carbonate along Elevation Transects in the Southern Great Basin, United States. *Geol. Soc. Am. Bull.* 101 (4), 464–475. doi:10.1130/0016-7606(1989)101<0464:svitca>2.3.co;2

Quade, J., Eiler, J., Daëron, M., and Achyuthan, H. (2013). The Clumped Isotope Geothermometer in Soil and Paleosol Carbonate. *Geochimica et Cosmochimica Acta* 105, 92–107. doi:10.1016/j.gca.2012.11.031

Quade, J., Garzione, C., and Eiler, J. (2007). Paleoelevation Reconstruction Using Pedogenic Carbonates. *Rev. Mineralogy Geochem.* 66, 53–87. doi:10.2138/rmg.2007.66.3

Rao, Z. G., Zhu, Z. Y., Chen, F. H., and Zhang, J. W. (2006). Does $\delta^{13}C_{carb}$ of the Chinese Loess Indicate Past C3/C4 Abundance? A Review of Research on Stable Carbon Isotopes of the Chinese Loess. *Quat. Sci. Rev.* 25, 22512257. doi:10.1016/j.quascirev.2006.03.013

Ringham, M. C., Hoke, G. D., Huntington, K. W., and Aranibar, J. N. (2016). Influence of Vegetation Type and Site-To-Site Variability on Soil Carbonate Clumped Isotope Records, Andean piedmont of Central Argentina (32-34°S). *Earth Planet. Sci. Lett.* 440 (June), 1–11. doi:10.1016/j.epsl.2016.02.003

Rousseau, D.-D., Antoine, P., Boers, N., Lagroix, F., Ghil, M., Lomax, J., et al. (2020). Dansgaard-Oeschger-like Events of the Penultimate Climate Cycle: the Loess point of View. *Clim. Past* 16 (2), 713–727. doi:10.5194/cp-16-713-2020

Rousseau, D.-D., Boers, N., Sima, A., Svensson, A., Bigler, M., Lagroix, F., et al. (2017). (MIS3 & 2) Millennial Oscillations in Greenland Dust and Eurasian Aeolian Records - A Paleosol Perspective. *Quat. Sci. Rev.* 169, 99–113. doi:10.1016/j.quascirev.2017.05.020

Rousseau, D.-D., Sima, A., Antoine, P., Hatté, C., Lang, A., and Zöller, L. (2007). Link between European and North-Atlantic Abrupt Climate Changes over the Last Glaciation. *Geophys. Res. Lett.* 34, L22713. doi:10.1029/2007gl031716

Rousseau, D. D., Antoine, P., Hatté, C., Lang, A., Zöller, L., Fontugne, M., et al. (2002). Abrupt Millennial Climatic Changes from Nussloch (Germany) Upper Weichselian Eolian Records during the Last Glaciation. *Quat. Sci. Rev.* 21, 1577–1582. doi:10.1016/s0277-3791(02)00034-3

Schaetzl, R. J., Forman, S. L., and Attig, J. W. (2014). Optical Ages on Loess Derived from Outwash Surfaces Constrain the advance of the Laurentide Ice Sheet Out of the Lake Superior Basin, USA. *Quat. Res.* 81 (2), 318–329. doi:10.1016/j.yqres.2013.12.003

Schubert, B. A., and Jahren, A. H. (2012). The Effect of Atmospheric CO2 Concentration on Carbon Isotope Fractionation in C3 Land Plants. *Geochimica et Cosmochimica Acta* 96, 29–43. doi:10.1016/J.GCA.2012.08.003

Shahriari, A., Khormali, F., Bläsing, M., Vlaminck, S., Kehl, M., Frechen, M., et al. (2017). Biomarkers in Modern and Buried Soils of Semi-desert and forest Ecosystems of Northern Iran. *Quat. Int.* 429, 62–73. doi:10.1016/j.quaint.2016.02.048

Sharifigarmdareh, J., Khormali, F., Scheidt, S., Rolf, C., Kehl, M., and Frechen, M. (2020). Investigating Soil Magnetic Properties with Pedogenic Variation along a

Precipitation Gradient in Loess-Derived Soils of the Golestan Province, Northern Iran. *Quat. Int.* 552, 100–110. doi:10.1016/j.quaint.2019.11.022

Shoaee, M. J., Vahdati Nasab, H., and Petraglia, M. D. (2021). The Paleolithic of the Iranian Plateau: Hominin Occupation History and Implications for Human Dispersals across Southern Asia. *J. Anthropological Archaeology* 62, 101292. doi:10.1016/j.jaa.2021.101292

Skonieczny, C., Bory, A., Bout-Roumazeilles, V., Abouchami, W., Galer, S. J. G., Crosta, X., et al. (2013). A Three-Year Time Series of mineral Dust Deposits on the West African Margin: Sedimentological and Geochemical Signatures and Implications for Interpretation of marine Paleo-Dust Records. *Earth Planet. Sci. Lett.* 364, 145–156. doi:10.1016/j.epsl.2012.12.039

Soil Survey Staff (2014). *Keys to Soil Taxonomy*. Washington, D.C., USA: U.S. Department of Agriculture, Natural Resources Conservation Service.

Song, Y., Li, Y., Cheng, L., Zong, X., Kang, S., Ghafarpour, A., et al. (2021). Spatio-temporal Distribution of Quaternary Loess across Central Asia. *Palaeogeogr. Palaeoclimatol. Palaeoecol.* 567, 110279. doi:10.1016/j.palaeo.2021.110279

Stevens, T., Adamiec, G., Bird, A. F., and Lu, H. (2013). An Abrupt Shift in Dust Source on the Chinese Loess Plateau Revealed through High Sampling Resolution OSL Dating. *Quat. Sci. Rev.* 82, 121–132. doi:10.1016/j.quascirev.2013.10.014

Stevens, T., and Lu, H. (2009). Optically Stimulated Luminescence Dating as a Tool for Calculating Sedimentation Rates in Chinese Loess: Comparisons with Grain-Size Records. *Sedimentology* 56 (4), 911–934. doi:10.1111/j.1365-3091.2008.01004.x

Stevens, T., Marković, S. B., Zech, M., Hambach, U., and Sümegi, P. (2011). Dust Deposition and Climate in the Carpathian Basin over an Independently Dated Last Glacial-Interglacial Cycle. *Quat. Sci. Rev.* 30, 662–681. doi:10.1016/j.quascirev.2010.12.011

Stevens, T., Sechi, D., Bradák, B., Orbe, R., Baykal, Y., Cossu, G., et al. (2020). Abrupt Last Glacial Dust Fall over Southeast England Associated with Dynamics of the British-Irish Ice Sheet. *Quat. Sci. Rev.* 250, 106641. doi:10.1016/j.quascirev.2020.106641

Stevenson, B. A., Kelly, E. F., McDonald, E. V., Busacca, A. J., and Welker, J. M. (2010). Oxygen Isotope Ratios in Holocene Carbonates across a Climatic Gradient, Eastern Washington State, USA: Evidence for Seasonal Effects on Pedogenic mineral Isotopic Composition. *The Holocene* 20, 575–583. doi:10.1177/0959683609356588

Sun, D., Bloemendal, J., Rea, D. K., Vandenberghe, J., Jiang, F., An, Z., et al. (2002). Grain-size Distribution Function of Polymodal Sediments in Hydraulic and Aeolian Environments, and Numerical Partitioning of Sedimentary Components. *Sediment. Geol* 152, 262–277. doi:10.1016/s0037-0738(02)00082-9

Sun, Y., Kutzbach, J., An, Z., Clemens, S., Liu, Z., Liu, W., et al. (2015). Astronomical and Glacial Forcing of East Asian Summer Monsoon Variability. *Quat. Sci. Rev.* 115, 132–142. doi:10.1016/j.quascirev.2015.03.009

Svensson, A., Biscaye, P. E., and Grousset, F. E. (2000). Characterization of Late Glacial continental Dust in the Greenland Ice Core Project Ice Core. *J. Geophys. Res.* 105 (D4), 4637–4656. doi:10.1029/1999jd901093

Sweeney, M. R., and Mason, J. A. (2013). Mechanisms of Dust Emission from Pleistocene Loess Deposits, Nebraska, USA. *J. Geophys. Res. Earth Surf.* 118, 1460–1471. doi:10.1002/jgrf.20101

Tan, H., Liu, Z., Rao, W., Jin, B., and Zhang, Y. (2017). Understanding Recharge in Soil-Groundwater Systems in High Loess hills on the Loess Plateau Using Isotopic Data. *Catena* 156, 18–29. doi:10.1016/J.CATENA.2017.03.022

Tripaldi, A., Ciccioli, P. L., Alonso, M. S., and Forman, S. L. (2010). Petrography and Geochemistry of Late Quaternary Dune fields of Western Argentina: Provenance of Aeolian Materials in Southern South America. *Aeolian Res.* 2 (1), 33–48. doi:10.1016/j.aeolia.2010.01.001

Újvári, G., Bernasconi, S. M., Stevens, T., Kele, S., Páll-Gergely, B., Surányi, G., et al. (2021). Stadial-Interstadial Temperature and Aridity Variations in East Central Europe Preceding the Last Glacial Maximum. *Paleoceanogr Paleoclimatol* 36, e2020PA004170. doi:10.1029/2020PA004170

Újvári, G., Kele, S., Bernasconi, S. M., Haszpra, L., Novothny, Á., and Bradák, B. (2019). Clumped Isotope Paleotemperatures from MIS 5 Soil Carbonates in Southern Hungary. *Palaeogeogr. Palaeoclimatol. Palaeoecol.* 518, 72–81.

Újvári, G., Kok, J. F., Varga, G., and Kovács, J. (2016). The Physics of Wind-Blown Loess: Implications for Grain Size Proxy Interpretations in Quaternary Paleoclimate Studies. *Earth. Sci. Rev.* 154, 247–278.

Újvári, G., Stevens, T., Svensson, A., Klötzli, U. S., Manning, C., Németh, T., et al. (2015). Two Possible Source Regions for central Greenland Last Glacial Dust. *Geophys. Res. Lett.* 42, 10,399–10,408.

Újvári, G., Varga, A., Ramos, F. C., Kovács, J., Németh, T., and Stevens, T. (2012). Evaluating the Use of clay Mineralogy, Sr–Nd Isotopes and Zircon U–Pb Ages in Tracking Dust Provenance: An Example from Loess of the Carpathian Basin. *Chem. Geol.* 304, 83–96.

Újvári, G., Wegner, W., Klötzli, U., Horschinegg, M., and Hippler, D. (2018). Sr-Nd-Hf Isotopic Analysis of < 10 Mg Dust Samples: Implications for Ice Core Dust Source Fingerprinting. *Geochem. Geophys. Geosyst.* 19 (1), 60–72.

Vandenberghe, J. (2013). Grain Size of fine-grained Windblown Sediment: a Powerful Proxy for Process Identification. *Earth-Science Rev.* 121, 18–30. doi:10.1016/j.earscirev.2013.03.001

Vandenberghe, J., Mücher, H. J., Roebroeks, W., and Gemke, D. (1985). Lithostratigraphy and palaeoenvironment of the Pleistocene deposits at Maastricht-Belvédère, southern Limburg, The Netherlands. *Med. Rijks Geol. Dienst.* 39, 7–18.

Vandenberghe, J., Renssen, H., Van Huissteden, K., Nugteren, G., Konert, M., Lu, H., et al. (2006). Penetration of Atlantic westerly Winds into Central and East Asia. *Quat. Sci. Rev.* 25, 2380–2389. doi:10.1016/j.quascirev.2006.02.017

Vandenberghe, J., Sun, Y., Wang, X., Abels, H. A., and Liu, X. (2018). Grain-Size Characterization of Reworked Fine-Grained Aeolian Deposits. *Earth Sci. Rev.* 177, 43–52. doi:10.1016/J.EARSCIREV.2017.11.005

Vandenberghe, J., Zhisheng, A., Nugteren, G., Huayu, L., and Van Huissteden, K. (1997). New Absolute Time Scale for the Quaternary Climate in the Chinese Loess Region by Grain-Size Analysis. *Geol* 25, 35. doi:10.1130/0091-7613(1997)025<0035:natsft>2.3.co;2

Varga, G., Gresina, F., Újvári, G., Kovács, J., and Szalai, Z. (2019b). On the Reliability and Comparability of Laser Diffraction Grain Size Measurements of Paleosols in Loess Records. *Sediment. Geology.* 389, 42–53. doi:10.1016/j.sedgeo.2019.05.011

Varga, G., Újvári, G., and Kovács, J. (2019a). Interpretation of Sedimentary (Sub)populations Extracted from Grain Size Distributions of Central European Loess-Paleosol Series. *Quat. Int.* 502, 60–70. doi:10.1016/j.quaint.2017.09.021

Vervoort, J. D., Plank, T., and Prytulak, J. (2011). The Hf-Nd Isotopic Composition of Marine Sediments. *Geochim. Cosmochim. Acta* 75, 5903–5926. doi:10.1016/j.gca.2011.07.046

Vlaminck, S., Kehl, M., Lauer, T., Shahriari, A., Sharifi, J., Eckmeier, E., et al. (2016). Loess-soil Sequence at Toshan (Northern Iran): Insights into Late Pleistocene Climate Change. *Quat. Int.* 399, 122–135. doi:10.1016/j.quaint.2015.04.028

Vlaminck, S., Kehl, M., Rolf, C., Franz, S. O., Lauer, T., Lehndorff, E., et al. (2018). Late Pleistocene Dust Dynamics and Pedogenesis in Southern Eurasia - Detailed Insights from the Loess Profile Toshan (NE Iran). *Quat. Sci. Rev.* 180, 75–95. doi:10.1016/j.quascirev.2017.11.010

Vriend, M., Prins, M. A., Buylaert, J.-P., Vandenberghe, J., and Lu, H. (2011). Contrasting Dust Supply Patterns across the north-western Chinese Loess Plateau during the Last Glacial-Interglacial Cycle. *Quat. Int.* 240, 167–180. doi:10.1016/j.quaint.2010.11.009

Wacha, L., Laag, C., Grizelj, A., Tsukamoto, S., Zeeden, C., Ivanišević, D., et al. (2021). High-resolution Palaeoenvironmental Reconstruction at Zmajevac (Croatia) over the Last Three Glacial/interglacial Cycles. *Palaeogeogr. Palaeoclimatol. Palaeoecol.* 576, 110504. doi:10.1016/j.palaeo.2021.110504

Xu, Y., Li, J., Yue, L., Jiang, J., Sun, F., and Zhang, L. (2015). Grain-size Characteristics of Red clay Deposits on the Eastern Edge of Chinese Loess Plateau and its Implications for Neogene Evolution of East Asian winter Monsoon. *Environ. Earth Sci.* 73 (11), 7445–7456. doi:10.1007/s12665-014-3918-x

Yang, S., and Ding, Z. (2008). Advance-retreat History of the East-Asian Summer Monsoon Rain- Fall belt over Northern China during the Last Two Glacial-Interglacial Cycles. *Earth Planet. Sci. Lett.* 274 (3–4), 499–510. doi:10.1016/j.epsl.2008.08.001

Yang, Y.-h., Zhang, H.-f., Chu, Z.-y., Xie, L.-w., and Wu, F.-y. (2010). Combined Chemical Separation of Lu, Hf, Rb, Sr, Sm and Nd from a Single Rock Digest and Precise and Accurate Isotope Determinations of Lu-Hf, Rb-Sr and Sm-Nd Isotope Systems Using Multi-Collector ICP-MS and TIMS. *Int. J. Mass Spectrom.* 290, 120–126. doi:10.1016/j.ijms.2009.12.011

Zamanian, K., Lechler, A. R., Schauer, A. J., Kuzyakov, Y., and Huntington, K. W. (2021). The $\delta^{13}C$, $\delta^{18}O$ and $\Delta 47$ Records in Biogenic, Pedogenic and Geogenic Carbonate Types from Paleosol-Loess Sequence and Their Paleoenvironmental Meaning. *Quat. Res.* 101, 256–272.

Zeeden, C., Kels, H., Hambach, U., Schulte, P., Protze, J., Eckmeier, E., et al. (2016). Three Climatic Cycles Recorded in a Loess-Palaeosol Sequence at Semlac (Romania) - Implications for Dust Accumulation in South-Eastern Europe. *Quat. Sci. Rev.* 154, 130–142. doi:10.1016/j.quascirev.2016.11.002

Zhao, W., Balsam, W., Williams, E., Long, X., and Ji, J. (2018). Sr-Nd-Hf Isotopic Fingerprinting of Transatlantic Dust Derived from North Africa. *Earth Planet. Sci. Lett.* 486, 23–31. doi:10.1016/j.epsl.2018.01.004

Zhao, W., Sun, Y., Balsam, W., Lu, H., Liu, L., Chen, J., et al. (2014). Hf-Nd Isotopic Variability in mineral Dust from Chinese and Mongolian Deserts: Implications for Sources and Dispersal. *Sci. Rep.* 4, 5837. doi:10.1038/srep05837

Zhao, W., Sun, Y., Balsam, W., Zeng, L., Lu, H., Otgonbayar, K., et al. (2015). Clay-sized Hf-Nd-Sr Isotopic Composition of Mongolian Dust as a Fingerprint for Regional to Hemispherical Transport. *Geophys. Res. Lett.* 42, 5661–5669. doi:10.1002/2015gl064357

Conflict of Interest: The authors declare that the research was conducted in the absence of any commercial or financial relationships that could be construed as a potential conflict of interest.

Publisher's Note: All claims expressed in this article are solely those of the authors and do not necessarily represent those of their affiliated organizations, or those of the publisher, the editors, and the reviewers. Any product that may be evaluated in this article, or claim that may be made by its manufacturer, is not guaranteed or endorsed by the publisher.

Copyright © 2021 Ghafarpour, Khormali, Meng, Tazikeh and Stevens. This is an open-access article distributed under the terms of the Creative Commons Attribution License (CC BY). The use, distribution or reproduction in other forums is permitted, provided the original author(s) and the copyright owner(s) are credited and that the original publication in this journal is cited, in accordance with accepted academic practice. No use, distribution or reproduction is permitted which does not comply with these terms.

frontiers
in Earth Science

ORIGINAL RESEARCH
published: 18 January 2022
doi: 10.3389/feart.2021.811181

Advancement of Megadunes and its Implications in the Badain Jaran Sand Sea

Peng Dong[1,2], **Aimin Liang**[3]* **and Yali Zhou**[3]

[1]College of Life Sciences, Hainan Normal University, Haikou, China, [2]College of Geography and Environmental Science, Hainan Normal University, Haikou, China, [3]School of Geography and Tourism, Shaanxi Normal University, Xi'an, China

The tallest megadunes on the Earth are developed in China's Badain Jaran Sand Sea, as a result of which a prolonged curiosity exists with regards to the existence and migration of such large dunes. However, our present understanding of movement of aeolian bedforms is largely limited to dunes with height ranging from several to several tens of meters. Difficulties in understanding the movement of megadunes predominantly exists in the monitoring methods. This study presents the evidence of the megadune advancement and its rate in the Badain Jaran Sand Sea, estimated by optically stimulated luminescence (OSL) dating of sediments on the slipfaces of several megadunes. It is suggested that megadunes experience similar advancement as the commonly observed sand dunes; the rate of advancement of megadunes fits the rate-height relationship. The rate of advancement varies linearly with the reciprocal of megadune height, which has been confirmed for dunes, extending the advancement rate-height relationship to a previously blind range of dune size. In addition, the advancement rate of megadunes exhibits far-reaching implications for megadune formation. In combination with other morphometric evidences, it exemplifies the assumption that the development of megadunes is predominantly controlled by wind rather than other factors such as the underlying relief and ground water, as accepted by most researchers.

Keywords: dune geomorphology, dune movement, advance rate-height relationship, megadune formation, Badain Jaran Sand Sea

OPEN ACCESS

Edited by:
Zhuolun Li,
Lanzhou University, China

Reviewed by:
Ruijie Lu,
Beijing Normal University, China
Bing Liu,
Northwestern Institute of Eco-Environment and Resources, China
Xin Gao,
Xinjiang Institute of Ecology and Geography (CAS), China

***Correspondence:**
Aimin Liang
aimliang@snnu.edu.cn

Specialty section:
This article was submitted to Quaternary Science, Geomorphology and Paleoenvironment, a section of the journal Frontiers in Earth Science

Received: *08 November 2021*
Accepted: *01 December 2021*
Published: *18 January 2022*

Citation:
Dong P, Liang A and Zhou Y (2022) Advancement of Megadunes and its Implications in the Badain Jaran Sand Sea. Front. Earth Sci. 9:811181. doi: 10.3389/feart.2021.811181

INTRODUCTION

Aeolian geomorphology has always attempted to understand the formation mechanism of aeolian bedforms that are organized into a hierarchical system consisting of ripples, dunes, and megadunes (i.e., large bedforms with a spacing exceeding 500 m and a height reaching 200 or 300 m and may occur as linear, crescentic, or star forms) (Wilson, 1972; Goudie, 2004; Livingstone and Warren, 2019). However, its development is unfavorable as the formation mechanism is highly differentiated by bedform scale, a behavior of nonlinear dynamical system (Phillips, 1992). It is now assumed that wind ripples are formed by air-particle movement interactions, dunes are developed through bedform-airflow feedback, and megadunes are possibly controlled by the thickness of atmospheric boundary layer. However, our understanding regarding the mechanism of aeolian bedforms is limited to selected dune types, typically barchan and linear dunes (Rozier et al., 2019; Qian et al., 2021).

The formation mechanism of megadunes has to be speculated. For example, several hypotheses have been proposed with respect to the formation of megadunes in the Badain Jaran Sand Sea. The underlying relief hypothesis holds that the megadunes are formed by aeolian sand covering on topographic prominences (Lou, 1962; Sun and Sun, 1964); groundwater hypothesis supported that the megadunes are maintained by internal moisture, which is extracted from groundwater through capillary action (Chen et al., 2004); aeolian hypothesis advocated that the megadunes are formed by wind, just like the common dunes (Dong et al., 2009). On the other hand, attempts to relate ripples, dunes, and megadunes are never abandoned because they share several morphological similarities (Dong et al., 2009). The distinction between the formation mechanism of ripples and dunes has been verified by extensive study including field observation and physical and numerical simulation (Richards, 1980; Pelletier, 2009; Lämmel et al., 2018). In contrast, the relationship between the formation mechanism of dunes and megadunes remains unknown because limited studies have been conducted with respect to megadunes, which are generally compound to complex with the superimposition of dunes and ripples. Till date, the formation of megadunes can only be speculated subjectively or based on a few weak evidences because it is not feasible to study megadunes like ripples and dunes (Dong et al., 2013). It is assumed that the similarity between megadunes and dunes should be implied in various aspects besides morphology. The analysis pertaining to Dong et al. (2009) on the geomorphological patterns characterized by height-spacing relationship of megadunes suggests that this relationship is consistent with superimposed dunes and wind ripples, and also with dunes and wind ripples distributed globally over the sand seas. It is therefore deduced that wind is predominantly responsible for the development of megadunes in the Badain Jaran Sand Sea. However, this deduction regarding the formation of megadune requires further evidences.

Mobility is the most conspicuous property of shifting dunes, although the overall activity varies as per different dune types (Thomas, 1992; Livingstone and Warren, 1996). Understanding sand dunes activity and dynamics not only is relevant to the studies of aeolian processes and the morphological development of different dune types but also has considerable implications for the recognition and interpretation of dunes to which further significance can be linked with paleoclimatic studies (Thomas, 1992). The movement of megadunes should also support information with respect to their formation. However, little is known regarding the movement of megadunes. Firstly, monitoring the movement of megadunes is very difficult largely because they are supposed to move at a rather slow rate. Secondly, it is impossible even to calculate a rough estimate as all the theoretical and empirical formulae developed for the movement rate of dunes have their own specific boundary conditions (Livingstone and Warren, 1996). Understanding megadune movement has to resort to field investigation.

Therefore, this study attempts to obtain information regarding the movement of megadunes in the Badain Jaran Sand Sea that features the tallest megadunes on the Earth (Wang et al., 2020). The study of megadunes in this sand sea will provide valuable clues to unravel the mystery of megadune formation, and therefore witnessed increasing interest in the last 2 decades (Chen et al., 2004; Dong et al., 2013). The present study aims to unravel more evidences for the megadune formation by testing evidences that exhibit similar mobility with other common dunes. Mobility is a character of shifting dunes. However, it can test existence of the underlying relief, as the underlying bedrock should be exposed due to the megadunes advancement.

PHYSIOGRAPHIC SETTING AND METHODS

Physiographic Setting

The Badain Jaran Sand Sea is a part of the Alxa Plateau in western Inner Mongolia, with an area of about 50,000 km^2, between latitudes 39° 20′ and 42° N and longitudes 99° 48′ and 104°14′ E (Yan et al., 2001). The sand sea is bounded to the south by the Heli Mountains, the Beidai Mountains, and the Heishantou Mountains that separate it from the gobis (gravel deserts) of the Hexi Corridor, to the north by the Guezihu wetland, which merges with the black gobis and plains of Mongolia, to the southeast by the Yabrai Mountains, which separate it from the Tengger Desert, and to the west and northwest by the flat lowlands of the Gulunai grassland. The Badain Jaran Sand Sea has a climate of extreme continental desert type according to Köppen's climate classification (Dong et al., 2004), with mean annual precipitation of less than 90 mm, annual potential evaporation of more than 2,500 mm, and mean annual air temperature range from 9.5 to 10.3°C. The Badain Jaran Sand Sea has a medium wind-energy environment, with the annual sand drift potential (DP) of 281 VU (mean value that calculated at per the result proposed by Zhang et al., 2015), as reported at the nearest meteorological stations.

The outstanding feature that characterizes the Badain Jaran Sand Sea is its megadune-lake landscape, which is comprised of megadunes and more than 100 lakes of different sizes. They are concentrated in the southeast within an area of approximately 4,000 km^2. The megadunes generally are 200–300 m tall, with the tallest megadune exceeding 400 m. These megadunes are classified as complex reversing megadunes developed from compound barchanoid megadunes, with their crests running from northeast (35°) to southwest (215°) (Dong et al., 2009), almost perpendicular to the resultant drift potential. Three megadunes in the hinterland of the megadune area are selected to investigate their advancement (**Figure 1**).

Methods

Movement of dunes is controlled by complex factors, but its dependence on dune height has sound scientific basis and is verified by several field observations (Livingstone and Warren, 1996). Megadunes with such height as those observed in the Badain Jaran Sand Sea are supposed to move at such a low rate that it is almost negligible. Hence, commonly implemented monitoring methods such as topographic survey and

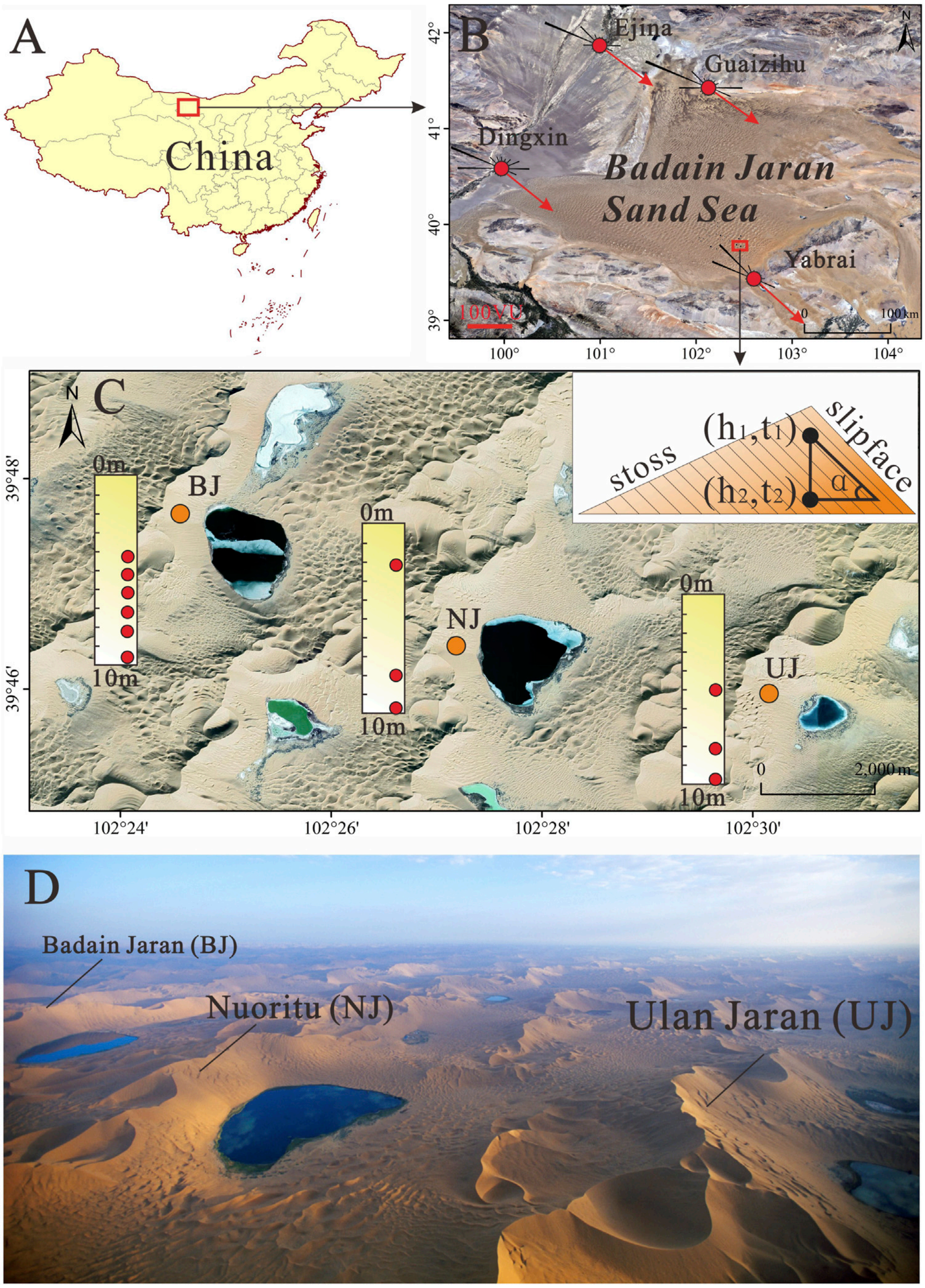

FIGURE 1 | (A, B) Location of the Badain Jaran Sand Sea and wind regime; the sand drift potential is calculated based on the ERA5 Reanalysis Data (www.ecmwf.int). **(C)** Three megadune drill cores (orange dots) in the Badain Jaran Sand Sea and OSL sampling sites (red dots). The inset graphical representation of the parameters used to estimate the rate of advancement. **(D)** Aerial image of the three megadunes (Source: Dong et al., 2013).

comparison of remote-sensing images fail to reveal the movement of these megadunes. Therefore, the present study attempts to estimate the advancement rate of megadunes in the Badain Jaran Sand Sea by means of optically stimulated luminescence (OSL) dating that can provide accurate dates of aeolian sediments (Yu and Lai, 2012). The mean advancement rate of a megadune can be estimated by dating sediments at different depth on the slipface through **Eq. 1** according to a principle illustrated by the inserted diagram in **Figure 1**. An important assumption is that the advancement of megadunes is realized by wind erosion on the stoss slope and deposition on the leeward slope or slipface. In addition, geometry of the megadune is fairly uniform in the process of its advancement. Rationality of this assumption will be discussed later.

TABLE 1 | Geographical information of the OSL sampling localities.

Megadune name	Height (m)	OSL sample location		
		Longitude	Latitude	Altitude (m)
Badain Jaran (BJ)	380	102° 24′ 43.96″ E	39° 47′ 42.32″ N	1245
Nouritu (NJ)	360	102° 27′ 18.43″ E	39° 46′ 19.06″ N	1244
Ulan Jaran (UJ)	430	102° 30′ 28.58″ E	39° 45′ 59.26″ N	1315

TABLE 2 | Environmental radioactivity and OSL dating results.

Sample ID	Depth (m)	U (ppm)	Th (ppm)	K (%)	Water content (%)	De (Gy)	Dose rate (Gy ka^{-1})	OSL age (ka)
BJ-01	4.3	1.20 ± 0.08	3.58 ± 0.17	1.47 ± 0.05	1.67	0.46 ± 0.04	2.18 ± 0.06	0.22 ± 0.02
BJ-02	5.3	1.08 ± 0.08	3.23 ± 0.18	1.63 ± 0.04	2.98	0.57 ± 0.06	2.16 ± 0.05	0.26 ± 0.03
BJ-03	6.3	1.44 ± 0.09	3.57 ± 0.17	1.60 ± 0.04	0.78	0.87 ± 0.06	2.29 ± 0.05	0.38 ± 0.03
BJ-04	7.3	1.2 ± 0.08	4.36 ± 0.19	1.69 ± 0.04	1.39	1.06 ± 0.09	2.35 ± 0.05	0.45 ± 0.04
BJ-05	8.3	1.18 ± 0.08	3.57 ± 0.18	1.44 ± 0.05	1.14	1.02 ± 0.11	2.04 ± 0.05	0.50 ± 0.06
BJ-06	9.6	1.08 ± 0.08	3.52 ± 0.19	1.48 ± 0.05	1.08	1.15 ± 0.05	2.02 ± 0.05	0.57 ± 0.03
NJ-01	2.1	1.25 ± 0.09	4.36 ± 0.20	1.58 ± 0.04	2.14	0.35 ± 0.22	2.32 ± 0.05	0.15 ± 0.09
NJ-02	8.0	0.95 ± 0.08	3.32 ± 0.17	1.30 ± 0.05	0.43	0.64 ± 0.10	1.88 ± 0.06	0.34 ± 0.05
NJ-03	9.7	1.10 ± 0.08	3.72 ± 0.19	1.42 ± 0.05	0.36	0.86 ± 0.09	2.023 ± 0.06	0.42 ± 0.05
UJ-01	5.0	0.97 ± 0.08	2.93 ± 0.18	1.34 ± 0.05	1.43	2.16 ± 0.13	1.88 ± 0.06	1.15 ± 0.08
UJ-02	8.1	1.00 ± 0.08	3.69 ± 0.17	1.39 ± 0.05	2.05	4.27 ± 0.37	1.94 ± 0.06	2.20 ± 0.20
UJ-03	9.7	1.14 ± 0.08	3.62 ± 0.17	1.40 ± 0.05	2.33	5.34 ± 0.31	1.97 ± 0.06	2.72 ± 0.18

$$D = (h_2 - h_1) / (t_2 - t_1) \tan \alpha \qquad (1)$$

where D is the mean advancement rate during the period between time t_1 and t_2, h_1 and h_2 are the depth corresponding to t_1 and t_2, respectively, and α is the angle of the slipface, about 30°. Hence, the advancement rate of megadunes can be estimated by dating aeolian sediments at different depths on the slipface.

Sediments at different depth on slipfaces of the three megadunes (**Figure 1**; **Table 1**) were sampled according to the OSL dating protocols. A sampling hand drill with an inner diameter of 100 mm was driven into the slipfaces of megadunes to extract underground sediment cores. A 200 mm long and 50 mm wide stainless tube was inserted to the sediment core to obtain OSL samples. The tubes containing sediment samples were sealed by aluminum foil and black plastic film. We finally collected 6 samples in the Badain Jaran megadune, and 3 samples in the Nuoritu and Ulan Jaran megadunes, respectively. Both ends (about 30 mm) of the sediment in the tube that were thought to be exposed were excluded in OSL dating.

The content of U, Th, and K of the OSL dating samples was measured by neutron activation method in China Institute of Atomic Energy. The moisture content was measured by oven drying method. OSL dating was carried out in the Shaanxi Normal University (Wang et al., 2021). We selected 90–125 μm quartz grains by wet sieving as the target measuring particles. Other detailed pretreatment procedures refer to Zhang et al. (2019). The annual dose rate of cosmic ray was calculated based on the parameters and equations proposed by Prescott and Hutton (1994). Equivalent dose of quartz originating from ceramics was obtained by OSL single aliquot regenerative dose (SAR) method, measured at 260°C of preheat and 220°C of cutheat. The ages of quartz particles were derived based on annual dose rate and equivalent dose.

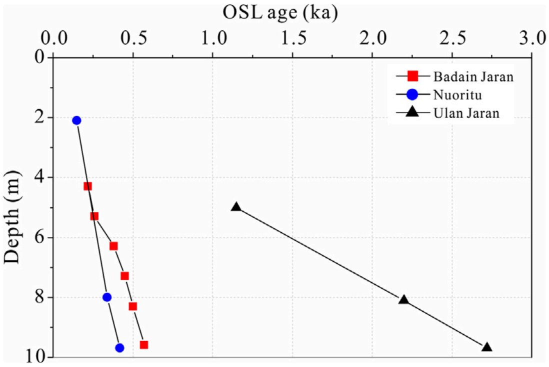

FIGURE 2 | OSL age-depth profiles of the three megadunes.

RESULTS AND DISCUSSION

The environmental radioactivity and OSL dating results of the three megadunes are listed in **Table 2**. The drilling depth of the three megadunes is similar, around 10 m (the maximum depth of the drill). However, the time span they cover is different, implying that the megadunes have different advancement rate. The taller is the megadune, the longer is the time span. The 10 m drill could drill through a stratum up to 2.7 ka old on the Ulan Jaran megadune, but only about 0.4 ka on the Nuoritu megadune. Consequently, the megadunes exhibit advancement rate on different time scale. The reliability of the OSL dating results is suggested in two aspects. Firstly, the OSL age-depth profiles of the three megadunes are similar (**Figure 2**), following a reasonable linear relationship reasonably well considering that the advancement rate of megadunes might have varied with time. Secondly, the Nuoritu megadune and Badain Jaran megadune demonstrate similar variation trend in advancement rate for the same period. Hence, we are confident that the OSL dating in this study provides reliable estimate pertaining to megadune advancement rate in the Badain Jaran Sand Sea.

Another question arises whether the sediments of different ages represent megadune advancement, involving the basic assumption to estimate the megadune advancement rate as mentioned in *Methods Section*. Net erosion of windward slope of the megadunes is manifested by the exposed stratification in several localities of the windward slopes, which are inclined with the same direction and angle (repose angle) of the slipfaces. Stratigraphic detections conducted on the windward slopes of two typical megadunes by Ground Penetrating Radar (GPR) revealed stratification consistent with the slipfaces of the megadunes, although the stratification in the upper sections was complicated by reversed crests (Li et al., 2009). The megadunes in Badain Jaran Sand Sea have been experiencing wind erosion on the windward slopes and deposition on the leeward slopes (slipfaces), resulting in overall advancement.

Advancement Rate of Megadunes

The advancement rate of megadunes at the order of meter per hundred years is much slower than the dunes commonly observed. Such a slow advancement rate can hardly be observed by conventional methods. Factors responsible for the slow advancement possibly include large size of the megadunes and the wind regime. Megadunes in the Badain Jaran Sand Sea are complex reversing megadunes. Their primary slipfaces are oriented towards the southeast in response to the dominant northwestern wind, and secondary slipfaces are oriented towards the northwest in response to the secondary southeastern wind (Dong et al., 2004). Hence, the megadunes advance towards southeast. The Badain Jaran Sand Sea generally has medium wind energy environments (Zhang et al., 2015). It usually has a wide unimodal to acute bimodal wind regime with intermediate directional variability characterized by RDP/DP (RDP is resultant drift potential, DP is drift potential) ranging from 0.5 to 0.8 (Dong et al., 2004). While the prevailing northwestern wind results in a general advancement toward the southeast, frequent southeastern wind especially in summer results in the reversed crest zones, at top 40–60 m of the megadunes (Dong et al., 2009). This reversed crest zone is the most active part of the megadune, and migrates back and forth in response to variations in wind direction. In addition, it forms reversed slipface by the southeastern wind. The reversed slipface partly offsets megadune advancement, though it cannot alter the general advancement as it consumes energy for the prevailing northwestern wind to adjust the slipface.

The slow advancement rate also partly contributes to the heightening of megadunes. Recent observations reveal that the megadune-lake system exists as a unique local air circulation with radiation of wind from lake throughout the year (**Figure 3**, unpublished data), resulting climbing sands on the slipfaces, retarding advancement, and heightening of megadunes. Therefore, the slow advancement rate of the megadunes in Badain Jaran Sand Sea is an aspect reflecting their formation mechanism. Morphology, movement, and lakes are interrelated to form this unique megadune-lake system.

Advance Rate-Height Relationship of Megadunes

Complex factors may influence the movement of sand dunes but the factors that influence the advancement of megadunes in the Badain Jaran Sand Sea due to the absence of vegetation and the underlying obstacles (Dong et al., 2009). In this context, it is meaningful to discuss the relationship between advancement rate and height of megadunes like other shifting dunes, although the advancement rate is solely available for three megadunes. Theories regarding the movement of barchans are followed here to understand the advancement of megadunes in the Badain Jaran Sand Sea. The age-depth profiles suggest that it is imperative to discuss the megadune advancement rate based on the average advancement rate of the three megadunes, though different megadunes represent different time periods. The longest time span that the advancement rate represents is less than 3 ka. The Late Holocene dune reaction stage in the arid regions of China (Yang, 2001), and the factors that influence megadune advancement can be considered relatively stable so that dune advancement rate did not vary widely with time (**Figure 4**). The following discussion on the relationship between advancement rate and megadune height and its geomorphologic implications are based on the average advancement rate.

A basic formula (**Eq. 2**) relating the movement rate and height has been derived for transverse dunes (Simons et al., 1965).

$$V_{\mathrm{d}} = q/kH\rho_{\mathrm{p}} \tag{2}$$

where V_{d} is the movement rate of a dune, q is the transport rate of the sand trapped by the slipface, approximately equaling the transport rate on the stoss slope $k = A/LH$, where A is the two-dimensional cross-sectional area of the dune, and L is its wavelength (distance between neighboring dunes), H is the height of the dune, and ρ_{p} is the bulk density of the sand in the dune. Variations of this basic formula have been produced for different purposes, but the fact that the movement rate of dunes changes linearly with the reciprocal of dune height is adequately confirmed by field observations (**Figure 5**). The curves in **Figure 5** represent a function $V_{\mathrm{d}} = a+b/H$, where a and b are regressive coefficients. However, uncertainty still exists on the size-movement curve at either extreme of the size range. Previous observations in **Figure 5** only represented dunes lower than 100 m. It is suggested that larger dunes seem to reach a plateau in their rate of movement beyond which the size has no role. This is possibly due to greater wind speed-up.

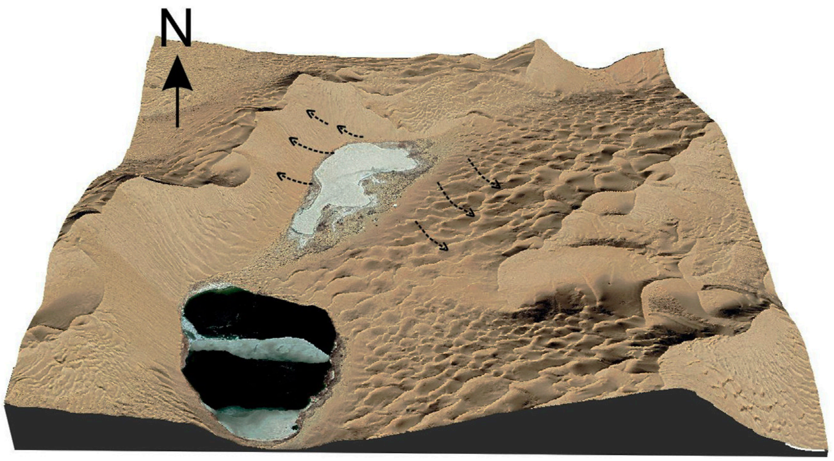

FIGURE 3 | Observed local air circulation that radiates from the interdune lakes (based on the unpublished data collected from wind towers).

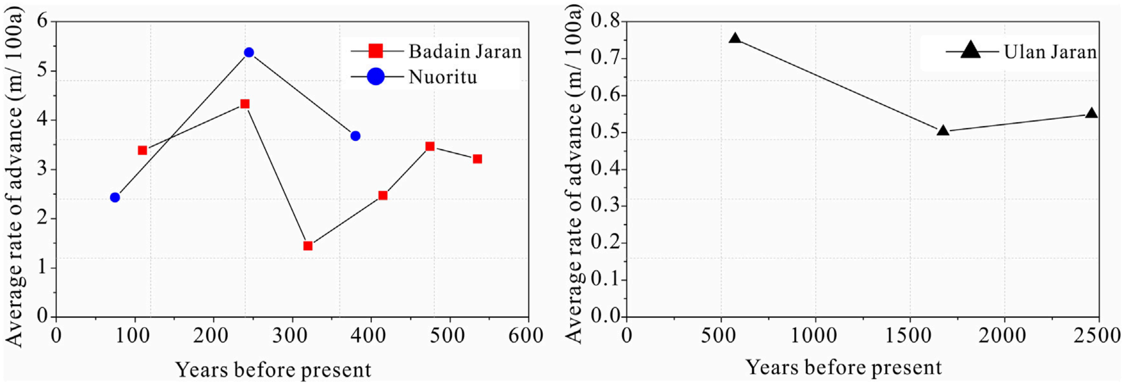

FIGURE 4 | Average advancement rate of the megadunes in different periods.

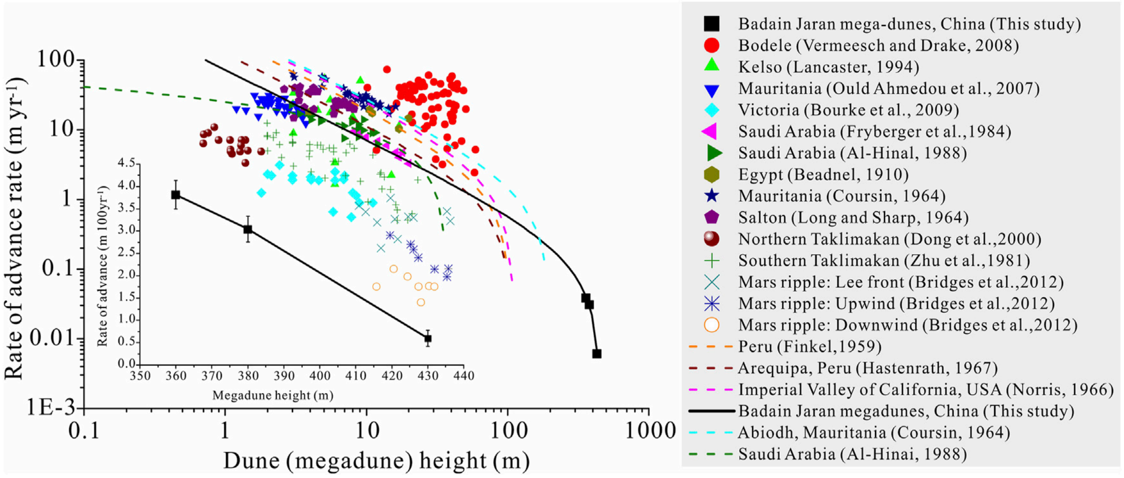

FIGURE 5 | Measured rates of transverse dune movement and the estimated advancement rate of megadunes in the Badain Jaran Sand Sea as a function of height. (Beadnell, 1910; Finkel, 1959; Coursin, 1964; Long and Sharp, 1964; Norris, 1966; Hastenrath, 1967; Zhu et al., 1981; Fryberger et al., 1984; Al-Hinai, 1988; Lancaster, 1994; Dong et al., 2000; Ould Ahmedou et al., 2007; Vermeesch and Drake, 2008; Bourke et al., 2009; Bridges et al., 2012)

Consequently, it is hypothesized that the relationship between movement rate and dune height should be exponential rather than linear (Sarnthein and Walger, 1974). However, few observations are available to confirm this. The advancement of the tallest megadunes on the Earth in the Badain Jaran Sand Sea gives us an opportunity to test the above hypothesis.

Figure 5 displays that the relationship between advancement rate and height of the three megadunes fall on a curve that fits the above linear function effectively. This linear relationship demonstrates that the slow advancement rate of Ulan Jaran megadune mostly resulted from its great height. However, several geomorphologic implications exist in this regard. Firstly, the tallest megadunes in the Badain Jaran Sand Sea experience similar advancement to sand dunes commonly observed. This is also verified by sedimentary structures of the megadunes, which are dominated by slipface beddings inclined towards the advancement direction and lack the gently-inclined stoss beddings (Yang, 2001; Li et al., 2009). Advancement of the megadunes is the consequence of piecemeal deflation on the windward slope, and of deposition in the lee side. Secondly, the possibility that the underlying relief controls the development of megadunes can be negated because no exposure of underlying bedrocks is observed on stoss side of the megadunes, which have undergone a long history of deflation. Increasing evidences support the fact that no bedrock relief underlies the megadunes (Yang et al., 2011). Thirdly, evidence from megadune advancement combined with previous morphometric features proves that the development of megadunes is controlled dominantly by wind rather than other factors such as the underlying relief and ground water as proposed previously (Dong et al., 2009).

CONCLUSION

It is suggested that the megadunes in Badain Jaran Sand Sea do advance, although their advancement rate is rather slow. The advancement of megadunes revealed in this study has several important implications:

1) The advancement of the megadunes explains the reason why the windward slopes of megadunes in Badain Jaran Sand Sea are dominated by slipface beddings inclined towards the advancement direction and lack the gently-inclined stoss beddings. In fact, the stoss beddings are preserved much less in fossil aeolian sand.
2) The megadunes in Badain Jaran Sand Sea have been experiencing piecemeal deflation on the windward slope, and of deposition in the lee. This justifies the assumption based on which the advancement rate of megadunes was estimated by dating the sediments at different depth of the slipfaces. The OSL dating method proves to be a good alternative to estimate the slow advancement rate such as that of the megadunes due to failure of the conventional methods.
3) The relationship between the advancement rate and height confirmed previously for dunes is extended to complex reversing megadunes. The large size of megadunes and the wind regime are largely responsible for the slow advancement rate of the megadunes in the Badain Jaran Sand Sea. In addition, unique local air circulation that radiates to form lakes partly retards megadune advancement and contributes to heightening of the megadunes. Morphology, movement, and lakes are interrelated to form the unique megadune lake system.
4) The advancement of megadunes adds more evidence to support the fact that the development of megadunes in the Badain Jaran Sand Sea is controlled dominantly by wind rather than other factors such as the underlying relieves, ground water, etc. However, more robust evidences are waiting for the deeper drill cores.

DATA AVAILABILITY STATEMENT

The original contributions presented in the study are included in the article/Supplementary material. Further inquiries can be directed to the corresponding author.

AUTHOR CONTRIBUTIONS

PD wrote the manuscript and done the field work. AL revised the manuscript and designed and did the field work. YZ did the OSL experiment.

FUNDING

This research was funded by the Fundamental Research Funds for the Central Universities (GK202103144).

ACKNOWLEDGMENTS

We are grateful to Prof. Luo Wanyin and Prof. Zhang Zhengcai (Northwest Institute of Eco-Environment and Resources, Chinese Academy of Sciences) for their assistance with our fieldwork. We also extend our deepest respect and appreciation to all the scientists who made substantial contributions to previous research in the Badain Jaran Sand Sea.

REFERENCES

Ai-Hinai, K. G. (1988). *Quaremary Aeolian Sand Mapping in Saudi Arabia, Using Remotely-Sensed Imagery*. London,UK: PhD, University of London.

Beadnell, H. J. L. (1910). The Sand-Dunes of the Libyan Desert. *Geographical J.* 36, 367–395. doi:10.2307/1777337

Bourke, M. C., Ewing, R. C., Finnegan, D., and McGowan, H. A. (2009). Sand Dune Movement in the Victoria Valley, Antarctica. *Geomorphology* 109 (3), 148–160. doi:10.1016/j.geomorph.2009.02.028

Bridges, N. T., Ayoub, F., Avouac, J.-P., Leprince, S., Lucas, A., and Mattson, S. (2012). Earth-like Sand Fluxes on Mars. *Nature* 485 (7398), 339–342. doi:10.1038/nature11022

Chen, J. S., Li, L., Wang, J. Y., Barry, D. A., Sheng, X. F., Gu, W. Z., et al. (2004). Groundwater Maintains Dune Landscape. *Nature* 432, 459–460. doi:10.1038/432459a

Coursin, A. (1964). *Observations et expériences faites en avril et mai 1956 sur les barkhans du Souehel el Abiodh (région est de Port-Étienne)*. Paris, France: Bulletin: Institut Française de l'Afrique Noire.

Dong, Z., Qian, G., Luo, W., Zhang, Z., Xiao, S., and Zhao, A. (2009). Geomorphological Hierarchies for Complex Mega-Dunes and Their Implications for Mega-Dune Evolution in the Badain Jaran Desert. *Geomorphology* 106 (3), 180–185. doi:10.1016/j.geomorph.2008.10.015

Dong, Z., Qian, G., Lv, P., and Hu, G. (2013). Investigation of the Sand Sea with the Tallest Dunes on Earth: China's Badain Jaran Sand Sea. *Earth-Science Rev.* 120, 20–39. doi:10.1016/j.earscirev.2013.02.003

Dong, Z., Wang, T., and Wang, X. (2004). Geomorphology of the Megadunes in the Badain Jaran Desert. *Geomorphology* 60 (1), 191–203. doi:10.1016/j.geomorph.2003.07.023

Dong, Z., Wang, X., and Chen, G. (2000). Monitoring Sand Dune advance in the Taklimakan Desert. *Geomorphology* 35 (3), 219–231. doi:10.1016/S0169-555X(00)00039-8

Finkel, H. J. (1959). The Barchans of Southern Peru. *J. Geology.* 67 (6), 614–647. doi:10.1086/626622

Fryberger, S. G., Al-Sari, A. M., Clisham, T. J., Rizvi, S. A. R., and Al-Hinai, K. G. (1984). Wind Sedimentation in the Jafurah Sand Sea, Saudi Arabia. *Sedimentology* 31, 413–431. doi:10.1111/j.1365-3091.1984.tb00869.x

Goudie, A. S. (2004). *Encyclopedia of Geomorphology*. London: Routledge.

Hastenrath, S. L. (1967). The Barchans of the Arequipa Region, Southern Peru. *Z. Geomorphol.* 11 (3), 300–331. doi:10.1086/626622

Lämmel, M., Meiwald, A., Yizhaq, H., Tsoar, H., Katra, I., and Kroy, K. (2018). Aeolian Sand Sorting and Megaripple Formation. *Nat. Phys* 14 (7), 759–765. doi:10.1038/s41567-018-0106-z

Lancaster, N. (1994). Controls on Aeolian Activity: Some New Perspectives from the Kelso Dunes, Mojave Desert, California. *J. Arid Environments* 27 (2), 113–125. doi:10.1006/jare.1994.1052

Li, X., Wang, Z., Chen, F., Lancaster, N., Li, Z., Li, G., et al. (2009). Deposition of Transverse Dune Mountains in Badain Jaran Desert. *Quat. Sci.* 29 (4), 797–805. doi:10.3969/j.issn.10017410.2009.04.16

Livingstone, I., and Warren, A. (2019). *Aeolian Geomorphology : A New Introduction*. Hoboken: John Wiley & Sons.

Livingstone, I., and Warren, A. (1996). *Aeolian Geomorphology: An Introduction*. London: Longman.

Long, J. T., and Sharp, R. P. (1964). Barchan-dune Movement in Imperial Valley, California. *Geol. Soc. America Bull.* 75 (2), 149–156. doi:10.1130/0016-7606(1964)75[149:bmiivc]2.0.co;2

Lou, T. (1962). *The Formation and Utilization of the Desert between Minqing and Badain Monastery*. Beijing: Science Press.

Norris, R. M. (1966). Barchan Dunes of Imperial Valley, California. *J. Geology.* 74 (3), 292–306. doi:10.1086/627164

Ould Ahmedou, D., Ould Mahfoudh, A., Dupont, P., Ould El Moctar, A., Valance, A., and Rasmussen, K. R. (2007). Barchan Dune Mobility in Mauritania Related to Dune and Interdune Sand Fluxes. *J. Geophys. Res.* 112 (F2). doi:10.1029/2006JF000500

Pelletier, J. D. (2009). Controls on the Height and Spacing of Eolian Ripples and Transverse Dunes: A Numerical Modeling Investigation. *Geomorphology* 105 (3), 322–333. doi:10.1016/j.geomorph.2008.10.010

Phillips, J. D. (1992). Nonlinear Dynamical Systems in Geomorphology: Revolution or Evolution? *Geomorphology* 5 (3), 219–229. doi:10.1016/0169-555X(92)90005-9

Prescott, J. R., and Hutton, J. T. (1994). Cosmic ray Contributions to Dose Rates for Luminescence and ESR Dating: Large Depths and Long-Term Time Variations. *Radiat. Meas.* 23 (2), 497–500. doi:10.1016/1350-4487(94)90086-8

Qian, G., Yang, Z., Tian, M., Dong, Z., Liang, A., and Xing, X. (2021). From Dome Dune to Barchan Dune: Airflow Structure Changes Measured with Particle Image Velocimetry in a Wind Tunnel. *Geomorphology* 382, 107681. doi:10.1016/j.geomorph.2021.107681

Richards, K. J. (1980). The Formation of Ripples and Dunes on an Erodible Bed. *J. Fluid Mech.* 99 (3), 597–618. doi:10.1017/S002211208000078X

Rozier, O., Narteau, C., Gadal, C., Claudin, P., and Courrech du Pont, S. (2019). Elongation and Stability of a Linear Dune. *Geophys. Res. Lett.* 46 (24), 14521–14530. doi:10.1029/2019GL085147

Sarnthein, M., and Walger, E. (1974). Der äolische Sandstrom aus der W-Sahara zur Atlantikküste. *Geol. Rundsch.* 63 (3), 1065–1087. doi:10.1007/BF01821323

Simons, D. B., Richardson, E. V., and Nordin, C. F., Jr (1965). *Bedload Equation for Ripples and Dunes*. Professional Paper. Washington, DC: US Government Printing Office.

Sun, P., and Sun, Q. (1964). *The Hydrological Geology of the Western Inner Mongolia*. Beijing: Science Press.

Thomas, D. S. G. (1992). Desert Dune Activity: Concepts and Significance. *J. Arid Environments* 22 (1), 31–38. doi:10.1016/S0140-1963(18)30654-2

Vermeesch, P., and Drake, N. (2008). Remotely Sensed Dune Celerity and Sand Flux Measurements of the World's Fastest Barchans (Bodélé, Chad). *Geophys. Res. Lett.* 35 (24). doi:10.1029/2008GL035921

Wang, H., Huang, C. C., Pang, J., Zhou, Y., Cuan, Y., Guo, Y., et al. (2021). Catastrophic Flashflood and Mudflow Events in the Pre-historical Lajia Ruins at the Northeast Margin of the Chinese Tibetan Plateau. *Quat. Sci. Rev.* 251, 106737. doi:10.1016/j.quascirev.2020.106737

Wilson, I. G. (1972). Aeolian Bedforms-Their Development and Origins. *Sedimentology* 19 (3-4), 173–210. doi:10.1111/j.1365-3091.1972.tb00020.x

Yan, M., Guangqian, W., Baosheng, L., and Guangrong, D. (2001). Formation and Growth of High Megadunes in Badain Jaran Desert. *Acta Geographica Sinica* 56 (1), 83–91. doi:10.11821/xb200101010

Yang, X. (2001). Landscape Evolution and Palaeoclimate in the Deserts of Northwestern China, with a Special Reference to Badain Jaran and Taklamakan. *Chin.Sci.Bull.* 46 (1), 6–10. doi:10.1007/BF03187228

Yang, X., Scuderi, L., Liu, T., Paillou, P., Li, H., Dong, J., et al. (2011). Formation of the Highest Sand Dunes on Earth. *Geomorphology* 135 (1), 108–116. doi:10.1016/j.geomorph.2011.08.008

Yu, L., and Lai, Z. (2012). OSL Chronology and Palaeoclimatic Implications of Aeolian Sediments in the Eastern Qaidam Basin of the Northeastern Qinghai-Tibetan Plateau. *Palaeogeogr. Palaeoclimatol. Palaeoecol.* 337-338, 120–129. doi:10.1016/j.palaeo.2012.04.004

Zhang, Y., Huang, C. C., Shulmeister, J., Guo, Y., Liu, T., Kemp, J., et al. (2019). Formation and Evolution of the Holocene Massive Landslide-Dammed Lakes in the Jishixia Gorges along the Upper Yellow River: No Relation to China's Great Flood and the Xia Dynasty. *Quat. Sci. Rev.* 218, 267–280. doi:10.1016/j.quascirev.2019.06.011

Zhang, Z., Dong, Z., and Li, C. (2015). Wind Regime and Sand Transport in China's Badain Jaran Desert. *Aeolian Res.* 17, 1–13. doi:10.1016/j.aeolia.2015.01.004

Zhu, Z., Chen, Z., Wu, Z., Li, J., Li, B., and Wu, G. (1981). *A Study on the Sand Dune Geomorphology of Taklimakan Desert*. Beijing: Science Press.

Conflict of Interest: The authors declare that the research was conducted in the absence of any commercial or financial relationships that could be construed as a potential conflict of interest.

Publisher's Note: All claims expressed in this article are solely those of the authors and do not necessarily represent those of their affiliated organizations, or those of the publisher, the editors and the reviewers. Any product that may be evaluated in this article, or claim that may be made by its manufacturer, is not guaranteed or endorsed by the publisher.

Copyright © 2022 Dong, Liang and Zhou. This is an open-access article distributed under the terms of the Creative Commons Attribution License (CC BY). The use, distribution or reproduction in other forums is permitted, provided the original author(s) and the copyright owner(s) are credited and that the original publication in this journal is cited, in accordance with accepted academic practice. No use, distribution or reproduction is permitted which does not comply with these terms.

frontiers
in Earth Science

ORIGINAL RESEARCH
published: 03 February 2022
doi: 10.3389/feart.2021.808157

Revisiting Late Pleistocene Loess–Paleosol Sequences in the Azov Sea Region of Russia: Chronostratigraphy and Paleoenvironmental Record

Jie Chen[1,2], *Thomas Stevens*[2], *Taibao Yang*[3]*, *Mingrui Qiang*[1], *Gennady Matishov*[4], *Evgeny Konstantinov*[5], *Redzhep Kurbanov*[6], *Biao Zeng*[3] *and Peihong Shi*[7]

[1]*School of Geography, South China Normal University, Guangzhou, China,* [2]*Department of Earth Sciences, Uppsala University, Uppsala, Sweden,* [3]*Institute of Glaciology and Ecogeography, College of Earth and Environmental Sciences, Lanzhou University, Lanzhou, China,* [4]*Southern Scientific Center, Russian Academy of Sciences, Rostov-on-Don, Russia,* [5]*Institute of Geography, Russian Academy of Sciences, Moscow, Russia,* [6]*Faculty of Geography, Lomonosov Moscow State University, Moscow, Russia,* [7]*College of Tourism and Environment, Shaanxi Normal University, Xi'an, China*

OPEN ACCESS

Edited by:
Kathryn Elizabeth Fitzsimmons,
University of Tübingen, Germany

Reviewed by:
Diana Jordanova,
National Institute of Geophysics,
Geodesy and Geography (BAS),
Bulgaria
Ulrich Friedrich Hambach,
University of Bayreuth, Germany

****Correspondence:***
Taibao Yang
yangtb@lzu.edu.cn

Specialty section:
This article was submitted to
Quaternary Science, Geomorphology
and Paleoenvironment,
a section of the journal
Frontiers in Earth Science

Received: *03 November 2021*
Accepted: *15 December 2021*
Published: *03 February 2022*

Citation:
Chen J, Stevens T, Yang T, Qiang M,
Matishov G, Konstantinov E,
Kurbanov R, Zeng B and Shi P (2022)
Revisiting Late Pleistocene
Loess–Paleosol Sequences in the
Azov Sea Region of Russia:
Chronostratigraphy and
Paleoenvironmental Record.
Front. Earth Sci. 9:808157.
doi: 10.3389/feart.2021.808157

Loess-paleosol sequences are the most intensively studied terrestrial archives used for the reconstruction of Late Pleistocene environmental and climatic changes in the Azov Sea region, southwest Russia. Here we present a refined chronostratigraphy and a multiproxy record of Late Pleistocene environmental dynamics of the most complete and representative loess–paleosol sequences (Beglitsa and Chumbur-Kosa sections) from the Azov Sea region. We propose a new chronostratigraphy following the Chinese and Danubean loess stratigraphic models that refines the subdivision of the Last Interglacial paleosol (S_1) complex in two Azov Sea sites, resolve the uncertainty of the stratigraphic position of the weakly developed paleosol (L_1SS_m) in Beglitsa section, and allow for direct correlation of the Azov Sea sections with those in the Danube Basin and the Chinese Loess Plateau. More importantly, it may serve as a basis for better constraining local and regional chronostratigraphic correlations, and facilitate the interpretation of climatic connections and possible forcing mechanisms responsible for the climatic trends in the region. In addition, a general succession of environmental dynamics is reconstructed from these two vital sections, which is broadly consistent with other loess records in the Dnieper Lowland and Lower Danube Basin, demonstrating similar climatic trends at Glacial–Interglacial time scales. Furthermore, our results have important implications for the chronostratigraphic representativeness of Beglitsa as a key regional loess section and for the reconstruction of the temporal and spatial evolution of Late Pleistocene climate in the Azov Sea region.

Keywords: quaternary stratigraphy, paleoenvironmental reconstruction, loess–paleosol sequences, Late Pleistocene, Azov Sea

INTRODUCTION

The loess–paleosol sequences (LPSs) of the Azov Sea in Eastern Europe–Western Russia are extensively distributed terrestrial deposits that preserve detailed evidence of past climatic and environmental changes in the region. However, they are also among the least well known and understood relative to loess deposits from elsewhere in Europe (Smalley et al., 2009; Schaetzl et al., 2018). The thickness of individual LPS varies between a few meters to several tens of meters, demonstrating multiple alternating series of loess and paleosol that indicate different environmental conditions extending through the mid Pleistocene to the present (Velichko, 1990; Dodonov et al., 2006; Velichko et al., 2009a).

Unlike the more uniform LPS further west in central Europe and further east in central Asia, Azov loess deposits and underlying alluvial/marine sediments contain small mammal faunas that are typically distributed along the Azov Sea shorelines, providing an important marker for bio-stratigraphic correlation between the continental and marine deposits (Dodonov et al., 2000; Dodonov et al., 2006). These fossil assemblages are also a vital advantage for the establishment of loess chronostratigraphy (Tesakov et al., 2007). Therefore, previous research on LPS of the Azov Sea was mainly focused on paleosol identification and stratigraphic subdivision at individual sites based on faunal composition of small mammals from alluvial/marine deposits and overlying buried soils (Dodonov et al., 2000; Markova, 2005; Markova, 2007; Tesakov et al., 2007; Velichko et al., 2009b; Sotnikova and Titov, 2009). In addition, a common way to establish the age of LPS horizons is based on stratigraphic correlations with previously dated paleosols known from regions farther north on the East European Plain (Dlussky, 2007; Chen et al., 2018a; Sycheva et al., 2020), or *via* patterns in the mineral magnetic characteristics of the LPS in the Black Sea and Azov Sea region (Dodonov et al., 2006; Velichko et al., 2009b; Panin et al., 2018). The latter approach of using magnetic variation in stratigraphic correlation is also widely applied elsewhere in Europe, such as the Danube Basin region (Buggle et al., 2009; Fitzsimmons et al., 2012; Marković et al., 2015; Sümegi et al., 2018) and the East European Plain (Rutter et al., 2003; Velichko et al., 2006; Hlavatskyi and Bakhmutov, 2020).

Generally, there are several stratigraphic models based on associations with marine isotope stages (MISs) that have been accepted in LPS records of the East European Plain. For detailed comparisons between these models see the illustrations in Velichko et al. (2011) and Zastrozhnov et al. (2018). It is worth noting that significant differences arise in the period between MIS 13 and 5 as a result of the unsatisfactory absolute chronology, as such the differences in models during the Late Pleistocene depends on choice paleosol corresponding to MIS 5 (**Table 1**). In addition, the nomenclatures for paleosol and loess at different horizons were usually derived from local place names or different research groups (**Table 1**), resulting in confusion and making correlation between sections difficult. These nomenclatures developed independently of one another and are substantially limiting for further research where these sequences are put into a wider context (Schaetzl et al., 2018; Krijgsman et al., 2019).

The existing loess stratigraphy of Azov Sea region was developed to a great extent based on a correlation between paleosols of the Azov Sea region and general stratigraphic schemes of East European Plain. As a consequence, there is inevitably the same challenge as witnessed in the general stratigraphic schemes of East European Plain. However, in spite of the difficulties mentioned above, it is still possible to establish a reliable stratigraphic model for LPS in the Azov Sea region. Supported by additional chronological approaches such as radiocarbon and luminescence dating, the record of alternation between loess and paleosol, clearly represented by multiple proxy variations including physical and geochemical parameters, allows for direct inter-section correlations from the Central Russian Upland to the Black/Azov Sea region. For instance, Chen et al. (2018a, b) applied optically stimulated luminescence (OSL) dating combined with magnetic susceptibility (MS) variations to develop a preliminary stratigraphic framework on two sections of the Azov Sea.

Moreover, a general succession of the Azov Sea area environmental changes at different timescales has been revealed by multiple paleoclimate proxy records from Azov LPS including MS and grain size (GS) variations (Velichko et al., 2009a; Liang et al., 2016; Chen et al., 2018b; Timireva et al., 2021), mammal faunal composition (Tesakov et al., 2007; Velichko et al., 2009b; Markova and Vislobokova, 2016), pollen and diatom assemblages (Matishov et al., 2013), and paleosol macro- and micromorphology (Panin et al., 2018). This integrated approach using multiproxy records has resulted in considerable progress in the understanding of paleoenvironmental changes recorded in the loess of the Azov Sea area despite being embedded in the poorly defined chronostratigraphy.

As such, it is now essential to better revisit the LPS chronostratigraphy of the Azov Sea region, hopefully providing opportunities not only to develop accurate past environmental reconstruction in the region but also to develop a complete and unified stratigraphic model that is comparable across loess of the whole European continent. The main purpose of this study is therefore to further refine the LPS stratigraphy of the Azov Sea region using a combined approach that involves reevaluation of previous absolute dating results and comparison of new climate proxies, mainly focusing on the Late Pleistocene and Holocene. It is then followed by a reconstruction of past environmental dynamics. Moreover, we followed the loess and soil stratigraphic nomenclature that has been already well accepted for Chinese and Danubean loess stratigraphy (Kukla and An, 1989; Marković et al., 2015; Schaetzl et al., 2018) and chose two representative sections that are located in different areas of the Azov Sea. The adoption of the refined chronostratigraphic scheme here offers potential for providing an important link to other regional LPS, even across the whole European continent, supporting a key record for comparison of the Black/Azov Sea Quaternary stratigraphy with the Danube loess model, and enabling better understanding of temporal and

TABLE 1 | Existing loess stratigraphic models with different nomenclatures on the East European Plain and correlations with L&S (loess and soil) stratigraphic nomenclatures initially presented by Kukla and An (1989) and marine isotope stages (MISs) since the Late Pleistocene.

Epoch	**Glacials and Interglacials**		**Black/Azov Sea region**	**Central Russian**	**Ukrainian Dnieper**	**Lower Volga region**		**L&S scheme**		**MIS**
			(Velchko. (1990); Velchko et al. (2011); Velchko et al. (2017))	**(Sycheva et al. (2020))**	**(Gerasimenko. (2006); Buggle et al. (2009))**	**(Zastrozhnov et al. (2018); Zastrozhnov et al. (2020))**		**(Kukla and An. (1989))**		
Holocene			Holocene S	Holocene S	Holocene S	Novocaspian S		S_0		1
Late Pleistocene	Last Glacial	Valdai Glacial	Altynovo L Trubchevsk S Desna L	Late Valdai L	Prychernomorsk L Dofinivka S Bug L	Khvalyn Horizon	Upper Khvalyn L	L_1	L_1LL_1	2
			Bryansk S	Bryansk S Tuskar’ L Aleksandrov S	Vytachiv S		Lower Khvalyn S		L_1SS_m	3
			Khotylevo L	Selikhovodvor L	Uday L	Atel L			L_1LL_2	4
	Last Interglacial			Streletsk S	Pryluky S	Upper Khazar S		S_1	S_1SS_1	5a
				Mlodat’ L					S_1LL_1	5b
			Krutitsa S	Kukuevo S					S_1SS_2	5c
			Sevsk L	Seim L	Tyasmin L				S_1LL_2	5d
		Mikulino Interglacial	Salyn S	Ryshkovo S	Kaydaky S				S_1SS_3	5e

spatial variability in environmental changes during the Late Quaternary (Marković et al., 2015; Sümegi et al., 2018).

STUDY AREA

The Azov Sea (45°~47°N, 35°~39°E) is one of the smallest seas in the world, with an average depth of 7 m up to a maximum value of 14 m, as well as a water surface area of 39,000 km^2 and water volume of 290 km^3 (Kosarev et al., 2007). It is an internal sea connected with the Black Sea *via* the narrow (up to 4 km) and shallow (up to 15 m) Kerch Strait (**Figure 1**). There are two primary rivers feeding into the sea, the Don and Kuban rivers, which account for more than 90% inflow volume. In the northeast, the largest bay, the Taganrog Gulf, penetrates into the land and coincides with the delta of the Don river. In the southeast, the Kuban river has vast alluvial plains and numerous channels extending over several tens of kilometers.

The present-day climate of the Azov Sea is temperate-continental, with distinct seasonality and occasional dry periods. It is characterized by mild and cold winters and warm, relatively dry summers. Easterly and northeasterly winds with speeds of 4–7 m s^{-1} and up to a maximum value of 15 m s^{-1} prevail in the autumn–winter period due to influence of a spur of the Siberian High anticyclone (Kosarev et al., 2007). The mean January temperature ranges from −5°C to 0°C (Matishov et al., 2013). In the spring–summer period, there are occasionally west and southwest winds with speeds of 4–6 m s^{-1} resulting from Mediterranean cyclonic systems passing over the sea. The mean monthly temperature in July is 22°C –24°C (Matishov et al., 2013). The Azov region receives, on average, ~580 mm of precipitation annually, which is unevenly distributed over the year. It can reach up to ~120 mm per month in winter (December, January) and early summer (May, June), compared with ~30 mm or more in other months (Panin et al., 2018). Such a climatic context develops a typical vegetation assemblage and steppe environment, which is presently dominated by stipa and sheep fescue (Matishov et al., 2013).

MATERIALS AND METHODS

Section Description and Sampling

The most extensive loess deposits are along the coastal area of the Azov Sea, in particular, the Taganrog Gulf. The Beglitsa (47°07′38″N, 38°30′56″E) and Chumbur-Kosa (46°57′48″N, 38°56′47″E) loess sections under study are situated on the northern and southern shores of the Taganrog Gulf, respectively (**Figure 1**). The Beglitsa section has an outcrop thickness of approximately 14 m, compared with ~16 m of the Chumbur-Kosa section. Both sections have several visible paleosols intercalated by loess horizons (**Figure 1**). Detailed pedostratigraphic descriptions and main paleosol macro- and micromorphology features for the two sections are presented by Chen et al. (2018a, b) and Panin et al. (2018). Bulk samples were collected continuously at 2-cm intervals for the Beglitsa and 5-cm intervals for the Chumbur-Kosa from the top to the base of the section, respectively. These samples were then used for physical and geochemical analyses, as outlined below.

Climate Proxies and Measurement Methods

Generally, the cyclicity of alternating high and low MS values between paleosols and loess units is indicative of the intensity of soil forming processes between Interglacial (interstadial) and Glacial periods, likely as a result of the pedogenetically formed fraction of fine ferrimagnetic minerals yielding higher MS values for paleosols in relation to loess units (Zhou et al., 1990; Maher et al., 2003). Thus, trends in MS are often used for establishing

FIGURE 1 | Study region and location of the investigated loess–paleosol sequences (LPSs) in this study indicated with red solid circles and other important LPSs mentioned in the main text represented by red solid rectangles. Photographs of the studied LPS sections are also shown.

magnetostratigraphy in European loess (Basarin et al., 2014; Song et al., 2018) and considered as reliable paleoclimate proxies to directly reflect climatically controlled soil formation variations (e.g., Buggle et al., 2014; Necula et al., 2015). Especially, the $\chi_{fd}\%$ is a main magnetic parameter that has been widely applied in MS as a sensitive indicator of ultrafine magnetic grains, increasing amounts of which also influence χ_{lf} (Dearing et al., 1996). In this study, the MS was measured at frequencies of 0.47 and 4.7 kHz in a static field of 300 mA m^{-1} using a Bartington MS2 susceptibility meter. Final MS is calculated from three measurements and expressed as low-frequency (0.47 kHz, χ_{lf}) and high-frequency (4.7 kHz, χ_{hf}) mass-specific MS in $m^3\,kg^{-1}$. In addition, the frequency-dependent MS ($\chi_{fd}\%$) was also determined as $\chi_{fd}\% = (\chi_{lf} - \chi_{hf})/\chi_{lf} \times 100\%$.

GS is a complex but important proxy in LPS for the reconstruction of eolian processes and wind circulation patterns, providing insights into characterizing different transport dynamics and relating to different depositional environments (Vandenberghe, 2013; Újvári et al., 2016; Chen et al., 2020). The GS was measured on a Malvern Mastersizer 2000 laser particle analyzer with a measurement range of 0.02 µm–2 mm. Bulk samples of 0.5 g were pretreated with successive procedures such as organic matter oxidation, carbonate dissolution, and particle dispersion prior to measurement. Clay is represented with grain size smaller than 5 µm since there is potential underestimation by the laser diffraction method in comparison with the traditional pipette method (Konert and Vandenberghe, 1997; Beuselinck et al., 1998). This is also in agreement with other published clay fractions in southeastern European loess sections (Obreht et al., 2014; Bösken et al., 2019; Chen et al., 2020). Fine silt is then expressed from 5 to 20 µm, coarse silt from 20 to 50 µm, and sand greater than 50 µm, respectively.

As the most visible difference between loess and paleosol in the field, changes in color are regarded as the most striking features of LPS. Thus, variations in color index have been commonly used to characterize different loess/paleosol horizons and further related to the intensity of pedogenesis in a more quantitative way (Basarin et al., 2011; Buggle et al., 2014; Panin et al., 2018). For measurements, dried and homogenized sediment samples were used to determine the color index using a X-Rite 948 spectrophotometer under standardized observation conditions (10° Standard Observer, 8 mm aperture, Illuminant C). Measured values were then represented in the form of the lightness, redness, and yellowness using the CIELAB color system (L*, a*, b*).

The carbonate content ($CaCO_3$%) and the total organic carbon content (TOC) can also be used as environmental proxies in LPS studies since they are indicative of physical–chemical characteristic variation between loess and paleosol horizons under different climate conditions (Velichko et al., 2009a; Basarin et al., 2011; Liang et al., 2016). In the present study, the $CaCO_3$% was measured using the calcimeter method of Bascomb (1961). Pretreatment procedure is the same as described by Fang et al. (1999). Due to the difficulty in separating the relative content of primary and secondary carbonate, it is important to note that the carbonate content includes both here. The TOC was determined by using the H_2SO_4–K_2CrO_7 oxidation method, following the procedure of Zhou et al. (1996).

As these climatic proxies with broadly accepted environmental significance and widely adopted in European loess (e.g., Bokhorst et al., 2011; Rousseau et al., 2011; Vandenberghe, 2013; Marković et al., 2015; Zeeden et al., 2016), we, hence, measured the MS, GS, soil color (L*, a*, b*), $CaCO_3$%, and TOC to better characterize loess/paleosol horizons and reveal paleoclimatic and paleoenvironmental conditions in the Azov Sea region. All climatic proxies above were measured at the College of Earth and Environmental Sciences, Lanzhou University. Data analyses were implemented at both the School of Geography, South China Normal University, and the Department of Earth Sciences, Uppsala University.

RESULTS

Combined with OSL ages and MS variations, Chen et al. (2018a, b) developed preliminary stratigraphic schemes for these two sections extending over the last full Glacial–Interglacial cycle (**Supplementary Figure S1**). However, this chronostratigraphy still needs to be further refined due to adopting several suboptimal ages that might exceed the upper limit of quartz OSL dating range and only individual MS proxy correlation. Detailed discussion on maximum age of quartz OSL dating and methodological errors of the dating procedure responsible for potential underestimation of these ages can be found in Chen et al. (2018a). Even so, the initial results showed that the whole ~11 m of the Beglitsa section formed since marine isotope stage (MIS) 5 (Chen et al., 2018a), while only the upper ~5 m of the Chumbur-Kosa section corresponds to the same period (Chen et al., 2018b). For better comparison, we, hence, present here the whole 14 m of the Beglitsa section and the upper 6 m of the Chumbur-Kosa section for investigation, which both covers the Holocene soil, the entire sequence of Last Glacial loess, the entire sequence of Last Interglacial soil complex, and the very upper part of the penultimate Glacial loess.

The χ_{lf} varies along the section between 4.12 and $58.46 \times 10^{-8}\ m^3\ kg^{-1}$ (average $21 \times 10^{-8}\ m^3\ kg^{-1}$) in Beglitsa and between 9.13 and $39.26 \times 10^{-8}\ m^3\ kg^{-1}$ (average $22.43 \times 10^{-8}\ m^3\ kg^{-1}$) in Chumbur-Kosa, respectively. In addition, the average χ_{fd}% is 6.82% in Beglitsa and 5.39% in Chumbur-Kosa. The MS record of two sections generally follows the pedostratigraphy, being enhanced in the paleosols compared with the loess units (**Figure 2**). However, there are also some stratigraphic paleosols that are visually discriminated in the field, while χ_{lf} and χ_{hf} do not significantly increase, such as depth intervals of 9.0–8.3 and 4.5–3.2 m of the Beglitsa section (**Figure 2**). This perhaps implies varying control on MS enhancement in the Beglitsa section.

Contents of fine silts (5–20 μm) range from 26.41% to 66.58% in Beglitsa and from 36.07% to 66.26% in Chumbur-Kosa, then followed by coarse silt, clay, and sand fractions (**Figure 3**). Similarly, variations of median grain size (MGS) are 10.75–42.53 μm (average 16.55 μm) in Beglitsa and 11.27–23.92 μm (average 16.05 μm) in the Chumbur-Kosa section (**Figure 3**). Both sand content and MGS are relatively stable except for some intervals featuring a marked peak, such as the sand horizon of the Beglitsa section and lower part around depth 5.5 m of the Chumbur-Kosa section (**Figure 3**). It is worth noting that the maximum MGS value in Beglitsa is much larger than that in Chumbur-Kosa due to the occurrence of this sand layer at a depth of 12.5–13.0 m of the Beglitsa section (**Figure 3**). In addition, the GS variations of two sections show little clear and consistent relationship to pedostratigraphy.

Three proxies (L*, a*, and b*) of color index show obvious variations that broadly match the pedostratigraphy of two sections, lightness L* in particular. This proxy (L*) generally exhibits lower values in paleosols and higher values in the intervening loess units, contrary to variations in MS (**Figure 4**). Values of L* for two sections fluctuate between 33.24 and 69.89 (Beglitsa), and 28.92 and 48.69 (Chumbur-Kosa), respectively. Notably, distinct fluctuations in L*can be observed approximately at a depth of 4 m at the Beglitsa section, compared with the subtle change in χ_{lf} and a* proxies at the same depth (**Figure 4**). It probably shows the sensitivity of this proxy to climate oscillations and potential to distinguish subordinate loess/paleosol horizons. Both a* and b* show broadly similar trends at the two sections (**Figure 4**).

With an average content of 12.59% for Beglitsa and 10.44% for Chumbur-Kosa over the whole sections in this study (**Figure 5**), $CaCO_3$% shows several obvious peaks and troughs oscillations at two sections. The lowest $CaCO_3$% interval (generally <10%) can be found within the paleosol at a depth of 6.4–5.5 m of the Beglitsa section, while a relatively higher $CaCO_3$% (generally >10%) content is observed within the paleosols at depths of 9.0–8.3 and 8.0–7.0 m. These two enriched $CaCO_3$% intervals within paleosols are even higher than those in the upper 6 m of loess horizons of the Beglitsa section (**Figure 5**). This

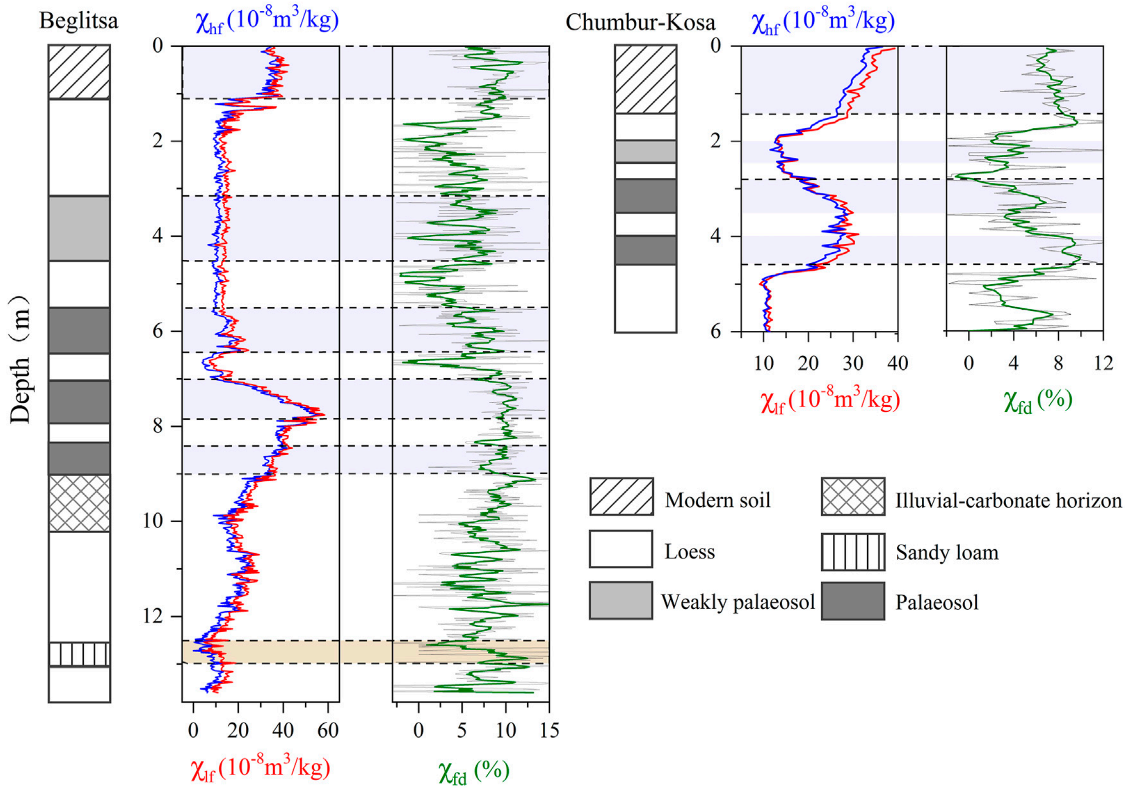

FIGURE 2 | Magnetic susceptibility(MS) variations in the Beglitsa and Chumbur-Kosa sections. The blue line represents χ_{hf}, the red line denotes χ_{lf}, and the green line is indicative of χ_{fd}%, respectively (the χ_{fd}% data have been smoothed by five points using adjacent-averaging method).

phenomenon is probably caused by high precipitation leading to carbonate leaching from the above paleosol or loess horizons (Liang et al., 2016). Additionally, TOC proxy also manifests peaks (paleosol) and troughs (loess) along the pedostratigraphy (**Figure 5**). In general, these two proxies are in good agreement with pedostratigraphy.

DISCUSSION

Refined Chronostratigraphy of Two Loess–Paleosol Sequence Sections at the Azov Sea

Figures 6 and **7** shows the refined chronostratigraphies of Beglitsa and Chumbur-Kosa sections, and correlations with the benthic LR04 stack records from Lisiecki and Raymo (2005). We here include further climatic proxies to better constrain the refined chronostratigraphy of these two sections. These new data enable constraints on the LPS sub-horizon phases, and correlations with Quaternary climate change archives and marine oxygen isotope stratigraphy.

The Last Interglacial Soil Complex

There is one interval of strongest MS enhancement (9.0–5.5 m) located in the middle of the MS curve compared with the surrounding MS values showing a clear baseline at the Beglitsa section (**Figures 2** and **6**). Three well-developed paleosols (i.e., S_1SS_3, S_1SS_2, and S_1SS_3) are also observed within this interval (**Figure 1**). By contrast, the L* and $CaCO_3$% proxy shows clearly opposing variations compared with χ_{lf} over the same interval. Similarly, other climate proxies, such as the clay content and TOC content, all exhibit peak and trough oscillations during this interval, although not as obviously as shown in the L* and $CaCO_3$% proxies (**Figure 6**). These variable climate proxies between depths of 9.0 and 5.5 m at the Beglitsa section suggest instability of climatic conditions during this period and potential for subdivision within this paleosol.

There are ages older than 80 ka reported from the middle of the most enhanced MS interval and the underlying carbonate horizon (Chen et al., 2018a). In addition, two minimum OSL ages of 203.8 ± 18.0 and 147.1 ± 12.2 ka were obtained from the lowermost part of the sand layer (depth interval 13–12.5 m) and the base of the overlying loess unit, respectively (**Figure 6**). It is likely that quartz OSL ages are underestimated when equivalent doses exceed 200 Gy due to (near) saturation of the quartz OSL signal (Murray et al., 2007; Timar-Gabor et al., 2015). Thus, potential age underestimation may occur at lower layers of the Beglitsa section (Chen et al., 2018a). Similarly, a minimum feldspar IRSL age of 204 ka by Pilipenko et al. (2005, 2011) was reported from the middle of sand horizon (corresponding to

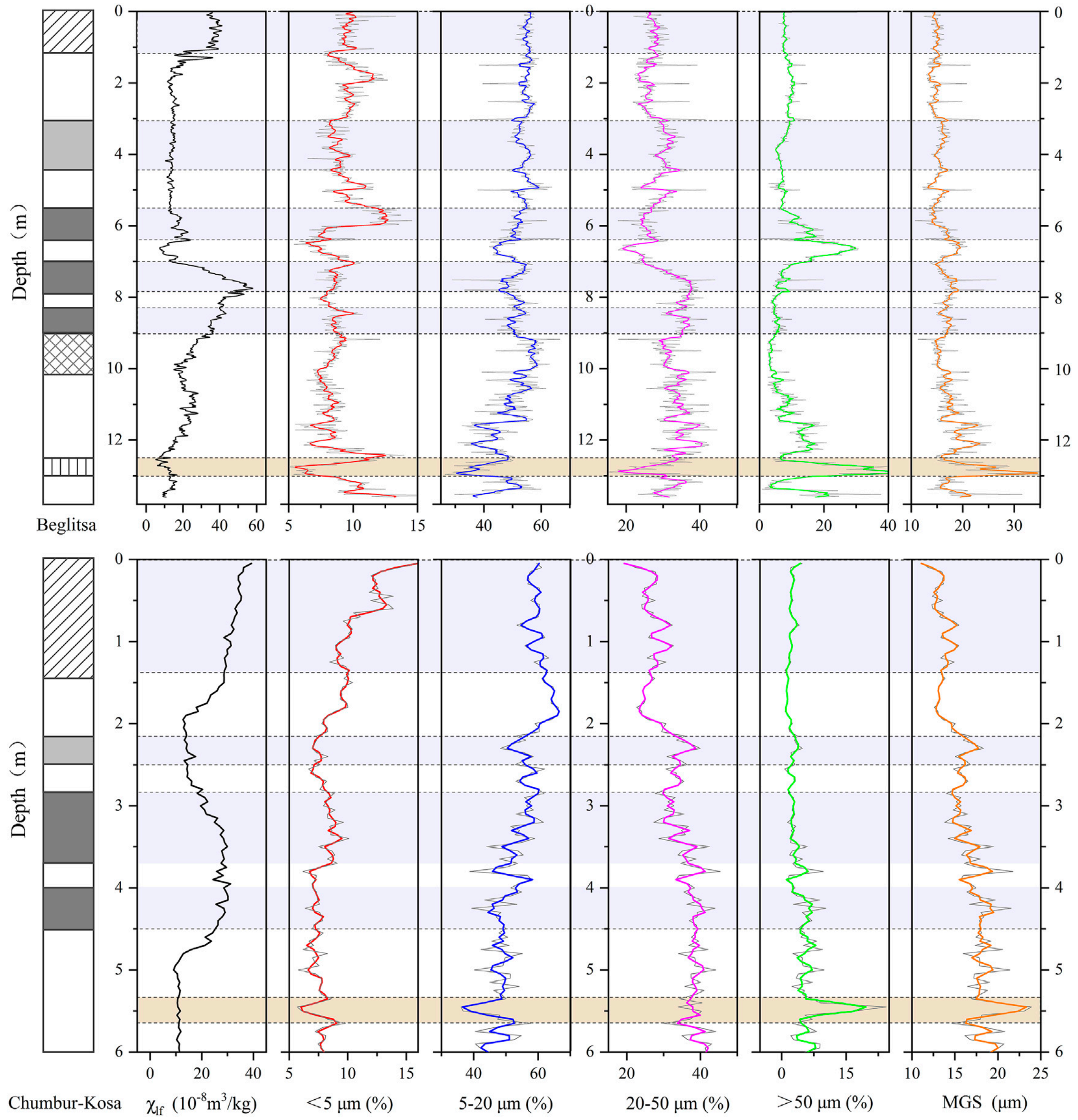

FIGURE 3 | Variations in different grain size (GS) fractions and median grain size (MGS) of the Beglitsa and Chumbur-Kosa sections against χ_{lf} (all GS data have been smoothed by five points using adjacent-averaging method).

the sand layer in our Beglitsa section) of the Pekla section, which is located on the northwestern part of the Taman Peninsula between the Black Sea and Azov Sea (**Figure 1**). Even though probably underestimated, these previous luminescence ages are still important in constraining the formation of lower stratigraphic levels of these sections, especially for the distinctive sand horizons. The deposition time of the sand horizon of Beglitsa section was at least confined to older than MIS 5. Moreover, similar sand horizons of Beglitsa and Pekla were also found at the lower part of Chumbur-Kosa in the form of high MGS and sand fraction content (**Figure 3**). The existence of this sand horizon at these sections that are all located on the Azov Sea coast probably indicates a widespread and distinct marine transgressive/regressive event. We, therefore, ascribed it to the uppermost Uzunlarian phase of the Black Sea, based on stratigraphic position and properties of these sandy deposits, which is correlated to the MIS 6 (Krijgsman et al., 2019).

From the above results, we correlate the enhanced MS interval above the sand horizon with MIS 5. In addition, a precipitous decrease in the $CaCO_3$% and L* proxy from the carbonate horizon to overlying substratum S_1SS_3 was observed at a depth of around 9 m, facilitating the identification of the lower boundary for this prominent paleosol complex (**Figure 6**). Thus, we attribute this lowermost S_1SS_3 of the main paleosol to the substage of MIS 5e.

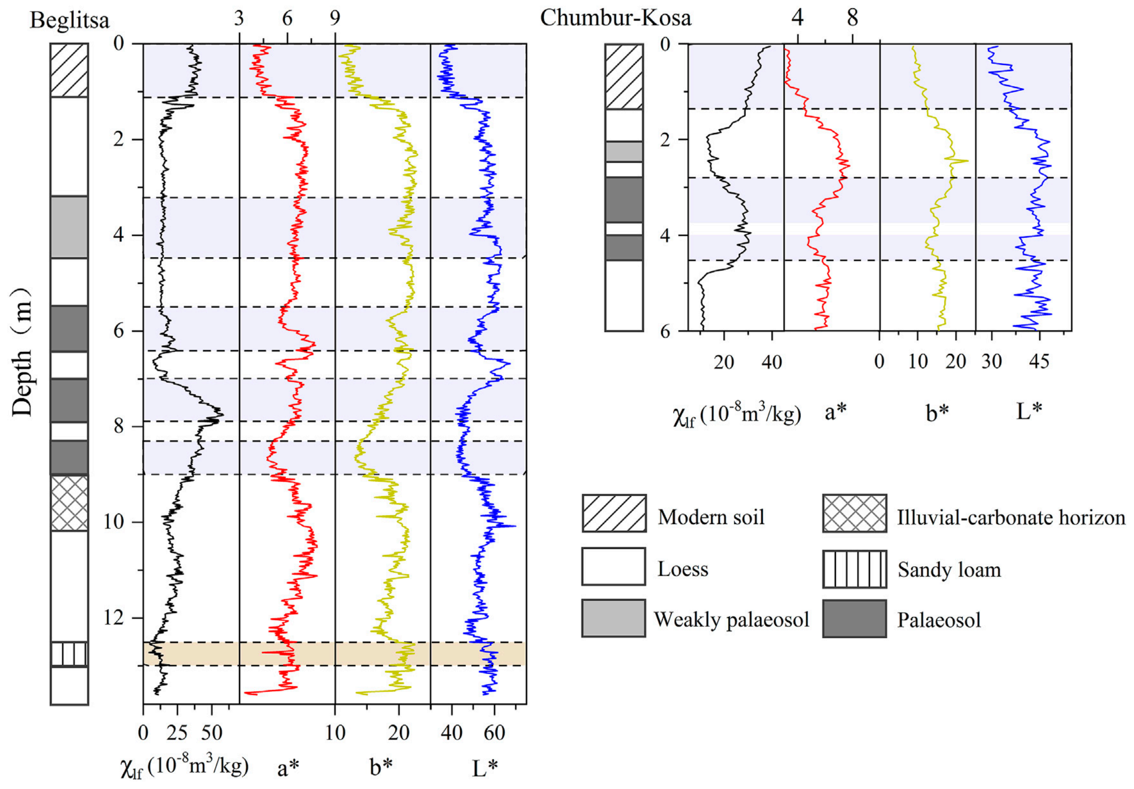

FIGURE 4 | Color index (L*, a*, b*) against the χ_{lf} variations in the Beglitsa and Chumbur-Kosa sections.

In the middle of this enhanced MS interval (i.e., S_1SS_2), the MS values reach a maximum, while L* and $CaCO_3$% show typical troughs with variations being very similar to the underlying substratum S_1SS_3 (**Figure 6**). Together with the previously published OSL age of 82.0 ± 7.4 ka in the upper part of S_1SS_2 as well as its stratigraphic position, we allocate this distinctive substratum, characterized by the highest MS and lowest L*values, to the substage of MIS 5c.

The uppermost subunit S_1SS_1 of the enhanced MS interval is distinguished by a weak increase in MS and TOC, a sharp increase in the clay content for the upper horizon, and relatively low L* and $CaCO_3$% values (**Figure 6**). A previously reported radiocarbon age of 29,340 ± 1,500 a (calibrated age of 34.07 ka) by Velichko et al. (2017) and an OSL age of 55.3 ± 4.9 ka by Chen et al. (2018a) were basically obtained at the same depth from this unit. These two ages made it difficult to determine the formation time of this unit, resulting in stratigraphic inconsistency. Velichko et al. (2017) referred this unit to MIS 3 and correlated it with reference sections in the center of the East European plain (Chen et al., 2018a). However, recent stratigraphic comparison of key sections based on litho- and pedostratigraphy, MS, GS, elemental and mineral composition, and luminescence dating in western Ciscaucasia (Azov Sea region and Stavropol Upland) showed that the three phases of soil formation within the S1 pedocomplex are probably a regional pattern and approximately corresponding to the warm stages within MIS 5-5a, 5c, and 5e (Mazneva et al., 2021). In addition, a detailed study of the depositional environment and pedostratigraphy on three paleosols of the MIS 5 pedocomplex of the Srednaya Akhtuba section was also conducted in nearby Lower Volga region further east of Azov Sea, with OSL ages ranging from 112.6 ± 5.4 to 68.3 ± 4.2 ka (Makeev et al., 2021). Especially the age of 68.3 ± 4.2 ka, obtained from the loess unit overlying the uppermost paleosol (corresponding to the S_1SS_1 in our Beglitsa section) of three soils (Yanina et al., 2017), is much older than the previously reported radiocarbon and OSL ages from the S_1SS_1 of the Beglitsa section. Thus, Mazneva et al. (2021) argued that the S_1SS_1 of the Beglitsa section is likely to be formed during MIS 5a rather than MIS 3.

Bioturbation in soils, reworked sediment mixing, or pedogenic overprinting may limit capacity for precisely dating soils using radiocarbon or luminescence, leading to depositional age underestimation and frequent age inversions (Stevens et al., 2006; Stevens et al., 2007). Thus, one possible explanation for producing these inconsistent ages at the uppermost subunit S_1SS_1 of the prominent paleosol complex is probably a consequence of intensive post-depositional pedogenic alteration (e.g., bioturbation) that leads to rejuvenation of the upper layer of S_1SS_1 due to bleaching of the luminescence signal and possible incorporation of older or younger carbon by mixing or excavating activities near this main paleosol surface (e.g., Bateman et al., 2003; Wang et al., 2003). The highest proportions of <5-μm fractions in the upper horizon of S_1SS_1 also hints at the more intense chemical weathering following pedogenetic overprinting

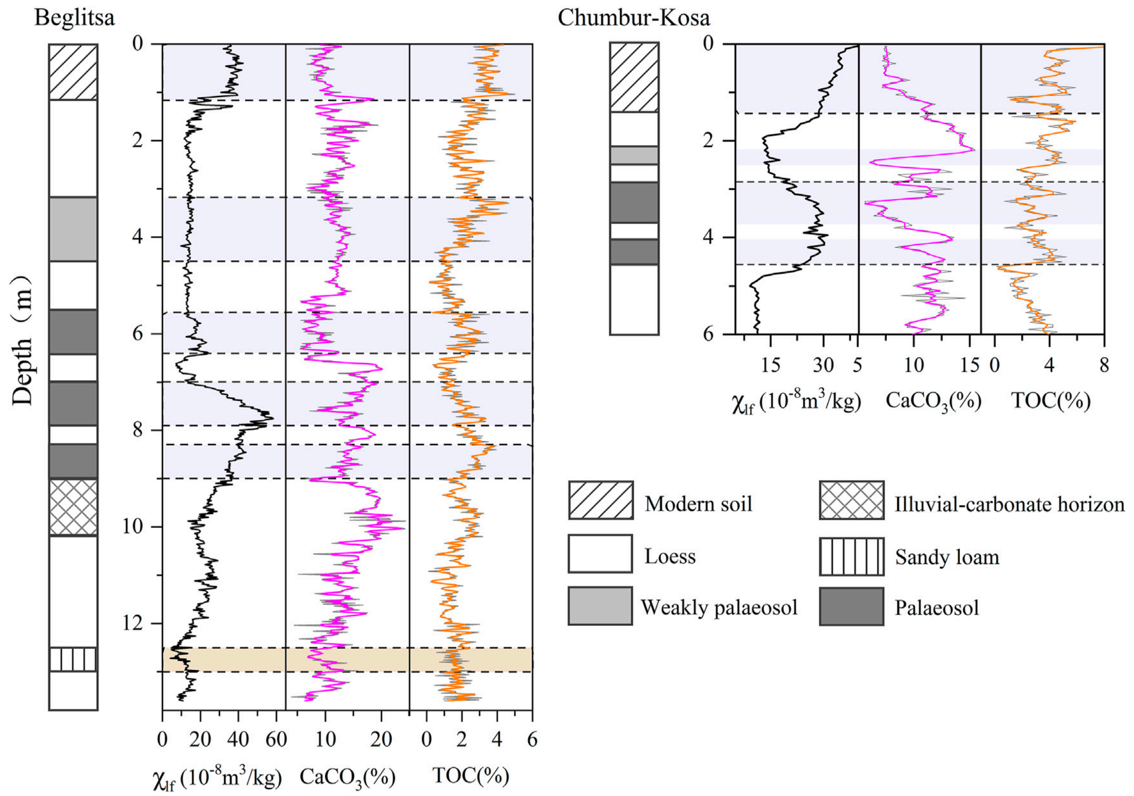

FIGURE 5 | $CaCO_3$% and total organic carbon content (TOC) proxies against χ_{lf} variations in the Beglitsa and Chumbur-Kosa sections (the $CaCO_3$% and TOC data have been smoothed by five points using adjacent-averaging method).

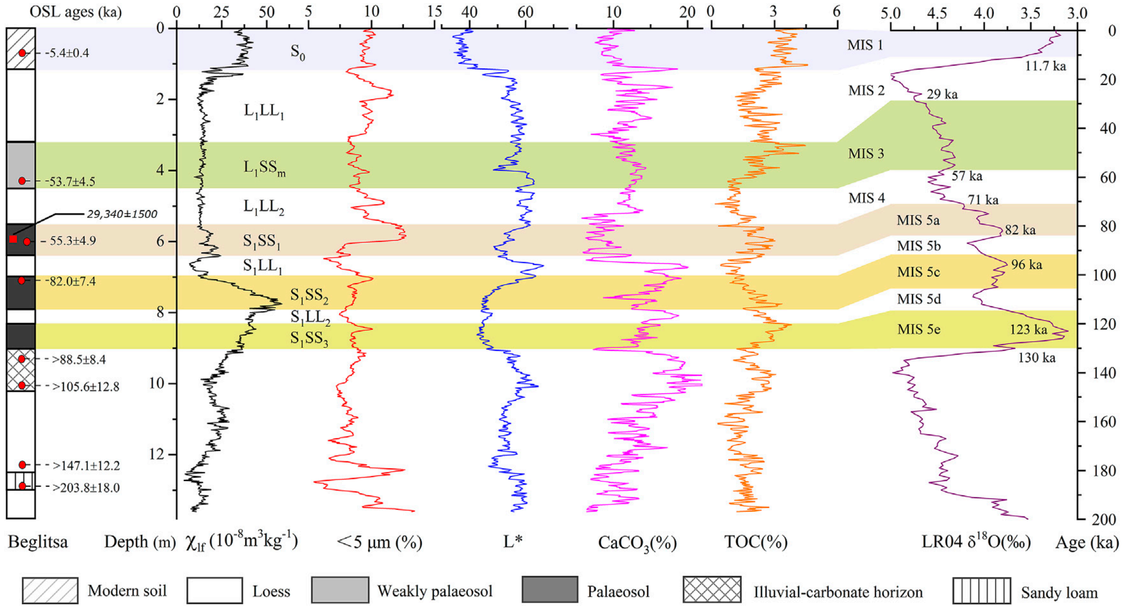

FIGURE 6 | Refined chronostratigraphy of the Beglitsa section with published luminescence and radiocarbon ages, together with multiple climate proxies (the χ_{lf}, <5 μm, L*, $CaCO_3$%, and TOC), and its correlation with benthic LR04 stack records from Lisiecki and Raymo (2005). Note that optically stimulated luminescence (OSL) and radiocarbon ages obtained by different researchers are illustrated with different forms: the red solid rectangle indicating radiocarbon age is derived from Velichko et al. (2017), and the red solid circles indicating luminescence ages are derived from Chen et al. (2018a).

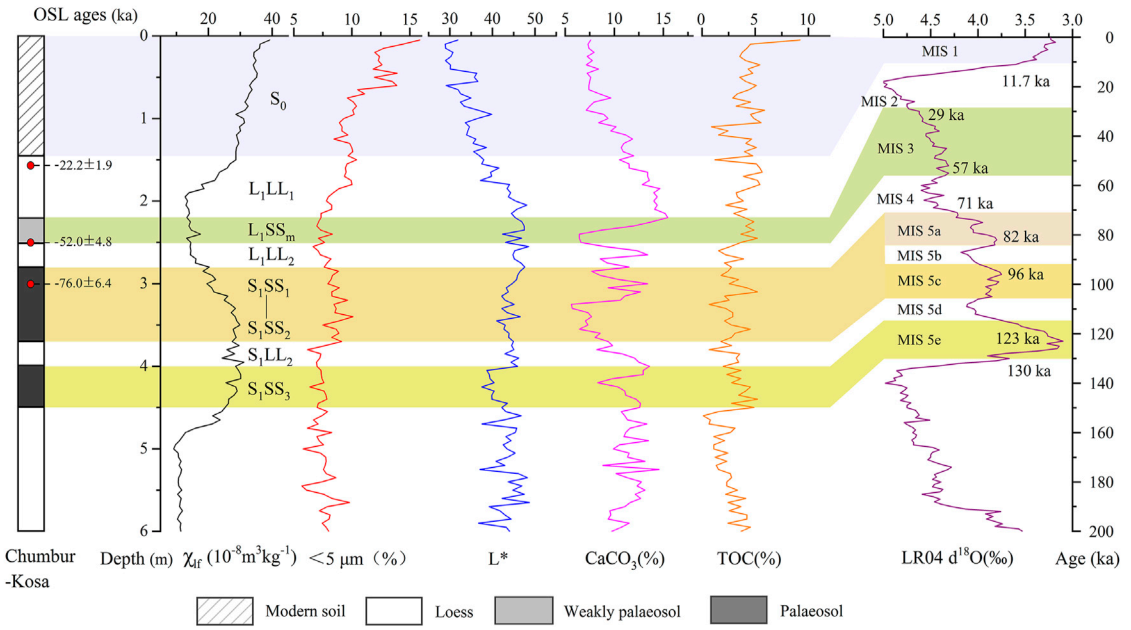

FIGURE 7 | Refined chronostratigraphy of the Chumbur-Kosa section with luminescence ages and multiple climate proxies (the χ_{lf}, <5 µm, L*, $CaCO_3$%, and TOC), and its correlation with benthic LR04 stack records from Lisiecki and Raymo (2005). The quartz OSL ages are derived from Chen et al. (2018b).

than the lower horizon of S_1SS_1 (**Figure 6**), which supports the aforementioned assertion. The previous ages obtained from the upper horizon of S_1SS_1 may not represent the true burial time of this uppermost substratum of the S_1 complex. Given its position in the stratigraphy and soil characteristics, we tend to correlate the S_1SS_1 with MIS 5a, which is consistent with stratigraphic correlation by Mazneva et al. (2021) but different from the previous study by Velichko et al. (2017) and Chen et al. (2018a).

Based on MS variations, **Figure 8** shows a stratigraphic correlation of the S_1 paleosol between the Beglitsa and other loess records on the East European Plain (Buggle et al., 2009; Hlavatskyi and Bakhmutov, 2020). This correlation is further compared with the high-resolution MS record through a luminescence-based chronostratigraphy from the Weinan section in China (Kang et al., 2011; Kang et al., 2013) and the benthic oxygen isotope stack (Lisiecki and Raymo, 2005). Except for the difference in sedimentary thickness and values within three well-developed paleosols, such a good consistency and correlation over the Eurasian continent supports the accuracy of the stratigraphic subdivision on S_1 for the Beglitsa section and correspondence of the substrata of S_1 with MIS 5a-e.

As for the Chumbur-Kosa section, a previous study has identified the prominent paleosol complex at 4.5–2.8 m below the modern top surface yielding MS values as high as those of the modern soil (Chen et al., 2018b). An OSL age of 76.0 ± 6.4 ka positioned in the uppermost part of this enhanced MS interval suggests this paleosol corresponds to the Late Last Interglacial complex, and probably can be assigned to the Late MIS 5 (Chen et al., 2018b). Moreover, there are two MS peaks with a dominant lower peak typically noted in the curve of χ_{fd} (**Figure 2**), denoting stronger intensity of soil-forming processes compared with the upper one. By contrast, two troughs with an intercalating sharp peak in $CaCO_3$% are observed within this interval, showing an opposing variation compared with χ_{fd} (**Figure 5**). Other climate proxies also show peak and trough oscillations within the S_1, although not as distinct as the χ_{fd} and $CaCO_3$% (**Figure 7**).

Due to limited luminescence ages obtained from the Chumbur-Kosa section, we have relied primarily on additional climate proxies and stratigraphic correlation with other well-dated loess sections near the Black–Azov Sea region to achieve the subunit identification within S_1 (**Figure 9**). The MS pattern of S_1 corresponding to the twin peak association and correlating to the MIS 5 can be found elsewhere of southeastern Europe. For instance, in the Kurortne section in the Black Sea Lowland of Southern Ukraine, the MIS 5 paleosol is presented by the two pedogenetic levels: Kaydaky paleosol (MIS 5e) and Pryluky paleosol (MIS 5a-c) and characterized by well-developed humus and high MS values (Tecsa et al., 2020). On the Black Sea shore of Romania (such as the Mircea Voda and Costinesti sections), the MIS 5 pedocomplex is composed of two strongly developed paleosols and covered by relatively unweathered loess deposits of MIS 4 (Constantin et al., 2014; Necula et al., 2013, Necula et al., 2015). It has been shown previously that a loess unit occurs rarely in the upper part of S_1 (or it has a very small thickness) probably due to low sediment accumulation rates and substantial transformation by soil-forming processes at a later stage; thus, the S_1SS_1 and S_1SS_2 paleosols are occasionally superimposed on each other and without an intercalating loess unit (**Figure 7**) (Hlavatskyi and Bakhmutov, 2020; Tecsa et al., 2020). At Chumbur-Kosa section, a sharp increase in the $CaCO_3$% within the upper MS peak of S_1 might indicate the presence of less altered loess material, although not enough to

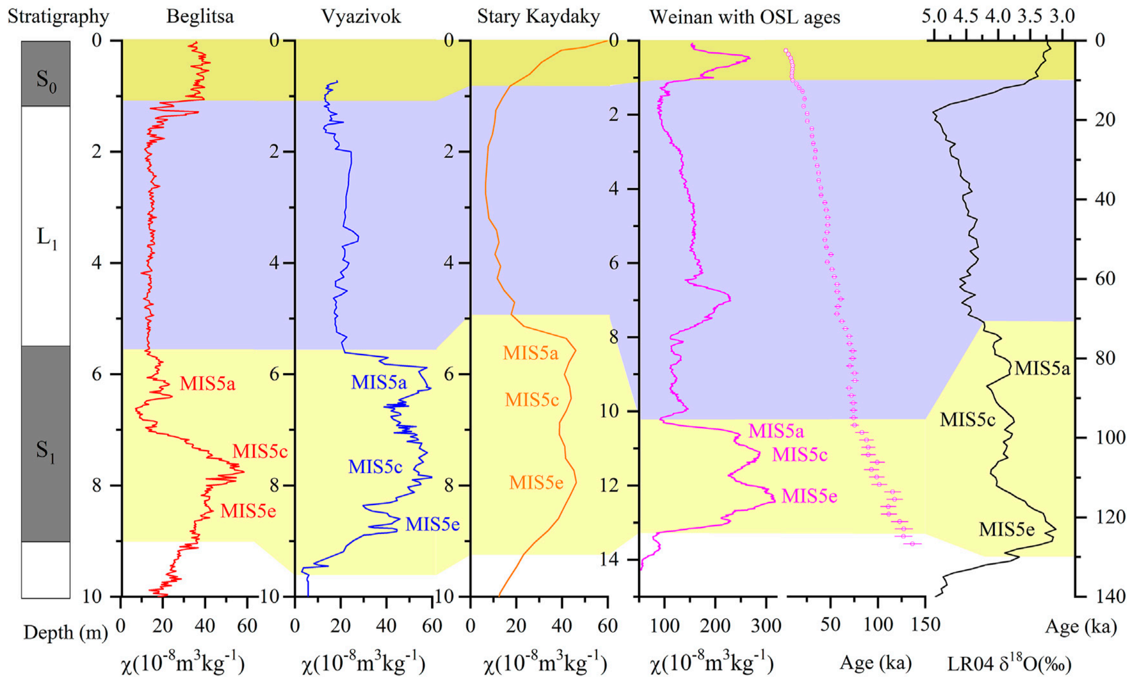

FIGURE 8 | Stratigraphy of the Beglitsa section and its correlation with other loess records on the East European Plain and CLP based on the χ_{lf} proxy, and with the benthic LR04 stack. Vyazivok, Ukraine (Hlavatskyi and Bakhmutov, 2020); Stary Kaydaky, Ukraine (Buggle et al., 2009); Weinan, China (Kang et al., 2011, 2013); and the benthic LR04 stack (Lisiecki and Raymo, 2005). For location of sections on the East European Plain, please refer to **Figure 1**.

form a loess unit due to overprinting by post-depositional pedogenic processes (**Figure 7**). In view of this, we followed this stratigraphic subdivision for the S_1 of the Chumbur-Kosa section according to its lithological facies and pedological characteristics, with previously independent ages providing stratigraphic control. That is, the depth interval of 4.5–4.0 m correlates with MIS 5e, and the depth interval of 3.7–2.8 m belongs to MIS 5a-c with the bracketing depth interval of 4.0–3.7 m corresponding to MIS 5d (**Figure 7**).

The Last Glacial Loess

The most substantial difference from the previous stratigraphy at the Azov Sea loess proposed in Chen et al. (2018a, b) in this new chronostratigraphy is the Last Glacial loess (L_1) subdivision. For the Beglitsa section, relatively clear variations in proxies at depths between 4.5 and 3.2 m indicate a weakly developed paleosol formation during this period, such as higher values in TOC and lower values in L* (**Figure 6**), probably corresponding to an interstadial event. This weakly developed paleosol can be observed in the field by a visible color change but hardly noticeable in MS data. A previous OSL age of 53.7 ± 4.5 ka at the lowermost part of this interval provides additional evidence. Considering the stratigraphic position of this interval, we attribute it to MIS 3 (57–29 ka), named L_1SS_m. Similarly, the depth interval of 2.5–2.2 m at the Chumbur-Kosa section is also suggestive of MIS 3 based on multiple proxy variations (especially a drastic drop in the $CaCO_3$%) and an OSL age of 52.0 ± 4.8 ka at a depth of 2.5 m (**Figure 7**).

The L_1SS_m paleosol, known as Bryansk soil in European Russia and Vytachiv soil in Ukraine, is widely distributed over the periglacial and extraglacial regions of the East European Plain and presents a key stratigraphic marker of sections (Sycheva and Khokhlova, 2016). Previously obtained radiocarbon and OSL ages in this paleosol from different sites on the East European Plain cover a wide interval older than 25 ka and younger than 55 ka (Rusakov and Sedov, 2012; Gozhik et al., 2014; Sedov et al., 2016; Veres et al., 2018; Sycheva et al., 2020). Moreover, morphological characteristics of this paleosol with silty-loam groundmass, farinaceous carbonates, granular aggregates, and irregular wedge-like structures are clearly recognizable in the central region of the East European Plain (Sycheva and Khokhlova, 2016; Sycheva et al., 2020). The previous OSL ages we obtained within the L_1SS_m paleosol at the Azov Sea sections are in reasonably good agreement with multiple radiocarbon and OSL ages obtained at other sections on the East European Plain (e.g., Sycheva and Khokhlova, 2016; Veres et al., 2018) and the lower limit of MIS 3 (e.g., Lisiecki and Raymo, 2005). In addition, the L_1SS_m paleosols expressed in the Azov sections are typically characterized by high contents of coarse silt and low values of carbonate content (**Figures 3**, **5**), which are similar to the main characteristics of similar paleosols in the central region of the East European Plain. Last but not the least, this weakly developed paleosol was also identified in the depth interval of ~4.0–2.0 m below the modern top surface at other different Azov Sea loess sections by a slight increase in MS and organic matter content in recent studies, suggesting the widespread existence of an L_1SS_m

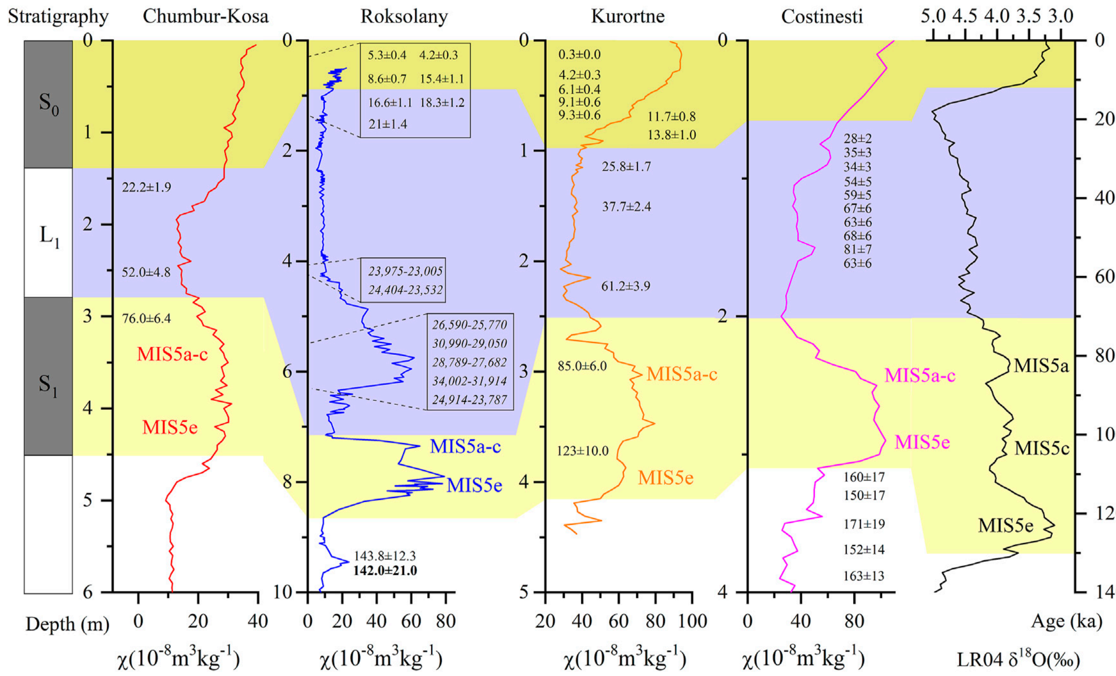

FIGURE 9 | Stratigraphy of the Chumbur-Kosa section and its correlation with well-dated loess records near the Black–Azov Sea region based on the χ_{lf} proxy, and with the benthic LR04 stack. Roksolany, Ukraine (Hlavatskyi and Bakhmutov, 2020); Kurortne, Ukraine (Tecsa et al., 2020); Costinesti, Romania (Constantin et al., 2014; Necula et al., 2015); and the benthic LR04 stack (Lisiecki and Raymo, 2005). Ages shown at the Chumbur-Kosa section are derived from Chen et al. (2018b); ages presented at the Roksolany section are cited from many references (Fedorowicz et al., 2012; Wulf et al., 2016; Constantin et al., 2019) and summarized in Hlavatskyi and Bakhmutov (2020); and ages presented at the Costinesti section are derived from Constantin et al. (2014). Note that there are three types of absolute ages illustrated: ages in regular type represent OSL ages, ages in italic are ^{14}C ages, and ages in bold show TL ages. For more information, please see the main text in this study and related references. For location of sections near the Black–Azov Sea region, please refer to **Figure 1**.

paleosol in the Azov Sea region (Mazneva et al., 2021; Timireva et al., 2021).

Chen et al. (2018a, b) failed to distinguish this substratum (L_1SS_m) due to a clear baseline of low MS values showing comparative constancy and small fluctuation at this depth interval. Especially for the Beglitsa section, two close-in-age OSL ages at different depths add to the difficulty in ascribing this interval to a specific MIS stage or stages (**Supplementary Figure S1**). Although the MS behavior of Beglitsa section generally follows the pedostratigraphy with higher values shown in paleosols and lower values in loess units, which is broadly consistent with the pedogenic enhancement model, there are χ_{lf} and χ_{hf} that do not significantly increase in this weaker paleosol L_1SS_m (**Figure 2**). In addition, the χ_{fd}% shows much more limited relation to pedostratigraphy, with changes not occurring at stratigraphic boundaries and inconsistent patterns between different units (**Figure 2**). These two parameters are likewise not covariant at certain stratigraphic horizons, such as a depth interval of 5.5–4.5 m (loess unit) and 4.5–3.2 m (paleosol L_1SS_m) (**Figure 2**). The inconsistent changes in χ_{lf} with pedostratigraphy, more complex pattern of χ_{fd}%, and noncovariant relationship along the section between these two parameters may indicate that other processes affect the magnetic signal in the Beglitsa section. A recent enviromagnetic study in nearby Lower Volga loess deposits further east of Azov showed that there are also other factors, such as magnetic mineral dissolution by hydromorphic processes (Taylor et al., 2014), magnetic mineral destruction by strong weathering (Baumgart et al., 2013), magnetic mineral alteration induced by weak pedogenesis (Ma et al., 2013), and surface oxidation of coarse magnetic grains (Van Velzen and Dekkers, 1999; Buggle et al., 2014; Buggle et al., 2014; Stevens et al., 2020), controlling the magnetic signal in this region (Költringer et al., 2020). These processes do not always lead to magnetic enhancement but can cause dissolution and magnetic depletion of certain components, depending on the type of soils and the characteristics of the environment in which the paleosol formed (Bradák et al., 2021). Magnetic enhancement in southern Russia is, thus, more complex than implied by the application of a simple pedogenic enhancement model, which requires further study in the future. As a result, it is difficult to identify this weakly developed paleosol based on only individual MS indicator.

Fortunately, the additional climate proxies in this study give us increased confidence to discriminate this sublayer within the loess horizon. It is, therefore, important to adopt a multiproxy approach for interpreting the stratigraphy and paleoclimatic significance of LPS. In contrast, single-proxy approaches may often provide merely fragmentary information and cause problematic interpretations (Vandenberghe et al., 2014). The stratigraphic position of L_1SS_m paleosol of the Beglitsa section determined here is different from the previous subdivision by Velichko et al. (2012, 2017). The newly identified L_1SS_m paleosol of the Chumbur-Kosa section has never been reported by previous study (e.g., Liang et al., 2016; Chen et al., 2018b, 2020).

After determining the position of L_1SS_m paleosols for two sections, it is much easier to attribute the under- and overlying loess units (L_1LL_2 and L_1LL_1) to MIS 4 and MIS 2, respectively (**Figures 6** and **7**). The L_1LL_2 and L_1LL_1 loess units, intercalated by the L_1SS_m paleosol, are strongly enriched in carbonates and depleted in humus, additionally with higher L* values in comparison with paleosols for two sections (**Figures 6** and **7**). Moreover, a previous OSL age of 22.2 ± 1.9 ka (Chen et al., 2018b) obtained for the upper part of the L_1LL_1 loess of the Chumbur-Kosa section further confirms the correlation of L_1LL_1 loess with MIS 2, thus, corroborating the accuracy of our subdivision and correlation of L_1 loess at the Azov Sea.

The Holocene Soil

Here our model is the same as those presented in a previous study of the Holocene soil (S_0) subdivision (Chen et al., 2018a, b), that is, depths of 1.2–0 m for the Beglitsa section and 1.4–0 m for the Chumbur-Kosa section belong to the Holocene soil (S_0) and correspond to MIS 1 (**Figures 6**, **7**). In the Beglitsa section, a large and rapid jump in all climatic proxy curves at a depth of 1.2 m, together with a previous OSL age (5.4 ± 0.4 ka) at a depth of 0.7 m, constitutes the whole evidence to ascertain forming phases of this uppermost soil horizon (**Figure 6**). As for the Chumbur-Kosa section, obvious variations can also be found from the curve of all climatic proxies at a depth of 1.4 m, although with no OSL ages obtained within this interval (**Figure 7**).

Environmental Changes at the Azov Sea

The Last Interglacial Complex (MIS 5)

During the Last Interglacial complex period, the climate in the Azov Sea region was generally characterized by warm, relatively humid conditions, although undergoing several obvious oscillations, as reflected in the intensity of pedogenesis responsible for paleosol S_1 (9.0–5.5 m in Beglitsa, 4.5–2.8 m in Chumbur-Kosa). The soil type resembles the modern soil, and MS values are as high as those of the modern soil, making this period as a potential analog for the present Interglacial. Patterns in paleoclimate proxy data within S_1 correlate well with warmer global climates, as demonstrated by the benthic LR04 stack records (Lisiecki and Raymo, 2005). Furthermore, high values of clay and TOC content and low values of L* and $CaCO_3$% (**Figures 6** and **7**), indices of climatic conditions favorable to forming soils, further confirm this general trend during the period. The climate trend is also consistent with the macro- and micromorphological studies performed on the LPS in the Azov Sea region, where the paleosol is represented as humus accumulation (dark brown dense loam, spots of Fe–Mn, biogenic pores, and fine gypsum crystals) and a series of genetic horizons (Acs-A-Bcy-BCks), suggesting abundant moisture supply and high humidity (Velichko et al., 2017; Panin et al., 2018). Additionally, the predominance of forb steppes inferred from palynological data and the presence of small mammal remains for paleosol S_1 of Azov loess sections, such as *Lagurus lagurus* and ground squirrels, are also indicators of mild steppe conditions with a dense vegetation cover (Dodonov et al., 2006; Tesakov et al., 2007; Velichko et al., 2012; Velichko et al., 2017). Furthermore, gastropod studies from the surrounding area of the Azov Sea, such as the Caucasus region, strongly support humid conditions during the formation of paleosol S_1, as expressed by the ecosystem with high-grass to forest-steppe biomes (Richter et al., 2020).

These climatic conditions inferred from different paleoclimate proxy data of S_1 are broadly similar with records in the Dnieper Lowland and Lower Danube Basin through regional loess comparison (**Figures 8** and **9**), providing insights into general climatic trends in these regions. However, also in the detail, there are differences seen when these records are compared under a better constrained chronostratigraphy.

The S_1SS_3 and S_1SS_2 paleosols show relatively higher MS values in the Beglitsa section, which sharply decrease toward the upper S_1SS_1 paleosol resulting in low MS values in the S_1SS_1, while a less distinctive pattern and a more constant change can be observed in the whole S_1 of the Chumbur-Kosa section (**Figures 8** and **9**). In addition, the MIS 5c seems to be the climatic optimum during the Last Interglacial complex as revealed by the highest χ_{lf} and χ_{fd}% values within S_1 of the Beglitsa section (**Figure 2**), while it is the MIS 5e in the Chumbur-Kosa section, as expressed by two χ_{fd}% peaks with much greater χ_{fd}% values in the lower S_1SS_3 paleosols compared with the upper one (**Figure 2**), if not taking into account the complexity in magnetic enhancement between these two sections. This is most probably related to specific features of the depositional and preservational environment at particular sections (Vandenberghe et al., 2014), as the Beglitsa and Chumbur-Kosa sections are separately exposed on the northern coast of the second terrace of the Azov Sea and southern shores of the sub-horizontal flat interfluves of the Azov Sea, and further isolated by the Gulf of Taganrog (**Figure 1**). Through a comparison between the Beglitsa and the Chumbur-Kosa sections of S_1 and other loess records from the Danube–Black/Azov Sea loess fields, we show that the investigated sequence extends over the Late Pleistocene, providing a key record for direct comparison of paleoclimatic trends over the vast European continent, revealing similarities in environmental magnetic loess records among these regions (e.g., Marković et al., 2015; Song et al., 2018; Sümegi et al., 2018), and further highlighting the dissimilarities of the site for the understanding of Eurasian continental temporal and spatial climatic evolution (Marković et al., 2018; Zeeden et al., 2018).

The Last Glacial (MIS 4-2)

The whole Last Glacial period was characterized by thick loess accumulation and clear background MS values associated with the L_1 loess in response to cold and dry climate conditions in the Azov region (5.5–1.2 m in Beglitsa, 2.8–1.4 m in Chumbur-Kosa). Multiproxy records indicate a similar climate condition, documented by low values of clay and TOC content and high values of L* and $CaCO_3$% (**Figures 6** and **7**). Cold glacial conditions inferred from the Black Sea records also support such climatic evolution in these adjacent areas (Ménot and Bard, 2012; Wegwerth et al., 2015).

However, a phase characterized by milder, relatively wetter conditions during the Last Glacial period, corresponding to MIS

3, was traced (4.5–3.2 m in Beglitsa, 2.5–2.2 m in Chumbur-Kosa) and also supported by distinct morphogenetic characteristics of the L_1SS_m paleosol in most of the loess sections located on the central part of the East European Plain. They are noted for wedge-like structures of the lower boundary of the humus horizon, farinaceous carbonates, and abundant granular aggregates from the upper horizon (Sycheva and Khokhlova, 2016). The granular aggregates can be considered as a cryogenic process indicator according to Todisco and Bhiry (2008) and Villagran et al. (2013). These characteristics suggest that the L_1SS_m paleosol formed under less cold and more moist climatic conditions but underwent intense cryogenic processes in the final stage of the paleosol development (Sedov et al., 2016; Sycheva and Khokhlova, 2016; Sycheva et al., 2020). In contrast, no obvious signs of cryoturbations in the L_1SS_m of Azov sections were found, indicating an insignificant cryogenic influence on this paleosol and relatively warmer climatic conditions at that time in this region (Panin et al., 2018). This is perhaps due to the fact that the geographic position of the Azov Sea is far from glacial areas compared with its analog in the central region of the East European Plain. It is also probably related to the moderating influence of the Black and Azov seas (Necula et al., 2015).

In summary, climate conditions in the Azov region during the Last Glacial period, as a whole, were characterized by two main cold and arid phases corresponding to the Early and Late Last Glacial, related to intensive accumulation of loess units L_1LL_2 and L_1LL_1, as well as separated by a phase of mild and wet climate corresponding to the Middle Last Glacial, associated with weakly developed soil L_1SS_m and noted for humus accumulation (high TOC content) and carbonate redistribution (low $CaCO_3\%$ content). These results are comparable with review studies of climatic oscillations during the Last Glacial period recorded in the Danube Basin LPS, except for the difference in thickness of the stratigraphic units (Marković et al., 2008; Fitzsimmons et al., 2012).

The Holocene (MIS 1)

The Holocene period is associated with the uppermost soil S_0, corresponding to climatic amelioration in the form of warmer, relatively more humid conditions (upper 1.2 m in Beglitsa and upper 1.4 m in Chumbur-Kosa), as demonstrated by higher χ_{lf}, <5 μm, and TOC values and lower L*, $CaCO_3\%$ values (**Figures 6** and **7**). The soil is represented by a Chernozem, a soil type close to the modern ones found in the area, and noted typically for humus accumulation and soil aggregation due to biogenic processes (Panin et al., 2018). Paleoclimatic records from other loess sections adjacent to the Azov Sea also yield evidence for a relatively warmer climate during this period (Velichko et al., 2012; Panin et al., 2019; Mazneva et al., 2021).

CONCLUSION

Following a multiproxy sedimentological investigation and chronological reevaluation, we show that two Late Quaternary loess sections around the Azov Sea are key sections for better constraining local and regional chronostratigraphic correlations. A more detailed and accurate chronostratigraphy was established with the help of various absolute ages and climatic proxies, compared with previous ones that are mainly following general stratigraphic schemes of the East European Plain. The new chronostratigraphy of the Azov Sea sections resolves many uncertainties in the stratigraphic position of loess units and soil complexes, and further correlates them with corresponding MIS, facilitating direct stratigraphic comparison between different regions. Besides, by this comparison and/or correlation with other terrestrial records from the Danube–East European Plain, we show that there are also some differences requiring further study in spite of general similarities.

In the studied records, the MIS 5 Interglacial complex period was the warmest and relatively most humid period, as reflected by intensively weathered paleosol. It was then followed by two main cold and arid periods corresponding to the MIS 4 and MIS 2 Glacial periods, interrupted by a phase of mild and wet climate corresponding to MIS 3. Finally, the Holocene is a period of climatic amelioration characterized by warmer, relatively more humid conditions, corresponding to MIS 1.

DATA AVAILABILITY STATEMENT

The raw data supporting the conclusions of this article will be made available by the authors, without undue reservation.

AUTHOR CONTRIBUTIONS

JC conceptualized the study, wrote the original draft, developed the methodology, performed the formal analysis, and conducted the investigation and visualization. TS wrote, reviewed, and edited the manuscript. TY supervised the study, acquired the resources, was in charge of the project administration, and acquired the funding. MQ wrote, reviewed, and edited the manuscript, and acquired the funding. GM acquired the resources and validated the study. EK and RK conducted the investigation and acquired the resources. BZ was in charge of the data curation. PS conducted the investigation and was in charge of the data curation.

FUNDING

This research was funded by the National Natural Science Foundation of China (Nos. 41271024 and 42071109), the Guangdong Basic and Applied Basic Research Foundation (2021A1515110246) and the Open Foundation of MOE Key Laboratory of Western China's Environmental System, Lanzhou University, and the Fundamental Research Funds for the Central Universities (lzujbky-2021-kb01). The Swedish

Research Council is gratefully acknowledged for funding TS for his part in this project (2017–03888).

ACKNOWLEDGMENTS

We are grateful to members from the Institute of Geography, Russian Academy of Sciences, for the help in the field, members from the Institute of Glaciology and Ecogeography, Lanzhou University, for the aid in the laboratory analyses, and Yan Qin for her assistance with **Figure 1**. We would also like to extend our sincere thanks to Dmytro Hlavatskyi, Cristian Necula, Daniel Veres, and Shugang Kang for providing the MS data of the different sections.

SUPPLEMENTARY MATERIAL

The Supplementary Material for this article can be found online at: https://www.frontiersin.org/articles/10.3389/feart.2021.808157/full#supplementary-material

REFERENCES

Basarin, B., Buggle, B., Hambach, U., Marković, S. B., Dhand, K. O. H., Kovačević, A., et al. (2014). Time-scale and Astronomical Forcing of Serbian Loess-Paleosol Sequences. *Glob. Planet. Change* 122, 89–106. doi:10.1016/j.gloplacha.2014.08.007

Basarin, B., Vandenberghe, D. A. G., Marković, S. B., Catto, N., Hambach, U., Vasiliniuc, S., et al. (2011). The Belotinac Section (Southern Serbia) at the Southern Limit of the European Loess belt: Initial Results. *Quat. Int.* 240, 128–138. doi:10.1016/j.quaint.2011.02.022

Bascomb, C. L. (1961). A Calcimeter for Routine Use on Soil Samples. *Chem. Industry* 45, 1826–1827.

Bateman, M. D., Frederick, C. D., Jaiswal, M. K., and Singhvi, A. K. (2003). Investigations into the Potential Effects of Pedoturbation on Luminescence Dating. *Quat. Sci. Rev.* 22, 1169–1176. doi:10.1016/s0277-3791(03)00019-2

Baumgart, P., Hambach, U., Meszner, S., and Faust, D. (2013). An Environmental Magnetic Fingerprint of Periglacial Loess: Records of Late Pleistocene Loess-Palaeosol Sequences from Eastern Germany. *Quat. Int.* 296, 82–93. doi:10.1016/j.quaint.2012.12.021

Beuselinck, L., Govers, G., Poesen, J., Degraer, G., and Froyen, L. (1998). Grain-size Analysis by Laser Diffractometry: Comparison with the Sieve-Pipette Method. *Catena* 32, 193–208. doi:10.1016/s0341-8162(98)00051-4

Bokhorst, M. P., Vandenberghe, J., Sümegi, P., Łanczont, M., Gerasimenko, N. P., Matviishina, Z. N., et al. (2011). Atmospheric Circulation Patterns in central and Eastern Europe during the Weichselian Pleniglacial Inferred from Loess Grain-Size Records. *Quat. Int.* 234, 62–74. doi:10.1016/j.quaint.2010.07.018

Bösken, J., Obreht, I., Zeeden, C., Klasen, N., Hambach, U., Sümegi, P., et al. (2019). High-resolution Paleoclimatic Proxy Data from the MIS3/2 Transition Recorded in Northeastern Hungarian Loess. *Quat. Int.* 502, 95–107. doi:10.1016/j.quaint.2017.12.008

Bradák, B., Seto, Y., Stevens, T., Újvári, G., Fehér, K., and Költringer, C. (2021). Magnetic Susceptibility in the European Loess Belt: New and Existing Models of Magnetic Enhancement in Loess. *Palaeogeogr. Palaeoclimatol. Palaeoecol.* 569, 110329. doi:10.1016/j.palaeo.2021.110329

Buggle, B., Hambach, U., Glaser, B., Gerasimenko, N., Marković, S., Glaser, I., et al. (2009). Stratigraphy, and Spatial and Temporal Paleoclimatic Trends in Southeastern/Eastern European Loess-Paleosol Sequences. *Quat. Int.* 196, 86–106. doi:10.1016/j.quaint.2008.07.013

Buggle, B., Hambach, U., Müller, K., Zöller, L., Marković, S. B., and Glaser, B. (2014). Iron Mineralogical Proxies and Quaternary Climate Change in SE-European Loess-Paleosol Sequences. *Catena* 117, 4–22. doi:10.1016/j.catena.2013.06.012

Chen, J., Yang, T., Matishov, G. G., Velichko, A. A., Zeng, B., He, Y., et al. (2018b). Luminescence Chronology and Age Model Application for the Upper Part of the Chumbur-Kosa Loess Sequence in the Sea of Azov, Russia. *J. Mt. Sci.* 15, 504–518. doi:10.1007/s11629-017-4689-0

Chen, J., Yang, T., Matishov, G. G., Velichko, A. A., Zeng, B., He, Y., et al. (2018a). A Luminescence Dating Study of Loess Deposits from the Beglitsa Section in the Sea of Azov, Russia. *Quat. Int.* 478, 27–37. doi:10.1016/j.quaint.2017.11.017

Chen, J., Yang, T., Qiang, M., Matishov, G. G., Velichko, A. A., Zeng, B., et al. (2020). Interpretation of Sedimentary Subpopulations Extracted from Grain Size Distributions in Loess Deposits at the Sea of Azov, Russia. *Aeolian Res.* 45, 100597. doi:10.1016/j.aeolia.2020.100597

Constantin, D., Begy, R., Vasiliniuc, S., Panaiotu, C., Necula, C., Codrea, V., et al. (2014). High-resolution OSL Dating of the Costineşti Section (Dobrogea, SE Romania) Using fine and Coarse Quartz. *Quat. Int.* 334-335, 20–29. doi:10.1016/j.quaint.2013.06.016

Constantin, D., Veres, D., Panaiotu, C., Anechitei-Deacu, V., Groza, S. M., Begy, R., et al. (2019). Luminescence Age Constraints on the Pleistocene-Holocene Transition Recorded in Loess Sequences across SE Europe. *Quat. Geochronol.* 49, 71–77. doi:10.1016/j.quageo.2018.07.011

Dearing, J. A., Dann, R. J. L., Hay, K., Lees, J. A., Loveland, P. J., Maher, B. A., et al. (1996). Frequency-dependent Susceptibility Measurements of Environmental Materials. *Geophys. J. Int.* 124, 228–240. doi:10.1111/j.1365-246x.1996.tb06366.x

Dlussky, K. G. (2007). Likhvin Interglacial Polygenetic Paleosol: A Reconstruction on the Russian Plain. *Quat. Int.* 162-163, 141–157. doi:10.1016/j.quaint.2006.10.029

Dodonov, A. E., Tchepalyga, A. L., Mihailescu, C. D., Zhou, L. P., Markova, A. K., Trubikhin, V. M., et al. (2000). Last-interglacial Records from central Asia to the Northern Black Sea Shoreline: Stratigraphy and Correlation. *Neth. J. Geosciences* 79, 303–311. doi:10.1017/s0016774600021788

Dodonov, A. E., Zhou, L. P., Markova, A. K., Tchepalyga, A. L., Trubikhin, V. M., Aleksandrovski, A. L., et al. (2006). Middle-Upper Pleistocene Bio-Climatic and Magnetic Records of the Northern Black Sea Coastal Area. *Quat. Int.* 149, 44–54. doi:10.1016/j.quaint.2005.11.017

Fang, X.-M., Ono, Y., Fukusawa, H., Bao-Tian, P., Li, J.-J., Dong-Hong, G., et al. (1999). Asian Summer Monsoon Instability during the Past 60,000 Years: Magnetic Susceptibility and Pedogenic Evidence from the Western Chinese Loess Plateau. *Earth Planet. Sci. Lett.* 168, 219–232. doi:10.1016/s0012-821x(99)00053-9

Fedorowicz, S., Woźniak, P., Halas, S., Łanczont, M., Paszkowski, M., and Wójtowicz, A. (2012). Challenging K-Ar Dating of the Quaternary Tephra from Roxolany, Ukraine. *Mineralogia-Special Pap.* 39, 102–105.

Fitzsimmons, K. E., Marković, S. B., and Hambach, U. (2012). Pleistocene Environmental Dynamics Recorded in the Loess of the Middle and Lower Danube basin. *Quat. Sci. Rev.* 41, 104–118. doi:10.1016/j.quascirev.2012.03.002

Gerasimenko, N. (2006). Upper Pleistocene Loess-Palaeosol and Vegetational Successions in the Middle Dnieper Area, Ukraine. *Quat. Int.* 149, 55–66. doi:10.1016/j.quaint.2005.11.018

Gozhik, P., Komar, M., Łanczont, M., Fedorowicz, S., Bogucki, A., Mroczek, P., et al. (2014). Paleoenvironmental History of the Middle Dnieper Area from the Dnieper to Weichselian Glaciation: A Case Study of the Maksymivka Loess Profile. *Quat. Int.* 334-335, 94–111. doi:10.1016/j.quaint.2013.11.037

Hlavatskyi, D. V., and Bakhmutov, V. G. (2020). Magnetostratigraphy and Magnetic Susceptibility of the Best Developed Pleistocene Loess-Palaeosol Sequences of Ukraine: Implications for Correlation and Proposed Chronostratigraphic Models. *Geol. Q.* 64, 723–753. doi:10.7306/gq.1544

Kang, S. G., Wang, X. L., and Lu, Y. C. (2013). Quartz OSL Chronology and Dust Accumulation Rate Changes since the Last Glacial at Weinan on the southeastern Chinese Loess Plateau. *Boreas* 42, 815–829. doi:10.1111/bor.12005

Kang, S., Lu, Y., and Wang, X. (2011). Closely-spaced Recuperated OSL Dating of the Last Interglacial Paleosol in the southeastern Margin of the Chinese Loess Plateau. *Quat. Geochronol.* 6, 480–490. doi:10.1016/j.quageo.2011.04.004

Költringer, C., Stevens, T., Bradák, B., Almqvist, B., Kurbanov, R., Snowball, I., et al. (2020). Enviromagnetic Study of Late Quaternary Environmental Evolution in Lower Volga Loess Sequences, Russia. *Quat. Res.* 103, 1–25. doi:10.1017/qua.2020.73

Konert, M., and Vandenberghe, J. (1997). Comparison of Laser Grain Size Analysis with Pipette and Sieve Analysis: A Solution for the Underestimation of the clay Fraction. *Sedimentology* 44, 523–535. doi:10.1046/j.1365-3091.1997.d01-38.x

Kosarev, A. N., Kostianoy, A. G., and Shiganova, T. A. (2007). *The Sea of Azov, the Black Sea Environment*. Berlin: Springer, 63–89.

Krijgsman, W., Tesakov, A., Yanina, T., Lazarev, S., Danukalova, G., Van Baak, C. G. C., et al. (2019). Quaternary Time Scales for the Pontocaspian Domain: Interbasinal Connectivity and Faunal Evolution. *Earth-Science Rev.* 188, 1–40. doi:10.1016/j.earscirev.2018.10.013

Kukla, G., and An, Z. (1989). Loess Stratigraphy in Central China. *Palaeogeogr. Palaeoclimatol. Palaeoecol.* 72, 203–225. doi:10.1016/0031-0182(89)90143-0

Liang, Y., Yang, T.-b., Velichko, A. A., Zeng, B., Shi, P.-h., Wang, L.-d., et al. (2016). Paleoclimatic Record from Chumbur-Kosa Section in Sea of Azov Region since Marine Isotope Stage 11. *J. Mt. Sci.* 13, 985–999. doi:10.1007/s11629-015-3738-9

Lisiecki, L. E., and Raymo, M. E. (2005). A Pliocene-Pleistocene Stack of 57 Globally Distributed Benthic δ^{18}O Records. *Paleoceanography* 20, 1–17. doi:10.1029/2004pa001071

Ma, M., Liu, X., Hesse, P. P., Lü, B., Guo, X., and Chen, J. (2013). Magnetic Properties of Loess Deposits in Australia and Their Environmental Significance. *Quat. Int.* 296, 198–205. doi:10.1016/j.quaint.2012.06.018

Maher, B. A., MengYu, H., Roberts, H. M., and Wintle, A. G. (2003). Holocene Loess Accumulation and Soil Development at the Western Edge of the Chinese Loess Plateau: Implications for Magnetic Proxies of Palaeorainfall. *Quat. Sci. Rev.* 22, 445–451. doi:10.1016/s0277-3791(02)00188-9

Makeev, A., Lebedeva, M., Kaganova, A., Rusakov, A., Kust, P., Romanis, T., et al. (2021). Pedosedimentary Environments in the Caspian Lowland during MIS5 (Srednaya Akhtuba Reference Section, Russia). *Quat. Int.* 590, 164–180. doi:10.1016/j.quaint.2021.03.015

Markova, A. K., and Vislobokova, I. A. (2016). Mammal Faunas in Europe at the End of the Early - Beginning of the Middle Pleistocene. *Quat. Int.* 420, 363–377. doi:10.1016/j.quaint.2015.07.065

Markova, A. K. (2005). Eastern European Rodent (Rodentia, Mammalia) Faunas from the Early-Middle Pleistocene Transition. *Quat. Int.* 131, 71–77. doi:10.1016/j.quaint.2004.07.020

Markova, A. K. (2007). Pleistocene Mammal Faunas of Eastern Europe. *Quat. Int.* 160, 100–111. doi:10.1016/j.quaint.2006.09.011

Marković, S. B., Bokhorst, M. P., Vandenberghe, J., McCoy, W. D., Oches, E. A., Hambach, U., et al. (2008). Late Pleistocene Loess-Palaeosol Sequences in the Vojvodina Region, north Serbia. *J. Quat. Sci.* 23, 73–84. doi:10.1002/jqs.1124

Marković, S. B., Stevens, T., Kukla, G. J., Hambach, U., Fitzsimmons, K. E., Gibbard, P., et al. (2015). Danube Loess Stratigraphy-Towards a Pan-European Loess Stratigraphic Model. *Earth-Science Rev.* 148, 228–258. doi:10.1016/j.earscirev.2015.06.005

Marković, S. B., Stevens, T., Mason, J., Vandenberghe, J., Yang, S., Veres, D., et al. (2018). Loess Correlations-Between Myth and Reality. *Palaeogeogr. Palaeoclimatol. Palaeoecol.* 509, 4–23. doi:10.1016/j.palaeo.2018.04.018

Matishov, G., Kovaleva, G., Novenko, E., Krasnorutskaya, K., and Pol'shin, V. (2013). Paleogeography of the Sea of Azov Region in the Late Holocene (Reconstruction by Diatom and Pollen Data from marine Sediments). *Quat. Int.* 284, 123–131. doi:10.1016/j.quaint.2012.05.044

Mazneva, E., Konstantinov, E., Zakharov, A., Sychev, N., Tkach, N., Kurbanov, R., et al. (2021). Middle and Late Pleistocene Loess of the Western Ciscaucasia: Stratigraphy, Lithology and Composition. *Quat. Int.* 590, 146–163. doi:10.1016/j.quaint.2020.11.039

Ménot, G., and Bard, E. (2012). A Precise Search for Drastic Temperature Shifts of the Past 40,000 Years in southeastern Europe. *Paleoceanography* 27, PA2210. doi:10.1029/2012PA002291

Murray, A. S., Svendsen, J. I., Mangerud, J., and Astakhov, V. I. (2007). Testing the Accuracy of Quartz OSL Dating Using a Known-Age Eemian Site on the River Sula, Northern Russia. *Quat. Geochronol.* 2, 102–109. doi:10.1016/j.quageo.2006.04.004

Necula, C., Dimofte, D., and Panaiotu, C. (2015). Rock Magnetism of a Loess-Palaeosol Sequence from the Western Black Sea Shore (Romania). *Geophys. J. Int.* 202, 1733–1748. doi:10.1093/gji/ggv250

Necula, C., Panaiotu, C., Heslop, D., and Dimofte, D. (2013). Climatic Control of Magnetic Granulometry in the Mircea Vodă Loess/paleosol Sequence (Dobrogea, Romania). *Quat. Int.* 293, 5–14. doi:10.1016/j.quaint.2012.03.043

Obreht, I., Buggle, B., Catto, N., Markovič, S. B., Bösel, S., Vandenberghe, D. A. G., et al. (2014). The Late Pleistocene Belotinac Section (Southern Serbia) at the Southern Limit of the European Loess belt: Environmental and Climate Reconstruction Using Grain Size and Stable C and N Isotopes. *Quat. Int.* 334-335, 10–19. doi:10.1016/j.quaint.2013.05.037

Panin, P. G., Timireva, S. N., Konstantinov, E. A., Kalinin, P. I., Kononov, Y. M., Alekseev, A. O., et al. (2019). Plio-Pleistocene Paleosols: Loess-Paleosol Sequence Studied in the Beregovoye Section, the Crimean Peninsula. *Catena* 172, 590–618. doi:10.1016/j.catena.2018.09.020

Panin, P. G., Timireva, S. N., Morozova, T. D., Kononov, Y. M., and Velichko, A. A. (2018). Morphology and Micromorphology of the Loess-Paleosol Sequences in the South of the East European plain (MIS 1-MIS 17). *Catena* 168, 79–101. doi:10.1016/j.catena.2018.01.032

Pilipenko, O. V., Sharonova, Z. V., Trubikhin, V. M., Abrahamsen, N., and Moerner, N.-A. (2005). Paleomagnetic and Petromagnetic Investigations of Rocks of the Pekla Loess-Soil Section (Krasnodar Territory) in the Interval 240-55 Ka. *Izvestiya, Phys. Solid Earth* 41, 492–501.

Pilipenko, O. V., and Trubikhin, V. M. (2011). Paleomagnetic Record in the Late Pleistocene Loess-Soil Deposits of the Pekla Section in the Time Interval 425-50 Ka. *Izv., Phys. Solid Earth* 47, 686–697. doi:10.1134/s106935131107007x

Richter, C., Wolf, D., Walther, F., Meng, S., Sahakyan, L., Hovakimyan, H., et al. (2020). New Insights into Southern Caucasian Glacial-Interglacial Climate Conditions Inferred from Quaternary Gastropod Fauna. *J. Quat. Sci* 35, 634–649. doi:10.1002/jqs.3204

Rousseau, D.-D., Antoine, P., Gerasimenko, N., Sima, A., Fuchs, M., Hatté, C., et al. (2011). North Atlantic Abrupt Climatic Events of the Last Glacial Period Recorded in Ukrainian Loess Deposits. *Clim. Past* 7, 221–234. doi:10.5194/cp-7-221-2011

Rusakov, A., and Sedov, S. (2012). Late Quaternary Pedogenesis in Periglacial Zone of Northeastern Europe Near Ice Margins since MIS 3: Timing, Processes, and Linkages to Landscape Evolution. *Quat. Int.* 265, 126–141. doi:10.1016/j.quaint.2012.03.002

Rutter, N. W., Rokosh, D., Evans, M. E., Little, E. C., Chlachula, J., and Velichko, A. (2003). Correlation and Interpretation of Paleosols and Loess across European Russia and Asia over the Last Interglacial-Glacial Cycle. *Quat. Res.* 60, 101–109. doi:10.1016/s0033-5894(03)00069-3

Schaetzl, R. J., Bettis, E. A., Crouvi, O., Fitzsimmons, K. E., Grimley, D. A., Hambach, U., et al. (2018). Approaches and Challenges to the Study of Loess-Introduction to the LoessFest Special Issue. *Quat. Res.* 89, 563–618. doi:10.1017/qua.2018.15

Sedov, S., Rusakov, A., Sheinkman, V., and Korkka, M. (2016). MIS3 Paleosols in the center-north of Eastern Europe and Western Siberia: Reductomorphic Pedogenesis Conditioned by Permafrost? *Catena* 146, 38–47. doi:10.1016/j.catena.2016.03.022

Smalley, I., O'Hara-Dhand, K., Wint, J., Machalett, B., Jary, Z., and Jefferson, I. (2009). Rivers and Loess: The Significance of Long River Transportation in the Complex Event-Sequence Approach to Loess deposit Formation. *Quat. Int.* 198, 7–18. doi:10.1016/j.quaint.2008.06.009

Song, Y., Guo, Z., Marković, S., Hambach, U., Deng, C., Chang, L., et al. (2018). Magnetic Stratigraphy of the Danube Loess: A Composite Titel-Stari Slankamen Loess Section over the Last One Million Years in Vojvodina, Serbia. *J. Asian Earth Sci.* 155, 68–80. doi:10.1016/j.jseaes.2017.11.012

Sotnikova, M., and Titov, V. (2009). Carnivora of the Tamanian Faunal Unit (The Azov Sea Area). *Quat. Int.* 201, 43–52. doi:10.1016/j.quaint.2008.05.019

Stevens, T., Armitage, S. J., Lu, H., and Thomas, D. S. G. (2006). Sedimentation and Diagenesis of Chinese Loess: Implications for the Preservation of Continuous, High-Resolution Climate Records. *Geol* 34, 849–852. doi:10.1130/g22472.1

Stevens, T., Sechi, D., Bradák, B., Orbe, R., Baykal, Y., Cossu, G., et al. (2020). Abrupt Last Glacial Dust Fall over Southeast England Associated with Dynamics of the British-Irish Ice Sheet. *Quat. Sci. Rev.* 250, 106641. doi:10.1016/j.quascirev.2020.106641

Stevens, T., Thomas, D., Armitage, S., Lunn, H., and Lu, H. (2007). Reinterpreting Climate Proxy Records from Late Quaternary Chinese Loess: A Detailed OSL Investigation. *Earth-Science Rev.* 80, 111–136. doi:10.1016/j.earscirev.2006.09.001

Sümegi, P., Gulyás, S., Molnár, D., Sümegi, B. P., Almond, P. C., Vandenberghe, J., et al. (2018). New Chronology of the Best Developed Loess/paleosol Sequence of Hungary Capturing the Past 1.1 Ma: Implications for Correlation and Proposed Pan-Eurasian Stratigraphic Schemes. *Quat. Sci. Rev.* 191, 144–166. doi:10.1016/j.quascirev.2018.04.012

Sycheva, S., Frechen, M., Terhorst, B., Sedov, S., and Khokhlova, O. (2020). Pedostratigraphy and Chronology of the Late Pleistocene for the Extra

Glacial Area in the Central Russian Upland (Reference Section Aleksandrov Quarry). *Catena* 194, 104689. doi:10.1016/j.catena.2020.104689

Sycheva, S., and Khokhlova, O. (2016). Genesis, 14C Age, and Duration of Development of the Bryansk Paleosol on the Central Russian Upland Based on Dating of Different Materials. *Quat. Int.* 399, 111–121. doi:10.1016/j.quaint.2015.08.055

Taylor, S.N., Lagroix, F., Rousseau, D.-D, and Antoine, P. (2014). Mineral Magnetic Characterization of the Upper Pleniglacial Nussloch loess Sequence (Germany): An Insight into Local Environmental Processes. *Geophys. J. Int.* 199, 1463–1480. doi:10.1093/gji/ggu331

Tecsa, V., Gerasimenko, N., Veres, D., Hambach, U., Lehmkuhl, F., Schulte, P., et al. (2020). Revisiting the Chronostratigraphy of Late Pleistocene Loess-Paleosol Sequences in Southwestern Ukraine: OSL Dating of Kurortne Section. *Quat. Int.* 542, 65–79. doi:10.1016/j.quaint.2020.03.001

Tesakov, A. S., Dodonov, A. E., Titov, V. V., and Trubikhin, V. M. (2007). Plio-Pleistocene Geological Record and Small Mammal Faunas, Eastern Shore of the Azov Sea, Southern European Russia. *Quat. Int.* 160, 57–69. doi:10.1016/j.quaint.2006.09.009

Timar-Gabor, A., Constantin, D., Buylaert, J. P., Jain, M., Murray, A. S., and Wintle, A. G. (2015). Fundamental Investigations of Natural and Laboratory Generated SAR Dose Response Curves for Quartz OSL in the High Dose Range. *Radiat. Measurements* 81, 150–156. doi:10.1016/j.radmeas.2015.01.013

Timireva, S. N., Kononov, Y. M., Sycheva, S. A., Taratunina, N. A., Kalinin, P. I., Filippova, K. G., et al. (2021). Revisiting the Taman peninsula Loess-Paleosol Sequence: Middle and Late Pleistocene Record of Cape Pekla. *Quat. Int.* doi:10.1016/j.quaint.2021.06.010

Todisco, D., and Bhiry, N. (2008). Micromorphology of Periglacial Sediments from the Tayara Site, Qikirtaq Island, Nunavik (Canada). *Catena* 76, 1–21. doi:10.1016/j.catena.2008.08.002

Újvári, G., Kok, J. F., Varga, G., and Kovács, J. (2016). The Physics of Wind-Blown Loess: Implications for Grain Size Proxy Interpretations in Quaternary Paleoclimate Studies. *Earth-Science Rev.* 154, 247–278. doi:10.1016/j.earscirev.2016.01.006

Van Velzen, A. J., and Dekkers, M. J. (1999). Low-temperature Oxidation of Magnetite in Loess-Paleosol Sequences: a Correction of Rock Magnetic Parameters. *Studia Geophysica et Geodaetica* 43, 357–375. doi:10.1023/a:1023278901491

Vandenberghe, J. (2013). Grain Size of fine-grained Windblown Sediment: A Powerful Proxy for Process Identification. *Earth-Science Rev.* 121, 18–30. doi:10.1016/j.earscirev.2013.03.001

Vandenberghe, J., Markovič, S. B., Jovanovič, M., and Hambach, U. (2014). Site-specific Variability of Loess and Palaeosols (Ruma, Vojvodina, Northern Serbia). *Quat. Int.* 334-335, 86–93. doi:10.1016/j.quaint.2013.10.036

Velichko, A. A., Borisova, O. K., Kononov, Y. M., Konstantinov, E. A., Kurbanov, R. N., Morozova, T. D., et al. (2017). Reconstruction of Late Pleistocene Events in the Periglacial Area in the Southern Part of the East European Plain. *Dokl. Earth Sc.* 475, 895–899. doi:10.1134/s1028334x17080098

Velichko, A. A., Catto, N. R., Yu Kononov, M., Morozova, T. D., Yu Novenko, E., Panin, P. G., et al. (2009a). Progressively Cooler, Drier Interglacials in Southern Russia through the Quaternary: Evidence from the Sea of Azov Region. *Quat. Int.* 198, 204–219. doi:10.1016/j.quaint.2008.06.005

Velichko, A. A., Catto, N., Tesakov, A. S., Titov, V. V., Morozova, T. D., Semenov, V. V., et al. (2009b). Structural Specificity of Pleistocene Loess and Soil Formation of the Southern Russian plain According to Materials of Eastern Priazovie. *Dokl. Earth Sc.* 429, 1364–1368. doi:10.1134/s1028334x09080273

Velichko, A. A., Faustova, M. A., Pisareva, V. V., Gribchenko, Y. N., Sudakova, N. G., and Lavrentiev, N. V. (2011). “Glaciations of the East European Plain,” in *Glaciations of the East European Plain: Distribution and Chronology, Developments in Quaternary Sciences* (Amsterdam: Elsevier), 337–359. doi:10.1016/b978-0-444-53447-7.00026-x

Velichko, A. A. (1990). Loess-paleosol Formation on the Russian plain. *Quat. Int.* 7-8, 103–114. doi:10.1016/1040-6182(90)90044-5

Velichko, A. A., Morozova, T. D., Nechaev, V. P., Rutter, N. W., Dlusskii, K. G., Little, E. C., et al. (2006). Loess/paleosol/cryogenic Formation and Structure Near the Northern Limit of Loess Deposition, East European Plain, Russia. *Quat. Int.* 152-153, 14–30. doi:10.1016/j.quaint.2005.12.003

Velichko, A., Morozova, T. D., Borisova, O. K., Timireva, S. N., Semenov, V. V., Kononov, Y. M., et al. (2012). Development of the Steppe Zone in Southern Russia Based on the Reconstruction from the Loess-Soil Formation in the Don-Azov Region. *Dokl. Earth Sc.* 445, 999–1002. doi:10.1134/s1028334x12080107

Veres, D., Tecsa, V., Gerasimenko, N., Zeeden, C., Hambach, U., and Timar-Gabor, A. (2018). Short-term Soil Formation Events in Last Glacial East European Loess, Evidence from Multi-Method Luminescence Dating. *Quat. Sci. Rev.* 200, 34–51. doi:10.1016/j.quascirev.2018.09.037

Villagran, X. S., Schaefer, C. E. G. R., and Ligouis, B. (2013). Living in the Cold: Geoarchaeology of Sealing Sites from Byers Peninsula (Livingston Island, Antarctica). *Quat. Int.* 315, 184–199. doi:10.1016/j.quaint.2013.07.001

Wang, H., Hackley, K. C., Panno, S. V., Coleman, D. D., Liu, J. C.-l., and Brown, J. (2003). Pyrolysis-combustion 14C Dating of Soil Organic Matter. *Quat. Res.* 60, 348–355. doi:10.1016/j.yqres.2003.07.004

Wegwerth, A., Ganopolski, A., Ménot, G., Kaiser, J., Dellwig, O., Bard, E., et al. (2015). Black Sea Temperature Response to Glacial Millennial-scale Climate Variability. *Geophys. Res. Lett.* 42, 8147–8154. doi:10.1002/2015gl065499

Wulf, S., Fedorowicz, S., Veres, D., Łanczont, M., Karátson, D., Gertisser, R., et al. (2016). The ’Roxolany Tephra’ (Ukraine) – New Evidence for an Origin from Ciomadul Volcano, East Carpathians. *J. Quat. Sci.* 31, 565–576. doi:10.1002/jqs.2879

Yanina, T. A., Svitoch, A. A., Kurbanov, R. N., Murray, A. S., Tkach, N. T., and Sychev, N. V. (2017). Opyt Datirovaniya Pleystotsenovykh Otlozheniy Nizhnego Povolzh’ya Metodom Opticheski Stimulirovannoy Lyuminestsentsii (Paleogeographic Analysis of the Results of Optically Stimulated Luminescence Dating of Pleistocene Deposits of the Lower Volga Area). *Vestnik MSU, Seriya 5 Geografiya* 1, 21–29.

Zastrozhnov, A., Danukalova, G., Golovachev, M., Titov, V., Osipova, E., Simakova, A., et al. (2020). Biostratigraphical Investigations as a Tool for Palaeoenvironmental Reconstruction of the Neopleistocene (Middle-Upper Pleistocene) at Kosika, Lower Volga, Russia. *Quat. Int.* 540, 38–67. doi:10.1016/j.quaint.2018.11.036

Zastrozhnov, A., Danukalova, G., Shick, S., and van Kolfshoten, T. (2018). State of Stratigraphic Knowledge of Quaternary Deposits in European Russia: Unresolved Issues and Challenges for Further Research. *Quat. Int.* 478, 4–26. doi:10.1016/j.quaint.2017.03.037

Zeeden, C., Hambach, U., Obreht, I., Hao, Q., Abels, H. A., Veres, D., et al. (2018). Patterns and Timing of Loess-Paleosol Transitions in Eurasia: Constraints for Paleoclimate Studies. *Glob. Planet. Change* 162, 1–7. doi:10.1016/j.gloplacha.2017.12.021

Zeeden, C., Kels, H., Hambach, U., Schulte, P., Protze, J., Eckmeier, E., et al. (2016). Three Climatic Cycles Recorded in a Loess-Palaeosol Sequence at Semlac (Romania) - Implications for Dust Accumulation in South-Eastern Europe. *Quat. Sci. Rev.* 154, 130–142. doi:10.1016/j.quascirev.2016.11.002

Zhou, L. P., Oldfield, F., Wintle, A. G., Robinson, S. G., and Wang, J. T. (1990). Partly Pedogenic Origin of Magnetic Variations in Chinese Loess. *Nature* 346, 737–739. doi:10.1038/346737a0

Zhou, W. J., Donahue, D. J., Porter, S. C., Jull, T. A., Li, X. Q., Stuiver, M., et al. (1996). Variability of Monsoon Climate in East Asia at the End of the Last Glaciation. *Quat. Res.* 46, 219–229.

Conflict of Interest: The authors declare that the research was conducted in the absence of any commercial or financial relationships that could be construed as a potential conflict of interest.

Publisher’s Note: All claims expressed in this article are solely those of the authors and do not necessarily represent those of their affiliated organizations, or those of the publisher, the editors, and the reviewers. Any product that may be evaluated in this article, or claim that may be made by its manufacturer, is not guaranteed or endorsed by the publisher.

Copyright © 2022 Chen, Stevens, Yang, Qiang, Matishov, Konstantinov, Kurbanov, Zeng and Shi. This is an open-access article distributed under the terms of the Creative Commons Attribution License (CC BY). The use, distribution or reproduction in other forums is permitted, provided the original author(s) and the copyright owner(s) are credited and that the original publication in this journal is cited, in accordance with accepted academic practice. No use, distribution or reproduction is permitted which does not comply with these terms.

frontiers in Earth Science

ORIGINAL RESEARCH
published: 10 February 2022
doi: 10.3389/feart.2022.832993

Holocene Aeolian Activity Recorded by Mountain Paleosols, Gonghe Basin, Northeast Qinghai-Tibet Plateau

Chunxia Xu[1,2], Chongyi E[1,2,3], Yunkun Shi[1,2], Jing Zhang[1,2], Manping Sun[1,2], Zhaokang Zhang[1,2] and Yongxin Zeng[1,2]*

[1]Key Laboratory of Tibetan Plateau Land Surface Processes and Ecological Conservation (Ministry of Education), Qinghai Normal University, Xining, China, [2]Qinghai Province Key Laboratory of Physical Geography and Environmental Process, College of Geographical Science, Qinghai Normal University, Xining, China, [3]Academy of Plateau Science and Sustainability, People's Government of Qinghai Province and Beijing Normal University, Xining, China

The Gonghe Basin (GHB) on the northeastern Qinghai-Tibet Plateau (NE-QTP) is sensitive to climatic change due to the interplay of the Asian summer monsoon and the westerlies. Extensive aeolian sediments in the basin represent important archives of regional environmental evolution. However, the paleosol development timing is still not clear because of limited number of optically stimulated luminescence (OSL) sampling and dating, which restricts our understanding of past aeolian activities during the Holocene in GHB. In this study, a loess-paleosol section, Najiao (NJ), from the southeastern margin of GHB was investigated. Eighteen OSL samples were obtained from the 400-cm section in order to construct a high-resolution chronological framework. Paleoenvironmental proxies including grain size distribution (GS), magnetic susceptibility (MS), total organic carbon (TOC), and geochemical elements were measured to reconstruct the Holocene aeolian activity. Results show a successive accumulation from Early to Middle Holocene at NJ section, but a c. 3 ka sedimentary hiatus is found between c. 5 and 1.5 ka. Paleosol ages are constrained by high-resolution OSL ages which are from c. 7–5 ka. Consistent with previous studies, strong aeolian activities occurred in GHB during the Early Holocene (c. 13–9 ka), indicating dry climate conditions. Initiation of pedogenesis was at c. 9 ka, and the intensified soil development and lowest aeolian activity were between c. 7 and 5 ka. The increased sand content after c. 1.5 ka indicates enhanced human activities in the interior of GHB in the Late Holocene.

Keywords: aeolian activity, high resolution, OSL dating, holocene climate, human activities

OPEN ACCESS

Edited by:
Zhiwei Xu,
Nanjing University, China

Reviewed by:
Ruijie Lu,
Beijing Normal University, China
Bernd Wünnemann,
Southwest Jiaotong University, China

****Correspondence:***
Chongyi E
echongyi@163.com

Specialty section:
This article was submitted to Quaternary Science, Geomorphology and Paleoenvironment, a section of the journal Frontiers in Earth Science

Received: *10 December 2021*
Accepted: *17 January 2022*
Published: *10 February 2022*

Citation:
Xu C, E C, Shi Y, Zhang J, Sun M, Zhang Z and Zeng Y (2022) Holocene Aeolian Activity Recorded by Mountain Paleosols, Gonghe Basin, Northeast Qinghai-Tibet Plateau. Front. Earth Sci. 10:832993. doi: 10.3389/feart.2022.832993

INTRODUCTION

The arid/semi-arid northeastern Qinghai-Tibet Plateau (NE-QTP) is particularly sensitive to climatic change as it is under the interplay between the Asian summer monsoon and the westerlies (An et al., 2012; Chen et al., 2016). Sediments, tree rings, and ice cores are important archives of regional environmental and climatic change on the NE-QTP (An et al., 2012; Chen et al., 2016). Aeolian deposits are widespread on the arid NE-QTP, and taken as an important proxy for reconstructing paleoclimatic change, which is well-studied since the 1980s (Xu, 1987; Liu et al., 2012; Qiang et al., 2013; Sun et al., 2014; Hu et al., 2015; Qiang et al., 2016; Liu et al., 2017; Qin et al., 2017; Li et al., 2020). Generally, aeolian activity was stronger and accumulation rates were higher under the dry-cold climate during the Late Glacial to Early Holocene, while dune activity was weaker in the more humid Mid-Holocene, and intensified again in the Late Holocene (Stauch et al., 2016; Chen et al., 2020). It has been reported that natural factor was the dominant control on millennial-scale dust storm activity during most of the Holocene, but an upturn in dust storms since c. 2 cal ka BP has been linked with increasing human populations/intensifying human disturbance in dust source regions of northern China (Chen et al., 2021). Thus, aeolian activity is not only related to climate change, but also to human activity, on different timescales.

Aeolian deposits contain occasional paleosols that were formed when dunes were stabilized due to vegetation development. Published optically stimulated luminescence (OSL) ages for paleosol formation show great variation between basins, and even for different parts of the same basin, due to its limited occurrence (Chen et al., 2020) and moisture effects of local terrain (Qiang et al., 2013). However, few studies have considered the role of soil development mode on paleosol age, which limits understanding of paleoenvironments. The ideal soil development mode for reconstructing paleoenvironmental variations is “aeolian dust aggradation”, i.e., continuous accumulation of aeolian sand or dust over at least the millennial scale in either dry-cold or warm-wet periods. In such cases, paleosol development is simultaneous with dust input and paleosol OSL ages directly reflect the timing of humidity (Ee et al., 2018; Zhang et al., 2020). However, at the millennial scale, aeolian sedimentation on the NE-QTP is not continuous (Chongyi et al., 2018; Zhang et al., 2018; Chongyi et al., 2019; Yan et al., 2019; Zhang et al., 2020). During periods of warm and humid climate, dust input reduces and strong pedogenesis may occur; the mode of soil development comprises (*in-situ*) chemical weathering of aeolian—or other—parent material (E et al., 2018b; Zhang et al., 2020). Due to the predominately aeolian parent material, paleosol OSL ages indicate the timing of dust or sand deposition rather than soil formation. Thus, quartz OSL ages can be taken to indicate an upper limit to soil formation (Miao et al., 2016; Zhang et al., 2020), and the duration of mountain soil development can be effectively constrained by high-resolution OSL ages of deposits at different depths. In addition, high-resolution OSL sampling is an effective means of verifying the continuity of aeolian sedimentation and underpins millennial-scale paleoenvironmental reconstruction during the Holocene (Lu et al., 2006).

The Gonghe Basin (GHB) is the largest intramontane basin on the NE-QTP (Stauch et al., 2016) and its location in the arid/semi-arid transition zone makes it sensitive to climate change and environmental evolution. The prevailing westerly wind and high vegetation coverage of mountain areas in the southwestern basin provide suitable trapping and preservation conditions of dust and there are thick aeolian deposits. In this study, high-resolution OSL dating of a mountain sediment profile at Najiao (NJ) in the southwestern GHB, combined with analysis of grain size (GS), low frequency magnetic susceptibility (MS), total organic carbon (TOC), and geochemical elements, is used to constrain the timing of paleosol development and reconstruct Holocene aeolian activity. The findings are used to discuss the forcing mechanisms of aeolian activity in the context of regional ecological and climatic change.

Regional Setting

GHB (average elevation 3,000 m asl) is bounded by mountains, with Xiqing Mountain of the Qinling system to the east, the Heka, Ela, Wahong Mountains of the Kunlun system to the south and southeast, Qinghai South Mountain (and Qinghai Lake) to the north, and the Waligong, and Riyue Mountains to the northeast (**Figure 1A**) (Liu et al., 2013a; Liu et al., 2013b). The basin trends NW-SE, with an area of 13,800 km^2, a width of 30–90 km, and a length of approximately 210 km (Liu et al., 2013a; Liu et al., 2013b). The region is characterized by a cold and dry alpine and arid/semi-arid climate, with an annual evaporation of 528–1937 mm, a temperature and precipitation of 1.0–5.2°C and 311.1–402.1 mm, with precipitation accounting for c. 80% in summer (Liu et al., 2020). The natural vegetation shows strong altitudinal zonation. Below 3,000 m, vegetation is mainly characterized by desert and desert steppe, with some mosaic meadows in lowland areas. Around 3,200 m, the vegetation consists of typical steppe adjacent to diluvial piedmont fans. Over 3,600 m, subalpine meadows dominate the community along the mountainside in the eastern GHB (Qiang et al., 2016). The main areas of desert comprise Muge Sands and Talatan Plain, with mobile, semi-fixed, and fixed sand dunes.

MATERIALS AND METHODS

Lithology and Sample Collection

The NJ section (35°40′23.15″N, 101°5′49.04″E, 3,629 m altitude) (**Figures 1A,B**) is in the eastern Muge Sand, in the southwestern GHB. Surface vegetation is the subalpine meadow, with an outcrop thickness of 4 m. Based on lithology, the section can be divided into six layers: 0–35 cm, modern soil; 35–185 cm, weak paleosol, of which 10–60 cm contains white pseudomycelium; 185–235 cm, paleosol; 235–385 cm, loess; 385–395 cm, weak paleosol; 395–400 cm, loess. Total 18 OSL samples were collected at 10 cm intervals in/close to the paleosol layer and at 40 cm intervals elsewhere. Proxy samples—for GS, TOC, MS, and geochemical elements analysis—were collected continuously at 5 cm intervals, giving a total of 108 samples.

Proxy Analyses

A total of 108 samples have been used for measurements of GS, MS and TOC. Composition of geochemical elements was collected from 64 samples to calculate the rubidium/strontium ratio (Rb/Sr) that reflects the leaching degree of aeolian sediment in the process of weathering and pedogenesis (Nesbitt and Young, 1989; Chen et al., 1999). The GS distribution taken as an indicator of the intensity of aeolian activity was measured by a Malvern 2000 laser particle size analyzer, using the method described by Lu and An (1997). After removing carbonates, the TOC content indicating vegetation coverage and biomass was performed on an Elementar Vario TOC Cube analyzer (Gasse et al., 1991). Geochemical elements were carried out using the wavelength

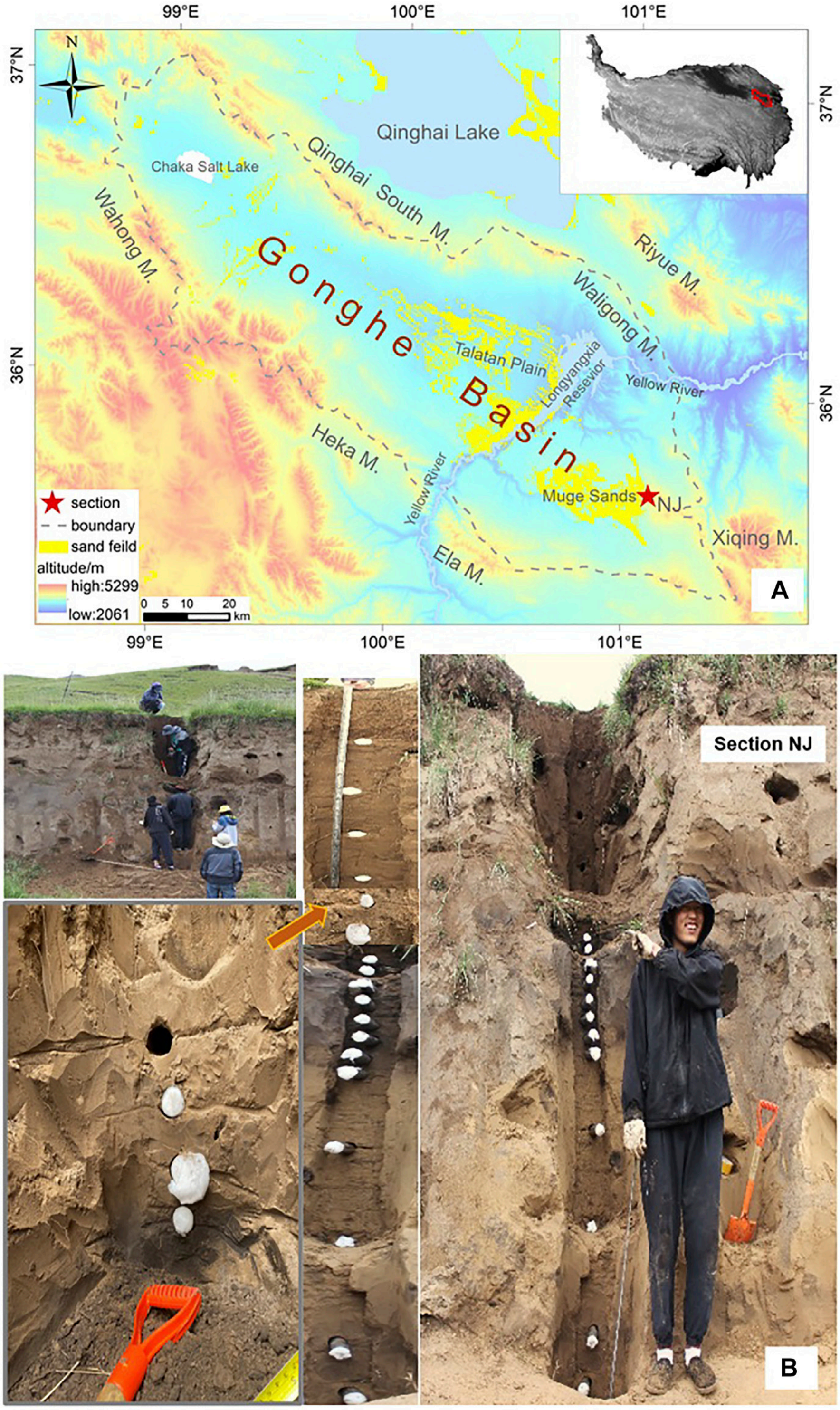

FIGURE 1 | Location maps and site details of the study area. The sand field data set is provided by National Tibetan Plateau Data Center (http://data.tpdc.ac.cn). **(A)** Location of Gonghe Basin on the Northeast Qinghai-Tibet Plateau and location of the study section (NJ) in Gonghe Basin. **(B)** Photos of Stratigraphies, landforms for section NJ.

TABLE 1 | OSL dating results for section NJ, Gonghe Basin, NE-QTP.

Sample No.	Depth /cm	^{40}K /%	^{238}U /ppm	^{232}Th /ppm	Water content /%	D_e /Gy	Dose rate /(Gy/ka)	Number /discs	Age /ka
NJ1	40	1.61 ± 0.04	1.36 ± 0.3	7.68 ± 0.6	10 ± 5	1.29 ± 0.07	3.22 ± 0.14	18	0.4 ± 0.03
NJ2	80	1.70 ± 0.04	1.40 ± 0.3	8.02 ± 0.6	10 ± 5	2.55 ± 0.15	2.80 ± 0.13	18	1.0 ± 0.07
NJ3	120	1.70 ± 0.04	1.31 ± 0.3	7.13 ± 0.6	10 ± 5	3.66 ± 0.18	2.70 ± 0.12	18	1.4 ± 0.1
NJ4	160	1.72 ± 0.04	1.31 ± 0.3	7.49 ± 0.6	10 ± 5	4.89 ± 0.29	2.72 ± 0.12	18	1.9 ± 0.1
NJ5	170	1.79 ± 0.04	1.90 ± 0.3	9.76 ± 0.6	10 ± 5	3.85 ± 0.51	3.07 ± 0.14	16	1.3 ± 0.2
NJ6	180	1.84 ± 0.04	2.03 ± 0.3	10.64 ± 0.7	10 ± 5	4.45 ± 0.58	3.2 ± 0.15	16	1.4 ± 0.2
NJ7	190	1.88 ± 0.04	1.46 ± 0.3	9.38 ± 0.6	10 ± 5	15.53 ± 0.40	2.88 ± 0.12	18	5.4 ± 0.3
NJ8	200	1.79 ± 0.04	1.49 ± 0.3	9.53 ± 0.6	10 ± 5	20.85 ± 0.62	2.81 ± 0.12	18	7.4 ± 0.4
NJ9	210	1.71 ± 0.04	1.36 ± 0.3	9.89 ± 0.6	10 ± 5	23.46 ± 0.44	2.74 ± 0.12	18	8.3 ± 0.4
NJ10	220	1.76 ± 0.04	1.41 ± 0.3	8.96 ± 0.6	10 ± 5	25.85 ± 0.46	2.72 ± 0.12	18	9.5 ± 0.5
NJ11	230	1.77 ± 0.04	1.65 ± 0.3	9.16 ± 0.6	10 ± 5	28.35 ± 1.14	2.97 ± 0.13	18	9.5 ± 0.7
NJ12	240	1.74 ± 0.04	1.50 ± 0.3	9.40 ± 0.6	10 ± 5	29.44 ± 1.12	2.75 ± 0.12	18	10.7 ± 0.7
NJ13	250	1.64 ± 0.04	1.38 ± 0.3	7.41 ± 0.6	10 ± 5	28.96 ± 1.99	2.50 ± 0.11	18	11.6 ± 1.0
NJ14	260	1.60 ± 0.04	1.38 ± 0.3	7.73 ± 0.6	10 ± 5	32.24 ± 1.72	2.48 ± 0.11	18	13.0 ± 0.9
NJ15	300	1.68 ± 0.04	1.49 ± 0.3	8.35 ± 0.6	10 ± 5	34.26 ± 1.43	3.00 ± 0.14	18	12.0 ± 0.8
NJ16	340	1.77 ± 0.04	1.70 ± 0.3	9.69 ± 0.6	10 ± 5	35.19 ± 1.45	2.94 ± 0.14	18	12.6 ± 0.8
NJ17	380	1.75 ± 0.04	1.79 ± 0.3	10.39 ± 0.6	10 ± 5	31.07 ± 0.86	2.98 ± 0.14	18	11.0 ± 0.6
NJ18	400	1.73 ± 0.04	1.70 ± 0.3	9.42 ± 0.6	10 ± 5	33.55 ± 1.67	2.87 ± 0.13	18	12.3 ± 0.9

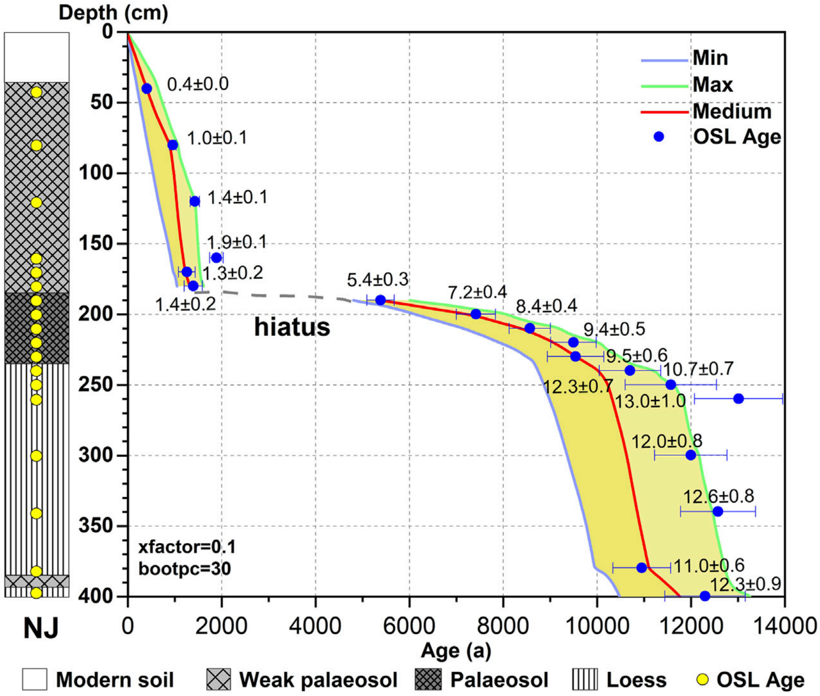

FIGURE 2 | Age-depth relationship for the NJ section based on the Undatable model (Lougheed and Obrochta, 2019).

dispersion type of X-ray fluorescence spectrometer following a routine pretreatment protocol (Liu et al., 2013a). MS was measured by a Bartington MS2 meter after drying the samples below 40°C.

OSL Dating

The quartz fraction of 63–90 μm was extracted for equivalent dose (D_e) determination. Extracted quartz was checked for purity using infrared stimulated luminescence (IRSL) measurements

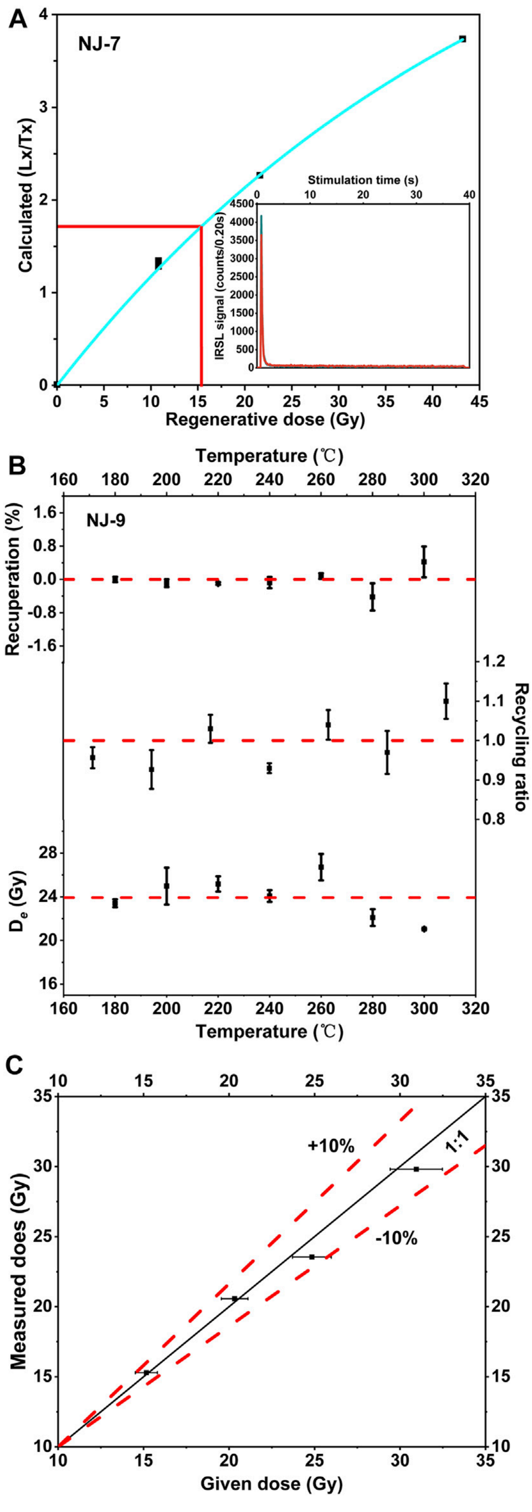

FIGURE 3 | OSL characteristics for samples, NJ section. **(A)** Growth and decay (inset) curves for sample NJ-7. **(B)** Preheat plateau tests (D_e) at sample NJ-9 showing a plateau between 180 and 300°C. **(C)** Dose recovery test. Given doses versus measured doses for four randomly selected samples. The solid black line is the slope of unity, where the ratio is 100%, and the two red dashed lines indicate 10% above and below the line. Error bars represent one standard error.

(Duller, 2003). D_e was determined by the single aliquot regenerative (SAR) protocol on a Risø TL/OSL-DA-20-C/D reader (Murray and Wintle, 2000; Wintle and Murray, 2006). For D_e calculations, the signal was derived from the first 0.16 s of stimulation and an early background (0.16–0.32 s) to minimize the influence of slow and medium components (Cunningham and Wallinga, 2010). D_e rejection criteria were restricted by two test measurements (e.g., 0.9 < R5/R1 < 1.1, and R4/N < 5%). Average D_e was calculated based on the results of 16–18 aliquots.

The concentrations of uranium (U), thorium (Th) and potassium (K) were measured by inductively coupled plasma mass spectrometry for calculating the environmental dose rate. Then the concentrations of U, Th and K were converted into infinite matrix dry dose rates using the conversion factors of Guérin et al. (2012). The cosmic ray contribution was from Prescott and Hutton (1994). Due to the modern mountain climate is relatively humid, water content was estimated as 10 ± 5%. Detailed dating information including radionuclide concentrations, dose rates, equivalent doses and age results are summarized in **Table 1**.

Age-Depth Model

The age-depth relationship was established in section NJ using the Undatable model to construct the chronological framework and verify continuity of the aeolian sediment accumulation on millenial scale (**Figure 2**). Undatable model is a rapid, deterministic age-depth modeling routine for geological sequences, using Matlab software and programming practices (Lougheed and Obrochta, 2019). For the NJ section, model parameters xfactor = 0.1 and bootpc = 30 were used.

RESULTS

Quartz Luminescence Characteristics

The quartz OSL signal of sample NJ-7 rapidly decreased to background in the first 2 s, indicating a fast component (**Figure 3A**). Preheat plateau tests were carried out on NJ-9 to select an appropriate preheating regime (**Figure 3B**). There is an apparent plateau between 180°C and 240°C. All of the recycling ratios are between 0.9 and 1.1 under different preheat temperature, and all recuperations are smaller than 5%. Consequently, a preheat temperature of 240°C and a cut-heat temperature of 200°C was selected to determine quartz De for all samples. Four randomly selected samples were chosen for dose recovery test, and all ratios lie within 10% of the slope of unity, indicating well dose recoveries (**Figure 3C**).

Dating Results

Within one standard error, OSL ages are generally grown with the increase of sampling depth, except for one age inversions in upper weak paleosol with an age of 1.9 ± 0.1 ka at the depth of 1.5 m. The 2-m deep upper weak paleosol layer was deposited in the last c. 1.5 ka. The loess age is concentrated from 12.3 ± 0.9 ka to 9.5 ± 0.6 ka. The apparent paleosol age is from 9.4 ± 0.5 ka to 5.4 ± 0.3 ka.

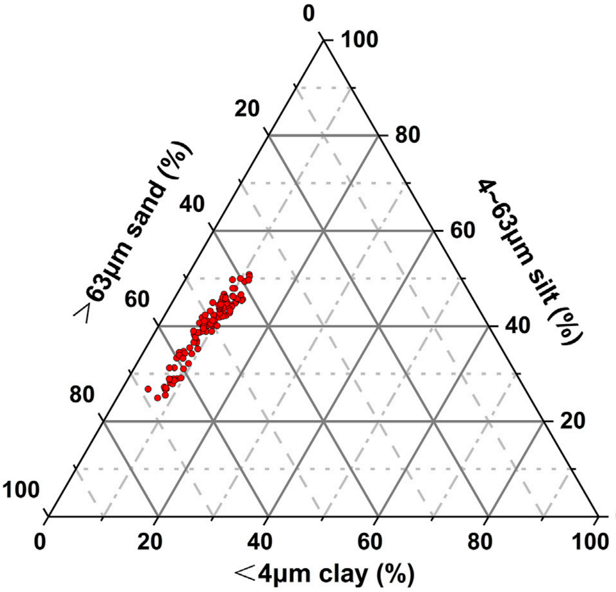

FIGURE 4 | Ternary diagram showing grain size components for samples from the NJ section.

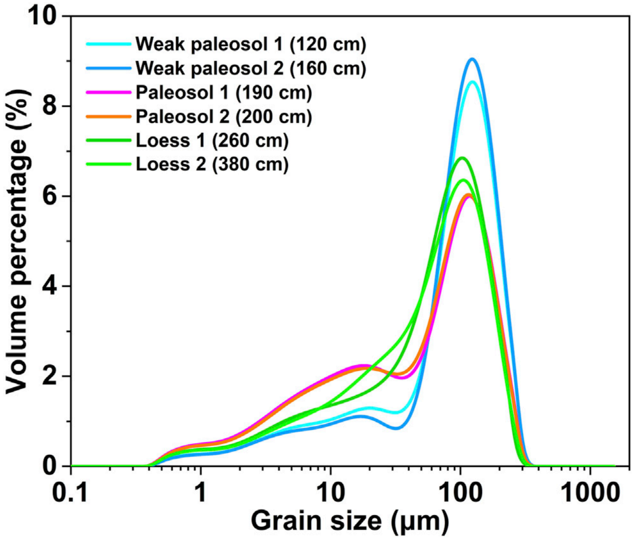

FIGURE 5 | Grain size distribution curves for selected samples from the NJ section.

The resulting age-depth curve (**Figure 2**) shows a continuous deposition from the Early to Middle Holocene and after 1.5 ka. A c. 3 ka hiatus in deposition took place in the Late Holocene (c. 5–1.5 ka). Similar millennial-scale hiatuses have been identified in other high-resolution OSL dated aeolian sections elsewhere on the NE-QTP (Zhang et al., 2018; E et al., 2019; Yan et al., 2019), indicating ubiquitous discontinuity in aeolian deposits over millennial-scale on the entire Qinghai-Tibet Plateau (QTP).

Proxy Results

The NJ section mainly comprises sand size sediment (>63 μm), ranging from 38.09 to 68.49% (average 51.31%) (**Figure 4**). Comparison of GS distributions between loess, weak paleosol, and paleosol samples (**Figure 5**) shows they are mostly unimodal grain size distribution with overlapping peaks, indicating they have a similar/single provenance and the material source has been stable over time. According to the prevailing wind direction in GHB is northwest, the desert in GHB should be the potential material source.

In the NJ section, MS varies from 23.4 to 65.8 × 10^{-8} m^3/kg (average 35.7 × 10^{-8} m^3/kg), with the highest value in paleosol and lowest in loess (**Figure 6**). But the MS in upper sandy weak paleosol is slightly higher than the lower loess. TOC varies from 1.05 to 4.5% (average 2.13%), with the highest proportion in modern soil with upper depth of 25 cm which is significantly affected by surface litter layer and root matter input (**Figure 6**). TOC in paleosol is much higher than loess and weak paleosol, but lowest in loess stratum. Rb/Sr ratio varies from 0.37 to 0.62, with an average of 0.5. Trend similar to TOC and MS is observed in the Rb/Sr ratio, which shows the highest value in paleosol and the lowest in loess (**Figure 6**).

DISCUSSION

Timing of Paleosol Development in the GHB

As mentioned above, the accuracy of paleosol OSL ages depends on the soil development mode. The ideal soil development mode for OSL dating is "aeolian dust aggradation", i.e., paleosol development is simultaneous with dust input (E et al., 2018b; Zhang et al., 2020). The high-resolution OSL dating of paleosol layer at NJ section indicates continuous dust deposition on the millennial scale. Thus, the paleosol OSL age falls well within the period of pedogenesis. According to the field observation (**Figure 1B**), the dark paleosol layer has a thickness of 50 cm (185–235 cm) dated from c. 9 ka to c.5 ka, indicating a very low dust accumulation rate during the pedogenic process. Then for obtaining a reliable paleosol age, the high-resolution OSL dating strategy is vital and necessary. The low-resolution OSL sampling strategy is difficult to differ the (*in-situ*) chemical weathering of previously deposited aeolian parent material or the "aeolian dust aggradation" at least on millennial scale. Therefore, it is not strange that the paleosol ages based on the low-resolution OSL sampling show great variations between basins, and even for different sites in the same basin.

Meanwhile, the environmental proxy indicator of paleoenvironment is equally important to verify the pedogenic intensity. In NJ, the highest MS, TOC, Rb/Sr and clay content indicate the strongest pedogenic process occurred during c. 7 to 5 ka in 185–200 cm (**Figure 6**). This result is consistent with the lake level highstands in Kuhai (**Figure 7F**) (Yan et al., 2018) and Qinghai Lake (Liu et al., 2015). Similarly, a high resolution OSL chronology at ND aeolian sand section (E et al., 2019) records the strongest pedogenesis from 6 to 4.5 ka in the neighboring Qinghai Lake area (**Figure 7E**). The tree ring (Yang et al., 2021) records a wet middle Holocene since 6.7 to 5 ka, and the precipitation

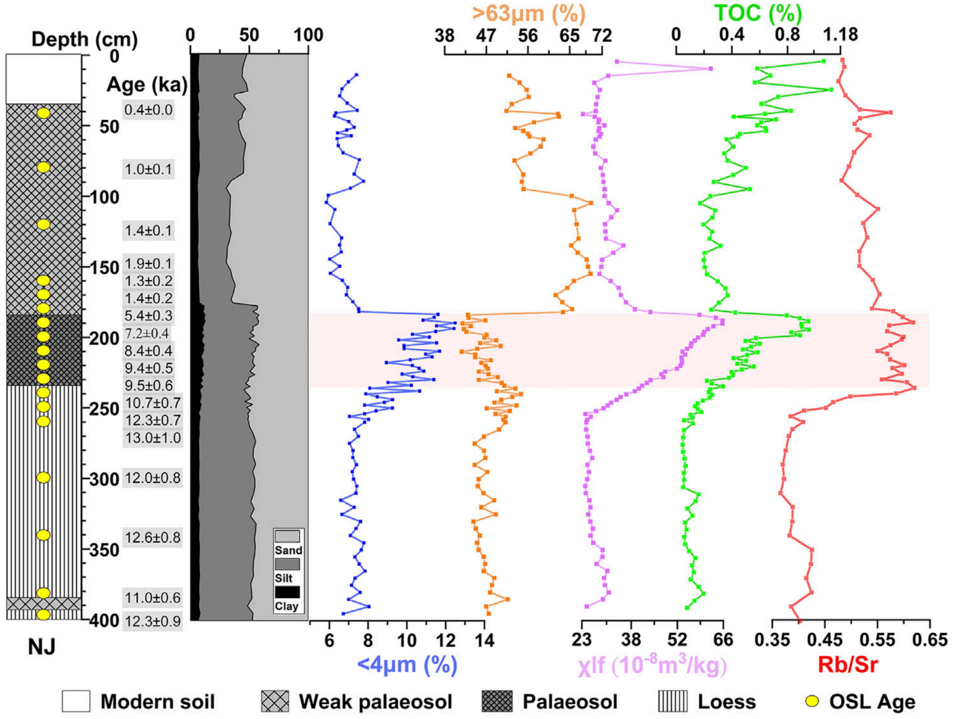

FIGURE 6 | Stratigraphic sequence of the NJ section showing OSL ages and variations in sediment size and various proxy indicators with depth.

decreased remarkably since 4 ka (**Figure 7H**). Although the deposition of 1.5–5 ka in NJ is absent, the strongest pedogenic period in GHB is clear in c. 7 to 5 ka.

History of Aeolian Activity in the GHB

The regional aeolian activity in GHB is reconstructed according to the records of different paleoclimate proxy indicators from neighboring sites on the NE-QTP in **Figure 7**. Three stages can be identified, designed I to Ⅲ.

Stage I. Late Glacial and Early Holocene (13–9 ka). NJ section lithostratigraphy is characterized by sandy loess with relatively high sand content, reflecting relatively strong and frequent wind. TOC and Rb/Sr are at their lowest in this period, indicating sparse vegetation, weak weathering, and dry climate conditions in general (**Figures 7B,C**). Aeolian sediment of ND in Qinghai Lake, high salinity of Qinghai Lake and low lake level from Kuhai Lake suggest a strengthened aeolian activity and dry climate condition in NE-QTP (**Figures 7E–G**) (Zhang et al., 1989; Yan et al., 2018; E et al., 2019). All these results are consistent with the climate change history in QTP (Chen et al., 2020). Overall, climatic conditions in GHB within NE-QTP show a consistent condition and reveal intensified aeolian activity during the early Holocene.

Stage II. Middle Holocene (9–5 ka). NJ section lithostratigraphy shifts to paleosol in this stage. The sand content decreased slightly, but the MS, TOC, clay content and Rb/Sr increased significantly. It could indicate increased precipitation, enhanced pedogenesis, high biomass and weakened aeolian activity under relatively stable warm and wet conditions (**Figure 6**). In the latter part of the period between c. 7–5 ka, sand content is at its lowest, TOC and Rb/Sr at highest (**Figures 7B,C**), indicating the strong pedogenesis. These findings are consistent with previous studies in GHB that show the highest moisture levels, and lowest aeolian activity in the Mid-Holocene (Stauch et al., 2016). Similar patterns are observed in other records in the NE-QTP including low mean grain size (Mz) at the ND section (**Figure 7E**); highest lake level in Kuhai Lake and lowest salinity in Qinghai Lake (**Figures 7F,G**); and maximal at Qilian Mountain (Yang et al., 2021) between c. 7.6–4 ka (**Figure 7H**). In general, the climatic optimum in the GHB between c. 7–5 ka corresponds with other parts of the NE-QTP that record their wettest conditions in the Middle Holocene.

Stage III. Late Holocene (after c. 1.5 ka). NJ section lithostratigraphy comprises weak paleosol. The sand content in this layer is much higher than the middle to early Holocene paleosol and sandy loess (**Figures 6**, **7A**). It indicates aeolian activities after c. 1.5 ka have been enhanced and are even stronger than early Holocene. Contradictorily, the Rb/Sr and TOC are higher than the lower sandy loess, and the MS is slightly higher than the lower sandy loess (**Figures 7B–D**). All these imply a wetter and better climate condition in the late Holocene than early Holocene. The prevailing wind direction in GHB is northwest, and straight distance from the mountain of NJ section to the Muge sands is less than 10 km (**Figure 1A**). Undoubtedly, NJ section recorded enhanced aeolian activities in GHB. Consistently, the stronger aeolian activity after c. 1.5 ka BP was reported in NE-QTP by the summarization of 93 aeolian sand OSL ages from 39 sections (Chen et al., 2016).

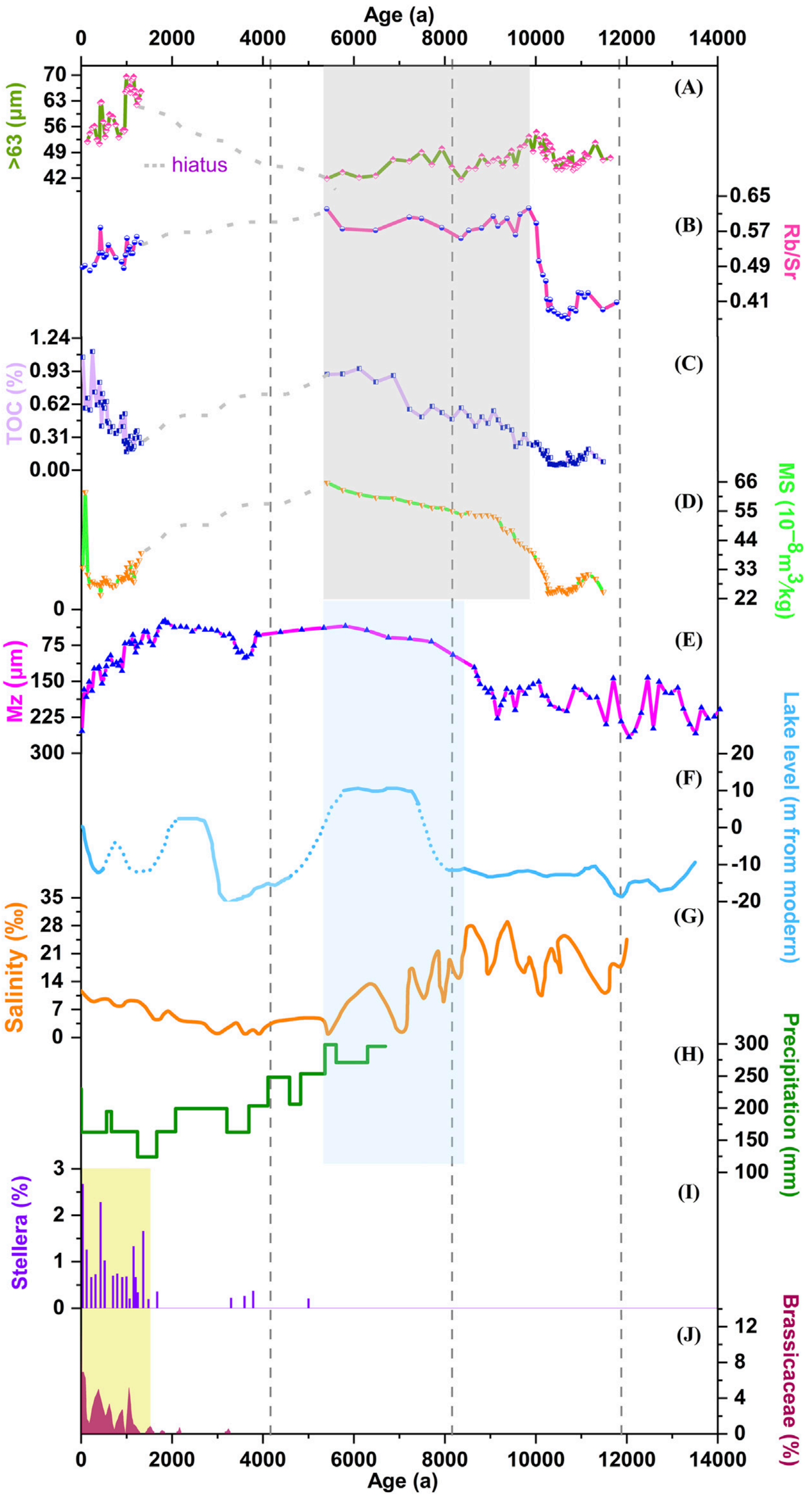

FIGURE 7 | Comparison of proxy indicators for the NJ section with published paleoclimate records for other sites on the Northeast Qinghai-Tibet Plateau (NE-QTP) (ages based on the Undatable model). **(A)** >63 μm content, NJ section. **(B)** Rb/Sr, NJ section. **(C)** Total organic carbon (TOC), NJ section. **(D)** Low frequency magnetic susceptibility (MS), NJ section. **(E)** Mean grain size (Mz), ND section, Qinghai Lake (E et al., 2019). **(F)** Lake level, core KH17, Kuhai Lake (Yan et al., 2018). **(G)** Salinity, Qinghai Lake (Zhang et al., 1989). **(H)** Precipitation, tree ring DLH, Qilian Mountains (Yang et al., 2021). **(I)** Stellera pollen, core GGHA, Gonghe Basin (Liu et al., 2016). **(J)** Brassicaceae pollen, core GGHA, Gonghe Basin (Huang et al., 2017).

However, there was no decreasing trend after 1.5 ka BP in the precipitation reconstruction based on tree rings from Qilian Mountain after 3.5 ka BP (**Figure 7H**) (Yang et al., 2021). It was inferred that the increased aeolian activity after c.1.5 ka BP is not related to climate change but a consequence of intensified human activity (Zhang et al., 1988; Chen et al., 2016). Pollen from Genggahai Lake in GHB suggests an intensification of human settlement and grazing activity after c. 1.4 ka by high percentages of Stellera and Brassicaceae pollen and Sporormiella spores (Liu et al., 2016; Huang et al., 2017, Huang et al., 2020) (**Figures 7I,J**). Repeated shifts between nomadic pasture and farmland in the Qinghai Lake area since the late Western Han Dynasty (2.0–1.8 ka, 1.9–1.5 ka) may promote aeolian activity (Sun et al., 2021; Wei et al., 2021). For broader northern China, increased dust storms since c. 2 ka BP were also closely linked to increasing human populations in the dust source regions of northern China (Chen et al., 2021). In the interior of GHB, the intensity of human activity is much stronger and the ecological resistance is much lower. With the enhancement of human activities in the interior of GHB, sand supply was increased to the mountain soils as parental material. Increased sand contents dilute clay contents and magnetic minerals that produced by pedogenesis, then the MS of weak plaeosol present a lower feature. Rb/Sr ratio is less affected by aeolian activity because it reflects the proportionality of the relative contents of two elements (Wang et al., 2020), so Rb/Sr ratio reflects pedogenesis more likely, similar with TOC.

Overall, strong aeolian activities in GHB since c. 1.5 ka BP is closely related to the enhanced human activities than natural variability of climate.

CONCLUSION

The duration of mountain soil development in GHB was effectively constrained by high-resolution OSL ages from c. 7–5 ka. The period of strong pedogenesis is consistent with the warm and wet climatic condition recorded with tree rings and high lake levels in NE-QTP. A successive accumulation at the NJ section was recorded over the millennial scale during the Early to Middle Holocene in GHB, but a c. 3 ka hiatus was found between c. 5 and 1.5 ka. The aeolian activities showed a strong aeolian activity in GHB during Early Holocene (13–9 ka), consistent with the paleoclimatic records on the NE-QTP. Pedogenesis began at c. 9 ka, with the most intensive paleosol development, and the lowest aeolian activity in c. 7–5 ka. Weak paleosol development after c. 1.5 ka, but increased sand content, imply that human activities were enhanced in the interior of GHB in the Late Holocene.

DATA AVAILABILITY STATEMENT

The original contributions presented in the study are included in the article/Supplementary Material, further inquiries can be directed to the corresponding author.

AUTHOR CONTRIBUTIONS

CX performed the OSL dating, proxy data measurement and analysis, and finished writing the manuscript. CE contributed to the conception of the study, organization of the manuscript and manuscript revision. YS, JZ, and MS contributed to the modifications and suggestions. ZZ contributed to the age-depth model. YZ helps in the experimental treatment of OSL dating and proxy analysis.

FUNDING

The research was funded by the National Natural Science Foundation of China (Grant Nos 42171011, 41761042), the Natural Science Foundation of Qinghai (Grant No. 2021-ZJ-918).

ACKNOWLEDGMENTS

We thank Ji Xianba, Qiang Peng, Liqian Xie, Fajun Su, Yang Li, Guochuan Xia for helps in the field and thank Barbara Rumsby for editing the manuscript. Special thanks to reviewers and editor Zhiwei Xu whose constructive suggestions and detailed comments helped to clarify and improve the paper.

REFERENCES

An, Z., Colman, S. M., Zhou, W., Li, X., Brown, E. T., Jull, A. J. T., et al. (2012). Interplay between the Westerlies and Asian Monsoon Recorded in Lake Qinghai Sediments since 32 Ka. *Sci. Rep.* 2, 619. doi:10.1038/srep00619

Chen, F., Wu, D., Chen, J., Zhou, A., Yu, J., Shen, J., et al. (2016). Holocene Moisture and East Asian Summer Monsoon Evolution in the Northeastern Tibetan Plateau Recorded by Lake Qinghai and its Environs: A Review of Conflicting Proxies. *Quat. Sci. Rev.* 154, 111–129. doi:10.1016/j.quascirev.2016.10.021

Chen, F., Zhang, J., Liu, J., Cao, X., Hou, J., Zhu, L., et al. (2020). Climate Change, Vegetation History, and Landscape Responses on the Tibetan Plateau during the Holocene: A Comprehensive Review. *Quat. Sci. Rev.* 243, 106444. doi:10.1016/j.quascirev.2020.106444

Chen, J., Wang, Y. J., Ji, J. F., Chen, Y., and Lu, H. Y. (1999). Rb/Sr Variations and its Climatic Stratigraphical Significance of a Loess-Paleosol Profile from Luochuan, Shanxi Province. *Quat. Sci.* 19 (4), 350–356.

Chen, S., Liu, J., Wang, X., Zhao, S., Chen, J., Qiang, M., et al. (2021). Holocene Dust Storm Variations over Northern China: Transition from a Natural Forcing to an Anthropogenic Forcing. *Sci. Bull.* 66, 2516–2527. doi:10.1016/j.scib.2021.08.008

Chongyi, E., Sohbati, R., Murray, A. S., Buylaert, J.-P., Liu, X., Yang, L., et al. (2018). Hebei Loess Section in the Anyemaqen Mountains, Northeast Tibetan Plateau: A High-Resolution Luminescence Chronology. *Boreas* 47, 1170–1183. doi:10.1111/bor.12321

ChongYi, E., Jing, Z., ZongYan, C., YongJuan, S., YaJuan, Z., Ping, L., et al. (2019). High Resolution OSL Dating of Aeolian Activity at Qinghai Lake, Northeast Tibetan Plateau. *Catena* 183, 104180. doi:10.1016/j.catena.2019.104180

Cunningham, A. C., and Wallinga, J. (2010). Selection of Integration Time Intervals for Quartz OSL Decay Curves. *Quat. Geochronol.* 5, 657–666. doi:10.1016/j.quageo.2010.08.004

Duller, G. A. T. (2003). Distinguishing Quartz and Feldspar in Single Grain Luminescence Measurements. *Radiat. Measurements* 37, 161–165. doi:10.1016/S1350-4487(02)00170-1

Ee, C., Zhang, J., Wu, C. Y., Sun, Y. J., Sun, M. P., Yan, W., et al. (2018). Study of Chronology of the Meadow Soil in the Qinghai Lake Basin by Means of Optically Stimulated Luminescence. *Acta Pedologica Sinica* 55, 1325–1335. doi:10.11766/trxb201801090021

Gasse, F., Arnold, M., Fontes, J. C., Fort, M., Gibert, E., Huc, A., et al. (1991). A 13,000-year Climate Record from Western Tibet. *Nature* 353, 742–745. doi:10.1038/353742a0

Guérin, G., Mercier, N., Nathan, R., Adamiec, G., and Lefrais, Y. (2012). On the Use of the Infinite Matrix assumption and Associated Concepts: A Critical Reviewfinite Matrix assumption and Associated Concepts: a Critical Review. *Radiat. Measurements* 47, 778–785. doi:10.1016/j.radmeas.2012.04.004

Hu, M. J., Yang, A. L., and Zhang, W. L. (2015). Environmental Evolution since the Middle-Late Holocene in the Maqu Plateau Reflected by Constant Element Oxides Content and Ratio. *J. Desert Res.* 35, 313–321. doi:10.7522/j.issn.1000-694X.2015.00002

Huang, X.-z., Liu, S.-s., Dong, G.-h., Qiang, M.-r., Bai, Z.-j., Zhao, Y., et al. (2017). Early Human Impacts on Vegetation on the Northeastern Qinghai-Tibetan Plateau during the Middle to Late Holocene. *Prog. Phys. Geogr. Earth Environ.* 41, 286–301. doi:10.1177/0309133317703035

Huang, X., Zhang, J., Storozum, M., Liu, S., Gill, J. L., Xiang, L., et al. (2020). Long-term Herbivore Population Dynamics in the Northeastern Qinghai-Tibetan Plateau and its Implications for Early Human Impacts. *Rev. Palaeobotany Palynology* 275, 104171. doi:10.1016/j.revpalbo.2020.104171

Li, G., Zhang, H., Liu, X., Yang, H., Wang, X., Zhang, X., et al. (2020). Paleoclimatic Changes and Modulation of East Asian Summer Monsoon by High-Latitude Forcing over the Last 130,000 Years as Revealed by Independently Dated Loess-Paleosol Sequences on the NE Tibetan Plateau. *Quat. Sci. Rev.* 237, 106283. doi:10.1016/j.quascirev.2020.106283

Liu, B., Jin, H. L., Sun, Z., Su, Z. Z., and Zhang, C. X. (2013b). Holocene Millennial-Scale Climatic Change Recorded by Grain Size and Chemical Elements of Peat Deposits in Gonghe Basin, Northeastern Tibetan Plateau. *J. Glaciology Geocryology* 35, 609–620. doi:10.7522/j.issn.1000-0240.2013.0070

Liu, B., Jin, H. L., Sun, Z., Sun, Z. Z., and Zhang, C. X. (2012). Geochemical Characteristics of Aeolian Deposits in Gonghe Basin, Northeastern Qinghai-Tibetan Plateau and the Indicating Climatic Changes. *Adv. Earth Sci.* 27, 788–799.

Liu, B., Jin, H., Sun, L., Su, Z., Zhang, C., and Zhao, S. (2017). History of Moisture Change Derived from Slope Sediments of the Eastern Gonghe Basin (Northeastern Qinghai-Tibetan Plateau) during the Last 17 Ka. *Geol. J.* 52, 583–593. doi:10.1002/gj.2795

Liu, B., Jin, H., Sun, L., Sun, Z., and Su, Z. (2013a). Winter and Summer Monsoonal Evolution in Northeastern Qinghai-Tibetan Plateau during the Holocene Period. *Geochemistry* 73, 309–321. doi:10.1016/j.chemer.2013.03.006

Liu, B., Zhao, H., Jin, H., and Chen, F. (2020). Holocene Moisture Variation Recorded by Aeolian Sand-Palaeosol Sequences of the Gonghe Basin, Northeastern Qinghai-Tibetan Plateau, China. *Acta Geologica Sinica - English Edition* 94, 668–681. doi:10.1111/1755-6724.14541

Liu, S. S., Huang, X. Z., Qiang, M. R., Lin, X. R., Bai, Z. J., and Peng, W. (2016). Vegetation and Climate Change during the Mid-late Holocene Reflected by the Pollen Record from Lake Genggahai, Northeastern Tibetan Plateau. *Quat. Sci.* 36, 247–256. doi:10.11928/j.issn.1001-7410.2016.02.01

Liu, X.-J., Lai, Z., Madsen, D., and Zeng, F. (2015). Last Deglacial and Holocene lake Level Variations of Qinghai Lake, north-eastern Qinghai-Tibetan Plateau. *J. Quat. Sci.* 30, 245–257. doi:10.1002/jqs.2777

Lougheed, B. C., and Obrochta, S. P. (2019). A Rapid, Deterministic Age-Depth Modeling Routine for Geological Sequences with Inherent Depth Uncertainty. *Paleoceanography and Paleoclimatology* 34, 122–133. doi:10.1029/2018PA003457

Lu, H., Stevens, T., Yi, S., and Sun, X. (2006). An Erosional Hiatus in Chinese Loess Sequences Revealed by Closely Spaced Optical Dating. *Chin. Sci Bull* 51, 2253–2259. doi:10.1007/s11434-006-2097-x

Lu, H. Y., and An, Z. S. (1997). An Experimental Study on the Impacts on Measurement of the Grain Size of Loess Sediment from Pretreatment. *Chin. Sci. Bull.* 42, 2535–2538. doi:10.1007/bf02882455

Miao, X., Wang, H., Hanson, P. R., Mason, J. A., and Liu, X. (2016). A New Method to Constrain Soil Development Time Using Both OSL and Radiocarbon Dating. *Geoderma* 261, 93–100. doi:10.1016/j.geoderma.2015.07.004

Murray, A. S., and Wintle, A. G. (2000). Application of the Single-Aliquot Regenerative-Dose Protocol to the 375°C Quartz TL Signal. *Radiat. Measurements* 32, 579–583. doi:10.1016/S1350-4487(00)00089-5

Nesbitt, H. W., and Young, G. M. (1989). Formation and Diagenesis of Weathering Profiles. *J. Geology.* 97, 129–147. doi:10.1086/629290

Prescott, J. R., and Hutton, J. T. (1994). Cosmic ray Contributions to Dose Rates for Luminescence and ESR Dating: Large Depths and Long-Term Time Variations. *Radiat. Measurements* 23, 497–500. doi:10.1016/1350-4487(94)90086-8

Qiang, M., Chen, F., Song, L., Liu, X., Li, M., and Wang, Q. (2013). Late Quaternary Aeolian Activity in Gonghe Basin, Northeastern Qinghai-Tibetan Plateau, China. *Quat. Res.* 79, 403–412. doi:10.1016/j.yqres.2013.03.003

Qiang, M., Jin, Y., Liu, X., Song, L., Li, H., Li, F., et al. (2016). Late Pleistocene and Holocene Aeolian Sedimentation in Gonghe Basin, Northeastern Qinghai-Tibetan Plateau: Variability, Processes, and Climatic Implications. *Quat. Sci. Rev.* 132, 57–73. doi:10.1016/j.quascirev.2015.11.010

Qin, X. G., Yin, Z. Q., Wang, M. H., Zhao, W. J., Mu, Y., and Zhang, L. (2017). Loess Records of the Holocene Climate Change of Gonghe and Guide Basins in the Northeastern Boundary of the Tibet Plateau. *Acta Pedologica Sinica* 91, 266–286.

Stauch, G., Lai, Z., Lehmkuhl, F., and Schulte, P. (2018). Environmental Changes during the Late Pleistocene and the Holocene in the Gonghe Basin, north-eastern Tibetan Plateau. *Palaeogeogr. Palaeoclimatol. Palaeoecol.* 509, 144–155. doi:10.1016/j.palaeo.2016.12.032

Sun, M., Sun, Y., Wei, H., Hou, G., Xianba, J., Xie, L., et al. (2021). Luminescence Dating of Relics in Ancient Cities Provides Absolute Dates for Understanding Human-Land Relationships in Qinghai Lake Basin, Northeastern Tibetan Plateau. *Front. Earth Sci.* 9, 701037. doi:10.3389/feart.2021.701037

Sun, Q. F., Cheng, B., and Zhao, L. (2014). Climate and Environment Phase Deviation Recorded by clay Minerals and Pollen since the Late Deglacial in the Gonghe Basin. *J. Desert Res.* 34, 1237–1247. doi:10.7522/j.issn.1000-694X.2013.00445

Wang, Y., Guo, F., Ma, L., Yan, Y., Liu, X., and Sun, Y. (2020). Millennial-scale Summer Monsoon Oscillations over the Last 260 Ka Revealed by High-Resolution Elemental Results of the Mangshan Loess-Palaeosol Sequence from the southeastern Chinese Loess Plateau. *Quat. Int.* 552, 164–174. doi:10.1016/j.quaint.2020.05.039

Wei, H. C., E, C. Y., Duan, R. L., Zhang, J., Sun, Y. J., Hou, G. L., et al. (2021). Fungal Spore Record of Pastoralism on the NE Qinghai-Tibetan Plateau since the Middle Holocene. *Sci. China Earth Sci.* 51, 1907–1922. doi:10.1007/s11430-020-9787-4

Wintle, A. G., and Murray, A. S. (2006). A Review of Quartz Optically Stimulated Luminescence Characteristics and Their Relevance in Single-Aliquot Regeneration Dating Protocols. *Radiat. Measurements* 41, 369–391. doi:10.1016/j.radmeas.2005.11.001

Xu, S. Y. (1987). Depositional Period and Sedimentary Environment of Gonghe Series in the Qinghai Province, China. Research Group of "Paleogeographical Evolution of the Late Cenozoic in the Northeast Marginal Regions of Qinghai-Xizang Plateau". *J. Lanzhou Univ. (Natural Sciences)* 23, 109–119. doi:10.13885/j.issn.0455-2059.1987.02.019

Yan, D., Wünnemann, B., Zhang, Y., Long, H., Stauch, G., Sun, Q., et al. (2018). Response of lake-catchment Processes to Holocene Climate Variability: Evidences from the NE Tibetan Plateau. *Quat. Sci. Rev.* 201, 261–279. doi:10.1016/j.quascirev.2018.10.017

Yan, W. T., E, C. Y., Jiang, Y. Y., Sun, Y. J., Lv, S. C., Zhang, J., et al. (2019). Study on the History of Eolian Sand Activities in Gonghe Basin Based on OSL Dating. *J. Salt Lake Res.* 27, 28–38. doi:10.12119/j.yhyj.201901004

Yang, B., Qin, C., Bräuning, A., Osborn, T. J., Trouet, V., Ljungqvist, F. C., et al. (2021). Long-term Decrease in Asian Monsoon Rainfall and Abrupt Climate Change Events over the Past 6,700 Years. *Proc. Natl. Acad. Sci. USA* 118, e2102007118. doi:10.1073/pnas.2102007118

Zhang, F. X., Lei, D. T., and Tian, Z. X. (1988). Ancient Graziery in Qinghai. *Agr. Archaeol.* 02, 358–365.

Zhang, J., E, C., Wu, C., Sun, Y., Li, P., Shi, Y., et al. (2020). An alpine Meadow Soil Chronology Based on OSL and Radiocarbon Dating, Qinghai Lake, Northeastern Tibetan Plateau. *Quat. Int.* 562, 35–45. doi:10.1016/j.quaint.2020.05.044

Zhang, J., E, C. Y., and Zhao, Y. J. (2018). A High-Density Optically Stimulated Luminescence (OSL) Dating at Heima He Loess Section in Qinghai Lake Area. *J. Earth Environ.* 9, 557–568. doi:10.7515/JEE182048

Zhang, P. X., Zhang, B. Z., and Yang, W. B. (1989). On the Model of post-glacial Palaeoclimatic Fluctuation in Qinghai Lake Region. *Quat. Sci.* 9, 66–77.

Conflicts of Interest: The authors declare that the research was conducted in the absence of any commercial or financial relationships that could be construed as a potential conflict of interest.

Publisher's Note: All claims expressed in this article are solely those of the authors and do not necessarily represent those of their affiliated organizations, or those of the publisher, the editors and the reviewers. Any product that may be evaluated in this article, or claim that may be made by its manufacturer, is not guaranteed or endorsed by the publisher.

Copyright © 2022 Xu, E, Shi, Zhang, Sun, Zhang and Zeng. This is an open-access article distributed under the terms of the Creative Commons Attribution License (CC BY). The use, distribution or reproduction in other forums is permitted, provided the original author(s) and the copyright owner(s) are credited and that the original publication in this journal is cited, in accordance with accepted academic practice. No use, distribution or reproduction is permitted which does not comply with these terms.

frontiers
in Earth Science

ORIGINAL RESEARCH
published: 02 March 2022
doi: 10.3389/feart.2022.850633

Quantitative Reconstruction of Precipitation and Lake Areas During Early to Middle Holocene in Mu Us Desert, North China

Dawei Li[1]*, Yongqiu Wu*[2]**, Lihua Tan*[1]*, Yanglei Wen*[1] *and Tianyang Fu*[1]

[1]*State Key Laboratory of Earth Surface Processes and Resource Ecology, Beijing Normal University, Beijing, China,* [2]*College of Geography and Environmental Sciences, Zhejiang Normal University, Jinhua, China*

Paleoclimatic researches have revealed that the East Asian summer monsoon (EASM) strengthened and precipitation increased in north China during the early to middle Holocene. The lacustrine landform and sediment recorded approximately simultaneous Holocene high lake levels. However, relatively few studies have been reported involving the quantitative reconstruction of precipitation and lake areas in the Mu Us Desert (MUD), northwest edge area of the modern EASM. Based on the lacustrine landform, and by using the lake hydrologic model, this study quantitatively reconstructed precipitation and lake areas during the early to middle Holocene in the MUD. The results revealed the following: 1) A total of 127 paleolakes existed in the closed drainage area during the early to middle Holocene. The area of paleolakes was 896.1 km^2, which is 2.96 times that of modern lakes. The relative height between the highstand and the modern lake surface is ~5–9 m. 2) Precipitation during the early to middle Holocene decreased from 550 mm in the southeast to 350 mm in the northwest. The 400 mm isohyet moved 130–170 km to the northwest, roughly coincident with the modern 250 mm isohyet. 3) The relative increase in precipitation was ~32–60%, and the increase in the west was significantly higher than in the east. The precipitation gradient in much of the MUD was lower than the present. The results show that the monsoon edge area and monsoon rain belt migrated to the northwest during the early to middle Holocene. The MUD was stably dominated by the EASM. Data also showed that the spatio-temporal pattern of the climate during the early to middle Holocene was relatively humid with a decreased precipitation gradient for millennia.

Keywords: Mu Us Desert, closed drainage area, early to middle Holocene, quantitative precipitation reconstruction, lake area

OPEN ACCESS

Edited by:
Zhuolun Li,
Lanzhou University, China

Reviewed by:
Xiaokang Liu,
Shaanxi Normal University, China
Li Wu,
Anhui Normal University, China

Correspondence:
Yongqiu Wu
wuyongqiu@zjnu.edu.cn

Specialty section:
This article was submitted to Quaternary Science, Geomorphology and Paleoenvironment, a section of the journal Frontiers in Earth Science

Received: *07 January 2022*
Accepted: *04 February 2022*
Published: *02 March 2022*

Citation:
Li D, Wu Y, Tan L, Wen Y and Fu T (2022) Quantitative Reconstruction of Precipitation and Lake Areas During Early to Middle Holocene in Mu Us Desert, North China. Front. Earth Sci. 10:850633. doi: 10.3389/feart.2022.850633

INTRODUCTION

There were variations in monsoon precipitation in the geological data recorded in China during the Holocene (An et al., 2000). The data showed that the East Asian summer monsoon (EASM) strengthened, the monsoon rain belt moved northwestward, and precipitation increased in the early to middle Holocene (Yang et al., 2015a). Holocene precipitation variations in north China have been quantitatively reconstructed with multiple methods. In the Chinese Loess Plateau, Sun et al. (1995) established a susceptibility-rainfall conversion function by regression analysis of magnetic susceptibility of surface soils and contemporary precipitation data. The reconstructed

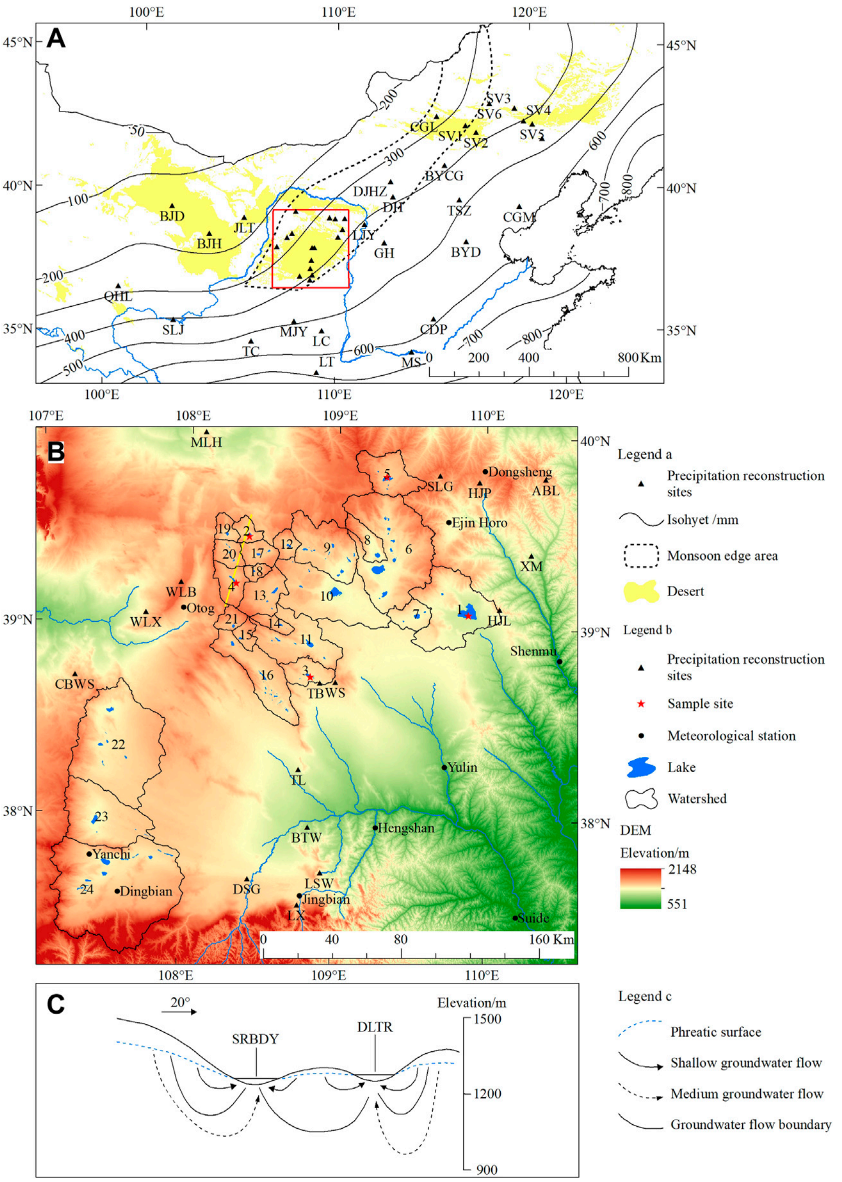

FIGURE 1 | Overview of the study area. **(A)** Map of northern China and location of study area. The modern isohyets are values averaged over 56 years (1961–2016); monsoon edge area is modified after Zhang et al. (1993); the red rectangle is the study area. **(B)** Topography of study area. The DEM data is from ASTER GDEM version2. **(C)** Diagrammatic section of groundwater flow system of SRBDY–DLTR Nuur drainage areas (modified after Hou et al., 2008); location of the section is shown by the yellow line in **Figure 1B**).

precipitation was 100–150 mm higher than the present in the loess-desert transitional zone during the Holocene optimum. Precipitation reconstruction from the Gonghai Lake in the north loess plateau revealed gradually increasing rainfall since the last deglaciation, reaching a maximum of 30% higher than the present during the middle Holocene (Chen et al., 2015). In eastern Inner Mongolia Plateau, pollen records of Chagan Nuur showed that the East Asian monsoon precipitation began to increase in the early Holocene and reached a maximum in the middle Holocene, which was 30–50% higher than modern rainfall (Li et al., 2020). The lake hydrologic model and Holocene shoreline records were used to reconstruct the precipitation in Dali Lake, located near the northwestern limit of the EASM domain. The results showed that rainfall in the Dali Lake area increased by 11–5.5 ka, and the EASM expanded northwest (Goldsmith et al., 2017). The Bayanchagan Lake in southern Inner Mongolia also recorded a wet period in the early to middle Holocene, with annual precipitation approximately 32% higher than the present (Jiang et al., 2006). In the Alxa Plateau, the reconstructed average precipitation of the Jilantai playa during 8.5–3.5 ka was 246 mm, about 75% higher than the present (Wu et al., 2018). In the Badain Jaran Desert, Yang and

Williams (2003) estimated precipitation of ~200 mm during the early to middle Holocene, at least twice that of the modern period. The reconstructed precipitation in the Shiyang River drainage area during the middle Holocene was approximately 70% higher than the present (Liu and Li, 2017). The reconstruction results showed that the increase percentage in precipitation during the early to middle Holocene ranged from ~30% to 100% compare with the present in north China, with significant differences near the northwestern limit of the EASM domain.

Lakes are treated as archives of earth history (Cohen, 2003). In structurally stable regions, lake level fluctuation is a sensitive response to catchment climatic change (Fritz, 2008). According to the quantitative reconstruction results, the climate in the early to middle Holocene was wetter than the present. Furthermore, the lacustrine landform and strata show the lakes' highstand during this period. For instance, the lacustrine strata revealed by cores in the Ulan Buh Desert show that a unified paleolake developed in the northern part of the desert during the early to middle Holocene (Chen et al., 2014). The lake highstand in Badain Jaran Desert occurred at ~10–6.6 cal ka BP (Wang et al., 2016). Evidence from ancient shorelines and lacustrine stratigraphy in Badain Jaran Desert indicate that the area of the lakes during this period was about five times that of modern lakes (Yang and Williams, 2003). The terrace of Baijian lake in Tengger Desert shows the lake level was ~15 m higher than present at 8.5–5.1 ka (Zhang et al., 2004). Furthermore, lacustrine landform and strata recorded the existence of lake highstands during the early and middle Holocene in the south and east Inner Mongolia Plateau (Yang et al., 2011; Yang et al., 2015b; Zhang et al., 2016).

The Mu Us Desert (MUD) is one of the twelve sandy areas in China. It is located northwest edge area of the modern EASM (**Figure 1A**). Precipitation reconstruction is of great significance to the study of climate change in the EASM edge area and the evolution of the MUD. In addition, it is beneficial to understand the desert's evolution and landform pattern by reconstructing paleolake area during the early to middle Holocene. Previous research has mainly focused on sediments in the southeast of the desert. Moreover, paleoclimatic records have been revealed from the aeolian sand-paleosol sequence, loess-paleosol sequence, and alluvial-lacustrine-peat deposition (Gao et al., 1993; Zhou et al., 1999; Jia et al., 2015; Liu et al., 2018a; Jia et al., 2018). Proxies such as magnetic susceptibility and pollen assemblage have been used to quantitatively reconstruct precipitation levels (Shi et al., 1988; Chen et al., 1993; Sun and Feng, 2013; Liu et al., 2017). The paleoclimatic research in the northwest of the desert has received relatively less attention. Moreover, current studies rarely involve the reconstruction of the paleolake area in the desert. Here, this study presents and discusses reconstructed precipitation and lake areas during the Holocene highstand based on the lakes in the closed drainage area of the west and north MUD.

REGIONAL SETTING

The MUD, with an area of about 4 × 10^4 km^2, is situated in the southeastern Ordos Plateau. Elevation ranges from 1600 m a.s.l. in the northwest to 1,200 m in the southeast. Bedrock hills from the arid denudation plateau in the northwest MUD extend to the southeast. Lakes and alluvial-lacustrine plains are distributed in valleys between bedrock hills. The aeolian landform presents a characteristically staggered distribution pattern of different forms of mobile, semi-fixed, and fixed dunes/land (Department of Geography of Peking University, 1983). The underlying bedrock in the MUD is Jurassic and Cretaceous sandstone, of which the weathered detritus provide one of the major provenances of the desert(Zhu et al., 1980). The mean annual precipitation decreased by about 450 mm to the northwest. Dominated by the East Asian monsoon, 60–70% of the annual rainfall occurs between July and September. The mean annual temperature ranges from 6.5 to 9°C.

There are 154 natural lakes in the MUD covering an area ≥0.1 km^2(Wu et al., 2017). Most of the lakes are distributed in bedrock valleys or aeolian depressions. Jurassic and Cretaceous sandstone constitute the lake floor. These lakes are salt lakes with a mineral concentration ranging from 75 to 400 g/L, except for some freshwater or brackish water lakes such as Hongjian Nuur and Daotuhaizi in the southeast MUD(Zheng et al., 1992). The average depth of most lakes is within 2 m. Hongjian Nuur is the deepest lake with an average depth of 8.2 m at 1230 m a.s.l (Wang and Dou, 1998). Groundwater resources in MUD are abundant with a salinity less than 1 g/L. The groundwater table in the inter-dune depressions is within 1 m (Department of Geography of Peking University, 1983). The lakes are convergent centers of surface and groundwater runoff in local watershed (Hou et al., 2005).

The west and north MUD belong to the Ordos Plateau closed drainage area, showing neither surface nor groundwater hydraulic connection with the Yellow River and its tributaries (Hou et al., 2008). There are 108 natural lakes distributed in closed drainage area. The total area of these lakes is 301.1 km^2. These lakes can be divided into twenty-four drainage basins according to surface watershed (**Figure 1B**). The surface watershed is approximately consistent with the groundwater watershed (Hou et al., 2005). Each basin contains a single lake or catenulated lakes connected by seasonal river channels. Groundwater renewal ability decreases with depth in the closed drainage area. The annual renewal rate of medium and deep groundwater flow is less than 0.5% and 0.02%, respectively. The vertical hydraulic connection between shallow groundwater and medium to deep groundwater is weak (Wan et al., 2010). Therefore, the lakes in each drainage basin are independent discharge centers of surface runoff and shallow groundwater flow (**Figure 1C**).

MATERIALS AND METHODS

Lacustrine Landform and Sample

Lacustrine plains, lake terraces, and lake shorelines are the landform relics of lake evolution. The lake terrace relics and corresponding lacustrine deposits, which represent the stable stage of lakes during their expansion period, are direct evidence of the evolutionary history of lakes and for

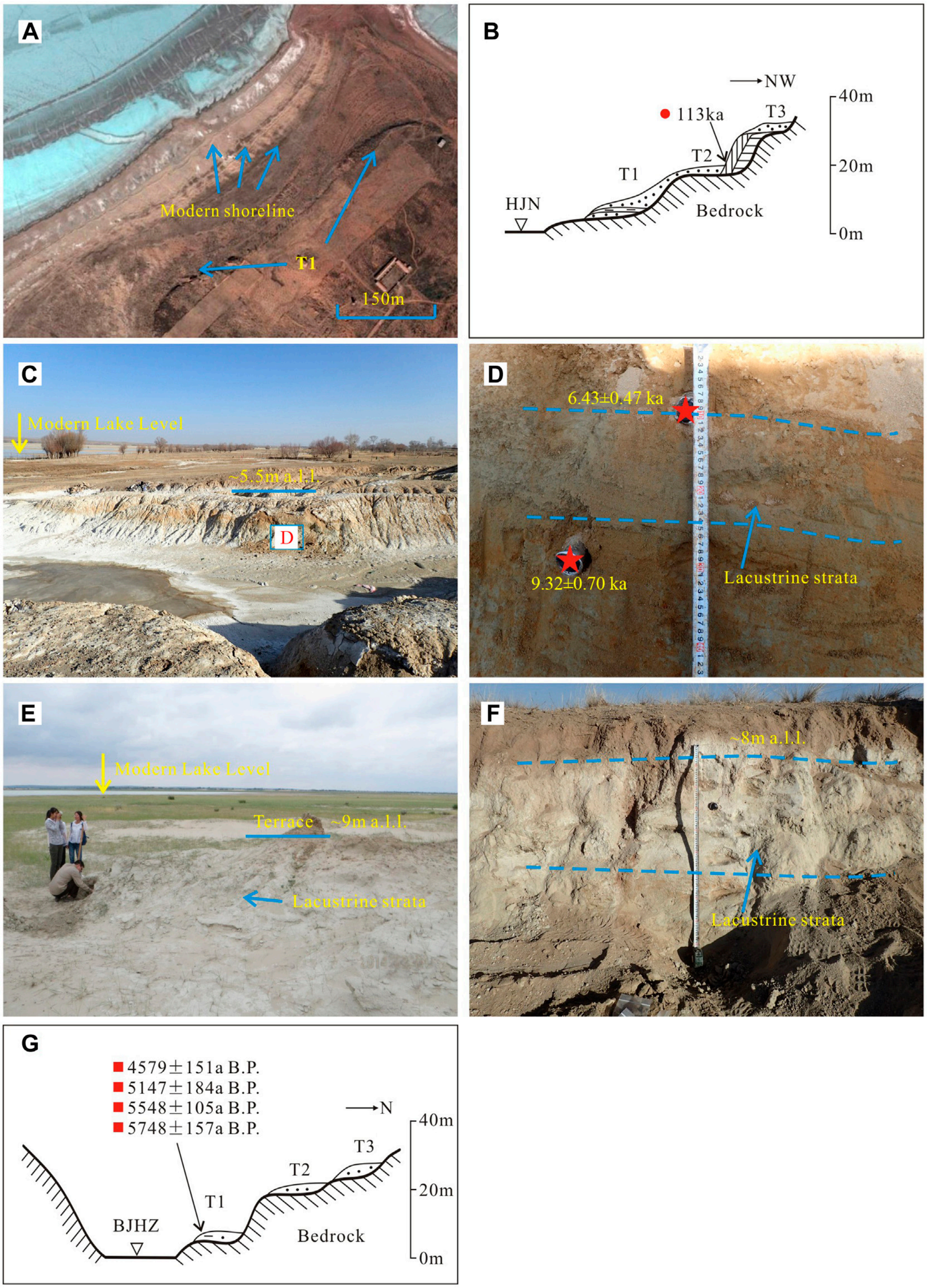

FIGURE 2 | Geomorphology and lacustrine strata of lakes in MUD. **(A)** Image of lake shorelines and T1in south HJN. **(B)** Sketch map of lake terraces of HJN (modified after Shi, 1991). **(C)** Image of lake terrace in the south DLTR. **(D)** Lacustrine strata in the terrace of the south DLTR. **(E)** Holocene lacustrine strata in the southeast beach of BZN. **(F)** Lake terrace and lacustrine strata in the east SRBDY. **(G)** Sketch map of lake terraces in BJHZ (modified after Long et al., 2007; Shi, 1991).The red star, circle, and square show OSL, TL, and ^{14}C dates, respectively. The ^{14}C dates were converted to calendar ages using Calib 7.02 based on the INTCAL 13 calibration (Reimer et al., 2013).

reconstructing high lake levels. The lakes on the Ordos Plateau have been retreating since the late Quaternary. Hongjian Nuur and Bojianghaizi developed three lake terraces (**Figure 2**). T2 and T3 developed before the late Pleistocene, and T1 developed in the early and middle Holocene (Yuan et al., 1987; Shi, 1991). Holocene lake terrace and lacustrine strata in the MUD are generally no more than 10 m higher than the modern lake surface. The lacustrine sediments are gray-white or gray-green silty sand and fine sand with horizontal bedding. The sedimentary texture is loose with poor cementation. The lake terraces are stepped terrain with a flat top and a steep front edge. Lacustrine strata remain partially on the terrace. Based on remote sensing image interpretation, lake basins of Hongjian Nuur (HJN), Dalengturu Nuur (DLTR), Baozhai Nuur (BZN), Sharibuduyin Nuur (SRBDY), and Bojianghaizi (BJHZ) were selected for field investigation and sampling (**Figure 1B**, No.1–5).

HJN is the largest lake in MUD. Shorelines and lake terraces are clearly visible in south HJN. The shorelines formed in recent decades are roughly parallel to the modern shoreline (**Figures 2A,B**). The top of the lacustrine strata in T1 is about 9 m above the modern lake. The sediment is gray-white very fine sand. The terrace of DLTR is in the south of the lake. The terrace is about 5.5 m higher than the modern lake, slightly inclined toward the lake (**Figure 2C**). The lacustrine strata is gray-green fine sand with clay, about 17 cm in thickness (**Figure 2D**). The Holocene terrace of BZN is located on the southeast beach of the lake about 9 m above the modern lake. The lacustrine layer is gray-white silt sand with well-developed horizontal bedding (**Figure 2E**). The lake terrace of SRBDY, located in the east of the lake, is about 8 m higher than the modern lake. The lacustrine strata at the top is about 40 cm, with gray-white fine sand and visible and well-developed horizontal bedding (**Figure 2F**). The T1 in the north of Bojianghaizi is about 7 m higher than the modern lake with gray-green and gray-black lacustrine clay (**Figure 2G**).

Two quartz Optical Stimulated Luminescence (OSL) dating samples were collected in the DLTR section. Pure quartz grains 38–63 μm size were extracted from the middle part of the sample tube using the procedure employed by the OSL Laboratory of the State Key Laboratory of Earth Surface Processes and Resource Ecology, Beijing Normal University. The SAR-SGC method was used to determine the equivalent dose (De) (Lai and Ou, 2013).The measurement equipment was a Risø DA-20 TL/OSL reader equipped with blue diodes (k = 470 ± 20 nm) and a 90Sr/90Y radioactive beta source. The concentrations of Uranium (U), Thorium (Th), and Potassium (K) were measured by inductively coupled plasma mass spectrometry (ICP-MS). The water content was measured by weighing the samples before and after drying. Finally, we obtained the boundary ages of the lacustrine deposit in the DLTR section.

Lake Hydrologic Model

The lake area is governed by lake inputs and outputs. The lake level remains stable when the water inputs equal outputs. Lake inputs are lake surface precipitation and drainage runoffs, whereas the outputs are water surface evaporation and groundwater discharge. Based on the reconstructed lake area, the lake hydrologic model can be used to calculate the precipitation of the corresponding period. The model used in this study followed Goldsmith et al. (2017):

$$\mathrm{P} \times A_C \times F_R + P \times A_L = E \times A_L + G \tag{1}$$

where P is mean annual precipitation(m); A_C is the catchment area (m^2) where the area of the lake is subtracted from the area of the catchment; F_R represents the fraction of the watershed precipitation that reaches the lake (including surface and groundwater runoff); A_L is the area of the lake (m^2); E represents the mean annual evaporation of the lake surface (m); and G represents groundwater discharge from the lake per year (m^3).

The catchment area (A_C) was calculated from topographic maps with contour lines of 5 and 10 m. Considering the inter-annual fluctuations of the lake level (Xu et al., 2019), the modern area of the lake (A_L) was averaged from data of two periods: a topographic map drawn in the 1970s and a geomorphic map of the MUD (Wu et al., 2017). The precipitation was interpolated from the mean annual precipitation of meteorological stations in the MUD for 56 years (1961–2016). The highstand area of five lakes was calculated from topographic maps according to the elevation of the lacustrine strata. The watershed area of the lake highstand was the same as the modern catchment area because the elevation of each watershed was much higher than the modern lake and Holocene highstand. All the catchments are closed basins with no hydraulic connection between them. Thus, groundwater discharge from the lake (G) can be neglected for the hydrologic model. The meteorological data of each basin was obtained by interpolation.

The evaporation of the lake surface was estimated using a modified Penman equation (Penman, 1948; Sene et al., 1991):

$$E_d = \frac{\Delta H/L + \gamma E_a}{\Delta + \gamma} \tag{2}$$

where E_d is evaporation per day (m/day); Δ is the slope of the saturation vapor pressure curve at air temperature t (hpa/°C); H is net radiation, J/(m^2·day); L represents latent heat of vaporization (J/kg); γ is psychrometric constant (hpa/°C); and E_a is atmospheric conductance (m/day).

The climatological data (radiation, temperature, air pressure, vapor pressure, wind velocity, and sunshine duration) were obtained from the Chinese Meteorological Agency for the period 1961–2016 for meteorological stations located in the MUD. The mean annual evaporation of each meteorological station was calculated by summing evaporation per day (E_d). The evaporation of each lake surface (E) was mathematically interpolated from these stations. The runoff fraction (F_R) can be calculated using the closed-basin hydrological model. In addition, it can be estimated by the Budyko relationship (Budyko, 1974; Koster et al., 2006):

$$F_R = 1 - \mathrm{E_c}/\mathrm{P} = 1 - [\mathrm{D}(\tanh 1/\mathrm{D})(1 - \cosh \mathrm{D} + \sinh \mathrm{D})]^{0.5} \tag{3}$$

where $\mathrm{E_c}$ is catchment evaporation calculated as D = R_{net}/P L, where D is the dryness index, R_{net} is mean annual net radiation, P is annual precipitation, L is latent heat of vaporization, and R_{net}/ L is potential evaporation. Potential

TABLE 1 | Quartz OSL ages of lacustrine strata in DLTR.

Sample No.	Lab No.	Depth (m)	Water content (%)	K (%)	U (ppm)	Th (ppm)	De (Gy)	Dose rate (Gy/ka)	Aliquots	Age (ka)
DLTR-2	BNU61	0.69	16.76	3.13 ± 0.05	16.97 ± 0.73	12.41 ± 0.81	41.43 ± 0.64	6.45 ± 0.46	15	6.43 ± 0.47
DLTR-3	BNU62	0.92	12.18	3.00 ± 0.05	11.12 ± 0.51	4.58 ± 0.58	43.76 ± 0.52	4.70 ± 0.35	13	9.32 ± 0.70

evaporation can be measured by the radiative balance or by pan evaporation (Koster et al., 2006; Goldsmith et al., 2017). It also can be approximately estimated using the Penman equation (Yang et al., 2012; Li et al., 2020).In our calculation, the Penman equation was used.

In the modern lake hydrologic model, the mean annual evaporation of meteorological stations in the MUD was calculated using the Penman equation. Then, the evaporation (E) of the five lake basins was calculated by mathematical interpolation. The modern runoff fraction (F_R) of each basin was calculated using the lake hydrologic model and Budyko relationship, respectively. The results show that the two runoff fractions (F_{R1} and F_{R2}) are similar, indicating that both the modern lake hydrological model and Budyko relationship produced suitable estimates.

In this paper, first, the model was applied to HJN, DLTR, BZN, SRBDY, and BJHZ to reconstruct precipitation during the lake highstand. Second, the paleolake areas of other drainages (No. 6–24 in **Figure 1B**) were estimated using this model under the reconstructed precipitation pattern. In the paleolake hydrologic model, the evaporation was also calculated using the Penman equation. Considering the influence of wind speed and temperature on evaporation, we estimated that the evaporation during the lake's highstand was at most 15% higher than the modern value. For the paleolakes, precipitation (or paleolake area) and runoff fraction could not be constrained independently. Therefore, we used both the closed-basin lake hydrologic model and the Budyko relationship to assess these parameters.

Extraction of Published Precipitation Data

A series of precipitation data was extracted from published articles to reconstruct the paleoprecipitation pattern in MUD combining with reconstructed precipitation by the model in **section 3.2**. The published precipitation data were extracted according to the following methods:1) the paleoprecipitation was extracted immediately from articles with exact data; 2) the paleoprecipitation was calculated using modern precipitation (1961–2016) multiplied by change percentage given in the articles; 3) with regard to data in precipitation series, data from the chosen period were digitalized and averaged. With the method above, forty precipitation data was extracted in the MUD and its surrounding region in north China.

RESULTS

Lake Highstand Reconstructed by Lacustrine Landform and Strata

Based on field investigations, the highstand of five lakes was reconstructed using a topographic map and a digital elevation model (**Figure 3**). The area of the paleolakes is 1.65–3.56 times that of modern lakes, with the smallest ratio in HJN. The total area of paleolakes in the five catchments is 158.2 km^2, which is 2.05 times that of modern lakes. There was only one lake during the highstand period in the DLTR and SRBDY drainage. The drainage basins in HJN, BJHZ, and BZN contain more than one lake. In each basin, the elevation of the watershed between lakes is the upper limit of the upstream paleolake level. We also inferred that paleolakes existed in some depressions during the highstand period. For example, the Shejiahaizi (*haizi* means lake in the dialect of study area), located in depression northeast of HJN, was a lake that regressed decades ago according to the topographic map and remote sensing image. During the Holocene highstand period, Shejiahaizi was probably an independent lake that was ~3 m higher than the HJN based on lacustrine landform. In the BZN drainage, lake Baozhai Nuur and the adjacent Baga Nuur were connected to a unified lake due to rising lake levels. In the west of the drainage, there are two depressions where paleolakes may develop. In the BJHZ drainage, two adjacent lakes were connected during the high lake level period.

The quartz optically stimulated luminescence (OSL) ages of the lacustrine strata in DLTR are listed in **Table 1**. The quartz OSL ages confirmed the lake highstand occurred during the early to middle Holocene.

Quantitative Precipitation Reconstruction Based on the Lake Hydrologic Model

The modern precipitation (P), modern and highstand evaporation (E), catchment area (A_C), and runoff fraction (F_R) required in the hydrologic model are listed in **Table 2**. The interpolated modern mean annual evaporation ranged from 995 to 1,065 mm with a rough trend of increasing from east to west. The evaporation of the paleolakes was calculated using modern values multiplied by 1.15. The runoff fraction (F_R) of the paleolake drainages during lake highstand was estimated by Budyko relationship. They ranged from 5% to 8%, higher than at present in each catchment. The runoff fraction (F_R) in both periods shows a decreasing trend from southeast to northwest.

The precipitation of five lakes during the highstand was estimated using the lake hydrologic model (**Table 2**). The reconstructed precipitation of HJN in the eastern MUD was 500 mm. In the middle MUD, the precipitation of BZN and BJHZ was 471 and 472 mm, respectively. The precipitation of DLTR and SRBDY in the west was 443 and 444 mm, respectively. The reconstructed precipitation was 120–165 mm higher than the modern value. The increase in precipitation was 32–60%, and the increase in the west was significantly higher than that in the east.

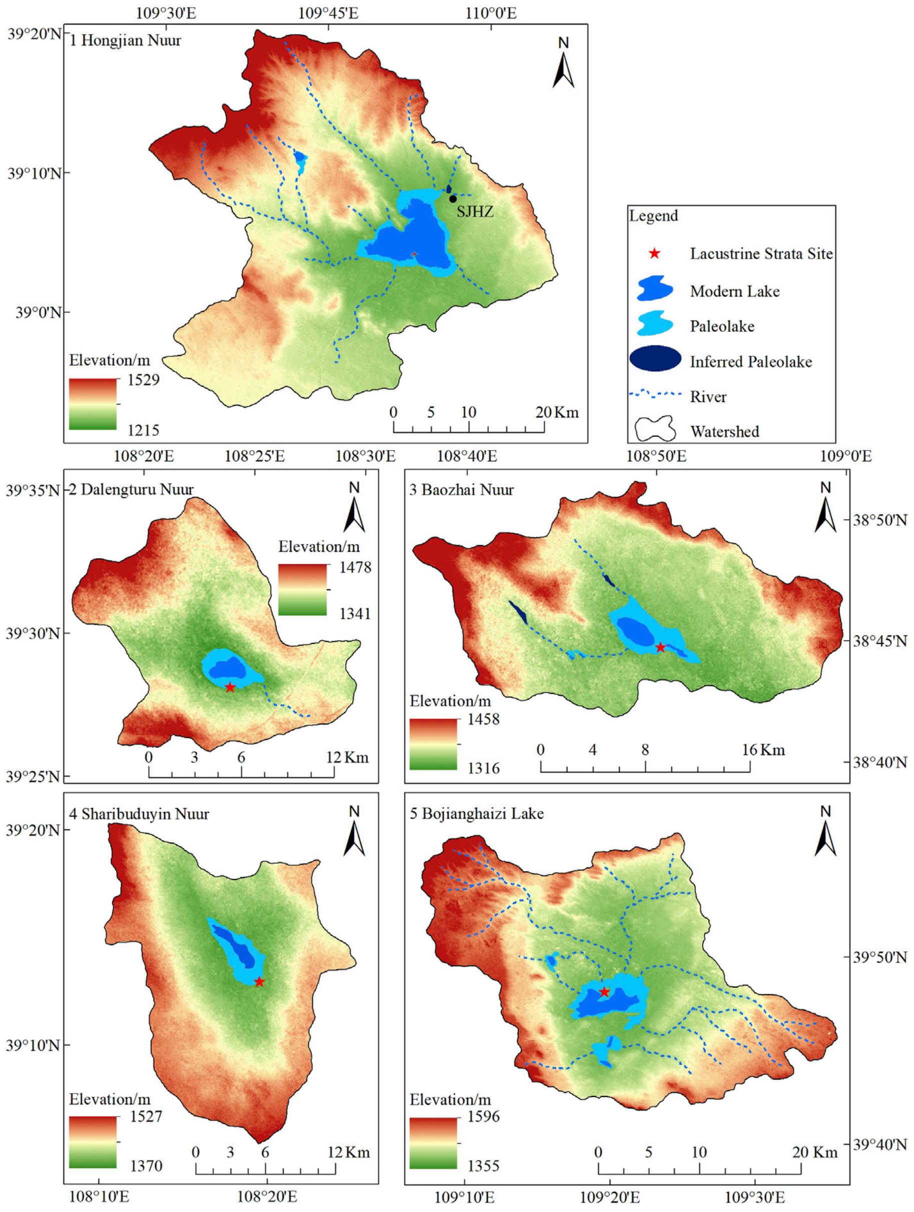

FIGURE 3 | Reconstructed highstand of five lake basins in the MUD (the DEM data is from ASTER GDEM version 2).

Reconstruction of Precipitation Patterns

Precipitation patterns in the MUD during the early to middle Holocene were reconstructed by synthesizing precipitation data in **section 4.2** and published data. A total of forty-five precipitation data from the early to middle Holocene in the MUD and surrounding areas were used (**Supplementary Table S1**). The isohyet of the MUD was reconstructed by interpolation (**Figure 4**). The results show that the precipitation during the early to middle Holocene in the MUD decreased from about 550 mm in the southeast to about 350 mm in the northwest, which is consistent with present levels. The 400 mm isohyet moved 130–170 km to the northwest, roughly consistent with the modern 250 mm isohyet. The moving distance in the southwest is slightly smaller than that in the northeast. The amplification of precipitation gradually increased from southeast to northwest. Due to the difference in amplification, the precipitation gradient in much of the MUD is lower than at present. The large gradient is distributed near the 400 mm isohyet in the west MUD.

Reconstructed Paleolakes

The lake highstand of five drainage areas was reconstructed based on lacustrine landform and strata in **section 4.1**. Based on the reconstructed precipitation pattern in the MUD, the paleolake area of each drainage (No. 6–24) during the early to middle Holocene was estimated. First,

TABLE 2 | The hydrological parameters of each lake basins in the MUD during the modern and highstand period.

No	Name	Period	P/m	E/m	$A_L/10^6m^2$	$A_C/10^6m^2$	$F_{R1}/\%$	$F_{R2}/\%$
1	Hongjian Nuur	Modern	0.380	0.996	54.92	1538.16	6.00	5.94
		Highstand	0.500	1.145	90.36		—	8.04
2	Dalengturu Nuur	Modern	0.288	0.971	2.36	168.36	3.37	3.13
		Highstand	0.443	1.117	6.90		—	6.50
3	Baozhai Nuur	Modern	0.322	1.003	5.29	353.35	3.21	3.87
		Highstand	0.471	1.153	16.15			6.94
4	Sharibuduyin Nuur	Modern	0.279	0.984	3.80	344.28	2.82	2.77
		Highstand	0.444	1.132	13.53		—	6.33
5	Bojianghaizi Lake	Modern	0.317	0.987	10.93	639.00	3.68	3.87
		Highstand	0.472	1.135	31.28		—	7.23
6	Qigai-Baahar Nuur	Modern	0.335	0.995	49.52	2267.19	4.40	4.38
		Highstand	0.485	1.144	119.13		—	7.54
7	Danao Lake	Modern	0.356	0.995	8.67	306.92	5.22	5.09
		Highstand	0.491	1.144	16.88		—	7.74
8	Wulan Nuur	Modern	0.326	0.994	6.16	294.30	4.29	4.09
		Highstand	0.479	1.143	14.82		—	7.35
9	Subei Nuur	Modern	0.314	0.993	15.97	1022.56	3.43	3.72
		Highstand	0.468	1.142	47.38			7.00
10	Hetongchagan Nuur	Modern	0.319	0.998	24.79	1517.12	3.54	3.83
		Highstand	0.476	1.148	73.51		—	7.19
11	Aobai Nuur	Modern	0.319	1.001	15.02	1000.17	3.26	3.80
		Highstand	0.467	1.151	44.61		—	6.84
12	Dakebo Lake	Modern	0.303	0.995	2.88	187.91	3.55	3.37
		Highstand	0.454	1.144	7.71		—	6.50
13	Muduchahan Nuur	Modern	0.301	0.994	7.15	522.60	3.19	3.31
		Highstand	0.453	1.143	21.34		—	6.48
14	Ketuoluohai Nuur	Modern	0.313	0.997	2.51	155.87	3.57	3.65
		Highstand	0.460	1.147	6.67		—	6.67
15	Kaikai Nuur	Modern	0.299	0.992	1.95	155.19	2.94	3.27
		Highstand	0.445	1.141	5.97		—	6.25
16	Haolebaoji Nuur	Modern	0.315	1.003	14.02	978.29	3.18	3.65
		Highstand	0.461	1.153	41.25		—	6.61
17	Baiyan Nuur	Modern	0.294	0.992	3.95	266.11	3.58	3.13
		Highstand	0.445	1.141	10.23		—	6.25
18	Haoqingzhao Nuur	Modern	0.290	0.992	1.15	114.34	2.45	3.01
		Highstand	0.446	1.141	4.43		—	6.29
19	Zhaoshao Lake	Modern	0.276	0.993	1.57	166.12	2.49	2.62
		Highstand	0.405	1.142	4.43		—	4.98
20	Nalin Nuur	Modern	0.285	0.985	3.11	236.37	3.27	2.93
		Highstand	0.416	1.133	7.21		—	5.42
21	Hadatu Nuur	Modern	0.290	0.988	2.33	177.96	3.19	3.05
		Highstand	0.434	1.136	6.32		—	5.95
22	Wuhudong Nuur	Modern	0.264	1.025	15.38	2638.69	1.69	2.11
		Highstand	0.418	1.179	70.29		—	4.98
23	Beidachi Lake	Modern	0.281	1.034	12.13	1397.54	2.35	2.46
		Highstand	0.475	1.189	58.81		—	6.60
24	Gouchi Lake	Modern	0.307	1.065	35.52	3751.55	2.36	2.90
		Highstand	0.509	1.236	176.88		—	7.07

F_{R1} and F_{R2} represent runoff fractions calculated by the lake hydrologic model and Budyko relationship, respectively.

the runoff fraction (F_{R2}) of each drainage basin was estimated using the Budyko relationship. Second, the lake area of each basin was calculated using the lake hydrologic model (**Table 2**). The total area of reconstructed paleolakes during the early to middle Holocene was 896.1 km^2, which is 2.96 times that of modern lakes. The lake area of each drainage is two to five times that of modern lakes with the largest increase in the southwest MUD. The area of the paleolake in the Wuhudong Nuur, Gouchi, and Beidachi basins (No. 22–24 in **Table 2**) are 4.57, 4.84, and 4.97 times that of modern lakes, respectively.

Based on the reconstructed lake area in each drainage (No. 6–24), we also attempted to reconstruct the paleolake pattern. For the catchment comprising one single lake, the paleolake expanded by topographic contour around the modern lake based on the calculated area. In the basin comprising a series of catenulated lakes, the elevation of the watershed between lakes was regarded as the altitude of the paleolake upstream. The upstream paleolake area was calculated using closed contour and the corresponding altitude. The downstream lake area was calculated as the total area minus the upstream lake area. Due to the rise in lake levels, adjacent lakes may have become unified lakes. Therefore, the

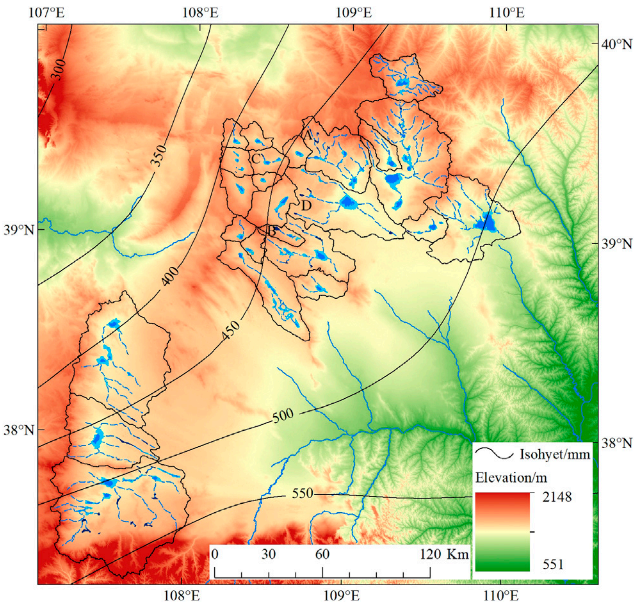

FIGURE 4 | Reconstructed precipitation and lake pattern in the MUD (the legends are same as **Figure 3**).

modern 108 lakes decreased to eighty-four during the early to middle Holocene. In addition, there are small, closed depressions in certain catchments. These depressions were inferred as paleolakes during the Holocene highstand. A total of forty-three inferred lakes with an area more than 0.1 km^2 were identified. According to the method above, there were 127 paleolakes in the closed flow area of MUD during the early to middle Holocene. The paleolake pattern is shown in **Figure 4**.

DISCUSSION

Estimation of Evaporation Used in the Lake Hydrologic Model

As one of the required parameters in the lake hydrologic model, open water evaporation is typically estimated by observing different pans. However, the observation data of a 20 m^2 evaporation pan, which is approximately equal to open water evaporation, is rare in the MUD. The observation data of D20 and 601B pans are significantly higher than open water evaporation in arid and semi-arid areas because of the pan wall. In certain regions, open water evaporation is estimated using observation data of pans multiplied by a conversion coefficient (Linacre, 1994). However, the conversion coefficient in the MUD was difficult to constrain. Therefore, a modified Penman equation was used to estimate the evaporation of the lake surface (Penman, 1948; Sene et al., 1991). The Penman equation has been used to calculate evaporation in arid and semi-arid China (Li et al., 2001; Yang et al., 2010). The difference between calculated values and measured data in 20 m^2 evaporation pans was no more than 10% according to experiments conducted in the arid regions of Xinjiang, in western China (Zhang and Zhou, 1992).

TABLE 3 | Evaporation of meteorological station in MUD.

Station	Mean annul			Mean May to September^b		
	E_{D20}/mm^a	E/mm	E_{D20}/ E	E_{601B}/mm	E/mm	E_{601B}/ E
Shenmu	1914.4	1000.6	0.52	690.8	673.1	0.97
Jingbian	1967.5	992.7	0.50	759.9	703.3	0.93
Yanchi	2042.0	1009.1	0.49	782.6	695.6	0.89
Hengshan	2084.4	1009.6	0.48	803.4	684.7	0.85
Suide	2108.2	1013.8	0.48	794.4	702.2	0.88
Dingbian	2289.0	1089.3	0.48	888.1	734.1	0.83
Dongsheng	2259.5	971.2	0.43	789.3	693.0	0.88
Otog	2453.2	979.2	0.40	835.9	681.1	0.81

^{a}*E_{D20} and E_{601B} represent observation data of D20 and 601B pans, respectively.*
^{b}*The 601B pan is generally used during May to September since 2002 in the MUD.*

The observed evaporation of two pans and calculated evaporation using the Penman equation are listed in **Table 3**. The ratios $E_{D20}/\ E$ and $E_{601B}/\ E$ are 0.4–0.52 and 0.81–0.97, respectively. Both ratios decreased from the semi-arid southeast to the arid northeast. The average conversion coefficient between D20 pan and open water evaporation in arid northwest China and Inner Mongolia Plateau was estimated at 0.44 and 0.52, respectively (Xie and Wang, 2007). The $E_{D20}/\ E$ ratio in the MUD was roughly between these two coefficients. The conversion coefficient between 601B pan and 20 m^2 pan in North China ranged from 0.83 to 0.93, which is close to the $E_{601B}/\ E$ ratio in the MUD. The decreasing trend from semi-humid Henan to semi-arid Inner Mongolia was also consistent with the MUD (Qian et al., 1998). This indicates the evaporation calculated using the Penman equation was approximately equal to the open water evaporation.

In the paleolake hydrologic model, the evaporation of lakes was also estimated using the Penman equation. The temperature during the early to middle Holocene was about 1°C higher than modern times (Fang et al., 2011). Based on the sensitivity of evaporation to temperature change, a 1°C rise would produce evaporation rate changes of about 5–6% in the MUD. We also examined the sensitivity of evaporation to wind speed change. A 20% change in wind speed can lead to about a 10% change in evaporation, which is nearly consistent with the examination in Dali Lake in eastern Inner Mongolia (Goldsmith et al., 2017). Thus, considering the possible change in temperature and wind speed, the evaporation was assumed at 15% higher than the modern value at most.

Reconstructed Precipitation in the MUD

The lake hydrologic model is one of the common methods for reconstructing precipitation. The precipitation reconstructed in HJN was 500 mm. The result is approximate to the value 510 ± 25 mm estimated from pollen data from the Hejialiang section about 15 km east of the lake (Chen et al., 1993). The reconstructed precipitation in BZN was 471 mm. The rainfall calculated based on pollen assemblage in Taobao and Wushen profiles was 470 ± 25 and 461.8 mm, respectively (Shi, 1991; Chen et al., 1993). These two profiles are about 7 and 15 km to the southeast of BZN, respectively. This indicated that the lake hydrologic model and pollen assemblage produced suitable estimates. The mean annual

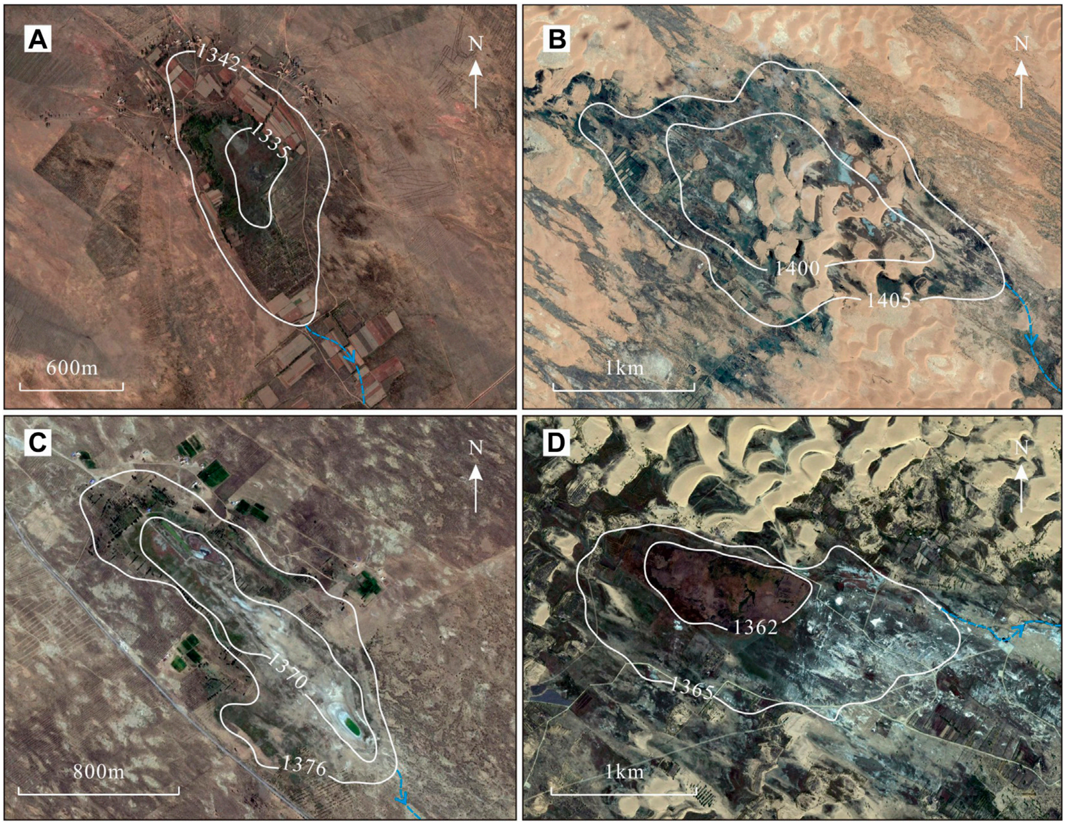

FIGURE 5 | Inferred paleolake in the MUD during the early to middle Holocene (The white curves represent contour lines extracted from topographic maps, the number means elevation/m. The blue line with arrow indicates the possible flow direction. **(A–D)** correspond to locations in **Figure 4**).

precipitation of the HJN lake was ~380 mm. The precipitation during the early to middle Holocene was ~32% higher than present. The result is consistent with reconstructed results near the 400 mm isohyet in the MUD and southeast Inner Mongolia Plateau (Jiang et al., 2006; Xu et al., 2010). However, the result was much smaller than the estimated precipitation of Qinghai Lake (Shi et al., 1992). This may reflect that the migration distance of the monsoon rain belt varied in different regions of the monsoon edge area.

In the EASM area of China, the relative increase in precipitation during the early to middle Holocene varied from ~10 to 15% in the humid southeastern coastal area to more than 70% in the arid northwest area (Yang and Williams, 2003; Stebich et al., 2015; Liu and Li, 2017; Li et al., 2018; Wu et al., 2018). The reconstructed relative increase in the MUD rose from ~32% in the southeast to ~60% in the northwest. The rising trend is consistent with the whole EASM area in China. However, the extent of relative increase ranges significantly from southeast to the northwest, indicating that the monsoon edge area was extremely sensitive to climatic change. During the early to middle Holocene, the precipitation gradient decreased significantly in the MUD due to the difference in precipitation increase. This probably reflects the monsoon rain belt and the monsoon edge area migration to the northwest. In consequence, the MUD was stably dominated by the EASM. The spatio-temporal pattern of climate showed a relatively stable, warm, and humid climate for millennia. It can also be confirmed from the peat and paleosol development process in the MUD. The development of peat and lacustrine in the MUD since the last deglaciation indicates the regional climate fluctuated considerably until 8.5 ka. Thereafter there were humid intervals until 6ka, during which lacustrine sediments were deposited (Liu et al., 2018b). The paleosol was generally regarded as the indicator of warm and humid climate. In the aeolian sand/paleosol sequence of the MUD, the duration of paleosol is much longer than the aeolian sand during the early to middle Holocene (Gao et al., 1993; Ding et al., 2021).

Paleolake Pattern in the Closed Drainage Area

The lakes in northern China generally reached their highstand due to the increase in precipitation in the early and middle Holocene. The lake landforms and lacustrine strata of HJN and BJHZ are direct evidence of the development of high lakes in the study area. The decrease in the grain size of lacustrine deposits in the lake cores of the Baahar Nuur and Qigai Nuur in north MUD indicates an increase in lake level during the early and middle Holocene (Guo et al., 2007; Sun and

Feng, 2013). The clay deposits in Chagan Nuur in the western MUD indicate a stable deep-water sedimentary environment of ~9–5 ka (Yang, 1997). Clay sediments in Hetongchahagan Nuur in the western MUD indicate a stable deep-water sedimentary environment at~9—6 ka (Bernasconi et al., 1997). Grain size analysis of the DSGL profile in the southern MUD showed that the Salawusu Lake began to form in the early Holocene and reached its maximum in the middle Holocene (Liu et al., 2018b). These lake records above indicate that the lake highstands during the early to middle Holocene in the MUD were almost simultaneous and stable.

The total area of lakes in the closed drainage area is 2.96 times that of modern lakes. The relative height between the highstand and the modern lake surface is about 5–9 m. The increase of height and area was smaller than the lakes in Badain Jaran Desert and Tengger Desert (Yang and Williams, 2003; Zhang et al., 2004). Most of the lakes in the study area locate in bedrock valleys or aeolian bedrock depressions. The topography of the lake basins is mainly controlled by bedrock gullies. The modern aeolian activity has little impact on topography. The stable terrain is conducive to the reconstruction of paleolake pattern. According to the reconstruction results, the number of paleolakes increased along with the rise of the lake level and the expansion of the lake area. The adjacent lakes in certain basins connected and formed unified lakes due to the rise in water level. In addition, closed depressions were extracted from topographic maps and remote sensing images. Geomorphic relics, such as lake shorelines, can be distinguished around the depressions. Salt crystals on the surface of depressions indicated paleolakes may have existed (**Figure 5**). We inferred these closed depressions formed lakes due to the rise of precipitation during the early to middle Holocene. In each catchment, the altitude of the lake highstands was lower than the watershed between drainages. The pattern of closed drainage area is consistent with the present. There is no evidence from the lake landform, lacustrine strata, and climatic conditions supporting the formation of a unified megalake in the closed drainage area during the early to middle Holocene.

CONCLUSION

The precipitation and lake areas of the MUD during the early and middle Holocene were quantitatively reconstructed based on the lacustrine landform, and by using the lake hydrologic model. A total of 127 paleolakes existed in the closed flow area during the early to middle Holocene. The paleolake area was 896.1 km^2, which is 2.96 times that of modern lakes. The relative height between the highstand and the modern lake surface is about 5–9 m. The precipitation during early to middle Holocene decreased from about 550 mm in the southeast to about 350 mm in the northwest. The 400 mm isohyet moved 130–170 km to the northwest, roughly consistent with the modern 250 mm isohyet. The relative increase in precipitation was ~32–60%, and the increase in the west was significantly higher than the east. The precipitation gradient in much of the MUD was lower than the present. The results above indicate that the monsoon edge area and monsoon rain belt have migrated to the northwest. Furthermore, the MUD was stably dominated by the EASM. The spatio-temporal pattern of the climate during the early to middle Holocene was relatively warm and humid with a decreased precipitation gradient for millennia.

DATA AVAILABILITY STATEMENT

The original contributions presented in the study are included in the article/**Supplementary Material**, further inquiries can be directed to the corresponding author.

AUTHOR CONTRIBUTIONS

DL, YWu, and LT contributed to conception and design of the study. DL, LT, YWe, and TF conducted investigation and methodology. DL, YWe, and TF performed the statistical analysis. YWu provided the funding. All authors contributed to manuscript revision, read, and approved the submitted version.

SUPPLEMENTARY MATERIAL

The Supplementary Material for this article can be found online at: https://www.frontiersin.org/articles/10.3389/feart.2022.850633/full#supplementary-material

REFERENCES

An, Z., Porter, S. C., Kutzbach, J. E., Wu, X. H., Wang, S. M., Liu, X. D., et al. (2000). Asynchronous Holocene Optimum of the East Asian Monsoon. *Quat. Sci. Rev.* 19, 743–762. doi:10.1016/S0277-3791(99)00031-1

Bernasconi, S. M., Dobson, J., Mckenzie, J. A., Ariztegui, D., Niessen, F., Hsu, K. J., et al. (1997). Preliminary Isotopic and Palaeomagnetic Evidence for Younger Dryas and Holocene Climate Evolution in NE Asia. *Terra Nova* 9 (5-6), 246–250. doi:10.1046/j.1365-3121.1997.d01-38.x

Budyko, M. I. (1974). *Climate and Life*. San Diego: Academic Press.

Chen, F., Li, G., Zhao, H., Jin, M., Chen, X., Fan, Y., et al. (2014). Landscape Evolution of the Ulan Buh Desert in Northern China during the Late Quaternary. *Quat. Res.* 81, 476–487. doi:10.1016/j.yqres.2013.08.005

Chen, F., Xu, Q., Chen, J., Birks, H. J. B., Liu, J., Zhang, S., et al. (2015). East Asian Summer Monsoon Precipitation Variability since the Last Deglaciation. *Sci. Rep.* 5, 1–11. doi:10.1038/srep11186

Chen, W. N., Gao, S. Y., Shao, Y. J., and Zhang, H. L. (1993). Palynological Assemblages and Paleoclimatic Change of Mu Us Sandy Land during Holocene. *J. Chin. Hist. Geogr.* 14 (01), 22–30.

Cohen, A. S. (2003). *Paleolimnology: The History and Evolution of Lake Systems*. Oxford, England: Oxford University Press.

Department of Geography of Peking University (1983). *Natural Features and Rehabilitation of Mu Us Sandy Land*. Beijing: Science Press.

Ding, Z., Lu, R., Wang, L., Yu, L., Liu, X., Liu, Y., et al. (2021). Early-mid Holocene Climatic Changes Inferred from Colors of Eolian Deposits in the Mu Us Desert. *Geoderma* 401, 115172. doi:10.1016/j.geoderma.2021.115172

Fang, X. Q., Liu, C. H., and Hou, G. L. (2011). Reconstruction of Precipitation Pattern of China in the Holocene Megathermal. *Scientia Geographica Sinica* 31 (11), 1287–1292. doi:10.13249/j.cnki.sgs.2011.011.1287

Fritz, S. C. (2008). Deciphering Climatic History from Lake Sediments. *J. Paleolimnol* 39, 5–16. doi:10.1007/s10933-007-9134-x

Gao, S. Y., Chen, W. N., Jin, H. L., Dong, G. R., Li, B. S., Yang, G. S., et al. (1993). A Preliminary Study on Desert Evolution in the Northwestern Fringe of Monsoon Area. *China. Sci. China, Ser. B.* 23 (2), 202–208. doi:10.3321/j.issn:1006-9240.1993.02.005

Goldsmith, Y., Broecker, W. S., Xu, H., Polissar, P. J., DeMenocal, P. B., Porat, N., et al. (2017). Northward Extent of East Asian Monsoon Covaries with Intensity on Orbital and Millennial Timescales. *Proc. Natl. Acad. Sci. USA* 114, 1817–1821. doi:10.1073/pnas.1616708114

Guo, L., Feng, Z., Li, X., Liu, L., and Wang, L. (2007). Holocene Climatic and Environmental Changes Recorded in Baahar Nuur Lake Core in the Ordos Plateau, Inner Mongolia of China. *Chin. Sci Bull* 52, 959–966. doi:10.1007/s11434-007-0132-1

Hou, G. C., Zhang, M. S., Liu, F., Wang, Y. H., Liang, Y. P., Tao, Z. P., et al. (2005). *Groundwater Exploration and Research in the Ordos Basin*. Beijing: Geological Publishing House.

Hou, G. C., Zhao, Z. H., Wang, X. Y., Gong, B., and Yin, L. H. (2008). Formation Mechanism of Interior Drainage Areas and Closed Drainage Areas of the Ordos Plateau in the Middle Reaches of the Yellow River, China Based on an Analysis of the Water Cycle. *Geol. Bull. China* 27 (8), 1107–1114. doi:10.3969/j.issn.1671-2552.2008.08.002

Jia, F., Lu, R., Gao, S., Li, J., and Liu, X. (2015). Holocene Aeolian Activities in the Southeastern Mu Us Desert, China. *Aeolian Res.* 19, 267–274. doi:10.1016/j.aeolia.2015.01.002

Jia, F., Lu, R., Liu, X., Zhao, C., Lv, Z., and Gao, S. (2018). Palaeoenvironmental Implications of a Holocene Sequence of Lacustrine-Peat Sediments from the Desert-Loess Transitional Zone in Northern China. *J. Asian Earth Sci.* 156, 167–173. doi:10.1016/j.jseaes.2018.01.030

Jiang, W., Guo, Z., Sun, X., Wu, H., Chu, G., Yuan, B., et al. (2006). Reconstruction of Climate and Vegetation Changes of Lake Bayanchagan (Inner Mongolia): Holocene Variability of the East Asian Monsoon. *Quat. Res.* 65 (3), 411–420. doi:10.1016/j.yqres.2005.10.007

Koster, R. D., Fekete, B. M., Huffman, G. J., and Stackhouse, P. W. (2006). Revisiting a Hydrological Analysis Framework with International Satellite Land Surface Climatology Project Initiative 2 Rainfall, Net Radiation, and Runoff Fields. *J. Geophys. Res.* 111. doi:10.1029/2006JD007182

Lai, Z. P., and Ou, X. J. (2013). Basic Procedures of Optically Stimulated Luminescence (OSL) Dating. *Prog. Geogr.* 32 (5), 683–693. doi:10.11820/dlkxjz.2013.05.001

Li, G., Wang, Z., Zhao, W., Jin, M., Wang, X., Tao, S., et al. (2020). Quantitative Precipitation Reconstructions from Chagan Nur Revealed Lag Response of East Asian Summer Monsoon Precipitation to Summer Insolation during the Holocene in Arid Northern China. *Quat. Sci. Rev.* 239, 106365. doi:10.1016/j.quascirev.2020.106365

Li, J., Dodson, J., Yan, H., Wang, W., Innes, J. B., Zong, Y., et al. (2018). Quantitative Holocene Climatic Reconstructions for the Lower Yangtze Region of China. *Clim. Dyn.* 50, 1101–1113. doi:10.1007/s00382-017-3664-3

Li, W. C., Li, S. J., and Pu, P. M. (2001). Estimates of Plateau Lake Evaporation:A Case Study of Zige Tangco. *J. Lake Sci.* 13, 227–232. doi:10.18307/20010305

Linacre, E. T. (1994). Estimating U.S. Class A Pan Evaporation from Few Climate Data. *Water Int.* 19, 5–14. doi:10.1080/02508069408686189

Liu, X., Lu, R., Lü, Z., Du, J., Jia, F., Li, T., et al. (2017). Magnetic Susceptibility of Surface Soils in the Mu Us Desert and its Environmental Significance. *Aeolian Res.* 25, 127–134. doi:10.1016/j.aeolia.2017.04.003

Liu, X., Lu, R., Jia, F., Chen, L., Li, T., Ma, Y., et al. (2018a). Holocene Water-Level Changes Inferred from a Section of Fluvio-Lacustrine Sediments in the Southeastern Mu Us Desert, China. *Quat. Int.* 469, 58–67. doi:10.1016/j.quaint.2016.12.032

Liu, X., Lu, R., Du, J., Lyu, Z., Wang, L., Gao, S., et al. (2018b). Evolution of Peatlands in the Mu Us Desert, Northern China, since the Last Deglaciation. *J. Geophys. Res. Earth Surf.Earth Surf.* 123, 252–261. doi:10.1002/2017JF004413

Liu, Y., and Li, Y. (2017). Quantitative Reconstruction of Precipitation and Runoff during MIS 5a, MIS 3a, and Holocene, Arid China. *Theor. Appl. Climatol* 130, 747–754. doi:10.1007/s00704-016-1921-8

Long, H., Wang, N. A., Li, Y., and Wang, C. H. (2007). Particle Size Characteristics of Deposits from PJHZ Section in Northern Edge of Mu Us Desert and Their Environmental Significance. *J. Desert Res.* 27 (02), 187–193. doi:10.3321/j.issn:1000-694X.2007.02.004

Penman, H. L. (1948). Natural Evaporation from Open Water, Bare Soil and Grass. *Proc. R. Soc. Lond. A.* 193, 120–145. doi:10.1098/rspa.1948.0037

Qian, Y. P., Wang, L., Li, W. Y., and Lin, Y. P. (1998). Water-surface Evaporation Research in Bayangaole Evaporation Experimental Station, Inner Mongolia. *J. China Hydrol.* 04, 35–38.

Reimer, P. J., Bard, E., Bayliss, A., Beck, J. W., Blackwell, P. G., Ramsey, C. B., et al. (2013). IntCal13 and Marine13 Radiocarbon Age Calibration Curves 0-50,000 Years Cal BP. *Radiocarbon* 55, 1869–1887. doi:10.2458/azu_js_rc.55.16947

Sene, K. J., Gash, J. H. C., and McNeil, D. D. (1991). Evaporation from a Tropical Lake: Comparison of Theory with Direct Measurements. *J. Hydrol.* 127, 193–217. doi:10.1016/0022-1694(91)90115-x

Shi, P. J., Jiang, T. M., and Liu, Q. F. (1988). Reconstruction of Precipitation during the Last Stage of the Late Pleistocene and the Middle Holocene in Ordos Plateau of North China. *J. Beijing Normal Univ. (Natural Science)* 24, 94–99.

Shi, P. J. (1991). *Theory and Practice of Research into Geography Environment Changes—Research into Geographical Environment Change during Late Quaternary Period in the Ordos Region of North China*. Beijing: Science Press.

Shi, Y. F., Kong, Z. C., Wang, S. M., Tang, L. Y., Wang, F. B., Yao, T. D., et al. (1992). The Climatic Fluctuation and Important Events of Holocene Megathermal in China. *Sci. China Ser. B* 22 (12), 1300–1308. doi:10.1360/zb1992-22-12-1300

Stebich, M., Rehfeld, K., Schlütz, F., Tarasov, P. E., Liu, J., and Mingram, J. (2015). Holocene Vegetation and Climate Dynamics of NE China Based on the Pollen Record from Sihailongwan Maar Lake. *Quat. Sci. Rev.* 124, 275–289. doi:10.1016/j.quascirev.2015.07.021

Sun, A., and Feng, Z. (2013). Holocene Climatic Reconstructions from the Fossil Pollen Record at Qigai Nuur in the Southern Mongolian Plateau. *The Holocene* 23, 1391–1402. doi:10.1177/0959683613489581

Sun, D. H., Zhou, J., Wu, X. H., and Porter, S. C. (1995). Preliminary Reconstruction of Annual Rainfall in Loess Plateau and Loess-Desert Transitional Regions in Suitable Climatic Period of Holocene. *J. Desert Res.* 15 (4), 339–344. doi:10.3321/j.issn:1000-694X.1995.04.012

Wan, Y. Y., Su, X. S., Dong, W. H., and Hou, G. C. (2010). Evaluation of Groundwater Renewal Ability in the Ordos Cretaceous Groundwater Basin. *J. Jilin Univ. (Earth Sci. Edition)* 40 (03), 623–630. doi:10.3969/j.issn.1671-5888.2010.03.020

Wang, N., Ning, K., Li, Z., Wang, Y., Jia, P., and Ma, L. (2016). Holocene High Lake-levels and Pan-lake Period on Badain Jaran Desert. *Sci. China Earth Sci.* 59, 1633–1641. doi:10.1007/s11430-016-5307-7

Wang, S. M., and Dou, H. S. (1998). *Lakes in China*. Beijing: Science Press.

Wu, Y. Q., Tan, L. H., Hao, C. Z., Fu, T. Y., Zhang, M., Wen, Y. L., et al. (2017). *Geomorphic Map of Mu Us Desert*. Harbin: Harbin Cartographic Publishing House.

Wu, Y. L., Wang, Y. B., Liu, X. Q., Yu, Z. T., and Ni, Z. Y. (2018). Holocene Climate Evolution in the Monsoonal Margin Region Revealed by the Pollen Record from Jilantai Playa. *J. Lake Sci.* 30 (4), 1161–1176. doi:10.18307/2018.0427

Xie, X. Q., and Wang, L. (2007). Changes of Potential Evaporation in Northern China over the Past 50 Years. *J. Nat. Resour.* 22 (05), 683–691. doi:10.11849/zrzyxb.2007.05.002

Xu, D. L., Ding, J. N., and Wu, Y. Q. (2019). Lake Area Change in the Mu Us Desert in 1989-2014. *J. Desert Res.* 39 (06), 40–47. doi:10.7522/j.issn.1000-694X.2018.00099

Xu, Q., Xiao, J., Li, Y., Tian, F., and Nakagawa, T. (2010). Pollen-based Quantitative Reconstruction of Holocene Climate Changes in the Daihai Lake Area, Inner Mongolia, China. *J. Clim.* 23, 2856–2868. doi:10.1175/2009JCLI3155.1

Yang, Q. T. (1997). Basic Sedimentary Characters and Paleoclimatic Implications of Saline Lakes in Inner Mongolia. *Geology. Chem. Minerals* 19 (01), 50–54.

Yang, S., Ding, Z., Li, Y., Wang, X., Jiang, W., and Huang, X. (2015a). Warming-induced Northwestward Migration of the East Asian Monsoon Rain Belt from the Last Glacial Maximum to the Mid-holocene. *Proc. Natl. Acad. Sci. USA* 112, 13178–13183. doi:10.1073/pnas.1504688112

Yang, X., Ma, N., Dong, J., Zhu, B., Xu, B., Ma, Z., et al. (2010). Recharge to the Inter-dune Lakes and Holocene Climatic Changes in the Badain Jaran Desert, Western China. *Quat. Res.* 73, 10–19. doi:10.1016/j.yqres.2009.10.009

Yang, X., Scuderi, L. A., Wang, X., Scuderi, L. J., Zhang, D., Li, H., et al. (2015b). Groundwater Sapping as the Cause of Irreversible Desertification of Hunshandake Sandy Lands, Inner Mongolia, Northern China. *Proc. Natl. Acad. Sci. USA* 112 (3), 702–706. doi:10.1073/pnas.1418090112

Yang, X., Scuderi, L., Paillou, P., Liu, Z., Li, H., and Ren, X. (2011). Quaternary Environmental Changes in the Drylands of China - A Critical Review. *Quat. Sci. Rev.* 30, 3219–3233. doi:10.1016/j.quascirev.2011.08.009

Yang, X., and Williams, M. A. J. (2003). The Ion Chemistry of Lakes and Late Holocene Desiccation in the Badain Jaran Desert, Inner Mongolia, China. *Catena* 51, 45–60. doi:10.1016/s0341-8162(02)00088-7

Yang, Z. C., Li, Y. L., Cui, D., Chen, J., and Zhao, X. Y. (2012). Changes of Main Climatic Parameters and Potential Evapotranspiration in Typical Semi-arid Sandy Lands of Northern China during 1951-2005. *J. Desert Res.* 32 (5), 1384–1392.

Yuan, B. Y., Cui, J. X., and Yin, Q. (1987). The Relationship between Gully Development and Climatic Changes in the Loess Yuan Region: Examples from Luochuan, Shaanxi Province. *Acta Geographica Sinica* 42 (4), 328–337. doi:10.11821/xb198704005

Zhang, G. W., and Zhou, Y. C. (1992). Evaporation Properties and Estimates in the Landlocked Arid Region in Xinjiang. China. *Adv. Water Sci.* 3, 226–232. doi:10.3321/j.issn:1001-6791.1992.03.010

Zhang, H. C., Peng, J. L., Ma, Y. Z., Chen, G. J., Feng, Z.-D., Li, B., et al. (2004). Late Quaternary Palaeolake Levels in Tengger Desert, NW China. *Palaeogeogr. Palaeoclimatol. Palaeoecol.* 211, 45–58. doi:10.1016/j.palaeo.2004.04.006

Zhang, J., Tsukamoto, S., Jia, Y., and Frechen, M. (2016). Lake Level Reconstruction of Huangqihai Lake in Northern China since Mis 3 Based on Pulsed Optically Stimulated Luminescence Dating. *J. Quat. Sci.* 31, 225–238. doi:10.1002/jqs.2861

Zhang, L. S., Shi, P. J., Hou, L. F., and Fang, X. Q. (1993). "Research on Precipitation Change and its Distributive Pattern of Monsoon Edge Area in Northern China during Holocene Period," in *Research on the Past Life-Supporting Environment Change of China(I)*. Editor L S Zhang (Beijing: Ocean Press), 147–154.

Zheng, X. Y., Zhang, M. G., Dong, J. H., Gao, Z. H., Xu, C., Han, Z. M., et al. (1992). *Salt Lakes in Inner Mongolia*. Beijing: Science Press.

Zhou, W., Head, M. J., Lu, X., An, Z., Jull, A. J. T., and Donahue, D. (1999). Teleconnection of Climatic Events between East Asia and Polar, High Latitude Areas during the Last Deglaciation. *Palaeogeogr. Palaeoclimatol. Palaeoecol.* 152, 163–172. doi:10.1016/S0031-0182(99)00041-3

Zhu, Z. D., Wu, Z., Liu, S., and Di, X. (1980). *An Outline of Chinese Deserts*. Beijing: Science Press.

Conflict of Interest: The authors declare that the research was conducted in the absence of any commercial or financial relationships that could be construed as a potential conflict of interest.

Publisher's Note: All claims expressed in this article are solely those of the authors and do not necessarily represent those of their affiliated organizations, or those of the publisher, the editors and the reviewers. Any product that may be evaluated in this article, or claim that may be made by its manufacturer, is not guaranteed or endorsed by the publisher.

Copyright © 2022 Li, Wu, Tan, Wen and Fu. This is an open-access article distributed under the terms of the Creative Commons Attribution License (CC BY). The use, distribution or reproduction in other forums is permitted, provided the original author(s) and the copyright owner(s) are credited and that the original publication in this journal is cited, in accordance with accepted academic practice. No use, distribution or reproduction is permitted which does not comply with these terms.

frontiers | Frontiers in Earth Science

ORIGINAL RESEARCH
published: 27 April 2022
doi: 10.3389/feart.2022.897640

The Effects of Wind Regime and Sand Supply on the Coexistence of Barchans and Linear Dunes in China's Qaidam Basin

Fang Ma[1,2], *Ping Lü*[1]* *and Min Cao*[1]

[1]School of Geography and Tourism, Shaanxi Normal University, Xi'an, China, [2]Key Laboratory of Desert and Desertification, Northwest Institute of Eco-Environment and Resources, Chinese Academic Sciences, Lanzhou, China

Dunes composed of granular materials are present in deserts and other environments, such as subaqueous environments and environments on other planets, with very different time and length scales for their evolution. In arid regions, barchans (transverse dunes) develop under a unimodal wind regime, and are oriented perpendicular to the sand transport direction, whereas linear (longitudinal) dunes develop under a bimodal wind regime and are oriented parallel to the sand transport direction. However, field survey results cannot be explained solely by the wind because barchans and linear dunes can coexist under the same wind regime. Here, we investigated China's Qaidam Basin, where barchans and linear dunes coexist. We measured dune morphology, analyzed wind data, and quantified the sand supply (equivalent sand thickness) to describe their development environment, and focused on the effect of sand supply to explore the combined effects of wind regime and sand supply on the coexistence of barchans and linear dunes. In our study area, barchans and linear dunes had low heights. The wind regime was narrowly bimodal, with low directional variability. The sand supply was limited (low equivalent sand thickness), but was greater for barchan chains than for barchans, and linear dunes had the smallest supply; the equivalent sand thickness in the linear dune areas was half that in barchan areas and one-quarter that in barchan chain areas. Except in the presence of topographical barriers and cohesive sediments, a unimodal or bimodal wind regime with an acute angle allows barchans and linear dunes to coexist under a low sand supply. The linear dunes and the barchans migrated along the resultant drift direction. Though we studied aeolian dunes, these findings will increase our understanding of these similar bedforms that develop in other planetary environments (e.g., Mars).

Keywords: equivalent sand thickness, sand supply, qaidam basin, linear dunes, barchan dunes, coexisting, wind regime

OPEN ACCESS

Edited by:
Zhuolun Li,
Lanzhou University, China

Reviewed by:
Kecun Zhang,
Northwest Institute of Eco-Environment and Resources (CAS), China
Dang Xiaohong,
Inner Mongolia Agricultural University, China

Correspondence:
Ping Lü
lvping@snnu.edu.cn

Specialty section:
This article was submitted to Quaternary Science, Geomorphology and Paleoenvironment, a section of the journal Frontiers in Earth Science

Received: *16 March 2022*
Accepted: *11 April 2022*
Published: *27 April 2022*

Citation:
Ma F, Lü P and Cao M (2022) The Effects of Wind Regime and Sand Supply on the Coexistence of Barchans and Linear Dunes in China's Qaidam Basin.
Front. Earth Sci. 10:897640.
doi: 10.3389/feart.2022.897640

INTRODUCTION

Dunes arise from the dynamic interactions between boundary-layer flows and the surface granular material. These processes occur on Earth, but have also been observed on several planets and moons, including Mars, Venus, and Titan (Lancaster, 2006; Lorenz and Zimbelman, 2014). In arid regions, subaqueous locations, and extraterrestrial environments, dunes develop with different temporal and

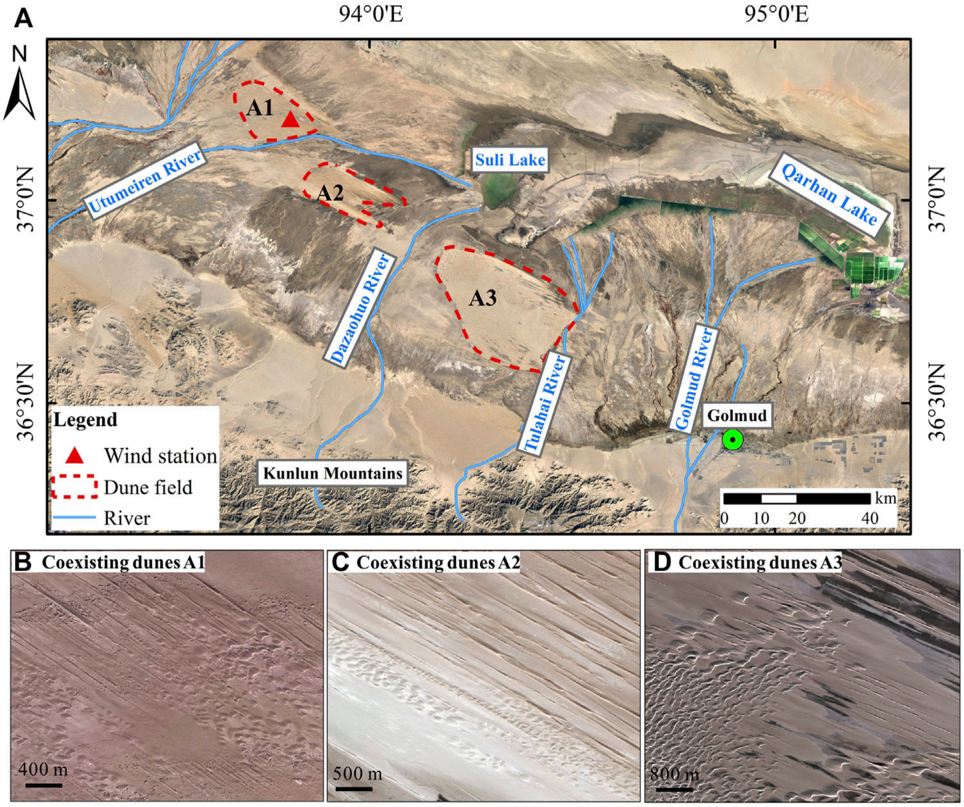

FIGURE 1 | (A) Location of the study area and wind sampling station; **(B–D)** images of areas A1, A2, and A3 (respectively) where barchans and linear dunes coexist in the Qaidam Basin. Image source: Google Earth (https://earth.google.com/).

spatial scales. The similar morphology on earth and Mars (C. Li et al., 2018; Parteli and Herrmann, 2007), the similar scaling laws followed by dunes (Claudin and Andreotti, 2006) and the fact that sand ripples and dunes can be explained by a unified model (Duran Vinent et al., 2019) suggest that the same mechanisms govern dune formation. Barchans and linear dunes are the most widely distributed and intensively studied dune types on earth. Barchans (transverse dunes) develop under a nearly unidirectional wind regime, with the dune's orientation perpendicular to the resultant sand transport direction (α, which represents the angle between the dune's orientation and the wind direction, is greater than 75°), whereas longitudinal dunes develop where the wind direction is bidirectional and moderately variable, with the dune's orientation parallel to the resultant sand transport direction (the angle α is less than 15°) (Fryberger and Dean, 1979; Hunter et al., 1983; Lancaster, 1995; Livinstone and Warren, 1996; Wasson and Hyde, 1983; D. Zhang et al., 2010; Z. Zhang et al., 2015). Although there is good evidence for these descriptions, the differences suggest that barchans and linear dunes should not coexist in the same area. However, field surveys and remote sensing images show that linear dunes coexist with barchans in areas such as the Qaidam Basin (**Figure 1**), and this kind of aeolian geomorphology also occurs in the Taklimakan Desert, the Rub'Al-Khali Desert, and the Sahara Desert (Lü et al., 2018; Lü et al., 2017; Ma and Lü, 2019). The coexistence of different types of dune under the same wind environment seems to contradict our traditional understanding of dune formation, so it is difficult to explain this coexistence based solely on wind dynamics.

The wind, sand supply, and surface conditions are the main factors that control dune formation and evolution (Wasson and Hyde, 1983; Baas, 2007; Courrech du Pont et al., 2014; Lü et al., 2018). Many scholars have investigated this phenomenon from the perspective of surface conditions, such as sediment cohesion due to high total silt, clay, and salt contents (C. Li et al., 2019; Rubin and Hesp, 2009; Rubin and Rubin, 2013; Yu and Lai, 2014), the soil water conditions (C. Li et al., 2018), wind erosion of ridges (Zhou et al., 2012), the wind regime, and topography, particularly including surface barriers (Z. Zhang et al., 2017). However, the effect of sand supply on dune formation has often been ignored, so how this supply affects the coexistence of the two dune types is unclear. Some researchers have recognized that sand supply may affect the coexistence of barchans and linear dunes (C. Li et al., 2018; Z. Zhang et al., 2017), but this hypothesis has not been supported by quantitative research.

We designed the present study to provide a quantitative explanation for the coexistence of barchans and linear dunes in China's Qaidam Basin. We measured dune morphology, and analyzed the wind regime using data measured at a wind station in areas A1 where the two dune types coexist, and quantified their

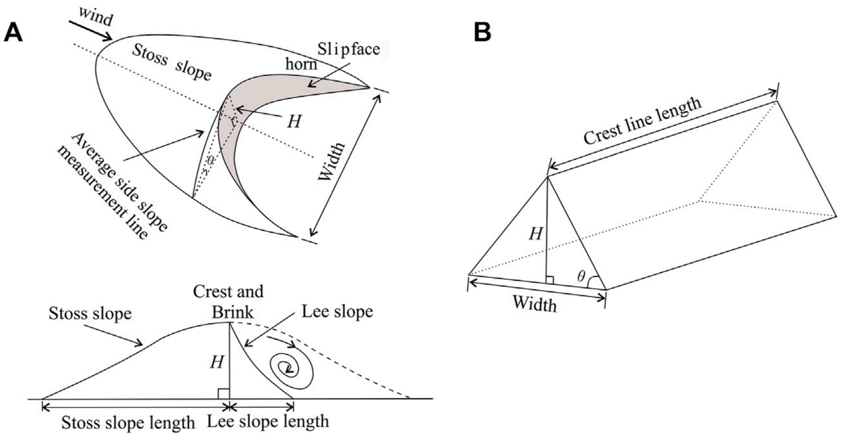

FIGURE 2 | Schematic diagram of the **(A)** barchans and **(B)** linear dunes, and their major morphological parameters. *H*, height of the dune's crest above the bed, θ, the average angle of one side slope of the dune with respect to the surface. Source: **(A)** modified after Hesp and Hastings (1998).

sand supply using the equivalent sand thickness (*EST*) to investigate the effect of this variable on the coexistence of barchan and linear dunes. Our goals were to 1) obtain details of the dune morphology and wind regime, 2) quantify the sand supply for both dune types, and 3) analyze the combined effects of the wind regime and sand supply on the coexistence of barchans and linear dunes. Our results offer insights into the combined effect of several dune-forming factors related to the wind regime and sand supply. Even though we studied aeolian dunes, our findings will help us to understand similar bedforms that develop in other planetary environments (e.g., Mars).

STUDY REGION AND METHOD

Study Area

The Qaidam Basin is located in the northeastern part of the Tibetan Plateau, at an average altitude of about 3,000 m. It is bounded by the Kunlun Mountains in the south and the Altyn Tagh and Qilian mountains in the north (J. Li et al., 2016). The climate in this region is a typical hyper-arid continental desert climate, with an annual precipitation less than 30 mm, and an evaporation rate greater than 3,000 mm, and desert covers 9 × 10^3 km^2 (Z. Zhang et al., 2017). The wind is mainly controlled by a meandering Westerly Jet Stream, and predominant wind is northwest wind.

The study area is located near the basin's center, where isolated salt lakes are distributed near the dune fields and form extensive dry playas. The three dune areas (A1, A2, and A3) are divided by the Utumeiren River and Dazaohuo River, and Suli Lake is located north of A3. The primary dune types in the study area are barchans, barchan chains, and linear dunes, and the barchans and linear dunes coexist in three parts of the dune field (**Figure 1B-D**). The mean grain size for the barchans and linear dunes was 0.24 and 0.23 mm, respectively. The linear dunes in all three areas extend from west-northwest to east-southeast. They resemble an isosceles triangle in cross-section. Three spatial patterns of coexistence of barchans and linear dunes along the wind direction can be seen: barchans are distributed downwind of or inside the linear dune field (**Figure 1B**), parallel to the linear dunes (**Figure 1C**), or upwind of the linear dunes (**Figure 1D**).

Data Sources and Methods

Dune Morphometry

Dune morphology was measured from Google Earth images with a spatial resolution of 3.8 m combined with field surveys. Dune morphological parameters were the crest-line length (L_L), width (W_L), height (H_L), spacing (distance between the crest lines of consecutive dunes) and orientation (D_L) of the linear dunes and the stoss slope length (S_B), lee slope length (L_B), width (W_B), height (H_B), spacing and orientation (D_B) of the barchans (**Figure 2**). In total, we measured 17, 41, and 35 linear dunes in areas A1, A2, and A3, respectively, and 34, 98, and 86 barchans in areas A1, A2, and A3, respectively. In addition, we measured three barchans and a linear dune in A1 during our field survey using a three-dimensional laser scanner (VZ-2000, RIEGL, Horn, Austria) with a resolution of 8 mm. To verify the results, we compared the Google Earth measurements with the field survey results. Because of the lower resolution, the values measured from the Google Earth images were greater than those in the field survey. Therefore, we used the following correction coefficients to correct the Google Earth values: 0.79 for the crest-line length and width of the linear dunes, and 0.96 for the width, 0.72 for the stoss slope, and 0.94 for the lee slope of the barchans.

We calculated the dune height (H) using trigonometry based on the assumption that the dune's cross-section was triangular:

$$H = W/2 \times \tan\theta \tag{1}$$

where W is the dune's width, and θ is the average angle of one side slope of the dune with respect to the surface, measured along the side slope measurement line, which was perpendicular to the central axis of the sand dune, and which runs from the dune crest to the inter-dunes area (**Figure 2**); we used $\theta = 11^\circ$ for barchans (Hesp and Hastings, 1998), and $\theta = 15^\circ$ for linear dunes (Lü et al., 2017; Lucas et al., 2015).

We measured the average dune height (H_{mean}) of two adjacent dunes and the spacing (λ, from crest to crest) based on 15 transects for barchans (n = 85) and 25 transects for linear dunes (n = 139). We used the average dune height and spacing for each transacts, and calculated the standard deviation (SD). We quantified the relationship between the height and spacing of the barchans and linear dunes using the H_{mean} of two adjacent dunes (Dong et al., 2009):

$$H_{\mathrm{mean}} = (H_1 + H_2)/2 \tag{2}$$

Wind Regime

Wind is a key factor for dune formation, as it provides the energy for sand entrainment and transport and controls the direction of dune movement**.** Topography and surface characteristics affect the wind velocity**.** To measure wind velocity, we installed a two-dimensional supersonic anemometer (WindSonic, Gill, Lymington, Hampshire, United Kingdom) in dune area A1 (93°46′54.4″E, 37°12′0.80″N), with the wind speed sensor at a height of 2 m above the surface. Wind data was recorded at 1-min intervals from July 2017 to June 2018 using a CR300 datalogger (Campbell Scientific, Logan, UT, United States). The threshold wind speed for sediment transport in this study area was 6 m s^{-1} at a height of 10 m (Z. Zhang et al., 2017). We calculated the drift potential (*DP*), resultant drift potential (*RDP*), resultant drift direction (*RDD*), and directional variability (*RDP/DP*) using Fryberger and Dean's method (1979). The equation is as follows:

$$DP = V^2 (V - V_{\mathrm{t}})\mathrm{t} \tag{3}$$

where *DP* is the sand drift potential in vector units (VU); *V* is the measured wind velocity in knots at 10 m height; V_{t} is the threshold wind velocity in knots; t is the proportion of time during which wind velocity is greater than the threshold velocity. Although this method makes a number of interpretative simplifications and assumptions (Bullard, 1997), previous studies of the wind energy environments of global sand seas have demonstrated the value of these parameters. We extrapolated the wind velocity at a height of 10 m above the surface from the velocity at 2 m above the surface according to Dong et al., 2010. The equation is as follows:

$$U_{10} = 0.17 + 1.08U_2 \tag{4}$$

where U_2 is the wind velocity at 2 m height, and U_{10} is the wind velocity at 10 m (Z. Zhang et al., 2017).

Equivalent Sand Thickness

Sand supply is clearly a vital factor for dune growth, and sediment thickness inside a dune field provides a good representation of the sand supply. The supply can be quantified using the equivalent sand thickness (*EST*) parameter, which is defined as the average sand thickness per unit area (Wasson and Hyde, 1983). We used the ALOS PALSAR Radiometric Terrain-Corrected (RTC) dataset with a 12.5-m horizontal resolution to calculate the equivalent sand thickness in the Qaidam Basin. The dataset can be downloaded from https://vertex.daac.asf.alaska.edu/. We used the method proposed by Bullard et al. (2011) to calculate equivalent sand thickness. First, we extracted each 1 km×1 km grid cell from the DEM, and defined it as a block. Next, based on the dune shapes and their orientations, we drew a 1-km transect in the DEM to define the profile for each dune in the block (**Figure 3**). The cross-sections of barchans are usually oriented perpendicular to the crest, whereas the cross-sections of linear dunes are orientated perpendicular to the dune's long axis. Based on this method, A1 region was divided into 138 blocks, obtained 113 transects, and sampled a total of 312 dunes. A2 region was divided into 135 blocks, obtained 129 transects and sampled a total of 370 dunes. A3 region was divided into 450 blocks, obtained 450 transects, and sampled a total of 1171 dunes. We measured the dune height (*H*), cross-sectional area (*CSA*), and dune spacing (λ) for each individual dune in each block (**Figure 3**).

Because the inter-dune elevation varies throughout a sand sea, we calculated the dune height (*H*) by subtracting the average elevation of the interdune areas between two adjacent dunes (E_1 and E_n) relative to the maximum elevation (E_{max}):

$$H = E_{\mathrm{max}} - \left(\frac{E_1 + E_n}{2}\right) \tag{5}$$

Dune spacing was measured between the highest elevations (E_{max}) of adjacent dunes along a transect.

The cross-sectional area (*CSA*) for a single dune is calculated as follows:

$$CSA = \left[\left(\frac{\sum E_{1-n}}{n}\right) - \left(\frac{E_1 + E_n}{2}\right)\right] \times W_d \tag{6}$$

where W_d is the distance between adjacent interdune elevations (E_1 to E_n). The equivalent sand thickness (*EST*) is then calculated as follows:

$$EST = \frac{\sum CSA_{1-n}}{L} \tag{7}$$

where *n* is the number of individual dunes in the transect, and *L* is the length of the transect line in each block.

Results

Dune Morphology

Table 1 summarizes the morphological parameters of the barchans and linear dunes in our study area. For the linear dunes, there was little difference in dune width among the three regions. The crestline was straight and its mean length ranged between 1.2 and 2.1 km, with an average width of about 32 m and a height of about 4 m. Controlled by the dominant northwest wind, the linear dune orientation was from the west-northwest and northwest towards the east-southeast and southeast. For the barchan dunes, the average dune height, length of the stoss slope, and length of the lee slope were much greater at A3 than at A1 and A2.

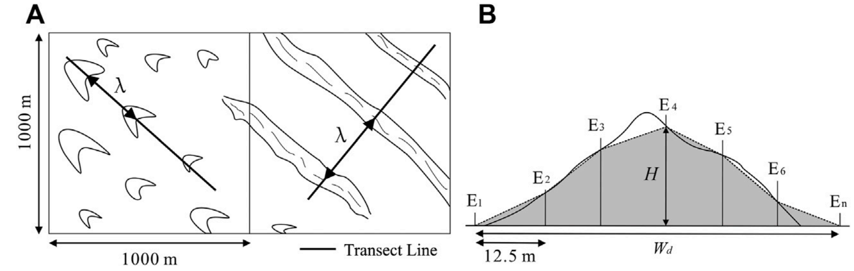

FIGURE 3 | (A) Orientation of the two-dimensional transects for the two dune types (where λ represents the dune spacing between crests) and **(B)** the dune cross-sectional profile, indicating the distribution of the DEM elevation points. E_1 to E_n represent sampling positions. H is the height of the dune's crest and W_d is the distance between adjacent interdune areas. Source: adapted from Bullard et al. (2011).

TABLE 1 | The morphological characteristics of the linear and barchan dunes. Values are means ± SD (n = 17, 41, and 35 for linear dunes in areas A1, A2, and A3, respectively, and n = 34, 98, and 86 for barchan dunes in areas A1, A2, and A3, respectively; the morphological characteristics including crest-line length (L_L), width (W_L), height (H_L), and orientation (D_L) of the linear dunes and the stoss slope length (S_B), lee slope length (L_B), width (W_B), orientation (D_B), and height (H_B) of the barchans).

Study area	**Linear Dunes**				**Barchan Dunes**				
	L_L (m)	**W_L (m)**	**D_L (°)**	**H_L (m)**	**S_B (m)**	**L_B (m)**	**W_B (m)**	**D_B (°)**	**H_B (m)**
A1	1155.43 ±567.16	31.94 ±11.82	124.76 ±0.91	4.27 ±1.58	48.93 ±19.15	11.26 ±4.44	57.67 ±24.46	45.31 ±15.26	6.50 ±2.56
A2	2110.63 ±968.72	33.77 ±15.73	122.17 ±1.97	4.52 ±2.11	45.28 ±20.77	7.03 ±2.74	37.31 ±15.27	39.25 ±18.67	3.63 ±1.48
A3	1814.69 ±804.31	31.89 ±11.14	113.60 ±1.07	4.27 ±1.49	88.08 ±40.21	14.93 ±4.86	97.02 ±41.97	45.50 ±16.58	9.43 ±4.08

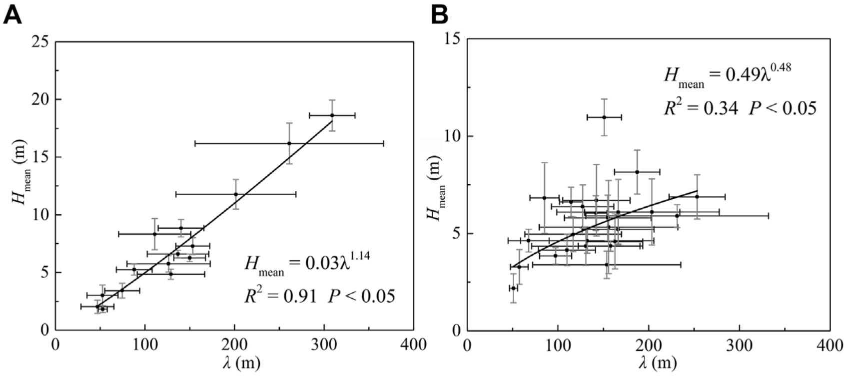

FIGURE 4 | The relationships between average dune height (H_{mean}) of two adjacent dunes and the spacing between crests (λ) in the areas where **(A)** barchans and **(B)** linear dunes coexisted. Values are means ± SD.

The relationship between dune height and spacing reflects the dynamic processes that control dune formation, and the relationship was statistically significant for both dune types. The mean dune height was strongly and significantly positively correlated with spacing for barchans (Pearson's r = 0.97, $p < 0.01$), whereas the correlation was significant and positive, but only moderately strong, for the linear dunes (r = 0.45, $p < 0.05$). Lancaster (1988) suggested that this relationship could be represented by a power function, so we used that equation form to model the relationship. **Figure 4** shows the relationship between the mean dune height (H_{mean}) and spacing (λ) for the barchans and linear dunes, which can be expressed as follows for our study data:

$$\text{For barchans: } H_{\text{mean}} = 0.03\lambda^{1.14}\left(R^2 = 0.91, P < 0.05\right) \quad (8)$$

$$\text{For linear dunes: } H_{\text{mean}} = 0.49\lambda^{0.48}\left(R^2 = 0.34, P < 0.05\right) \quad (9)$$

The relationship was stronger for the barchans, as it explained 91% of the variation, versus only 34% for the

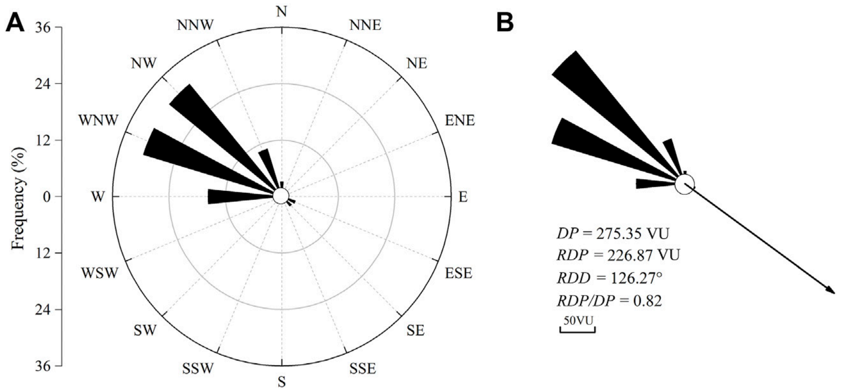

FIGURE 5 | (A) Wind rose for the distribution of threshold wind directions (i.e., for winds strong enough to entrain sediment) and **(B)** the annual drift potential statistics in the areas where linear dunes and barchans coexisted. *DP*, drift potential (in vector units, VU); *RDP*, resultant drift potential (VU); *RDD*, resultant drift potential; *RDP/DP*, directional variability.

linear dunes, and the exponent of 1.14 for barchans. However, although the function for linear dunes was statistically significant, there was considerable scatter in the data for the linear dunes and much of the variance (66%) was not explained. In addition, the exponent of 0.48 for the linear dunes was much smaller than Bullard results, which ranged from 0.683 to 0.913.

Wind Regime

Threshold Wind Speed and Wind Direction

In the Qaidam Basin, the mean annual wind speed in the areas where linear dunes and barchans coexist is 3.96 ± 1.08 m s^{-1} (mean ± SD) at a height of 10 m, with the maximum monthly average wind speed of 5.26 m s^{-1} in summer and spring, followed by autumn and winter (2.36 m s^{-1}), and the maximum wind speed ranged between 9.67 and 18.54 m s^{-1}. Compared with other areas where these dune types coexist (Ma and Lü, 2019), the annual mean wind speed is greater than the value for the Taklimakan Desert (1.68 m s^{-1}), and lower than those in the Rub'Al-Khali Desert and the Sahara Desert (4.31 and 4.55 m s^{-1}, respectively).

The wind rose for sand-driving wind (i.e., wind faster than the particle entrainment threshold) clearly shows a primarily unimodal distribution, but with main and secondary wind directions (Z. Zhang et al., 2017). **Figure 5A** shows the wind rose for the threshold wind direction in the study area. The direction of the sand-driving wind is stable, with an obvious primary wind between west-northwest and northwest, with 61.7% of the sand-driving wind originating within this range. Winds from 270° to 337.5° represent 88.0% of the total winds. The Qaidam Basin desert shows little influence by the East Asian summer monsoon and is mainly controlled by a meandering Westerly Jet Stream (Yu and Lai, 2014), so the threshold wind direction is relatively unimodal.

Drift Potential

DP is the most important and frequently used index for judging wind energy, and this parameter can be combined with the evolution of aeolian geomorphology to provide a crucial reference standard for definition of the wind energy environment. It is widely used in the study of aeolian geomorphology (Lancaster, 1995; Pye and Tsoar, 1990; Z.; Zhang et al., 2017; Zu et al., 2008).

Figure 5B shows the annual *DP* in the areas where linear dunes and barchans coexist. In the study area, annual *DP* was 275.36 vector units (VU) and the *RDP* was 226.87 VU, which represents a medium wind energy environment according to classification from Fryberger and Dean (1979). The *RDD* was from northwest to southeast (126.27°). The linear dunes elongated roughly parallel to this direction (**Table 1**). The *RDP/DP* ratio (directional variability of the wind) is a major factor that affects the dune type, and increases gradually from barchans to star dunes (Fryberger and Dean, 1979; Hereher, 2018; Wasson and Hyde, 1983; Zu et al., 2008), the value of 0.82 for our study area represents low directional variability, which agrees with the wind rose (**Figure 5A**).

Figure 6 shows the seasonal variation of *DP* and the associated components of sand transport in the areas where linear dunes and barchans coexist. The largest *DP* was in the spring, followed by summer, and the smallest values were in autumn and winter. *RDD* ranged from 123.28° to 136.14°, which shows low variation, and was oriented in the same direction as the linear dunes and perpendicular to the wide axis of the barchans. Except for winter, which showed moderate variability (*RDP/DP* = 0.55), the sand transport direction was also stable, with low directional variability (*RDP/DP* values ranged from 0.83 to 0.85).

Dune Morphology and Sand Supply

Dune development requires a sufficient sand supply. To explore the effects of sand supply on the coexistence of linear and barchan dunes, we used *EST* to assess the sand supply for both dune types.

Comparison of the ALOS PALSAR RTC Data With Field Survey Data

Thus far, DEMs have been unable to estimate dune cross-sectional profiles as accurately as field surveys (Bullard et al., 2011; White et al., 2015). Prior to carrying out any data analysis

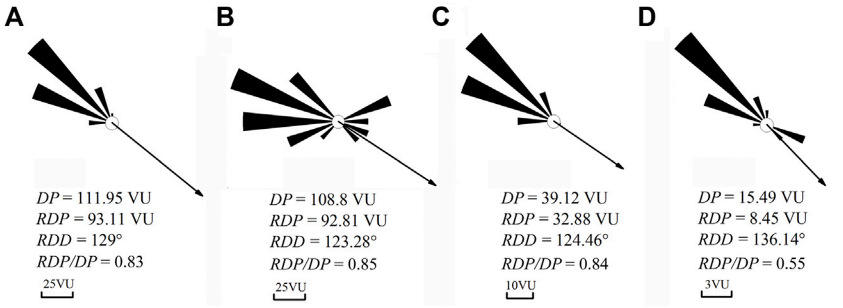

FIGURE 6 | The seasonal variations of drift potential (*DP*) and associated parameters in the areas where linear dunes and barchans coexisted. **(A)** spring, **(B)** summer, **(C)** autumn, and **(D)** winter. *RDP*, resultant drift potential; *RDD*, resultant drift potential; *RDP/DP*, directional variability. Note that the scales differ among the graphs.

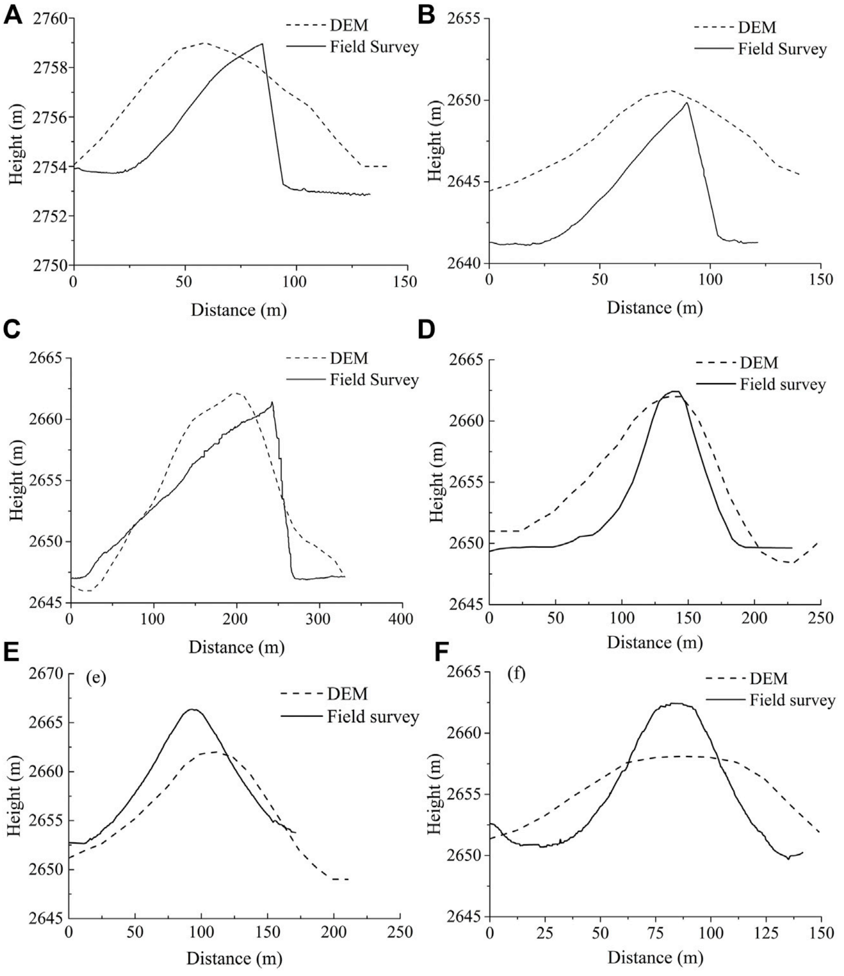

FIGURE 7 | Comparison of dune profiles based on a digital elevation model (DEM) and field surveys for **(A,B,C)** three barchans and **(D,E)**, and **(F)** three linear dunes. The barchan coordinates are 93°46′39.3″E and 37°14′10.8″N, and the linear dune coordinates are 93°46′55.99″E and 37°11′55.84″N.

TABLE 2 | Comparison of the digital elevation model (DEM) and field survey estimates of dune cross-sectional area (*CSA*) for the six dunes whose profiles are shown in **Figure 7**.

Dune	*CSA* from the field Survey(m^2)	*CSA* from the DEM(m^2)	Ratio (Field/DEM)
Barchan 1	267.52	546.53	0.4895
Barchan 2	309.93	363.73	0.8521
Barchan 3	1943.74	2219.81	0.8756
Linear Dune 1	740.92	1162.17	0.6375
Linear Dune 2	629.93	549.05	0.8716
Linear Dune 3	936.16	1125.17	0.8320

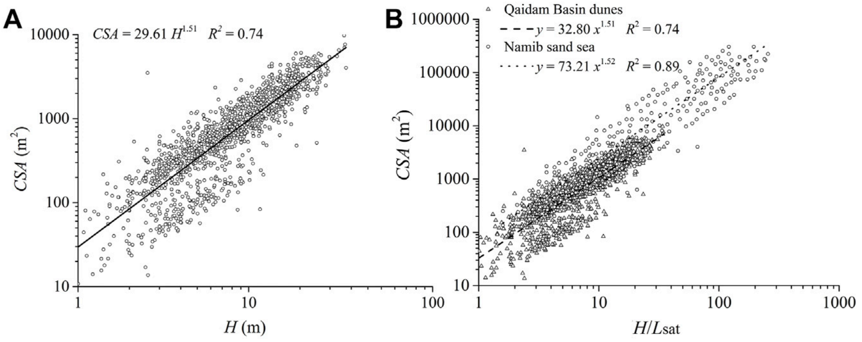

FIGURE 8 | (A) Relationship between individual dune height (H) and individual cross-sectional area (*CSA*) for the dune field in the Qaidam Basin. **(B)** Relationship between the rescaled individual dune height (H/L_{sat}, where L_{sat} represents the saturated length) and the cross-sectional area (*CSA*) for the dune field. Data for the Namib sand sea were obtained from Bullard et al. (2011).

with the ALOS PALSAR RTC data, we compared six dune cross-sectional profiles (three for barchans and three for linear dunes) created from the DEM with the corresponding profiles created from the field survey data. **Figure 7** shows the resulting cross-sectional profiles for these dunes. The cross-sectional area (*CSA*) from the DEM was larger than that from the field surveys.

Table 2 shows that the ratio of field-estimated *CSA* to the DEM-estimated *CSA* ranged from 0.49 to 0.88. We therefore used the arithmetic mean ratio of 0.74 for barchans and the arithmetic mean value of 0.78 for linear dunes to estimate *CSA* from the DEM data.

The relationship between dune height and *CSA* is a key parameter of Wasson and Hyde's (1983) methodology for calculating *EST* from transect data (Bullard et al., 2011). **Figure 8A** shows the relationship between dune height and the adjusted *CSA* for the dunes in areas A1, A2, and A3, which can be expressed as:

$$CSA = 29.61H^{1.51}\left(R^2 = 0.74, P < 0.05\right) \tag{10}$$

Bullard et al. (2011) researched the relationship between *CSA* and the height of individual dunes using ASTER GDEM data for the Namib Sand Sea, and found the following relationship:

$$CSA = 77.06H^{1.524} \tag{11}$$

We attempted to use the saturation length, to normalize the dune height and compare our results with those from the Namib Sand Sea:

$$L_{sat} \cong 2.2\left(\rho_s/\rho_f\right)d \tag{12}$$

where ρ_s and ρ_f represent the sand and fluid densities, respectively, and d is the mean diameter of the sand particles (Andreotti et al., 2010; Gadal et al., 2020). The mean particle diameters in the Namib sand sea and the Qaidam Basin are 0.20 and 0.23 mm, respectively, and the grain to fluid density ratio (ρ_s/ρ_f) for the Namib sand sea and the Qaidam Basin are 2125 and 2128, respectively (Lancaster, 1981; Zhang et al., 2017). The corresponding L_{sat} values were 0.95 and 1.07 m. The rescaled values equal H/L_{sat}. We compared the rescaled results with the results from the Namib Sand Sea (**Figure 8B**), and found that the range of possible *CSA* values for a given height increased as the height increased with the same growth rate. However, for a given value of *H*, especially for low sand dunes, the value of *CSA* in the Qaidam Basin was less than the corresponding value in the Namib sand sea. This difference can be interpreted based on the complexity of the dune types. Simple barchans and linear dunes are the primary dune types in the Qaidam Basin, but these dune types covered only 12% of the total areas of the Namib sand sea, where the majority of the dune types were compound and complex dunes (Bullard et al., 2011).

Dune Morphology and Sand Supply for Area A1

Figure 9 shows the spatial patterns of the *EST*, height, and spacing for area A1 (Areas A2 and A3 are discussed in the following sections.) Barchans and barchan chains were mainly distributed north of the dry river bed, whereas linear dunes and

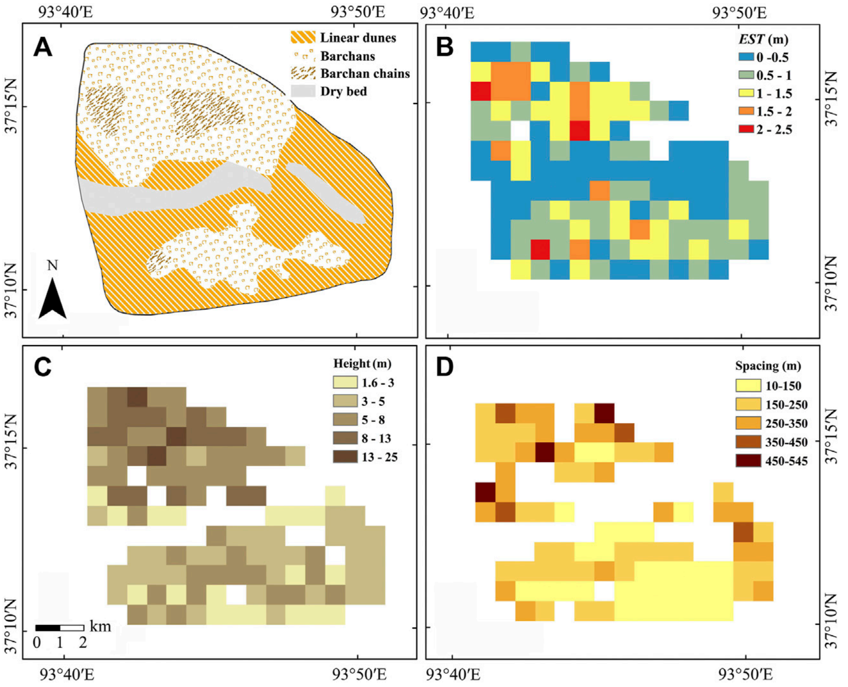

FIGURE 9 | Maps of the **(A)** dune distribution, **(B)** equivalent sand thickness (*EST*), **(C)** dune crest height, and **(D)** crest to crest dune spacing for area A1 **(Figure 1)**.

barchans were mostly distributed south of the dry river bed, but barchans were also distributed inside the area of linear dunes in the south.

The spatial distribution of *EST* shows that the *EST* in this area was low, with values ranging from 0 to 2.5 m and averaging 0.75 m. From the spatial distribution of *EST*, the thickness was higher in the centers of the two areas with barchans than at their edges, and the *EST* of the barchan chains was larger than those of the barchans and linear dunes. *EST* was lowest in the linear dunes area, where the sand supply was lowest.

The mean dune height for the blocks ranged from 1.6 to 25.0 m and averaged 5.75 m, with dunes shorter than 10 m accounting for 85% of the total, and tall dunes were found mainly in the barchan chains. The spatial pattern shows that dune height was higher north of the dry river bed than in the south, and higher in the center of the two barchan areas than at the edges. Dune spacing is also an essential reflection of sediment supply (Dong et al., 2009; Dong et al., 2010; Hugenholtz and Barchyn, 2010). Dune spacing ranged from 10 to 545 m, and followed a pattern similar to that for the dune height; that is, the greater the dune height, the greater the dune spacing. North of the dry river bed, the dominant dune types were barchans and barchan chains, and the dunes were tall and relatively widely spaced; south of the dry river bed, short barchans and linear dunes with narrow dune spacing were dominant.

Dune Morphology and Sand Supply for Area A2

In this dune field, the primary dunes are linear dunes. Barchans are found only in two small areas in the northwestern part of this area, and are roughly parallel to the linear dunes, and some of these barchans are upwind of linear dunes. **Figure 10** shows that the *EST* is quite low, with values ranging from 0.1 to 2.9 m and averaging 1.2 m; that is, the sand supply is low. The thickness decreases from the central desert towards the surrounding areas.

Dune height ranged from 1 to 11 m, and averaged 5.01 m. Dune spacing ranged from 105 to 569 m, with an average spacing of 201.61 m. The linear dunes distributed in the central desert area, had an average spacing of 225.78 m, versus 141.04 m for the barchans. There appeared to be no similarity between the maps of dune spacing and dune height.

Dune Morphology and Sand Supply for Area A3

Figure 11 shows that barchans, barchan chains, linear dunes, parabolic dunes, and shrub dunes coexist in this area. The barchan chains were distributed from northwest to southeast in the central part of the desert, surrounded by simple barchans. Linear dunes were located in the eastern part of the desert, and were distributed parallel to the barchans and barchan chains. In the southern and southeastern parts of the desert, extensive parabolic dunes and shrub dunes occur.

EST ranged from 0 to 9 m, averaged 3.6 m, and decreased gradually from northwest and west to east. Based on the prevailing wind directions (**Figure 5**) and the geomorphology, the main sources of regional sediments are probably sediments from the Dazaohuo River. *EST* was relatively large for the barchans and barchan chains, which means that the sand

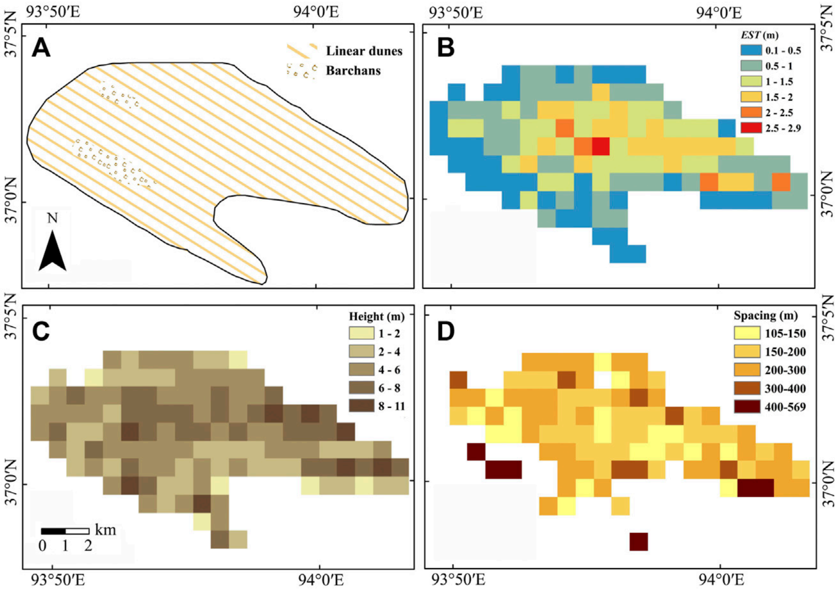

FIGURE 10 | Maps of the **(A)** dune distribution, **(B)** equivalent sand thickness (*EST*), **(C)** dune crest height, and **(D)** crest to crest dune spacing for area A2 **(Figure 1)**.

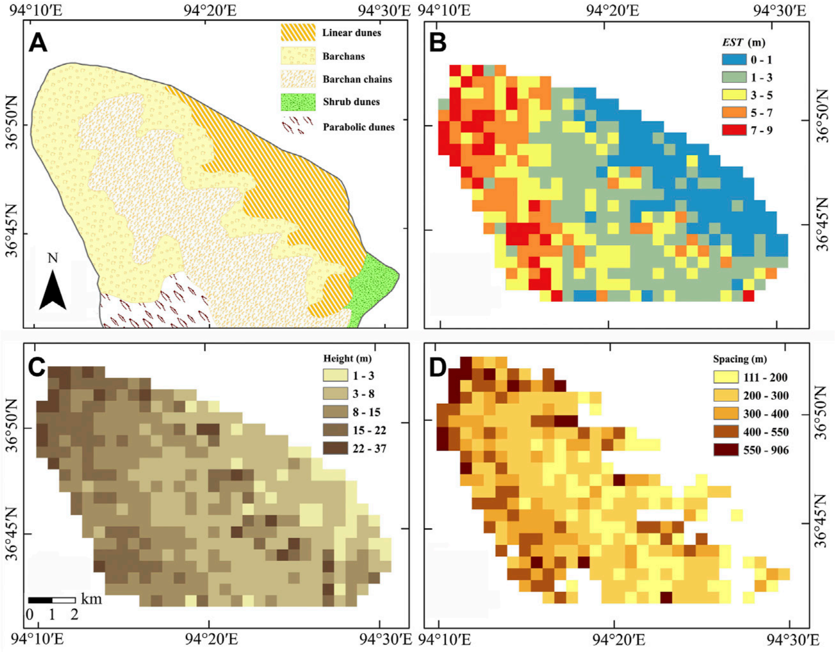

FIGURE 11 | Maps of the **(A)** dune distribution, **(B)** equivalent sand thickness (*EST*), **(C)** dune crest height, and **(D)** crest to crest dune spacing for area A3 **(Figure 1)**.

supply is relatively abundant. In contrast, *EST* for the linear dunes was much smaller, and ranged from 0 to 3 m.

Dune height in area A3 ranged from 1 to 37 m, with an average height of about 9.84 m. The mean dune height for the barchan chains (12.86 m) was higher than that of the barchans (10.28 m), and the linear dunes had the lowest mean height (4.78 m). Dune spacing ranged from 111 to 906 m, and avenged 316.9 m. The dune height and spacing appeared to follow spatial patterns similar to those for dune height; that is, dunes with greater height were more widely spaced.

TABLE 3 | The equivalent sand thickness (*EST*) for the different dune types.

Region	*EST* (m)		
	Linear Dunes	Barchans	Barchan Chains
A1	0.53 ± 0.30	0.91 ± 0.42	1.74 ± 0.29
A2	0.89 ± 0.58	1.03 ± 0.45	—
A3	0.71 ± 0.49	2.17 ± 1.19	3.45 ± 1.61

Sand Supply for the Different Dune Types

Sand supply is also a crucial factor that determines which dune types will evolve. **Table 3** shows that the three areas where linear dunes and barchans coexist have low *EST*, but that the different dune types had different sand supplies. Except for A2, where we did not find barchan chains, the *EST* was greater for barchan chains than for barchans, and linear dunes had the smallest *EST* in all three areas. From the barchans to the linear dunes, *EST* decreases greatly; that is, the sand supply decreases greatly. Generally speaking, the linear dunes appear to have developed under a low sediment supply. The sand supply in the linear dune area is extremely low, with an *EST* only half of the value for the barchans and one-quarter of the value for barchan chains. The distribution of *EST* for three areas (**Figure 12**) also shows that the *EST* of linear dunes with the lowest value compared with barchan dunes and barchan chains, and present concentrated distribution, the value less than 1.5 count for 75%.

DISCUSSION

We designed the present study to provide a quantitative explanation for the coexistence of barchans and linear dunes in China's Qaidam Basin. We measured dune morphology, and analyzed the wind regime using data provided by a wind station in areas where the two dune types coexist, and quantified their sand supply using *EST* to investigate the effect of this variable on coexistence of the barchan and linear dunes. Our ultimate goals were to characterize the development environment in areas where the dunes coexist, and quantify the sand supply using *EST* to explore how the wind regime and sand supply together affect coexistence of the barchans and linear dunes.

Dune Morphological Factors Responsible for the Coexistence of Barchans and Linear Dunes

Dune morphology is shaped by the wind, sand supply, vegetation, topography, and other factors (J. Li et al., 2016). The primary dune types in our study area were barchans and linear dunes, scarcely compound dunes. Simple dune types suggest that there is no stable sand supply large enough to support dune growth and evolution to produce more complex dunes (Bullard et al., 2011; Kocurek et al., 1992). The dune heights of the barchans and linear dunes in our study area were relatively low, which might indicate that a low sand supply constrains dune growth. The relationship between height and spacing reflects the combined effects of the local wind conditions, richness of the sand supply, and dynamic processes (Baddock et al., 2007; Dong et al., 2009; Dong et al., 2010; Lancaster, 1995; Lü et al., 2017). Where the dune height increases faster than the dune spacing, this indicates a tendency for vertical growth of the dunes that is permitted by an abundant sand supply (Lancaster, 1988). The large exponent in the height–spacing relationship for barchans (1.14) may reflect an abundant sand supply, whereas the smaller exponent for linear dunes (0.48) may reflect limitation of the dune size by the low availability of sand.

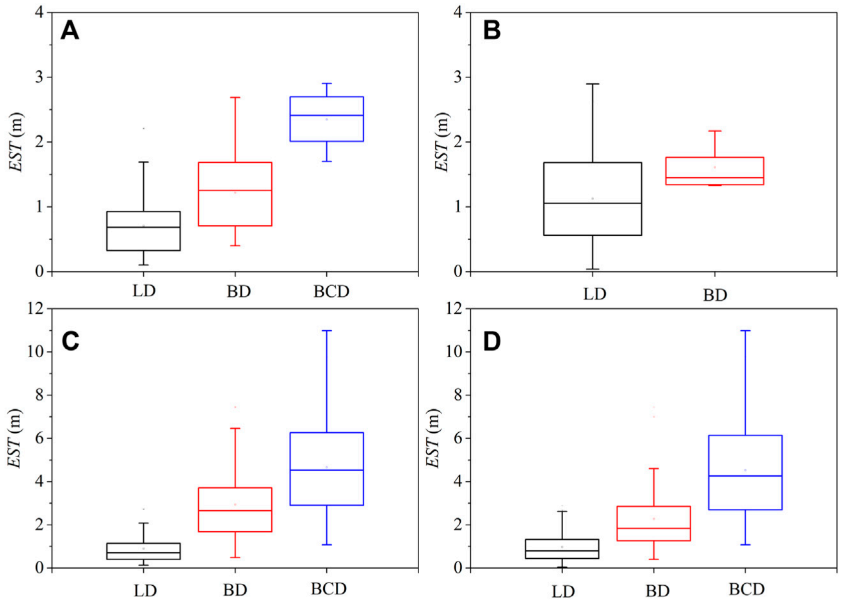

FIGURE 12 | Distribution characteristics of *EST* for area A1 **(A)**, A2 **(B)**, A3 **(C)**, and all three areas **(D)**. LD, linear dunes; BD, barchan dunes; BCD, barchan chain dunes.

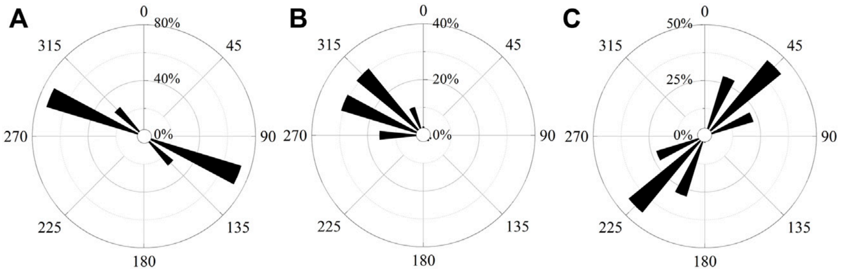

FIGURE 13 | Probability distributions for the orientation of the **(A)** linear dunes, **(B)** sand-driving wind, and **(C)** barchans.

However, the goodness of fit for the height–spacing relationship for linear dunes was only 0.34. This support, but does not prove, our hypothesis that the sand supply was more limited for the linear dunes than for the barchans.

Wind Regime for the Coexistence of Barchans and Linear Dunes

Wind regime is the primary factor that controls dune formation, as the wind drives sand transport and controls the direction of dune movement (Lancaster, 1995; Z. Zhang et al., 2017; Zu et al., 2008). Previous research shows that barchans develop under a unimodal wind regime, whereas linear dunes develop under a narrowly bimodal wind regime (Fryberger and Dean, 1979; Livinstone and Warren, 1996; Wasson and Hyde, 1983). Barchans and linear dunes can generally coexist when the divergence angle between the two wind directions approaches 90° (Gadal et al., 2019; Reffet et al., 2010). In the Qaidam Basin, the orientation of the linear dunes was parallel to the sand-driving wind direction, whereas the orientation of the barchans was almost perpendicular to the wind direction (**Figure 13**). The wind rose for sand-driving wind showed an obvious primary wind direction from the west-northwest (30.9%) and another from the northwest (30.8%), there is a narrowly bimodal wind regime with low directional variability (an overall mean *RDP/DP* value of 0.82 and *RDD* values of 123°–136°; **Figure 6**). The resultant drift direction in our areas were stable throughout the year. This wind regime always corresponding to barchans according to traditional theory, which indicate that sand availability or other factors might play a key role of the barchan and linear dunes coexist in the Qaidam basin desert.

Sand Supply Required for Coexistence of Barchans and Linear Dunes

Sand supply is an essential factor for understanding the geomorphological characteristics of dunes, it is also inextricably bound up with concepts, such as sediment availability, *EST*, and sediment supply models (Hugenholtz and Barchyn, 2010). Combine with the wind regime, sand supply or sediment availability for transport control both the dune type and the dune orientation (Courrech du Pont et al., 2014; Gao et al., 2018; Gao et al., 2015; Lü et al., 2018). When the sand availability is stable, dunes grow in height and migrate to create an orientation that maximizes the components of transport that are normal (perpendicular) to the crest. In our study area, barchan chains developed in area where there is the largest equivalent sand thickness. When the sand supply is limited, barchans and linear dunes can coexist under a bidirectional wind (Gao et al., 2015; Lü et al., 2018). Our findings show that there are sediment-starved regions in our study area with low equivalent sand thickness. Limited sand supply controled barchan and linear dunes coexist. Besides this, our investigation shows that *EST* gradually decreased along the sequence from barchan chains to barchans and linear dunes (**Table 3**), and dunefields dominated by linear dunes occurred at the lowest *EST* values. We proposed that under unidirectional wind regime, barchan chains develped in the central of dune field with high sediment availability. With the decreased sand availability, linear dunes extend downwind from barchans originate possibly from their wake as sediment availability (*EST*) drops, and sand will accumulate in the lee of the localized sand source. Meanwhile, this linear dune stabilized by downwind accumulation of salts and mud, as explained by Rubin and Hesp (2009), allowing the dune itself to function as an obstacle that induces subsequent deposition farther downwind, and become aligned with the sand transport.

Although we did not study a wide range of conditions for dune fields where barchans and linear dunes coexist in other sand seas due to limited availability of high-resolution terrain data, our results suggest that a limited sand supply is an important factor responsible for the coexistence of these dunes.

CONCLUSION

In this study, we described the conditions under which barchans and linear dunes coexist in the Qaidam Basin, and explored the effects of wind regime and sand supply on dune formation and coexistence.

The morphology of the barchans and linear dunes revealed a relatively low mean dune height. The relationship between dune height and spacing was strong for barchans, but although the relationship was significant for the linear dunes, it was much weaker. The wind regime was narrowly bimodal, with low directional variability, and the threshold wind distribution showed obvious primary winds from the west-northwest (30.9%) and northwest (30.8%). This combination led to sand transport from northwest to southeast (*RDD* = 126°), and the linear dunes elongated and moved parallel to *RDD*. *EST* was greatest for the barchan chains, followed by the barchans, and both dune types had much larger *EST* than the linear dunes. In the linear dune fields, the sand supply was extremely low relative to the other dune fields, so sand will accumulate in the lee of the sand source. The linear dunes then develop by elongating at the downwind end and become aligned with the sand transport direction. In summary, under a unimodal wind regime or a bimodal wind regime with an acute angle between the dominant wind directions, coexistence of the two dune types appears to result from a deficient sand supply, although this may interact with the presence of topographical barriers or with the sand's salt, silt, and clay contents, which affect the cohesiveness of the sand supply. These conditions cause the linear dunes to extend parallel to the *RDD*, whereas in adjacent areas with higher *EST*, there is enough sand for barchans to form and migrate parallel to the *RDD*.

DATA AVAILABILITY STATEMENT

The original contributions presented in the study are included in the article/Supplementary Material, further inquiries can be directed to the corresponding author.

AUTHOR CONTRIBUTIONS

LP and MF designed the research. MF carried out the field measurements, data analysis and wrote the manuscript. LP, MF and CM discussed the result.

FUNDING

This study was financially supported by the National Natural Science Foundation of China (41871011) and the Fundamental Research Funds for the Central Universities of China (2020TS101).

REFERENCES

Andreotti, B., Claudin, P., and Pouliquen, O. (2010). Measurements of the Aeolian Sand Transport Saturation Length. *Geomorphology* 123 (3-4), 343–348. doi:10.1016/j.geomorph.2010.08.002

Baas, A. C. W. (2007). Complex Systems in Aeolian Geomorphology. *Geomorphology* 91 (3-4), 311–331. doi:10.1016/j.geomorph.2007.04.012

Baddock, M. C., Livingstone, I., and Wiggs, G. F. S. (2007). The Geomorphological Significance of Airflow Patterns in Transverse Dune Interdunes. *Geomorphology* 87 (4), 322–336. doi:10.1016/j.geomorph.2006.10.006

Bullard, J. E. (1997). A Note on the Use of the "Fryberger Method" for Evaluating Potential Sand Transport by Wind. *J. Sediment. Res.* 67 (3), 499–501. doi:10.1306/D42685A9-2B26-11D7-8648000102C1865D

Bullard, J. E., White, K., and Livingstone, I. (2011). Morphometric Analysis of Aeolian Bedforms in the Namib Sand Sea Using ASTER Data. *Earth Surf. Process. Landforms* 36 (11), 1534–1549. doi:10.1002/esp.2189

Claudin, P., and Andreotti, B. (2006). A Scaling Law for Aeolian Dunes on Mars, Venus, Earth, and for Subaqueous Ripples. *Earth Planet. Sci. Lett.* 252 (1-2), 30–44. doi:10.1016/j.epsl.2006.09.004

Courrech du Pont, S., Narteau, C., and Gao, X. (2014). Two Modes for Dune Orientation. *Geology* 42 (9), 743–746. doi:10.1130/g35657.1

Dong, Z., Qian, G., Luo, W., Zhang, Z., Xiao, S., and Zhao, A. (2009). Geomorphological Hierarchies for Complex Mega-Dunes and Their Implications for Mega-Dune Evolution in the Badain Jaran Desert. *Geomorphology* 106 (3-4), 180–185. doi:10.1016/j.geomorph.2008.10.015

Dong, Z., Wei, Z., Qian, G., Zhang, Z., Luo, W., and Hu, G. (2010). "Raked" Linear Dunes in the Kumtagh Desert, China. *Geomorphology* 123 (1-2), 122–128. doi:10.1016/j.geomorph.2010.07.005

Duran Vinent, O., Andreotti, B., Claudin, P., and Winter, C. (2019). A Unified Model of Ripples and Dunes in Water and Planetary Environments. *Nat. Geosci.* 12 (5), 345–350. doi:10.1038/s41561-019-0336-4

Fryberger, S. G., and Dean, G. M. (1979). "Dune Forms and Wind Regime," in *A Study of Global Sand Seas*. Editors E. D. McKee (Washington, DC: U.S. Government Printing Office)

Gadal, C., Narteau, C., Courrech du Pont, S., Rozier, O., and Claudin, P. (2019). Incipient Bedforms in a Bidirectional Wind Regime. *J. Fluid Mech.* 862, 490–516. doi:10.1017/jfm.2018.978

Gadal, C., Narteau, C., Ewing, R. C., Gunn, A., Jerolmack, D., Andreotti, B., et al. (2020). Spatial and Temporal Development of Incipient Dunes. *Geophys. Res. Lett.* 47 (16), e2020GL088919. doi:10.1029/2020gl088919

Gao, X., Gadal, C., Rozier, O., and Narteau, C. (2018). Morphodynamics of Barchan and Dome Dunes under Variable Wind Regimes. *Geology* 46 (9), 743–746. doi:10.1130/g45101.1

Gao, X., Narteau, C., Rozier, O., and du Pont, S. C. (2015). Phase Diagrams of Dune Shape and Orientation Depending on Sand Availability. *Sci. Rep.* 5, 14677. doi:10.1038/srep14677

Hereher, M. E. (2018). Geomorphology and Drift Potential of Major Aeolian Sand Deposits in Egypt. *Geomorphology* 304, 113–120. doi:10.1016/j.geomorph.2017.12.041

Hesp, P. A., and Hastings, K. (1998). Width, Height and Slope Relationships and Aerodynamic Maintenance of Barchans. *Geomorphology* 22 (1998), 193–204. doi:10.1016/S0169-555X(97)00070-6

Hugenholtz, C. H., and Barchyn, T. E. (2010). Spatial Analysis of Sand Dunes with a New Global Topographic Dataset: New Approaches and Opportunities. *Earth Surf. Process. Landforms* 35 (8), 986–992. doi:10.1002/esp.2013

Hunter, R. E., Richmond, B. M., and Rho Alpha, T. (1983). Storm-controlled Oblique Dunes of the Oregon Coast. *Geol. Soc. America Bull.* 94, 1450–1465. doi:10.1130/0016-7606(1983)94<1450:sodoto>2.0.co;2

Kocurek, G., Townsley, M., Yeh, E., Havholm, K. G., and Sweet, M. L. (1992). Dune and Dune-Field Development on Padre Island, Texas, with Implications for Interdune Deposition and Water-Table-Controlled Accumulation. *Sepm Jsr* 62 (4), 622–635. doi:10.1306/D4267974-2B26-11D7-8648000102C1865D

Lancaster, N. (1981). Grain Size Characteristics of Namib Desert Linear Dunes. *Sedimentology* 28, 115–122. doi:10.1111/j.1365-3091.1981.tb01668.x

Lancaster, N. (1988). Controls of Eolian Dune Size and Spacing. *Geol* 16 (11), 972–975. doi:10.1130/0091-7613(1988)016<0972:coedsa>2.3.co;2

Lancaster, N. (1995). *Geomorphology of Desert Dunes*. Routledge, London: Geomorphology of Desert Dunes.

Lancaster, N. (2006). Linear Dunes on Titan. *Science* 312 (5774), 702–703. doi:10.1126/science.1126292

Li, C., Dong, Z., Chen, G., Yang, J., Cui, X., and Li, J. (2018). Qaidam Basin as an Analog for Linear Dune Formation in Chasma Boreale, Mars: A Comparative Analysis. *Geomorphology* 322, 29–40. doi:10.1016/j.geomorph.2018.08.033

Li, C., Dong, Z., Yin, S., Chen, G., and Yang, J. (2019). Influence of Salinity and Moisture on the Threshold Shear Velocity of saline Sand in the Qarhan Desert, Qaidam Basin of China: A Wind Tunnel experiment. *J. Arid Land* 11, 674–684. doi:10.1007/s40333-019-0058-x

Li, J., Dong, Z., Qian, G., Zhang, Z., Luo, W., Lu, J., et al. (2016). Pattern Analysis of a Linear Dune Field on the Northern Margin of Qarhan Salt Lake, Northwestern China. *J. Arid Land* 8 (5), 670–680. doi:10.1007/s40333-016-0052-5

Livinstone, I., and Warren, A. (1996). *Aeolian Geomorphology: An Introduction*. England: Addison Wesley Longman

Lorenz, R. D., and Zimbelman, J. R. (2014). *Dune Worlds: How Windblown Sand Shapes Planetary Landscapes*. Heidelberg: Springer Science & Business Media.

Lü, P., Dong, Z., and Rozier, O. (2018). The Combined Effect of Sediment Availability and Wind Regime on the Morphology of Aeolian Sand Dunes. *J. Geophys. Res. Earth Surf.* 123, 2878–2886. doi:10.1029/2017JF004361

Lü, P., Narteau, C., Dong, Z., Rozier, O., and Courrech du Pont, S. (2017). Unravelling Raked Linear Dunes to Explain the Coexistence of Bedforms in Complex Dunefields. *Nat. Commun.* 8, 14239. doi:10.1038/ncomms14239

Lucas, A., Narteau, C., Rodriguez, S., Rozier, O., Callot, Y., Garcia, A., et al. (2015). Sediment Flux from the Morphodynamics of Elongating Linear Dunes. *Geology* 43 (11), 1027–1030. doi:10.1130/g37101.1

Ma, F., and Lü, P. (2019). Wind Regime in Coexisting Region of Barchan and Linear Dunes. *J. Desert Res.* 39 (3), 98–106. doi:10.7522/j.issn.1000-694X.2018.00072

Parteli, E. J. R., and Herrmann, H. J. (2007). Dune Formation on the Present Mars. *Phys. Rev. E* 76 (4 Pt 1), 041307. doi:10.1103/PhysRevE.76.041307

Pye, K., and Tsoar, H. (1990). *Aeolian Sand and Sand Dunes*. London: Unwin Hyman.

Reffet, E., Courrech du Pont, S., Hersen, P., and Douady, S. (2010). Formation and Stability of Transverse and Longitudinal Sand Dunes. *Geology* 38 (6), 491–494. doi:10.1130/g30894.1

Rubin, D. M., and Hesp, P. A. (2009). Multiple Origins of Linear Dunes on Earth and Titan. *Nat. Geosci* 2 (9), 653–658. doi:10.1038/ngeo610

Rubin, D. M., and Rubin, A. M. (2013). Origin and Lateral Migration of Linear Dunes in the Qaidam Basin of NW China Revealed by Dune Sediments, Internal Structures, and Optically Stimulated Luminescence Ages, with Implications for Linear Dunes on Titan: Discussion. *Geol. Soc. America Bull.* 125 (11-12), 1943–1946. doi:10.1130/b30780.1

Wasson, R. J., and Hyde, R. (1983). Factors Determining Desert Dune Type. *Nature* 304 (5924), 337–339. doi:10.1038/304337a0

White, K., Bullard, J., Livingstone, I., and Moran, L. (2015). A Morphometric Comparison of the Namib and Southwest Kalahari Dunefields Using ASTER GDEM Data. *Aeolian Res.* 19, 87–95. doi:10.1016/j.aeolia.2015.09.006

Yu, L., and Lai, Z. (2014). Holocene Climate Change Inferred from Stratigraphy and OSL Chronology of Aeolian Sediments in the Qaidam Basin, Northeastern Qinghai-Tibetan Plateau. *Quat. Res.* 81 (3), 488–499. doi:10.1016/j.yqres.2013.09.006

Zhang, D., Narteau, C., and Rozier, O. (2010). Morphodynamics of Barchan and Transverse Dunes Using a Cellular Automaton Model. *J. Geophys. Res.* 115 (F3041). doi:10.1029/2009jf001620

Zhang, Z., Dong, Z., and Li, C. (2015). Wind Regime and Sand Transport in China's Badain Jaran Desert. *Aeolian Res.* 17, 1–13. doi:10.1016/j.aeolia.2015.01.004

Zhang, Z., Dong, Z., Qian, G., Li, J., Luo, W., and Tyrrell, S. (2017). Formation and Development of Dunes in the Northern Qarhan Desert, central Qaidam Basin, China. *Geol. J.* 53, 1123–1134. doi:10.1002/gj.2947

Zhou, J., Zhu, Y., and Yuan, C. (2012). Origin and Lateral Migration of Linear Dunes in the Qaidam Basin of NW China Revealed by Dune Sediments, Internal Structures, and Optically Stimulated Luminescence Ages, with Implications for Linear Dunes on Titan. *Geol. Soc. America Bull.* 124 (7-8), 1147–1154. doi:10.1130/b30550.1

Zu, R., Xue, X., Qiang, M., Yang, B., Qu, J., and Zhang, K. (2008). Characteristics of Near-Surface Wind Regimes in the Taklimakan Desert, China. *Geomorphology* 96 (1-2), 39–47. doi:10.1016/j.geomorph.2007.07.008

Conflict of Interest: The authors declare that the research was conducted in the absence of any commercial or financial relationships that could be construed as a potential conflict of interest.

Publisher's Note: All claims expressed in this article are solely those of the authors and do not necessarily represent those of their affiliated organizations, or those of the publisher, the editors and the reviewers. Any product that may be evaluated in this article, or claim that may be made by its manufacturer, is not guaranteed or endorsed by the publisher.

Copyright © 2022 Ma, Lü and Cao. This is an open-access article distributed under the terms of the Creative Commons Attribution License (CC BY). The use, distribution or reproduction in other forums is permitted, provided the original author(s) and the copyright owner(s) are credited and that the original publication in this journal is cited, in accordance with accepted academic practice. No use, distribution or reproduction is permitted which does not comply with these terms.

frontiers | Frontiers in Earth Science

ORIGINAL RESEARCH
published: 19 May 2022
doi: 10.3389/feart.2022.891032

Geochemical Composition of Surface Sediments in the Bashang Area, North China and its Environmental Significance

Linjing Liu[1,2], Gaolei Jiang[1,2]*, Xin Mao[1,2]*, Hongmei Zhao[1,2], Yongjie Zhao[3], Yuecong Li[3], Hua Zhao[1,2] and Zhiwei Bi[1,2]

[1]Institute of Hydrogeology and Environmental Geology, Chinese Academy of Geological Sciences, Shijiazhuang, China, [2]Key Laboratory of Quaternary Chronology and Hydrological Environment Evolution, China Geological Survey, Shijiazhuang, China, [3]College of Geographical Sciences, Hebei Normal University, Shijiazhuang, China

The geochemical characteristics of sediments are important for reconstructing paleoclimatic and paleoenvironmental conditions in the Asian summer monsoon marginal area. However, robust reconstructions require an understanding of the key factors and mechanisms governing the spatial variations in the composition and ratio of chemical elements in the modern sediments of the Asian summer monsoon marginal area. In this study, 128 surface sediment samples were collected from the Bashang area, which is situated in the Asian summer monsoon marginal area, and examined for their major and trace element compositions and grain size. Principal component analysis (PCA) and redundancy analysis (RDA) were used to analyse the relationship between geochemical data and modern temperature and precipitation data. The results showed that the CIA values of sediments in the Bashang area are mainly affected by temperature rather than precipitation and the Rb/Sr value in the study area reflects the level of precipitation in the corresponding period and the temperature controlling the leaching and weathering. In addition, SiO_2/Al_2O_3 and Zr/Ti ratios have good positive relationships with the coarse-grained fraction of sediments and thus can be used as grain size proxies. We propose that the exact environmental significance indicated by these proxies should be stated explicitly before using them as proxies for paleoenvironmental reconstructions of the Asian summer monsoon marginal area.

Keywords: geochemistry, chemical index of alteration (CIA), rb/sr, SiO2/Al2O3, bashang area, environmental significance

OPEN ACCESS

Edited by:
Zhiwei Xu,
Nanjing University, China

Reviewed by:
Mengying He,
Nanjing Normal University, China
Hongya Wang,
Peking University, China
Xusheng Li,
Nanjing University, China

***Correspondence:**
Gaolei Jiang
jianggl198899@163.com
Xin Mao
maoxin.iheg@cnu.edu.cn

Specialty section:
This article was submitted to Quaternary Science, Geomorphology and Paleoenvironment, a section of the journal Frontiers in Earth Science

Received: 07 March 2022
Accepted: 15 April 2022
Published: 19 May 2022

Citation:
Liu L, Jiang G, Mao X, Zhao H, Zhao Y, Li Y, Zhao H and Bi Z (2022) Geochemical Composition of Surface Sediments in the Bashang Area, North China and its Environmental Significance. Front. Earth Sci. 10:891032. doi: 10.3389/feart.2022.891032

1 INTRODUCTION

The geochemical characteristics of sediments can provide information on provenance and weathering, transport, and sedimentation processes (Wittkop et al., 2020; Yang et al., 2021). Thus, the geochemical characteristics of sediments can help determine the provenance of aeolian deposits, elucidate weathering processes, and further serve as proxies for reconstructing paleoclimatic and paleoenvironmental conditions (Zhao et al., 2019; Skurzyński et al., 2020). For example, the chemical index of alteration (CIA) is often used to evaluate the intensity of chemical weathering (Xiong et al., 2010; Buggle et al., 2011; Dinis et al., 2020), and the Rb/Sr ratios in loess-paleosol sequences can reveal the East Asian winter monsoon intensity (Chen et al., 1999; Jin et al., 2006). In addition, the SiO_2/Al_2O_3 ratio can be used as a grain size proxy (Hatano et al., 2019). Geochemical proxies are influenced by various factors, such as the mineral composition of parent rocks, changes in material sources and sedimentary processes (Borges et al., 2008; Garzanti et al., 2011; Wang et al., 2012; Shang et al., 2013; Hu and Yang, 2016; Peng et al., 2016; Chen et al., 2018; Guo et al., 2018; Li et al., 2019; Chen C. et al., 2021). Borges et al. (2008) found that the continuous cycle of sedimentation and the inheritance of the material from the previous sedimentary cycle greatly influence the application of chemical weathering indicators. Garzanti et al. (2011) suggested that hydraulics, such as suspension screening and selective entraining, greatly impact the elemental composition of sediments, and the CIA and other chemical weathering indicators lose their significance in indicating the degree of chemical weathering during hydraulic processes.

The East Asian summer monsoon (EASM) margin environment, defined as the semiarid zone in northern China, with mean annual precipitation ranging from 400 to 200 mm, is highly vulnerable to climate change (Jiang et al., 2020; Ming et al., 2021). In this region, widespread aeolian deposits, paleosols and lacustrine sediments have recorded a long history of changing environmental conditions under the influence of Asian monsoons (Yang and Ding, 2008; Zhen et al., 2021). Therefore, this region is a focus for historical reconstructions of monsoon changes (Xiao et al., 2006; Fan et al., 2017; Sun et al., 2018; Ding et al., 2019). Elemental compositions and ratios are commonly used reconstruction proxies (Liu B. et al., 2018; Liu J. et al., 2018; Chen Q. et al., 2021; Liu M. et al., 2021). However, robust reconstructions require an understanding of the key factors governing the spatial variations in the compositions and ratios of chemical elements in the modern sediments of the marginal Asian summer monsoon area.

The Bashang area, which connects the southeastern margin of the Inner Mongolia Plateau and the northern part of the Yan Mountains, northern China, is situated in the northeast Asian summer monsoon marginal area. The Asian monsoon margin is the most sensitive region to changes in monsoons. Specifically, environmental changes in northernmost margin of the EASM reflect the advance and retreat of the summer monsoon system and its interaction with the surrounding climate system (Gao et al., 2020). Moreover, this region is a representative agro-pastoral transitional zone and has a fragile ecological environment (Liu X. et al., 2021). Therefore, this region is ideal for studying the spatial variability of the composition and ratio of chemical elements in modern sediments, as well as its influential factors in the Asian summer monsoon marginal area. However, the spatial variability of chemical elements in modern sediments, as well as its influential factors in the Bashang area, remain uncertain.

In this study, 128 surface sediment samples were collected from the Bashang area and examined for their major and trace element contents and grain size. The objectives of this study were to investigate the mechanisms that control the spatial variability of chemical proxies in the surface sediments of the Asian summer monsoon marginal area, such as the CIA, Rb/Sr ratio, and SiO_2/Al_2O_3 ratio, which are commonly used indices for paleoenvironmental reconstruction, and to assess the potential for the use of those chemical proxies as indicators of environmental conditions.

2 STUDY AREA

The Bashang area is situated in the transition zone from the Inner Mongolia Plateau to the mountainous area in the northern mountains of Hebei Province (**Figure 1**). The area is surrounded by mountain ranges, such as the Yinshan Mountains to the north, the Yanshan Mountains to the south, and the Greater Khingan Range to the east (**Figure 1**). The Bashang area ranges from 1,350 m to 1,600 m in elevation, and the elevation decreases from south to north.

Climatologically, the Bashang area is located in the Asian summer monsoon marginal area and is characterized by a continental climate (Liu M. et al., 2021). The wind directions are dominated by northwest winds, which are driven by winter monsoonal winds from the Siberian high-pressure system. The mean annual temperature (MAT) values in this region range from 2 to 5°C, and they increase from east to west. Precipitation is mainly concentrated from July to September. The windy days and frost-free periods are 60–90 days and 80–100 days, respectively. The mean annual precipitation (MAP) gradually increases from 260 in the northwest to 400 mm in the southeast. Moreover, the mean annual potential evaporation values range from 1700 to 1800 mm, which are 4–5 times the MAP. The soil types are mainly chestnut soil and sandy soil. The soil textures are mainly sandy and clayey, and the soil layer is relatively thin (Wu and Zhao, 2017).

3 MATERIALS AND METHODS

3.1 Sample Collection

In this study, 128 surface sediment samples were collected from the Bashang area (**Figure 1A**). These samples were obtained mainly from areas that are less affected by human activities. The sediment types were mainly alluvial and lacustrine deposits. A representative 10 m × 10 m quadrat was selected, and then surface samples were collected from the top 1–2 cm at the four corners and centre of the quadrat according to the plum blossom point method. The lithology of the samples is mainly fine sand, with small amounts of medium sand and silt.

3.2 Sample Analysis

Approximately 5 g dried samples were ground to less than 200 mesh with an agate mortar and then pressed into tablets using the boric acid pressing method (Ji et al., 2003) at a high pressure of 30 tonnes. The concentrations of major elements and trace elements in our samples were determined by X-ray fluorescence (XRF) spectrometry (Panalytica) at Nanjing Normal University. The instrument used Hongze Lake Sediment GSS-9 (GBW07423) as a standard material for quality control. The analytical uncertainties (relative standard deviations) were less than 10%.

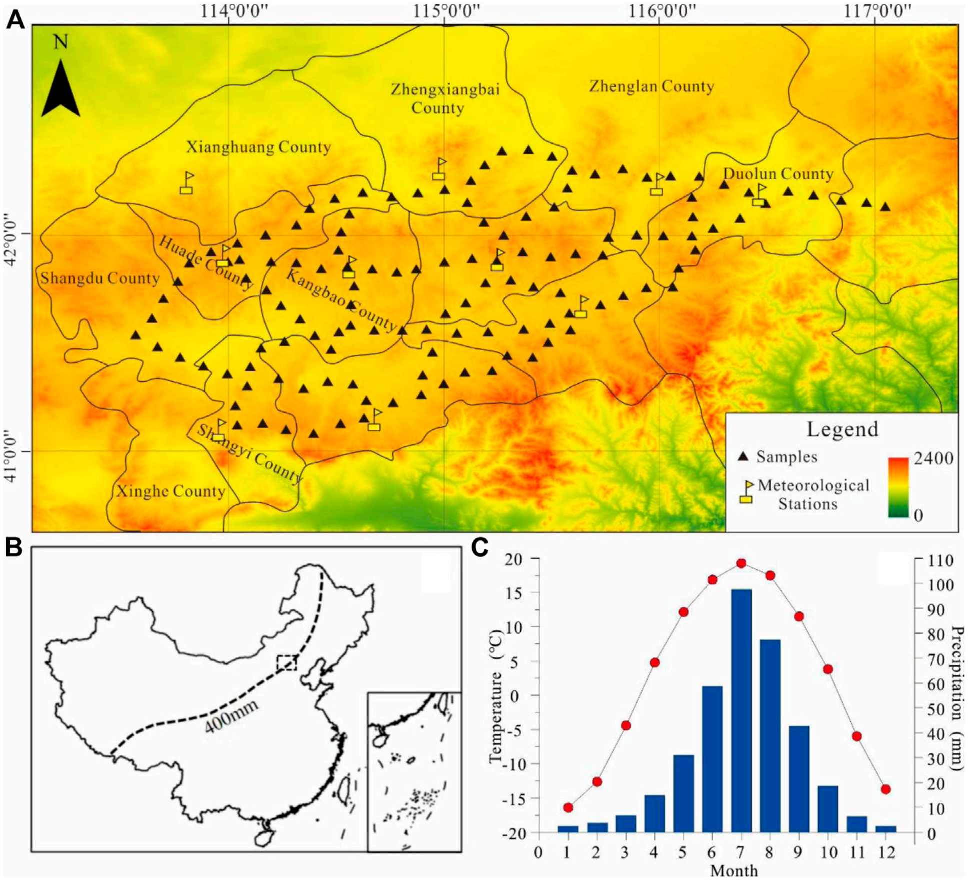

FIGURE 1 | (A) and (B) Location of the study area (C) Monthly mean temperatures and monthly mean precipitation values in the Bashang area.

TABLE 1 | Climatic conditions of the Bashang area, including the MAT and MAP, calculated based on meteorological data between 1960 and 2018 from ten meteorological stations in the Bashang area obtained from the China Meteorological Data Sharing Service System.

Meteorological Station	Longitude	Latitude	Annual Average Temperature (MAT; °C) (°C)	Annual Precipitation (MAP; mm)
Xianghuang County	113.8333	42.2333	3.7	262.9
Zhengxiangbai County	115.0000	42.3000	2.5	351.3
Zhenglan County	116.0000	42.2333	2.3	364.1
Duolun County	116.4667	42.1833	2.5	376.0
Taipusi County	115.2667	41.8833	2.1	393.4
Huade County	114.0000	41.9000	2.9	320.2
Kangbao County	114.5833	41.8500	1.9	347.6
Guyuan County	115.6500	41.6667	2.1	398.2
Shangyi County	113.9833	41.1000	3.8	415.7
Zhangbei County	114.7000	41.1500	3.4	387.6

The grain size of the samples was determined using a Malvern Mastersizer 2000 at the Key Laboratory of Quaternary Chronology and Hydrological Environment Evolution, China Geological Survey. This apparatus, with a measurement range of 0.02–2000 μm, was produced by Malvern Instruments Ltd., United Kingdom. Samples were first pretreated with 10% H_2O_2 and 30% HCl to remove organic matter and carbonates, respectively, and then dispersed by ultrasonication with 10 ml 10% boric acid solution. Then, the samples were analysed. Replicate analyses indicate that the mean particle size measurement error is <2%.

3.3 Meteorological Data

The MAT and MAP were calculated based on meteorological data between 1960 and 2018 from ten meteorological stations in the

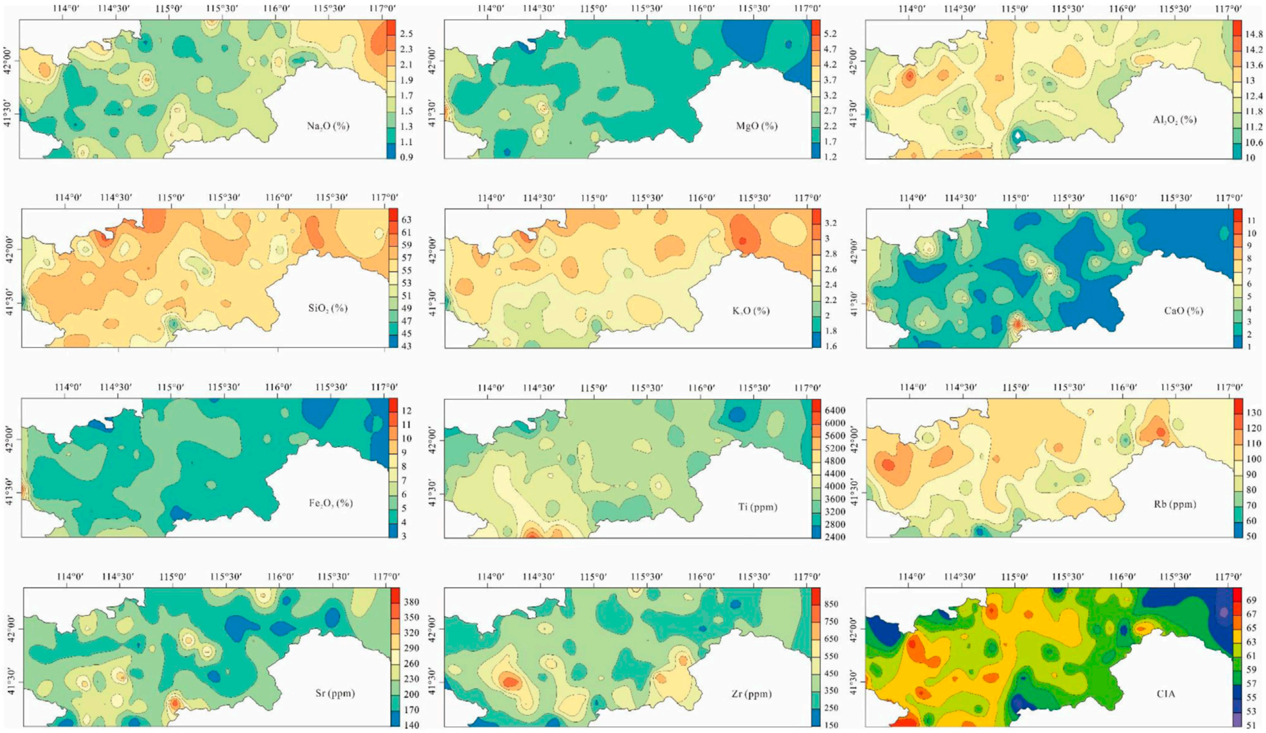

FIGURE 2 | Spatial distribution of elements in the surface sediments of the Bashang area.

Bashang area (**Table 1**). Then, the kriging model data interpolation method was used to obtain the MAT and MAP at each sampling point.

3.4 Data Analysis

Common element proxies, such as the CIA and Rb/Sr and SiO_2/Al_2O_3 ratios, were determined from the surface sediments of this study. The CIA (Nesbitt and Young, 1982) was calculated as follows:

$$CIA = Al_2O_3/(Al_2O_3 + K_2O + Na_2O + CaO^*) \times 100$$

where CaO* refers to the amount of CaO incorporated in the silicate fraction of the samples, which was determined in our study following the method of McLennan (1993).

Principal component analysis (PCA) and redundancy analysis (RDA) were used for ordination of the geochemical data and the temperature, precipitation and mean grain size of the sediment samples. Log(x+1) transformations were applied before ordination analysis. Ordination analysis was used to explore the spatial distribution of element contents and the relation between the element contents and environmental variables. Log(x+1) transformations were applied before ordination analysis. Monte Carlo permutation tests (499 unrestricted permutations) were conducted to test the significance of variables, and forward selection was used to determine the minimum subset of significant variables. The ordinations were performed using the CANOCO program, version 5.0 (Šmilauer and Lepš, 2014).

4 RESULTS

4.1 Major and Trace Element Compositions

SiO_2 had the highest mean concentration of 56.28%, and the concentrations ranged from 43.36 to 62.92%. The concentrations of Al_2O_3 in the surface sediments ranged from 9.25 to 15.31%, with a mean concentration of 12.49%. The concentrations of Fe_2O_3 ranged from 3.07 to 11.99%, with a mean concentration of 4.89%. The K_2O, Na_2O, CaO, and MgO concentrations were 1.53% (0.94–2.56%), 2.63% (1.64–3.28%), 2.89% (1.23–12.36%), and 2.21% (1.26–5.31%), respectively. Among the trace elements, the mean concentrations of Rb, Sr, Ti and Zr in the surface sediments were 96.96 ppm (50.50–128.20 ppm), 210.71 ppm (137.00–400.90 ppm), 3892.90 ppm (2479.10–6506.80 ppm) and 387.88 ppm (190–840 ppm), respectively. The concentration of SiO_2 showed relatively small spatial variations within the Bashang area (**Figure 2**), while other major and trace elements showed considerable spatial variations. Higher concentrations of Al_2O_3 and Rb occurred in the western part of the Bashang area, while higher concentrations of both Zr and Ti were observed in the southern and western parts of the Bashang area (**Figure 2**).

The average CIA value was 61.59, and the values ranged from 51.17 to 69.34, while the average Rb/Sr value was 0.477, and the values ranged from 0.16 to 0.75. Higher CIA values occurred in the western part of the Bashang area, and Rb/Sr values were the highest in the northwestern part of the Bashang area (**Figure 2**).

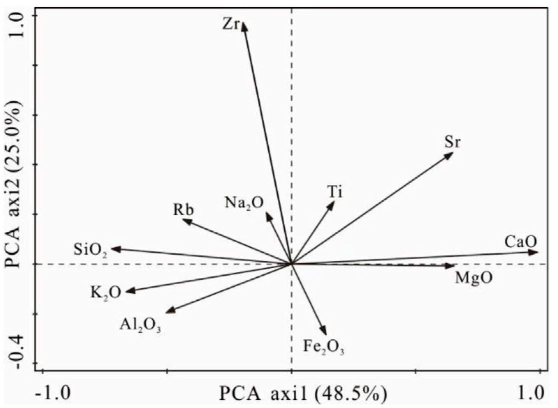

FIGURE 3 | PCA biplot of different elements in the surface sediments of the Bashang area.

The PCA results showed two principal components that accounted for 73.5% of the total variance (**Figure 3**). The first principal component (PC1) was positively correlated with MgO, CaO, and Sr and negatively correlated with SiO_2, K_2O, Al_2O_3 and Rb in the sediments (**Figure 3**). The second principal component (PC2) had high positive loadings of Zr and Ti and negative correlations with Fe_2O_3 (**Figure 3**). The RDA results showed that the first axis of the RDA captured 13% of the total variance, and the second axis captured 8%. The results showed one strong positive relationship between the CIA and Ti, temperature and clay content (**Figure 5**), and the arrows of the first axis were positioned in the negative direction. Zr and Si/Al and the fine and coarse sand contents had a positive relationship, and the arrows were positioned in the negative direction of the first axis. Rb/Sr had a weak relationship with the environmental parameters.

4.2 Grain Size

The grain size analysis revealed that the samples were dominated by fine sand (64–255 μm) and silt (4–63 μm). The mean contents of the clay (<4 μm), silt (4–63 μm), and fine sand (64–255 μm) fractions were 15.80, 44.36 and 28.30%, respectively. Moreover, the mean contents of the medium sand (256–512 μm) and coarse sand (512–2000 μm) fractions were relatively low.

The mean contents of the clay, silt and fine sand fractions showed relatively small spatial variations within the Bashang area (**Figure 4**). The mean contents of the medium and coarse sand fractions showed considerable spatial variations, and higher medium and coarse sand fractions were identified in the southwestern and northeastern parts of the Bashang area (**Figure 4**).

5 DISCUSSION

5.1 Proxy Interpretation

5.1.1 CIA

The CIA was first proposed by Nesbitt and Young (1982) to reconstruct the paleoclimate from the early Proterozoic sediments of the Huronian Supergroup, north of Lake Huron. The CIA has been widely used to quantitatively evaluate the chemical weathering intensity (Guo et al., 2018; Wang et al., 2020) and represents the ratio of mobile soluble elements (i.e., CaO, Na_2O, and K_2O) to immobile insoluble elements (i.e., Al_2O_3). Generally, higher CIA values indicate stronger chemical weathering (Xie et al., 2018; Chen C. et al., 2021). CIA values <50 indicate virtually no weathering; CIA values of approximately 50–60 indicate weak chemical weathering; and CIA values >80 indicate strong chemical weathering (Zhao et al., 2018).

Previous studies have suggested that climate, especially precipitation, exerts a dominant control on silicate weathering (White and Blum, 1995; Dinis et al., 2020). However, in this study, the RDA results show that the CIA exhibits better correlations with the MAT values and clay fractions and poorer correlations with the MAP values. The intensity of weathering at the Earth's surface largely depends on climate, and the weathering intensity is higher in warmer and more humid settings. Based on the Arrhenius equation, the mineral decomposition rate at the watershed scale increases as temperature increases, and the reaction rate can be doubled for each 10 °C increase (White and Blum, 1995; Dessert et al., 2003). The influence of temperature on the weathering rate is dependent on precipitation (White and Blum, 1995). In the study area, precipitation gradually decreased from east to west due to the weakening of the Asian monsoon. However, temperature increased from east to west. The increase in the CIA values from east to west (**Figure 2**) and the RDA result (**Figure 5**) indicate that the CIA values of sediments in the Bashang area are mainly affected by temperature rather than precipitation.

5.1.2 Rb/Sr Ratio

Rb and Sr usually exhibit different geochemical behaviours in sediments during the processes of weathering, denudation, and transport (Amorosi et al., 2021). In comparison to Sr, Rb is relatively insoluble and can be immobilized by adsorption onto clay minerals (Chen et al., 1999; Liu et al., 2014; An et al., 2018). Thus, the Rb/Sr ratio is often considered a good proxy for the chemical weathering intensity in lacustrine sediments (Jin et al., 2001), loess-paleosol sediments (Liang et al., 2013), and aeolian sediments (Liu et al., 2014). Previous studies of weathering crusts and loess-paleosol sediments have suggested that higher Rb/Sr values in the residual component indicate stronger chemical weathering. The higher chemical weathering intensity of lake sediments in catchments corresponds to the low Rb/Sr ratios of lake sediments resulting from more dissolved Sr in the basin (Jin and Zhang, 2002; Jin et al., 2006).

In this study, the RDA results show that the Rb/Sr ratio has a negative correlation with the MAT and MAP values. The studies of loess-paleosol sequences show that the Rb/Sr value of the residual component gradually increases with the strengthening of chemical weathering (Chen et al., 1999; Chen et al., 2001). Accordingly, the Rb/Sr value in lacustrine sediments decreases with increasing chemical weathering rate in the basin (Jin et al., 2001). Therefore, generally, in dry and cold climate environments, chemical weathering is weak and the Rb/Sr value of lacustrine sediments is high. Under warm and humid conditions, chemical weathering is strong and the Rb/Sr value of lacustrine sediments is low. On the other hand, the variation

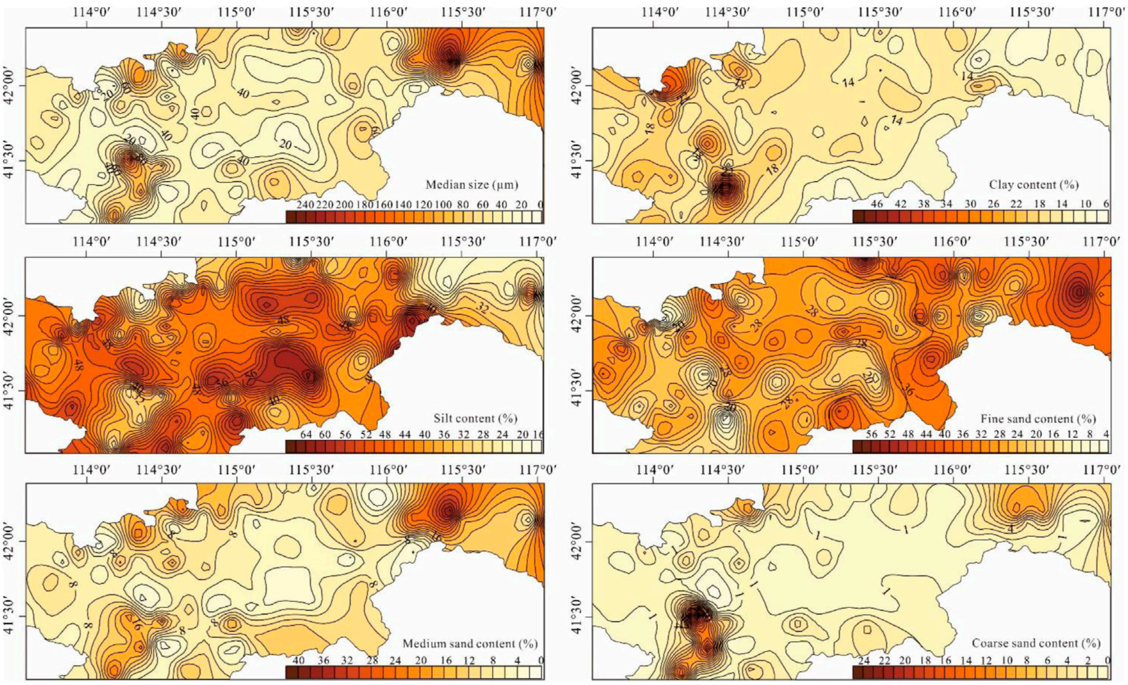

FIGURE 4 | Spatial distribution of grain size parameters.

range of Rb content in lacustrine sediments is very small, and the variation of Rb/Sr value mainly depends on the activity of Sr (Chen, et al., 1997). This is because the element Rb and Sr are easy to separate during rainwater leaching, Rb has a strong affinity with clay, and Sr easily enters the solution (Chen et al., 1997). Therefore, the Rb/Sr value in well preserved lacustrine sediments essentially indicates the degree of material leaching in the source area, and further reflects the level of precipitation in the corresponding period in the basin and the temperature controlling the leaching and weathering behavior.

5.1.3 SiO_2/Al_2O_3 Ratio

In general, coarse-grained sediments are enriched in quartz that has a high SiO_2 content. In contrast, fine-grained sediments usually tend to be enriched in micaceous and/or clay minerals that have high Al_2O_3 contents (Liang et al., 2013). Consequently, SiO_2/Al_2O_3 ratios are used as a grain size index (Hatano et al., 2019). In this study, the RDA results show that the mean and median grain sizes have significant positive correlations with the SiO_2/Al_2O_3 ratio. **Figure 6** also indicates that grain size exerts a strong influence on the SiO_2/Al_2O_3 ratio.

5.1.4 Ti and Zr Contents and Zr/Ti Ratio

Ti and Zr are presumably the least mobile elements during weathering and are mainly found in weathering-resistant silicate minerals, such as zircon and rutile, respectively (Dypvik and Harris, 2001; Kylander et al., 2013). Changes in the Ti and Zr contents can thus be used to qualitatively or semiquantitatively estimate detrital matter abundances (Francke et al., 2020). When the regional precipitation increases, large Ti and Zr abundances are brought into the lake during heavy runoff and heavy precipitation, and vice

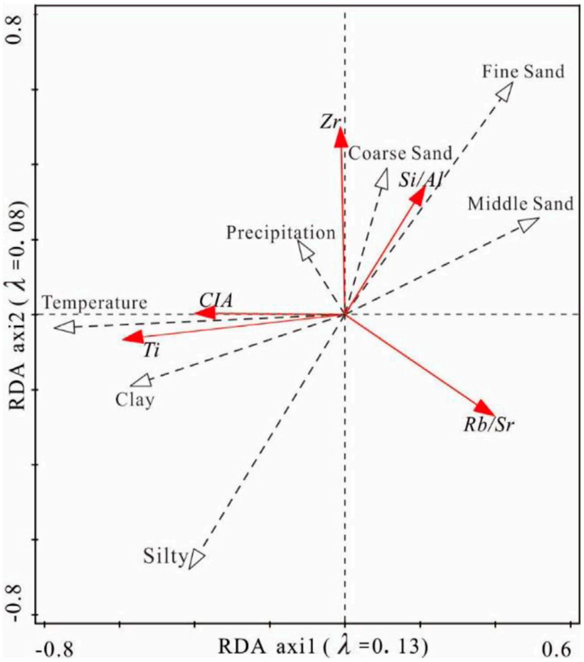

FIGURE 5 | RDA plot of environmental indices and factors.

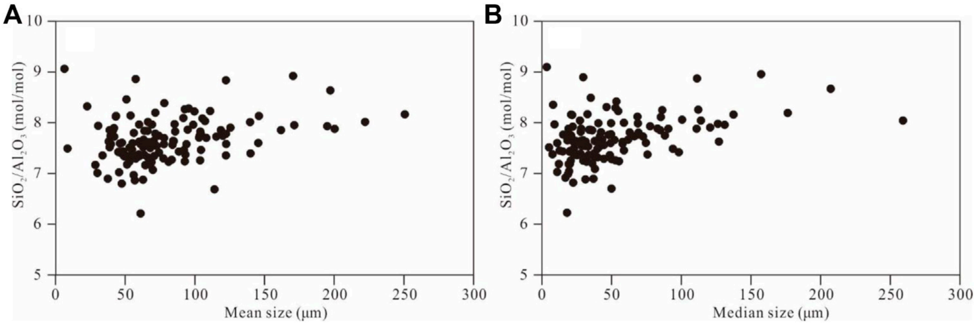

FIGURE 6 | Relationship between the SiO_2/Al_2O_3 ratio and the mean grain size **(A)** and median grain size **(B)** of sediments.

versa. Therefore, the Ti contents indicate the amounts of detrital sediments brought into the lake by regional precipitation or surface runoff to a certain extent (Shen et al., 2010; Biskaborn et al., 2012). In this study, the RDA results show that Zr exhibits a good correlation with the sand fraction, while Ti is associated with the clay and silt fractions. Thus, increases in the Zr/Ti ratio may be indicative of less clay and silt or more sand and can be used as a proxy for alterations in silicate sources.

5.2 Implications for Paleoenvironmental Reconstruction

As common geochemical proxies, the CIA, Rb/Sr ratio, SiO_2/Al_2O_3 ratio, and Zr/Ti ratio are widely used to assess various sediments (Roy et al., 2013; Francke et al., 2020). The CIA and Rb/Sr ratio are often used to evaluate the chemical weathering intensity (Garzanti et al., 2018). In this study, the CIA values have a good correlation with the clay components of sediments and temperature. The study area is located at the margin of the Asian monsoon, and the precipitation in this area is affected by the advance and retreat of the monsoon. The RDA results indicate that the CIA values of sediments in the Bashang area are mainly affected by temperature rather than precipitation. In the study area, the mean annual precipitation (MAP) gradually increases from 260 in the northwest to 400 mm in the southeast. It is possible that the changes in precipitation have a limited effect on the regional CIA. The Rb/Sr ratio has a negative correlation with the MAT and MAP values. The Rb/Sr ratio is affected by complex factors. Especially for the lacustrine sediments, the source of sediments has a great influence on Rb/Sr ratio (An et al., 2018). These negative correlations suggested that the Rb/Sr value in well preserved lacustrine sediments in the study area reflects the level of precipitation in the corresponding period in the basin and the temperature controlling the leaching and weathering behavior. The negative correlation between Rb/Sr ration and CIA value also indicates this point. The PCA results show that PC1 is positively correlated with MgO, CaO and Sr, which are easily transported elements, and is negatively correlated with SiO_2, K_2O, Al_2O_3 and Rb in the sediments, which are not easily transported (**Figure 3**). PC1 accounts for 48.5% of the total variance. Therefore, the changes in PC1 can be used as a comprehensive proxy of paleoclimate change.

Many studies have suggested that SiO_2/Al_2O_3 and Zr/Ti ratios can be used as grain size indices for aeolian sands (Chen Q. et al., 2021) and lake sediments (Kylander et al., 2013) in semiarid and arid regions. Our findings are consistent with these conclusions. The SiO_2/Al_2O_3 and Zr/Ti ratios in this study have a good positive relationship with the coarse-grained fraction of sediments and thus can be used as proxies for grain size.

6 CONCLUSION

The CIA values of sediments in the Bashang area are mainly affected by temperature. The Rb/Sr value in well preserved lacustrine sediments in the study area reflects the level of precipitation in the corresponding period in the source area and the temperature controlling the leaching and weathering behavior. Therefore, different geochemical proxies in the same sediments have different interpretation. The exact environmental significance indicated by these proxies should be stated explicitly before using them as proxies for paleoenvironmental reconstructions of the Asian summer monsoon marginal area. Statistical analyses of chemical changes may be able to identify more appropriate climate change proxies.

The mean and median grain sizes have significant positive correlations with the SiO_2/Al_2O_3 ratio. The SiO_2/Al_2O_3 ratio can therefore be used as a grain size index. Zr exhibits a good correlation with the sand fraction, while Ti is associated with the clay and silt fractions. Thus, the Zr/Ti ratio can be used as a proxy for alterations in silicate sources.

DATA AVAILABILITY STATEMENT

The original contributions presented in the study are included in the article/**Supplementary Material**, further inquiries can be directed to the corresponding authors.

AUTHOR CONTRIBUTIONS

All authors listed have made substantial, direct, and intellectual contributions to the work and have approved it for publication.

FUNDING

This research was financially supported by the National Natural Science Foundation of China (42177428, 41807420, 41907375, U20A20116, and 41602194) and the Basic Research Programme of the Institute of Hydrogeology and Environmental Geology, Chinese Academy of Geological Sciences (CAGS) (SK202007).

ACKNOWLEDGMENTS

We are grateful to Jiayi Xiao at Nanjing Normal University and other colleagues at the Institute of Hydrogeology and Environmental Geology, CAGS, who contributed to our field work and data analysis.

SUPPLEMENTARY MATERIAL

The Supplementary Material for this article can be found online at: https://www.frontiersin.org/articles/10.3389/feart.2022.891032/full#supplementary-material

REFERENCES

Amorosi, A., Bruno, L., Campo, B., Di Martino, A., and Sammartino, I. (2021). Patterns of Geochemical Variability across Weakly Developed Paleosol Profiles and Their Role as Regional Stratigraphic Markers (Upper Pleistocene, Po Plain). *Palaeogeogr. Palaeoclimatol. Palaeoecol.* 574, 110413. doi:10.1016/j.palaeo.2021.110413

An, F., Lai, Z., Liu, X., Fan, Q., and Wei, H. (2018). Abnormal Rb/Sr Ratio in Lacustrine Sediments of Qaidam Basin, NE Qinghai-Tibetan Plateau: A Significant Role of Aeolian Dust Input. *Quat. Int.* 469, 44–57. doi:10.1016/j.quaint.2016.12.050

Biskaborn, B. K., Herzschuh, U., Bolshiyanov, D., Savelieva, L., and Diekmann, B. (2012). Environmental Variability in Northeastern Siberia during the Last ~ 13,300 Yr Inferred from Lake Diatoms and Sediment-Geochemical Parameters. *Palaeogeogr. Palaeoclimatol. Palaeoecol.* 329-330, 22–36. doi:10.1016/j.palaeo.2012.02.003

Borges, J. B., Huh, Y., Moon, S., and Noh, H. (2008). Provenance and Weathering Control on River Bed Sediments of the Eastern Tibetan Plateau and the Russian Far East. *Chem. Geol.* 254, 52–72. doi:10.1016/j.chemgeo.2008.06.002

Buggle, B., Glaser, B., Hambach, U., Gerasimenko, N., and Marković, S. (2011). An Evaluation of Geochemical Weathering Indices in Loess-Paleosol Studies. *Quat. Int.* 240, 12–21. doi:10.1016/j.quaint.2010.07.019

Chen, C., Tao, S., Zhao, W., Jin, M., Wang, Z., Li, H., et al. (2021). Holocene Lake Level, Vegetation, and Climate at the East Asian Summer Monsoon Margin: A Record from the Lake Wulanhushao Basin, Southern Inner Mongolia. *Palaeogeogr. Palaeoclimatol. Palaeoecol.* 561, 110051. doi:10.1016/j.palaeo.2020.110051

Chen, J., An, Z., and Head, J. (1999). Variation of Rb/Sr Ratios in the Loess-Paleosol Sequences of Central China during the Last 130,000 Years and Their Implications for Monsoon Paleoclimatology. *Quat. Res.* 51, 215–219. doi:10.1006/qres.1999.2038

Chen, J., An, Z., Liu, L., Ji, J., Yang, J., and Chen, Y. (2001). Variations in Chemical Compositions of the Eolian Dust in Chinese Loess Plateau over the Past 2.5 Ma and Chemical Weathering in the Asian Inland. *Sci. China Ser. D-Earth Sci.* 44 (5), 403–413. doi:10.1007/bf02909779

Chen, J., Qiu, G., Lu, H., and Ji, J. (1997). Variation of Summer Monsoon Intensity on the Loess Plateau of Central China during the Last 130 000 a. *Chin. Sci. Bull.* 42, 473–476. doi:10.1007/bf02882595

Chen, Q., Li, Z., Dong, S., Wang, N. a., Lai, D. Y. F., and Ning, K. (2018). Spatial Variations in the Chemical Composition of Eolian Sediments in Hyperarid Regions: a Case Study from the Badain Jaran Desert, Northwestern China. *J. Sediment. Res.* 88, 290–300. doi:10.2110/jsr.2018.11

Chen, Q., Li, Z., Dong, S., Yu, Q., Zhang, C., and Yu, X. (2021). Applicability of Chemical Weathering Indices of Eolian Sands from the Deserts in Northern China. *CATENA* 198, 105032. doi:10.1016/j.catena.2020.105032

Dessert, C., Dupré, B., Gaillardet, J., François, L. M., and Allègre, C. J. (2003). Basalt Weathering Laws and the Impact of Basalt Weathering on the Global Carbon Cycle. *Chem. Geol.* 202, 257–273. doi:10.1016/j.chemgeo.2002.10.001

Ding, Z., Lu, R., Lyu, Z., and Liu, X. (2019). Geochemical Characteristics of Holocene Aeolian Deposits East of Qinghai Lake, China, and Their Paleoclimatic Implications. *Sci. Total Environ.* 692, 917–929. doi:10.1016/j.scitotenv.2019.07.099

Dinis, P. A., Garzanti, E., Hahn, A., Vermeesch, P., and Cabral-Pinto, M. (2020). Weathering Indices as Climate Proxies. A Step Forward Based on Congo and SW African River Muds. *Earth-Science Rev.* 201, 103039. doi:10.1016/j.earscirev.2019.103039

Dypvik, H., and Harris, N. B. (2001). Geochemical Facies Analysis of Fine-Grained Siliciclastics Using Th/U, Zr/Rb and (Zr+Rb)/Sr Ratios. *Chem. Geol.* 181, 131–146. doi:10.1016/S0009-2541(01)00278-9

Fan, J., Xiao, J., Wen, R., Zhang, S., Wang, X., Cui, L., et al. (2017). Carbon and Nitrogen Signatures of Sedimentary Organic Matter from Dali Lake in Inner Mongolia: Implications for Holocene Hydrological and Ecological Variations in the East Asian Summer Monsoon Margin. *Quat. Int.* 452, 65–78. doi:10.1016/j.quaint.2016.09.050

Francke, A., Holtvoeth, J., Codilean, A. T., Lacey, J. H., Bayon, G., and Dosseto, A. (2020). Geochemical Methods to Infer Landscape Response to Quaternary Climate Change and Land Use in Depositional Archives: a Review. *Earth-Science Rev.* 207, 103218. doi:10.1016/j.earscirev.2020.103218

Gao, Y. H., Li, Z. L., Zhu, R. X., and Wang, N. A. (2020). Quantitative Reconstruction of Holocene Millennial-Scale Precipitation in the Asian Monsoon Margin of Northwest China, Revealed by Phytolith Assemblages from Calcareous Root Tubes in the Tengger Desert. *Clim. Dyn.* 55 (3), 755–770. doi:10.1007/s00382-020-05293-4

Garzanti, E., Andó, S., France-Lanord, C., Censi, P., Vignola, P., Galy, V., et al. (2011). Mineralogical and Chemical Variability of Fluvial Sediments 2. Suspended-Load Silt (Ganga-Brahmaputra, Bangladesh). *Earth Planet. Sci. Lett.* 302, 107–120. doi:10.1016/j.epsl.2010.11.043

Garzanti, E., Dinis, P., Vermeesch, P., Andò, S., Hahn, A., Huvi, J., et al. (2018). Dynamic Uplift, Recycling, and Climate Control on the Petrology of Passive-Margin Sand (Angola). *Sediment. Geol.* 375, 86–104. doi:10.1016/j.sedgeo.2017.12.009

Guo, Y., Yang, S., Su, N., Li, C., Yin, P., and Wang, Z. (2018). Revisiting the Effects of Hydrodynamic Sorting and Sedimentary Recycling on Chemical Weathering Indices. *Geochimica Cosmochimica Acta* 227, 48–63. doi:10.1016/j.gca.2018.02.015

Hatano, N., Yoshida, K., Adachi, Y., and Sasao, E. (2019). Intense Chemical Weathering in Southwest Japan during the Pliocene Warm Period. *J. Asian Earth Sci.* 184, 103971. doi:10.1016/j.jseaes.2019.103971

Hu, F., and Yang, X. (2016). Geochemical and Geomorphological Evidence for the Provenance of Aeolian Deposits in the Badain Jaran Desert, Northwestern China. *Quat. Sci. Rev.* 131, 179–192. doi:10.1016/j.quascirev.2015.10.039

Jiang, M., Han, Z., Li, X., Wang, Y., Stevens, T., Cheng, J., et al. (2020). Beach Ridges of Dali Lake in Inner Mongolia Reveal Precipitation Variation during the Holocene. *J. Quat. Sci.* 35, 716–725. doi:10.1002/jqs.3195

Jin, Z., Cao, J., Wu, J., and Wang, S. (2006). A Rb/Sr Record of Catchment Weathering Response to Holocene Climate Change in Inner Mongolia. *Earth Surf. Process. Landforms* 31, 285–291. doi:10.1002/esp.1243

Jin, Z., Wang, S., Shen, J., Zhang, E., Li, F., Ji, J., et al. (2001). Chemical Weathering since the Little Ice Age Recorded in Lake Sediments: a High-Resolution Proxy of Past Climate. *Earth Surf. Process. Landforms* 26, 775–782. doi:10.1002/esp.224

Jin, Z., and Zhang, E. (2002). Paleoclimate Implications of Rb/Sr Ratios from Lake Sediments. *Sci. Technol. Eng.* 2, 20–22. CNKI:SUN:KXJS.0.2002-03-008

Kylander, M. E., Klaminder, J., Wohlfarth, B., and Löwemark, L. (2013). Geochemical Responses to Paleoclimatic Changes in Southern Sweden since the Late Glacial: the Hässeldala Port Lake Sediment Record. *J. Paleolimnol.* 50, 57–70. doi:10.1007/s10933-013-9704-z

Li, Z., Chen, Q., Zhang, C., Yu, Q., Dong, S., Zhao, L., et al. (2019). Environmental Significance of the Chemical Composition of Sediments in Groundwater-Recharged Lakes of the Badain Jaran Desert, NW China. *Geochem. Geophys. Geosyst.* 20, 1026–1040. doi:10.1029/2018GC007967

Liang, L., Sun, Y., Beets, C. J., Prins, M. A., Wu, F., and Vandenberghe, J. (2013). Impacts of Grain Size Sorting and Chemical Weathering on the Geochemistry of Jingyuan Loess in the Northwestern Chinese Loess Plateau. *J. Asian Earth Sci.* 69, 177–184. doi:10.1016/j.jseaes.2012.12.015

Liu, B., Jin, H., Sun, L., Niu, Q., Zhang, C., Xue, W., et al. (2018). Multiproxy Records of Holocene Millennial-Scale Climatic Variations from the Aeolian Deposit in Eastern Horqin Dune Field, Northeastern China. *Geol. J.* 54, 351–363. doi:10.1002/gj.3184

Liu, B., Jin, H., Sun, L., Sun, Z., Niu, Q., Xie, S., et al. (2014). Holocene Moisture Change Revealed by the Rb/Sr Ratio of Aeolian Deposits in the Southeastern Mu Us Desert, China. *Aeolian Res.* 13, 109–119. doi:10.1016/j.aeolia.2014.03.006

Liu, J., Wang, Y., Wang, Y., Guan, Y., Dong, J., and Li, T. (2018). A Multi-Proxy Record of Environmental Changes during the Holocene from the Haolaihure Paleolake Sediments, Inner Mongolia. *Quat. Int.* 479, 148–159. doi:10.1016/j.quaint.2016.12.015

Liu, M., Min, L., Zhao, J., Shen, Y., Pei, H., Zhang, H., et al. (2021). The Impact of Land Use Change on Water-Related Ecosystem Services in the Bashang Area of Hebei Province, China. *Sustainability* 13, 716. doi:10.3390/su13020716

Liu, X., Lu, R., Ding, Z., Lyu, Z., Li, Y., and Dong, Z. (2021). Holocene Environmental Changes Inferred from an Aeolian-Palaeosol-Lacustrine Profile in the Mu Us Desert, Northern China. *Front. Earth Sci.* 9, 799935. doi:10.3389/feart.2021.799935

McLennan, S. M. (1993). Weathering and Global Denudation. *J. Geol.* 101, 295–303. doi:10.1086/648222

Ming, G., Zhou, W., Wang, H., Shu, P., Cheng, P., Liu, T., et al. (2021). Grain Size Variation in Two Lakes from Margin of Asian Summer Monsoon and its Paleoclimate Implications. *Palaeogeogr. Palaeoclimatol. Palaeoecol.* 567, 110295. doi:10.1016/j.palaeo.2021.110295

Nesbitt, H. W., and Young, G. M. (1982). Early Proterozoic Climates and Plate Motions Inferred from Major Element Chemistry of Lutites. *Nature* 299, 715–717. doi:10.1038/299715a0

Peng, S., Hao, Q., Wang, L., Ding, M., Zhang, W., Wang, Y., et al. (2016). Geochemical and Grain-Size Evidence for the Provenance of Loess Deposits in the Central Shandong Mountains Region, Northern China. *Quat. Res.* 85, 290–298. doi:10.1016/j.yqres.2016.01.005

Roy, P. D., Quiroz-Jiménez, J. D., Pérez-Cruz, L. L., Lozano-García, S., Metcalfe, S. E., Lozano-Santacruz, R., et al. (2013). Late Quaternary Paleohydrological Conditions in the Drylands of Northern Mexico: a Summer Precipitation Proxy Record of the Last 80 Cal Ka BP. *Quat. Sci. Rev.* 78, 342–354. doi:10.1016/j.quascirev.2012.11.020

Shen, H. Y., Jia, Y. L., and Guo, F. (2010). Characteristics and Environmental Significance of the Magnetic Susceptibility in Sediment of Huangqihai Lake, Inner Mongolia, China. *Arid. Land Geogr.* 33, 151–157. doi:10.13826/j.cnki.cn65-1103/x.2010.02.002

Skurzyński, J., Jary, Z., Kenis, P., Kubik, R., Moska, P., Raczyk, J., et al. (2020). Geochemistry and Mineralogy of the Late Pleistocene Loess-Palaeosol Sequence in Złota (Near Sandomierz, Poland): Implications for Weathering, Sedimentary Recycling and Provenance. *Geoderma* 375, 114459. doi:10.1016/j.geoderma.2020.114459

Šmilauer, P., and Lepš, J. (2014). *Multivariate Analysis of Ecological Data Using CANOCO 5*. Cambridge, UK: Cambridge University Press.

Sun, Q., Chu, G., Xie, M., Zhu, Q., Su, Y., and Wang, X. (2018). An Oxygen Isotope Record from Lake Xiarinur in Inner Mongolia since the Last Deglaciation and its Implication for Tropical Monsoon Change. *Glob. Planet. Change* 163, 109–117. doi:10.1016/j.gloplacha.2018.01.017

Wang, P., Du, Y., Yu, W., Algeo, T. J., Zhou, Q., Xu, Y., et al. (2020). The Chemical Index of Alteration (CIA) as a Proxy for Climate Change during Glacial-Interglacial Transitions in Earth History. *Earth-Science Rev.* 201, 103032. doi:10.1016/j.earscirev.2019.103032

Wang, X., Xia, D., Zhang, C., Lang, L., Hua, T., and Zhao, S. (2012). Geochemical and Magnetic Characteristics of Fine-Grained Surface Sediments in Potential Dust Source Areas: Implications for Tracing the Provenance of Aeolian Deposits and Associated Palaeoclimatic Change in East Asia. *Palaeogeogr. Palaeoclimatol. Palaeoecol.* 323-325, 123–132. doi:10.1016/j.palaeo.2012.02.005

White, A. F., and Blum, A. E. (1995). Effects of Climate on Chemical_ Weathering in Watersheds. *Geochimica Cosmochimica Acta* 59, 1729–1747. doi:10.1016/0016-7037(95)00078-E

Wittkop, C., Bartley, J. K., Krueger, R., Bouvier, A., Georg, R. B., Knaeble, A. R., et al. (2020). Influence of Provenance and Transport Process on the Geochemistry and Radiogenic (Hf, Nd, and Sr) Isotopic Composition of Pleistocene Glacial Sediments, Minnesota, USA. *Chem. Geol.* 532, 119390. doi:10.1016/j.chemgeo.2019.119390

Wu, A. B., and Zhao, Y. X. (2017). Analysis of Ecological Land Pattern Evolution and Ecosystem Service Value in Bashang Plateau. *Trans. Chin. Soc. Agric. Eng.* 33 (2), 283–290.

Xiao, J., Wu, J., Si, B., Liang, W., Nakamura, T., Liu, B., et al. (2006). Holocene Climate Changes in the Monsoon/arid Transition Reflected by Carbon Concentration in Daihai Lake of Inner Mongolia. *Holocene* 16, 551–560. doi:10.1191/0959683606hl950rp

Xie, Y., Yuan, F., Zhan, T., Kang, C., and Chi, Y. (2018). Geochemical and Isotopic Characteristics of Sediments for the Hulun Buir Sandy Land, Northeast China: Implication for Weathering, Recycling and Dust Provenance. *CATENA* 160, 170–184. doi:10.1016/j.catena.2017.09.008

Xiong, S., Ding, Z., Zhu, Y., Zhou, R., and Lu, H. (2010). A ~6Ma Chemical Weathering History, the Grain Size Dependence of Chemical Weathering Intensity, and its Implications for Provenance Change of the Chinese Loess-Red Clay Deposit. *Quat. Sci. Rev.* 29, 1911–1922. doi:10.1016/j.quascirev.2010.04.009

Yang, S., and Ding, Z. (2008). Advance-retreat History of the East-Asian Summer Monsoon Rainfall Belt over Northern China during the Last Two Glacial-Interglacial Cycles. *Earth Planet. Sci. Lett.* 274, 499–510. doi:10.1016/j.epsl.2008.08.001

Yang, S., Luo, Y., Li, Q., Liu, W., Chen, Z., Liu, L., et al. (2021). Comparisons of Topsoil Geochemical Elements from Northwest China and Eastern Tibetan Plateau Identify the Plateau Interior as Tibetan Dust Source. *Sci. Total Environ.* 798, 149240. doi:10.1016/j.scitotenv.2021.149240

Yuan, S., Rui-Jie, L., Fei-Fei, J., Li-Hui, T., Qing-Liang, T., Yuan, C., et al. (2013). Paleoclimatic Evolution Indicated by Major Geochemical Elements from Aeolian Sediments on the East of Qinghai Lake. *Sci. Cold Arid Regions* 5, 301–308. doi:10.3724/SP.J.1226.2013.00301

Zhao, W., Liu, L., Chen, J., and Ji, J. (2019). Geochemical Characterization of Major Elements in Desert Sediments and Implications for the Chinese Loess Source. *Sci. China Earth Sci.* 62, 1428–1440. doi:10.1007/s11430-018-9354-y

Zhao, Z., Wen, X., Tang, L., Li, B., Niu, D., Meng, J., et al. (2018). Applicability of Chemical Alteration Index to Indication of Paleoclimate Change by Different Sedimentary Facies. *Acta Sedimentol. Sin.* 36, 343–353. doi:10.14027/j.issn.1000-0550.2018.026

Zhen, Z., Li, W., Xu, L., Zhang, X., and Zhang, J. (2021). Lake-level Variation of Dali Lake in Mid-east of Inner Mongolia since the Late Holocene. *Quat. Int.* 583, 62–69. doi:10.1016/j.quaint.2021.03.003

Conflict of Interest: The authors declare that the research was conducted in the absence of any commercial or financial relationships that could be construed as a potential conflict of interest.

Publisher's Note: All claims expressed in this article are solely those of the authors and do not necessarily represent those of their affiliated organizations, or those of the publisher, the editors and the reviewers. Any product that may be evaluated in this article, or claim that may be made by its manufacturer, is not guaranteed or endorsed by the publisher.

Copyright © 2022 Liu, Jiang, Mao, Zhao, Zhao, Li, Zhao and Bi. This is an open-access article distributed under the terms of the Creative Commons Attribution License (CC BY). The use, distribution or reproduction in other forums is permitted, provided the original author(s) and the copyright owner(s) are credited and that the original publication in this journal is cited, in accordance with accepted academic

frontiers | Frontiers in Earth Science

BRIEF RESEARCH REPORT
published: 31 May 2022
doi: 10.3389/feart.2022.835281

Variation in Luminescence Characteristics and Paramagnetic Defect Centres in Fine-Grained Quartz From a Loess-Palaeosol Sequence in Tajikistan: Implications for Provenance Studies in Aeolian Environments

Aditi K. Dave[1*†], *Alida Timar-Gabor*[3,4], *Giancarlo Scardia*[5], *Nosir Safaraliev*[6] and *Kathryn E. Fitzsimmons*[1,2]

[1]Research Group for Terrestrial Palaeoclimates, Max Planck Institute for Chemistry, Mainz, Germany, [2]Department of Geosciences, University of Tübingen, Tübingen, Germany, [3]Faculty of Environmental Sciences and Engineering, Babes Bolyai University, Cluj-Napoca, Romania, [4]Interdisciplinary Research Institute on Bionanoscience, Babes Bolyai University, Cluj-Napoca, Romania, [5]Instituto de Geociências e Ciências Exatas, Universidade Estadual Paulista (UNESP), Rio Claro, Brazil, [6]Department of Geology, Tajik National University, Dushanbe, Tajikistan

Trapped charge characteristics in quartz are of increasing interest for their utility as indicators of sediment provenance. These include sensitivity of optically stimulated luminescence (OSL) and thermoluminescence (TL) signal and paramagnetic E_1' defect centre in quartz. Up until now, these methods have largely been used independently in provenance investigations, especially in aeolian systems. Variations in quartz OSL and TL signal sensitivity in loess-palaeosol sequences has been linked to shifts in sediment source corresponding to climatic fluctuations. However, the processes responsible for observed variation in OSL and TL sensitivity in quartz, including its link to the original rock source and/or its sedimentary history, remains a topic of contention. On the other hand, the intensity of E_1' defect centre in quartz is known to reflect the provenance of quartz, and is also routinely utilised as a provenance indicator in aeolian studies. In this study we aim to understand the variations in E_1' intensity and OSL (and TL) sensitivity by direct comparison of these characteristics in fine-grained quartz from a c. 60 m-thick loess-palaeosol sequence in Tajikistan. In doing so, we investigate the natural processes that may have led to variability in trapped-charge characteristics over the c. 500 ky timespan covered by the sequence. Our results suggest that apart from the inherent link to its provenance signature, the observed luminescence sensitivity of quartz especially in loess-palaeosol sequences are largely influenced by depositional and post-depositional processes during soil formation.

Keywords: provenance, luminescence sensitivity, defect centres, Tajikistan, Central Asia, loess

OPEN ACCESS

Edited by:
David K. Wright,
University of Oslo, Norway

Reviewed by:
Sumiko Tsukamoto,
Leibniz Institute for Applied Geophysics (LIAG), Germany
Manoj Kumar Jaiswal,
Indian Institute of Science Education and Research Kolkata, India

****Correspondence:***
Aditi K. Dave
aditi-krishna.dave@uni-tuebingen.de

†Present address:
Aditi K. Dave,
Department of Geosciences,
University of Tübingen, Tübingen,
Germany

Specialty section:
This article was submitted to Quaternary Science, Geomorphology and Paleoenvironment, a section of the journal Frontiers in Earth Science

Received: *14 December 2021*
Accepted: *02 May 2022*
Published: *31 May 2022*

Citation:
Dave AK, Timar-Gabor A, Scardia G, Safaraliev N and Fitzsimmons KE (2022) Variation in Luminescence Characteristics and Paramagnetic Defect Centres in Fine-Grained Quartz From a Loess-Palaeosol Sequence in Tajikistan: Implications for Provenance Studies in Aeolian Environments. Front. Earth Sci. 10:835281. doi: 10.3389/feart.2022.835281

INTRODUCTION

Deposits of aeolian dust, or loess, have long been recognised as excellent terrestrial archives of past environmental change (Liu, 1985; Kukla et al., 1988; Schaetzl et al., 2018). These deposits form stacked sequences of primary loess and buried soils—commonly known as loess-palaeosol sequences - that largely reflect colder, drier, more windy phases, and more humid, warmer, less windy periods respectively (Marković et al., 2015). Whilst *in situ* evidence of past climatic conditions can be extracted from the physical and chemical characteristics of loess sediments (e.g., Fitzsimmons et al., 2012 and references therein), identifying the source of loess—its provenance—is equally valuable for elucidating dust transport pathways, thereby providing insights into past wind dynamics and atmospheric circulation in a region (Ding et al., 2000; Muhs et al., 2008). A number of provenance techniques have been applied to distinguish source change in loess, including various isotopic (Sr, Nd; Smith et al., 2003; Rao et al., 2006) and geochemical (major and trace elements; Sun, 2002; Buggle et al., 2008) approaches. However, these methods are derived from bulk sediments, which can lead to indeterminate results (Újvári et al., 2012). The limitations of radiogenic and elemental approaches in loess provenance studies have led to an increased interest in targeting specific minerals, such as zircon (Stevens et al., 2010; Fenn et al., 2018) and quartz (Nagashima et al., 2007; Sun et al., 2008). Provenance techniques based on detrital zircon U-Pb ages in loess are, however, often limited by the low concentrations of zircon grains (Fenn et al., 2018). By contrast, quartz is ubiquitous, and its resistance to weathering provides an excellent material for provenance analysis in loess sediments.

In recent years, lattice defects and impurities in quartz have been increasingly investigated as potential indicators of sedimentary history and transport processes (Pietsch et al., 2008; Fitzsimmons, 2011; Sawakuchi et al., 2012) and provenance (Nagashima et al., 2007; Toyoda et al., 2016; Nagashima et al., 2017; Sawakuchi et al., 2018). A range of characteristics are exploited for this purpose. These involve various components of the optically stimulated luminescence (OSL) and thermoluminescence (TL) signals (Tsukamoto et al., 2011; Jeong and Choi, 2012), including its sensitivity characteristics (Zheng et al., 2009; Lü and Sun, 2011; Sawakuchi et al., 2012; Zular et al., 2015), or specific intrinsic or impurity-related defect centres in quartz such as E_1', Al-hole and Ti-Li centres using electron spin resonance (ESR; Nagashima et al., 2007; Shimada et al., 2013; Tissoux et al., 2015; Wei et al., 2020).

Luminescence sensitivity, conventionally defined as the luminescence emitted per unit dose per unit mass of the sample, is an intrinsic property of the quartz crystal lattice. The luminescence sensitivity of quartz is often linked to 1) the thermal history of the quartz-bearing source rocks, which forms the basis of its use as a provenance indicator (Fitzsimmons, 2011; Sawakuchi et al., 2011); and 2) the sedimentary history of the grain, whereby quartz is sensitised by repeated processes of erosion, transport, storage and burial (Pietsch et al., 2008; Fitzsimmons et al., 2010). As such, the technique shows promise for application in long profiles of aeolian loess. Recent investigations of quartz OSL and TL sensitivity down loess profiles in Tajikistan (Li and Zhou, 2021), as well as from the Chinese loess plateau (CLP; Lü et al., 2014; Lü et al., 2021) yield distinctions in the sensitivity of quartz between loess and palaeosol units. The variability observed within individual profiles has been attributed to the impact of climatic fluctuations on geomorphic processes, such as the expansion and contraction of nearby deserts leading to sensitivity change related to transport distance from the source (deserts) to the sink (loess) (Lü et al., 2014); increased glacial erosion in mountain regions during cold phases leading to increased production of low sensitivity quartz (Lü et al., 2014); and preferential weathering of certain rock types in response to long-term climate fluctuations, thereby leading to availability of quartz of different origin for loess deposition (Li and Zhou, 2021).

One of the most commonly used ESR-based quartz provenance technique utilises the heat-treated E_1' centre (or HT-E_1' centre) in combination with the crystallinity index of quartz (Nagashima et al., 2007; Toyoda et al., 2016). This method has been applied to distinguish between quartz from different inland Asian desert sources (Sun et al., 2007; Sun et al., 2008) and ocean sediment cores (Nagashima et al., 2011; Wang et al., 2020). The use of HT-E_1' centre as a provenance indicator is based on the premise that HT-E_1' reflects the total number of oxygen vacancies (*Si*=*Si*) in a quartz crystal and increases with rock age, a quantity which is characteristic of the source rock (Toyoda and Hattori, 2000; Toyoda et al., 2016). In a recent study (Dave et al., 2022), an alternate provenance technique is proposed based on the measurement of natural (not heat-treated) intensity of E_1' and peroxy defect centres in detrital quartz, both these parameters are known to increase with the age of the host rock (Odom and Rink, 1989). This study was successful in differentiating loess deposits from two different basins in Central Asia, as well as identified temporal variations in provenance in response to climatic fluctuations at a long loess sequence (Karamaidan) in Tajikistan.

Ultimately, the aim of sediment provenance analysis is to identify the parent rock from which sediments are derived. However, the process of sediment cycling is complicated by multiple factors that affect the fate of the material from source to sink (Weltje and von Eynatten, 2004). With this in mind, one of the first considerations for the application of a provenance technique lies in its sensitivity to detect changes in sediment composition, and therefore source, at a site. In this study, we compare two different approaches based on trapped charge within fine-grained aeolian quartz which appear to reflect different aspects of the sediment cycling process. The natural E_1' signal from quartz measures a single defect type and largely reflects the signature of the host rock (through its age: Odom and Rink, 1989; Dave et al., 2022). By contrast, the OSL and TL signals are more complex and may reflect either the signature of the parent rock (through its thermal history: Fitzsimmons, 2011; Sawakuchi et al., 2011; Sawakuchi et al., 2018), and/or its sedimentary and transport history (Pietsch et al., 2008; Fitzsimmons et al., 2010). Consequently, at any given point in a sedimentary setting, the quartz OSL and TL sensitivity may record the influence of both, and the degree of influence of either

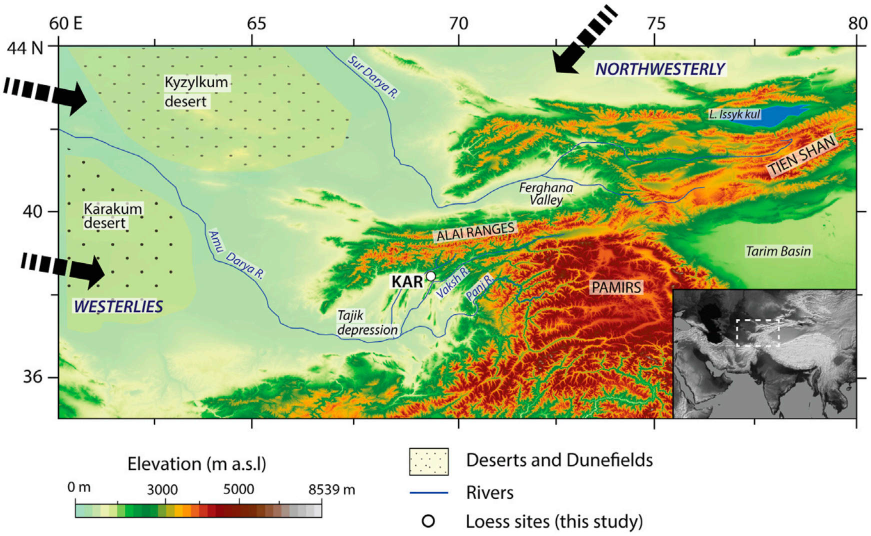

FIGURE 1 | Regional setting and location of study site KAR within western Central Asia. The elevation map was created using Shuttle Radar Topography Mission (SRTM) data from AW3D of the Japan Aerospace Exploration Agency.

depends on which parameters act as a dominating factor at that time (Fitzsimmons, 2011; Lü and Sun, 2011; Sawakuchi et al., 2011). Recent studies based on multi-spectroscopic techniques (Sharma, 2017), as well as laboratory-based experiments on repeated irradiation and bleaching of natural quartz (Bartyik et al., 2021; Li and Zhou, 2021) show that its OSL signal exhibits preferential sensitisation, the magnitude of which may vary depending on the quartz source. Thus, at this stage, understanding the reasons for sensitisation of quartz remain poorly understood. Therefore, a combined approach based on measurement of both the natural E_1' intensity and luminescence sensitivity of the OSL and TL signals, offers an alternative approach to interpret luminescence sensitivity data in loess records, as well as assess the influence of depositional and post-depositional processes in aeolian environments on luminescence sensitivity.

MATERIALS AND METHODS

Site Setting and Sampling

The site of Karamaidan (KAR; 38° 34′ 33.47″ N, 69° 16′ 40.79″ E, 1,629 m a.s.l.) lies in the foothills of the Gissar Range, on the northern margins of the Afghan-Tajik depression (**Figure 1**). The Afghan-Tajik depression is a seismically active sedimentary basin, the northern part of which is interrupted by a series of north-south oriented folds and ridges (McNab et al., 2019) that are traversed by a number of rivers arising from the glaciated Alai, Trans-Alai and Pamir ranges. These drainage systems are tributaries to the Amu Darya River and provides vast glacio-/fluvial outwash plain that acts as local dust source area (Li et al., 2019). The farther west and northwest located, Karakum and Kyzylkum deserts, act as additional dust sources for the Afghan-Tajik depression (Li et al., 2019). Given this setting, the margins of this depression preserve some of the thickest loess deposits in Eurasia, several of which represent quasi-continuous deposition over the last million years (Forster and Heller, 1994; Dodonov and Baiguzina, 1995). The loess deposits at KAR provide one such palaeoclimatic archive, which is known to preserve a record of climate change over the past 1 million years (Ma; Forster and Heller, 1994) and thus, provides an ideal test site to investigate long term variations in dust source and their relationship to changing climatic conditions.

The KAR profile represents a >100 m thick package of alternating primary loess and buried soils (Forster and Heller, 1994), exposed as a result of a recent earthquake-induced landslide. In this study we investigate a c. 56 m stratigraphic interval from the lower part of the KAR section, comprising of six loess and five palaeosol units, with three additional weak to moderately developed soils observed within the primary loess intervals (**Figure 2**). The relative chronology of the c. 56 m subsection sampled for this study is described and interpreted to span marine isotope stages (MIS) 9-19 (Dave et al., 2022), based on the correlation of *in-situ* magnetic susceptibility with the global marine isotope stack (Lisiecki and Raymo, 2005; **Figure 2**) as well as the previous chronostratigraphy obtained by Forster and Heller (1994) (**Supplementary Figure S1**). A description of the stratigraphy of the subsection, magnetic susceptibility measurements and relative chronology can be found in the **Supplementary Material S1**.

Sampling at KAR was carried out by abseiling down the exposed vertical cliff to ensure continuous down-profile observation and sample collection. Prior to sampling, more than 1 m of the overlying sediment on the cliff-face was removed to prevent contamination by recent displacement and to expose undisturbed stratigraphy. We collected a total of 55 samples every 0.5–1 m by hammering opaque tubes into the cleaned and exposed vertical section.

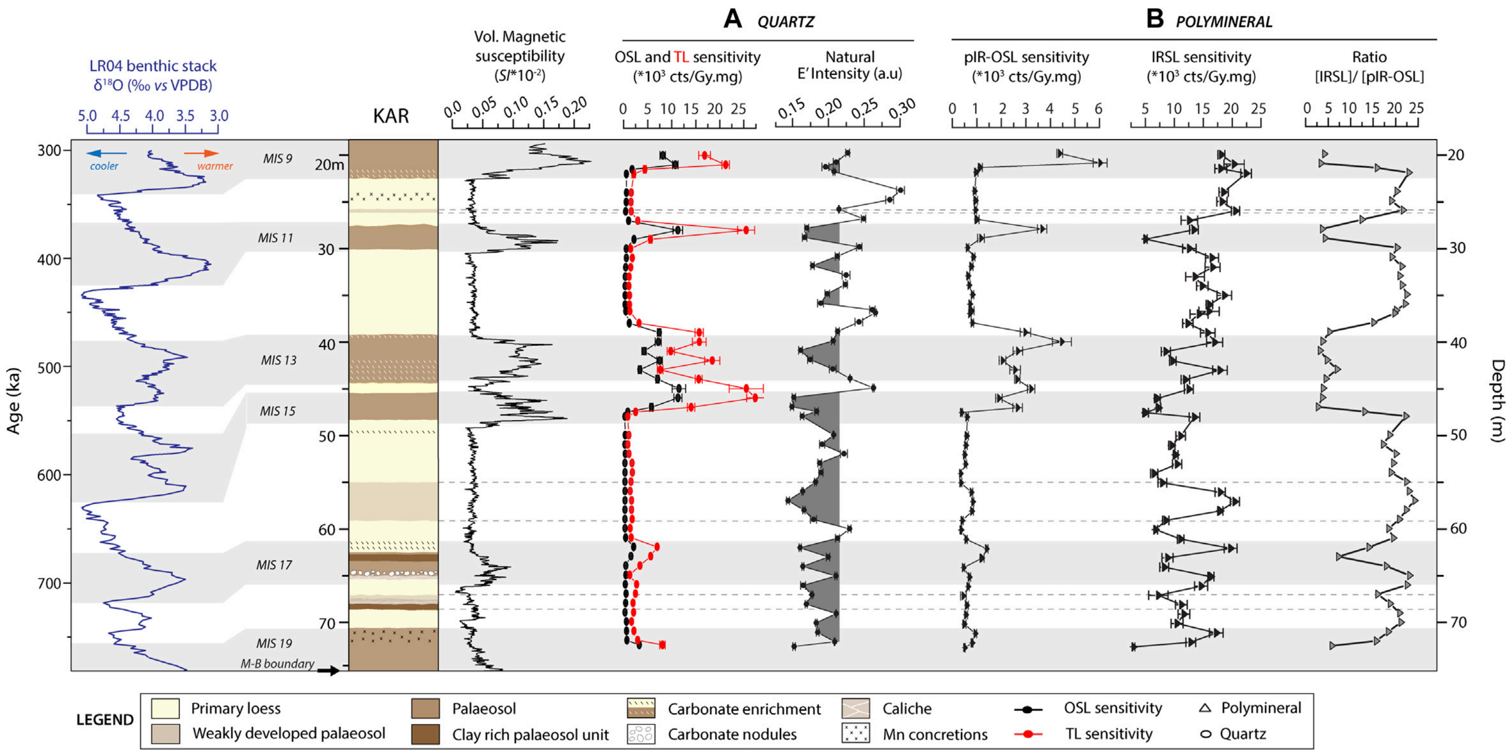

FIGURE 2 | Down-profile variations in **(A)** the sensitivity of the OSL and 110°C TL signal and the natural E_1' intensity from fine grain quartz and **(B)** the sensitivity of the pIR-OSL signal, the IRSL signal and the ratio of [IRSL]/[pIR-OSL] signal from fine grain polymineral samples for the KAR loess sequence. Stratigraphy of KAR and its correlation to the global benthic curve (Lisiecki and Raymo, 2005) is based on *in-situ* magnetic susceptibility measurements at the site (modified after Dave et al., 2022).

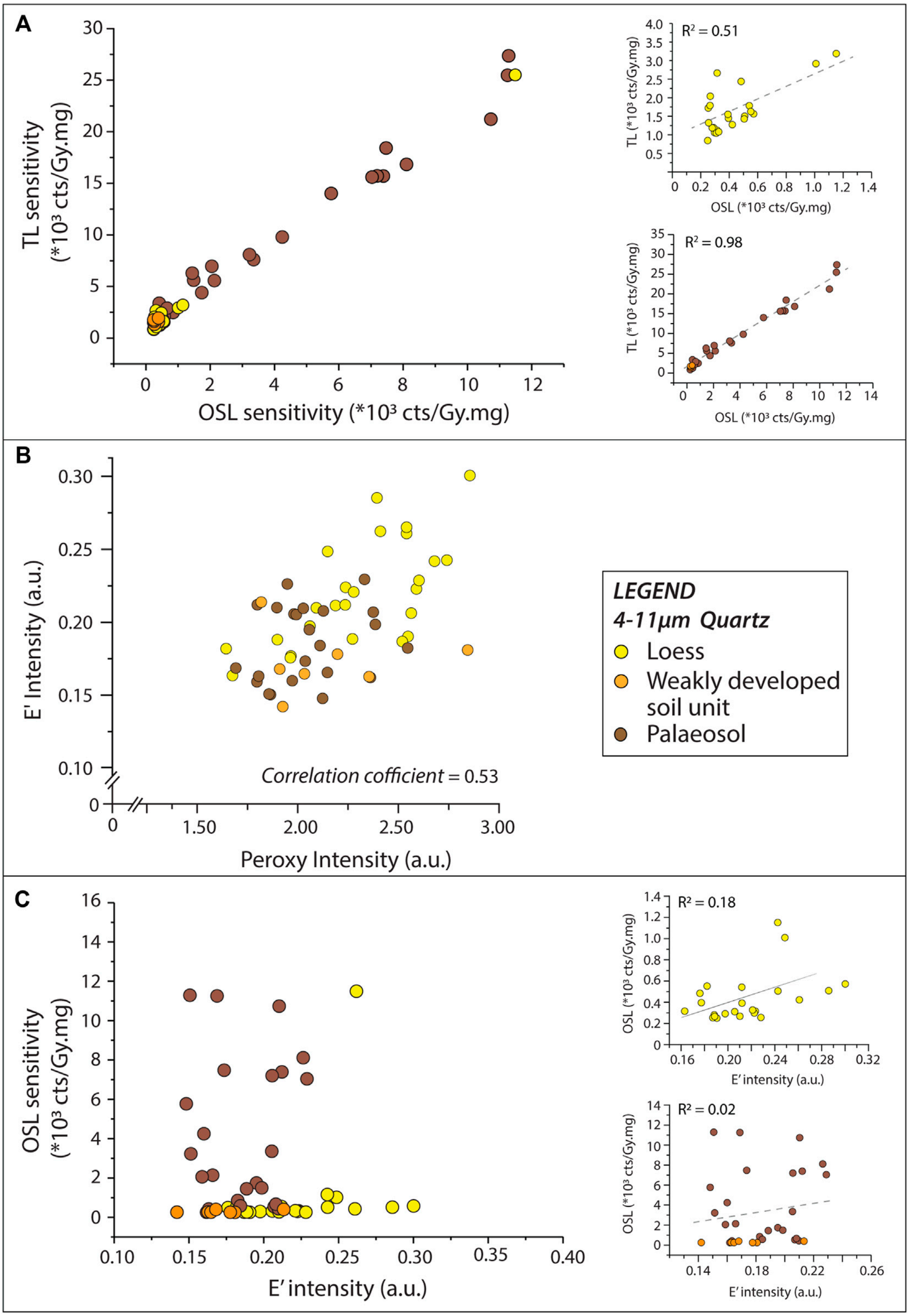

FIGURE 3 | (A) Plot comparing the sensitivity of OSL and 110°C TL signal from fine-grained quartz with respect to different stratigraphic units (loess, palaeosol, weakly developed soil) **(B)** Cross-plot of the E_1' and peroxy centre intensity from fine grain quartz with respect to stratigraphic units (modified from Dave et al., 2022) **(C)** Plot comparing E_1' intensity and sensitivity of the OSL signal from fine-grained quartz with respect to stratigraphic units. Note: The anomalous value of the loess sample (A0301, at depth c. 45 m), that occurs as an "outlier" in the main plots of **(A)** and **(C)**, is not plotted in the inset plots to avoid rescaling of the *y*-axis.

TABLE 1 | Protocol for luminescence sensitivity measurements from fine-grained quartz and polymineral samples (modified after Sawakuchi et al., 2018; Li and Zhou, 2021).

Step	Protocol for quartz
1	OSL 125°C, Blue LED 100 s at 5°C/s
2	β dose = 47.5 Gy
3	TL 240°C, 10 s at 5°C/s
4	IRSL 50°C, 50 s at 5°C/s
5	OSL 125°C, Blue LEDs for 100 s at 5°C/s
Step	**Protocol for polyminerals**
1	OSL 125°C for 100 s at 5°C/s
2	β irradiation, given dose = 47.5 Gy
3	Preheat at 240°C for 10 s
4	IRSL at 60°C for 300 s at 5°C/s
5	OSL (Blue LED) at 125°C for 100 s at 5°C/s

Luminescence Measurements

All samples were processed under subdued red-light conditions in dedicated laboratories at the Johannes Gutenberg University and Max Planck Institute for Chemistry in Mainz to extract fine-grained (4–11 µm) quartz and polymineral grains using published procedures (Frechen et al., 1996). Details of sample preparation, instrumentation and luminescence sensitivity measurements are given in the supplementary. The protocols for measurement of OSL and TL sensitivity of fine-grained quartz and the infrared stimulated luminescence (IRSL) and post infrared-optically stimulated luminescence (pIR-OSL) of polymineral grains are outlined in **Table 1**. Since luminescence sensitivity entails the measurement of luminescence emitted (counts, cts) per unit dose (Gy) per unit mass (mg), the luminescence measurements from all aliquots were normalised to the given laboratory dose and the corresponding aliquot mass. The sensitivity is expressed as cts/Gy.mg and uncertainties as 1σ standard deviation.

In addition, we conducted preliminary experiments to assess the effect of repeated laboratory- irradiation and bleaching cycles (80 cycles) on four fine-grained quartz samples from loess and soil units respectively. The protocol for these experiments is briefly described and outlined in **Supplementary Table S1** in the **Supplementary Materials S1**.

Electron Spin Resonance Measurements

ESR allows the measurement of paramagnetic (containing an unpaired electron) species in a material. In this study we focus on the natural intensity of two paramagnetic defect centres in fine-grained quartz from KAR: the E_1' centre and the peroxy centre. The measurement of these centres was carried out at Babeş-Bolyai-University in Cluj-Napoca and is reported in Dave et al. (2022). A summarised account of sample measurement procedures and parameters is presented in the **Supplementary Materials S1**.

RESULTS

Figure 2 illustrates the down-profile variations in luminescence sensitivity of the OSL and 110°C TL (hereon referred to as TL) signal and E_1' defect centre intensity from fine-grained quartz, and the pIR_{60}-OSL, IR_{60} (here 60°C refers to temperature of IRSL wash and is hereon referred to as pIR-OSL and IRSL respectively) and the ratio [IRSL]/[pIR-OSL] from polymineral fine grains. We observe that the quartz luminescence sensitivity of the TL and OSL signals is higher in the palaeosol horizons compared to primary loess units, and correlates with the variability in magnetic susceptibility (**Figure 2A**). In addition, **Figure 3A** shows the correlation between the 110°C TL and OSL signal, which is stronger in fine-grained quartz from soils as compared to that extracted from loess samples. This may be a result of either a difference in the inherent properties of quartz related to its origin and/or to the sensitisation of quartz during its sedimentary and depositional history. Jain et al. (2003) observed that not all components of the OSL signal in quartz sensitise in an identical manner, which implies that the degree of correlation between the 110°C TL and the different OSL components may vary between samples. Albeit at this stage, making a distinction between the sensitisation process of the different OSL components is not possible.

The ratio [IRSL]/[pIR-OSL] in polymineral grains has been proposed as a proxy for weathering intensity in loess-palaeosol sequences in the CLP (Wang and Miao, 2006). This ratio was proposed to indicate the relative enrichment of quartz in palaeosols due to weathering of feldspar minerals in these units. However, it must be noted that this is a "relative feldspar-content" driven interpretation and does not consider the inherent sensitivity of feldspar due to source change and/or its variation due to its sedimentary history. Our results on down-profile variability in the pIR-OSL and IRSL signal from polymineral fine-grains show that the pIR-OSL signal increases in soils and decreases in loess units while the IRSL signal does not show any apparent trend down the loess-palaeosol section (**Figure 2B**). Thus, the ratio [IRSL]/[pIR-OSL] from fine-grained polymineral samples at KAR shows a decrease within palaeosol horizons and an increase in loess horizons (**Figure 2B**), suggesting that in this case, the ratio is predominantly driven by the strong variation of the pIR-OSL signal from the quartz fraction as compared to the IRSL signal from the feldspar fraction in the polymineral.

Down-profile variation in the intensity of the natural E_1' signal of fine-grained quartz in general, indicates lower intensity in the palaeosol units and higher values in the primary loess horizons (**Figure 2A**). The variation in peroxy intensity of fine-grained quartz with depth correlates with the variations in natural E_1' values (**Supplementary Figure S2**) and hence, only the E_1' trend is shown in **Figure 2A**. Also, the variations in E_1' are more pronounced above c. 60 m depth. While, below c. 60 m (prior to MIS 16), the natural E_1' intensity is generally lower but fluctuates at a higher frequency and appears to be inconsistent with the observed stratigraphy of loess and soil units (**Figure 2A**). Nonetheless, the plot comparing natural E_1' and peroxy intensities in fine-grained quartz highlights the difference between loess and soil units (**Figure 3B**). Additionally, a brief look at **Figures 3A, B** suggests that the TL and OSL sensitivity is higher while the E_1' and peroxy intensity is lower in soils and vice versa for loess horizons. However, the comparison of the E_1'

intensity with the OSL sensitivity of fine-grained quartz in **Figure 3C** does not show any correlation. Thus, the fundamental relationship between E_1' intensity and OSL sensitivity of quartz as yet remains elusive (Poolton et al., 2000; Schilles et al., 2001).

DISCUSSION

Climate modelling studies and down-profile grain size variations in loess-palaeosol sequences in southern Tajikistan suggest stronger Westerly winds during glacial periods as compared to interglacials; thereby indicating dust transport from distal sources during glacial periods (Vandenberghe et al., 2006). Based on these studies, we suggest that the low natural E_1' intensities observed at KAR in the warmer, more humid soil units (interglacial conditions) is linked to proximal source signature. There are also phases within loess accumulating glacial stages, particularly during interstadial periods which oversaw weak pedogenesis, when E_1' intensity values were also low and which likewise indicate a net input of proximal source material (**Figure 2A**). At the same time, throughout the KAR profile, natural E_1' intensities, while variable, are relatively low, which suggests that proximal source sediments dominate the net background sediment contribution to the site throughout its depositional history. This observation is in tune with recent observations made by Li et al. (2019) that propose an increased likelihood of proximally sourced dust in loess deposits in the Tajik basin based on elemental geochemistry data from loess and modern meteorological analysis. Nevertheless, during glacial phases there is a stronger shift towards quartz with higher E_1' intensities (**Figure 2A**), particularly above c. 60 m depth. Below this depth the distinction between primary loess and palaeosols based on E_1' intensity is less pronounced. This is most likely due to the presence of multiple palaeosol horizons, low sedimentation rates, and compaction of the sediment, which may have contributed to over-printing of the quartz E_1' signature. Furthermore, the c. 60 m depth marker at KAR coincides with the end of the mid-Pleistocene transition (MPT; Clark et al., 2006), after which the Earth's climate shifted to lower-frequency (c. 100 kyr), higher-amplitude glacial-interglacial cycles. The MPT transition has been observed to manifest in other loess regions as more distinct loess-palaeosol oscillations with higher sedimentation rates (e.g., Fitzsimmons et al., 2012; Marković et al., 2015), which may explain the more distinct high E_1' intensity values within the glacial loess above c. 60 m at KAR.

The natural E_1' intensity values from fine-grained quartz add nuance to, and raises questions about, the interpretation derived from the OSL and TL sensitivity record at KAR. Within the primary loess and weak palaeosol layers accreted during the glacial and interstadial periods, OSL and TL sensitivity remains consistently low in relation to quartz from the more strongly developed interglacial palaeosols with high sensitivity values (**Figure 2A**). The net background input of proximally sourced material to the site, as proposed from the E_1' results, accounts for the comparatively constant sensitivity of the quartz OSL and TL signal observed in the loess units at KAR. However, it is unclear why the OSL and TL sensitivity shows minimal variation during loess accumulating glacial periods, which is unlike the variations shown by the E_1' signal. We hypothesise that the net OSL and TL sensitivity remains unaffected by the source shifts recorded by the E_1' during loess accumulating (glacial) stages because E_1' is a more sensitive proxy which measures a specific defect centre in quartz, whereas luminescence sensitivity is emitted from multiple traps as a result of recombination in both electron and hole centres (Aitken, 1998; Yukihara and McKeever, 2011). As a result, the proximal signal dominates the OSL and TL sensitivity values and masks more subtle changes due to input from a distal source.

It is likewise unclear what caused the increase in OSL and TL sensitivity observed during the formation of interglacial palaeosols. We propose this to be due to depositional and post-depositional processes associated with soil formation. Most of these processes may be linked to factors like the effect of dose rate from the surrounding sediment, repeated cycles of bleaching and irradiation during extended periods of soil formation and the possible effect of diagenesis during burial on the sensitivity of quartz. Of these factors, firstly, previous studies (e.g., Lü et al., 2014; Li and Zhou, 2021; Lü et al., 2021) demonstrate no correlation between the dose rate (i.e., ionising radiation received during burial) and OSL and TL sensitivity in long loess-palaeosol sequences and therefore, we suggest that downcore variability in dose rate is unlikely to explain the observed sensitivity changes. Secondly, it is well known that quartz is a stable mineral and least susceptible to *in-situ* weathering, however not much is known about the effect of diagenesis of quartz during burial on luminescence sensitivity. However, we envisage that these changes (if any) are likely to be insignificant over Quaternary timescales. This brings us to the role of repeated cycles of bleaching and irradiation associated with extended and intense periods of pedogenesis, aided by reduced sedimentation rates as the most likely factor contributing to enhanced sensitivity values observed in soil units. Since, the sensitisation of quartz via such a process is unlikely to be consistent, it would also explain the high degree of scatter observed in quartz OSL and TL sensitivity within the palaeosol horizons as compared to primary loess (**Figure 3A**). Our premise is also supported by the recent study from Li and Zhou (2021), who observed a three-fold increase in OSL sensitivity of fine-grained quartz from Tajik loess, after repeated laboratory induced irradiation and bleaching cycles. Additionally, our experiments based on limited (80 cycles) but repeated cycles of laboratory induced irradiation and bleaching in quartz from KAR loess, shows a 15–25% increase in OSL and TL sensitivity (**Supplementary Figure S3**), which further supports our hypothesis.

We also observe that the fine-grained quartz from the weakly developed soil units within the loess exhibits similar natural E_1' and peroxy characteristics to quartz from the well-developed palaeosol units (**Figure 3B**), suggesting a proximal source signature as observed during interglacial stages. However, the same quartz from weakly developed soils yields lower OSL and TL sensitivities similar to that observed in loess (**Figure 3A**). This agrees with our premise that repeated irradiation and bleaching cycles during soil formation aids the sensitisation of quartz, since quartz from weakly developed soils which represent weak pedogenesis under higher sedimentation rate are less likely to experience prolonged and repeated cycles of irradiation and bleaching post-deposition and therefore, do not exhibit increased sensitivity unlike the well-developed palaeosols.

At this stage, it must be noted from the work of previous studies that the inherent sensitivity of quartz as well as its preferential ability to sensitise (i.e., the degree and rate of sensitisation) related to its origin (Sharma, 2017; Sawakuchi et al., 2018; Bartyik et al., 2021; Li and Zhou, 2021) are crucial factors in dictating the OSL and TL sensitivity of quartz. Nonetheless, during formation of loess-palaeosol sequences, additional external factors like extended periods of irradiation and bleaching during pedogenesis aided by the low sedimentation rates during soil formation can lead to sensitisation of the OSL and TL signals in quartz. This post-depositional sensitisation of quartz in soil horizons can overprint the inherent luminescence sensitivity characteristics of the quartz.

CONCLUSION

This study utilises the natural E_1' and peroxy characteristics of quartz as a provenance indicator to assess the observed variations in luminescence (OSL and TL) sensitivity down a long loess-palaeosol sequence in Tajikistan. Previous studies link down-profile variations in luminescence sensitivity with climatic fluctuations that occur over glacial-interglacial timescales (Lü et al., 2014; Li and Zhou, 2021; Lü et al., 2021). However, the cause for the observed luminescence sensitivity variations in quartz is still debated (Lü et al., 2014; Li and Zhou, 2021; Lü et al., 2021). Our comparison of luminescence characteristics with E_1' and peroxy centres in quartz suggest that the high OSL and TL sensitivity in the soil horizons is likely to reflect sensitisation of quartz due to repeated irradiation and bleaching cycles during pedogenesis. At the same time, luminescence sensitivity variations that may have otherwise occurred due to changes in sediment source - for instance, as a result of input of some distal material at the loess site during glacial periods, is likely to be masked by the dominant input of proximally derived material. Nevertheless, the OSL and TL sensitivity of quartz from aeolian environments holds great potential for identifying spatial variability in luminescence characteristics between sites.

DATA AVAILABILITY STATEMENT

The raw data supporting the conclusion of this article will be made available by the authors, without undue reservation.

AUTHOR CONTRIBUTIONS

AD, AT-G and KF conceptualized the research. AD processed the samples, designed and performed the experiments, analysed the results and wrote the original draft of the manuscript. GS carried out the magnetic susceptibility measurements in the field. AD, KF, GS and NS carried out fieldwork and sample collection. All authors contributed to the manuscript revision and read and approved the submitted manuscript.

FUNDING

This research was supported by the Independent Max Planck Research grant awarded to KF. AT-G acknowledges the financial support of UEFISCDI PN-III-P4-ID-PCE-2020-0542 no 114/2021. We acknowledge open access publication support by Open Access Publishing Fund of the University of Tübingen, Germany.

ACKNOWLEDGMENTS

AD would like to thank the Luminescence Laboratory at the Max Planck Institute for Evolutionary Anthropology, Leipzig, Germany for access to the HF etching laboratory, and R Schiebel at the Max Planck Institute for Chemistry (MPIC) for access to a high precision mass balance. We would also like to thank our colleagues for their assistance during fieldwork: S Yusupov, A Safarov, ZN Nadjmudinov and RS Pavlatov (Tajik National University); C Prud'homme, A Engström Johansson, L Marquer, Z Perić, S de Graaf, M Notwatzki and K Reetz (MPIC).

SUPPLEMENTARY MATERIAL

The Supplementary Material for this article can be found online at: https://www.frontiersin.org/articles/10.3389/feart.2022.835281/full#supplementary-material

REFERENCES

Aitken, M. J. (1998). *An Introduction to Optical Dating: The Dating of Quaternary Sediments by the Use of Photon-Stimulated Luminescence*. Oxford: Oxford University Press.

Bartyik, T., Magyar, G., Filyó, D., Tóth, O., Blanka-Végi, V., Kiss, T., et al. (2021). Spatial Differences in the Luminescence Sensitivity of Quartz Extracted from Carpathian Basin Fluvial Sediments. *Quat. Geochronol.* 64, 101166. doi:10.1016/j.quageo.2021.101166

Buggle, B., Glaser, B., Zöller, L., Hambach, U., Marković, S., Glaser, I., et al. (2008). Geochemical Characterization and Origin of Southeastern and Eastern

European Loesses (Serbia, Romania, Ukraine). *Quat. Sci. Rev.* 27 (9), 1058–1075. doi:10.1016/j.quascirev.2008.01.018

Clark, P. U., Archer, D., Pollard, D., Blum, J. D., Rial, J. A., Brovkin, V., et al. (2006). The Middle Pleistocene Transition: Characteristics, Mechanisms, and Implications for Long-Term Changes in Atmospheric pCO2. *Quat. Sci. Rev.* 25 (23-24), 3150–3184. doi:10.1016/j.quascirev.2006.07.008

Dave, A. K., Timar-Gabor, A., Kabacińska, Z., Scardia, G., Safaraliev, N., Nigmatova, S., et al. (2022). A Novel Proxy for Tracking the Provenance of Dust Based on Paired E1'-Peroxy Paramagnetic Defect Centres in Fine-Grained Quartz. *Earth Space Sci. Open Archive*. [Preprint]. doi:10.1002/essoar.10510943.1

Ding, Z. L., Rutter, N. W., Sun, J. M., Yang, S. L., and Liu, T. S. (2000). Rearrangement of Atmospheric Circulation at about 2.6Ma over Northern China: Evidence from Grain Size Records of Loess-Palaeosol and Red Clay Sequences. *Quat. Sci. Rev.* 19 (6), 547–558. doi:10.1016/S0277-3791(99)00017-7

Dodonov, A. E., and Baiguzina, L. L. (1995). Loess Stratigraphy of Central Asia: Palaeoclimatic and Palaeoenvironmental Aspects. *Aeolian Sediments Quat. Rec.* 14 (7), 707–720. doi:10.1016/0277-3791(95)00054-2

Fenn, K., Stevens, T., Bird, A., Limonta, M., Rittner, M., Vermeesch, P., et al. (2018). Insights into the Provenance of the Chinese Loess Plateau from Joint Zircon U-Pb and Garnet Geochemical Analysis of Last Glacial Loess. *Quat. Res.* 89 (3), 645–659. doi:10.1017/qua.2017.86

Fitzsimmons, K. (2011). An Assessment of the Luminescence Sensitivity of Australian Quartz with Respect to Sediment History. *Geochronometria* 38 (3), 199–208. doi:10.2478/s13386-011-0030-9

Fitzsimmons, K. E., Rhodes, E. J., and Barrows, T. T. (2010). OSL Dating of Southeast Australian Quartz: A Preliminary Assessment of Luminescence Characteristics and Behaviour. *Quat. Geochronol.* 5 (2), 91–95. doi:10.1016/j.quageo.2009.02.009

Fitzsimmons, K. E., Marković, S. B., and Hambach, U. (2012). Pleistocene Environmental Dynamics Recorded in the Loess of the Middle and Lower Danube Basin. *Quat. Sci. Rev.* 41, 104–118. doi:10.1016/j.quascirev.2012.03.002

Forster, Th., and Heller, F. (1994). Loess Deposits from the Tajik Depression (Central Asia): Magnetic Properties and Paleoclimate. *Earth Planet. Sci. Lett.* 128 (3–4), 501–512. doi:10.1016/0012-821X(94)90166-X

Frechen, M., Schweitzer, U., and Zander, A. (1996). Improvements in Sample Preparation for the Fine Grain Technique. *Anc. TL* 14 (2), 15–17. Available at: http://ancienttl.org/ATL_14-2_1996/ATL_14-2_Frechen_p15-17.pdf.

Jain, M., Murray, A. S., and Bøtter-Jensen, L. (2003). Characterisation of Blue-Light Stimulated Luminescence Components in Different Quartz Samples: Implications for Dose Measurement. *Radiat. Meas.* 37 (4), 441–449. doi:10.1016/S1350-4487(03)00052-0

Jeong, G. Y., and Choi, J.-H. (2012). Variations in Quartz OSL Components with Lithology, Weathering and Transportation. *Quat. Geochronol.* 10, 320–326. doi:10.1016/j.quageo.2012.02.023

Kukla, G., Heller, F., Ming, L. X., Chun, X. T., Sheng, L. T., and Sheng, A. Z. (1988). Pleistocene Climates in China Dated by Magnetic Susceptibility. *Geol* 16 (9), 811–814. doi:10.1130/0091-7613(1988)016<0811:pcicdb>2.3.co;2

Li, Y., Song, Y., Kaskaoutis, D. G., Chen, X., Mamadjanov, Y., and Tan, L. (2019). Atmospheric Dust Dynamics in Southern Central Asia: Implications for Buildup of Tajikistan Loess Sediments. *Atmos. Res.* 229, 74–85. doi:10.1016/j.atmosres.2019.06.013

Li, Y., and Zhou, L. (2021). Variations of Thermally and Optically Stimulated Luminescence Sensitivity of Loess and Pedocomplex Samples from Southern Tajikistan, Central Asia. *Geochronometria* 48 (1), 242–252. doi:10.1515/geochr-2015-0118

Lisiecki, L. E., and Raymo, M. E. (2005). A Pliocene-Pleistocene Stack of 57 Globally Distributed Benthic δ18O Records. *Paleoceanography* 20 (1), a–n. doi:10.1029/2004PA001071

Liu, T. S. (1985). *Loess and Environment*. Beijing: China Ocean Press.

Lü, T., Sun, J., Li, S.-H., Gong, Z., and Xue, L. (2014). Vertical Variations of Luminescence Sensitivity of Quartz Grains from Loess/paleosol of Luochuan Section in the Central Chinese Loess Plateau since the Last Interglacial. *Quat. Geochronol.* 22, 107–115. doi:10.1016/j.quageo.2014.04.004

Lü, T., Sun, J., Feathers, J. K., and Sun, D. (2021). Spatiotemporal Variations and Implications of Luminescence Sensitivity of Quartz Grains on the Chinese Loess Plateau since the Last Interglaciation. *Quat. Res.* 99, 190–203. Cambridge Core. doi:10.1017/qua.2020.53

Lü, T., and Sun, J. (2011). Luminescence Sensitivities of Quartz Grains from Eolian Deposits in Northern China and Their Implications for Provenance. *Quat. Res.* 76 (2), 181–189. doi:10.1016/j.yqres.2011.06.015

Marković, S. B., Stevens, T., Kukla, G. J., Hambach, U., Fitzsimmons, K. E., Gibbard, P., et al. (2015). Danube Loess Stratigraphy - towards a Pan-European Loess Stratigraphic Model. *Earth-Science Rev.* 148, 228–258. doi:10.1016/j.earscirev.2015.06.005

McNab, F., Sloan, R. A., and Walker, R. T. (2019). Simultaneous Orthogonal Shortening in the Afghan-Tajik Depression. *Geology* 47 (9), 862–866. doi:10.1130/G46090.1

Muhs, D. R., Bettis, E. A., Aleinikoff, J. N., McGeehin, J. P., Beann, J., Skipp, G., et al. (2008). Origin and Paleoclimatic Significance of Late Quaternary Loess in Nebraska: Evidence from Stratigraphy, Chronology, Sedimentology, and Geochemistry. *Geol. Soc. Am. Bull.* 120 (11–12), 1378–1407. doi:10.1130/B26221.1

Nagashima, K., Tada, R., Tani, A., Toyoda, S., Sun, Y., and Isozaki, Y. (2007). Contribution of Aeolian Dust in Japan Sea Sediments Estimated from ESR Signal Intensity and Crystallinity of Quartz. *Geochem. Geophys. Geosyst.* 8 (2), a–n. doi:10.1029/2006GC001364

Nagashima, K., Nishido, H., Kayama, M., Kurosaki, Y., Ohgo, S., and Hasegawa, H. (2017). Composition of Asian Dust from Cathodoluminescence Spectral Analysis of Single Quartz Grains. *Geology* 45 (10), 879–882. doi:10.1130/G39237.1

Nagashima, K., Tada, R., Tani, A., Sun, Y., Isozaki, Y., Toyoda, S., et al. (2011). Millennial-scale Oscillations of the Westerly Jet Path during the Last Glacial Period. *J. Asian Earth Sci.* 40 (6), 1214–1220. doi:10.1016/j.jseaes.2010.08.010

Odom, A. L., and Rink, W. J. (1989). Natural Accumulation of Schottky-Frenkel Defects: Implications for a Quartz Geochronometer. *Geol* 17 (1), 55–58. doi:10.1130/0091-7613(1988)017<0055:naosfd>2.3.co;2

Pietsch, T. J., Olley, J. M., and Nanson, G. C. (2008). Fluvial Transport as a Natural Luminescence Sensitiser of Quartz. *Quat. Geochronol.* 3 (4), 365–376. doi:10.1016/j.quageo.2007.12.005

Poolton, N. R. J., Smith, G. M., Riedi, P. C., Bulur, E., Bøtter-Jensen, L., Murray, A. S., et al. (2000). Luminescence Sensitivity Changes in Natural Quartz Induced by High Temperature Annealing: A High Frequency EPR and OSL Study. *J. Phys. D. Appl. Phys.* 33 (8), 1007–1017. doi:10.1088/0022-3727/33/8/318

Rao, W., Yang, J., Chen, J., and Li, G. (2006). Sr-Nd Isotope Geochemistry of Eolian Dust of the Arid-Semiarid Areas in China: Implications for Loess Provenance and Monsoon Evolution. *Sci. Bull.* 51 (12), 1401–1412. doi:10.1007/s11434-006-2008-1

Sawakuchi, A. O., Blair, M. W., DeWitt, R., Faleiros, F. M., Hyppolito, T., and Guedes, C. C. F. (2011). Thermal History versus Sedimentary History: OSL Sensitivity of Quartz Grains Extracted from Rocks and Sediments. *Quat. Geochronol.* 6 (2), 261–272. doi:10.1016/j.quageo.2010.11.002

Sawakuchi, A. O., Guedes, C. C. F., DeWitt, R., Giannini, P. C. F., Blair, M. W., Nascimento, D. R., et al. (2012). Quartz OSL Sensitivity as a Proxy for Storm Activity on the Southern Brazilian Coast during the Late Holocene. *Quat. Geochronol.* 13, 92–102. doi:10.1016/j.quageo.2012.07.002

Sawakuchi, A. O., Jain, M., Mineli, T. D., Nogueira, L., Bertassoli, D. J., Häggi, C., et al. (2018). Luminescence of Quartz and Feldspar Fingerprints Provenance and Correlates with the Source Area Denudation in the Amazon River Basin. *Earth Planet. Sci. Lett.* 492, 152–162. doi:10.1016/j.epsl.2018.04.006

Schaetzl, R. J., Bettis, E. A., Crouvi, O., Fitzsimmons, K. E., Grimley, D. A., Hambach, U., et al. (2018). May)Approaches and Challenges to the Study of Loess—Introduction to the LoessFest Special Issue. *Quat. Res.* 89, 563–618. doi:10.1017/qua.2018.15

Schilles, T., Poolton, N. R. J., Bulur, E., Bøtter-Jensen, L., Murray, A. S., Smith, G. M., et al. (2001). A Multi-Spectroscopic Study of Luminescence Sensitivity Changes in Natural Quartz Induced by High-Temperature Annealing. *J. Phys. D. Appl. Phys.* 34 (5), 722–731. doi:10.1088/0022-3727/34/5/310

Sharma, S. K. (2017). Understanding the Reasons for Variations in Luminescence Sensitivity of Natural Quartz Using Spectroscopic and Chemical Studies. *Proc. Indian Natl. Sci. Acad.* 92 (0), 9024. doi:10.16943/ptinsa/2017/49024

Shimada, A., Takada, M., and Toyoda, S. (2013). Characteristics of ESR Signals and TLCLs of Quartz Included in Various Source Rocks and Sediments in Japan: A Clue to Sediment Provenance. *Geochronometria* 40 (4), 334–340. doi:10.2478/s13386-013-0111-z

Smith, J., Vance, D., Kemp, R. A., Archer, C., Toms, P., King, M., et al. (2003). Isotopic Constraints on the Source of Argentinian Loess – with Implications for

Atmospheric Circulation and the Provenance of Antarctic Dust during Recent Glacial Maxima. *Earth Planet. Sci. Lett.* 212 (1), 181–196. doi:10.1016/s0012-821x(03)00260-7

Stevens, T., Palk, C., Carter, A., Lu, H., and Clift, P. D. (2010). Assessing the Provenance of Loess and Desert Sediments in Northern China Using U-Pb Dating and Morphology of Detrital Zircons. *Geol. Soc. Am. Bull.* 122 (7–8), 1331–1344. doi:10.1130/B30102.1

Sun, J. (2002). Provenance of Loess Material and Formation of Loess Deposits on the Chinese Loess Plateau. *Earth Planet. Sci. Lett.* 203 (3), 845–859. doi:10.1016/S0012-821X(02)00921-4

Sun, Y., Tada, R., Chen, J., Chen, H., Toyoda, S., Tani, A., et al. (2007). Distinguishing the Sources of Asian Dust Based on Electron Spin Resonance Signal Intensity and Crystallinity of Quartz. *Atmos. Environ.* 41 (38), 8537–8548. doi:10.1016/j.atmosenv.2007.07.014

Sun, Y., Tada, R., Chen, J., Liu, Q., Toyoda, S., Tani, A., et al. (2008). Tracing the Provenance of Fine-Grained Dust Deposited on the Central Chinese Loess Plateau. *Geophys. Res. Lett.* 35 (1), L01804. doi:10.1029/2007GL031672

Tissoux, H., Voinchet, P., Lacquement, F., and Despriée, F. (2015). ESR as a Method for the Characterization of Alluvial Sediments. *Radiat. Meas.* 81, 2–8. doi:10.1016/j.radmeas.2015.05.010

Toyoda, S., and Hattori, W. (2000). Formation and Decay of the E1′ Center and of its Precursor. *Appl. Radiat. Isotopes* 52 (5), 1351–1356. doi:10.1016/S0969-8043(00)00094-4

Toyoda, S., Nagashima, K., and Yamamoto, Y. (2016). ESR Signals in Quartz: Applications to Provenance Research - A Review. *Quat. Int.* 397, 258–266. doi:10.1016/j.quaint.2015.05.048

Tsukamoto, S., Nagashima, K., Murray, A. S., and Tada, R. (2011). Variations in OSL Components from Quartz from Japan Sea Sediments and the Possibility of Reconstructing Provenance. *Quat. Int.* 234 (1), 182–189. doi:10.1016/j.quaint.2010.09.003

Újvári, G., Varga, A., Ramos, F. C., Kovács, J., Németh, T., and Stevens, T. (2012). Evaluating the Use of Clay Mineralogy, Sr-Nd Isotopes and Zircon U-Pb Ages in Tracking Dust Provenance: An Example from Loess of the Carpathian Basin. *Chem. Geol.* 304-305, 83–96. doi:10.1016/j.chemgeo.2012.02.007

Vandenberghe, J., Renssen, H., van Huissteden, K., Nugteren, G., Konert, M., Lu, H., et al. (2006). Penetration of Atlantic Westerly Winds into Central and East Asia. *Quat. Sci. Rev.* 25 (17), 2380–2389. doi:10.1016/j.quascirev.2006.02.017

Wang, K., Tada, R., Zheng, H., Irino, T., Zhou, B., and Saito, K. (2020). Provenance Changes in Fine Detrital Quartz in the Inner Shelf Sediments of the East China Sea Associated with Shifts in the East Asian Summer Monsoon Front during the Last 6 Kyrs. *Prog. Earth Planet Sci.* 7 (1), 5. doi:10.1186/s40645-019-0319-5

Wang, X., and Miao, X. (2006). Weathering History Indicated by the Luminescence Emissions in Chinese Loess and Paleosol. *Quat. Sci. Rev.* 25 (13), 1719–1726. doi:10.1016/j.quascirev.2005.11.009

Wei, C., Yin, G., Li, Y., Liu, C., Li, W., and Guo, R. (2020). Quartz Electron Spin Resonance Signal Intensity of Al and Ti-Li Centers as a Provenance Indicator: An Example from the Yangtze River Basin. *Quat. Int.* 562, 76–84. doi:10.1016/j.quaint.2020.06.023

Weltje, G. J., and von Eynatten, H. (2004). Quantitative Provenance Analysis of Sediments: Review and Outlook. *Sediment. Geol.* 171 (1), 1–11. doi:10.1016/j.sedgeo.2004.05.007

Yukihara, E. G., and McKeever, S. W. S. (2011). *Optically Stimulated Luminescence: Fundamentals and Applications.* John Wiley & Sons. doi:10.1002/9780470977064

Zheng, C. X., Zhou, L. P., and Qin, J. T. (2009). Difference in Luminescence Sensitivity of Coarse-Grained Quartz from Deserts of Northern China. *Radiat. Meas.* 44 (5), 534–537. doi:10.1016/j.radmeas.2009.02.013

Zular, A., Sawakuchi, A. O., Guedes, C. C. F., and Giannini, P. C. F. (2015). Attaining Provenance Proxies from OSL and TL Sensitivities: Coupling with Grain Size and Heavy Minerals Data from Southern Brazilian Coastal Sediments. *Radiat. Meas.* 81, 39–45. doi:10.1016/j.radmeas.2015.04.010

Conflict of Interest: The authors declare that the research was conducted in the absence of any commercial or financial relationships that could be construed as a potential conflict of interest.

Publisher's Note: All claims expressed in this article are solely those of the authors and do not necessarily represent those of their affiliated organizations, or those of the publisher, the editors and the reviewers. Any product that may be evaluated in this article, or claim that may be made by its manufacturer, is not guaranteed or endorsed by the publisher.

Copyright © 2022 Dave, Timar-Gabor, Scardia, Safaraliev and Fitzsimmons. This is an open-access article distributed under the terms of the Creative Commons Attribution License (CC BY). The use, distribution or reproduction in other forums is permitted, provided the original author(s) and the copyright owner(s) are credited and that the original publication in this journal is cited, in accordance with accepted academic practice. No use, distribution or reproduction is permitted which does not comply with these terms.

frontiers | Frontiers in Earth Science

ORIGINAL RESEARCH
published: 03 June 2022
doi: 10.3389/feart.2022.818338

Dune Field Patterns and Their Control Factors in the Middle Areas of China's Hexi Corridor Desert

*Yan Zhang and Zhengcai Zhang**

Key Laboratory of Desert and Desertification, Northwest Institute of Eco-environment and Resources, Chinese Academy of Sciences, Lanzhou, China

The middle areas of China's Hexi Corridor Desert are distributed within or at the edge of oases in continental river basins in Northern China. Recently, researchers found that rivers can provide sediment material for dune formation and development, but the mechanism has not been investigated in detail. In this study, the relationships among the wind environment, spatial distribution of continental rivers, sand availability, and dune field patterns in the middle area of Hexi Corridor Desert were analyzed. In terms of the wind energy environment, the study area can be divided into three regions: high-energy environment in the north, intermediate-energy environment in the middle, and low-energy environment in the south. The results showed that the resultant drift potential is predominantly from the NW quadrant. The directional variability of wind is intermediate in the northern and middle region and low in the southern region. The directions of winds with critical speed are SW in the northern region, NW and WNW in the middle region, and NW in the southern region. The main dune types are barchans, reticulate dunes, star dunes, linear dunes, and coppice dunes, which differ from previous results (mainly barchans and coppice dunes). Dune field patterns are controlled by the wind energy environment. In addition, the spatial distribution of continental rivers and sand availability are important factors affecting dune formation and development. Sand dunes are distributed downwind of continental rivers, which confirms the hypothesis that rivers can provide sediment material for dune formation. The spatial distribution and different dune types in the middle area of Hexi Corridor Desert reveal that their formation and development are controlled by the wind regime and sediment supply.

Keywords: Hexi corridor, desert, wind energy environment, dune patterns, factor

OPEN ACCESS

Edited by:
Zhuolun Li,
Lanzhou University, China

Reviewed by:
Jiyan Li,
Taiyuan Normal University, China
Shipei Dong,
Lanzhou University, China
Ping Lu,
Shaanxi Normal University, China

****Correspondence:***
Zhengcai Zhang
zhangzhsi@sina.com

Specialty section:
This article was submitted to Quaternary Science, Geomorphology and Paleoenvironment, a section of the journal Frontiers in Earth Science

Received: *19 November 2021*
Accepted: *25 April 2022*
Published: *03 June 2022*

Citation:
Zhang Y and Zhang Z (2022) Dune Field Patterns and Their Control Factors in the Middle Areas of China's Hexi Corridor Desert.
Front. Earth Sci. 10:818338.
doi: 10.3389/feart.2022.818338

INTRODUCTION

The wind regime, sediment supply, and surface characteristics (vegetation and topography) of a region are the main factors controlling dune formation and development in the region (Hack, 1941; Thomas, 1997; Zhang et al., 2015a; Lü et al., 2018). In particular, the formation of aeolian geomorphology is driven by energy from wind, which also guides subsequent development. Therefore, wind regime and wind energy environment have both been widely used in studies of aeolian geomorphology, including the classification of this geomorphology (Melton, 1940; Fedorovich, 1948; Wu, 1987; Lancaster, 1995; Thomas, 1997). For example, a narrow unimodal wind regime creates transverse dunes, a bimodal wind regime creates linear dunes, and a complex

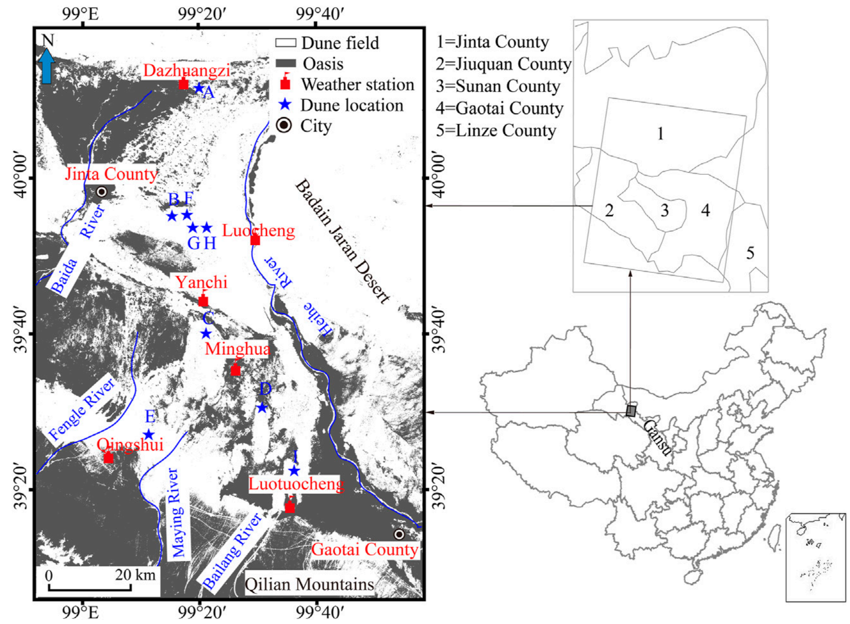

FIGURE 1 | Locations of the six weather stations in the present study and location of the study region.

wind regime creates star dunes (Fryberger and Dean, 1979). Fryberger and Dean studied the wind regime and wind energy environments associated with several classic dune types (crescent, linear, and star dunes), and found that the ratio of the resultant drift potential to the drift potential (*RDP*/*DP*) tended to decrease from crescent dunes to star dunes. For crescent and linear dunes, both wind energy and *RDP*/*DP* were high. Other researchers have confirmed that the wind regime is strongly related to the dune types that form in a given environment (Wasson and Hyde, 1983; Lancaster, 1994; Livingstone and Warren, 1996). Specifically, persistent winds control dune formation and development, but strong winds control dune orientation (Fitzsimmons et al., 2020).

The formation and development of dunes are undoubtedly affected by sediment supply, geometry of the sediment source and deposition areas, and size of the dune field, but these factors have not been extensively investigated (Beveridge et al., 2006; Ewing et al., 2006; Derickson et al., 2008; Ewing and Kocurek, 2010a, Ewing and Kocurek, 2010b). Lü et al. (2018) suggested that sediment availability has an important effect on dune types and dune formation and development. Recently, aeolian–fluvial interactions in dryland environments have been widely studied worldwide (Bullard and McTainsh, 2003; Nottebaum et al., 2015; Yan et al., 2015; Han et al., 2016; Liu and Coulthard, 2017). However, such interactions in the arid and semiarid region of northwestern China have rarely been studied (Yan et al., 2015; Han et al., 2016). Yan et al. (2015) and Zhang et al. (2021) investigated the interactions between deserts and large rivers in Northern China and confirmed the hypothesis of Bullard and McTainsh (2003), which states that rivers can provide sediment material for dune formation and development. Nevertheless, they also noted that the relationship between smaller rivers and dunes require further investigation.

Surface characteristics, such as vegetation and geomorphology, also control the types, formation, and development processes of dunes. The formation of almost all linear dunes and nebkhas is determined by the presence of an obstacle (Livingstone and Warren, 1996). Nevertheless, different sand dune types can occur in a region with different wind directions (Zhang and Dong, 2015; Lü et al., 2018).

Within the Hexi Corridor in Northern China, desert areas occur in the middle and western parts of Gansu Province (**Figure 1**). These areas have received little attention owing to their small coverage (approximately 1,100 km^2) compared with other Chinese deserts. To fill in some of the missing data, this study investigated the wind energy environment and dune field patterns in these desert areas. To this end, variations of the wind energy environment, sand dune patterns, and controlling factors of dune geomorphology were analyzed. The objectives of the research are as follows: 1) assessing the effect of the wind energy environment on dune pattern variations; 2) considering the implications of sediment supply on dune pattern variations; 3) determining the relationship between continental rivers and sand dunes; 4) comparing the results of this study with those of previous studies in the Hexi Corridor Desert.

MATERIALS AND METHODS

Study Region

The middle area of Hexi Corridor is located in the temperate zone hungriness taken in the middle latitudes of the northern hemisphere, with arid climate and little rainfall (40–410 mm)

TABLE 1 | Weather conditions of Gaotai and Jinta.

Location	Wind speed (m s^{-1})	Air humidity (%)	Air temperature (°C)	Precipitation (mm)
Gaitai	1.8	52	7.9	103.2
Jinta	2.4	43	8.5	60.5

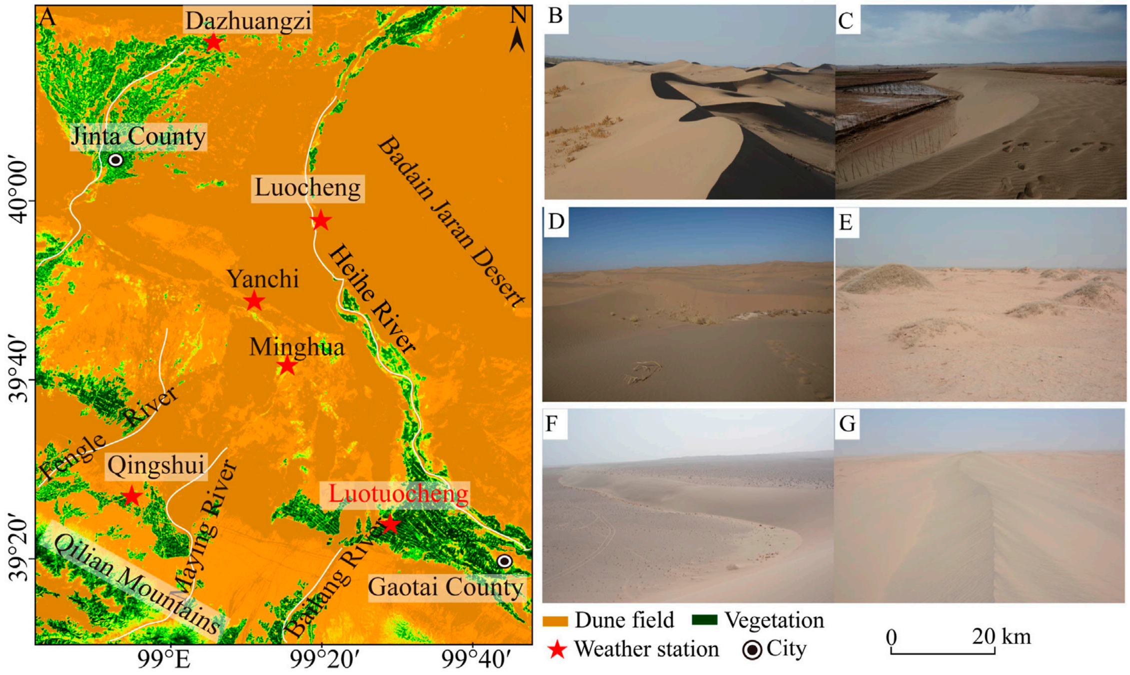

FIGURE 2 | (A) Spatial distribution of vegetation cover (based on NDVI values). **(B)** and **(C)** crescent dunes and chains; **(D)** reticulate dunes; **(E)** coppice dunes; **(F)** raked linear dunes; **(G)** reversing linear dunes.

and large annual evaporation (1,500–3,311 mm) (Jia, 2012; Luo et al., 2021). The region's weather is affected by the cold front in the winter seasons, with frequent windy days, and the wind direction is mainly northwest wind, west wind, and southwest wind. In the summer seasons, it is influenced by the monsoon, and the wind speed is low and the east wind increases (Guo, 2015). Also, the region's weather is characterized by the same period of wind and drought. The study area is sparsely distributed at the edges of the middle and lower reaches of a continental river basin. The study area includes two large continental rivers: the middle reaches of the Heihe River and the lower reaches of the Baida River. From east to west, three small continental rivers run through the study area: the Bailang River, Maying River, and Fengle River. The middle areas of the Hexi Corridor lie between the Baida River and Heihe River and in the lower reaches of the Bailang, Maying, and Fengle rivers. In the lower reaches of these rivers, large amounts of alluvial sediments are deposited, serving as the source areas of sediments for downwind dune formation and development (Nottebaum et al., 2015, **Figure 1**). Nottebaum et al. (2015) suggested that sand material in the middle area of the Hexi Corridor Desert was derived from the Qilian Mountains and transported by hydrological processes. However, Zhang et al. (2021) suggested that eolian sediments in the middle area of Hexi Corridor Desert were derived from the Qilian Mountains in the southwest and the Beishan Mountains in the north. Upwind sediment sources control dune formation and development in the middle area of the Hexi Corridor Desert. Barchans that formed on the Gobi surface move at an average rate of 8–53 m year^{-1}, and their movement is related to their width (Zhang et al., 2018). Sand grains in this area are mainly very fine sand and fine sand (Zhang and Dong, 2015).

Dunes are mainly distributed in two regions. The first is in the western part of the Jinta County and the lower reaches of the Baida River. This dune area covers approximately 40 km from north to south and 10–20 km from west to east, with a total area of approximately 650 km^2. The main dunes were reported to be coppice dunes (Wu, 2009). The second area is in the northwestern part of the Gaotai County, along the middle reaches of the Heihe River. This dune area covers approximately 10–30 km from north to south and 75 km from west to east, with a total area of 450 km^2 (Li, 1998). The main dune types are crescent dunes, crescent dune sheets, and sand sheets (Wu, 2009). The weather conditions of the Gaotai and Jinta are shown in **Table 1**.

Vegetation cover influences the development of dune fields and sand seas. **Figure 2** shows the vegetation cover in the study region in 2010. The vegetation cover is denser near and in the lower reaches of the rivers, with values of the normalized-difference vegetation index (*NDVI*) usually larger than 0.3; in some areas, the *NDVI* is between 0 and 0.1. The land surface is mainly covered by the Gobi (gravel), and dune fields (with *NDVI* < 0) are discontinuously distributed between rivers and in the northeastern part of the study area.

METHODS

We used automatic weather station data (wind speeds), HJ-1A/B remote-sensing images, and Google Earth high-resolution images to investigate the wind energy environment, wind regimes, and eolian dune geomorphology of the study area. Using these data, we examined the relationships between dune types and wind characteristics to extract information on the regional sand environment.

Wind data were obtained from six automatic weather stations in the study area: Dazhuangzi, Luocheng, Yanchi, Luotuocheng, Minghua, and Qingshui (**Figure 1**). Wind speed data were acquired at 1-h intervals in 2010, which is the earliest year for which wind data were recorded at these stations. At each station, wind speed and direction sensors were installed in a clear area at a height of 10 m above the land surface. We calculated the following parameters of the wind energy environment using Fryberger and Dean's (1979) method: drift potential (*DP*, in vector units), resultant drift potential (*RDP*), and resultant drift direction (*RDD*, which represents the direction of sand transportation) and directional variability (*RDP*/*DP*).

$$DP = u^2 (u - u_t)t, \tag{1}$$

$$RDD = Arctan(C/D), \tag{2}$$

$$C = \mathrm{Sum}(\mathrm{VU})\sin(\theta), \tag{3}$$

$$D = \mathrm{Sum}(\mathrm{VU})\cos(\theta), \tag{4}$$

$$RDP = \left(C^2 + D^2\right)^{1/2}, \tag{5}$$

where u is the wind velocity, in knots; u_t is the threshold wind velocity (the velocity required to entrain the sediment), in knots; t is the proportion of time during which the wind velocity is greater than the threshold velocity required to entrain the sediment; θ is the angle measured clockwise from 0° (north); and VU is the drift potential in each orientation class. u_t in the study region was estimated to be 12 knots under dry conditions (Fryberger and Dean, 1979), and the mean sediment size is approximately 0.22 mm. Accordingly, the threshold wind velocity was also set as 12 knots.

Livingstone and Warren (1996) classified dune field patterns as transverse dunes, linear dunes, and star dunes. In our study region, the patterns also included crescent dunes and chains, coppice dunes, and sand sheets (Cook et al., 1993). For the desert and oases boundary were not our main research aims, we used HJ-1A/B remote-sensing images with 30 m spatial resolution obtained from the China Center for Resources Satellite Data and Applications (http://www.cresda.com/n16/n92006/n92162/index.html). Data analysis methods were similar to those used by Han et al. (2015).

We determined dune crest orientations through visual interpretation and manual tracking using Google Earth high-resolution images with 1.5 m spatial resolution. The images were extracted using ArcGIS software (Esri, Redlands, CA, United States). We have enlarged every satellite image at a scale of 1:250 before drawing the dune's contour by hand. The detailed methods can be found in the study by Zhang et al. (2018).

An expectation-maximization (EM) algorithm was applied to fit the distribution of dune and wind orientation using a Gaussian mixture model (Lü et al., 2014). We assumed that the probability distribution function of critical wind and dune orientation may be described by a sum of normal distributions:

$$\mathcal{P}(\theta) = \sum_{i=1}^{n_\theta} \frac{wi}{\sigma_i \sqrt{2\pi}} \exp\left(-\frac{(\theta - \theta_i)^2}{2\sigma_i^2}\right), \tag{6}$$

where θ_i is the mean wind or dune orientation; w_i is the weight of wind or dune orientation in the θ_i direction; σ_i is the standard deviation of wind or dune orientation in the θ_i direction. Using the wind data set, the dune crest orientation was determined following the gross bedform-normal transport rule (Rubin and Hunter, 1987). According to this rule, dune orientation can be predicted using the transport ratio between primary and secondary winds and the angle between primary and secondary winds, as shown in **Eq. 7**.

$$\mathrm{Tan}\alpha = \pm \frac{R + |\cos\gamma|}{|\sin\gamma|}, \tag{7}$$

where α is the angle between primary wind and dune crest orientation; R is the transport ratio between primary and secondary winds ($R = w_2/w_1$, in this $w_2 > w_1$); and γ is the angle between primary and secondary winds.

In this study, we calculated sediment availability with the t/P' ratio, where t is the percentage of the time when the wind is above the threshold velocity for sediment entrainment and P' is the effective precipitation. Effective precipitation is expressed as P/Etp, where P is the precipitation and Etp is the potential evapotranspiration.

RESULTS

Wind Regime

The wind regimes in Chinese deserts are controlled by high-pressure systems and large-scale geomorphology (Wang et al., 2005). In the middle areas of China's Hexi Corridor Desert, winds associated with the Mongolia–Siberia high-pressure system occur in late spring and early summer, dominantly in the NW, W, and SW directions (Dong et al., 1993; Wang et al., 2005; Zhang et al., 2016).

Considering that only winds above the threshold wind speed (u_t) are important for dune formation, we focused on the proportion of winds above this threshold. Wind data from the

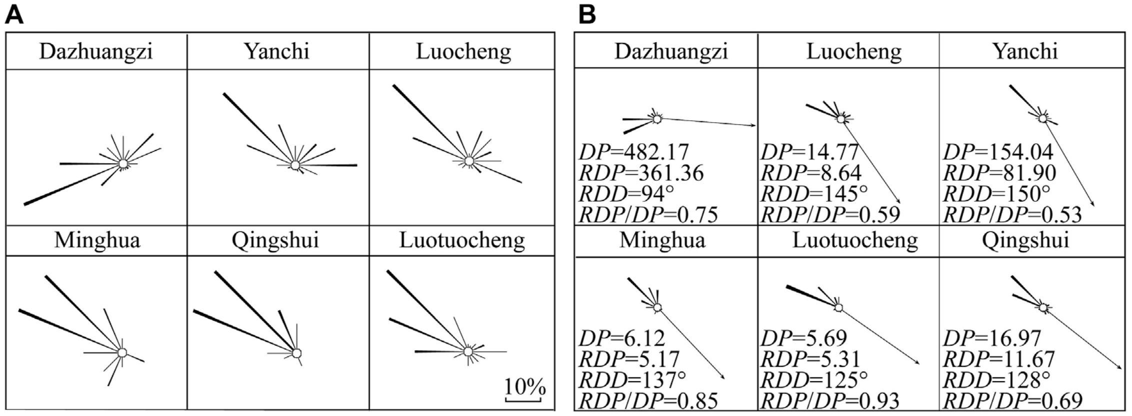

FIGURE 3 | (A) Critical wind directions (with wind speeds above the threshold wind velocity required to entrain sediment). **(B)** Annual wind energy environments.

TABLE 2 | Wind speed and wind energy environments at the six stations in 2010. *M*s, mean speed, m s^{-1}; *M*ws, maximum wind speed, m s^{-1}; *DP*, drift potential, VU; *RDP*, resultant drift potential, VU; *RDD*, resultant drift direction, °; *RDP/DP*, directional variability.

Station	Dazhuangzi	Luocheng	Yanchi	Minghua	Luotuocheng	Qingshui
*M*s	3.95	2.05	3.07	1.87	1.49	2.25
*M*ws	18.4	17.4	20.5	13.4	15.8	18.5
DP	482.17	14.77	154.04	6.12	5.69	16.97
RDP	361.36	8.64	81.90	5.17	5.31	11.67
RDD	94	145	150	137	125	128
RDP/DP	0.75	0.59	0.53	0.85	0.93	0.69

six weather stations are summarized in **Figure 3**. In the study region, the directions of winds exceeding the threshold were generally bimodal, except Luocheng, but the primary and secondary wind directions varied in different parts of the study region (**Figure 3A**).

The threshold wind direction can be divided to three categories: Dazhuangzi, Yanchi, and Luocheng and Minghua, Qingshui, and Luotuocheng. At Dazhuangzi, the primary wind direction was WSW (27.2% of the annual time) and the secondary direction was W (15.6%). At Yanchi and Luocheng, the primary threshold wind direction was from NW (25.7% and 25.8%, respectively of the time) and the secondary direction was from WNW at Yanchi (14.8%) and E at Luocheng (15.2%). At Minghua, Qingshui and Luotuocheng, the primary threshold wind direction was from NW (28.5–34.2%), and the secondary direction was from WNW (21.5–32.9%).

The wind speed and wind energy environments at the six weather stations in 2010 are summarized in **Table 2**. The mean wind speeds were the highest in the west (3.95 m s^{-1} at Dazhuangzi) and lowest in the east (1.49 m s^{-1} at Luotuocheng), with the highest maximum wind speed in the middle of the region (20.5 m s^{-1} at Yanchi) and the lowest maximum in the south (13.4 m s^{-1} at Minghua).

Wind Energy Environment

Fryberger and Dean's (1979) parameters of the wind energy environment can be used to identify areas with high (*DP* > 400) and low (*DP* < 200) wind energy in 2010 (**Table 2**; **Figure 3B**). According to their criteria, high wind energy occurred in the north (Dazhuyangzi) and low wind energy occurred in the middle and south of the region (Luocheng, Yanchi, Minghua, Luotuocheng, and Qingshui). This indicated that potential sand transport was larger in the north region than in the middle and south.

RDD ranged from 274 to 330° and could be divided into three regions: in the north, *RDD* was about 274° at Dazhuangzi; in the middle of the region (at Luocheng, Yanchi, and Minghua), *RDD* is between 317 and 330°; and in the south (Luotuocheng and Qingshui), *RDD* is between 305 and 308°. These results showed that sand transport directions were from northwest to southeast, and sand dunes moved to the southeast.

RDP/*DP* ranged from 0.53 to 0.93, indicating intermediate (Dazhuangzi, Luocheng, Yanchi, and Qingshui) and low (Minghua and Luotuocheng) directional variability. *RDP*/*DP* was the highest in the southeast and lowest in the middle of the study area.

Figures 4, **5** shows the monthly wind energy environment at the six stations. *DP* reached its maximum in April for most stations, except Dazhuangzi in December, when the *RDD* was SE (**Table 3**). The *RDD* was SE for almost all stations. The directional variability (*RDP*/*DP*) was generally low to intermediate.

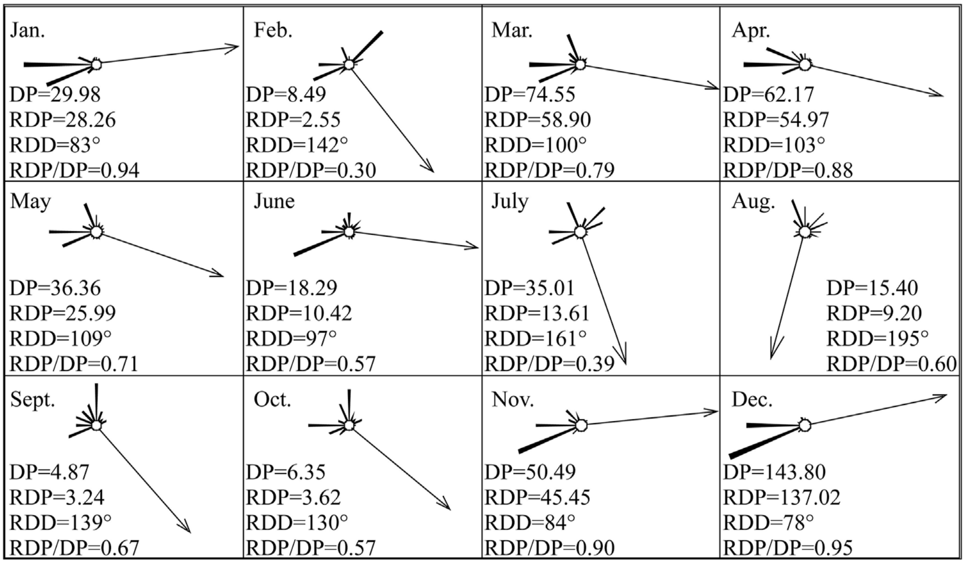

FIGURE 4 | Monthly wind energy environment at Dazhuangzi; other sites shown in **Supplementary Figures S1–S5**.

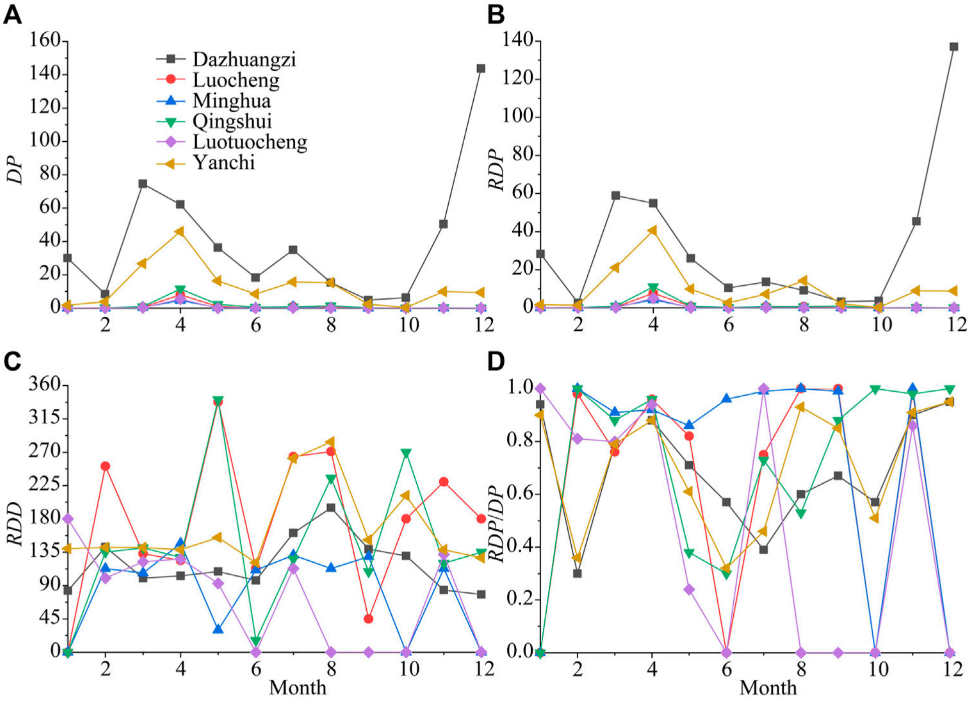

FIGURE 5 | Monthly wind energy environment in the study region. **(A)** DP, drift potential, VU; **(B)** RDP, resultant drift potential, VU; **(C)** RDD, resultant drift direction, °; **(D)** RDP/DP, directional variability.

Dune Field Patterns

According to a previous study, the main dune patterns in the study area are crescent dunes, coppice dunes, and sand sheets (Wu, 2009). In the present study, we used HJ-1A/B remote-sensing images, field investigation data, and Google Earth high-resolution images to identify the dune field patterns. Dunes in this desert include crescent dunes, coppice dunes, reticulate dunes, linear dunes, star dunes, and so on. Reticulate dunes are also known as "dune networks," "dune reticules," "*aklés*," "rhombic waffle patterns," or "alveolar dunes" (Cook et al., 1993). They

TABLE 3 | Monthly wind energy environment characteristics at the six stations. DZZ, Dazhuangzi; LC, Luocheng; YC, Yanchi; MH, Minghua; LTC, Luotuocheng; QS, Qingshui; T-max, maximum *DP* time; Period, total *DP* = 0 months; C, complicated.

Stations	DP		DP = 0	RDD	RDP/DP
	T-max	*RDD*	Period		
DZZ	December	ENE	0	S	Intermediate
LC	April	SE	4	C	6 months low; 6 months intermediate
YC	April	SE	0	SSE	6 months low; 6 months intermediate
MH	April	SE	3	S	low
LTC	April	SE	5	SE	6 months low; 1 month high
QS	April	SE	1	SSE	7 months low; 4 months intermediate

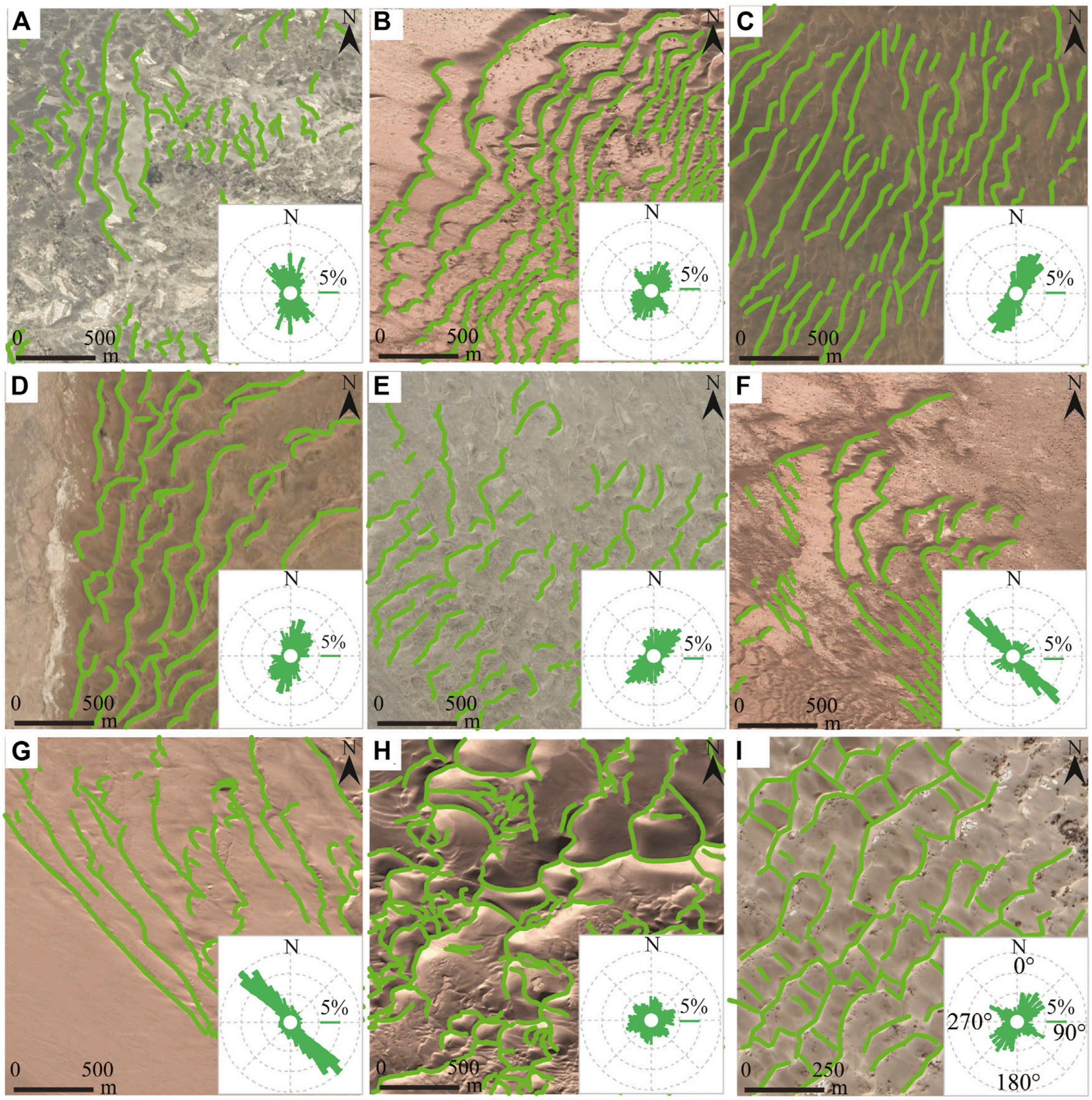

FIGURE 6 | Dune field patterns and dune orientation rose plots at nine locations in the study area. **(A)** Crescent and coppice dunes; **(B)** crescent dunes and chains; **(C)** crescent chains; **(D)** crescent dunes and chains; **(E)** crescent dunes and chains; **(F)** crescent chains and linear dunes; **(G)** linear dunes; **(H)** star dunes; **(I)** reticulate dunes.

TABLE 4 | Dune orientation statistics at nine locations in the study area. A, crescent and coppice dunes; B, crescent dunes and chains; C, crescent chains; D, crescent dunes and chains; E, crescent dunes and chains; F, crescent chains and linear dunes; G, linear dunes; H, star dunes; I, reticulate dunes. *N* is the analyzed dunes number. Locations are shown in **Figure 1**.

Dune fields	Dune orientation					
	Primary (°)	Percentage (%)	Secondary (°)	Percentage (%)	Tertiary (°)	Percentage (%)
A (*N* = 624)	123–176	50	2–57	44	—	—
B (*N* = 511)	2–91	68	127–177	30	—	—
C (*N* = 411)	2–66	85	—	—	—	—
D (*N* = 448)	2–90	79	148–177	19	—	—
E (*N* = 634)	1–77	74	143–177	20	—	—
F (*N* = 348)	118–168	68	2–63	21	—	—
G (*N* = 449)	128–177	81	—	—	—	—
H (*N* = 730)	47–107	41	123–173	24	2–38	18
I (*N* = 358)	8–72	62	113–143	22	—	—

develop under a wind regime with a bidirectional wind regime where the dominant wind directions are perpendicular (Cook et al., 1993; Livingstone and Warren, 1996; Hasi et al., 1999; Ewing et al., 2006; Zhang et al., 2015) and are characterized by network patterns (Zhang et al., 2015b, Zhang et al., 2015c). Crescent dunes and chains develop under a unidirectional wind regime or a bidirectional wind regime with dominant winds in opposite directions. Linear dunes develop under bidirectional wind regimes with winds that were not oriented in opposite directions. Star dunes develop under complex wind regimes. **Figure 6** shows the main patterns in the study region. The dune patterns included crescent dunes and chains (**Figures 6A–E**), linear dunes (**Figures 6F,G**), star dunes (**Figure 6H**), and reticulate dunes (**Figure 6I**), coppice dunes (**Figure 6A**), and sand sheets (**Figure 6E**). Reticulate and crescent dunes were distributed in most parts of the study region, whereas star and linear dunes were uncommon and found mostly in the eastern and northeastern parts of the study area.

Crescent dunes are mainly distributed at the edges of the desert or in areas with low vegetation cover (**Figure 6A**). Coppice dunes are mainly distributed near oases, with some interspersed with crescent dunes (**Figure 6A**). Linear dunes are mainly distributed in the middle part of the study region, usually at the edges of dune fields (**Figures 6F,G**). Star dunes are uncommon and distributed in the east of the Jinta County and north of the Gaotai County (**Figures 6D,H**). Reticulate dunes are relatively common and mostly distributed in the north of the Gaotai County (**Figure 6I**).

The middle area of Hexi Corridor Desert has a wide range of dune crest orientations (0°–180°) (**Table 4**; **Figure 6**). Nevertheless, the dune crest orientations are mainly NE–SW, followed by NW–SE. Moreover, the dune crest orientations in the Hexi Corridor Desert are spatially heterogeneous. In dune fields A, C, D, E, and G, dune crest orientation is unidirectional, with mean orientations of 176°, 26°, 22°, 25°, and 155°, respectively (**Table 5**). In dune fields B, F, and I, dune crest orientations are bidirectional, with mean primary (secondary) orientations of 44° (158°), 140° (47°), and 41° (128°), respectively. Dune field H has three orientations, with mean orientations of 78° (primary), 154° (secondary), and 16° (tertiary).

DISCUSSION

Wind Regime and Sand Dunes

The wind regime is a very important factor for dune formation and development. In this study, we used wind data from only 1 year (2010) to analyze the relationships between dune types and wind regime because detailed weather station data of the study region before 2010 are lacking. Moreover, detailed weather stations are difficult to acquire and not freely available. We used wind velocity and direction data from 2010 to analyze dune evolution, mainly because wind velocity in Jinta and Gaotai counties has been relatively larger in the recent 28 years (**Figure 7**). We believe that these data are representative of the wind climatology for linking with dune types. At present, a number of interpretative simplifications and assumptions are applied in the estimation of the wind energy environment (Bullard et al., 1996; Bullard, 1997), such as acquired wind data time-scale (Zhang et al., 2016), wind direction section range, and wind velocity classification values (Pearce and Walker, 2005). However, the wind energy environment is widely used for studying sand dune classification and formation (Bullard et al., 1996; Al-Awadhia et al., 2005; Wang et al., 2005; Saqqa and Saqqa, 2007; Hereher, 2010).

Spatial variations in the wind regime and sand supply can lead to the formation of different dune patterns. Crescent dunes are mainly distributed at the upwind edge of dune fields but with different crest orientations in different regions. Here, we focus on crescent dunes in the southeast of Dazhuangzi (**Figure 6A**), the west of Luocheng (**Figure 6B**), and the northeast of Qingshui (**Figure 6E**).

Southeast of Dazhuangzi (**Figure 6A**), the crest orientation (longest extension) was between 175° and 200° and the dunes moved ESE (85–110°). The calculated *RDD* was 94° (i.e., E), indicating similarities between the actual and predicted dune movement directions. In this region, the primary wind direction changes between SW and NW due to which the southwestern wings of some crescent dunes were elongated, forming

TABLE 5 | Results of the Gaussian mixture model fitting the dune crest and wind orientation distribution and the real and predicted values of dune crest orientation. (H* is a star-shaped dune with three directions of crest orientation and the tertiary direction of w_3, θ_3 and σ_3 are 0.19,16, and 10, respectively). DZZ, Dazhuangzi; LC, Luocheng; YC, Yanchi; MH, Minghua; LTC, Luotuocheng; QS, Qingshui. D, Dune orientation. Locations shown in **Figure 1**.

	w_1	θ_1 (°)	σ_1 (°)	w_2	θ_2 (°)	σ_2 (°)	D (°)
A/DZZ	0.52/0.71	150/275	17/36	0.48/0.29	27/54	22/29	176/173
C/YC	0.88/0.57	32/308	19/21	0.12/0.43	170/83	8/39	26/28
D/MH	0.8/0.81	39/308	26/19	0.2/0.19	162/180	11/72	22/18
E/QS	0.79/0.77	41/302	25/22	0.21/0.23	161/102	13/38	25/27
I/LTC	0.65/0.95	41/309	21/22	0.35/0.05	128/131	23/89	41/39
B	0.7	43	26	0.3	151	15	44
F	0.7	141	12	0.3	47	26	140
G	0.82	145	12	0.18	39	32	155
H*	0.55	78	29	0.26	154	18	78
LC	0.46	95	34	0.54	289	33	12

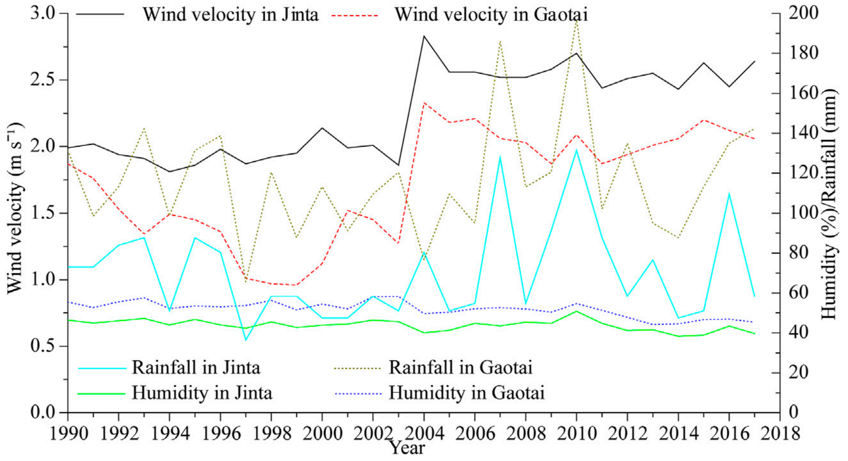

FIGURE 7 | Annual wind velocity in the Jinta and Gaotai County from 1990 to 2017.

asymmetrical crescent dunes. West of Luocheng (**Figure 6B**), the dune crest orientation is between 195° and 213°, and the dunes move SE (105–123°). The predicted *RDD* was 145°, indicating differences between the actual and predicted dune movement directions. In this region, the primary wind direction changes between SW and NW due to which the southwestern wings of some crescent dunes were elongated, forming asymmetrical crescent dunes. Northeast of Qingshui (**Figure 6E**), at the edge of the dune field, there were some single crescent dunes, but the inner dune field was dominated by crescent dunes and dune chains due to changes in the sediment supply. Specifically, sediment supply increased from the edge to the inner part of the dune field. In this region, dune crest orientation also changed from the upwind edge (between 166 and 210°) to the downwind edge (about 225°) of the dune field, and the dunes move ENE or ESE (76–120°) at the upwind edge of the dune field and SE (135°) at the downwind edge, but the calculated *RDD* was 128°.

The dune spacing of the crescent dunes decreases from 220 m in the northwest (with a maximum of 344 m) to 40 m in the southeast. Linear dunes are mainly distributed northwest of Luocheng and formed by the merger of crescent dunes (**Figures 6F,G**). In this region, dune spacing ranges from 36 to 81 m (**Figure 6F**) and from 124 to 156 m (**Figure 6G**). The dune crest orientation ranges between 145° and 161°, but the calculated *RDD* was between 145 and 150°. Star dunes are mainly distributed northwest of Luocheng (**Figure 6H**) and east of Minghua (**Figure 6I**). In this region, star dunes are common, with spacing between 161 and 540 m. Reticulate dunes are widely distributed in the middle and southern parts of the study region (**Figure 6I**). The primary crest orientation ranges between 201° and 226°, but it is mostly around 215°; the secondary crest orientation ranges between 114° and 153°, but it is mostly around 114°. The dune spacing is approximately 70 m between primary crests and approximately 40 m between secondary crests.

Spatial variations in wind direction can lead to different dune patterns. Changes in wind direction may cause crescent dunes to evolve into linear dunes or into reticulate and star dunes. In the desert area of Jinta County, dune patterns include crescent dunes (**Figures 2B,C**), reticulate dunes (**Figure 2D**), coppice dunes (**Figure 2E**), and linear dunes (comprising raked linear dunes and reversing linear dunes (**Figures 2F,G**). According to wind data from the two nearest meteorological stations (Yanchi and Luocheng), wind directions in this region are NW, SE, and NE. The critical wind direction from the NW quadrant (270° ≤ wind direction ≤360°) in Yanchi and Luocheng is 53 and 56%, respectively, and from the NE quadrant (22.5° ≤ wind direction ≤90°) is 26 and 36%, respectively. Crescent dunes and linear dunes are formed under the NW wind direction, whereas linear dunes are mainly distributed in the upwind edge of the dune areas. This implies that these two dune types formed under the same wind regimes (**Figure 2** Yanchi and Luocheng). The coexistence of barchan dunes and linear dunes was also found in a previous study, and the linear dunes are mainly caused by the asymmetry of sand sources in the upwind (Lü et al., 2018; Zhang et al., 2018). Reticulate dunes are distributed in the downwind of the dune areas and formed under NW and NE wind directions (**Figure 2** Yanchi and Luocheng). In this region, the movement direction of linear dunes was reversed by the action of ES winds (**Figure 2** Luocheng) and reversing linear dunes formed (**Figure 2G**).

In the northwestern part of the desert area of Gaotai County, dune patterns are mainly crescent dunes (**Figures 6C–E**) and reticulate dunes (**Figure 6I**). According to wind data from three meteorological stations (Minghua, Qingshui, and Luotuocheng), the wind direction in this region is mainly NW. Qingshui and Luotuocheng receive little wind from the SW quadrant, promoting the formation of reticulate dunes.

Using wind speed data from meteorological stations, the dune crest orientations were predicted according to the gross bedform-normal transport rule and compared with the dune crest orientation of the nearest dune field determined based on visual interpretation and manual tracking. Regarding the dominant dune crest orientation of dune fields, A, C, D, E, and I, the actual values (176°, 26°, 22°, 25°, and 41°) corresponded well to the predicted values (173°, 28°, 18°, 27°, and 39°) with an angular deviation of 3 ± 1°. Dune fields A, C, D, E, and I are consistent with Rubin and Hunters' theory. In contrast, dune fields B, F, G, and H did not exhibit such correspondence. This suggests that wind direction is the main factor controlling dune crest alignment in dune fields A, C, D, E, and I. Moreover, other factors such as degree of surface relief and sand availability influence dune development in dune fields B, F, G, and H. These areas feature many tall sand hills, which can change the near-surface airflow field, such as the formation of helical vortices, resulting in a deviation of the dune crest orientation from the gross bedform-normal transport rule.

We reanalyzed *DP* and mean annual wind velocity given by Zhang et al. (2015b), and found that *DP* is directly related to mean wind velocity ($DP = 3.92u_{\mathrm{mean}}^{3.39}$, $R^2 = 0.87$, $p < 0.05$, Zhang et al., 2015b). Therefore, we calculated *DP* in Jinta and Gaotai with annual mean wind velocity and found that the wind environment corresponded to a low-energy environment (DP < 200) in the recent 28 years. Nevertheless, *DP* in Jinta was larger than that in Gaotai (about 1–11 times). The higher *DP* at the upwind of the study region is conducive to the transport of erodible sediment to the downwind region, supporting the formation of sand dunes. Accordingly, the downwind region includes larger areas of sand dunes than the upwind region (**Figure 1**).

Sand Availability and Sand Dunes

Aeolian geomorphology reflects the complex external environment within which dune patterns develop, and the key factors responsible for their formation and evolution include the local wind regime, wind energy, sediment supply, source and deposition area geometry, areal limits (deposition area), and antecedent environmental conditions (Ewing and Kocurek, 2010a, Ewing and Kocurek, 2010b; Kocurek et al., 2010; Lü et al., 2018).

Aeolian sediment supply includes sediments with a sufficiently small grain size that can be transported by wind. The generation of aeolian sediment supply involves the accumulation of fluvial, alluvial, lacustrine, or coastal sediments, which may subsequently undergo deflation by wind (Kocurek and Lancaster, 1999). Sediment supply, sediment availability, and transport capacity correspond to the basin-scale sediment state of aeolian dune fields and sand seas (Kocurek and Lancaster, 1999). In sediment supply, the actual transport rate is used as a proxy for sediment availability, and the potential transport rate is used as a measure of the transport capacity of wind (Kocurek and Lancaster, 1999). Although this parameter is difficult to quantify, the dune mobility index is widely used as a measure of sediment mobility (e.g., Muhs and Maat, 1993; Bullard et al., 1997). For this calculation, we used data from 1980 to 2010 obtained from the meteorological stations in each part of the study area (**Figure 1**). The dune mobility index reached its maximum value in the northern part of the study region (10.19), followed by the middle part (4.92). In contrast, the minimum value (0.19) was observed in the southern part. This phenomenon indicated that dunes formed easily in the north than south.

In the arid regions, rivers are very important for the formation and development of aeolian dunes and sand sea distribution (Bullard and McTainsh, 2003; Yan et al., 2015). Rivers can not only serve as an index of sand sediment supply and sand availability, but they also affect the spatial distribution of aeolian dunes patterns. For instance, rivers can limit the downwind expansion of dune fields, particularly in wide parts of rivers. One such example is the north (Luocheng) and south (Luotuocheng). In the north, sediment materials are not transported across the river, but farther south, where the river is relatively narrow, they are transported across the river.

Crescent dunes form in areas with relatively low sediment availability, under a unimodal wind regime (Cook et al., 1993). Under the same wind conditions, several factors, such as sediment supply, dune formation age, and climate change, could affect variations in dune types. For the same dune formation age under the same wind regime, sediment supply is the key factor because sediment supply increases during the evolution from crescent dunes to reticulate and star dunes. However, under different dune formation ages, climate could be the key factor, such as in the study region (**Figures 6G,H**). **Figure 6H** shows high star dunes, which lie adjacent to linear dunes (**Figure 6G**). At the edges of oases and upwind of dune fields, the limited sediment supply and unimodal wind regime lead to the formation of crescent dunes (**Figures 2**; **Figures 6A,B**). With increasing distance downwind of the upwind edge of oases, the sediment supply increases and the dune field pattern changes to reticular dunes and a few star dunes (**Figures 6H,I**), as is the case southeast of Jinta County. Northwest of Luocheng, small linear dunes formed due to changes in wind direction and the limited sediment supply. The primary wind direction in Dazhuangzi is SW, but it changes to NW in Luocheng. As a result, the southwestern wings of crescent dunes eventually elongate to become linear dunes (**Figures 2F, 6G**), as Bagnold (1941) hypothesized.

Dune field patterns have been described using many classification systems, such as those by Melton (1940), Bagnold (1941), Fedorovich (1948), McKee (1979), Wu (1987), Cook et al. (1993), Lancaster (1995), Livingstone and Warren (1996), and Thomas (1997). However, no consensus has been reached on the nomenclature of dune patterns. For example, reticulate and star dunes are considered to be different patterns in the Fedorovich (1948) and Cooke et al. (1993) classification systems, whereas McKee (1979), Lancaster (1995), and Thomas (1997) do not include reticulate dunes. Furthermore, Livingstone and Warren (1996) consider reticulate dunes and star dunes to be the same pattern, and Wu (1987) suggested that reticulate dunes are part of the group of transverse dunes, whereas star dunes form under multidirectional wind directions. All these disputes are caused by reticulate dunes located in remote regions. In our study region, there are many reticulate dunes, and based on the local wind regime and sediment supply characteristics, reticulate dunes should belong to the category of star dunes. This is supported by the fact that reticulate dunes are frequently distributed in the same locations as the star dunes, and in some areas, linkages between two or more large reticulate dunes resemble star dunes. This suggests that reticulate dunes belong to the group of star dunes.

CONCLUSION

In this study, we analyzed the wind regime, wind energy environment, and dune patterns in the middle areas of China's Hexi Corridor Desert. The results provide information on regional aeolian geomorphology and wind energy environment in a part of northern China that has rarely been studied. The main conclusions are as follows:

In the middle area of Hexi Corridor Desert, the dune patterns include crescent, reticulate, coppice, star, and linear dunes, and sand sheets. In particular, reticulate dunes are distributed in the same areas as star dunes, suggesting that reticulate dunes belong to the group of star dunes.

The region's wind energy environment ranges from high to low, with the energy decreasing from NW to SE. The *RDD* is from NW to SE, but there are some differences within the region. The directional variability is low to intermediate and increases from north to south.

Dune crest orientations were calculated according to the gross bedform-normal transport rule. The predicted dominant orientation showed good correspondence with the actual orientation.

The middle areas of Hexi Corridor Desert lie between the middle and lower reaches of two large continental rivers. Along with these rivers, other rivers in the region provide large amounts of alluvial source materials. Therefore, sand dune types in the middle area of Hexi Corridor Desert are controlled by the wind regime, and the spatial distributions of sand coverage are controlled by the spatial distribution of rivers.

Although our study demonstrated that the types and spatial distributions of sand dunes are controlled by the wind regime and sediment supply, the development and migration of dunes require further investigation. It is noteworthy that we analyzed data from only 1 year because wind regime data are not freely available and difficult to obtain. Therefore, additional monitoring will be required to determine whether these results are representative of long-term patterns.

DATA AVAILABILITY STATEMENT

The raw data supporting the conclusion of this article will be made available by the authors, without undue reservation.

AUTHOR CONTRIBUTIONS

All authors listed have made a substantial, direct, and intellectual contribution to the work and approved it for publication.

ACKNOWLEDGMENTS

We gratefully acknowledge funding from the National Natural Science Foundation of China (Nos. 41971014 and 41771011). We are also indebted to the China Center for Resources Satellite Data and Applications, which provided the HJ-1A/B images.

SUPPLEMENTARY MATERIAL

The Supplementary Material for this article can be found online at: https://www.frontiersin.org/articles/10.3389/feart.2022.818338/full#supplementary-material

REFERENCES

Al-Awadhi, J. M., Al-Helal, A., and Al-Enezi, A. (2005). Sand Drift Potential in the Desert of Kuwait. *J. Arid Environ.* 63, 425–438. doi:10.1016/j.jaridenv.2005.03.011

Bagnold, R. A. (1941). *The Physics of Blown Sand and Desert Dunes*. London: Methuen.

Beveridge, C., Kocurek, G., Ewing, R. C., Lancaster, N., Morthekai, P., Singhvi, A. K., et al. (2006). Development of Spatially Diverse and Complex Dune-Field Patterns: Gran Desierto Dune Field, Sonora, Mexico. *Sedimentology* 53, 1391–1409. doi:10.1111/j.1365-3091.2006.00814.x

Bullard, J. E. (1997). A Note on the Use of the "Fryberger Method" for Evaluating Potential Sand Transport by Wind. *J. Sediment. Res.* 67, 499–501. doi:10.1306/d42685a9-2b26-11d7-8648000102c1865d

Bullard, J. E., and McTainsh, G. H. (2003). Aeolian-fluvial Interactions in Dryland Environments: Examples, Concepts and Australia Case Studyfluvial Interactions in Dryland Environments: Examples, Concepts, and Australia Case Study. *Prog. Phys. Geogr. Earth Environ.* 27, 471–501. doi:10.1191/0309133303pp386ra

Bullard, J. E., Thomas, D. S. G., Livingstone, I., and Wiggs, G. F. S. (1996). Wind Energy Variations in the Southwestern Kalahari Desert and Implications for Linear Dunefield Activity. *Earth Surf. Process. Landforms* 21, 263–278. doi:10.1002/(sici)1096-9837(199603)21:3<263::aid-esp627>3.0.co;2-i

Bullard, J. E., Thomas, D. S. G., Livingstone, I., and Wiggs, G. S. F. (1997). Dunefield Activity and Interactions with Climatic Variability in the Southwest Kalahari Desert. *Earth Surf. Process. Landforms* 22, 165–174. doi:10.1002/(sici)1096-9837(199702)22:2<165::aid-esp687>3.0.co;2-9

Cook, R., Warren, A., and Goudie, A. (1993). *Desert Geomorphology*. London: UCL.

Derickson, D., Kocurek, G., Ewing, R. C., and Bristow, C. (2008). Origin of a Complex and Spatially Diverse Dune-Field Pattern, Algodones, Southeastern California. *Geomorphology* 99, 186–204. doi:10.1016/j.geomorph.2007.10.016

Dong, G. R., Li, B. S., and Wen, X. (1993). "Aeolian Landforms in China," in *Features and Evolution of Landforms in China*. Editor J. Yang (Beijing: China Ocean Press), 149–172.

Ewing, R. C., and Kocurek, G. (2010b). Aeolian Dune Interactions and Dune-Field Pattern Formation: White Sands Dune Field, New Mexico. *Sedimentology* 57, 1199–1219. doi:10.1111/j.1365-3091.2009.01143.x

Ewing, R. C., and Kocurek, G. (2010a). Aeolian Dune-Field Pattern Boundary Conditions. *Geomorphology* 114 (3), 175–187. doi:10.1016/j.geomorph.2009.06.015

Ewing, R. C., Kocurek, G., and Lake, L. W. (2006). Pattern Analysis of Dune-Field Parametersfield Parameters. *Earth Surf. Process. Landforms* 31, 1176–1191. doi:10.1002/esp.1312

Fedorovich, B. A. (1948). The Relief of Asian Sands as a Reflection of Atmospheric Circulation Processes. *Probl. Fiz. Geogr.* 6 (13), 91–109.

Fitzsimmons, K. E., Nowatzki, M. N., Dave, A. K., and HartwigHarder, H. (2020). Intersections between Wind Regimes, Topography and Sediment Supply: Perspectives from Aeolian Landforms in Central Asia. *Palaeogeogr. Palaeoclimatol. Palaeoecol.* 540 (15), 109531. doi:10.1016/j.palaeo.2019.109531

Fryberger, S. G., and Dean, G. (1979). "Dune Forms and Wind Regime," in *A Study of Global Sand Seas*. Editor E. D. McKee (Washington, D.C. Professional Paper: USGS).

Guo, X. L. (2015). *Study on Wind Speed Variation Characteristics and Influencing Factors in Hexi Region in Recent 40 Years*. Lanzhou: Lanzhou Jiaotong University.

Hack, J. T. (1941). Dunes of the Western Navajo Country. *Geogr. Rev.* 31, 240–263. doi:10.2307/210206

Han, G., Zhang, G., You, L., Wang, Y., Yang, L., Yang, J., et al. (2016). Deflated Rims along the Xiangshui River on the Xiliaohe Plain, Northeast China: A Case of Active Fluvial-Aeolian Interactionsflated Rims along the Xiangshui River on the Xiliaohe Plain, Northeast China: A Case of Active FLuvial–Aeolian Interactions. *Geomorphology* 257, 47–56. doi:10.1016/j.geomorph.2015.12.025

Han, L., Zhang, Z., Zhang, Q., and Wan, X. (2015). Desertification Assessments in the Hexi Corridor of Northern China's Gansu Province by Remote Sensing. *Nat. Hazards* 75, 2715–2731. doi:10.1007/s11069-014-1457-0

Hasi, E., Dong, G. R., and Wang, G. Y. (1999). Morphodynamic study of reticulate dunes at Southeastern fringe of the Tengger Desert. *Science. China Series D: Earth Science.* 42 (02), 207–215. doi:10.1007/BF02878520

Hereher, M. E. (2018). Geomorphology and Drift Potential of Major Aeolian Sand Deposits in Egypt. *Geomorphology* 304, 113–120. doi:10.1016/j.geomorph.2017.12.041

Hereher, M. E. (2010). Sand Movement Patterns in the Western Desert of Egypt: an Environmental Concern. *Environ. Earth Sci.* 59, 1119–1127. doi:10.1007/s12665-009-0102-9

ITT (2008). *ITT Corporation ENVI 4.4 Software, 1133*. Avenue, White Plains, NY, USA: LLC.

Jia, W. X. (2012). Temporal and Spatial Changes of Precipitation in Qilian Mountain and Hexi Corridor during 1960-2009[J]. *Acta Geogr. Sin.* 67 (5), 631–644. doi:10.11821/xb201205006

Kocurek, G., Ewing, R. C., and Mohrig, D. (2010). How Do Bedform Patterns Arise? New Views on the Role of Bedform Interactions within a Set of Boundary Conditions. *Earth Surf. Process. Landforms* 35, 51–63. doi:10.1002/esp.1913

Kocurek, G., and Lancaster, N. (1999). Aeolian System Sediment State: Theory and Mojave Desert Kelso Dune Field Example. *Sedimentology* 46, 505–515. doi:10.1046/j.1365-3091.1999.00227.x

Lancaster, N. (1994). "Dune Morphology and Dynamics," in *Geomorphology of Desert Environments*. Editors A. D. Abrahams and A. J. Parsons (London: Chapman & Hall). doi:10.1007/978-94-015-8254-4_18

Lancaster, N. (1995). *Geomorphology of Desert Dunes*. London: Routledge.

Li, B. C. (1998). An Investigation and Study on the Desertification of the Ancient Oases from Han to Tang Dynamic in the Hexi Corridor. *Acta Geogr. Sin.* 53, 106–115.

Liu, B., and Coulthard, T. J. (2017). Modelling the Interaction of Aeolian and Fluvial Processes with a Combined Cellular Model of Sand Dunes and River Systemsfluvial Processes with a Combined Cellular Model of Sand Dunes and River Systems. *Comput. Geosciences* 106, 1–9. doi:10.1016/j.cageo.2017.05.003

Livingstone, I., and Warren, A. (1996). *Aeolian Geomorphology: An Introduction*. Harlow: Addison Wesley Longman Limited.

Lü, P., Dong, Z. B., and Rozier, O. (2018). The Combined Effect of Sediment Availability and Wind Regime on the Morphology of Aeolian Sand Dunes. *J. Geophys. Res. Earth Surf.* 123, 2878–2886. doi:10.1029/2017JF004361

Lü, P., Narteau, C., Dong, Z. B., Zhang, Z. C., and Pont, S. C. D. (2014). Emergence of Oblique Dunes in a Landscape-Scale Experiment. *Nat. Geosci.* 7, 99–103. doi:10.1038/ngeo2047

Luo, X. L., Li, Y. G., and Yan, Z. M. (2021). Evolution Characteristic of Sandstorm and Meteorological Influence Factors in Hexi Corridor in Recent 60 Years. *Res. soil water conservation* 28 (05), 254–267. doi:10.13869/j.cnki.rswc.2021.05.029

McKee, E. D. (1979). "Introduction to a Study of Global Sand Seas," in *A Study of Global Sand Seas, 3-19*. Editor E. D. McKee (Washington, D.C. Professional Paper: USGS).

Melton, F. A. (1940). A Tentative Classification of Sand Dunes its Application to Dune History in the Southern High Plains. *J. Geol.* 48, 113–174. doi:10.1086/624871

Muhs, D. R., and Maat, P. B. (1993). The Potential Response of Eolian Sands to Greenhouse Warming and Precipitation Reduction on the Great Plains of the U.S.A. *J. Arid Environ.* 25, 351–361. doi:10.1006/jare.1993.1068

Nottebaum, V., Lehmkuhl, F., Stauch, G., Lu, H., and Yi, S. (2015). Late Quaternary Aeolian Sand Deposition Sustained by Fluvial Reworking and Sediment Supply in the Hexi Corridor - an Example from Northern Chinese Drylands. *Geomorphology* 250, 113–127. doi:10.1016/j.geomorph.2015.08.014

Pearce, K. I., and Walker, I. J. (2005). Frequency and Magnitude Biases in the 'Fryberger' Model, with Implications for Characterizing Geomorphically Effective Winds. *Geomorphology* 68, 39–55. doi:10.1016/j.geomorph.2004.09.030

Rubin, D. M., and Hunter, R. E. (1987). Bedform Alignment in Directionally Varying Flows. *Science* 237, 276–278. doi:10.1126/science.237.4812.276

Saqqa, W. A., and Saqqa, A. W. (2007). A Computer Program (WDTSRP) Designed for Computation of Sand Drift Potential (DP) and Plotting Sand Roses. *Earth Surf. Process. Landforms* 32, 832–840. doi:10.1002/esp.1451

Thomas, D. S. G. (1997). "Sand Seas and Aeolian Bedforms," in *Arid Zone Geomorphology*. Editor D. S. G. Thomas (London: Belhaven Press).

Wang, X., Dong, Z., Yan, P., Zhang, J., and Qian, G. (2005). Wind Energy Environments and Dunefield Activity in the Chinese Deserts. *Geomorphology* 65, 33–48. doi:10.1016/j.geomorph.2004.06.009

Wasson, R. J., and Hyde, R. (1983). Factors Determining Desert Dune Type. *Nature* 304, 337–339. doi:10.1038/304337a0

Wu, Z. (1987). *Aeolian Geomorphology (In Chinese)*. Beijing: Science Press.

Wu, Z. (2009). *Sandy Deserts and its Control in China (In Chinese)*. Beijing: Science Press.

Yan, P., Li, X., Ma, Y., Wu, W., and Qian, Y. (2015). Morphological Characteristics of Interactions between Deserts and Rivers in Northern China. *Aeolian Res.* 19, 225–233. doi:10.1016/j.aeolia.2015.01.005

Zhang, Z. C., Dong, Z. B., Wen, Q., and Jiang, C. W. (2015c). Wind Regimes and Aeolian Geomorphology in the Western and Southwestern Tengger Desert. *Geol. J.* 50, 707–719. doi:10.1002/gj.2586

Zhang, Z. C., Dong, Z. B., and Zhao, A. G. (2016b). The Effect of the Time Interval Used to Calculatemean Wind Velocity on the Calculated Drift Potential, Relative Drift Potential, and Resultant Drift Direction for Sands from Three Deserts in Northern China. *Theor. Appl. Climatol.* 123, 151–160. doi:10.1007/s00704-014-1345-2

Zhang, Z., and Dong, Z. (2015). Grain Size Characteristics in the Hexi Corridor Desert. *Aeolian Res.* 18, 55–67. doi:10.1016/j.aeolia.2015.05.006

Zhang, Z., Dong, Z., Hu, G., and Parteli, E. (2018). Migration and Morphology of Asymmetric Barchans in the Central Hexi Corridor of Northwest China. *Geosciences* 8, 204. doi:10.3390/geosciences8060204

Zhang, Z., Dong, Z., and Li, C. (2015a). Wind Regime and Sand Transport in China's Badain Jaran Desert. *Aeolian Res.* 17, 1–13. doi:10.1016/j.aeolia.2015.01.004

Zhang, Z., Dong, Z., and Li, J. (2015b). Grain-size Characteristics of Dune Networks in china's Tengger Desert. *Geogr. Ann. Ser. A, Phys. Geogr.* 97, 681–693. doi:10.1111/geoa.12108

Zhang, Z., Dong, Z., Li, J., Qian, G., and Jiang, C. (2016a). Implications of Surface Properties for Dust Emission from Gravel Deserts (Gobis) in the Hexi Corridor. *Geoderma* 268, 69–77. doi:10.1016/j.geoderma.2016.01.011

Zhang, Z., Liang, A., Zhang, C., and Dong, Z. (2021). Gobi Deposits Play a Significant Role as Sand Sources for Dunes in the Badain Jaran Desert, Northwest China. *Catena* 206, 105530. doi:10.1016/j.catena.2021.105530

Conflict of Interest: The authors declare that the research was conducted in the absence of any commercial or financial relationships that could be construed as a potential conflict of interest.

Publisher's Note: All claims expressed in this article are solely those of the authors and do not necessarily represent those of their affiliated organizations, or those of the publisher, the editors, and the reviewers. Any product that may be evaluated in this article, or claim that may be made by its manufacturer, is not guaranteed or endorsed by the publisher.

Copyright © 2022 Zhang and Zhang. This is an open-access article distributed under the terms of the Creative Commons Attribution License (CC BY). The use, distribution or reproduction in other forums is permitted, provided the original author(s) and the copyright owner(s) are credited and that the original publication in this journal is cited, in accordance with accepted academic practice. No use, distribution or reproduction is permitted which does not comply with these terms.

frontiers | Frontiers in Earth Science

ORIGINAL RESEARCH
published: 13 June 2022
doi: 10.3389/feart.2022.901629

Investigating Potential Links Between Fine-Grained Components in Loess and Westerly Airflow: Evidence From East and Central Asia

Yue Li[1,2], Yougui Song[1,3]*, Kathryn E. Fitzsimmons[4,5], Aditi K. Dave[4,5], Yuming Liu[1], Xiulan Zong[1], Huanyu Sun[6], Huifang Liu[1] and Rustam Orozbaev[7,8]

[1]State Key Laboratory of Loess and Quaternary Geology, Institute of Earth Environment, Chinese Academy of Sciences, Xi'an, China, [2]Key Laboratory of Desert and Desertification, Northwest Institute of Eco-Environment and Resources, Chinese Academy of Sciences, Lanzhou, China, [3]CAS Center for Excellence in Quaternary Science and Global Change, Xi'an, China, [4]Department of Geosciences, University of Tübingen, Tübingen, Germany, [5]Research Group for Terrestrial Palaeoclimates, Max Planck Institute for Chemistry, Mainz, Germany, [6]College of Resource Environment and Tourism, Capital Normal University, Beijing, China, [7]Institute of Geology, National Academy of Sciences of Kyrgyz Republic, Bishkek, Kyrgyzstan, [8]Research Center for Ecology and Environment of Central Asia (Bishkek), Bishkek, Kyrgyzstan

Loess is a ubiquitous, silty aeolian sediment common across the semiarid to subhumid regions in the Northern Hemisphere. As such, the physical characteristics of loess sediment, such as modal grain size and quartz crystallinity index, have the potential to inform us about dust transport pathways and corresponding atmospheric circulation responsible for entrainment, transport, and deposition. In this article, we combine detailed granularity analyses and non-parametric end-member modeling with investigations of the quartz crystallinity index of three loess deposits, extending from East to Central Asia, with the aim of identifying dust transport processes and the climate subsystems responsible for them. We find marked differences in the grain size characteristics of Eastern and Central Asian loess. Given potential linkages of fine particles to the westerly jet stream, here we focused on the fine-grained end-members in the loess. The fine-grained components of the Central Asian Bishkek (BSK) and Chashmanigar (CMG) loess may be derived from individual particles carried at high altitude by major climate subsystems such as the westerlies. However, similar quartz crystallinity indexes of fine- and coarse-grained components in the Central Asian loess indicated that surface-level wind strength might influence the releases from proximal-sourced regions and abundances in the upper atmosphere for the fine particles. By contrast, the fine-grained component of the East Asian [Fanshan18 (FS18)] loess seems to yield physical similarities to the Tertiary Red Clays underlying many loess stratigraphies, and has been interpreted to relate to transport associated with the East Asian winter monsoon. It was further supported by quartz crystallinity indexes of the <16 μm fractions in the FS18 loess, basically consistent with those of the deserts in North China, highlighting the near-surface northwesterly winter monsoon as the dominant transport dynamics of fine-grained dust. In addition, comparisons of quartz crystallinity indexes of fine-grained components between the East and Central Asian loess also suggest that variations in fine particles within the loess might not be related to transport by the higher-level westerlies, which is in

OPEN ACCESS

Edited by:
Steven L. Forman,
Baylor University, United States

Reviewed by:
György Varga,
Research Centre for Astronomy and Earth Sciences, Hungary
Xinbo Gao,
Institute of Geology and Geophysics (CAS), China

***Correspondence:**
Yougui Song
syg@ieecas.cn

Specialty section:
This article was submitted to Quaternary Science, Geomorphology and Paleoenvironment, a section of the journal Frontiers in Earth Science

Received: 22 March 2022
Accepted: 27 April 2022
Published: 13 June 2022

Citation:
Li Y, Song Y, Fitzsimmons KE, Dave AK, Liu Y, Zong X, Sun H, Liu H and Orozbaev R (2022) Investigating Potential Links Between Fine-Grained Components in Loess and Westerly Airflow: Evidence From East and Central Asia.
Front. Earth Sci. 10:901629.
doi: 10.3389/feart.2022.901629

disagreement with the previous model. Therefore, our results indicate that variations in fine-grained end-members in loess are difficult to reliably document the variabilities of higher-level westerlies.

Keywords: loess, grain size, end-member modeling, quartz crystallinity index, westerlies

1 INTRODUCTION

Aeolian loess deposits cover about 10% of the global land surface and are extensively distributed in the semiarid to subhumid regions around the world (Taylor et al., 1983; Liu, 1985; Tsoar and Pye, 1987; Rousseau and Hatté, 2021). The enhanced dustiness and the associated climatic effects over Late Quaternary make it especially important to understand past dust activity (Claquin et al., 2003; Sun and An, 2005; Antoine et al., 2009; Rasmussen et al., 2014; Kang et al., 2015; Stevens et al., 2016; Újvári et al., 2017), which play a key role in reducing the large uncertainties that exist in Earth system models (Shao et al., 2011; Choobari et al., 2014; Liu et al., 2018). Loess archives act as a direct indicator of paleo-dust activity, and its formation generally occurs in four stages, production, deflation, transport, and deposition of particles (Smalley, 1966; Pye, 1995; Wright, 2001; Muhs et al., 2014). The latter three stages have important consequences for landform evolution, biogeochemical cycles, regional climate, human health, and desertification (Ravi et al., 2011, and references therein). Therefore, loess records can serve as the reliable tools to reconstruct past atmospheric circulation patterns and dynamic environments (e.g., Qin et al., 2005; Bokhorst et al., 2011; Vandenberghe, 2013; Obreht et al., 2015; Újvári et al., 2016; DiPietro et al., 2017).

Loess grain size properties also improved our understanding of dust source areas (Dong et al., 2016), transportation pathways (Varga, 2011), and paleo-atmospheric circulation (Bokhorst et al., 2011; Varga, 2011). Multiple peaks in loess grain size distribution (GSD) were related to different transport modes (Folk and Ward, 1957; Weltje, 1997; Sun et al., 2004; Qin et al., 2005). Consequently, the analysis of GSD is a promising way to strengthen the physical basis for interpreting aeolian processes using loess records. Recent years have seen increasing statistical analysis of loess grain size to identify subpopulation [grain size end-member (EM)] within bulk samples (Weltje, 1997; Sun et al., 2002; Sun et al., 2004; Prins et al., 2007; Prins and Vriend, 2007; Vriend et al., 2011; Vandenberghe, 2013; Li et al., 2018a; Vandenberghe et al., 2018; Varga et al., 2019; Jiang et al., 2020). The different EMs were interpreted to reveal distinct atmospheric transport mechanisms, modes, and travel distances (e.g., Újvári et al., 2016; Vandenberghe, 2013, and references therein). In some cases, the end-member approach has also been employed to indicate variations in the geological context or source area (e.g., Prins et al., 2007; Bokhorst et al., 2011). Therefore, the grain size partitioning model provides a clearer perspective for identifying the natural processes where aeolian loess was transported. There have been two different unmixing methods of grain size spectra: parametric decomposition and non-parametric decomposition (Prins et al., 2007; Dietze et al., 2014; Vandenberghe et al., 2018). The former uses parametric curve-fitting procedures to disintegrate the polymodal grain size distribution curve of a single sample into aggregates of unimodal statistical probability distribution functions with the Weibull function or normal function (Sun et al., 2002; Sun et al., 2004; Qin et al., 2005; Sun D. H. et al., 2008; Varga, 2011; Wang et al., 2017). The latter is performed based on the whole grain size database, and a numerical–statistical inversion technique is employed to identify fixed sedimentary populations (EMs) from the measured grain size distribution curves of the samples by weighting them with an appropriate score (Weltje, 1997; Varga et al., 2019). Generally, the EMs obtained by non-parametric decomposition are polymodal, and those of parametric curve fitting are logically unimodal (Varga et al., 2019). For interpretations of (sub)populations, non-parametric decomposition can only provide results of more simultaneous sedimentation mechanisms, such as seasonal dust signal, yet the results of parametric curve fitting can indicate process-related elements of background and dust storm depositional components for each sample (Varga et al., 2019). Hateren et al. (2017) reviewed several non-parametric end-member modeling algorithms and evaluated their accuracies, and Weltje and Prins (2003) argued that for the parametric end-member fitting, defects exist in the uniqueness of results and physical theory on GSDs. While Dietze et al. (2022) also indicated constraints and limitations of non-parametric end-member modeling analysis (EMMA). Regardless of those debates, despite theoretical differences, the two methods can produce similar results and both have been intensively employed (Sun, 2004; Park et al., 2014; Nottebaum et al., 2015; Újvári et al., 2016; DiPietro et al., 2017; Li et al., 2018a; Varga et al., 2019; Jiang et al., 2020).

However, the origin of the fine-grained EMs in loess is relatively complex: 1) deposition as individual particle, which is transported by large-scale high-altitude winds in long-term suspension mode from distant source (Sun et al., 2004; Sun D. H. et al., 2008; Park et al., 2014); 2) attachment to larger grains from near-source regions (Pye, 1987); 3) deposition as silt- or sand-sized aggregates (Derbyshire et al., 1995; Pye, 1995; Falkovich et al., 2001; Mason et al., 2003; Qiang et al., 2010b; Mason et al., 2011; Újvári et al., 2016); and 4) production by post-depositional weathering and pedogenic processes (Xiao et al., 1995; Bland, 1998; Wang et al., 2006; Hao et al., 2008). As a result, the controversial interpretations for the fine-grained components in loess have hampered detailed understanding of their potential links to the westerlies (Sun, 2004; Prins et al., 2007; Vriend et al., 2011; Nottebaum et al., 2014).

In this article, we carried out non-parametric EMMA to elucidate aeolian dust dispersal patterns in East and Central

Asia based on the loess GSDs. Given the complexity of explanations to finer components (Mason et al., 2011; Újvári et al., 2016), we separated the bulk samples into two or three size fractions, and measured crystallinity index (hereafter referred to as CI) of quartz mineral in size fractions to examine different origins for the fine- and coarse-grained particles. Quartz is an ubiquitous and weather-resistant rock-forming mineral. Quartz CI reflects temperature and crystallization rates during formation and depends on the types of source rocks (Murata and Norman, 1976). From this, the index has been applied to the identification of the dust sources in the Chinese Loess Plateau (CLP) and the Japan Sea (Ono et al., 1998; Toyoda and Naruse, 2002; Nagashima et al., 2007; Sun et al., 2007; Sun Y. et al., 2008; Nagashima et al., 2011; Sun et al., 2013). It has benefited from the successful distinguishment of the major Gobi and sandy deserts in North and Northwest China (Sun et al., 2013).

This study aims to shed light on the aeolian processes responsible for loess accumulation in different geographical provinces of Asia, and in particular to assess the imprint of the westerlies in the loess records by comparisons of the end-member subpopulations and the CI results. In addition, this study contributes toward correcting the deviation in genetic interpretations of end-members for the loess grain size.

2 MATERIALS AND METHODS

2.1 Study Area

The mid-latitudes of Eurasia is the most important loess area in the Northern Hemisphere (Muhs, 2013). The Siberian High (SH) as a semipermanent anticyclone dominates Eurasia, and cold and dense air masses produced by the SH lead to strong outbreaks of cold and dry northerly winds in a belt stretching from East Asia through portions of West Asia and central and northern Europe (Aizen et al., 2001; Cohen et al., 2001; Gong and Ho, 2002). While high-altitude atmosphere over Eurasia prevails westerly stream, and northward and southward migration of the westerly winds can directly modulate spatial distributions of precipitation in Europe and Central Asia (Aizen et al., 2001; Luetscher et al., 2015; Wassenburg et al., 2016; Perşoiu et al., 2019; Lan et al., 2021). Meanwhile, the intimate relationship between spatial variations in East Asian summer monsoon precipitation and the westerly jet path across East Asia during Holocene has also been identified (Nagashima et al., 2013; Herzschuh et al., 2019).

The study area involves East and Central Asia. In East Asia, the CLP loess is well known for its vast area of coverage and continuous deposition during the Quaternary (Liu, 1985; Liu and Ding, 1998; An, 2000; Guo et al., 2000). The CLP in north-central China covers an area of ~36 × 10^4 km^2 (Li and Lu, 2010), extending from ~100 to 115°E to ~35 to 45°N (Maher, 2016). Loess accumulation on the CLP is driven by winter monsoon near-surface winds associated with the SH pressure system and/or westerly circulation of the Northern Hemisphere (Liu, 1985; Porter et al., 2001; Roe, 2009; Lu et al., 2010; Maher, 2016; Sun et al., 2020). By contrast, comparatively patchy piedmont loess deposits of varying thickness are widely distributed along the high mountains in Central Asia (Song et al., 2021), including the Pamir and Alai ranges (Dodonov, 1991; Dodonov and Baiguzina, 1995; Dodonov et al., 1999; Ding et al., 2002), the Tian Shan (Zhou et al., 1995; Fang et al., 2002; Song et al., 2014; Youn et al., 2014; Fitzsimmons et al., 2018; Li G. et al., 2020), and the Altai (Zykin and Zykina, 2015) mountain margins. Since climate change in Central Asia is mainly controlled by the dynamics of westerly air masses (Aizen et al., 2001; Chen et al., 2019; Guan et al., 2019), deposition of the piedmont loess over the region could respond to the changes of the westerly (Ding et al., 2002; Vandenberghe et al., 2006; Li et al., 2016a; Li et al., 2019b; Fan et al., 2021; Jia et al., 2022) despite strong influences of the SH pressure system and the Asiatic polar fronts (Sorrel et al., 2007; Machalett et al., 2008; Groll et al., 2013; Li et al., 2018a). Particularly, our areas of interest are the Kyrgyz Tian Shan (northern Central Asia), the Afghan–Tajik Basin (southern Central Asia), and the Yanqin-Huailai-Zhoulu Basin (East Asia) (**Figure 1**). Comparisons of loess records from these sites would contribute to deciphering potential links between fine-grained components in loess and westerly airflow in consideration of the aforementioned descriptions and position of the Yanqin-Huailai-Zhoulu Basin downwind of the Kyrgyz Tian Shan and the Afghan–Tajik Basin (**Figure 2**).

The Kyrgyz Tian Shan is located in the southwestern Central Asia Orogenic Belt (CAOB) (Yakubchuk, 2004). It mainly consists of Precambrian continental fragments intruded by Cambrian to Silurian granitoids (Glorie et al., 2010; Kroner et al., 2013; Alexeiev et al., 2016), connecting to the Ili Block in China (Han et al., 2016). This region is mainly influenced by the mid-latitude westerlies, the SH, northerly polar fronts, and Asian monsoon systems (Machalett et al., 2008; Cheng et al., 2012; Sorg et al., 2012; Groll et al., 2013; Karger et al., 2017; Fitzsimmons et al., 2018; Guan et al., 2019). Maximum rainfall occurs in spring (March, April, and May) along the loess piedmonts over the region (Li et al., 2020c) (**Figure 1**). The SH expands southward in winter and brings with it cold temperatures, dry conditions, and strong wind and associated dust activity to the Kyrgyz Tian Shan (Cheng et al., 2012; Li et al., 2018a; Shi et al., 2020). The thickness of the outcropped loess in the Kyrgyz Tian Shan generally ranges from several meters to 20 m according to field observations (Song et al., 2021), while the thickest loess section already reported in the region is the 80 m-thick Remisowka section near Almaty (Machalett et al., 2006). The loess section with a thickness of ~20 m in the northern Krygyz Tian Shan was accumulated since the last glacial period based on quartz optically stimulated luminescence (OSL) dating (Youn et al., 2014); by comparison, the preliminary estimate of the paleomagnetic age of the Remisowka section is older than 800 ka (Song et al., 2021), though needs further chronological assessment (Machalett et al., 2006; Machalett et al., 2008; Fitzsimmons et al., 2018). The Moyun-Kum and Taukum deserts are located in about 180–200 km northwest and north of the Kyrgyz Tian Shan, respectively; however, a recent study suggested that the deserts are not the main source of the fine-grained loess, while piedmont slopes and alluvial–proluvial plains are common sources for both deserts and loess over the region (Li et al., 2020b).

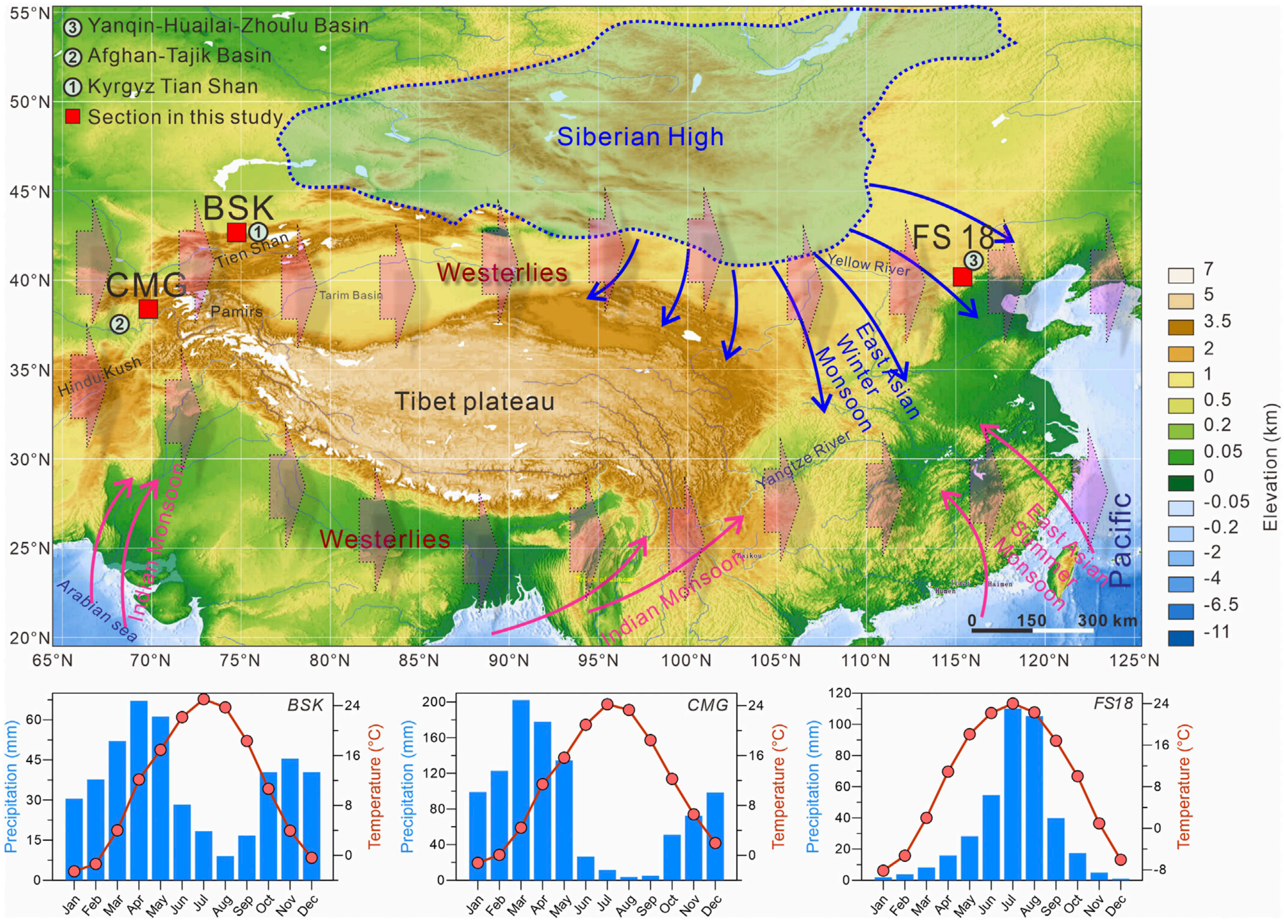

FIGURE 1 | Locations of the studied loess sections and monthly precipitation and temperature at the sampling sites.

The Afghan–Tajik Basin is bordered by the Tian Shan Mountains to the north and northeast, by the western Pamir Mountains to the east, and by the Hindu Kush Mountains to the south. The SH has a dominant impact on the precipitation variability during winter season (Feng et al., 2011). In summer, the subtropical high occupies the basin due to the onset of the Indian summer monsoon (Li et al., 2016b). The dust emissions and accumulations maximize during the hot and dry summer season (Dodonov et al., 1999; Ding et al., 2002; Li et al., 2019a), and dust activity in the basin are largely controlled by changes in the intensity of the Caspian Sea–Hindu Kush Index (CasHKI) (Li et al., 2019a). The loess mantle in the basin is extremely thick, attaining a thickness of 100–200 m (Dodonov, 1991; Frechen and Dodonov, 1998; Parviz et al., 2020b). The early magnetostratigraphic correlation estimated that the oldest loess in Tajikistan started to accumulate since Gauss polarity period (2.6 Ma) (Dodonov and Penkov, 1977). Ding et al. (2002) demonstrated the bottom paleomagnetic age of 1.77 Ma for the Chashmanigar section, and recent paleomagnetic analysis extended the basal age of this section to 2.13 Ma about the Reunion subchron (Parviz et al., 2020a). The great deserts such as Karakum and Kyzylkum are situated to the west and northwest of the basin (Ding et al., 2002). However, based on loess trace elements and meteorological reanalysis data, Li et al. (2019a) suggested that the deserts may have a minor contribution to loess formation in southern Tajikistan.

The Yanqin-Huailai-Zhoulu Basin is a fault basin, located at the margins of the NE CLP (Wang et al., 2014; Xiong et al., 2001). The annual precipitation and the highest temperature in the basin primarily occur during summer (**Figure 1**) (Xiong et al., 2001). The pedostratigraphic properties of the loess in the Yanqin-Huailai-Zhoulu Basin indicated loess deposition occurred during glacial periods with strengthened East Asian winter monsoon, whereas the palaeosols were developed during interglacial periods with the predominant East Asian summer monsoon (Xiong et al., 2001). Loess in the basin mainly occurs on uplands along the piedmonts of the mountains and covers terraces of different heights; loess over the region is commonly about 10–20 m thick, with a maximum thickness of about 100 m in the southern basin (Xiong et al., 2001). According to Xiong et al. (2001), the thickest loess deposit consists of 14 loess-paleosol couplets, underlain by fluvial pebbly conglomerates, and its paleomagnetic age extends back to 1.1 Ma. The present margin of the Hunshandake desert is about 180–200 km northwest of the

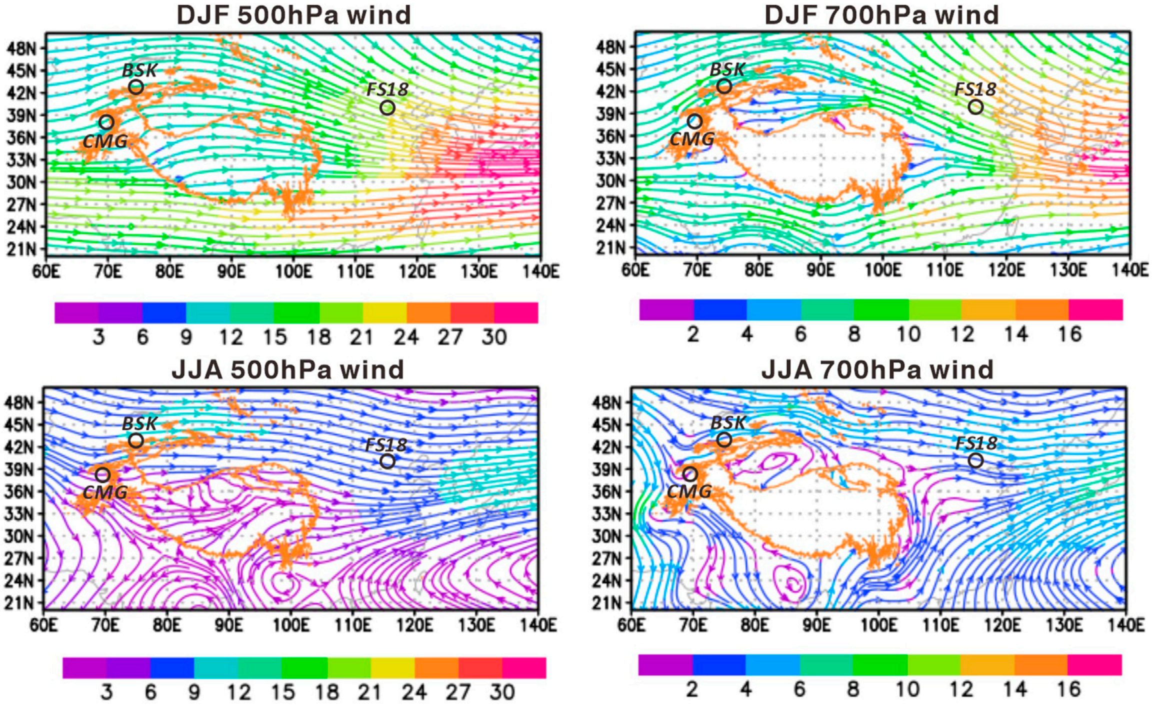

FIGURE 2 | Mean winter and summer streamlines (m s^{-1}) at 500 hPa (~5,000 m.a.s.l.) and 700 hPa (~3,000 m.a.s.l.) for 1980–2016 across East and Central Asia (URL: https://gmao.gsfc.nasa.gov/reanalysis/MERRA-2/). The orange lines represent the 1,700 m isohypse lines.

loess regions in the Yanqin-Huailai-Zhoulu Basin (Xiong et al., 1999a; Xiong et al., 2001), and correspondingly, the loess can provide essential information on evolution of the desert (Xiong et al., 1999b).

2.2 Field Sampling

We analyzed GSDs of bulk samples and CI of quartz mineral for the loess samples from the BSK, CMG, and FS18 sections, which are located in the Kyrgyz Tian Shan, the Afghan–Tajik Basin, and Yanqin-Huailai-Zhoulu Basin, respectively (**Figure 1**). The FS18 section is located downwind of the BSK and CMG sections, with the westerlies as an important connection (**Figure 2**). Therefore, as stated earlier, our results could be used to examine the significance of the westerlies during the process of loess transport in the study area.

The BSK loess section (74°46′50.1″E, 42°42′15.5″N, 1,432 m a.s.l; **Figures 3A,D**) is located in the Kyrgyz Tian Shan (**Figure 1**), near the Norus River in the Chui region, Kyrgyzstan and 24 km from the southeast part of Bishkek city (Li et al., 2020c). The section was exposed by road excavation, with a thickness of ~18 m. According to the OSL dating results of Youn et al. (2014), the BSK section roughly spans MIS1-5. The detailed lithologic features of the BSK section have been described in Li et al. (2020c), and its stratigraphy is also shown in **Figure 3A**.

The CMG loess section (69°49′54.7″E, 38°23′18.9″N, 1,549 m a.s.l; **Figures 3B,D**) is almost located in the same position as the Chashmanigar section studied by Ding et al. (2002). The section has a thickness of 25 m, which is exposed by gravitational sliding. The section is assumed to span MIS1-5 based on paleomagnetic dating and orbitally tuned time scale (Ding et al., 2002; Yang et al., 2006). In the section, upper 0.2 m is grayish-brown modern soil, characterized by a loose soil texture, and enriched in modern plant roots (**Figure 3B**). The 0.2–17.5 m depth is homogeneous and yellow loess unit, with a massive, loose, and porous structure (**Figure 3B**). Calcareous pseudo mycelium is heavily distributed from top to bottom of the loess layer. Carbonate concretions with a diameter of >10 cm occur in the 14.5–15.25 m horizon. The 17.5–24.75 m depth is a reddish brown paleosol unit (**Figure 3B**), implying strong pedogenesis. The paleosol layer evenly contains root-like calcareous channels. The 24.75–25 m depth is a grayish-yellow loess layer with loose structure. Carbonate concretions of 2–3 cm in diameter occur at depths of 22.8–22.95 m and 24.9 m.

The FS18 loess section (115°23′51.2″ E, 40°11′46.5″ N, 853 m a.s.l; **Figures 3C,D**) is located in approximately 90 km northwest of Beijing. The section is a composite of two vertical subsections [A (7 m thick) and B (8 m thick), **Figure 3D**], which are 40 m apart. Thus, the section has a total thickness of 15 m. The 0–0.4 m depth is modern surface soil; the 0.4–11.2 m depth is the loess unit, characterized by grayish-yellow, silt, loose and porous structure, with uniform texture, vertical joint, and very few black Fe–Me oxide, and calcareous mycelium. A weak paleosol unit at 11.2–13.4 m depth is brown, fine silt, or clayey silt, with compaction structure and abundant calcareous mycelium. The 13.4–15 m depth is the second loess unit, which is grayish-yellow silt. In addition, calcareous nodules of ϕ = 1–3 cm occur at the 13.1–13.9 cm depth.

We collected some bracketing samples from the FS18 section for luminescence dating (**Supplementary Text S1**;

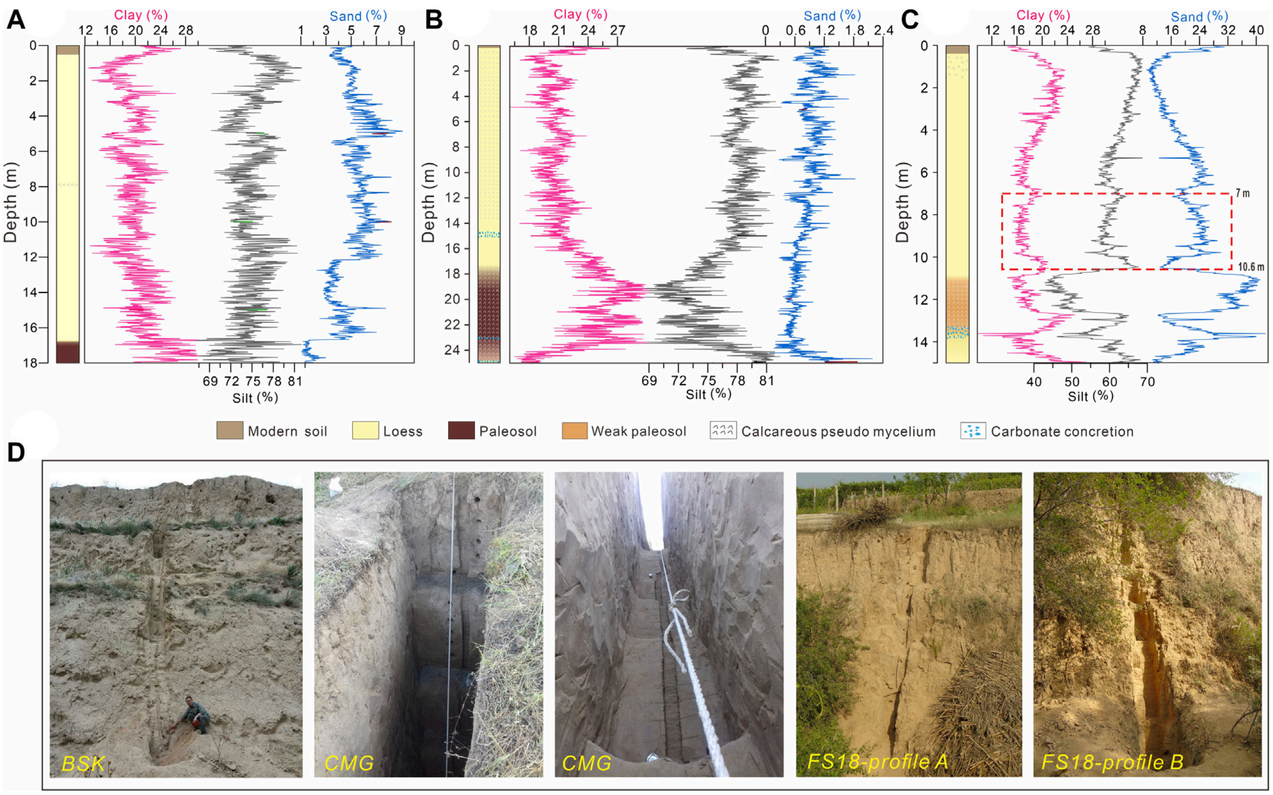

FIGURE 3 | Stratigraphic logs **(A–C)**, grain size results **(A–C)** and photos **(D)** of the BSK, CMG and FS18 loess sections. The red dashed box in **(C)** indicates the depth interval [7–10.6 m in FS18-subsection **(B)**] that is not used for the analyses due to its chronological overlap with the upper 7 m (**Supplementary Material**).

Supplementary Table S1; **Supplementary Figure S2**), and the results show that the section also spans MIS1-5. We initially assumed that the subsections A and B represented a continuous sequence. However, luminescence dating of key levels (**Supplementary Figure S2**) showed substantial temporal overlap between the subsections. Without additional samples we were unable to develop a robust age model incorporating the two subsections in order to integrate our granulometry data and therefore we treat the two subsections as separate, with a gap in the depths, but nevertheless discontinuously spanning the last full glacial cycle. Specifically, the luminescence dating results indicated a chronological overlap between 0–7 m and 7–10.6 m depths (**Supplementary Text S2**). **Figure 3C** also showed similar variation trends in grain sizes between them despite of striking differences shown in the top of the upper 7 m. Therefore, subsection A (0–7 m) and 10.6–15 m depth in subsection B were used to conduct the EMMA in the consideration of the relatively higher sedimentation rate for the upper 7 m (**Supplementary Figure S2**).

After removing the superficial weathered sediment from the three sections, samples were collected at 2-cm resolution. A total of 900 samples for BSK section, 1,250 samples for CMG section, and 750 samples for FS18 section were prepared for grain size tests (**Supplementary Table S2**). Subsequently, 48 samples (14 from BSK section, 16 from CMG section, and 17 from FS18 section) were selected and separated into two or three size fractions (BSK and CMG section: <16 μm and >16 μm; FS18 section: <16 μm, 16–63 μm and >63 μm) for measuring the quartz CI.

2.3 Experimental Methods

2.3.1 Grain Size

Prior to grain size measurements, 0.5 g of dry bulk sample was pretreated by the removal of organic matter and carbonate using H_2O_2 and HCl, respectively (Lu and An, 1997). Samples were then dispersed for 10 min by ultrasonification with 10 ml 10% $(NaPO_3)_6$ solution. The Mie theory was used to obtain the relationship between the particles size and the light intensity distribution pattern (Grehan and Gouesbet, 1979; Wiscombe, 1980). Therefore, the information on both refractive index (RI) and absorptive index (AI or imaginary refractive index) of analyzed materials are required (Eshel et al., 2004). In this study, water was used as the dispersant with a RI = 1.33 at 20°C, and the default setting of RI = 1.52 and AI = 0.1 were applied, primarily because these parameters are targeted at soil samples (e.g., loess) (Eshel et al., 2004; Malvern Instruments, 2009). Particle size distribution was calculated for 100 grain size classes within a measuring range of 0.02–2,000 μm. Replicate analyses indicated an analytical error of <2%. The grain size results used in this study can be seen in **Supplementary Table S1**. Grain size distribution was analyzed using a Malvern 3000 laser instrument at the State Key Laboratory of Loess and Quaternary

Geology, Institute of Earth Environment, Chinese Academy of Sciences.

2.3.2 Crystallinity Index (CI) of Quartz

A total of 48 CI samples are selected from the three sections (**Figure 7**; **Supplementary Table S3**). Five grams of each sample were treated with 30% H_2O_2 and 30% HCl to remove organic matter and carbonate, respectively (Sun et al., 2007; Zhao et al., 2012). The fractions of <16 μm and >16 μm were then isolated by gravitational settling based on Stokes' law (Gibbs, 1974). In addition, the fraction of >63 μm within the FS18 loess was also extracted by wet sieving due to its higher contents.

CI was measured by following Ma et al. (2013), using an X'pert Pro MPD X-ray diffractometer (XRD) at the State Key Laboratory of Loess and Quaternary Geology, Institute of Earth Environment, Chinese Academy of Sciences. Powders of the aforementioned different fractions were placed in the glass holder and irradiated with a Cu Kα source with voltage at 40 kV and 40 mA. The scanning angle ranges from 66° to 69° (2θ), with a scan speed of $0.01\ s^{-1}$ and a step speed of 25.0 s (Zhao et al., 2012). The CI was calculated using the following equation (Murata and Norman, 1976):

$$\mathrm{CI} = \mathrm{F} \times (a/b), \tag{1}$$

where the factor F is estimated as 12.24 (Zhao et al., 2012); a refers to the difference between the crest value at 67.74° (2θ) and the valley value at 67.84 (2θ); b is the difference between the crest value at 67.74° (2θ) and the background value. Absolute error of multiple measurements of CI for standard quartz sample (CI = 10) is ±0.15 (Ma et al., 2013). The XRD spectra for calculating the CI and the CI values of each fraction are accessible in **Supplementary Table S3**.

2.4 End-Member Modeling Analysis (EMMA) of Grain Size Distributions

As mentioned earlier, non-parametric EMMA is simultaneously conducted with a whole sequence based on the covariance structure of the dataset. They use the principles of eigenspace analysis and different scaling procedures to describe GSDs as a linear combination of end-members and their weighting scores (Weltje, 1997; Dietze et al., 2012). After the estimation of minimum number of EMs required for an appropriate approximation of the measured data, the size distributions and weighting scores for every end-members are determined (Varga et al., 2019), which makes the interpretation of EMs more statistically and physically descriptive (Paterson and Heslop, 2015). Various numerical techniques have recently become available, such as AnalySize (Paterson and Heslop, 2015), BEMMA (Yu et al., 2016), and EMMAgeo (Dietze et al., 2012). Hateren et al. (2017) suggested that AnalySize can yield accurate reproductions of artificial grain size datasets. Therefore, AnalySize was employed in this study. The relevant theories and calculative processes can be seen in Paterson and Heslop (2015).

The parametric curve-fitting technique is also applied here to evaluate the explanations of grain size EMs in previous studies. The parametric EMMA assumes that under steady and known dynamics of the transport mode and transport agent, the grain size of sediment displays a single-component distribution, which is controlled by a single factor (Sun et al., 2002; Sun et al., 2004), namely, different transport mechanisms produce unique modal grain sizes in the sediment they deposit (Ashley, 1978; Bagnold and Barndorff-Nielsen, 1980). The grain size distribution curves were decomposed using Weibull functions, an approach that is developed by Sun et al. (2002). Moreover, grain size parameters of the end-members were calculated from the analytical data with GRADISTAT (Version 4.0; Blott and Pye, 2001).

3 RESULTS

3.1 Grain Size

The mean particle size distribution and the range of volume frequency for each size class of the BSK section are similar to those of the CMG section, both distinctly differing from those of the FS18 section (**Figures 4A–C**). The size ranges of the BSK and CMG sections generally span 0.2–300 μm, with the primary modes of ~13 μm. The overall mean particle size distributions of the BSK and CMG sections show a unimodal pattern, with a slight skewness toward the coarse part of distribution (**Figures 4A,B**). An additional small peak occurs at 0.4–1.8 μm for the BSK and CMG loess (**Figures 4A,B**). The mean particle size distribution of the FS18 section presents a multimodal pattern, with peaks centering in 0.6 μm, 7 μm, and 50 μm (**Figure 4C**). In addition, the maximum values of each size class for the FS18 section also show obvious peak at 500–2,000 μm, despite lack of the peak in mean particle size distribution (**Figure 4C**).

Figures 3A–C shows the variations in clay, silt, and sand fractions in the BSK, CMG, and FS18 loess. The BSK and CMG loess are dominated by silt fraction, with mean proportions of 75 and 77%, respectively. While the silt fraction in the FS18 loess is relatively less, with an average of 60%. The silt fraction decreases lightly down the BSK section with significant fluctuations, and the clay fraction displays a variation trend opposite to the silt fraction (**Figure 3A**). The proportions of sand fraction in the BSK section range from 1.1 to 12.8%. The clay and silt fractions in the CMG section show more significant inverse relationship (**Figure 3B**). The proportions of clay fraction are much higher in the paleosol unit than in the loess unit. The sand fraction of the CMG loess displays the low contents, compared to that of the BSK section, with gradually decreasing trend (**Figure 3B**). In contrast, the proportions of silt fraction in the FS18 section follows the opposite trend of the sand fraction (**Figure 3C**). Notably, the sand-sized contents in the FS18 section are relatively higher (21.2%) than those in the BSK and CMG sections. The clay and silt fractions in the FS18 loess synchronously change; whereas the clay-sized contents vary with small amplitudes, relative to the silt-sized content.

3.2 Non-Parametric End-Member Modeling of Grain Size Data

The two criteria used for selecting the number of EM are parsimony and reproducibility (Prins and Weltje, 1999).

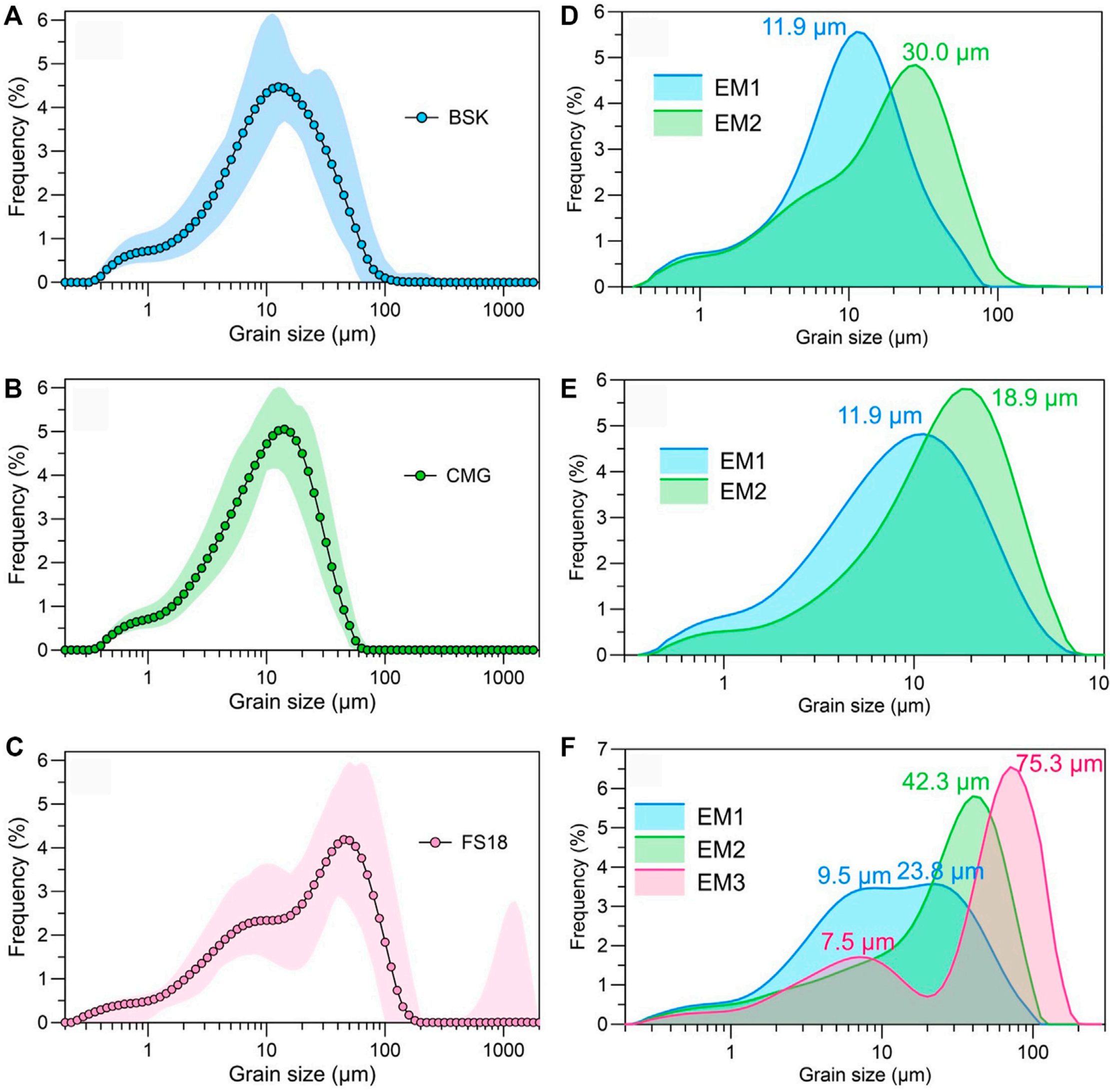

FIGURE 4 | Mean grain size distribution and range of volume frequency for each size class in loess for the BSK **(A)**, CMG **(B)**, FS18 **(C)** loess sections, and grain size partitioned components of the BSK **(D)**, CMG **(E)**, and FS18 **(F)** loess. The minimum and maximum values of the GSDs [colored shade in **(A)**, **(B)**, **(C)**] were found in each size class and the averages refer to the mean volume frequencies of each size class.

Specifically, parsimony is the minimum number of EMs, and for reproducibility, it is generally accepted that the number of EMs should explain over 95% of the variance of the entire grain size dataset. The coefficient of determination (R^2) and mean angular deviation (θ) are calculated to identify the minimal numbers of EMs necessary for a good statistical explanation of the data. Relatively higher R^2 and lower θ suggest a better statistical fit (Paterson and Heslop, 2015). In the correlation map of the BSK loess between R^2 and end-member quantity (**Supplementary Figure S3a**), end-member modeling yields the best results with 2 EMs; for models with more than 1 EMs, θ is less than 5°. Therefore, two EMs were modeled for the BSK loess, which yield $R^2 > 0.98$. The same is true for the CMG loess (**Supplementary Figure S3b**). However, the 3-EM model provides a realistic resolution for the FS18 loess (**Supplementary Figure S3c**), which meets the requirements of a minimum EM number and maximum reproducibility (Paterson and Heslop, 2015).

Figures 4D–F show the GSD of each EM for the three loess sections, with the modal sizes being exhibited. The two EMs of the BSK and CMG loess present a unimodal pattern (**Figures 4D,E**). The modal size of the EM1s for both sections is same (11.9 µm); whereas, the mode of the EM2 of the BSK loess is significantly larger than that of the CMG loess. The three identified EMs in the FS18 loess display very different grain size distributions from each other (**Figure 4F**). The EM1 and EM3 of the FS18 loess show a bimodal pattern; the frequencies for the two modes (9.5 and 23.8 µm) of the EM1 are of essential equality; the primary mode of the EM3 is 75.3 µm, and the secondary one is 7.5 µm. The EM2

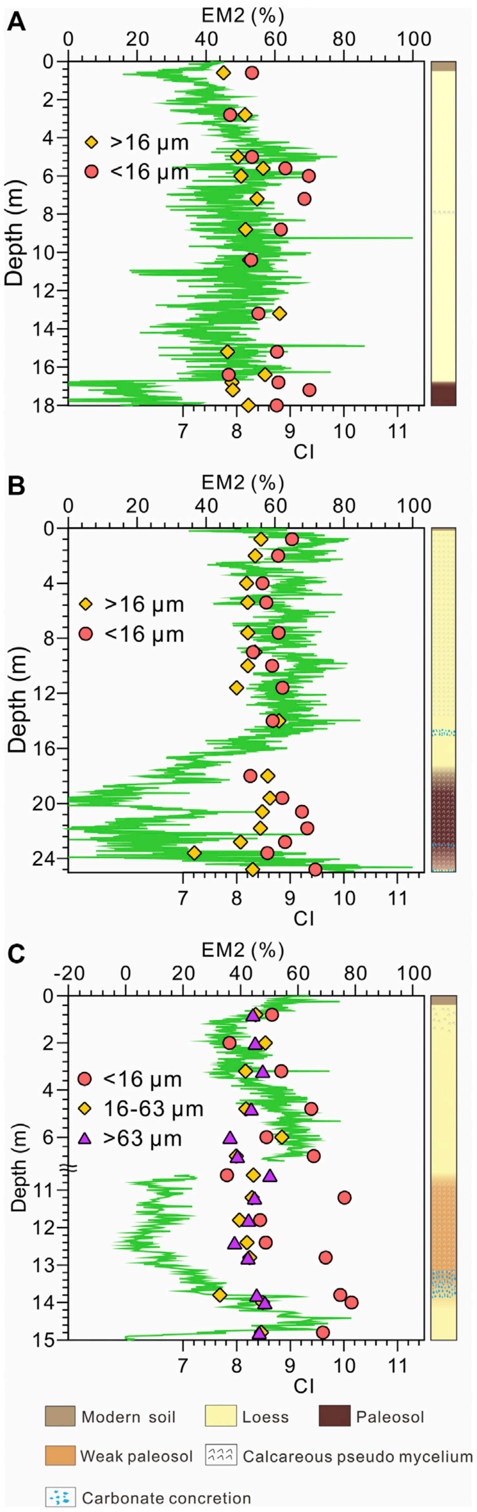

FIGURE 5 | Variations in CI and mean grain size of the BSK **(A)**, CMG **(B)**, and FS18 **(C)** sections.

unmixed in the FS18 loess shows a unimodal pattern (modal grain size of 42.3 μm), markedly skewed toward the coarser side.

3.3 Quartz CI

The CI values of quartz for the >16 μm and <16 μm fractions do not show evident variabilities down the BSK and CMG section (**Figures 5A,B**). Overall, both the BSK and CMG sections have similar CI values for the >16 μm and <16 μm fractions, respectively. In comparison to the BSK and CMG sections, the CI differences between fine- and coarse-grained quartz particles in the FS18 loess are significantly higher (**Figure 5C**), likely indicating that different size fractions are probably originated from different host rocks (Sun et al., 2013). However, the CI values of the coarse-grained fractions of the FS18 loess (including 16–63 μm and >63 μm fractions) are similar to those of the BSK and CMG loesses (**Figure 5**).

4 DISCUSSION

4.1 Likely Processes Responsible for Fine-Grained EMs in East and Central Asia

Coarse components of the BSK and CMG loesses were deposited during dust storms and non-dust storm processes, respectively, while coarse particles in the FS18 loess was also related to seasonal dust storms, but with higher energies, relative to the BSK loess, due to relative closeness to the SH pressure center (**Supplementary Text S3**). Moreover, the sand-grained EM in the FS18 loess was affected by availability of sediments (**Supplementary Text S3**). As a result, coarse-size fractions are unlikely to be transported by high-altitude westerly air streams. Inversely, the size of 20–30 μm is often regarded as the maximum grain size subjected to long-distance dust transport (Tsoar and Pye, 1987; Kok et al., 2012; Ryder et al., 2013). Therefore, here we exclusively discuss physical implications of fine-grained EM, and their links to the high-altitude westerlies because of the possibility that westerly jet stream is responsible for fine-grained dust transportation and deposition processes.

EM1s of both BSK and CMG loess have a modal grain size of 11.9 μm (**Figures 4D,E**), whereas Vandenberghe (2013) did not point out a subgroup with such a modal size. Fine-grained fractions in loess deposits can be produced by post-depositional weathering and pedogenic processes (Xiao et al., 1995; Bland, 1998; Wang et al., 2006; Hao et al., 2008). However, weathering process rarely influence ~2–10 μm fraction of aeolian sediments (Sun D. H. et al., 2008). Although weathering process produces a small amount of superfine grains, their sizes are seldom larger than 1 μm in diameter (Paton, 1978; Bronger and Heinkele, 1990), and even the chemical mechanism of grain size variation is unimportant for mineral dust particles larger than 0.3 μm (Qin et al., 2005). Moreover, we have used the reasonable pretreatment approach of size measurement (Lu and An, 1997) to eliminate the soil organic matter (SOM) and carbonate, which are easily influenced by chemical weathering and pedogenesis. Consequently, we exclude the influences of chemical weathering and post-depositional pedogenesis on the EM1s.

Particle size distributions of modern dust from the Kyrgyz Tian Shan typically yield a modal peak of approximately 10 μm (Schettler et al., 2014). **Figure 8** also shows that the primary end-member components identified from the GSDs of modern eolian dusts at a height of 100 m have a modal size of ~10 μm (Sun et al., 2003). Dust particles in the Dunde ice core in the western Qilian Shan, Northern China, also has a majority of its mass distribution concentrated within a modal grain size of 4–12 μm (Wu et al., 2009). Similarly, the modal sizes of long-range transported (LRT) dust on the glacier surface of the NE-TP range from 9.8 to 12 μm (Wei et al., 2019). In the eastern Tian Shan, the modal size of dust at Miaoergou glacier is 13 μm, that at glacier No. 1 is 11.5 μm and that at glacier No. 51 is 11.0 μm (Dong et al., 2009). The mode size of the microparticles in Muztagata ice core from the eastern Pamirs centers at ~10 μm (Wu et al., 2006). The mode of LRT dust size distribution for the cryoconite particles deposited on the TP glaciers generally ranges at 5–21 μm (Dong et al., 2020, and references therein). Thus, observational data from the dust modal size in glaciers and ice-cores demonstrate that fine particles with a modal grain size similar to that of EM1 in the BSK and CMG loess can be transported and deposited in the upper-level troposphere as individual mineral grains (Sun, 2004).

However, fine particles may also be deposited by attachment to larger grains from near-source regions (Pye, 1987), or as silt- or sand-sized aggregates (Derbyshire et al., 1995; Pye, 1995; Falkovich et al., 2001; Mason et al., 2003; Qiang et al., 2010b; Mason et al., 2011; Újvári et al., 2016). Based on the observed dust storms, Qiang et al. (2010b) suggested that the fine-grained components in the deposits of dust storm were most likely to settle by forming aggregates and/or adhering to larger grains, which deciphered the independence of the depositions of fine particles on the variations in wind strength during the most severe dust storms. Formation of aggregates that increases particle mass, and/or attachment to larger particles, enables fine grains to be deposited during dust storms; as a result, fine- and coarse-grained dust are transported together by low-level dust storms from the same adjoining sources (Pye, 1995; Mctainsh et al., 1997; Qiang et al., 2010b). Therefore, it cannot be ruled out that the EM1s in Central Asian loess were also possibly transported as aggregates and/or adhering to larger particles at a relatively low level in the atmosphere from the proximal source areas.

EM1 of the FS18 loess is characterized by two distinct modal sizes (**Figure 4F**), which is rarely observed for the typical Quaternary loess in the CLP (Prins and Vriend, 2007). In contrast, it was found that the GSDs of the EM1 is in good agreement with those of red clay in the CLP, as a fraction that cannot be further unmixed (**Figure 6**). Therefore, the EM1 was deposited under the very similar depositional environment to that of the Tertiary Red Clay. The GSDs of the original Red Clay have been modified by the post-depositional pedogenic process (Sun et al., 2006; Shang et al., 2016). Inversely, Vandenberghe et al. (2004) concluded that the clay fraction of the Xifeng Red Clay may not have a pedogenic origin but was transported by wind. Regardless of the influence of pedogenesis, Sun et al. (2006) suggested that the Red Clay deposits revealed significant fluctuations of the paleo-monsoon climate in East Asia at since late Miocene time. The size distributions of Red Clay indicated that its accumulation was most likely controlled by East Asian monsoon circulation rather than westerlies (Cao et al., 2001). Based on the mean grain sizes of both bulk samples and chemically isolated quartz grains of the Late Tertiary Red Clay deposits from six localities spanning across 550 km on the CLP, Miao et al. (2004) indicated that the Red Clay was transported mainly by northerly low-level winds, or the winds at least with a strong northerly component, associated with East Asian winter monsoon. In addition, study of the CLP dust source indicated that the dust source largely remained unchanged across the Pliocene–Pleistocene boundary, suggesting that the East Asian Monsoon played an important role in the deposition of the Red Clay as well as in the Quaternary loess and that the main winds transporting dust have not drastically changed trajectory since the Miocene (Bird et al., 2020). Therefore, we considered the FS18 EM1 to be transported by a weaker winter monsoon wind based on GSD characterizations.

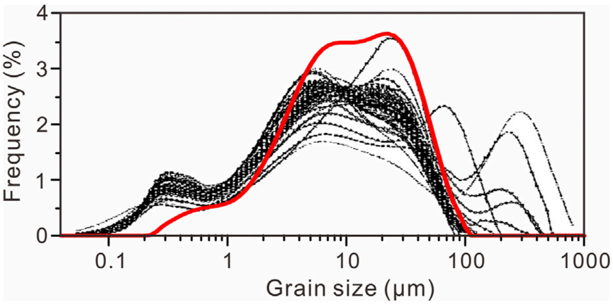

FIGURE 6 | Comparisons between GSDs of the EM1 identified in the FS18 loess (red line) and the red clay in the CLP (black lines, Cao et al., 2001).

4.2 Assessing the Ability of Loess Grain Sizes to Track Variabilities of the Westerlies

4.2.1 Evidence From Fine-Grained EM

Optical satellite data showed that the LRT dust in the Kyrgyz Tian Shan was sourced from a minor part of a dust plume moving northward from northeastern Afghanistan (Schettler et al., 2014). Dust in Muztagata ice core from the eastern Pamirs might be sourced from the Central Asian deserts, such as Kyzylkum and Karakum(Wu et al., 2006). Dust particles in the glaciers from eastern Tian Shan were released from the dust sources of Central Asia (e.g., the Taklimakan and Gobi deserts) (Dong et al., 2009). The potential sources of LRT dust in TP glaciers include the northern Chinese deserts (e.g., Gobi deserts, Qaidam deserts, Badain Jaran, and Tengger deserts) and Taklimakan deserts (Dong et al., 2020). Therefore, the LRT dust with finer grain size in the Tian Shan, Muztagata, and TP glaciers also originated from the nearby Asian dust sources, which were fed by the surrounding orogenic belts (ultimate provenances). It implies that dust storms in those sources strongly affected the concentration of dust deposited to the high mountains, for example, in eastern Tian Shan (Dong et al., 2009). The stronger surface winds, producing more frequent and/or intensive dust storms in the dust source regions, would enhance the atmospheric dust loadings and vice versa (Ruth et al., 2007; Qiang et al., 2010a; Xu et al., 2018). Consequently, dust on the glacier surface showed significant differences in concentrations and particle size distributions during the Asian dust and non-dust seasons, implying aeolian dust activity changed with seasonality and reached a different glacial elevation (Dong et al., 2020). Based on the aforementioned genetic interpretations of the non-parametric EMs of the BSK and CMG loess, they partially represent the LRT dust. In analogy to case of the LRT dust, grain sizes, and percentages of the EM1s in the BSK and CMG loess also depended on changes of near-surface winds, even if they are transported by the westerly wind circulations after being lifted to the high elevation. However, that added more uncertainties to the hypothesis that the fine-grained EMs are an indicator of change in intensity and pathway of high-altitude westerly circulation (Sun, 2004). Therefore, variations in the EM1s did not merely respond to variability in the westerlies, and thus were not expected to fully indicate changes of the westerlies. In addition, the revelation of variations in large-scale westerly circulations using loess deposits is based on the direct linkages between the dust-bearing wind systems and the larger atmospheric circulations. However, these linkages are usually complicated by the overland geomorphological settings. The Tian Shan, Alai, and Altai mountain ranges and Pamirs in Central Asia have a huge topographic effect on the mid-latitude westerlies (Rugenstein and Chamberlain, 2018; Kang et al., 2020; Wang et al., 2020). Therefore, the complex topography over the region results in varying wind trajectories and influences transport of aeolian loess sediments (Fitzsimmons et al., 2018; Li et al., 2018b; Sprafke et al., 2018; Li et al., 2020b). In this context, it also implies that large uncertainties exist in the investigation of the regional westerly circulations based on sedimentary properties of loess deposits in Central Asia.

The EM1 of the FS18 loess was derived from a transport-deposition mode similar to the Tertiary Red Clay, as stated earlier. Thus, it was mainly transported by low-level East Asian winter monsoon over short distances, rather than high-altitude westerly (Miao et al., 2004; Bird et al., 2020). Meanwhile, interpretation of coarser populations (EM2) indicates the FS18 section is close to the source areas and the SH pressure center (**Supplementary Text S3b**), which may also overwhelm the influence of the westerlies. Therefore, it is not straightforward to examine the signal of westerlies based on the FS18 loess. Moreover, even for the loess records from the central and southeastern CLP, dominant transport dynamics of the fine-grained particles therein is strongly associated with changes in the intensity of the near-surface northwesterly winter monsoon (Sun Y. et al., 2008). In conclusion, the present results, combined with the previous study of loess provenance, suggest that fine-grained EMs identified from the CLP loess are still primarily related to East Asian winter monsoon, rather than the westerly jet.

We also considered the results of parametric EMMA for the BSK, CMG, and FS18 loesses using Weibull function (**Supplementary Figure S5**). The fine-grained EM of the FS18 loess shows a mode size of 7.43 μm. Fine component in the CLP loess generally has a mode size range of 3–6 μm (Sun et al., 2004) or 2–8 μm (Sun D. H. et al., 2008). While loess deposits from the west coast of South Korea displayed a fine component with mode sizes of 2.7–4.4 μm (Park et al., 2014). Thus, it is plausible that the downwind of the westerlies yielded finer component with a smaller modal size than that in the upwind. However, the finer components in the BSK and CMG loesses showed peaks around modal particle sizes of 0.86 and 3.32 μm, respectively. This was also against the transport of fine particles by westerlies.

4.2.2 Evidence From Quartz CI

Supports for the aforementioned conclusions also come from the analyses of quartz CI. Previous studies indicated that the fine-grained EMs in Chinese loess obtained by non-parametric EMMA originated from long-term suspension transport by high-altitude westerlies (Prins et al., 2007; Vriend et al., 2011; Nottebaum et al., 2014). It assumes that the fine grains have a different source area from the coarse grains (Xie et al., 2014). However, our CI values indicated the similar sources between the fine- and coarse-grained fractions of the BSK and CMG loesses (**Figures 5A,B**), which thereby might not lend support to the assumption that the fine-grained components of loess deposits were hypothesized to be transported by the high-altitude westerlies. Therefore, our CI results and the previous findings (e.g., Qiang et al., 2010b; Xie et al., 2014) calls for a crucial problem that whether variations in the finer EMs of loess sediments were associated with the intensity and pathways of the westerlies and to what extent the loess grain sizes might document changes in the westerlies.

Figure 7 shows that most of the <16 μm fractions in the FS18 loess have CI values consistent with those of the deserts in North China (Tengger, Badain Juran, and Mu Us Deserts). By contrast, these CI values evidently differ from those of Taklamakan Desert (>2,000 km away from the CLP) (**Figure 7**). Therefore, based on the observations, fine-grained components in the CLP loess were still dominated by proximal sources (such as the deserts in North China) (Sun Y. et al., 2008), which were largely affected by dust input of the weak low-level winds (Miao et al., 2004), instead of the high-altitude westerlies in a long-distance transport. On the other hand, the EM2 of the FS18 loess was interpreted to indicate frequency and intensity of dust storm (**Supplementart Text S3**). When the percentage of the EM2 increased (frequent, strong dust storm), the CI values of the fine (<16 μm) fractions were similar to those of Mongolia Gobi (**Figures 5C**, **7**), suggesting increased contributions of fine-grained dust from the distant Gobi Desert in southern Mongolia to the CLP due to the intensified northwesterly winter monsoon. When the percentage of the EM2 decreased (weaker winds), the CI values of the fine fractions were consistent with those of deserts in North China (**Figures 5C**, **7**), seemingly indicating that the westerlies were responsible for dust transportation and deposition processes in the FS18 section (**Figure 7**) due to the weakened near-surface northwesterly winter monsoon. However, the notably different CI values of the fine-grained components between the FS18 loess and Taklamakan Desert demonstrated less input of fine particles from the distant dust source in long-term suspension. While dust from the Taklamakan Desert can be transported by the westerly jet stream for long distance, once entrained to elevations >5,000 m (Sun, 2002a, b). Consequently, the high-altitude westerly jet did not act as a major dynamics of fine-grained dust transportation for the FS18 loess. Although more research is required to reveal

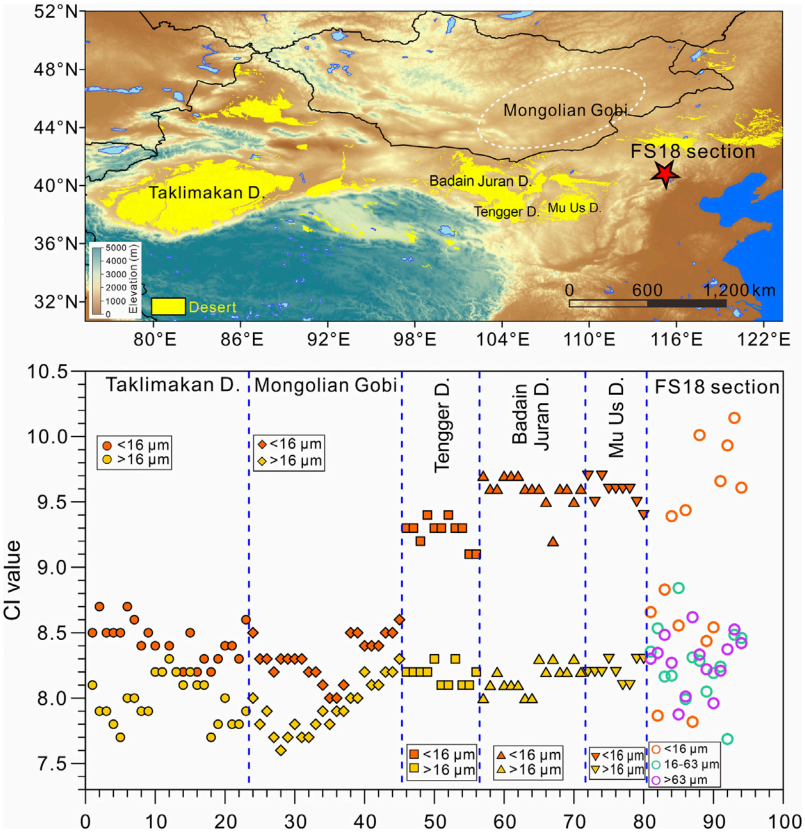

FIGURE 7 | Upper panel: locations of the involved sites. Lower panel: crystallinity indices of quartz for <16 μm and >16 μm fractions from the five deserts in North and Northwest China (Sun et al., 2013), and for <16 μm, 16–63 μm and >63 μm fractions from the FS18 loess.

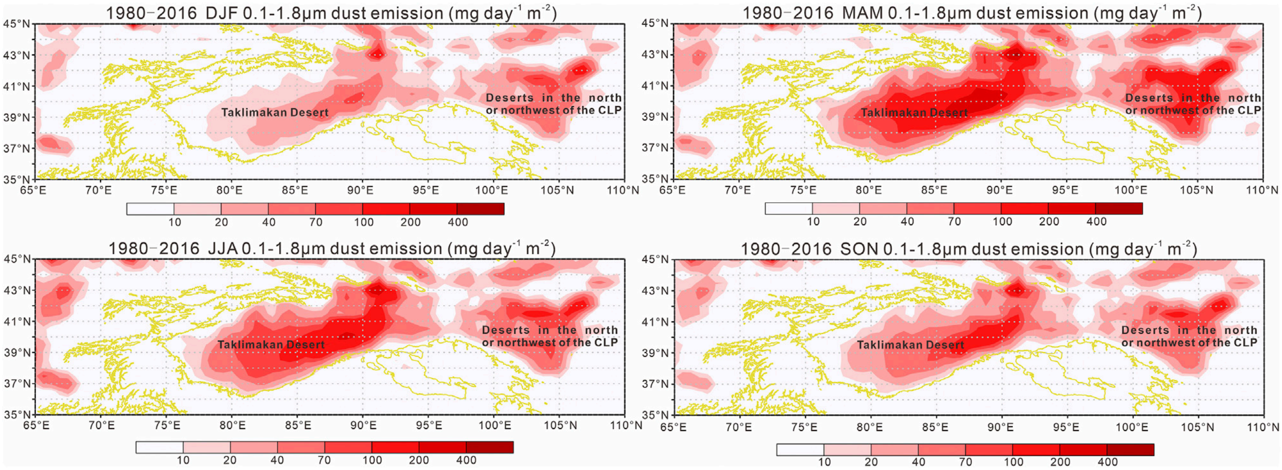

FIGURE 8 | DUFLUXU dust emission flux (kg m^{-1} s^{-1}) of winter (DJF), spring (MAM), summer (JJA), autumn (SON), and for the year 1980–2016. Particle size of the dust is 0.1–1.8 μm, and the positive/negative flux value represents eastbound/westbound direction. Data are collected from MERRA2 reanalysis data (https://disc.gsfc.nasa.gov/daac-bin/FTPSubset2.pl, Gelaro et al., 2017), with spatial resolution of 0.625° × 0.5° (longitude × latitude). The yellow line represents 1,700 m isohypse line.

the aeolian processes for the supply of fine particles from deserts in North China to the FS18 section during interglacial, the present provenance-tracing results emphasized the near-surface northwesterly winter monsoon as the dominant transport dynamics of fine-grained dust (Zhang et al., 1999; Sun Y. et al., 2008).

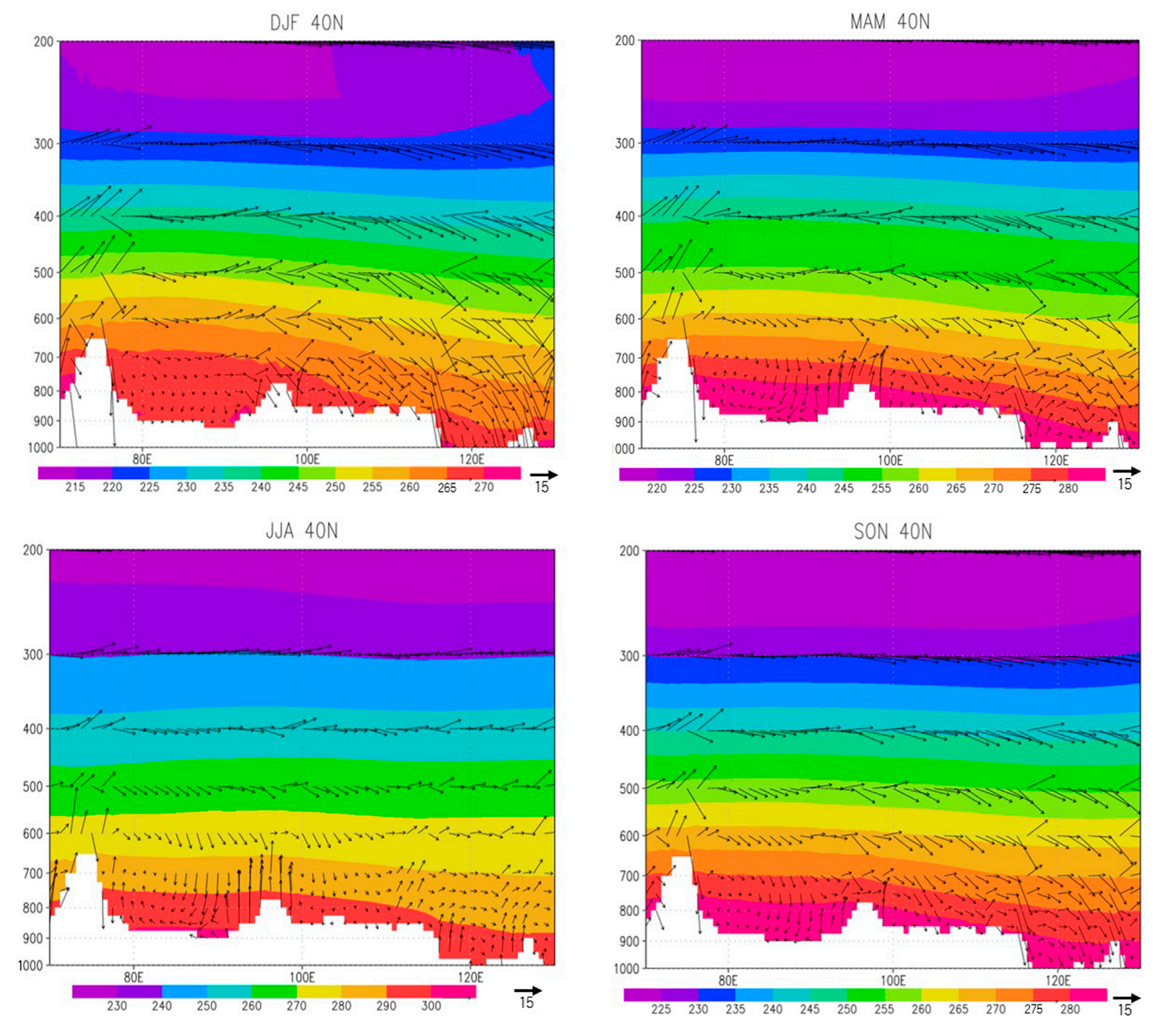

FIGURE 9 | Longitude pressure cross section of wind vectors (horizontal unit: m s^{-1}, vector unit: -10^{-2} Pa s^{-1}) and air temperature (colored, unit: K) in the Modern-Era Retrospective Analysis for Research and Applications, version 2 (MERRA2), dataset (Gelaro et al., 2017), along 40°N for climatological mean. DJF: winter; MAM: spring; JJA: summer; SON: fall.

Although Taklamakan dust can be easily transported eastward by high-altitude westerly airflow (Sun, 2002a; Sun, 2002b), particularly in spring (Yuan et al., 2019), it is expected that deposition of fine particles decreases when wind speed increases for their U_f/u^* ratio of <0.1 (U_f: the settling velocity of particle; u^*: the drag velocity of wind current) (Tsoar and Pye, 1987; Qiang et al., 2010b). Conversely, finer dust particles can be emitted from the deserts in the north or northwest of the CLP (e.g., Tengger and Badain Juran Deserts) (**Figure 8**) by strong saltation bombardment in the low-level atmosphere (Shao et al., 2020) that is supported by the consistent ε_{Nd} isotopic values between those deserts and the CLP loess (Zhao, 2015). Thus, it is possible that the fine dust particles were transported by the northwesterly winter monsoon winds in short suspension from the nearby source areas, in agreement with our earlier mentioned argument.

Figure 9 shows that near-surface air streams can be lifted into the upper westerly jet due to block of the Tian Shan ranges, and the higher-level westerlies have the capacity to carry mineral aerosols from Central Asia to East Asia. Subsequently, we compared the CI values of the <16 μm fractions of BSK and CMG loess with the FS18 loess. The differences in CI (**Figures 5C, 7**) indicates that the fine grains at FS18 located at northeastern margins of the CLP are different from those observed in the BSK and CMG sections, suggesting that the fine-grained component observed at FS18 is unlikely to be sourced from Central Asia, consequently raising caution on previous assumptions that fine particles of loess in the CLP were transported by westerlies.

4.2.3 Evidence From Previous Studies

Once off the ground, the fine-grained fraction can be dispersed for thousands of kilometers from the source areas at a much higher atmospheric level (Glaccum and Prospero, 1980; Rea et al., 1985; Pye, 1987; Tsoar and Pye, 1987), and the grain sizes of the uplifted fine-grained dust changes very little with increasing transport distance (Rea et al., 1985; Rea and Hovan, 1995; Nilson and Lehmkuhl, 2001; Sun D. H. et al., 2008). However, Sun (2004) observed the temporal and spatial variations in the modal size of the fine components for both glacial loess and interglacial paleosol across the CLP. Therefore, the model size changes possibly provided an evidence for the delivery of fine components in loess deposits by northwesterly winter monsoon from relatively nearby sources, such as deserts in northern China, instead of high-altitude westerlies. Furthermore, orbital- and suborbital-scale meridional movements of the pathway of the westerlies may reach ~10° in latitude (Toggweiler and Russell, 2008), significantly larger than that shown by Sun (2004), which also appeared not to support the links between fine components in the CLP loess and the westerly jet stream. Therefore, whether grain sizes of the CLP loess were imprinted with signs of the westerlies is worth revisiting. Based on the comparisons of the quartz CI values and analyses of the fine-grained EMs, as discussed earlier, this study suggested that variations in fine-grained fractions in loess are difficult to reliably document the variabilities of higher-level westerlies.

5 CONCLUSION

With the loess records from East (FS18 section) and Central (BSK and CMG sections) Asia, non-parametric EMMAs of grain size data and quartz CI tests were carried out to examine signals of the westerlies in the loess grain size records. Three EMs are distinguished in the FS18 loess, and two EMs in the BSK and CMG sections, respectively, which are able to characterize the dust transportation and deposition processes over the regions. In this study, we focused on the fine EMs in the loess in consideration of their potential linkages to the westerly jet stream. However, complicated origins and transportation and deposition processes of the fine-grained components in the BSK and CMG loess introduced some uncertainties in the model that variations in fine-grained EM of the loess were related to variations in high-altitude westerlies. While the fine component of the FS18 loess was derived from the transport-deposition mode controlled by the East Asian winter monsoon as the case of the Tertiary Red Clay, rather than the high-altitude westerlies. These interpretations were strengthened by the provenance-tracing results of coarse- and fine fractions in the loess based on quartz CI. Comparisons of the quartz CI values suggested that the fine-grained particles were characterized by relatively nearby sources, and that their transport-deposition mode might not be associated with the high-altitude westerlies. Consequently, it is suggested that variations in fine-grained fractions in loess are difficult to reliably document the variabilities of higher-level westerlies.

DATA AVAILABILITY STATEMENT

The original contributions presented in the study are included in the article/**Supplementary Material**; further inquiries can be directed to the corresponding author.

AUTHOR CONTRIBUTIONS

YuL and YS contributed to conception and design of the study. YuL, AD, XZ, HS, HL, and RO organized the database. YuL, AD, and YmL performed the statistical analysis. YuL wrote the first draft of the manuscript. YuL, KF, and AD wrote sections of the manuscript. All authors contributed to manuscript revision, read, and approved the submitted version.

FUNDING

This work was supported by the Natural Science Foundation of China (grant numbers 42102238 and 41977385), Key Laboratory of Desert and Desertification, Chinese Academy of Sciences (grant number KLDD-2020-009), the project of Special Research Assistant, Chinese Academy of Sciences, and an independent Max Planck Research Group awarded to KEF from the Max Planck Society.

ACKNOWLEDGMENTS

The authors thank Heng Liu from Xi'an Institute for Innovative Earth Environment Research for his help in plotting and Z Peric from Max Planck Institute for Chemistry for assistance in the luminescence dating laboratory.

SUPPLEMENTARY MATERIAL

The Supplementary Material for this article can be found online at: https://www.frontiersin.org/articles/10.3389/feart.2022.901629/full#supplementary-material

REFERENCES

Aizen, E. M., Aizen, V. B., Melack, J. M., Nakamura, T., and Ohta, T. (2001). Precipitation and Atmospheric Circulation Patterns at Mid-Latitudes of Asia. *Int. J. Climatol.* 21 (5), 535–556. doi:10.1002/joc.626

Alexeiev, D. V., Kröner, A., Hegner, E., Rojas-Agramonte, Y., Biske, Y. S., Wong, J., et al. (2016). Middle to Late Ordovician Arc System in the Kyrgyz Middle Tianshan: From Arc-Continent Collision to Subsequent Evolution of a Palaeozoic Continental Margin. *Gondwana Res.* 39, 261–291. doi:10.1016/j.gr.2016.02.003

An, Z. (2000). The History and Variability of the East Asian Paleomonsoon Climate. *Quat. Sci. Rev.* 19 (1-5), 171–187. doi:10.1016/s0277-3791(99)00060-8

Antoine, P., Rousseau, D.-D., Moine, O., Kunesch, S., Hatté, C., Lang, A., et al. (2009). Rapid and Cyclic Aeolian Deposition During the Last Glacial in European Loess: A High-Resolution Record from Nussloch, Germany. *Quat. Sci. Rev.* 28 (25–26), 2955–2973. doi:10.1016/j.quascirev.2009.08.001

Ashley, G. M. (1978). Interpretation of Polymodal Sediments. *J. Geol.* 86 (4), 411–421. doi:10.1086/649710

Bagnold, R. A., and Barndorff-Nielsen, O. (1980). The Pattern of Natural Size Distributions. *Sedimentology* 27 (2), 199–207. doi:10.1111/j.1365-3091.1980.tb01170.x

Bird, A., Millar, I., Rodenburg, T., Stevens, T., Rittner, M., Vermeesch, P., et al. (2020). A Constant Chinese Loess Plateau Dust Source Since the Late Miocene. *Quat. Sci. Rev.* 227, 106042. doi:10.1016/j.quascirev.2019.106042

Bland, W. (1998). *Weathering: An Introduction to the Scientific Principles*. New York: Oxford University Press.

Blott, S. J., and Pye, K. (2001). GRADISTAT: A Grain Size Distribution and Statistics Package for the Analysis of Unconsolidated Sediments. *Earth Surf. Process. Landforms* 26 (11), 1237–1248. doi:10.1002/esp.261

Bokhorst, M. P., Vandenberghe, J., Sümegi, P., Łanczont, M., Gerasimenko, N. P., Matviishina, Z. N., et al. (2011). Atmospheric Circulation Patterns in Central and Eastern Europe During the Weichselian Pleniglacial Inferred from Loess Grain-Size Records. *Quat. Int.* 234, 62–74. doi:10.1016/j.quaint.2010.07.018

Bronger, A., and Heinkele, T. (1990). Mineralogical and Clay Mineralogical Aspects of Loess Research. *Quat. Int.* 7-8, 37–51. doi:10.1016/1040-6182(90)90037-5

Cao, J., Zhang, X., Cheng, Y., and Lu, H. (2001). Size Distribution of the Late Cenozoic Red Clay and the Winter Monsoon Variations. *Mar. Geol. Quat. Geol.* 21 (3), 99–106. (in Chinese with English Abstract). doi:10.16562/j.cnki.0256-1492.2001.03.016

Chen, F., Chen, J., Huang, W., Chen, S., Huang, X., Jin, L., et al. (2019). Westerlies Asia and Monsoonal Asia: Spatiotemporal Differences in Climate Change and Possible Mechanisms on Decadal to Sub-Orbital Timescales. *Earth-Sci. Rev.* 192, 337–354. doi:10.1016/j.earscirev.2019.03.005

Cheng, H., Zhang, P. Z., Spötl, C., Edwards, R. L., Cai, Y. J., Zhang, D. Z., et al. (2012). The Climatic Cyclicity in Semiarid-arid Central Asia over the Past 500,000 Years. *Geophys. Res. Lett.* 39 (1), 1705. doi:10.1029/2011gl050202

Choobari, O. A., Zawar-Reza, P., and Sturman, A. (2014). The Global Distribution of Mineral Dust and its Impacts on the Climate System: A Review. *Atmos. Res.* 138, 152–165. doi:10.1016/j.atmosres.2013.11.007

Claquin, T., Roelandt, C., Kohfeld, K., Harrison, S., Tegen, I., Prentice, I., et al. (2003). Radiative Forcing of Climate by Ice-Age Atmospheric Dust. *Clim. Dyn.* 20 (2), 193–202. doi:10.1007/s00382-002-0269-1

Cohen, J., Saito, K., and Entekhabi, D. (2001). The Role of the Siberian High in Northern Hemisphere Climate Variability. *Geophys. Res. Lett.* 28 (2), 299–302. doi:10.1029/2000gl011927

Derbyshire, E., Kemp, R., and Meng, X. M. (1995). Variations in Loess and Palaeosol Properties as Indicators of Palaeoclimatic Gradients across the Loess Plateau of North China. *Quat. Sci. Rev.* 14 (7-8), 681–697. doi:10.1016/0277-3791(95)00077-1

Dietze, E., Hartmann, K., Diekmann, B., Ijmker, J., Lehmkuhl, F., Opitz, S., et al. (2012). An End-Member Algorithm for Deciphering Modern Detrital Processes from Lake Sediments of Lake Donggi Cona, NE Tibetan Plateau, China. *Sediment. Geol.* 243-244, 169–180. doi:10.1016/j.sedgeo.2011.09.014

Dietze, E., Maussion, F., Ahlborn, M., Diekmann, B., Hartmann, K., Henkel, K., et al. (2014). Sediment Transport Processes across the Tibetan Plateau Inferred from Robust Grain-Size End Members in Lake Sediments. *Clim. Past.* 10 (1), 91–106. doi:10.5194/cp-10-91-2014

Dietze, M., Schulte, P., and Dietze, E. (2022). Application of End-Member Modelling to Grain-Size Data: Constraints and Limitations. *Sedimentology* 69 (2), 845–863. doi:10.1111/sed.12929

Ding, Z. L., Ranov, V., Yang, S. L., Finaev, A., Han, J. M., and Wang, G. A. (2002). The Loess Record in Southern Tajikistan and Correlation with Chinese Loess. *Earth Planet. Sci. Lett.* 200 (3-4), 387–400. doi:10.1016/s0012-821x(02)00637-4

DiPietro, L. M., Driese, S. G., Nelson, T. W., and Harvill, J. L. (2017). Variations in Late Quaternary Wind Intensity From Grain-Size Partitioning of Loess Deposits in the Nenana River Valley, Alaska. *Quat. Res.* 87 (2), 258–274. doi:10.1017/qua.2017.3

Dodonov, A. E., and Baiguzina, L. L. (1995). Loess Stratigraphy of Central Asia: Palaeoclimatic and Palaeoenvironmental Aspects. *Quat. Sci. Rev.* 14 (7-8), 707–720. doi:10.1016/0277-3791(95)00054-2

Dodonov, A. E. (1991). Loess of Central Asia. *Geojournal* 24 (2), 185–194. doi:10.1007/bf00186015

Dodonov, A. E., Shackleton, N., Zhou, L. P., Lomov, S. P., and Finaev, A. F. (1999). Quaternary Loess-Paleosol Stratigraphy of Central Asia: Geochronology, Correlation, and Evolution of Paleoenvironments. *Stratigr. Geol. Correl.* 7 (6), 581–593.

Dodonov, A., and Penkov, A. (1977). Some Data on the Stratigraphy of the Watershed Loesses in the Tajik Depression. *Quat. Res.* 47, 67–76.

Dong, X. X., Yang, S. L., Tang, Z. H., and Ding, Z. L. (2016). A Grain-Size-Based Model for Dust Source-To-Sink Distance Reconstruction: A Case Study From Chinese Loess (In Chinese). *Sci. Sin. Terrae* 46, 1406–1412. doi:10.1360/N072016-00102

Dong, Z., Brahney, J., Kang, S., Elser, J., Wei, T., Jiao, X., et al. (2020). Aeolian Dust Transport, Cycle and Influences in High-Elevation Cryosphere of the Tibetan Plateau Region: New Evidences from Alpine Snow and Ice. *Earth-Science Rev.* 211, 103408. doi:10.1016/j.earscirev.2020.103408

Dong, Z., Li, Z., Wang, F., and Zhang, M. (2009). Characteristics of Atmospheric Dust Deposition in Snow on the Glaciers of the Eastern Tien Shan, China. *J. Glaciol.* 55 (193), 797–804. doi:10.3189/002214309790152393

Eshel, G., Levy, G. J., Mingelgrin, U., and Singer, M. J. (2004). Critical Evaluation of the Use of Laser Diffraction for Particle-Size Distribution Analysis. *Soil Sci. Soc. Am. J.* 68 (3), 736–743. doi:10.2136/sssaj2004.7360

Falkovich, A. H., Ganor, E., Levin, Z., Formenti, P., and Rudich, Y. (2001). Chemical and Mineralogical Analysis of Individual Mineral Dust Particles. *J. Geophys. Res.* 106 (D16), 18029–18036. doi:10.1029/2000jd900430

Fan, Y., Jia, J., Xia, D., Meadows, M., and Wang, Z. (2021). Seasonality of Response to Millennial-Scale Climate Events of the Last Glacial: Evidence From Loess Records Over Mid-Latitude Asia. *Geochem. Geophys. Geosyst.* 22 (10), e2021GC009903. doi:10.1029/2021gc009903

Fang, X., Shi, Z., Yang, S., Yan, M., Li, J., and Jiang, P. A. (2002). Loess in the Tian Shan and its Implications for the Develop-Ment of the Gurbantunggut Desert and Drying of Northern Xinjiang. *Chin. Sci. Bull.* 47 (16), 1381–1387. doi:10.1360/02tb9305

Feng, Z. D., Ran, M., Yang, Q. L., Zhai, X. W., Wang, W., Zhang, X. S., et al. (2011). Stratigraphies and Chronologies of Late Quaternary Loess-Paleosol Sequences in the Core Area of the Central Asian Arid Zone. *Quatern. Int.* 240 (1), 156–166. doi:10.1016/j.quaint.2010.10.019

Fitzsimmons, K. E., Sprafke, T., Zielhofer, C., Günter, C., Deom, J.-M., Sala, R., et al. (2018). Loess Accumulation in the Tian Shan Piedmont: Implications for Palaeoenvironmental Change in Arid Central Asia. *Quat. Int.* 469, 30–43. doi:10.1016/j.quaint.2016.07.041

Folk, R. L., and Ward, W. C. (1957). Brazos River Bar: A Study in the Significance of Grain Size Parameters. *J. Sediment. Res.* 27 (1), 3–26. doi:10.1306/74d70646-2b21-11d7-8648000102c1865d

Frechen, M., and Dodonov, A. E. (1998). Loess Chronology of the Middle and Upper Pleistocene in Tadjikistan. *Geol. Rundsch.* 87 (1), 2–20. doi:10.1007/s005310050185

Gelaro, R., McCarty, W., Suárez, M. J., Todling, R., Molod, A., Takacs, L., et al. (2017). The Modern-Era Retrospective Analysis for Research and Applications, Version 2 (MERRA-2). *J. Clim.* 30 (14), 5419–5454. doi:10.1175/Jcli-D-16-0758.1

Gibbs, R. J. (1974). *Suspended Solids in Water*. Boston, MA: Springer US.

Glaccum, R. A., and Prospero, J. M. (1980). Saharan Aerosols Over the Tropical North-Atlantic - Mineralogy. *Mar. Geol.* 37 (3-4), 295–321.

Glorie, S., De Grave, J., Buslov, M. M., Elburg, M. A., Stockli, D. F., Gerdes, A., et al. (2010). Multi-Method Chronometric Constraints on the Evolution of the Northern Kyrgyz Tien Shan Granitoids (Central Asian Orogenic Belt): From Emplacement to Exhumation. *J. Asian Earth Sci.* 38 (3-4), 131–146. doi:10.1016/j.jseaes.2009.12.009

Gong, D. Y., and Ho, C. H. (2002). The Siberian High and Climate Change Over Middle to High Latitude Asia. *Theor. Appl. Climatol.* 72 (1-2), 1–9. doi:10.1007/s007040200008

Grehan, G., and Gouesbet, G. (1979). Mie Theory Calculations: New Progress, with Emphasis on Particle Sizing. *Appl. Opt.* 18 (20), 3489–3493. doi:10.1364/ao.18.003489

Groll, M., Opp, C., and Aslanov, I. (2013). Spatial and Temporal Distribution of the Dust Deposition in Central Asia - Results from a Long Term Monitoring Program. *Aeolian Res.* 9 (9), 49–62. doi:10.1016/j.aeolia.2012.08.002

Guan, X., Yang, L., Zhang, Y., and Li, J. (2019). Spatial Distribution, Temporal Variation, and Transport Characteristics of Atmospheric Water Vapor Over Central Asia and the Arid Region of China. *Glob. Planet. Change* 172, 159–178. doi:10.1016/j.gloplacha.2018.06.007

Guo, Z., Biscaye, P., Wei, L., Chen, X., Peng, S., and Liu, T. (2000). Summer Monsoon Variations Over the Last 1.2 Ma from the Weathering of Loess-Soil Sequences in China. *Geophys. Res. Lett.* 27 (12), 1751–1754. doi:10.1029/1999gl008419

Han, Y., Zhao, G., Sun, M., Eizenhöfer, P. R., Hou, W., Zhang, X., et al. (2016). Late Paleozoic Subduction and Collision Processes During the Amalgamation of the Central Asian Orogenic Belt along the South Tianshan Suture Zone. *Lithos* 246-247, 1–12. doi:10.1016/j.lithos.2015.12.016

Hao, Q., Oldfield, F., Bloemendal, J., and Guo, Z. (2008). Particle Size Separation and Evidence for Pedogenesis in Samples from the Chinese Loess Plateau Spanning the Past 22 m.Y. *Geology* 36 (9), 727–730. doi:10.1130/g24940a.1

Hateren, J. A. V., Prins, M. A., and Balen, R. T. V. (2017). On the Genetically Meaningful Decomposition of Grain-Size Distributions: A Comparison of Different End-Member Modelling Algorithms. *Sediment. Geol.* 375, 49–71. doi:10.1016/j.sedgeo.2017.12.003

Herzschuh, U., Cao, X., Laepple, T., Dallmeyer, A., Telford, R. J., Ni, J., et al. (2019). Position and Orientation of the Westerly Jet Determined Holocene Rainfall Patterns in China. *Nat. Commun.* 10 (1), 2376. doi:10.1038/s41467-019-09866-8

Jia, J., Wang, N., Wang, Z., Wang, S., Meadows, M., Wang, L., et al. (2022). Weakened Dust Activity in Southern Central Asia During Heinrich Events. *Palaeogeog. Palaeoclimatol. Palaeoecol.* 587, 110805. doi:10.1016/j.palaeo.2021.110805

Jiang, Q., Qingzhen, H., Peng, S., and Qiao, Y. (2020). Grain-Size Evidence for the Transport Pathway of the Xiashu Loess in Northern Subtropical China and its Linkage with Fluvial Systems. *Aeolian Res.* 46, 100613. doi:10.1016/j.aeolia.2020.100613

Kang, J., Zan, J., Bai, Y., Fang, X., Chen, C., Guan, C., et al. (2020). Critical Altitudinal Shift from Detrital to Pedogenic Origin of the Magnetic Properties of Surface Soils in the Western Pamir Plateau, Tajikistan. *Geochem. Geophy. Geosy.* 21 (2), e2019GC008752. doi:10.1029/2019gc008752

Kang, S., Wang, X., Lu, Y., Liu, W., Song, Y., and Wang, N. (2015). A High-Resolution Quartz OSL Chronology of the Talede Loess Over the Past ~30 Ka and its Implications for Dust Accumulation in the Ili Basin, Central Asia. *Quat. Geochronol.* 30, 181–187. doi:10.1016/j.quageo.2015.04.006

Karger, D. N., Conrad, O., Böhner, J., Kawohl, T., Kreft, H., Soria-Auza, R. W., et al. (2017). Climatologies at High Resolution for the Earth's Land Surface Areas. *Sci. Data* 4, 170122. doi:10.1038/sdata.2017.122

Kok, J. F., Parteli, E. J. R., Michaels, T. I., and Karam, D. B. (2012). The Physics of Wind-Blown Sand and Dust. *Rep. Prog. Phys.* 75 (10), 106901. doi:10.1088/0034-4885/75/10/106901

Kröner, A., Alexeiev, D. V., Rojas-Agramonte, Y., Hegner, E., Wong, J., Xia, X., et al. (2013). Mesoproterozoic (Grenville-Age) Terranes in the Kyrgyz North Tianshan: Zircon Ages and Nd-Hf Isotopic Constraints on the Origin and Evolution of Basement Blocks in the Southern Central Asian Orogen. *Gondwana Res.* 23 (1), 272–295. doi:10.1016/j.gr.2012.05.004

Lan, J., Wang, T., Dong, J., Kang, S., Cheng, P., Zhou, K. e., et al. (2021). The Influence of Ice Sheet and Solar Insolation on Holocene Moisture Evolution in Northern Central Asia. *Earth-Sci. Rev.* 217, 103645. doi:10.1016/j.earscirev.2021.103645

Li, G., Yang, H., Stevens, T., Zhang, X., Zhang, H., Wei, H., et al. (2020a). Differential Ice Volume and Orbital Modulation of Quaternary Moisture Patterns Between Central and East Asia. *Earth Planet. Sci. Lett.* 530, 115901. doi:10.1016/j.epsl.2019.115901

Li, L., and Lu, H. (2010). A Preliminarily Quantitative Estimation of the Sedimentation and Erosion Rates of Loess Deposits in Chinese Loess Plateau Over the Past 250 Ka. *Acta Geog. Sin.* 65 (1), 37–52. doi:10.11821/xb201001005

Li, Y., Song, Y., Lai, Z., Han, L., and An, Z. (2016a). Rapid and Cyclic Dust Accumulation During MIS 2 in Central Asia Inferred from Loess OSL Dating and Grain-Size Analysis. *Sci. Rep.* 6 (1), 32365. doi:10.1038/srep32365

Li, Y., Song, Y., Chen, X., Li, J., Mamadjanov, Y., and Aminov, J. (2016b). Geochemical Composition of Tajikistan Loess and its Provenance Implications. *Palaeogeog. Palaeoclimatol. Palaeoecol.* 446, 186–194. doi:10.1016/j.palaeo.2016.01.025

Li, Y., Song, Y., Fitzsimmons, K. E., Chang, H., Orozbaev, R., and Li, X. (2018a). Eolian Dust Dispersal Patterns Since the Last Glacial Period in Eastern Central Asia: Insights from a Loess-Paleosol Sequence in the Ili Basin. *Clim. Past.* 14 (3), 271–286. doi:10.5194/cp-14-271-2018

Li, Y., Song, Y., Fitzsimmons, K. E., Chen, X., Prud'homme, C., and Zong, X. (2020b). Origin of Loess Deposits in the North Tian Shan Piedmont, Central Asia. *Palaeogeog. Palaeoclimatol. Palaeoecol.* 559, 109972. doi:10.1016/j.palaeo.2020.109972

Li, Y., Song, Y., Fitzsimmons, K. E., Chen, X., Wang, Q., Sun, H., et al. (2018b). New Evidence for the Provenance and Formation of Loess Deposits in the Ili River Basin, Arid Central Asia. *Aeolian Res.* 35, 1–8. doi:10.1016/j.aeolia.2018.08.002

Li, Y., Song, Y., Kaskaoutis, D. G., Chen, X., Mamadjanov, Y., and Tan, L. (2019a). Atmospheric Dust Dynamics in Southern Central Asia: Implications for Buildup of Tajikistan Loess Sediments. *Atmos. Res.* 229, 74–85. doi:10.1016/j.atmosres.2019.06.013

Li, Y., Song, Y., Orozbaev, R., Dong, J., Li, X., and Zhou, J. (2020c). Moisture Evolution in Central Asia Since 26 Ka: Insights from a Kyrgyz Loess Section, Western Tian Shan. *Quat. Sci. Rev.* 249, 106604. doi:10.1016/j.quascirev.2020.106604

Li, Y., Song, Y., Yin, Q., Han, L., and Wang, Y. (2019b). Orbital and Millennial Northern Mid-latitude Westerlies Over the Last Glacial Period. *Clim. Dyn.* 53 (5), 3315–3324. doi:10.1007/s00382-019-04704-5

Liu, T., and Ding, Z. (1998). Chinese Loess and the Paleomonsoon. *Annu. Rev. Earth Planet. Sci.* 26 (1), 111–145. doi:10.1146/annurev.earth.26.1.111

Liu, T. S. (1985). *Loess and the Environment (In Chinese)*. Beijing: Ocean Press.

Liu, Y., Zhang, M., Liu, Z., Xia, Y., Huang, Y., Peng, Y., et al. (2018). A Possible Role of Dust in Resolving the Holocene Temperature Conundrum. *Sci. Rep.* 8 (1), 4434. doi:10.1038/s41598-018-22841-5

Lu, H., Wang, X., and Li, L. (2010). Aeolian Sediment Evidence that Global Cooling Has Driven Late Cenozoic Stepwise Aridification in Central Asia. *Geol. Soc. Lond. Spec. Publ.* 342 (1), 29–44. doi:10.1144/sp342.4

Lu, H. Y., and An, Z. S. (1997). Pretreatment Methods in Loess–Palaeosol Granulometry. *Chin. Sci. Bull.* 42, 237–240. doi:10.1007/bf03182616

Luetscher, M., Boch, R., Sodemann, H., Spötl, C., Cheng, H., Edwards, R. L., et al. (2015). North Atlantic Storm Track Changes During the Last Glacial Maximum Recorded by Alpine Speleothems. *Nat. Commun.* 6 (1), 6344. doi:10.1038/ncomms7344

Ma, L., Zhao, J., and Sun, Y. (2013). Variability of the Crystallinity Index of Quartz from Eolian Deposits on the Chinese Loess Plateau. *J. Earth Environ.* 4 (2), 1255–1260. (In Chinese with English Abstract). doi:10.7515/JEE201302003

Machalett, B., Frechen, M., Hambach, U., Oches, E. A., Zöller, L., and Marković, S. B. (2006). The Loess Sequence from Remisowka (Northern Boundary of the Tien Shan Mountains, Kazakhstan)-Part I: Luminescence Dating. *Quatern. Int.* 152–153, 192–201. doi:10.1016/j.quaint.2005.12.014

Machalett, B., Oches, E. A., Frechen, M., Zoller, L., Hambach, U., Mavlyanova, N. G., et al. (2008). Aeolian Dust Dynamics in Central Asia During the Pleistocene: Driven by the Long-Term Migration, Seasonality, and Permanency of the Asiatic Polar Front. *Geochem. Geophy. Geosy.* 9 (8), Q08Q09. doi:10.1029/2007gc001938

Maher, B. A. (2016). Palaeoclimatic Records of the Loess/Palaeosol Sequences of the Chinese Loess Plateau. *Quat. Sci. Rev.* 154, 23–84. doi:10.1016/j.quascirev.2016.08.004

Malvern Instruments (2009). Determination of the Particle Absorption for Laser Diffraction Size Calculations, 1–4. Malvern Application Note (MRK1308-01).

Mason, J. A., Greene, R. S. B., and Joeckel, R. M. (2011). Laser Diffraction Analysis of the Disintegration of Aeolian Sedimentary Aggregates in Water. *Catena* 87 (1), 107–118. doi:10.1016/j.catena.2011.05.015

Mason, J. A., Jacobs, P. M., Greene, R. S. B., and Nettleton, W. D. (2003). Sedimentary Aggregates in the Peoria Loess of Nebraska, USA. *Catena* 53 (4), 377–397. doi:10.1016/s0341-8162(03)00073-0

Mctainsh, G. H., Nickling, W. G., and Lynch, A. W. (1997). Dust Deposition and Particle Size in Mali, West Africa. *Catena* 29 (3), 307–322. doi:10.1016/s0341-8162(96)00075-6

Miao, X., Sun, Y., Lu, H., and Mason, J. A. (2004). Spatial Pattern of Grain Size in the Late Pliocene 'Red Clay' Deposits (North China) Indicates Transport by Low-Level Northerly Winds. *Palaeogeog. Palaeoclimatol. Palaeoecol.* 206 (1-2), 149–155. doi:10.1016/j.palaeo.2004.01.018

Muhs, D. R., Cattle, S. R., Crouvi, O., Rousseau, D. D., Sun, J. M., and Zárate, M. A. (2014). *Loess Records*. Berlin: Springer-Verlag.

Muhs, D. R. (2013). The Geologic Records of Dust in the Quaternary. *Aeolian Res.* 9, 3–48. doi:10.1016/j.aeolia.2012.08.001

Murata, K. J., and Norman, M. B. (1976). An Index of Crystallinity for Quartz. *Am. J. Sci.* 276 (9), 1120–1130. doi:10.2475/ajs.276.9.1120

Nagashima, K., Tada, R., Tani, A., Sun, Y., Isozaki, Y., Toyoda, S., et al. (2011). Millennial-Scale Oscillations of the Westerly Jet Path During the Last Glacial Period. *J. Asian Earth Sci.* 40 (6), 1214–1220. doi:10.1016/j.jseaes.2010.08.010

Nagashima, K., Tada, R., Tani, A., Toyoda, S., Sun, Y., and Isozaki, Y. (2007). Contribution of Aeolian Dust in Japan Sea Sediments Estimated from ESR Signal Intensity and Crystallinity of Quartz. *Geochem. Geophys. Geosyst.* 8 (2), Q02Q04. doi:10.1029/2006GC001364

Nagashima, K., Tada, R., and Toyoda, S. (2013). Westerly Jet-East Asian Summer Monsoon Connection During the Holocene. *Geochem. Geophys. Geosyst.* 14 (12), 5041–5053. doi:10.1002/2013gc004931

Nilson, E., and Lehmkuhl, F. (2001). Interpreting Temporal Patterns in the Late Quaternary Dust Flux from Asia to the North Pacific. *Quat. Int.* 76-77, 67–76. doi:10.1016/s1040-6182(00)00090-2

Nottebaum, V., Lehmkuhl, F., Stauch, G., Hartmann, K., Wünnemann, B., Schimpf, S., et al. (2014). Regional Grain Size Variations in Aeolian Sediments Along the Transition Between Tibetan Highlands and North-Western Chinese Deserts - The Influence of Geomorphological Settings on Aeolian Transport Pathways. *Earth Surf. Process. Landforms* 39 (14), 1960–1978. doi:10.1002/esp.3590

Nottebaum, V., Stauch, G., Hartmann, K., Zhang, J., and Lehmkuhl, F. (2015). Unmixed Loess Grain Size Populations Along the Northern Qilian Shan (China): Relationships Between Geomorphologic, Sedimentologic and Climatic Controls. *Quatern. Int.* 372, 151–166. doi:10.1016/j.quaint.2014.12.071

Obreht, I., Zeeden, C., Schulte, P., Hambach, U., Eckmeier, E., Timar-Gabor, A., et al. (2015). Aeolian Dynamics at the Orlovat Loess-Paleosol Sequence, Northern Serbia, Based on Detailed Textural and Geochemical Evidence. *Aeolian Res.* 18, 69–81. doi:10.1016/j.aeolia.2015.06.004

Ono, Y., Naruse, T., Ikeya, M., Kohno, H., and Toyoda, S. (1998). Origin and Derived Courses of Eolian Dust Quartz Deposited During Marine Isotope Stage 2 in East Asia, Suggested by ESR Signal Intensity. *Glob. Planet. Change* 18 (3-4), 129–135. doi:10.1016/s0921-8181(98)00012-5

Park, C.-S., Hwang, S., Yoon, S.-O., and Choi, J. (2014). Grain Size Partitioning in Loess-Paleosol Sequence on the West Coast of South Korea Using the Weibull Function. *Catena* 121, 307–320. doi:10.1016/j.catena.2014.05.018

Parviz, N., Shen, Z. S., Yunus, M., and Zulqarnain, S. (2020b). Loess Deposits in Southern Tajikistan (Central Asia): Magnetic Properties and Paleoclimate. *Quat. Geochronol.* 60, 101114. doi:10.1016/j.quageo.2020.101114

Parviz, N., Shen, Z., Yunus, M., and Zulqarnain, S. (2020a). Loess Deposits in Southern Tajikistan (Central Asia): Magnetic Properties and Paleoclimate. *Quat. Geochronol.* 60, 101114. doi:10.1016/j.quageo.2020.101114

Paterson, G. A., and Heslop, D. (2015). New Methods for Unmixing Sediment Grain Size Data. *Geochem. Geophys. Geosyst.* 16 (12), 4494–4506. doi:10.1002/2015gc006070

Paton, T. R. (1978). *The Formation of Soil Material*. London: George Allen and Uniwin Press.

Perşoiu, A., Ionita, M., and Weiss, H. (2019). Atmospheric Blocking Induced by the Strengthened Siberian High Led to Drying in West Asia During the 4.2 Ka BP Event–A Hypothesis. *Clim. Past.* 15 (2), 781–793. doi:10.5194/cp-15-781-2019

Porter, S. C., Hallet, B., Wu, X., and An, Z. (2001). Dependence of Near-Surface Magnetic Susceptibility on Dust Accumulation Rate and Precipitation on the Chinese Loess Plateau. *Quat. Res.* 55 (3), 271–283. doi:10.1006/qres.2001.2224

Prins, M. A., and Vriend, M. (2007). Glacial and Interglacial Eolian Dust Dispersal Patterns Across the Chinese Loess Plateau Inferred from Decomposed Loess Grain-Size Records. *Geochem. Geophy. Geosy.* 8 (7), Q07Q05. doi:10.1029/2006gc001563

Prins, M. A., Vriend, M., Nugteren, G., Vandenberghe, J., Lu, H., Zheng, H., et al. (2007). Late Quaternary Aeolian Dust Input Variability on the Chinese Loess Plateau: Inferences from Unmixing of Loess Grain-Size Records. *Quat. Sci. Rev.* 26 (1-2), 230–242. doi:10.1016/j.quascirev.2006.07.002

Prins, M. A., and Weltje, G. J. (1999). "End-Member Modelling of Grain-Size Distributions of Sediment Mixture," in *Geologica Ultraiectina* (Utrecht: Utrecht University).

Pye, K. (1987). *Aeolian Dust and Dust Deposits*. London: Academic Press.

Pye, K. (1995). The Nature, Origin and Accumulation of Loess. *Quat. Sci. Rev.* 14 (7-8), 653–667. doi:10.1016/0277-3791(95)00047-x

Qiang, M., Chen, F., Wang, Z., Niu, G., and Song, L. (2010a). Aeolian Deposits at the Southeastern Margin of the Tengger Desert (China): Implications for Surface Wind Strength in the Asian Dust Source Area Over the Past 20,000 Years. *Palaeogeog. Palaeoclimatol. Palaeoecol.* 286 (1-2), 66–80. doi:10.1016/j.palaeo.2009.12.005

Qiang, M., Lang, L., and Wang, Z. (2010b). Do Fine-Grained Components of Loess Indicate Westerlies: Insights from Observations of Dust Storm Deposits at Lenghu (Qaidam Basin, China). *J. Arid. Environ.* 74 (10), 1232–1239. doi:10.1016/j.jaridenv.2010.06.002

Qin, X., Cai, B., and Liu, T. (2005). Loess Record of the Aerodynamic Environment in the East Asia Monsoon Area Since 60,000 Years Before Present. *J. Geophys. Res. Solid Earth* 110 (B1), B01204. doi:10.1029/2004jb003131

Rasmussen, S. O., Bigler, M., Blockley, S. P., Blunier, T., Buchardt, S. L., Clausen, H. B., et al. (2014). A Stratigraphic Framework for Abrupt Climatic Changes During the Last Glacial Period Based on Three Synchronized Greenland Ice-Core Records: Refining and Extending the INTIMATE Event Stratigraphy. *Quat. Sci. Rev.* 106, 14–28. doi:10.1016/j.quascirev.2014.09.007

Ravi, S., D'Odorico, P., Breshears, D. D., Field, J. P., Goudie, A. S., Huxman, T. E., et al. (2011). Aeolian Processes and the Biosphere. *Rev. Geophys.* 49. doi:10.1029/2010RG000328

Rea, D. K., and Hovan, S. A. (1995). Grain Size Distribution and Depositional Processes of the Mineral Component of Abyssal Sediments: Lessons from the North Pacific. *Paleoceanography* 10 (2), 251–258. doi:10.1029/94pa03355

Rea, D. K., Leinen, M., and Janecek, T. R. (1985). Geologic Approach to the Long-Term History of Atmospheric Circulation. *Science* 227 (4688), 721–725. doi:10.1126/science.227.4688.721

Roe, G. (2009). On the Interpretation of Chinese Loess as a Paleoclimate Indicator. *Quat. Res.* 71 (2), 150–161. doi:10.1016/j.yqres.2008.09.004

Rousseau, D. D., and Hatté, C. (2021). *Ground-Air Interface: The Loess Sequences, 13Markers of Atmospheric Circulation*. Switzerland: Springer.

Rugenstein, J. K. C., and Chamberlain, C. P. (2018). The Evolution of Hydroclimate in Asia Over the Cenozoic: A Stable-Isotope Perspective. *Earth-Science Rev.* 185, 1129–1156. doi:10.1016/j.earscirev.2018.09.003

Ruth, U., Bigler, M., Röthlisberger, R., Siggaard-Andersen, M.-L., Kipfstuhl, S., Goto-Azuma, K., et al. (2007). Ice Core Evidence for a Very Tight Link Between North Atlantic and East Asian Glacial Climate. *Geophys. Res. Lett.* 34 (3), L03706. doi:10.1029/2006GL027876

Ryder, C. L., Highwood, E. J., Lai, T. M., Sodemann, H., and Marsham, J. H. (2013). Impact of Atmospheric Transport on the Evolution of Microphysical and Optical Properties of Saharan Dust. *Geophys. Res. Lett.* 40 (10), 2433–2438. doi:10.1002/grl.50482

Schettler, G., Shabunin, A., Kemnitz, H., Knoeller, K., Imashev, S., Rybin, A., et al. (2014). Seasonal and Diurnal Variations in Dust Characteristics on the Northern Slopes of the Tien Shan - Grain-Size, Mineralogy, Chemical Signatures and Isotope Composition of Attached Nitrate. *J. Asian Earth Sci.* 88, 257–276. doi:10.1016/j.jseaes.2014.03.019

Shang, Y., Beets, C. J., Tang, H., Prins, M. A., Lahaye, Y., Van Elsas, R., et al. (2016). Variations in the Provenance of the Late Neogene Red Clay Deposits in Northern China. *Earth Planet. Sci. Lett.* 439, 88–100. doi:10.1016/j.epsl.2016.01.031

Shao, Y., Wyrwoll, K.-H., Chappell, A., Huang, J., Lin, Z., McTainsh, G. H., et al. (2011). Dust Cycle: An Emerging Core Theme in Earth System Science. *Aeolian Res.* 2 (4), 181–204. doi:10.1016/j.aeolia.2011.02.001

Shao, Y., Zhang, J., Ishizuka, M., Mikami, M., Leys, J., and Huang, N. (2020). Dependency of Particle Size Distribution at Dust Emission on Friction Velocity and Atmospheric Boundary-Layer Stability. *Atmos. Chem. Phys.* 20, 12939–12953. doi:10.5194/acp-20-12939-2020

Shi, L., Zhang, J., Yao, F., Zhang, D., and Guo, H. (2020). Temporal Variation of Dust Emissions in Dust Sources Over Central Asia in Recent Decades and the Climate Linkages. *Atmos. Environ.* 222, 117176. doi:10.1016/j.atmosenv.2019.117176

Smalley, I. (1966). The Properties of Glacial Loess and the Formation of Loess Deposits. *J. Sediment. Res.* 36 (3), 669–676. doi:10.1306/74d7153c-2b21-11d7-8648000102c1865d

Song, Y., Chen, X., Qian, L., Li, C., Li, Y., Li, X., et al. (2014). Distribution and Composition of Loess Sediments in the Ili Basin, Central Asia. *Quatern. Int.* 334-335, 61–73. doi:10.1016/j.quaint.2013.12.053

Song, Y., Li, Y., Cheng, L., Zong, X., Kang, S., Ghafarpour, A., et al. (2021). Spatio-Temporal Distribution of Quaternary Loess Across Central Asia. *Palaeogeog. Palaeoclimatol. Palaeoecol.* 567, 110279. doi:10.1016/j.palaeo.2021.110279

Sorg, A., Bolch, T., Stoffel, M., Solomina, O., and Beniston, M. (2012). Climate Change Impacts on Glaciers and Runoff in Tien Shan (Central Asia). *Nat. Clim. Change* 2 (10), 725–731. doi:10.1038/nclimate1592

Sorrel, P., Popescu, S.-M., Klotz, S., Suc, J.-P., and Oberhänsli, H. (2007). Climate Variability in the Aral Sea Basin (Central Asia) During the Late Holocene Based on Vegetation Changes. *Quat. Res.* 67 (3), 357–370. doi:10.1016/j.yqres.2006.11.006

Sprafke, T., Fitzsimmons, K. E., Grützner, C., Elliot, A., Marquer, L., and Nigmatova, S. (2018). Reevaluation of Late Pleistocene Loess Profiles at Remizovka (Kazakhstan) Indicates the Significance of Topography in Evaluating Terrestrial Paleoclimate Records. *Quat. Res.* 89, 674–690. doi:10.1017/qua.2017.103

Stevens, T., Buylaert, J.-P., Lu, H., Thiel, C., Murray, A., Frechen, M., et al. (2016). Mass Accumulation Rate and Monsoon Records from Xifeng, Chinese Loess Plateau, Based on a Luminescence Age Model. *J. Quat. Sci.* 31 (4), 391–405. doi:10.1002/jqs.2848

Sun, D., Bloemendal, J., Rea, D. K., An, Z., Vandenberghe, J., Lu, H., et al. (2004). Bimodal Grain-Size Distribution of Chinese Loess, and its Palaeoclimatic Implications. *Catena* 55 (3), 325–340. doi:10.1016/s0341-8162(03)00109-7

Sun, D., Bloemendal, J., Rea, D. K., Vandenberghe, J., Jiang, F., An, Z., et al. (2002). Grain-Size Distribution Function of Polymodal Sediments in Hydraulic and Aeolian Environments, and Numerical Partitioning of the Sedimentary Components. *Sediment. Geol.* 152, 263–277. doi:10.1016/s0037-0738(02)00082-9

Sun, D. H., Chen, F. H., Bloemendal, J., and Su, R. X. (2003). Seasonal Variability of Modern Dust over the Loess Plateau of China. *J. Geophys Res-Atmos* 108 (D21), 4665. doi:10.1029/2003jd003382

Sun, D. H. (2004). Monsoon and Westerly Circulation Changes Recorded in the Late Cenozoic Aeolian Sequences of Northern China. *Glob. Planet. Change* 41 (1), 63–80. doi:10.1016/j.gloplacha.2003.11.001

Sun, D. H., Su, R. X., Bloemendal, J., and Lu, H. Y. (2008a). Grain-Size and Accumulation Rate Records from Late Cenozoic Aeolian Sequences in Northern China: Implications for Variations in the East Asian Winter Monsoon and Westerly Atmospheric Circulation. *Palaeogeog. Palaeoclimatol. Palaeoecol.* 264 (1-2), 39–53. doi:10.1016/j.palaeo.2008.03.011

Sun, J. M. (2002a). Provenance of Loess Material and Formation of Loess Deposits on the Chinese Loess Plateau. *Earth Planet. Sci. Lett.* 203 (3-4), 845–859. doi:10.1016/s0012-821x(02)00921-4

Sun, J. M. (2002b). Source Regions and Formation of the Loess Sediments on the High Mountain Regions of Northwestern China. *Quat. Res.* 58 (3), 341–351. doi:10.1006/qres.2002.2381

Sun, Y., and An, Z. (2005). Late Pliocene-Pleistocene Changes in Mass Accumulation Rates of Eolian Deposits on the Central Chinese Loess Plateau. *J. Geophys. Res.: Atmos.* 110 (D23), D23101. doi:10.1029/2005JD006064

Sun, Y., Chen, H., Tada, R., Weiss, D., Lin, M., Toyoda, S., et al. (2013). ESR Signal Intensity and Crystallinity of Quartz from Gobi and Sandy Deserts in East Asia and Implication for Tracing Asian Dust Provenance. *Geochem. Geophy. Geosy.* 14 (14), 2615–2627. doi:10.1002/ggge.20162

Sun, Y., Lu, H., and An, Z. (2006). Grain Size of Loess, Palaeosol and Red Clay Deposits on the Chinese Loess Plateau: Significance for Understanding Pedogenic Alteration and Palaeomonsoon Evolution. *Palaeogeog. Palaeoclimatol. Palaeoecol.* 241 (1), 129–138. doi:10.1016/j.palaeo.2006.06.018

Sun, Y., Tada, R., Chen, J., Chen, H., Toyoda, S., Tani, A., et al. (2007). Distinguishing the Sources of Asian Dust Based on Electron Spin Resonance Signal Intensity and Crystallinity of Quartz. *Atmos. Environ.* 41 (38), 8537–8548. doi:10.1016/j.atmosenv.2007.07.014

Sun, Y., Tada, R., Chen, J., Liu, Q., Toyoda, S., Tani, A., et al. (2008b). Tracing the Provenance of Fine-Grained Dust Deposited on the Central Chinese Loess Plateau. *Geophys. Res. Lett.* 35 (1), L01804. doi:10.1029/2007GL031672

Sun, Y., Yan, Y., Nie, J., Li, G., Shi, Z., Qiang, X., et al. (2020). Source-to-Sink Fluctuations of Asian Aeolian Deposits Since the Late Oligocene. *Earth-Sci. Rev.* 200, 102963. doi:10.1016/j.earscirev.2019.102963

Taylor, S. R., Mclennan, S. M., and Mcculloch, M. T. (1983). Geochemistry of Loess, Continental Crustal Composition and Crustal Model Ages. *Geochim. Cosmochim. Acta* 47 (11), 1897–1905. doi:10.1016/0016-7037(83)90206-5

Toggweiler, J. R., and Russell, J. (2008). Ocean Circulation in a Warming Climate. *Nature* 451 (7176), 286–288. doi:10.1038/nature06590

Toyoda, S., and Naruse, T. (2002). Eolian Dust from the Asian Deserts to the Japanese Islands Since the Last Glacial Maximum: The Basis for the ESR Method. *Trans. Jpn. Geomorphol. Union* 23, 811–820. Available at: http://ci.nii.ac.jp/naid/110001273013

Tsoar, H., and Pye, K. (1987). Dust Transport and the Question of Desert Loess Formation. *Sedimentology* 34 (1), 139–153. doi:10.1111/j.1365-3091.1987.tb00566.x

Újvári, G., Kok, J. F., Varga, G., and Kovács, J. (2016). The Physics of Wind-Blown Loess: Implications for Grain Size Proxy Interpretations in Quaternary Paleoclimate Studies. *Earth-Science Rev.* 154, 247–278. doi:10.1016/j.earscirev.2016.01.006

Újvári, G., Stevens, T., Molnár, M., Demény, A., Lambert, F., Varga, G., et al. (2017). Coupled European and Greenland Last Glacial Dust Activity Driven by North Atlantic Climate. *P. Natl. A. Sci. India. A.* 114 (50), E10632–E10638. doi:10.1073/pnas.1712651114

Vandenberghe, J. (2013). Grain Size of Fine-Grained Windblown Sediment: A Powerful Proxy for Process Identification. *Earth-Sci. Rev.* 121, 18–30. doi:10.1016/j.earscirev.2013.03.001

Vandenberghe, J., Lu, H., Sun, D., Huissteden, J. V., and Konert, M. (2004). The Late Miocene and Pliocene Climate in East Asia as Recorded by Grain Size and Magnetic Susceptibility of the Red Clay Deposits (Chinese Loess Plateau). *Palaeogeog. Palaeoclimatol. Palaeoecol.* 204 (3-4), 239–255. doi:10.1016/s0031-0182(03)00729-6

Vandenberghe, J., Renssen, H., van Huissteden, K., Nugteren, G., Konert, M., Lu, H., et al. (2006). Penetration of Atlantic Westerly Winds into Central and East Asia. *Quat. Sci. Rev.* 25 (17-18), 2380–2389. doi:10.1016/j.quascirev.2006.02.017

Vandenberghe, J., Sun, Y., Wang, X., Abels, H. A., and Liu, X. (2018). Grain-Size Characterization of Reworked Fine-Grained Aeolian Deposits. *Earth-Sci. Rev.* 177, 43–52. doi:10.1016/j.earscirev.2017.11.005

Varga, G. (2011). Similarities Among the Plio–Pleistocene Terrestrial Aeolian Dust Deposits in the World and in Hungary. *Quatern. Int.* 234 (1), 98–108. doi:10.1016/j.quaint.2010.09.011

Varga, G., Újvári, G., and Kovács, J. (2019). Interpretation of Sedimentary (Sub) Populations Extracted from Grain Size Distributions of Central European Loess-Paleosol Series. *Quatern. Int.* 502, 60–70. doi:10.1016/j.quaint.2017.09.021

Vriend, M., Prins, M. A., Buylaert, J.-P., Vandenberghe, J., and Lu, H. (2011). Contrasting Dust Supply Patterns Across the North-Western Chinese Loess Plateau During the Last Glacial-Interglacial Cycle. *Quatern. Int.* 240 (1), 167–180. doi:10.1016/j.quaint.2010.11.009

Wang, H., Mason, J. A., and Balsam, W. L. (2006). The Importance of Both Geological and Pedological Processes in Control of Grain Size and Sedimentation Rates in Peoria Loess. *Geoderma* 136 (1-2), 388–400. doi:10.1016/j.geoderma.2006.04.005

Wang, X., Carrapa, B., Sun, Y., Dettman, D. L., Chapman, J. B., Caves Rugenstein, J. K., et al. (2020). The Role of the Westerlies and Orography in Asian Hydroclimate Since the Late Oligocene. *Geology* 48, 728–732. doi:10.1130/g47400.1

Wang, X., Løvlie, R., Chen, Y., Yang, Z., Pei, J., and Tang, L. (2014). The Matuyama-Brunhes Polarity Reversal in Four Chinese Loess Records: High-Fidelity Recording of Geomagnetic Field Behavior or a Less Than Reliable Chronostratigraphic Marker? *Quat. Sci. Rev.* 101, 61–76. doi:10.1016/j.quascirev.2014.07.005

Wang, X., Wei, H., Khormali, F., Taheri, M., Kehl, M., Frechen, M., et al. (2017). Grain-Size Distribution of Pleistocene Loess Deposits in Northern Iran and its Palaeoclimatic Implications. *Quatern. Int.* 429, 41–51. doi:10.1016/j.quaint.2016.01.058

Wassenburg, J. A., Dietrich, S., Fietzke, J., Fohlmeister, J., Jochum, K. P., Scholz, D., et al. (2016). Reorganization of the North Atlantic Oscillation During Early Holocene Deglaciation. *Nat. Geosci.* 9 (8), 602–605. doi:10.1038/ngeo2767

Wei, T., Dong, Z., Kang, S., Rostami, M., Ulbrich, S., and Shao, Y. (2019). Hf-Nd-Sr Isotopic Fingerprinting for Aeolian Dust Deposited on Glaciers in the Northeastern Tibetan Plateau Region. *Glob. Planet. Change* 177 (JUN), 69–80. doi:10.1016/j.gloplacha.2019.03.015

Weltje, G. J. (1997). End-Member Modeling of Compositional Data: Numerical-Statistical Algorithms for Solving the Explicit Mixing Problem. *Math. Geol.* 29 (4), 503–549. doi:10.1007/bf02775085

Weltje, G. J., and Prins, M. A. (2003). Muddled or Mixed? Inferring Palaeoclimate from Size Distributions of Deep-Sea Clastics. *Sediment. Geol.* 162 (1), 39–62. doi:10.1016/s0037-0738(03)00235-5

Wiscombe, W. J. (1980). Improved Mie Scattering Algorithms. *Appl. Opt.* 19 (9), 1505–1509. doi:10.1364/ao.19.001505

Wright, J. S. (2001). "Desert" Loess Versus "Glacial" Loess: Quartz Silt Formation, Source Areas and Sediment Pathways in the Formation of Loess Deposits. *Geomorphology* 36 (3-4), 231–256. doi:10.1016/s0169-555x(00)00060-x

Wu, G. J., Zhang, C. L., Gao, S. P., Yao, T. D., Tian, L. D., and Xia, D. S. (2009). Element Composition of Dust from a Shallow Dunde Ice Core, Northern China. *Glob. Planet. Change* 67 (3-4), 186–192. doi:10.1016/j.gloplacha.2009.02.003

Wu, G., Yao, T., Xu, B., Li, Z., Tian, L., Duan, K., et al. (2006). Grain Size Record of Microparticles in the Muztagata Ice Core. *Sci. China Ser. D. Earth Sci.* 49 (001), 10–17. doi:10.1007/s11430-004-5093-5

Xiao, J., Porter, S. C., An, Z., Kumai, H., and Yoshikawa, S. (1995). Grain Size of Quartz as an Indicator of Winter Monsoon Strength on the Loess Plateau of Central China During the Last 130,000 Yr. *Quat. Res.* 43 (1), 22–29. doi:10.1006/qres.1995.1003

Xie, Y., Meng, J., and Guo, L. (2014). REE Geochemistry of Modern Eolian Dust Deposits in Harbin City, Heilongjiang Province, China: Implications for Provenance. *Catena* 123, 70–78. doi:10.1016/j.catena.2014.07.008

Xiong, S., Ding, Z., and Liu, D. (1999a). Comparisons of Grain Size Characteristics of Red Earth from Southern China with that of Loess and Dune Sand from Bering Region. *Chin. Sci. Bull.* 44 (18), 1690–1693. doi:10.1007/bf03183492

Xiong, S., Ding, Z., and Liu, T. (2001). Climatic Implications of Loess Deposits from the Beijing Region. *J. Quat. Sci.* 16 (6), 575–582. doi:10.1002/jqs.618

Xiong, S., Ding, Z., and Liu, T. (1999b). Loess Deposits in Beijing Region since Last 1.2 Ma and Desert Expansion over Northern China (In Chinese). *Mar. Geol. Quat. Geol.* 19 (3), 67–73.

Xu, B., Wang, L., Gu, Z., Hao, Q., Wang, H., Chu, G., et al. (2018). Decoupling of Climatic Drying and Asian Dust Export During the Holocene. *J. Geophys. Res. Atmos.* 123 (2), 915–928. doi:10.1002/2017JD027483

Yakubchuk, A. (2004). Architecture and Mineral Deposit Settings of the Altaid Orogenic Collage: A Revised Model. *J. Asian Earth Sci.* 23 (5), 761–779. doi:10.1016/j.jseaes.2004.01.006

Yang, S., Ding, F., and Ding, Z. (2006). Pleistocene Chemical Weathering History of Asian Arid and Semi-Arid Regions Recorded in Loess Deposits of China and Tajikistan. *Geochim. Cosmochim. Acta* 70 (7), 1695–1709. doi:10.1016/j.gca.2005.12.012

Youn, J. H., Seong, Y. B., Choi, J. H., Abdrakhmatov, K., and Ormukov, C. (2014). Loess Deposits in the Northern Kyrgyz Tien Shan: Implications for the Paleoclimate Reconstruction During the Late Quaternary. *Catena* 117, 81–93. doi:10.1016/j.catena.2013.09.007

Yu, S.-Y., Colman, S. M., and Li, L. (2016). BEMMA: A Hierarchical Bayesian End-Member Modeling Analysis of Sediment Grain-Size Distributions. *Math. Geosci.* 48 (6), 723–741. doi:10.1007/s11004-015-9611-0

Yuan, T., Chen, S., Huang, J., Wu, D., Lu, H., Zhang, G., et al. (2019). Influence of Dynamic and Thermal Forcing on the Meridional Transport of Taklimakan Desert Dust in Spring and Summer. *J. Clim.* 32 (3), 749–767. doi:10.1175/jcli-d-18-0361.1

Zhang, X. Y., Arimoto, R., and An, Z. S. (1999). Glacial and Interglacial Patterns for Asian Dust Transport. *Quat. Sci. Rev.* 18 (6), 811–819. doi:10.1016/s0277-3791(98)00028-6

Zhao, J., Chen, H., Song, Y., and Sun, Y. (2012). Determination of Quartz Content and Crystallinity Index from Loess Samoles. *Mar. Geol. Quat. Geol.* 32 (5), 131–135. (In Chinese with English Abstract). doi:10.3724/SP.J.1140.2012.05131

Zhao, W. (2015). *Geochemistry Characteristics of Clay-Sized Fractions from East Asian Deserts — Mineral Dust Provenance, Transport and Tracer (In Chinese, Nanjing University)*. Nanjing: School of Earth Science and Engineering. Nanjing University.

Zhou, L. P., Dodonov, A. E., and Shackleton, N. J. (1995). Thermoluminescence Dating of the Orkutsay Loess Section in Tashkent Region, Uzbekistan, Central Asia. *Quat. Sci. Rev.* 14 (7-8), 721–730. doi:10.1016/0277-3791(95)00056-9

Zykin, V. S., and Zykina, V. S. (2015). The Middle and Late Pleistocene Loess-Soil Record in the Iskitim Area of Novosibirsk Priobie, South-Eastern West Siberia. *Quatern. Int.* 365, 15–25. doi:10.1016/j.quaint.2014.07.011

Conflict of Interest: The authors declare that the research was conducted in the absence of any commercial or financial relationships that could be construed as a potential conflict of interest.

Publisher's Note: All claims expressed in this article are solely those of the authors and do not necessarily represent those of their affiliated organizations, or those of the publisher, the editors, and the reviewers. Any product that may be evaluated in this article, or claim that may be made by its manufacturer, is not guaranteed or endorsed by the publisher.

Copyright © 2022 Li, Song, Fitzsimmons, Dave, Liu, Zong, Sun, Liu and Orozbaev. This is an open-access article distributed under the terms of the Creative Commons Attribution License (CC BY). The use, distribution or reproduction in other forums is permitted, provided the original author(s) and the copyright owner(s) are credited and that the original publication in this journal is cited, in accordance with accepted academic practice. No use, distribution or reproduction is permitted which does not comply with these terms.

Advantages of publishing in Frontiers

OPEN ACCESS
Articles are free to read
for greatest visibility
and readership

FAST PUBLICATION
Around 90 days
from submission
to decision

HIGH QUALITY PEER-REVIEW
Rigorous, collaborative,
and constructive
peer-review

TRANSPARENT PEER-REVIEW
Editors and reviewers
acknowledged by name
on published articles

Frontiers
Avenue du Tribunal-Fédéral 34
1005 Lausanne | Switzerland

Visit us: www.frontiersin.org
Contact us: frontiersin.org/about/contact

REPRODUCIBILITY OF RESEARCH
Support open data
and methods to enhance
research reproducibility

DIGITAL PUBLISHING
Articles designed
for optimal readership
across devices

FOLLOW US
@frontiersin

IMPACT METRICS
Advanced article metrics
track visibility across
digital media

EXTENSIVE PROMOTION
Marketing
and promotion
of impactful research

LOOP RESEARCH NETWORK
Our network
increases your
article's readership